54.24
B665(c)
4:2

Comprehensive Treatise of Electrochemistry

Volume 4: Electrochemical Materials Science

Edited by

J. O'M. Bockris
Texas A & M University
College Station, Texas

Brian E. Conway
University of Ottawa
Ottawa, Ontario, Canada

Ernest Yeager
Case Western Reserve University
Cleveland, Ohio

Ralph E. White
Texas A & M University
College Station, Texas

PLENUM PRESS NEW YORK AND LONDON

Library of Congress Cataloging in Publication Data

Main entry under title:

Electrochemical materials science.

(Comprehensive treatise of electrochemistry; v. 4)
Includes bibliographic references and indexes.
1. Corrosion and anti-corrosives. 2. Stress corrosion. 3. Electrochemistry. I. Bockris, J. O'M. (John O'M.), 1923- . II. Series.
QD552.C64 [TA462] 541.3'7s 81-4780
ISBN 0-306-40614-4 [620.1'1223] AACR2

© 1981 Plenum Press, New York
A Division of Plenum Publishing Corporation
233 Spring Street, New York, N. Y. 10013

All rights reserved

No part of this book may be reproduced, stored in a retrieval system, or transmitted, in any form or by any means, electronic, mechanical, photocopying, microfilming, recording, or otherwise, without written permission from the Publisher

Printed in the United States of America

Comprehensive Treatise of Electrochemistry

Volume 4: Electrochemical Materials Science

COMPREHENSIVE TREATISE OF ELECTROCHEMISTRY

Volume 1	THE DOUBLE LAYER Edited by J. O'M. Bockris, Brian E. Conway, and Ernest Yeager
Volume 2	ELECTROCHEMICAL PROCESSING Edited by J. O'M. Bockris, Brian E. Conway, Ernest Yeager, and Ralph E. White
Volume 3	ELECTROCHEMICAL ENERGY CONVERSION AND STORAGE Edited by J. O'M. Bockris, Brian E. Conway, Ernest Yeager, and Ralph E. White
Volume 4	ELECTROCHEMICAL MATERIALS SCIENCE Edited by J. O'M. Bockris, Brian E. Conway, Ernest Yeager, and Ralph E. White
Volume 5	THERMODYNAMIC AND TRANSPORT PROPERTIES OF AQUEOUS AND MOLTEN ELECTROLYTES Edited by Brian E. Conway, J. O'M. Bockris, and Ernest Yeager
Volume 6	ELECTRODICS: TRANSPORT Edited by Ernest Yeager, J. O'M. Bockris, and Brian E. Conway

Contributors

J. O'M. Bockris, Department of Chemistry, Texas A & M University, College Station, Texas 77843

Genady P. Cherepanov, Tomilino (Moscow Region), 140070, USSR

M. J. Dignam, Department of Chemistry, University of Toronto, Toronto, Canada M5S 1A1

Israël Epelboin, Groupe de Recherche No. 4 du C.N.R.S. "Physique des Liquides et Electrochimie," associé à l'Université Pierre et Marie Curie, 75230 Paris Cedex 05, France

Claude Gabrielli, Groupe de Recherche No. 4 du C.N.R.S "Physique des Liquides et Electrochimie," associé à l'Université Pierre et Marie Curie, 75230 Paris Cedex 05, France

V. Guruswamy, Department of Chemistry, Texas A & M University, College Station, Texas 77843

Michel Keddam, Groupe de Recherche No. 4 du C.N.R.S. "Physique des Liquides et Electrochimie," associé à l'Université Pierre et Marie Curie, 75230 Paris Cedex 05, France

Go Okamoto, Applied Chemistry Division, Faculty of Science, Science University of Tokyo, Tokyo, Japan

R. N. Parkins, Department of Metallurgy and Engineering Materials, The University, Newcastle upon Tyne, England

J. P. Randin, ASULAB SA, CH 2001 Neuchâtel, Switzerlan

Norio Sato, Electrochemistry Laboratory, Faculty of Engineering, Hokkaido University, Sapporo, Japan

William H. Smyrl, Sandia Laboratories, Albuquerque, New Mexico 87185

P. K. Subramanyan, Gould Laboratories, Gould, Inc., Cleveland, Ohio 44108

Hisasi Takenouti, Groupe de Recherche No. 4 du C.N.R.S. "Physique des Liquides et Electrochimie," associé à l'Université Pierre et Marie Curie, 75230 Paris Cedex 05, France

Jean Van Muylder, CEBELCOR and Department of Metallurgy and Electrochemistry, Université Libre de Bruxelles, B-1050 Brussels, Belgium

Preface to Comprehensive Treatise of Electrochemistry

Electrochemistry is one of the oldest defined areas in physical science, and there was a time, less than 50 years ago, when one saw "Institute of Electrochemistry and Physical Chemistry" in the chemistry buildings of European universities. But, after early brilliant developments in electrode processes at the beginning of the twentieth century and in solution chemistry during the 1930s, electrochemistry fell into a period of decline which lasted for several decades. Electrochemical systems were too complex for the theoretical concepts of the quantum theory. They were too little understood at a phenomenological level to allow their ubiquity in application in so many fields to be comprehended.

However, a new growth began faintly in the late 1940s, and clearly in the 1950s. This growth was exemplified by the formation in 1949 of what is now called The International Society for Electrochemistry. The usefulness of electrochemistry as a basis for understanding conservation was the focal point in the founding of this Society. Another very important event was the choice by NASA in 1958 of fuel cells to provide the auxiliary power for space vehicles.

With the new era of diminishing usefulness of the fossil fuels upon us, the role of electrochemical technology is widened (energy storage, conversion, enhanced attention to conservation, direct use of electricity from nuclear–solar plants, finding materials which interface well with hydrogen). This strong new interest is not only in the technological applications of electrochemistry. Quantum chemists have taken great interest in redox processes. Organic chemists are interested in situations where the energy of electrons is as easily controlled as it is at electrodes. Some biological processes are now seen in electrodic terms, with electron transfer to and from materials which would earlier have been considered to be insulators.

It is now time for a comprehensive treatise to look at the whole field of electrochemistry.

The present treatise was conceived in 1974, and the earliest invitations to authors for contributions were made in 1975. The completion of the early volumes has been delayed by various factors.

There has been no attempt to make each article emphasize the most recent situation at the expense of an overall statement of the modern view. This treatise is not a collection of articles from *Recent Advances in Electrochemistry* or *Modern Aspects of Electrochemistry*. It is an attempt at making a mature statement about the present position in the vast area of what is best looked at as a new interdisciplinary field.

Texas A & M University	J. O'M. Bockris
University of Ottawa	B. E. Conway
Case Western Reserve University	Ernest Yeager
Texas A & M University	Ralph E. White

Preface to Volume 4

The science of degradation of materials involves a vast area of science and technology, the economic importance of which rivals that of any other clearly defined area affecting the standard of life. The basis of the corrosion process is the electrochemical charge-transfer reaction, and the center of the subject of the degradation of materials is electrochemical material science.

It is obviously correct to begin this volume with a chapter on the treatment of the thermodynamics of corrosion. Next we include a chapter on corrosion kinetics. Chapter 3, on electrochemical passivation, comes from a very noted school that was ahead of its time regarding present theories of passivation. The next chapter covers the electrochemical passivation of metals.

The kinetics of the growth of oxides (Chapter 5) is a vital area, less discussed than the more commonly referred to "inhibition" problem (Chapter 6).

One of the more puzzling aspects of corrosion—not clearly integrated into the discipline of electrochemistry until the mid-1900s—was that of stress corrosion cracking (Chapter 7); the most important corrosion occurs beneath the surface. The subject of corrosion is also associated with the latent effects of hydrogen, the catalyst of cracking (Chapter 8).

In the last two chapters we discuss topics that are somewhat different in character than those treated in earlier chapters. We felt it necessary to have a chapter on friction, because it is a vital and much neglected subject, describing how electrochemical forces can affect the contacts of two solids through the medium of an ionic liquid (Chapter 9). Chapter 10, on nonmetallic electrode materials, stresses the fact that electrochemistry no longer deals with metals only—in many instances it need not deal with metals at all—and will soon involve not only the treatment of the semiconductor–solution interface but also that of the insulator–solution interface, which is now a part of the electrodic treatment of bioelectrochemical problems.

Texas A & M University	J. O'M. Bockris
University of Ottawa	B. E. Conway
Case Western Reserve University	Ernest Yeager
Texas A & M University	Ralph E. White

Notation

$a_\pm$	mean activity; a_i, a_j activities of species i, j
c	concentration (molar); velocity of light (cm s^{-1})
C_1, C_2, etc.	differential capacities of regions 1, 2, etc.
cn	coordination number
d	thickness, e.g., of a film, or of a dielectric
D	diffusion coefficient
D_{x_ψ}	dissociation energy for molecule x_ψ
$\mathbf{D}$	dielectric displacement
e	electron charge
E	potential (cf. electrode, on metal–solution potential difference, in kinetics)
E_{cal}	measured potential on the scale of the normal calomel electrode
E_{CB}	energy of conduction band
E_{F}	Fermi level
E_{H}	measured potential on the hydrogen scale in the *same* solution
E_{NHE}	measured potential on the scale of the normal hydrogen electrode
E_{SS}	energy of surface states
E_{VB}	energy of valence band
$\mathscr{E}$	electrostatic field
$f_\pm$	rational activity coefficient (mean)
F	Faraday constant
g	interaction parameter, in non-Langmuir isotherms
$g_{ij}(r_{ij})$	radial distribution function (of distance r_{ij}); pair correlation function

G, H, S	free energy enthalpy, and entropy (per mole)
h	Planck's constant
i	current density
I_0	intensity of light
I	current moment of inertia
J	flux; quantum number for rotation
k	with subscript, rate constants
k_s	salting out (Setschenow) coefficient
k	Boltzmann constant
K	thermodynamic equilibrium constant
K_1, K_2, etc.	integral capacities of regions 1, 2, etc.
m	concentration (molal); mass of particle
M	molarity; N no longer used; number of particles
n	solvation number; quantum number for vibration
n_{CB}	density of electronic states in the conduction band
n_e	concentration of electrons
n_e^s	concentration of electrons at the surface
n_e^0	concentration of electrons in bulk
n_p	concentration of holes
n_e^s	concentration of holes at the surface
n_p^0	concentration of holes in bulk
N_A	concentration of charge acceptors
N_D	concentration of charge donors
N_{SS}	concentration of surface states
P	pressure (Pa), e.g., P_{O_2}, presence of a gas, O_2; momentum
$P(E)$	probability (for state of energy E)
q, Q	partition function
Q_i	charge for some species, i, e.g., on a surface
r_i	radius of an ion
r_{ij}	distance between particles i, j
R	molar gas constant; resistance
t	time
T	absolute temperature (K); with subscript, nmr relaxation times (T_1, T_2)
U	internal energy
v	velocity (usually of a reaction); mobility of ion under 1 V cm^{-1} charge
V	volume; partial molar volume
x, y, z	coordinate system; distances
$y_\pm$	stoichiometric activity coefficient (mean, molar)
$\neq$	activated state (used as superscript)

Greek Symbols

α	light absorption coefficient; transfer coefficient; specific expansibility
β	charge-transfer symmetry factor; specific compressibility
γ	surface tension
$\gamma_{\pm}$	stoichiometric activity coefficient (mean) molal
δ	diffusion-layer thickness; barrier thickness
$\Delta_i^{i,b}\varphi$	potential inside a metal ($i = m$), semiconductor (i = sc), or insulator (i = ins)
$\Delta_1^{i}\varphi$	potential drop at the inner Helmholtz plane φ ($i = M$, sc, ins, etc.)
$\Delta_b^{2}\varphi$	potential in the diffuse (Gouy) double layer
$\Delta_2^{i}\varphi$	potential in the Helmholtz layer (i = M, sc, or ins)
Γ_i	surface excess of species i
ε	permittivity; quantum efficiency
ζ	zeta potential
η	overpotential; viscosity
θ	fractional surface coverage; relative permittivity; dielectric constant
κ	conductivity; Debye–Hückel parameter
$\Lambda_{\pm,c}$	molar ionic conductivity at concentration c
Λ_c	molar conductivity at concentration c
Λ_{∞}	molar conductivity at infinite dilution
$\Lambda_{\pm,\infty}$	molar ionic conductivity at infinite dilution
μ	electric dipole moment; or chemical potential
μ_e	mobility of electrons
μ_p	mobility of holes
μ^0	standard chemical potential
$\tilde{\mu}$	electrochemical potential
ν	stoichiometric number; frequency of vibration (s^{-1})
$\tilde{\nu}$	wave number (cm^{-1})
ρ	density of space change; resistivity
$\rho(E)$	volume charge density
$\rho_i(E)$	density of states ($i = M$, sc, or ins)
σ	surface charge density in distribution; charge in double-layer region (subscripted) divided by area
σ_e	capture cross section of electrons
σ_m	charge on metal surface, divided by area

σ_p	capture cross section of holes
τ	relaxation time
ϕ	double-layer potential (subscripted for indication of region)
ϕ_x	apparent molar function of x; with subscript $\bar{x}$, partial molar function of x
φ	inner potential
$\Delta\varphi$	Galvani potential
χ	surface potential
$\Delta\chi$	surface potential difference
ψ	outer potential
$\Delta\psi$	Volta potential
ω	angular frequency

r 277 B 1

Contents

1. Thermodynamics of Corrosion

Jean Van Muylder

1. Introduction 1
2. Application of Chemical Thermodynamics 3
   2.1. General Statements 3
   2.2. Chemical Thermodynamics 4
3. Application of Electrochemical Thermodynamics 6
   3.1. General Statements 6
   3.2. Electrochemical Thermodynamics 8
   3.3. Principles of Electrochemical Thermodynamics 13
4. Diagrams of Potential–pH Electrochemical Equilibria in Aqueous Solutions at 25°C 15
   4.1. General Statements 15
   4.2. Diagrams of E–pH Electrochemical Equilibria 15
5. Electrochemical Equilibria in Aqueous Solutions at Elevated Temperatures 27
   5.1. General Statements 27
   5.2. Determination of Standard Free Energy at T K 27
   5.3. Specific Heat of Dissolved Species 30
   5.4. Determination of Temperature Coefficient of Standard Equilibrium Potential—Method of de Béthune 34
   5.5. E-pH Equilibria Diagrams of the Binary System 36
6. Applications 40
   6.1. Thermodynamic Nobility and Practical Nobility 40
   6.2. Passivation and Activation of Metals 43
   6.3. Efficiency of Oxidizing Inhibitors of Corrosion 45
   6.4. Localized Corrosion of Copper and Iron 49
7. Electrode Potential Measurements in Corrosion Studies 63
   7.1. General Statements 63
   7.2. Electrochemical Experiments of Corrosion 68

References 86

2. Electrochemistry and Corrosion on Homogeneous and Heterogeneous Metal Surfaces

William H. Smyrl

1. Thermodynamics . . . 97
2. Kinetics of Corrosion Reactions . . . 100
    2.1. Corrosion and Fundamental Electrode Kinetics . . . 100
    2.2. Basic Concepts of Electrode Kinetics . . . 101
    2.3. Coupled Reactions . . . 104
    2.4. Superposition of Simultaneous Reactions . . . 106
    2.5. Coupled Corrosion Reactions . . . 107
    2.6. Corrosion with Soluble Products . . . 113
3. Corrosion of Copper in Acidic Aqueous Solutions . . . 114
    3.1. Copper Dissolution Kinetics and Corrosion . . . 115
    3.2. Copper Dissolution Kinetics in H_2SO_4 . . . 116
    3.3. Copper Dissolution in Acidic Chloride Solutions . . . 118
    3.4. Copper Corrosion in Deoxygenated H_2SO_4 and HCl . . . 121
    3.5. Copper Corrosion in Oxygenated HCl and H_2SO_4 . . . 126
4. Nonuniform Corrosion and Heterogeneous Systems . . . 136
    4.1. Mathematics of Modeling Corrosion Systems . . . 137
    4.2. Modeling of Composition-Driven Nonuniform Corrosion . . . 139
    4.3. Modeling of Galvanic Corrosion . . . 142
5. Summary . . . 147

References . . . 147

3. The Study of the Passivation Process by the Electrode Impedance Analysis

Israël Epelboin, Claude Gabrielli, Michel Keddam, and Hisasi Takenouti

1. Introduction . . . 151
    1.1. Brief Review of the Literature . . . 153
    1.2. Electrochemical Impedance . . . 155
    1.3. Formal Model of the Passivation Process Impedance . . . 156
2. Plotting of the Polarization Curve and Impedance Measurement . . . 160
    2.1. Accessibility of the Steady State . . . 160
    2.2. Stability of the Electrochemical Interface . . . 161
    2.3. Impedance Measurement . . . 163
3. Passivation of Iron in a Weakly Acidic Medium . . . 166
    3.1. Experimental Results . . . 166
    3.2. Reaction Model . . . 166
4. Passivation of Titanium . . . 168
    4.1. Experimental Results . . . 168
    4.2. Reaction Model . . . 169
5. Transpassivity of Nickel . . . 171
    5.1. Experimental Results . . . 171
    5.2. Reaction Model . . . 172

6. Passivity of Iron in 1 M H_2SO_4 . . . 173
  6.1. Experimental Results . . . 173
  6.2. Reaction Model . . . 174
7. Passivation of Iron in 1 M H_2SO_4 . . . 177
  7.1. Experimental Results . . . 177
  7.2. Models of Z-Shaped Curve . . . 179
8. Iron in HNO_3 Solutions . . . 183
  8.1. Experimental Results . . . 183
  8.2. Reaction Model . . . 186
Auxiliary Notation . . . 187
References . . . 188

4. Electrochemical Passivation of Metals

Norio Sato and Go Okamoto

1. Introduction . . . 193
2. Potentiostatic Anodic Polarization Curves . . . 196
  2.1. General View . . . 196
  2.2. Iron . . . 199
  2.3. Nickel . . . 201
  2.4. Chromium . . . 203
  2.5. Cobalt . . . 203
3. Active–Passive Transition . . . 204
  3.1. Electrode Impedance . . . 204
  3.2. Flade Potential . . . 206
  3.3. Galvanostatic Passivation . . . 208
  3.4. Potentiostatic Passivation . . . 209
  3.5. Effect of Anions . . . 212
4. Passive Films . . . 213
  4.1. Iron . . . 213
  4.2. Nickel . . . 217
  4.3. Cobalt . . . 220
  4.4. Chromium . . . 221
  4.5. Stainless Steel . . . 222
5. Dissolution of Passive Metals . . . 222
  5.1. Dissolution in Steady States . . . 222
  5.2. Dissolution in Non-Steady-States . . . 224
  5.3. Ionic Current through Passive Barrier Films . . . 226
6. Theory of Passivity . . . 226
  6.1. Passivation Processes . . . 226
  6.2. Theory of Passivity . . . 227
7. Chemical Breakdown of Passive Films . . . 230
  7.1. Passivity Breakdown due to Aggressive Anions . . . 230
  7.2. Film Breakdown . . . 232
  7.3. Film Breakdown Models . . . 234
  7.4. Pit Generation Kinetics . . . 234
  7.5. Stability of Pitting . . . 235

8. Transpassive Dissolution 236
  8.1. Transpassivity 236
  8.2. Anodic Brightening 237
9. Electode Transfer Reactions at Passive Metal Electrodes 238
  9.1. Oxygen Electrode Reaction 238
  9.2. Redox Reactions 240
10. Concluding Remarks 242
References 242

5. The Kinetics of the Growth of Oxides

M. J. Dignam

1. Introduction 247
  1.1. The Nature of the Problem 247
  1.2. Commonly Observed Kinetic Behavior 248
2. Theory of Ionic Transport through Solids 256
  2.1. Approximate One-Dimensional Model for Bulk Transport 256
  2.2. Transport Rate Controlled by Defect Injection 258
  2.3. Transport Rate Controlled by Both Bulk Transport and Injection Process 259
  2.4. Intrinsic Ionic Conduction 261
  2.5. Second-Order Effects 266
  2.6. Local Field Model 270
  2.7. The Direct Logarithmic Equation 272
  2.8. Summary of Ionic Transport Equations 273
3. The Metal–Oxide and Oxide–Electrolyte Interfaces 275
  3.1. Introduction 275
  3.2. Transition Layer Model: Thermodynamic Properties 275
  3.3. Transition Layer Model: Distribution of Charge and Potential 276
  3.4. Consequences for Oxide Growth Kinetics 277
4. Kinetics of Growth of Valve Metal Oxides 278
  4.1. Steady State Kinetics 278
  4.2. Isothermal Transient Kinetics 281
5. Other Metal–Oxide Systems 289
  5.1. Porous Anodic Oxide Films—Al, Al_2O_3 289
  5.2. Growth of Thick Films by Dissolution, Precipitation Mechanism—Ag, Ag_2O 291
  5.3. Formation and Growth of Oxide Nuclei 296
6. Concluding Remarks 301
Auxiliary Notation 302
References 303

6. Corrosion Inhibition

R. N. Parkins

1. Introduction 307
2. Polarization Curves and Inhibition 308

3. The Inhibition of General Corrosion 309
4. Mechanisms of the Inhibition of General Corrosion 317
5. Inhibition of Localized Corrosion 323
6. Conclusions 329
References 330

7. Stress Corrosion Cracking

Genady P. Cherepanov

1. Introduction 333
2. Pit Growth (Pitting) 336
    2.1. General Equations of Transport Processes 336
    2.2. Some One-Dimensional Pitting Processes 340
3. Fracture Mechanics Approach 345
    3.1. General Functional Method 345
    3.2. Energy Method 350
    3.3. Arbitrary System of Tunnels in Elastic Body 352
    3.4. Crack Twinning 354
    3.5. Experimental Determination of the $\dot{l}$–Γ Diagram 355
4. Electrochemical Mechanism of Crack Growth 358
    4.1. Equations of Motion of Electrolyte Ions in Narrow Slits 360
    4.2. The Corrosion Crack Growth Rate 363
    4.3. The Tunnel Model of the Crack Growth 368
    4.4. Analysis of Some Experimental Data 375
    4.5. Some Models of the Tunnel Growth 378
5. Crack Growth in Metals due to Local Hydrogen Embrittlement 383
    5.1. Theoretical Consideration 384
    5.2. Analysis of Test Data 388
    5.3. Threshold Stress Intensity Factor 394
6. The Environmental Growth of Fatigue Cracks 397
7. Conclusion: The Comparative Analysis of Major Mechanisms of Subcritical Crack Growth in Metals 403
References 406

8. Electrochemical Aspects of Hydrogen in Metals

P. K. Subramanyan

1. Introduction 411
2. Experimental Study of H in Metals 412
    2.1. Principle of the Electrochemical Method 413
    2.2. Solution of the Diffusion Equation 414
    2.3. Solution of the Diffusion Equation when the Charging Current Is Switched Off 417
    2.4. Experimental Method of Studying H Permeation 419
    2.5. Analysis of the Buildup Permeation Transient 420

3. Solubility of H in Metals 421
    3.1. Sievert's Law 422
    3.2. Significance of the Solubility of H Measured in Electrochemical Permeation Method 423
4. Chemical Potential of Hydrogen in Metals. 424
    4.1. The Basic Relationship of the Chemical Potential of Hydrogen to the Hydrogen Evolution Kinetics 425
    4.2. The Kinetics of Hydrogen Evolution and the Possible Pressure of Hydrogen in Internal Cracks, Cavities, or Voids in Metals. . . . 426
5. Permeation of H in Relationship to the Mechanism of Hydrogen Evolution Reaction 429
    5.1. Mode of Entry of H into the Lattice 430
    5.2. Dependence of Permeation Current on the Mechanism of h.e.r. . . 431
6. Influence of the Composition of the Ambient Solution on Permeation of Hydrogen in Metals 434
7. Effect of Hydrostatic Pressure on the Kinetics of h.e.r. and Hydrogen Permeation in Iron 436
8. Effect of Stress on the Chemical Potential of H in Metals 437
9. Tensile Stress and Hydrogen Pump 441
10. Effect of Stress on the Solubility of H in Metals 443
11. Hydrogen Embrittlement of Metals 449
    11.1. Pressure Theory of Hydrogen Embrittlement 449
    11.2. Petch's Theory of Hydrogen Embrittlement 452
    11.3. Decohesion Theory of H Embrittlement 453
    11.4. Hydride Embrittlement 453
    11.5. Stress Corrosion and Hydrogen Embrittlement 453
    11.6. Concluding Remarks 453
12. Usefulness of the Study of Hydrogen in Metals 454
    12.1. Storage of H in Metals 454
    12.2. Rechargeable H Electrode 455
    12.3. Fusion Reactors 456
    12.4. Fast Hydrogen-Permeating Membranes 457
    12.5. Materials Impermeable to Hydrogen 457
    12.6. Codeposition of Hydrogen in Electrodeposition of Metals . . . 458
    12.7. Study of Changes in the Crystal Structure of Metals and Alloys. . 458
    12.8. Development of Materials for H_2-Burning Internal Combustion Engines 458
References 459

9. Triboelectrochemistry

V. Guruswamy and J. O'M. Bockris

1. Introduction 463
2. Historical 463
3. The Rehbinder Effect on Hardness 464
4. The Dependence of Friction on Potential 464
5. Wear Resistance and Surface Deformation 469

6. Practical Usage of Friction Dependence on Potential 469
7. Conclusion 470
Auxiliary Notation 470
References 470

10. Nonmetallic Electrode Materials

J. P. Randin

1. Introduction 473
2. Carbon and Graphite Electrodes 474
    2.1. Electrochemical Stability in Aqueous Solutions 474
    2.2. Electrocatalytic Activity for the Oxygen Reduction Reaction . . . 486
    2.3. Electrochemical Stability in Fused Salts 489
3. Carbide, Boride, Nitride, Phosphide, and Sulfide Electrodes 496
    3.1. Electrochemical Stability 497
    3.2. Electrocatalytic Activity 500
    3.3. Electroanalytical Applications 504
    3.4. Intercalation Compounds as the Cathode of Reversible Batteries . . 505
4. Mixed Transition Metal Oxide Electrodes 507
    4.1. Transition Metal Oxides of the Perovskite Structure 508
    4.2. Transition Metal Oxides of the Spinel Structure 517
5. Conclusions 519
References 521

Addendum to Chapter 1 539
Index 545

1

Thermodynamics of Corrosion

JEAN VAN MUYLDER

1. Introduction

One designates by the word *corrosion* the unwanted destruction of a material through the chemical or electrochemical action of the surrounding environment. It is well known that iron and commonly used kinds of steel corrode very easily. If appropriate and burdensome precautions are not taken to protect them (e.g., by means of protective coverings, such as paints), the bridges, cranes, wagons, car bodies, ship hulls—in short, iron objects of all kinds—are generally and very rapidly ruined by corrosion. In this respect, the unique case of the ancient iron column of Delhi (India), which, although not protected, has until now not been noticeably damaged by corrosion, seems to be an entirely exceptional case, which can be attributed to very particular circumstances in the metal composition (low content of S, high content of P) and the dryness and purity of the local air.(1,2)

The corrosion of metallic materials is a calamity of major importance, whose action is frequently aggravated by its often hidden and insidious character. The economic and technical importance of this calamity has grown considerably in recent years with the installation of relatively new equipment whose functioning depends on a very low susceptibility to corrosion. As Pourbaix(3) has stated, corrosion can cause and has, in fact, already caused

---

JEAN VAN MUYLDER • CEBELCOR and Department of Metallurgy and Electrochemistry, Université Libre de Bruxelles, B-1050 Brussels, Belgium.

considerable disasters in nuclear reactors, planes, mills, and automated industries. Corrosion constitutes at present a determining problem in nuclear, aerospace, and electronic industries.

The economic importance of the problem is shown convincingly by the following estimates concerning the destruction of metals and the enormous sums spent by public agencies, industries, and consumers to renew what has been destroyed and to protect what has been built.

According to the best estimates, the quantity of iron destroyed annually by corrosion lies between 25% and 33% of the annual production.

At an exhibition concerning corrosion, organized by Shell at Brussels in 1937, the following inscription was placed: "While you are reading this, 760 kilograms of iron are being corroded."

In 1949, Uhlig estimated the annual cost of corrosion in the United States at 5.5 billion dollars,(3,5,8) and more recent estimates by Liechtenstein have brought this cost to 10 billion dollars.(3,6–8)

In a report published in 1971 by the Department of Trade and Industry of Great Britain, Hoar put the cost of corrosion in that country at 1365 million pounds per year (about 3 billion dollars or 55 dollars per person per year), which is approximately 3.5% of its gross national product.(3,9)

The figures mentioned by Uhlig in 1949 take into account only the direct losses corresponding to the cost of protection and replacement of corroded equipment. They do not account for indirect losses, which result from incapacitation of businesses, product losses, lowering of return, explosions, contamination, and even loss of human lives.

These corrosion phenomena are characterized not only by their economic and technical importance, but also by their complexity. It is, in fact, frequent that one states that materials, presumably resistant against corrosion, are ruined rapidly under certain circumstances. On the other hand, it less frequently happens that materials which are supposedly vulnerable behave perfectly well under specific conditions. Even in the case of experiments, seemingly simple at first and with a small number of experimental parameters, one comes up against apparently contradictory or paradoxical results.

In 1923, Evans placed two iron specimens connected by a galvanometer into two KCl solutions separated by a porous wall. He observed that by paddling air in one of these solutions and nitrogen in the other, he caused the passage of an electric current between the two iron specimens, in the sense that the iron submerged in the solution without air corroded, and the iron in contact with the aired solution remained free of corrosion.(10)

In distilled water, iron corrodes. If one adds chromate, the corrosion can be either enhanced or eliminated. If, when the corrosion is eliminated, one adds chloride to the solution, a strong localized corrosion develops.

In distilled water, an immobile zinc plate corrodes. In the same water, a moving zinc plate is covered with a protective layer and corrosion is stopped (Pourbaix(11)).

It has been known for a long time that one can protect iron against corrosion by connecting it to the negative pole of a continuous source of electric current, a procedure which is the basis for the technology called cathodic protection. Conversely, one generally activates the corrosion of iron by connecting it to the positive pole. However, the results are sometimes reversed. A positive current can bring about the protection of the iron, and a negative current can provoke the corrosion of the iron.(12-14) An analogous phenomenon has been observed by Dodero(15) in the case of igneous electrolysis of sodium hydroxide.

In boiler technology, one makes an effort to eliminate oxygen by means of physically working degassers or by the addition of reducing agents (sulfite, hydrazine, morpholine, etc.). These precautions have allowed reduction of boiler corrosion considerably. However, in the Hamberg Elektrizitätswerke, Freier(16) managed to operate a boiler without corrosion for 12,000 hr (500 days) at 200°C.

All of this is complicated and apparently contradictory. This appearance of complexity is precisely what brought about the feeling that corrosion is an inevitable evil to which one must resign oneself without trying to control it.

In one of his studies on corrosion, Evans wrote that the strangeness of corrosion reactions, resulting in the belief that they do not obey well-defined laws, has caused the orthodox physicochemists to look at the entire subject with suspicion. Because of this, the scientific study of corrosion has been confined to empiricism for a long period of time.(17)

The fact is, however, that corrosion reactions are no less subject to laws and principles than are the chemical and electrochemical reactions, of which they are integral parts.

2. Application of Chemical Thermodynamics

2.1. General Statements

Like all other phenomena, the manifestations of corrosion obey the laws of thermodynamics. Metals tend to return to their original state. Except for the "noble" metals, i.e., gold, silver, and platinum, which are found in the native state, the majority of the metals are found on earth in the state of minerals, i.e., oxides, sulfurs, sulfates, carbonates, silicates, etc. By different metallurgical procedures, the metals are extracted from them. Exposed under the conditions of utilization, to the action of water, oxygen, solar radiation, temperature variations, and other atmospheric and pollutive agents, they are progressively destroyed by corrosion and transform into thermodynamically more stable substances whose composition frequently comes close to that of the original minerals, i.e., iron transforms into rust close to limonite, copper changes into a green patina similar to brochantite, etc.

This return to the original form is well illustrated in a verse found in Genesis(3,19): "... until you return to the earth from which you were taken, as you were dust and you shall be turned into dust again." Pourbaix reports that "certain people have seen in this text an early expression of the second principle of thermodynamics."(3,8) The great imperative of thermodynamics is, in fact, that a system, whatever it may be, tends to develop toward its most stable form.

2.2. Chemical Thermodynamics

General Formula of Chemical Equilibria

Referring to special studies for more details concerning fundamental principles,(18–21) we shall mention here only the essential aspects of chemical thermodynamics applied to systems in the following pages. To define these systems, it is convenient to select as independent variables the absolute temperature, T, the pressure exerted by the outer world, p, and the number of moles, n, of the different constituents. The thermodynamic function relative to these variables is the function, G, the thermodynamic potential at constant pressure and temperature, generally designated as "Gibbs free energy" or "free enthalpy."

This function is connected with the enthalpy or heat function of reaction at constant pressure, H, by the equation

$$G = H - TS \tag{1}$$

where S is the entropy of the system.

Equation (1) represents, for any substance under the given physicochemical conditions, the maximum portion of its energy susceptible for transformation into mechanical work. In the course of each spontaneous transformation at constant temperature and pressure, the value of G decreases. In other terms, an isothermic and isobaric reaction is spontaneously possible only if it lowers the free energy of the system, or

$$\Delta G < 0 \tag{2}$$

Conversely, in order for spontaneous isothermic and isobaric transformations to take place, condition (2) has to be verified.

The application of this condition, derived from the first and second principles of classical thermodynamics, determines whether a certain reaction can take place or not. Furthermore, it allows a predetermination of the equilibrium conditions and the direction of the chemical reactions.

The chemical molar potential, μ_γ, of the constituent, γ, of a chemical system which contains n_γ moles of it, is connected with the value of free energy,

G, of the system by the partial derivation

$$\mu_\gamma = \left(\frac{\partial G}{\partial n_\gamma}\right)_{p,T,n_\delta} \qquad (\delta \neq \gamma) \tag{3}$$

The indicators indicate that pressure, temperature, and number of moles of all constituents other than γ are kept constant.

For the given values of pressure, p, and temperature, T, one can therefore write

$$\mu_\gamma = \frac{\partial G}{\partial n_\gamma} = g_\gamma \qquad \text{specific molar free energy} \tag{4}$$

$$= h_\gamma - Ts_\gamma \qquad \text{specific molar free enthalpy} \tag{5}$$

where h_γ and s_γ are the specific molar enthalpy and the specific molar entropy, respectively.

Generally, any chemical transformation is written according to the model of De Donder$^{(22)}$:

$$\Sigma_\gamma \nu_\gamma M_\gamma = 0 \tag{6}$$

where the coefficients are positive or negative according to whether the reactants, M_γ, are situated in a member of the usual reaction equation or in the other. The state of thermodynamic equilibrium is achieved when the variation of free energy, relative to the transformation under consideration, is zero:

$$\Delta G \equiv \Sigma_\gamma \nu_\gamma \mu_\gamma = 0 \tag{7}$$

the summation, $\Sigma_\gamma \nu_\gamma \mu_\gamma$, being equal in size and sign to the variation of free energy of the reaction.

If one represents by the same symbol (M_γ) the fugacity φ_γ or "corrected" partial pressure of the gaseous bodies, $(M_\gamma) \equiv \varphi_\gamma = p_\gamma f_\gamma$, and the activity a_γ or "corrected" concentration of the dissolved species $(M_\gamma) \equiv a_\gamma = c_\gamma f_\gamma$, the values of the chemical potential μ_γ of the reaction substances can be expressed by the equation

$$\mu_\gamma = \mu_\gamma^{\circ} + RT \ln M_\gamma \tag{8}$$

where μ_γ° represents the normal chemical potential of the compound under consideration [i.e., its chemical potential in the state of reference, or $(M_\gamma) =$ 1 mole/l for the dissolved bodies and 1 atm for the gaseous bodies].

So, the condition of equilibrium of any chemical reaction$^{(6)}$ can be written

$$\Sigma_\gamma \nu_\gamma \mu_\gamma^{\circ} + RT \Sigma_\gamma \nu_\gamma \ln M_\gamma = 0 \tag{9}$$

or

$$\Sigma_\gamma \nu_\gamma \mu_\gamma^{\circ} + 4.5756 T \Sigma_\gamma \nu_\gamma \log M_\gamma = 0 \tag{10}$$

or also

$$\Sigma_\gamma \nu_\gamma \mu_\gamma \log M_\gamma = -\frac{\Sigma_\gamma \nu_\gamma \mu_\eta}{4.5756T} \tag{11}$$

or, finally

$$\Sigma_\gamma \nu_\gamma \log M_\gamma = \log K \tag{12}$$

$$\log K_T = -\frac{\Sigma_\gamma \nu_\gamma \mu_\gamma}{4.5756\,T} \tag{13}$$

K_T is the equilibrium constant, which is normally designated, according to the nature of the transformation under consideration, under the following traditional denominations: Guldberg and Waage constant, Ostwald constant, Henry constant, vapor pressure, solubility, or product of solubility.

As has been indicated by Pourbaix,(3,8,23) the group of equations (12) and (13) represent a synthesis of the different laws of chemical equilibrium. The knowledge of the equilibrium constant of a chemical reaction is thus referred back to the knowledge of molar chemical potentials.

In cases where the temperature is 25°C (298.15 K), generally adopted as reference, Eqs. (12) and (13) become, respectively,

$$\Sigma \nu_\gamma \log M_\gamma = \log K_{298} \tag{14}$$

$$\log K_{298} = -\frac{\Sigma_\gamma \nu_\gamma \mu_\gamma{}^\circ}{1364} \tag{15}$$

$\mu_\gamma{}^\circ$ representing the standard chemical potentials of the reaction bodies (i.e., normal chemical potential at 25°C).

These standard chemical potentials $\mu_\gamma{}^\circ$ present well-defined values, which are recorded in the tables of thermodynamic data(23–29) or in the tables of thermodynamic data included in other works,(30–34) or in the form of stability constants.(35,36)†

3. Application of Electrochemical Thermodynamics

3.1. General Statements

The application of chemical thermodynamics to the study of metal corrosion phenomena in the presence of aqueous solutions has brought meager results and proved to be insufficient for the problem.

The fundamental cause for the insufficiency of chemical thermodynamics is due to the fact that corrosion manifestations are not solely chemical. Rather they are primarily electrochemical reactions, which contain, besides chemical substances (ions charged negatively and positively), free electric charges under the form of electrons, e^-. This was brought to light by the classical experiments of Evans.(10)

---

† When consulting sources of documentation referred to, care must be taken, as these thermodynamic magnitudes are frequently named and noted differently.

The laws of chemical equilibrium [Eqs. (12) and (13)] which influence partial pressures, p (or fugacities, φ_γ) and concentrations, c_γ (or activities, a_γ)

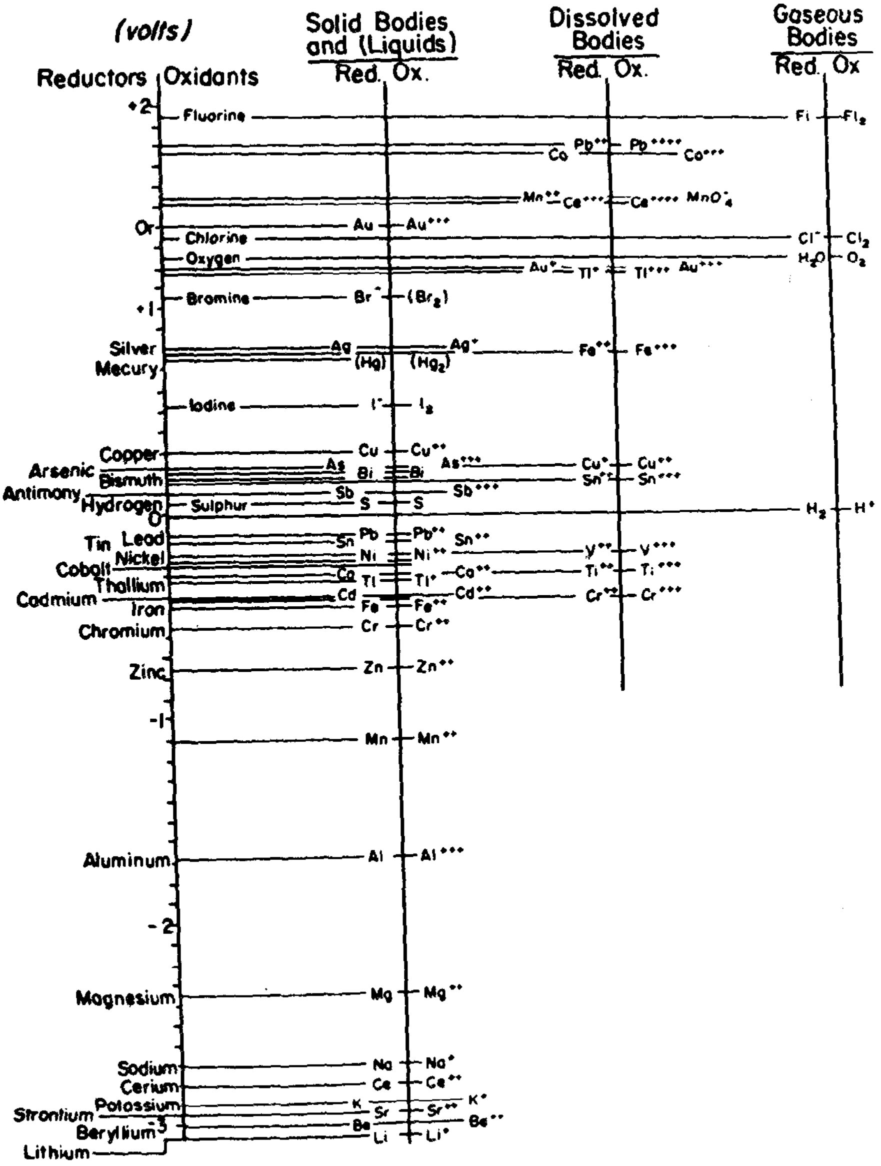

Figure 1. Standard equilibrium potentials.

are, therefore, insufficient to address the study of all the phenomena participating in corrosion. In order to reach that goal, consideration must be given also to a third term, which will express the energetic influence of the electrons in the form of an electrode potential, E.

One can attribute this electric magnitude, which is easily measured, to the great interest taken by numerous corrosion specialists in the "dissolution potential" scale of Nernst(37) (equilibrium potentials). Figure 1 shows a diagram which reproduces the classification established by Nernst.

The values of electrode potential refer to the equilibria of metals and nonmetals with aqueous solutions, containing one ion-gram of metal or nonmetal per liter at pH = 0 and at 25°C.

In conformity with this classification, metals whose dissolution potential is lower than the dissolution potential of hydrogen (0 V) can be corroded in aqueous solutions with the freeing of hydrogen giving a weaker dissolution potential (Pb, Sn, Ni, Co, Tl, Cd, Fe, Cr, Zn, Mn, Al, Mg, Na, Ca, K, Sr, Be, Li).

Metals such as Sb, Bi, Cu, and Ag, whose dissolution potential lies between that of hydrogen (0 V) and oxygen (+1.29 V), cannot be corroded by freeing hydrogen, but they can be in solutions containing oxygen.

Metals whose dissolution potential is above that of oxygen (+1.29 V) generally cannot be corroded in aqueous solutions (Au, Pt).

In reality there are multiple exceptions to this rule. Metals which should corrode often remain corrosion free. Conversely, metals which should remain free of corrosion often corrode. These apparent contradictions cannot be explained by the scheme shown in Figure 1, as the reactions which occur when a metal is corroded are generally multiple ones and frequently irreversible.

3.2. Electrochemical Thermodynamics

3.2.1. General Formula of Electrochemical Equilibria

An electrochemical reaction (or electrode reaction) may be defined as a reaction in which chemical bodies, M_γ (neutral molecules and/or cations and anions), and free electric charges in the form of electrons, e^-, take part. This can be written in a manner similar to that applied to the chemical reactions (6):

$$\Sigma_\gamma \nu_\gamma M_\gamma + ne^- = 0 \qquad (16)$$

The condition of equilibrium(3,8,23) can be written

$$\Sigma_\gamma \nu_\gamma \mu_\gamma - 23{,}061\, nE_0 = 0 \qquad (17)$$

In addition to the molar chemical potentials, μ_γ, of the reaction bodies, an electrode potential, E_0, is added, which measures the influence of electric charges. The magnitude, 23,061, is the conversion factor for the volt-faraday (used for the measurement of the electric potential, E_0) in calories.†

Using Eq. (17), one obtains

$$\Sigma_\gamma \nu_\gamma \mu_\gamma^{\cdot} + RT\Sigma_\gamma \nu_\gamma \ln M_\gamma - 23{,}061\, nE_0 = 0 \tag{18}$$

By replacing R by its value and Naperian logarithms to decimal logarithms, one obtains

$$\Delta_\gamma \nu_\gamma \mu_\gamma^{\cdot} + 4.5756 T\Sigma_\gamma \nu_\gamma \log M_\gamma - 23{,}061\, nE_0 = 0 \tag{19}$$

which expresses the equilibrium condition of electrochemical reaction (16).

Equation (19) can also be written

$$E_0 = \frac{\Sigma_\gamma \nu_\gamma \mu_\gamma^{\cdot}}{23{,}061\, n} + \frac{4.5756\, T}{23{,}061\, n} \Sigma_\gamma \nu_\gamma \log M_\gamma \tag{20}$$

or

$$E_0 = E_0^\circ + \frac{4.5756\, T}{23{,}061\, n} \Sigma_\gamma \nu_\gamma \log M_\gamma \tag{21}$$

and

$$E_0^\circ = \frac{\Sigma_\gamma \nu_\gamma \mu_\gamma}{23{,}061\, n} \tag{22}$$

where E_0 is the equilibrium potential of the electrochemical reaction and E_0° its normal equilibrium potential (in the special case where all constituents of the reaction are at the state of reference: $[M] = 1$ mol/l for the dissolved species and 1 atm for the gaseous bodies).

As in the case of the equilibrium constant, K, of the chemical reaction (13), the knowledge of the normal equilibrium potential, E_0°, of an electrochemical reaction is based upon molar chemical potentials.

At a temperature of 25°C (298.15 K), the equations (20) and (21) become, respectively,

$$\Sigma_\gamma \nu_\gamma \mu_\gamma{}^\circ + 1364\, \Sigma_\gamma \nu_\gamma \log M_\gamma - 23{,}061\, nE_0^\circ = 0 \tag{23}$$

and

$$E_0 = E_0^\circ + \frac{0.05915}{n} \Sigma_\gamma \nu_\gamma \log M_\gamma \tag{24}$$

$$E_0^\circ = \frac{\Sigma_\gamma \nu_\gamma \mu_\gamma{}^\circ}{23{,}061\, n} \tag{25}$$

where E_0 is the equilibrium potential of the electrochemical reaction under consideration, and E_0° and μ° the standard equilibrium potential of that reaction and the standard chemical potential of the reaction bodies at 25°C, respectively.

---

† 1 volt-faraday is the energy used in the displacement of a charge of 1 faraday (96,487.0 C) with a potential difference of 1 V.

Conforming with Pourbaix[3,6,23] the equations (24) and (25) constitute a synthesis of the laws of electrochemical equilibrium, where it is customary to speak of the following:

1. Oxidation–reduction potential: The reaction species are all in a dissolved state and constitute a homogeneous system.
2. Dissolution potential: One of the constituents is a solid body. The system is a heterogeneous solid–solution.
3. Gas electrode potential: One of the constituents is a gaseous body. The system is a heterogeneous gas–solution.

Each of these cases deals with equilibrium potentials of electrochemical reactions of different characters.

3.2.2. Definition and Determination of the Electrode Potential

In comparison with chemical reactions, the determination of the equilibrium circumstances of the electrochemical reactions presents a fundamental difficulty, due to the fact that there is no method of determining the absolute value of the electrode potential.

This can be overcome by setting an arbitrary zero potential and measuring all the electrode potentials in relation to this conventional reference. This reference can be held by any electrode on whose surface the equilibrium state of a reversible electrochemical reaction is realized. The choice of the electrochemist has been the standard hydrogen electrode at a temperature of 25°C, she(25), where the state of equilibrium of the reversible electrochemical reaction

$$H_2 = 2H^+ + 2e^- \tag{26}$$

is realized.

In actual practice, this reference electrode is made of an electrode of platinised platinum, saturated with gaseous hydrogen, under pressure of 1 atm ($p_{H_2} = 1$ atm) and immersed into a solution of hydrochloric acid, 1.17 M HCl ($a_{H^+} = 1$, pH = 0.00).

Figure 2 shows a measurement arrangement of the electrode potential by means of a standard hydrogen electrode, she. This electrode is connected with the reaction solution by an electrolytic junction, avoiding a difference of diffusion potential between the two solutions (i.e., saturated agar agar gel of KCl, NH_4NO_3, salts where the ions have similar mobilities). When an electric current circulates in the reaction solution, this junction opens up upon the immediate neighborhood of the electrode surface on which the reaction occurs (Haber–Luggin capillary[38] or capillary device of Piontelli[39] with lateral split).

Unless indicated otherwise, values of the electrode potentials in the text refer to the standard hydrogen electrode, she.

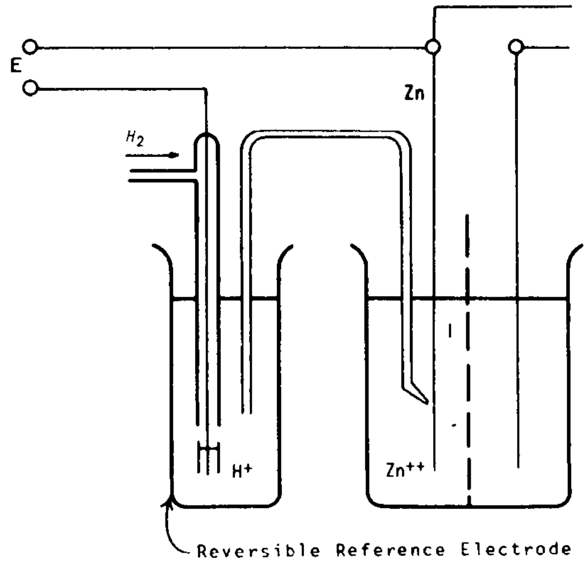

Figure 2. Measurement of electrode potential (Haber and Luggin's method).

The above-mentioned convention implies that the standard chemical potentials of the constituents of the standard hydrogen electrode (gaseous hydrogen, H_2, under pressure of 1 atm and $a_{H^+} = 1$) should equal zero, as

$$\mu_{H_2}{}^\circ = 0 \text{ cal mol}^{-1} \tag{27}$$

$$\mu_{H^+}{}^\circ = 0 \text{ cal mol}^{-1}$$

$$\Sigma \nu \mu_{\text{she}}{}^\circ = 0 \text{ cal mol}^{-1} \tag{28}$$

Conforming with this convention, and applying Eqs. (24) and (25), the equilibrium potential of such an electrode is given by

$$E_0 = 0.000 - 0.0591 \text{ pH} - 0.0295 \log p_{H_2} \tag{29}$$

It becomes necessary to extend the convention relative to the zero of reference of electrode potentials, to temperatures above 25°C, so that, in agreement with what is now called the "universal convention," the potential of the standard hydrogen electrode is equal to zero at all temperatures†:

$$(E_0^\circ)_{\text{she}}(T \text{ K}) = 0.000 \text{ V} \tag{30}$$

---

† This "universal convention" has not, however, been adopted by all authors. Some authors use the standard state, which is "not conventional," where the potential of the standard hydrogen electrode $(E_0^\circ)_{\text{she},298}$ is equal only to 0.000 V at 25°C (ΔG_{298}° relative to the equilibrium $2H^+ + 2e^- = H_2$ equals 0 cal). This potential differs from 0 V at other temperatures, TK: $(E_0^\circ)_{\text{she},T} \neq 0.00$ V (ΔG_T° relative to the equilibrium $2H^+ + 2e^- = H_2$ is then different from zero calories).

The electrode potential of any electrochemical reaction (16) which can be written now in a less condensed form:

$$aA + cH_2O = bB + mH^+ + ne^- \qquad (31)$$

thus represents the equilibrium potential of the simple galvanic cell which achieves the general chemical reaction

$$aA + cH_2O = bB + (m - n)H^+ + \frac{n}{2}H \qquad (32)$$

resulting from the simultaneous realization of two joined electrochemical reactions

$$aA + cH_2O = bB + mH^+ + 2e^- \quad \text{(any electrochemical reaction)} \qquad (31)$$

$$\frac{n}{2}H_2 = nH^+ + 2e^- \quad \text{(electrochemical reaction of the reference system)} \qquad (26)$$

As pointed out by de Béthune and Loud,(40) the electrode potential of an element is a voltage measurement of the maximum electrical energy which can be gathered by reaction of this element with hydrogen.

Resulting from this situation, the variation of free energy

$$\Delta G^\circ = \Sigma \nu \mu^\circ \qquad (33)$$

determined for reaction (31) represents the variation of free enthalpy for the general chemical reaction (32). Consequently, the fundamental thermodynamic equation of Gibbs–Helmholtz

$$\Delta G^\circ = \Delta H^\circ - T\Delta S^\circ \qquad (34)$$

cannot be applied to individual electrochemical reactions [Eq. (31)] but solely to reference chemical systems [Eq. (32)].

The important consequence is the calculation of the value $E_0^\circ(T)$ of the standard equilibrium potential of any electrochemical reaction (31) at a temperature T K. From this, it is necessary to determine the variation of standard free energy

$$\Delta G^\circ(T) = \Sigma \nu \mu^\circ(T) \qquad (35)$$

relative to the general chemical reaction (32). The value E_0°, relative to the electrochemical reaction (31), can then be deduced by means of the equation

$$E_0^\circ(T) = \frac{\Delta G^\circ(T)}{23{,}061\, n} = \frac{\Sigma \nu \mu^\circ(T)}{23{,}061\, n} \qquad (36)$$

In the terms of a resolution adopted by the International Union of Pure and Applied Chemistry (IUPAC) in Stockholm in 1953,(41) the electrode potential of a metal, M_1, is the difference $(\psi_1 - \psi_{ref})$ between the potential of the metal, M_1, and the potential of the reference electrode. It is not the inverse difference ($\psi_{ref} - \psi_1$) between the potential of the reference electrode and the potential of the metal, M_1. According to this convention, the electrode potential of the reduction system is negative and that of the oxidizing system is positive.

For example, the standard electrode potential of zinc is −0.76 V and not +0.76 V.

It is incorrect to speak of a potential of a metal in relation to an aqueous solution, since neither of these environments contains free electrons. Potential can only be spoken of in relation to a predetermined reference electrode, submerged in a solution or other conductive electrolytic environment.

3.3. Principles of Electrochemical Thermodynamics

3.3.1. First Principle—Possibility of Oxidation and Reduction

Equations (24) and (25) determine the direction—oxidation or reduction—at which it is thermodynamically possible for an electrochemical reaction to be achieved at equilibrium at the interface between a metal and a solution. When the potential of an electrode is superior to the equilibrium potential, this can be accomplished only by oxidation. If the electrode potential is lower than the equilibrium potential, the reaction can only take place by reduction. If the electrode potential and equilibrium potential of the reaction are equal, neither oxidation nor reduction can take place. The two antagonistic reactions can then be measured by the "exchange current."

If, under standard conditions,

$$E = E_0 \qquad (37a)$$

then there is neither oxidation nor reduction; if

$$E > E_0 \qquad (37b)$$

there is the possibility of oxidation; if

$$E < E_0 \qquad (37c)$$

then there is the possibility of reduction.

This triad of conditions expresses the first principle of electrochemical thermodynamics,(3,8,23) which states that for each electrochemical reaction which occurs in the presence of an electrolytic environment, there exists a certain value, E_0 (or reversible value) of the electrode potential where the state of thermodynamic equilibrium is realized. On an electrode whose potential represents this equilibrium value, a reaction cannot take place either by oxidation or by reduction.

1277

3.3.2. Second Principle—Affinity, Overpotential, and Velocity

In the case of electrochemical reactions, written according to De Donder

$$Av \geq 0 \tag{38}$$

which connects the direction of a chemical reaction (defined by the sign of its velocity) to the sign of its affinity, A. The velocity, v, of a chemical reaction is always either zero or has the same sign as its affinity. Pourbaix$^{(3,8,23,43)}$ has established the equation†

$$(E - E_0)i \geq 0 \tag{39}$$

This constitutes the mathematical expression of a second principle of electrochemical thermodynamics.

Here, the difference $(E - E_0)$ shows (in magnitude and sign) the affinity divided by n faradays, or the overpotential, η, of the considered reaction according to the equation

$$A = n(E - E_0)\text{ volts} \tag{40}$$

$$A = 23{,}061\, n(E - E_0)\text{ calories} \tag{41}$$

The intensity of the reaction current, i, measures the speed of the reaction, according to Faraday's law. Conventionally, it is given the sign " + " in the case of oxidation, and the sign " − " in the case of reduction.

Equation (39) connects the direction of an electrochemical reaction (defined by the sign of the intensity of its reaction current, i) with the sign of the difference $(E - E_0)$ between the electrode potential and the equilibrium potential of the reaction at the electrode.

If, at standard conditions,

$$E > E_0, \qquad i \geq 0 \tag{42}$$

then there is either oxidation or no reaction; if, at standard conditions,

$$E < E_0, \qquad i \leq 0 \tag{43}$$

then there is reduction or no reaction.

The second principle of electrochemical thermodynamics thus requires the velocity to be zero or of the same sign as its overpotential $(E - E_0) \equiv \eta$.

The practical importance of the measure of the electrode potentials and of their thermodynamic interpretation in corrosion studies is based on Eq. (39).

---

† *Editor's note*: The author chooses to express things in their standard state. Analogous equations of course apply to the rest of the states.

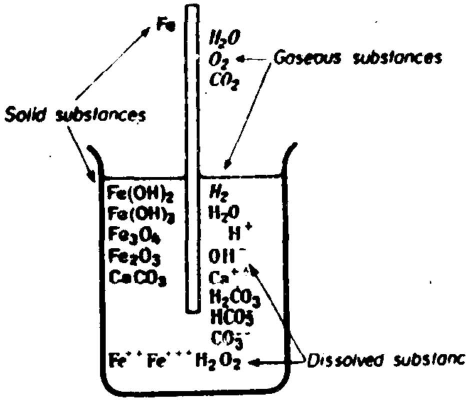

Figure 3. Iron in the presence of tap water (after M. Pourbaix(3,8)).

4. Diagrams of Potential–pH Electrochemical Equilibria in Aqueous Solutions at 25°C†

4.1. General Statements

The corrosion of metal in the presence of water or aqueous solutions is generally a complex problem. An obvious example is iron, which corrodes in the water containing calcium that is distributed in cities. As Pourbaix(3,8) indicated, this environment contains a large number of substances (Figure 3) which react chemically and electrochemically among each other.

When studying the possible reactions in isolation, it has turned out to be more productive to use the graphic method of diagrams of E-pH electrochemical equilibria, also called "Pourbaix diagrams,"(3,8,23,43–45) which give a true thermodynamic framework to the total of the reactions in which an aqueous solution takes part. These express the conditions of thermodynamic stability of all bodies which can be formed in the presence of a given electrolytic solution. They can also lead to theoretical diagrams of corrosion (stability of dissolved species), of immunity (stability of the metal),‡ and of passivation (stability of oxides, hydroxides and/or insoluble salts).§

The utilization of such diagrams is explained in detail in previous publications of Pourbaix.(3,8,23,33,34)

4.2. Diagrams of E–pH Electrochemical Equilibria

To illustrate the significance and practical usage of the Pourbaix diagrams, we shall examine in succession the cases of the binary $Fe–H_2O$ system and the ternary $Cu–CO_2–H_2O$ system.

[†] See the Addendum to this chapter on page 539, for a general bibliography.

[‡] It is conventionally agreed that there is no corrosion when the maximum quantity of a metal, which a solution can dissolve and which is initially exempt from it, is equal to or lower than 10^{-6} g-at./l.

[§] Passivation implies an absence of corrosion only if the oxide, hydroxide, or salt forms a perfect protective cover on the metal, thus creating passivity.

4.2.1. Binary Diagrams

Figures 4a to 4c present three diagrams of electrochemical equilibria of the Fe–H_2O system, where iron oxide has been considered, as well as the magnetite Fe_3O_4 ($\mu° = 242{,}700\ \mathrm{cal\ mol^{-1}}$), three different forms of ferric oxide of decreasing thermodynamic stability, the "aged" goethite α-FeOOH (Figure 4a), the "fresh" goethite α-FeOOH (Figure 4b), and the lepidocrocite γ-FeOOH (Figure 4c).(3,46,47)

The following are the free energy values (in cal $\mathrm{mol^{-1}}$) of formation of six varieties of iron oxide and hydroxide (III) recognized by de Miranda,(47) calculated for Fe_2O_3, and classified by decreasing stability of considered species†:

a. $-\underline{180{,}51}0$: "aged" goethite, α-FeOOH (most stable form)
b. $-\underline{177{,}4}00$: hematite, α-Fe_2O_3
c. $-\underline{172{,}91}0$: "fresh" goethite, α-FeOOH
d. $-\underline{169}{,}466$: maghemite, γ-Fe_2O_3
e. $-\underline{168{,}3}10$: lepidocrocite, γ-FeOOH
f. $-\underline{161{,}9}30$: hydroxide, $Fe(OH)_3$ (least stable form)

Figure 4 shows the domain of thermodynamic stability of iron totally situated below the domain of thermodynamic stability of water under atmospheric pressure (lines a and b). Metallic iron is never stable thermodynamically in the presence of 25°C water under 1 atm pressure, no matter what the pH of the solution. Simultaneous stability of water and iron at 25°C can only be obtained by sufficiently strong elevation of pressure to decrease the equilibrium potential of the H_2O–O_2 system below the equilibrium potential of the Fe–Fe_3O_4 system. This circumstance can be realized at pH between 10 and 12 only for pressures equal or above 750 atm. With weaker pressures, unpassivated metallic iron always tends to corrode by reducing the water with a release of hydrogen. Between the H_2O–O_2 equilibrium and the Fe–Fe^{2+} equilibrium, the value of the electrode potential is thermodynamically inaccessible; it depends on the kinetics of the phenomenon, especially the overpotential of hydrogen on iron. Corrosion of iron can lead to a dissolving of the metal with a predominant formation of green Fe^{2+} and $FeOH^+$ cations or hypoferrite $HFeO_2^-$ and FeO_2^- anions which are also green, according to whether the pH is lower or higher than ~10.6. For pH above 6–7, these cations can be converted into magnetic oxide Fe_3O_4, which is black (magnetite) or into ferrous hydroxide $Fe(OH)_2$, which is white. The last, whose domain of stability is entirely covered by that of Fe_3O_4, is thermodynamically unstable compared to Fe_3O_4 and tends to be transformed into this body. In the presence of oxygen and other oxidizing agents, ferrous ions and magnetite Fe_3O_4, which exist below the H_2O–O_2 equilibrium, can be oxidized into ferric ions, Fe^{3+} and $FeOH^{2+}$, as well as ferric oxides, Fe_2O_3 or FeOOH.

---

† Underlined figures indicate the precision.

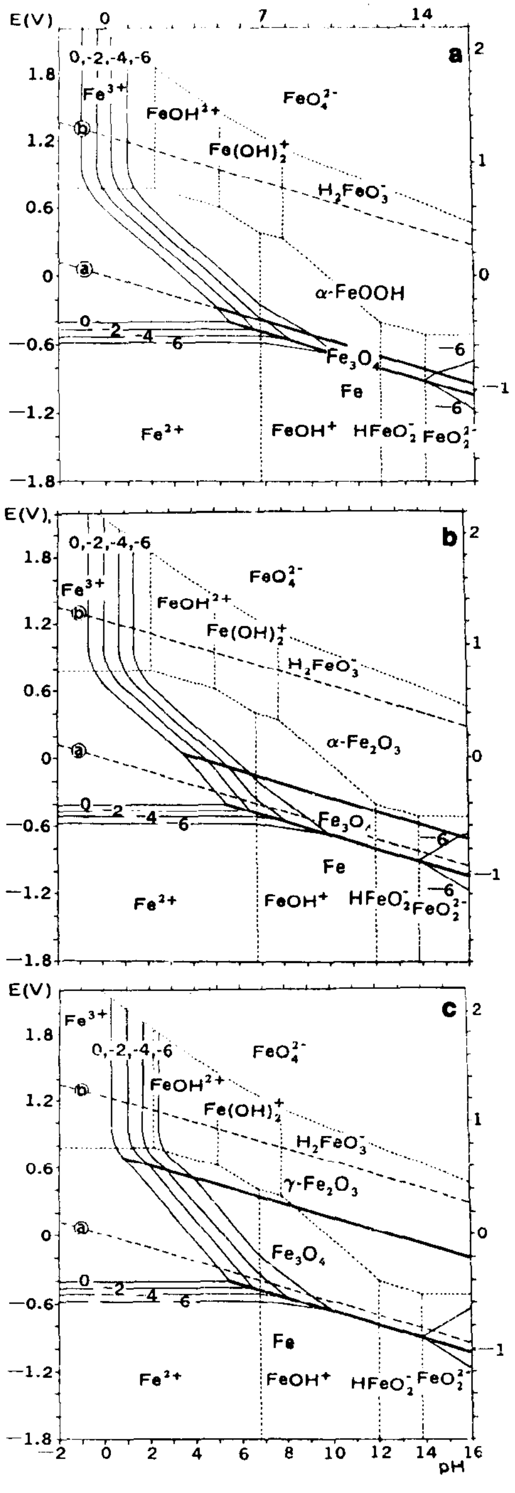

Figure 4. Equilibrium potential–pH diagrams for the Fe–H_2O system, when considering, as iron oxides, magnetite Fe_3O_4 and three different ferric oxides: (a) Aged goethite α-FeOOH. $\mu FeOOH = -118{,}600$, i.e., $\mu Fe_2O_3 = -180{,}510$ cal. (b) Fresh goethite α-FeOOH. $\mu FeOOH = -114{,}800$, i.e., $\mu Fe_2O_3 = -172{,}910$ cal. (c) Lepidocrocite γ-FeOOH. $\mu FeOOH = -112{,}500$, i.e., $\mu Fe_2O_3 = -168{,}310$ cal.

Thus, from bottom to top, one sees in succession, the ions and compounds where the iron is in its most current degree of oxidation: 0, +2, +2.67, +3, and +6. From left to right, the effects of a progressive alkalinization are shown: precipitation of hydroxides and oxides and redissolution in very alkaline and reducing environments.

Between the lines a (H_2–H_2O equilibrium) and b (H_2O–O_2 equilibrium), corrosion and passivation of the iron is effected without release of hydrogen or oxygen and can be produced only under the action of an oxidizer.

Figures 5a–5c and 6a–6c represent, for a total content of dissolved iron equal to 10^{-6} g-at./liter (absence of corrosion) the theoretical diagrams called corrosion–immunity–passivation, which corresponds to the three equilibrium diagrams 4a, 4b, and 4c. In the case of Figures 5a–5c, the magnetite Fe_3O_4 and the ferric oxide are both protectors, whereas in the case of Figures 6a–6c, the protective nature rests solely on the ferric oxide. In the domains of protective passivation represented in these two series of diagrams, a line is traced below which the ferric oxide is unstable, compared to the magnetite. As stressed by Pourbaix,(3) the choice between these six diagrams for the study of a specific case of corrosion or noncorrosion cannot be made on a purely thermodynamic basis. It must be determined beforehand the protective oxides which are effectively formed on the metal in experimental circumstances, as well as their condition of stability, if possible.

At present, it seems that at 25°C layers of Fe_3O_4 are not protective. This is shown in numerous works: Mayne and Pryor,(48) Nagayama and Cohen,(49) Bloom and Goldenberg,(50) Foley, Kruger, and Bechtoldt,(51) and Yolken, Kruger, and Calvert.(52) It is a film of maghemite γ-Fe_2O_3, containing a small quantity of hydrogen, of thermodynamic stability similar to lepidocrocite γ-FeOOH (Figure 4c) which confers a state of passivity to the active iron.

According to Wagner,(53) this oxide γ-Fe_2O_3 is in reality a magnetite deficient in iron of the formula $Fe_{2.67}O_4$. According to Nagoyama and Cohen,(49) passivity can result from the formation of an overlaying film of γ-Fe_2O_3 on a layer of Fe_3O_4.

Among the six diagrams represented in Figures 5 and 6, it is the judgment of Pourbaix that the series in Figure 6 corresponds most to the real circumstances of corrosion and noncorrosion of iron in the presence of aqueous solutions without chlorine. Among the diagrams of this figure, it is 6c which seems the most valid in the case of passivation of iron that was initially active. Figure 7 shows the experimental and theoretical conditions of corrosion together [Pourbaix(3,8,46,53) for the first, 6c for the second] with immunity and the passivation of iron. In the area of protective passivation (Figure 6c), a protective γ-Fe_2O_3 layer (or γ-FeOOH with similar stability) can be formed in direct contact with the iron. Above the dashed line in the domain of passivity, where the oxidation of Fe_3O_4 to γ-Fe_2O_3 (or γ-FeOOH) is theoretically possible, a nonprotective layer of Fe_3O_4 can be made protective by covering it with a film of γ-Fe_2O_3 (or γ-FeOOH).

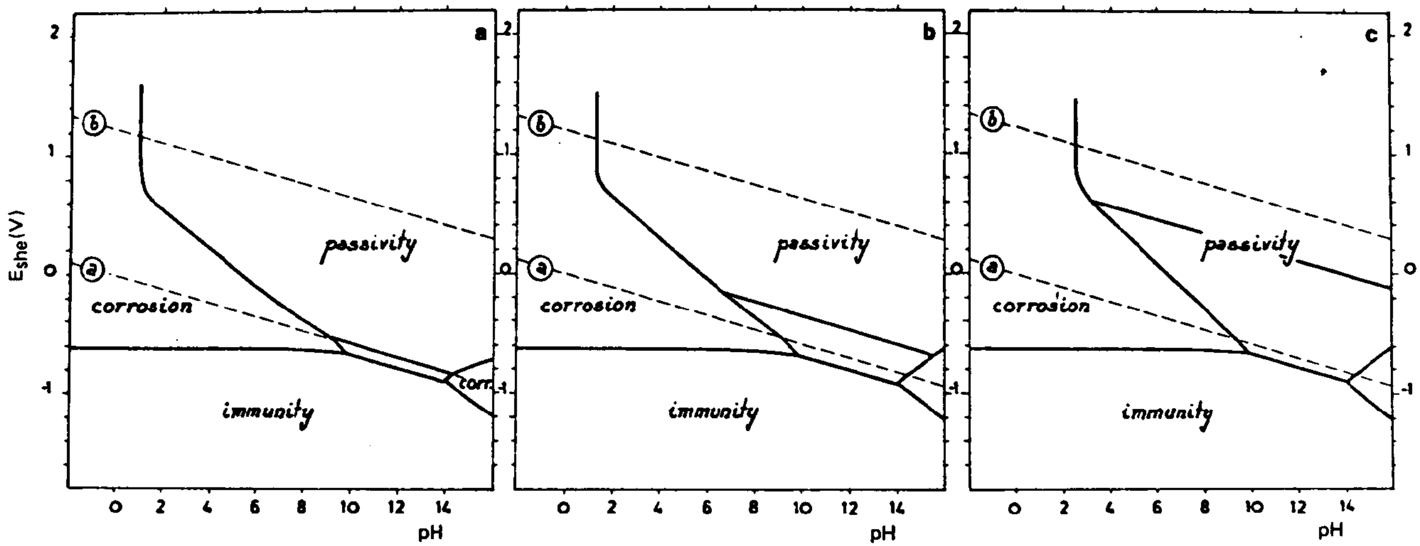

Figure 5. Theoretical conditions of corrosion, immunity, and passivation of iron, when admitting that Fe_3O_4 is not protective and that ferric oxides are protective. (a) Aged goethite α-FeOOH, (b) fresh goethite α-FeOOH, (c) lepidocrocite γ-FeOOH. (After M. Pourbaix[(3)].)

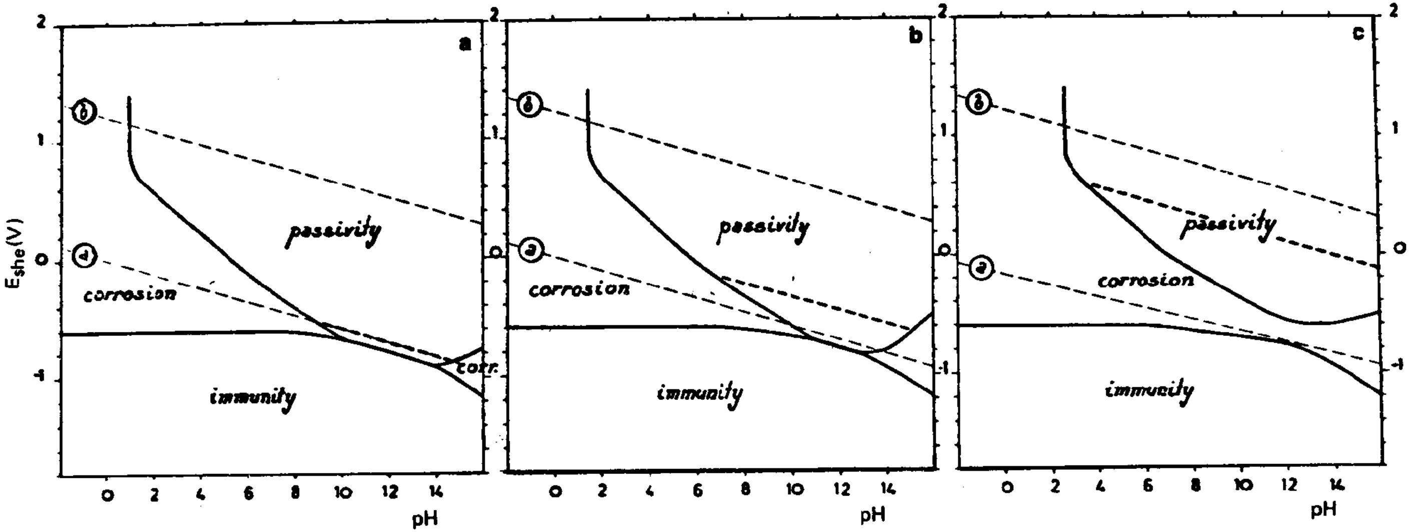

Figure 6. Theoretical conditions of corrosion, immunity, and passivation of iron, when admitting that both Fe_3O_4 and the ferric oxides are protective. (a) Fe_3O_4 and aged goethite α-FeOOH. (b) Fe_3O_4 and fresh goethite α-FeOOH. (c) Fe_3O_4 and lepidocrocite γ-FeOOH. (After M. Pourbaix.$^{(3)}$)

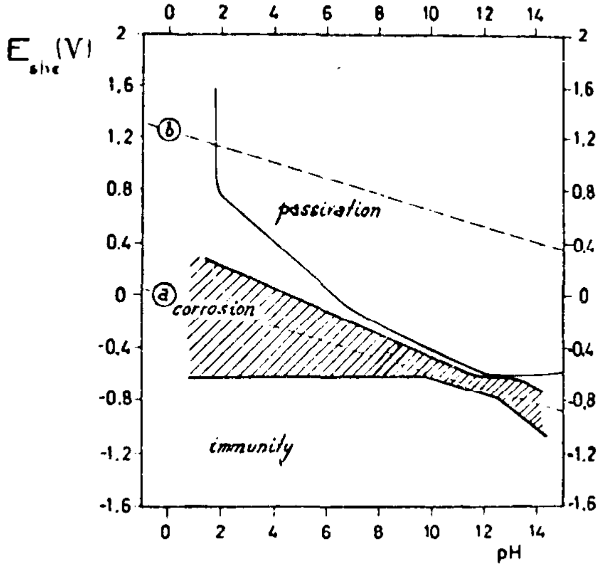

Figure 7. Experimental and theoretical conditions of corrosion, immunity, and passivation of iron, at 25°C (after M. Pourbaix[3,46]).

Pourbaix is of the opinion that under such conditions, passivation films of iron can become progressively less soluble and thus will acquire a stability similar to that of the "aged" goethite α-FeOOH, which is the most stable of the varieties of ferric oxide considered by us. It follows that the conditions of passivity defined in Figure 6c can develop in time toward those presented in Figures 6b and 6a. Feitknecht and Schindler(54) have observed that a compound obtained at the reaction of an alkaline solution and a ferric salt solution, is, after a prolonged contact with the mother liquid, essentially constituted by goethite α-FeOOH.

According to de Miranda,(47) a layer of goethite, containing copper and other alloys coming from steel, confers the protective character to rust formed in atmospheric corrosion on weathering steels.

4.2.2. Ternary Diagrams

Since their introduction, diagrams of electrochemical equilibria, E-pH, relative to binary systems at 25°C, have proven to be useful in the study of numerous corrosion problems, in the fight against it, as well as in areas such as general chemistry, analytical chemistry, electrodeposition, geology, and hydrometallurgy.

However, binary diagrams can strictly be applied only in the absence of substances which can form with the element under consideration, solvable complex species, or insoluble salts. In the opposite case, it is imperative, along with the necessary thermodynamic data, to establish electrochemical *E*–pH diagrams which conform to experimental conditions. These more complex diagrams take into consideration, not only the element under consideration, its oxides, hydroxides and hydrides, water and its constituents and ions, but all other dissolved, condensed, and gaseous substances known, and derived from the element studied. *X*-nary systems (ternary, quarternary, systems with five compounds, etc.) follow. For similar systems, we shall consider, for example, the following ternary $Cu–CO_2–H_2O$ system at 25°C.(3,8,55)

Compared to the binary $Cu–H_2O$ system,(3,8,33,34,56) the following eight supplementary substances have to be considered:

Condensed bodies

$CuCO_3{\cdot}Cu(OH)_2$ (malachite)

$2CuCO_3{\cdot}Cu(OH)_2$ (azurite)

Dissolved species

H_2CO_3, HCO_3^-, CO_3^{2-}

$CuCO_3(aq)$, $Cu(CO_3)_2^{2-}$, $CuCO_3(OH)_2^{2-}$

The four diagrams of Figure 8 represent the influence of pH on the solubility of the azurite, malachite, and tenorite (CuO) for four activities, in totally dissolved CO_2 [$CO_2(aq) + H_2CO_3 + HCO_3^- + CO_3^{2-}$], respectively, equal at 10^{-3}, 10^{-2}, 10^{-1}, and 1 mol/liter, i.e., the conditions of pH and total content of dissolved CO_2 for which each of the three condensed bodies is most stable.

Figure 9 shows four diagrams of electrochemical *E*–pH equilibria, related, respectively, to the four activities in totally dissolved CO_2 allowed in Figure 8. By allowing that the lines of equal solubility of number −6 (10^{-6} g-at. Cu(aq)/liter) separate the areas of corrosion from areas of passivation and immunity (Figure 9), the diagrams in Figure 10 can be obtained, which describe the theoretical conditions of corrosion, immunity, and passivation of copper in the presence of carbonic solutions.

According to this figure, weak contents of CO_2 (10^{-3} and 10^{-2} *M*) exert a passivating influence in neutral and slightly alkaline solution, because of the stability of the malachite $CuCO_3{\cdot}Cu(OH)_2$. Stronger contents of CO_2 (10^{-1} and 1 *M*) are activating due to the stability of the soluble complexes $CuCO_3(aq)$, $Cu(CO_3)_2^{2-}$ and $CuCO_3(OH)_2^{2-}$. Some experiments have shown that predictions based on Figures 9 and 10 are fairly accurate.(56)

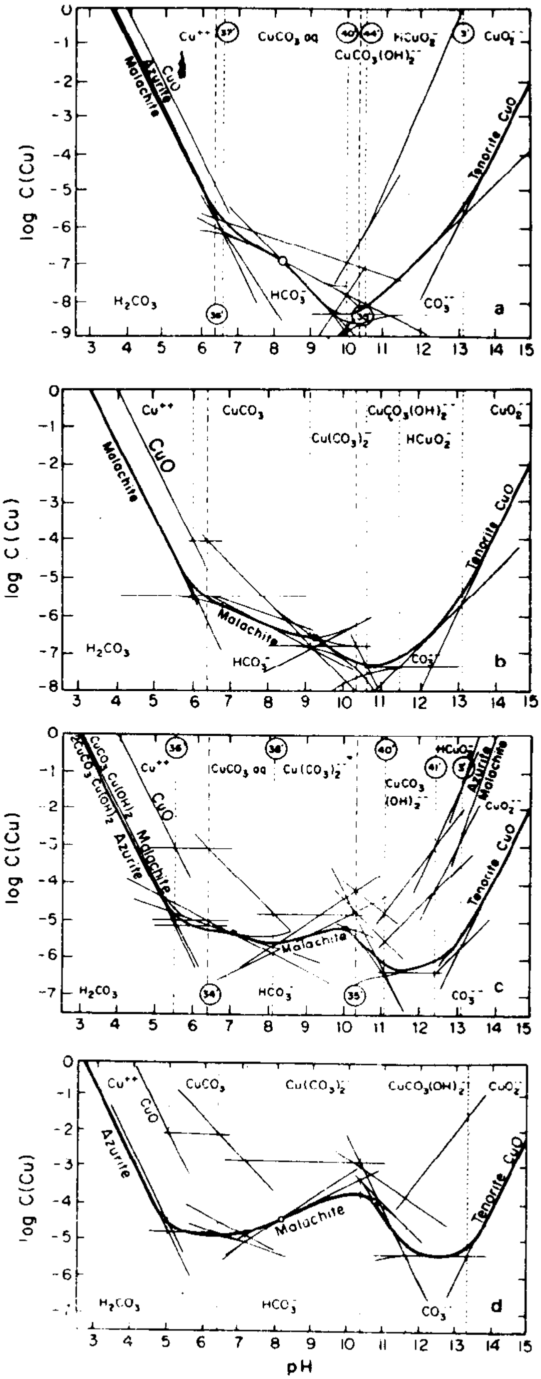

Figure 8. Influence of pH on the solubility of tenorite, CuO; azurite, $2CuCO_3 \cdot Cu(OH)_2$; and malachite, $CuCO_3 \cdot Cu(OH)_2$ at 25°C for (a) 10^{-3}, (b) 10^{-2}, (c) 10^{-1} and (d) 1 mol CO_2 per liter (44, 440, 4400, and 44,000 ppm).

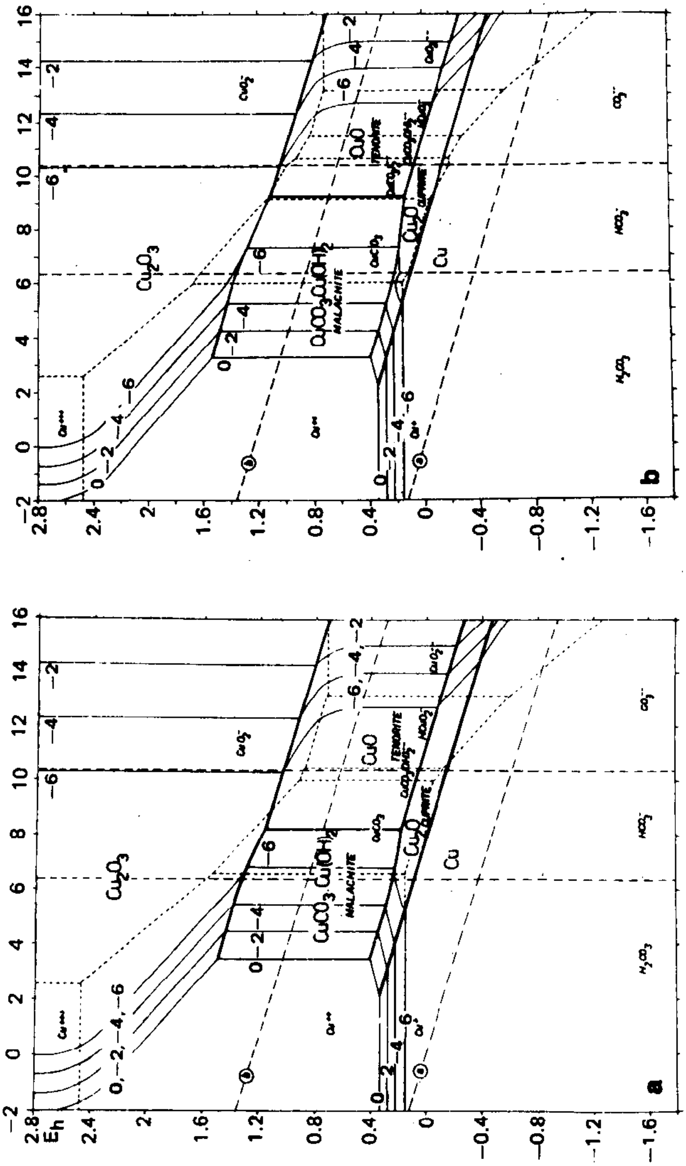
a
b
Eh
2.8
2.4
2
1.6
1.2
0.8
0.4
0
−0.4
−0.8
−1.2
−1.6
−2
0
2
4
6
8
10
12
14
16
Cu+++
Cu++
Cu+
Cu2O3
CuO2−
CuO
TENORITE
Cu2O
CUPRITE
Cu
CuCO3.Cu(OH)2
MALACHITE
CuCO3
HCuO2−
Cu(CO3)2−−
CuO2−−
H2CO3
HCO3−
CO3−−
0, −2, −4, −6
−2
−4
−6

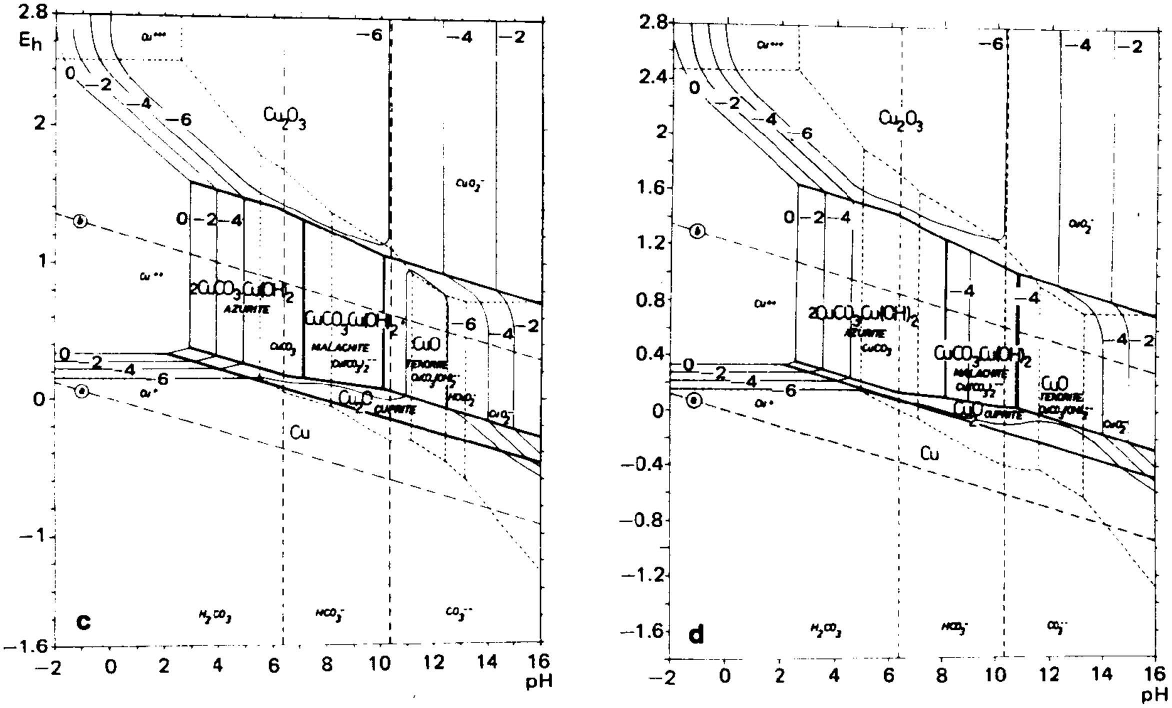

Figure 9. Equilibrium potential-pH diagrams for the ternary system Cu-CO_2-H_2O at 25°C: (a) 10^{-3} mol/liter CO_2 total dissolved (44 ppm); (b) 10^{-2} mol/liter CO_2 total dissolved (440 ppm); (c) 10^{-1} mol/liter CO_2 total dissolved (4400 ppm); and (d) 1 mol/liter CO_2 total dissolved (44,000 ppm).

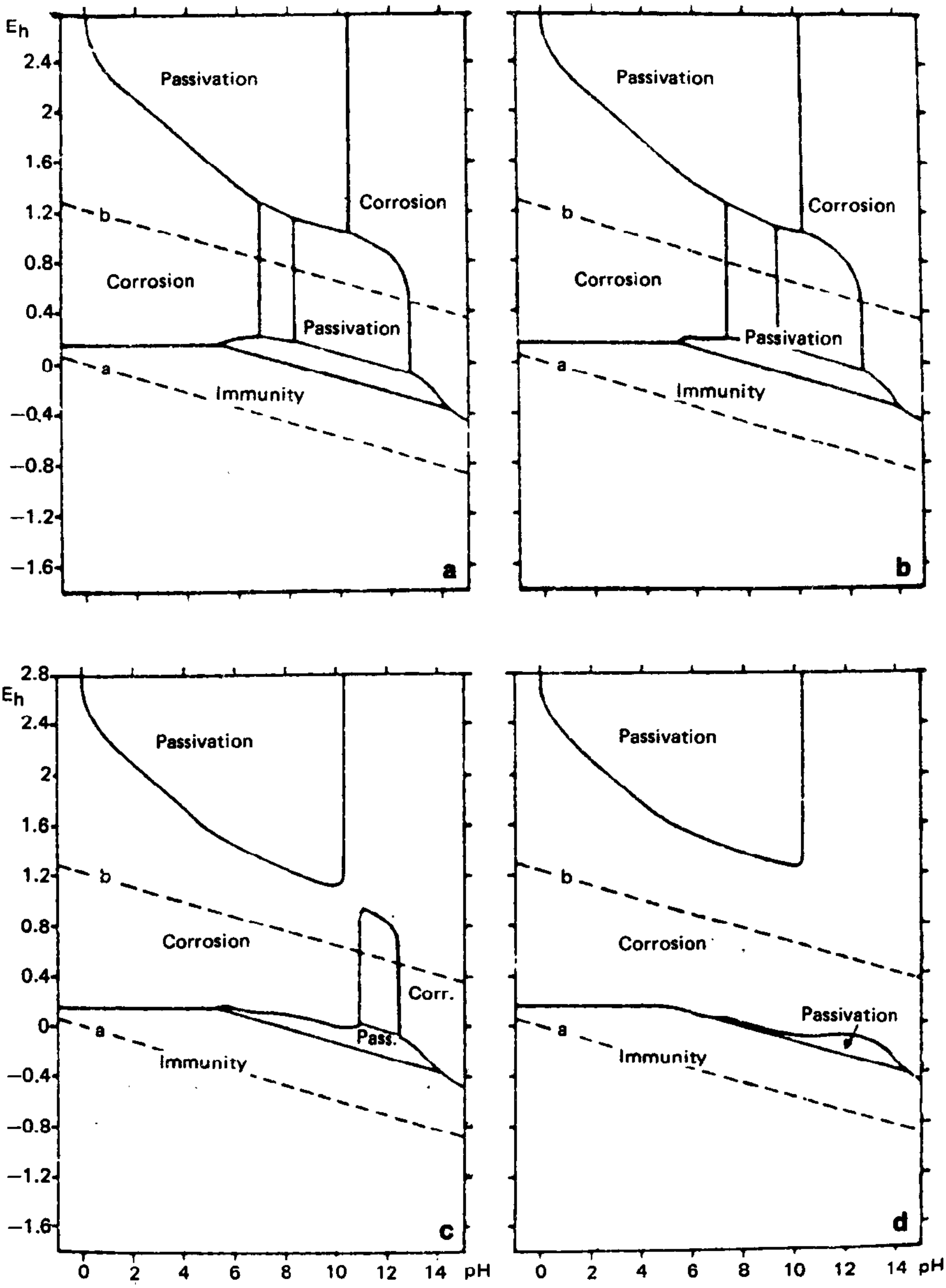

Figure 10. Influence of the content in CO_2 total dissolved on the theoretical conditions of immunity, corrosion, and passivation of copper, at 25°C: (a) 10^{-3} mol g liter^{-1}; (b) 10^{-2} mol g liter^{-1}; (c) 10^{-1} mol g liter^{-1}; (d) 1 mol g liter^{-1}.

5. Electrochemical Equilibria in Aqueous Solutions at Elevated Temperatures[†]

5.1. General Statements

Electrochemical behavior of metals, their oxides, hydroxides, and their ions in the presence of aqueous solutions at elevated temperatures has evoked considerable scientific and technological interest. Numerous reactions take place under such circumstances; not only in the wide field of aqueous corrosion, but also in geochemistry, hydrometallurgy under pressure, the energy industry, desalination of seawater, etc. In this respect, the knowledge of which equilibria will coexist in the system of a metal in an aqueous environment at an elevated temperature would prove a valuable guide, allowing a quick identification of possible and impossible reactions. Thus it was necessary to extend the E–pH equilibrium diagrams originally established for 25°C to higher temperatures. However, there are little thermodynamic data available for species dissolved in water. Many determinations have been carried out between 25 and 60°C, but from 60 to 100°C less is known, with little available information on temperatures above 100°C. Researchers have tried to avoid this problem by establishing E–pH equilibrium diagrams to 300°C by extrapolation, i.e., with the help of thermodynamic data with the reference temperature of 25°C, supplemented by empirical hypotheses on the influence of temperature on molar heat values. By devising a correlation between thermodynamic properties at ordinary and higher temperatures, some authors have established "principles of correspondence," which makes possible the calculation of the entropies of the ions at 60, 100, 150, 200, 250, and 300°C if their entropies at 25°C are known (C. M. Criss and J. W. Cobble,(99,100) I. L. Khodakovski(101,108)).

A different approach to the problem is the determination of temperature coefficients of standard equilibrium potentials of electrochemical reactions [de Béthune(103,104)].

Each of these three methods will be considered with regard to dissolved species at temperatures between 25 and 300°C. Manning and Melling(105) and Lowson(106) have written papers on the first two methods.

Potential–pH equilibrium diagrams for high temperatures are being established in increasing numbers, following these three principal methods, for numerous metals and nonmetals.

5.2. Determination of Standard Free Energy of Reaction at T K

5.2.1. Extrapolation of Thermodynamic Data at 25°C

5.2.1.1. Standard Free Energies of Reaction, $\Delta G^\circ(T)$

The standard free energy of a chemical reaction at constant temperature and pressure can be expressed by the equation of Gibbs–Helmholtz,

$$\Delta G^\circ(T) = \Delta H^\circ(T) - T\Delta S^\circ(T) \qquad (44)$$

[†] See the Addendum to this chapter on page 539, for a general bibliography.

where $\Delta H^\circ(T)$ and $\Delta S^\circ(T)$ are the standard enthalpies and entropies of reaction at temperature T K, respectively.

At 25°C, this equation becomes

$$\Delta G^\circ(298) = \Delta H^\circ(298) - 298\Delta S^\circ(298) \tag{45}$$

The variation of standard free energy produced by bringing the temperature from 298 to T K is obtained by subtracting, member by member, Eqs. (44) and (45):

$$\Delta G^\circ(T) - \Delta G^\circ(298) = \Delta H^\circ(T) - \Delta H^\circ(298) - T\Delta S^\circ(T) + 298\Delta S^\circ(298) \tag{46}$$

Otherwise, the variations of standard enthalpy and entropy of reaction as a function of temperature, with constant pressure, are expressed by the respective equations

$$\Delta H^\circ(T) - \Delta H^\circ(298) = \int_{298}^{T} \Delta C_p^\circ\, dT \qquad \text{(Kirchhoff's equation)} \tag{47}$$

$$\Delta S^\circ(T) - \Delta S^\circ(298) = \int_{298}^{T} \Delta C_p^\circ \frac{dT}{T} \tag{48}$$

where C_p° is the variation of specific molar heat with constant pressure of the total of the reaction bodies (or variation of specific molar heat of reaction).

Equation (46) can, therefore, be written

$$\Delta G^\circ(T) - \Delta G^\circ(298) = -(T\text{-}298)\Delta S^\circ(298) + \int_{298}^{T} \Delta C_p^\circ\, dT - T\int_{298}^{T} \Delta C_p^\circ \frac{dT}{T} \tag{49}$$

or

$$\Delta G^\circ(T) = \Delta G^\circ(298) - (T\text{-}298)\Delta S^\circ(298) + \int_{298}^{T} \Delta C_p^\circ\, dT - T\int_{298}^{T} \Delta C_p^\circ \frac{dT}{T} \tag{50}$$

Equation (50) shows that the free energy of a reaction can be determined at any temperature if the following data are known:

(i) standard free energy of reaction ΔG° at 298 K,
(ii) standard entropy of reaction ΔS° at 298 K,
(iii) influence of temperature, from 298 to T K, on variations of specific molar heat of reaction.

In the case of a chemical reaction, $\Sigma \upsilon M = 0$, the following equations exist between the free energies, the enthalpies, the entropies, and the specific molar heat of the chemical species, M, which takes part in the equation:

$$\begin{aligned} \Delta G &= \Sigma \nu g = \Sigma \nu \mu \\ \Delta H &= \Sigma \nu h \\ \Delta S &= \Sigma \nu s \\ \Delta C_p &= \Sigma \nu c_p \end{aligned} \tag{51}$$

Knowledge of standard free energies of reaction, $\Delta G°(298)$ and standard free entropies of reaction, $\Delta S°(298)$, implies knowledge of specific molar free energies of formation, $g°$ (or standard chemical potentials, $\mu°$), of the reaction bodies, and also their standard entropies, $s°$, at 298 K.

5.2.1.2. *Standard Free Energies of Formation*

The development which was carried out in Section 5.2.1. for standard free energy of reaction, can also be done for the standard free energy of formation, $g°(T)$ of a specific compound. In this way, one obtains the following expression:

$$g°(T) = g°(298) - (T\text{-}298)s°(298) + \int_{298}^{T} c_p° \, dT - T\int_{298}^{T} c_p° \frac{dT}{T} \tag{52}$$

where $g°$ and $s°$ are free energy and specific molar entropy of formation, respectively, at 298 K and $c_p°$ the specific molar heat at constant pressure.

5.2.2. *Method for Integration of the Gibbs–Helmholtz Equation*

5.2.2.1. *Standard Free Energies of Formation*

The standard enthalpy of formation, $h°(T)$, of a substance at temperature T is the integral of its specific molar heat, $c_p°$, between the reference temperature (for example, 298 K) and the temperature under consideration, T K:

$$h°(T) = \int_{298}^{T} c_p \, dT \tag{53}$$

The enthalpy of formation at temperature T can thus be obtained if the variation of the specific molar heat in the interval of the temperature assigned to the integration is known.

The specific heat of substances other than dissolved bodies and ions in aqueous solution are frequently expressed by an empirical or semiempirical expression as follows:

$$c_p° = a + bT + cT^2 + dT^{-2} + \cdots \tag{54}$$

where not all terms appear in all cases. When Eqs. (53) and (54) are introduced, the following expression of standard enthalpy of formation is obtained:

$$h°(T) = aT + \tfrac{1}{2}bT^2 + \tfrac{1}{3}cT^3 - dT^{-1} + k \tag{55}$$

The value of the integration constant, k, is determined by equating T to 298 K and searching in the numerical data table for the corresponding value of $h°(298)$.

Finally, when $h°(T)$ is carried into the Gibbs–Helmholtz equation, the following is obtained:

$$g°(T) = -T\int_{298}^{T} \frac{h°(T)}{T^2}\, dT \tag{56}$$

or

$$g°(T) = -aT \ln T - \tfrac{1}{2}bT^2 - \tfrac{1}{6}cT^3 - \tfrac{1}{2}\, dT^{-1} + k + k'T \tag{57}$$

The value of the second integration constant, k', is obtained by taking $T = 298$ K and searching the value of $g°(298)$ in the special tables.

5.2.2.2. Standard Free Energies of Reaction, $\Delta G°(T)$

The development carried out in 5.2.2.1 can be transposed for the determination of the standard free energy of reaction, $\Delta G°(T)$.

5.3. Specific Heat of Dissolved Species

Since thermodynamic quantities $g°$ (or $\mu°$), $h°$, and $s°$ at 298 K, which intervene implicitly or explicitly in Eqs. (50), (52), and (57) are generally well known, $g°(T)$ and $G°(T)$ can be calculated most often without difficulties, if the thermal dependence of specific molar heat at constant pressure $c_p°(T)$ is known.

This dependence is generally known in the case of solid, liquid, and gaseous neutral chemical bodies, such as elements, oxides, hydroxides, hydrates, chlorides, fluoride, etc. It is not generally known in the case of dissolved species, neutral molecules, and ions charged positively or negatively.

Different hypotheses (e.g., simplifying, empirical, or semiempirical) have been proposed on the influence of temperature on the specific heat of dissolved species.

5.3.1. Hypothesis of Zero Value of Variation of Specific Molar Heat

The hypothesis $\Delta C_p° = 0$ at all temperatures implies that the algebraic sum of the specific molar heat of all reaction substances is zero:

$$\Delta C_p° = \Sigma \nu c_p° = 0 \tag{58}$$

Expressed differently, the sum of the specific molar heat of the substances formed by the reaction equal sum of the specific molar heat of the substances which disappear with the reaction:

$$\Sigma \nu c_p° \text{ (products)} - \Sigma \nu c_p° \text{ (reactants)} = 0 \tag{59}$$

According to Duby,(107) this simplifying hypothesis, designed to facilitate the integration of the van't Hoff equation, is valid only for limited temperature differences and small variations of specific heats. In other cases, it can lead to serious errors, and the potential-pH diagrams based on this hypothesis have to be regarded with reservations.

Also, following Manning and Melling,(105) it can only be a first approximation, usable only when other information is lacking, as ΔC_p° can vary between -100 and $+100$ cal deg^{-1} mol^{-1}.

The error which can result from application of this hypothesis has been stressed by Barnes and Kullerod(108) in the system $H_2S_{aq} = HS^- - H^+$, by Robins and Biernat(109) for the system $HSO_4^- = SO_4^{2-} + H^+$, and by H. C. Helgeson(110,111) in the case of numerous dissociation equilibria.

The postulate $\Delta C_p^\circ = 0$ simplifies Eq. (50), which is then presented as

$$\Delta G^\circ(T) = \Delta G^\circ(298) - (T\text{-}298)\Delta S^\circ(298) \tag{60}$$

which, as observed by Manning and Melling,(105) is the equivalent of the integrated form of the van't Hoff equation:

$$d\frac{\Delta G}{T} = -\Delta H\frac{dT}{T^2} = \Delta H d\, 1/T \tag{61}$$

or

$$\frac{\Delta G^\circ(T)}{T} - \frac{\Delta G^\circ(298)}{298} = \Delta H^\circ(298)\left(\frac{1}{T} - \frac{1}{298}\right) \tag{62}$$

5.3.2. Hypothesis of Constancy of Variation of Specific Molar Heat

This hypothesis implies that the algebraic sum of the specific molar heat, $\Sigma \nu c_p^\circ$, of the reaction substances is a constant which does not depend on the temperature, expressed

$$\Delta C_p^\circ = k \tag{63}$$

where k is a constant.

When Eqs. (47) and (54) are considered, the hypothesis proposed means the energy of reaction varies in proportion to the absolute temperature. Equation (50) then becomes

$$\Delta G^\circ(T) = \Delta G^\circ(298) - (T - 298)\Delta S^\circ(298) + k\left(T - 298 - T\ln\frac{T}{298}\right) \tag{64}$$

According to Manning and Melling,(105) the hypothesis of the constancy of ΔC_p° is applicable in the case of nonionic species in temperatures of 25–300°C. The case of ionic species is more complex, as the specific heat is not constant and a maximum or minimum can be observed between 50 and 100°C, as indicated by several authors.

Concerning the value given to k, the two following cases can be considered:

5.3.2.1. *The Constant Value for the Variation of the Specific Molar Heat of a Reaction Is That Existing at 25°C*

$$\Delta C_p^\circ = k = \Delta C_p^\circ(298) \tag{65}$$

Helgeson[(103)] examined this case in studies on the influence of the temperature on equilibrium constants of numerous reactions of dissociation in aqueous solutions. Manning and Melling[(100)] state that the value $k = \Delta C_p^\circ(298)$ has never been adopted for the establishment of potential–pH diagrams at elevated temperatures. However, according to the results of comparative calculations carried out on the influence of temperature on the dissociation of water and on reactions of hydrolysis of cations of iron and anions of arsenic, the results are similar to those furnished by more complex techniques.

5.3.2.2. *The Constant Value for the Variation of Specific Molar Heat of a Reaction Is the Mean Between the Value at 25°C and the Value at the Maximal Temperature Considered—Method of Criss and Cobble*[(99,100)]

In this hypothesis, the specific heat at the temperature T, $c_p^\circ(T)$ of a dissolved species is assigned a value equal to the mean of the value of $c_p^\circ(T)$ between 298 and T K, as

$$c_p^\circ(T) \equiv c_p^\circ]_{298}^{T} \tag{66}$$

With this value of c_p° introduced into Eq. (48), connecting the entropy to the specific heat, the following is obtained

$$c_p^\circ]_{298}^{T} = \frac{s^\circ(T) - s^\circ(298)}{\ln T/298} \tag{67}$$

which allows the value of $c_p^\circ]_{298}^{T}$ to be calculated with no knowledge of c_p° at any temperature, provided that the entropy at 298 and T K is known.

In the case of nondissolved chemical substances $c_p^\circ]_{298}^{T}$ is, according to Manning and Melling,[(105)] similar to the arithmetic mean of the specific heat between 298 and T K. Either method can be utilized according to the disposal properties of c_p° and s° at elevated temperatures.

In the case of dissolved substances, c_p° is generally unknown and $c_p^\circ]_{298}^{T}$ can only be obtained by applying Eq. (67).

Two empirical equations have been proposed for connecting the entropy at 298.15 K of a dissolved substance $s^\circ(298)$ to the entropy $s^\circ(T)$ at a temperature T K.

5.3.2.2.1. ***Correspondence Principle of Criss and Coble***[(99,100)]. This principle is based on the experimental observation that a standard state can be selected so that the specific molar entropies of the ions are linearly connected at the temperature under consideration, expressed by

$$s_T^\circ = a_T + b_T s_{298}^\circ(\text{abs}) \tag{68}$$

where a_T and b_T are constants† which depend on temperature and category of ion under consideration, and where $s_{298}^\circ(\text{abs})$ is the specific molar entropy at 298.15 K. The entropy of an ion cannot be determined in a direct manner, for an ion is always associated with ions of the opposite sign, and all measurement results from the ionic whole. An arbitrary entropy has been attributed to the proton, H^+, from which calculations can be made of the entropies of the other ions. Latimer(31) has introduced $s_{298}^\circ(H^+) = 0\ \text{cal deg}^{-1}\ \text{mol}^{-1}$ as the basis of the "conventional scale" of the ionic entropies. It has later been stated thermodynamically that the properties of the ions were better explained if another value were attributed to the entropy of the proton, H^+, the best being $s_{298}^\circ(H^+) = -5.0\ \text{cal deg}^{-1}\ \text{mol}^{-1}$.

At 298.15 K (25°C) the correspondence between conventional and absolute entropy is given,

$$s_{298}^\circ(\text{abs}) = s_{298}^\circ(\text{conv}) - 5.0z \tag{69}$$

where z is the ionic charge.

At any temperature, a suitable entropy can be selected for the proton, H^+, which in turn does not adhere to the principle of correspondence.

Substituting absolutes for conventional entropies, Eqs. (67) and (68) can be combined to give the following equation, established by Criss and Cobble:

$$c_p^\circ]_{298}^T = \alpha_T + \beta_T s_{298}^\circ(\text{abs}) \tag{70}$$

With this equation, the value of $c_p^\circ]_{298}^T$ can be determined without calculating $s_T^\circ(\text{abs})$. The knowledge of $s_{298}^\circ(\text{abs})$ is sufficient. In Eq. (70) α_T and β_T depend on temperature and ionic categories.

By considering smaller temperature differences in relation to 298.15 K, Criss and Cobble established an equation which allows the calculation of the specific heat at 298 K:

$$c_{p(298)}^\circ = A + B s_{298}^\circ(\text{abs}) \tag{71}$$

where the specific heat is referred to an "absolute scale," in which $c_{p(298)}^\circ(H^+)(\text{abs}) = 28\ \text{cal deg}^{-1}\ \text{mol}^{-1}$. This will give

$$c_p^\circ(\text{abs}) = c_p^\circ(\text{conv}) + 28z \tag{72}$$

where A and B depend on ionic categories.

5.3.2.2.2. Correspondence Principle of Khodakovski(101,102). By a different method, Khodakovski *et al.* established another correspondence principle of ionic entropies at 298 K and T K, formulated

$$s_T^\circ = a_T - \alpha_T |z| + c_T s_{298}^\circ \tag{73}$$

---

† The values of the constants a, b, α, and β are indicated in the publications of Criss and Cobble.

where $|z|$ is the absolute value of the ionic charge, and a_T, c_T, and d_T are constants which depend on the absolute temperature and ionic categories.†

In Khodakovski's expression of the correspondence principle of the entropies, s° is the conventional entropy based on $s^\circ_{298}(\mathrm{H}^+) = 0$ cal deg^{-1} mol^{-1}. Following the author, the validity of Eq. (73) has been confirmed up to 300°C.

Khodakovski has also expressed the relation between specific heat and entropy at 298.15 K as

$$c^\circ_{p(298)} = a - d|z| - \tfrac{2}{3}s^\circ_{298} \tag{74}$$

5.3.3. *Proportionality between Specific Molar Heat and Temperature—Method of Khodakovski*

In his studies on free energies of formation of ions in aqueous solutions, Khodakovski[(101,102)] has shown that specific molar heat is proportionate to the absolute temperature, as

$$c^\circ_p = bT \tag{75}$$

where b is a constant which can easily be deduced from the experimental values of c°_p at any temperature. It is preferable, however, to use the reference temperature of 298.15 K, as it gives the best agreement between calculated values and experimental values until 300°C.

Equation (75) can then be written

$$c^\circ_p = d^\circ_{p(298)}\frac{T}{298.15} = 3554.10^{-3}\,Tc^\circ_{p(298)} \tag{76}$$

Equation (50) then becomes

$$\Delta G^\circ(T) = \Delta G(298) - (T\text{-}298)\Delta S^\circ(298) - \frac{\Delta C^\circ_{p(298)}}{2 \times 298.15}(T\text{-}298)^2 \tag{77}$$

or

$$\Delta G^\circ(T) = \Delta G^\circ(298) - (T\text{-}298)\Delta S^\circ(298) - 1677.10^{-3}\Delta C^\circ_{p(298)}(T\text{-}298)^2 \tag{77}$$

5.4. Determination of Temperature Coefficient of Standard Equilibrium Potential—Method of de Béthune[(103,104)]

The temperature coefficient of the standard equilibrium potential, E°_0, of an electrochemical reaction can be experimentally defined in relation to a standard hydrogen electrode in two ways:

(i) in relation to the reference hydrogen electrode brought to the same temperature as the electrode being studied, i.e., the "isothermal coefficient" of de Béthune, or

(ii) in relation to the reference hydrogen electrode kept at a given temperature, i.e., the "thermal coefficient" of de Béthune.

---

† Values of constants a_T, c_T, and d_T are indicated in publications of Khodakovski. Values of the constants α, β, A, and B are indicated in publications of Criss and Cobble.

de Béthune has shown that the value of these two coefficients can be determined from thermodynamic data at 298.15 K. Only the practical results of theory will be presented here, which could help to establish E–pH equilibria diagrams at high temperatures.

The "isothermal coefficient" of temperature of standard equilibrium potential includes two terms:

(i) the "first" isothermic coefficient, which is the first to be derived from standard equilibrium potential in relation to the absolute temperature is:

$$\left(\frac{dE_0^\circ}{dT}\right)_{\text{iso}} = \frac{\Delta S^\circ(298)}{nF} \tag{78}$$

(ii) the "second" isothermal coefficient, which is the second derivative of the same standard equilibrium potential, is

$$\left(\frac{d^2E_0^\circ}{dT^2}\right)_{\text{iso}} = \frac{\Delta C^\circ_{p(298)}}{nFT} \tag{79}$$

where ΔS° and ΔC_p° are, respectively, the variation of the entropy:

$$\Delta S^\circ_{(298)} = bS^\circ_B + (m-n)s^\circ_{H^+} + n/2s^\circ_{H_2} - as^\circ_A - cs^\circ_{H_2O} \tag{80}$$

and the variation of specific heat

$$\Delta C^\circ_{p(298)} = bc^\circ_{p,B} + (m-n)c^\circ_{p,H^+} + n/2c^\circ_{p,H_2} - ac^\circ_{p,A} - cc^\circ_{p,H_2O} \tag{81}$$

at 298 K of the general chemical reaction

$$a\mathrm{A} + c\mathrm{H_2O} = b\mathrm{B} + (m-n)H^+ + n/2H_2 \tag{32}$$

which is carried out at the two electrodes of the simple isothermic galvanic cell:

$$\text{shc}\|\text{electrolyte}|\text{electrode}^\dagger \tag{82}$$

where nF and T are the number of faradays transported at reaction (32) and the absolute temperature at which (82) applies, respectively.

Finally, the influence of the temperature on the standard equilibrium potential of an electrochemical reaction can be expressed

$$E^\circ_{0(t)} = E^\circ_{0(25)} + \left(\frac{dE_0^\circ}{dT}\right)_{\text{iso}}(t-25) + \tfrac{1}{2}\left(\frac{d^2E_0^\circ}{dT^2}\right)(t-25)^2 \tag{83}$$

or

$$E^\circ_{0(T)} = E^\circ_{0(298)} + \left(\frac{dE_0^\circ}{dT}\right)_{\text{iso}}(T-298) + \tfrac{1}{2}\frac{d^2E_0^\circ}{dT^2}(T-298)^2 \tag{84}$$

The "thermal coefficient" of temperature of the standard equilibrium potential of an electrochemical reaction is defined

$$\left(\frac{dE_0^\circ}{dT}\right) = \frac{\Delta S^{*\circ}_{E298}}{nF} \tag{85}$$

---

† The double vertical signifies that the potential of liquid junction has been eliminated or minimized, i.e., by use of appropriate saline bridges.

when, in the thermal cell

$$\begin{aligned}&\mathrm{M}(T_1)|\text{electrode}(T_1)|\text{electrolyte}(T_1)|\text{electro-}\\&\quad\text{lyte}(T_2)|\text{electrode}(T_2)|\text{electrode}(T_1)|\mathrm{M}(T_1)\end{aligned} \tag{86}$$

the effects of metallic thermocouple, thermodiffusion (Soret effect), and thermal liquid junction potential are eliminated.

In Eq. (85), $\Delta S^{*\circ}_{E_{298}}$ represents the standard ionic entropy of electrochemical transport for the electrochemical reaction carried out in the thermal cell (86). The standard entropy of electrochemical transport $S^{*\circ}_E$ (H^+) of the H^+ ion being equal to -4.48 cal deg^{-1} mol^{-1}, the standard entropies of electrochemical transport $S^{*\circ}_E$ of the other ions are obtained by

$$S^{*\circ}_E = s^\circ + z(-4.48)\,\text{cal deg}^{-1}\,\text{mol}^{-1} \tag{87}$$

where z is the ionic charge including sign.

5.5. E–pH Equilibria Diagrams of the Binary System Fe–H_2O, at High Temperatures

The Fe–H_2O system studied by Townsend[118] was selected arbitrarily as an example for E–pH diagrams at elevated temperatures. According to the method of Criss and Cobble, diagrams were established of the E–pH equilibria of the Fe–H_2O system in relation to various temperatures, including three dissolved species (Fe^{2+}, $HFeO_2^-$, and Fe^{3+}) and three condensed bodies (Fe, Fe_3O_4, and α-Fe_2O_3). The inaccuracy affecting the value of the standard entropy of the $HFeO_2^-$ ion is indicated by a double equilibrium line for every reaction in which this ion takes place. The scale of the electrode potentials refers to the standard "conventional" state where the potential for the standard hydrogen electrode is equal to 0.000 V at all temperatures.

The influence of temperature on the stability of the system is characterized by the following:

(i) expansion of the domain of corrosion in strong alkaline environment by enlargement of the domain of existence of the $HFeO_2^-$ anion to the disadvantage of Fe, Fe_3O_4, and α-Fe_2O_3, with a maximum of enlargement around 200°C;

(ii) decrease of stability of the Fe^{2+} cation vs. Fe, Fe_3O_4, and α-Fe_2O_3, and of the Fe^{3+} cation vs. α-Fe_2O_3, and an improvement of the stability of the condensed bodies in an acid environment;

(iii) increase of relative stability of the Fe^{2+} cation versus the Fe^{3+} cation by a raising of the border between these two dissolved species.

The expansion of the domain of "alkaline corrosion" by elevating the temperature has been confirmed experimentally by many authors. The speed of corrosion of steel, relatively low in the presence of caustic soda NaOH at ordinary temperature, strongly increases from 25 to 105°C. However, at higher temperatures, i.e., 300–350°C, the speed decreases. These facts, illustrating a maximum corrosion speed between 105 and 300°C, are in good qualitative

T211 B 3

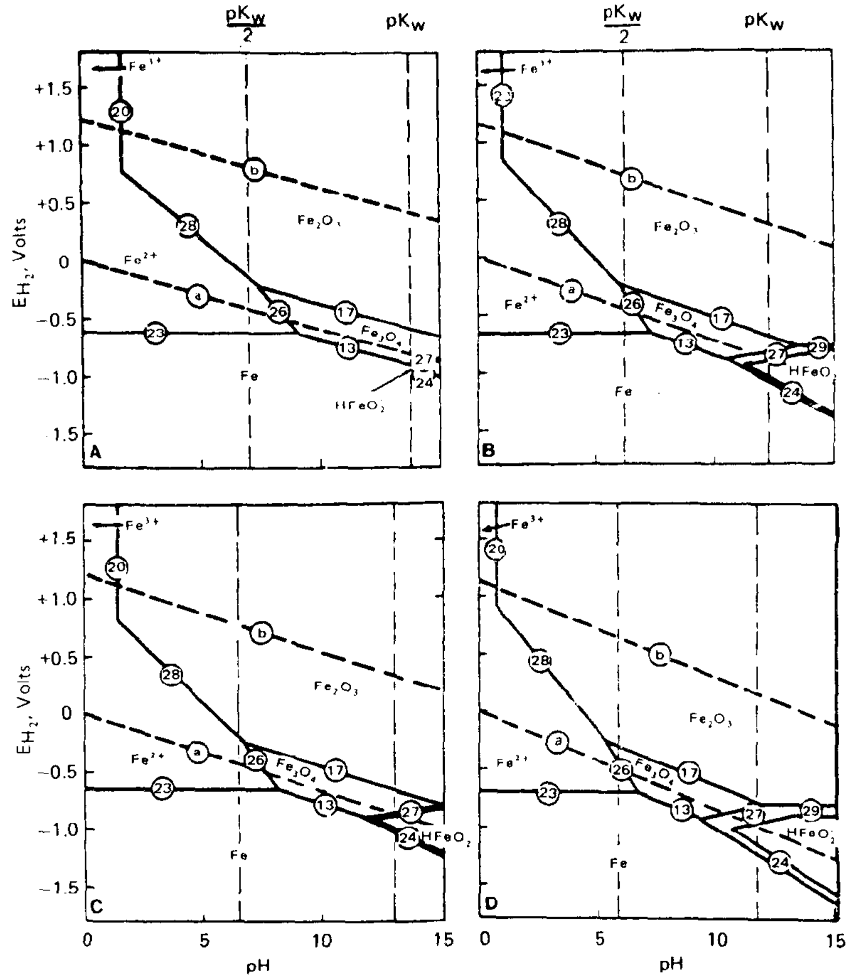

Figure 11. Potential-pH diagrams for Fe-H_2O systems at elevated temperatures. (A) Conventional potential-pH diagram at 25°C for Fe-H_2O, constructed according to Pourbaix assuming Fe, Fe_3O_4, and Fe_2O_3 as solid substances. Activities of dissolved substances taken as 10^{-6} mol. Pressure taken as 1 atm. (B)Potential-pH diagrams as in Figure 11A constructed for 60°C using the method of Criss and Cobble, taking $\bar{S}^{\circ}_{HFeO_2}$ (25) = 10 ± 5 e.u. (C) Potential-pH diagram as in Figure 11B constructed for 100°C. (D) Potential-pH diagram as in Figure 11B constructed for 150°C. (After H. E. Townsend.⁽¹¹⁸⁾)

agreement with the maximum stability of the $HFeO_2^-$ anion, predicted by the E-pH equilibrium diagrams (see Figures 11-13) of Townsend.⁽¹¹⁸⁾ These diagrams have served as a basis of discussion for cathodic protection at elevated temperatures and caustic fragility. In respect to cathodic protection, the elevation of temperature, which has little effect on thermodynamic immunity in a neutral or acid environment, can change them noticeably in an alkaline

T277 A 3

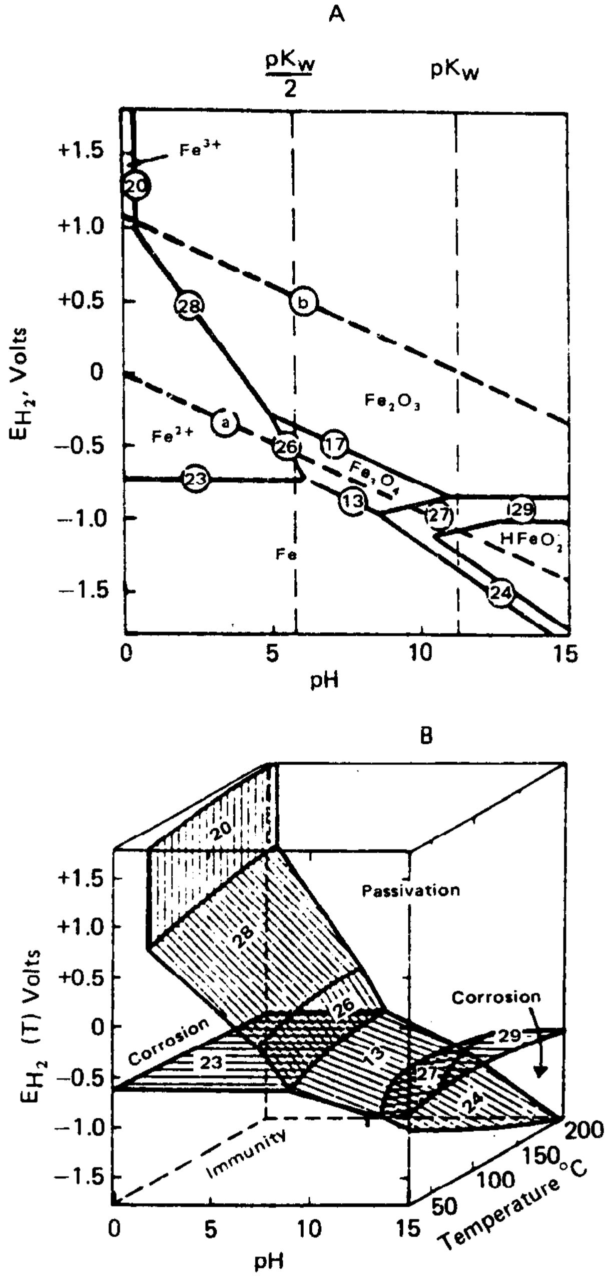

Figure 12. Potential-pH diagrams for Fe-H_2O systems at elevated temperatures. (A) Potential-pH diagram as in Figure 11B constructed for 200°C. (B) Potential-pH-temperature diagram formed by combining Figures 11A, 11B, 11C, 11D, and 12A and assuming passivation by films of Fe_3O_4 and Fe_2O_3, taking $\bar{S}^{\circ}_{HFeO_2^-}$ (25) = 10 e.u. (After H. E. Townsend.[118])

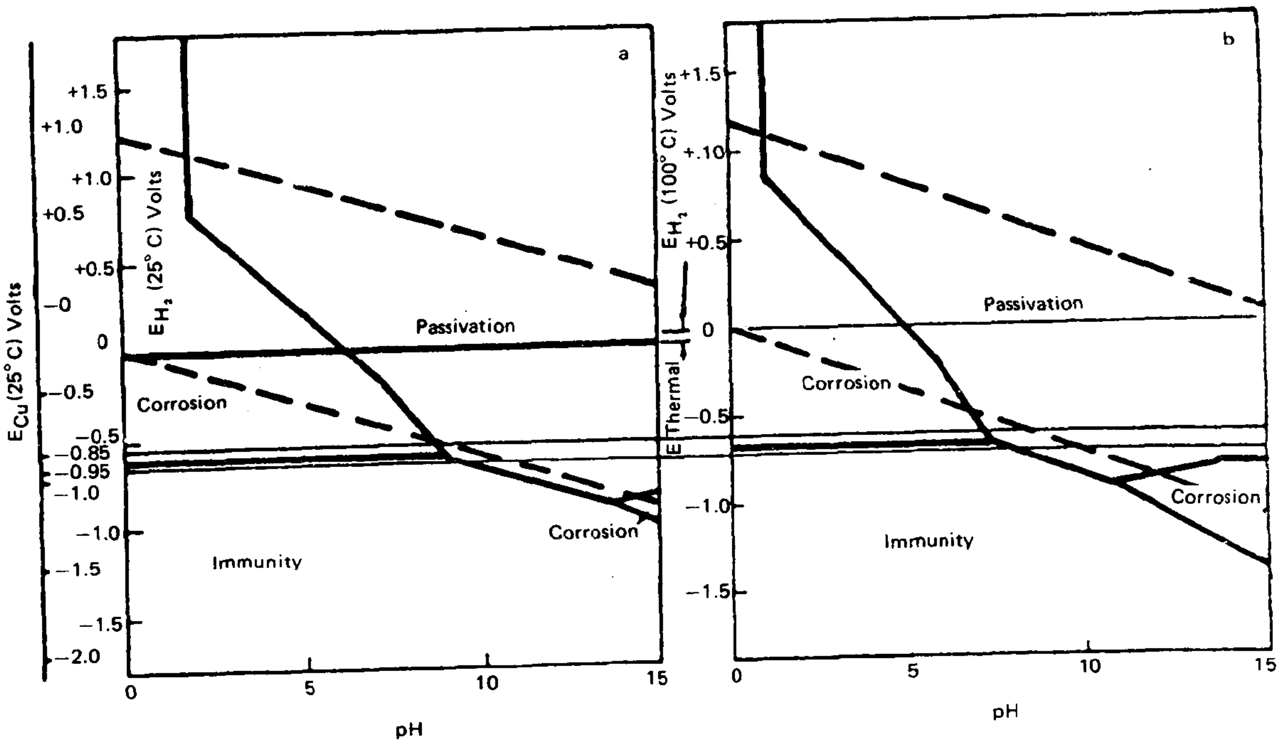

Figure 13. Comparison of potential-pH diagrams at (a) 25°C and (b) 100°C with respect to the same potential scale assuming passivation by films of Fe_3O_4 and Fe_2O_3 taking $S^{\circ}_{HFeO_2^-}$ (25) = 10 e.u. Copper-saturated copper sulfate potential scale at 25°C at far left. (After H. E. Townsend.[118])

environment. Cathodic protection of iron, even disregarding the embrittlement phenomena through hydrogen, may become, in alkaline media, more difficult at elevated temperatures, where more negative potentials are needed to insure immunity.

Regarding caustic embrittlement, the diagrams show that the three crucial factors for a catastrophic situation are:

(i) elevated temperatures,
(ii) concentrated solutions of NaOH,
(iii) critical values of potential (−950 to −750 mV_{she}).

These correspond well with the stability of the $HFeO_2^-$ anion. Townsend has concluded that the diagrams correctly predict the corrosion of iron and steel in hot concentrated environments of NaOH, that with stability of the $HFeO_2^-$ ion. This can help define requirements of immunity in alkaline and hot environments for safe cathodic protection.

6. Applications

6.1. Thermodynamic Nobility and Practical Nobility

Metals and nonmetals with an immunity area below line *a* (see, e.g., Figure 11) (H_2–H_2O or H_2–H^+ equilibrium under pressure of 1 atm) can be oxidized with corrosion or passivation and release of hydrogen. The affinity of that reaction will be stronger, the more negative the immunity potential is (i.e., Pb, Sn, Ni, Co, Cd, Fe, Cr, Zn, Mn, Al, Mg). The metals whose immunity extends above line *a*, but not reaching line *b* (H_2O–O_2 equilibrium under pressure of 1 atm) cannot be oxidized in water and aqueous solutions with evolution of hydrogen, but they can be oxidized in the presence of oxygen and other oxidizers. This is easily facilitated as their area of immunity approaches line *b* (i.e., As, Sb, Bi, Cu, Ag, Hg). Metals whose immunity passes beyond line *b* generally cannot be corroded by aqueous solutions containing oxygen or oxidizers with a reduction potential lower than the immunity potential of the metal (i.e., Au).

The degree of nobility of a metal or nonmetal can therefore be connected to the extent of its area of thermodynamic immunity. Otherwise, disregarding kinetic factors, and supposing passivation layers are protective, it can be seen that nobility may result not only from immunity, but also from passivation.

Figure 14 shows theoretical "corrosion, immunity, and passivation" diagrams for 43 metals and nonmetals, the most frequently encountered in practice, in the order of decreasing thermodynamic nobility. The corrosion areas are represented by fine hatching with lines descending from right to left for the most frequent case of corrosion by dissolution, and by traits descending from left to right for the rare case of corrosion by gasification. Passivation areas have been marked by coarse hatching with lines descending from left to right

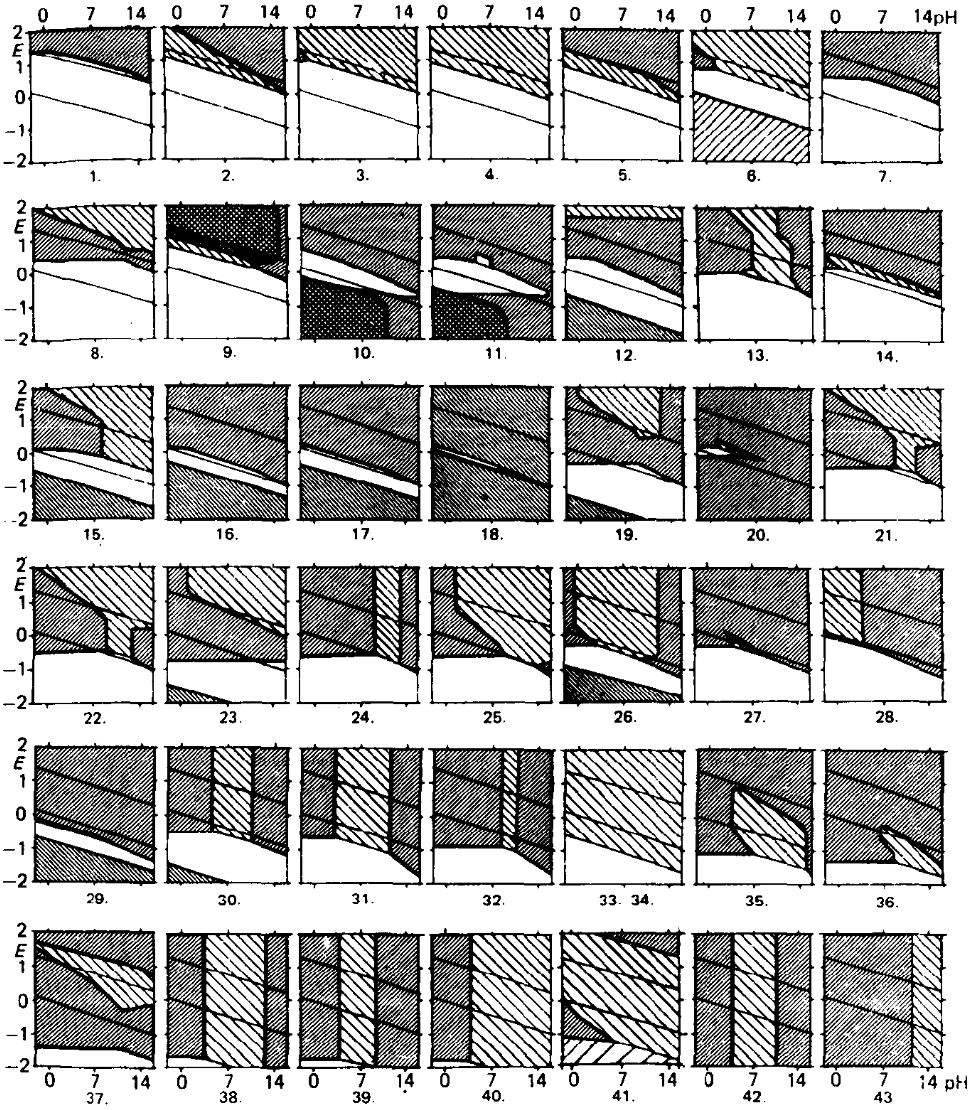

Figure 14. Corrosion, immunity, and passivation domains of metals and nonmetals classified in order of thermodynamic nobility. 1, Gold; 2, iridium; 3, platinum; 4, rhodium; 5, ruthenium; 6, palladium; 7, mercury; 8, silver; 9, osmium; 10, selenium; 11, tellurium; 12, polonium; 13, copper; 14, technetium; 15, bismuth; 16, antimony; 17, arsenic; 18, carbon; 19, lead; 20, rhenium; 21, nickel; 22, cobalt; 23, thallium; 24, cadmium; 25, iron; 26, tin; 27, molybdenum; 28, tungsten; 29, germanium; 30, indium; 31, gallium; 32, zinc; 33, niobium; 34, tantalum; 35, chromium; 36, vanadium; 37, manganese; 38, zirconium; 39, aluminum; 40, hafnium; 41, titanium; 42, beryllium; 43, magnesium. Key: ▨, corrosion yielding soluble products; ▧, corrosion yielding gaseous products; ▧, passivation by a film of oxide or hydroxide; ▨, passivation by a film of hydride; ☐, immunity. (After M. Pourbaix.(33,34))

Table 1
Classifications of Metals and Nonmetals in Order of Thermodynamic Nobility[a]

	A (Immunity)	B (Immunity and passivation)	
	Noble metals		
1	Gold	Rhodium	1
2	Iridium	Niobium	2
3	Platinum	Tantalum	3
4	Rhodium	Gold	4
5	Ruthenium	Iridium	5
6	Palladium	Platinum	6
7	Mercury	Titanium	7
8	Silver	Palladium	8
9	Osmium	Ruthenium	9
10	Selenium	Osmium	10
11	Tellurium	Mercury	11
12	Polonium	Gallium	12
13	Copper	Zirconium	13
14	Technetium	Silver	14
15	Bismuth	Tin	15
16	Antimony	Copper	16
17	Arsenic	Hafnium	17
18	(Carbon)	Beryllium	18
19	Lead	Aluminum	19
20	Rhenium	Indium	20
21	(Nickel)	Chromium	21
22	(Cobalt)	Selenium	22
23	Thallium	Technetium	23
24	Cadmium	Tellurium	24
25	Iron	Bismuth	25
26	Tin	Polonium	26
27	Molybdenum	Tungsten	27
28	Tungsten	Iron	28
29	Germanium	(Nickel)	29
30	Indium	(Cobalt)	30
31	Gallium	Antimony	31
32	Zinc	Arsenic	32
33	Niobium	(Carbon)	33
34	Tantalum	Lead	34
35	Chromium	Rhenium	35
36	Vanadium	Cadmium	36
37	Manganese	Zinc	37
38	Zirconium	Molybdenum	38
39	Aluminum	Germanium	39
40	Hafnium	Vanadium	40
41	Titanium	Magnesium	41
42	Beryllium	Thallium	42
43	Magnesium	Manganese	43
	Non-noble metals		

---

[a] Following M. Pourbaix.(33,34)

for the frequent case of passivation by formation of oxide or hydroxide, and with lines from right to left for the rare case of passivation by formation of hydride. Immunity areas are represented in white.

Pourbaix has established in Table 1 a double classification based, on one side, on the criterion of the extent of the domain of immunity and the distance to the H_2–H_2O equilibrium (line *a* of the diagrams): classification by order of thermodynamic nobility (column A); and, on the other side, on the criterion of combined extent of immunity and passivation domains (in absence of chloride): classification by order of practical nobility (column B).

The 23 elements of column A whose immunity is in common with the stability of water can be considered as possessing, to a decreasing degree, thermodynamic nobility. This agrees with the classical "scale of dissolution potentials" of Nernst (Figure 1).† However, neither the classification of column A nor the classification of Nernst correspond well to experienced facts of corrosion. Rather, the metals which, according to the above-mentioned rules, ought to corrode often remain free of corrosion, with the converse effects as well. The classification of column B, according to practical nobility, generally appears to conform to reality to a greater degree. It brings out considerably nobility conferred by passivation on the following metals: Nb, Ta, Ti, Ga, Sn, Hf, Be, Al, In, Cr.

The classifications indicated in columns A and B of Table 1 can only be accepted with certain reservations because of the following:

(i) Diagrams of binary electrochemical equilibria on which they are based will be improved with the development and refinement of knowledge in chemistry and thermodynamics. For certain elements (i.e., Ni and Co), the thermodynamic data available are insufficient to consider the diagrams totally accurate. These two metals passivate more easily than their *E*–pH equilibria diagrams predict.

(ii) Reaction of corrosion and passivation can be irreversible. The circumstances of real stability of an element may be more extended than what is indicated by the area of immunity (i.e., C).

(iii) The protective power of oxides, hydrated oxides, and hydroxides of numerous metals can be ruined in aqueous solutions whose chloride content exceeds a critical value. Thus chlorides frequently are harmful to passivation and provoke a localized corrosion, with a subsequent lowering of potential. Classification B, therefore, can be considered reasonably valid only in solutions low in chloride.

6.2. Passivation and Activation of Metals

As shown by Pourbaix,(3,8,33,34) metals which passivate by oxidization and activate by reduction are those which have a higher oxide less soluble than a lower oxide and present a corrosion domain in a triangular form.

---

† Dissolution potentials refer to the case where the metal, Me, is in equilibrium with an aqueous solution of pH = 0, where M^{n+} cation is equal to 1.

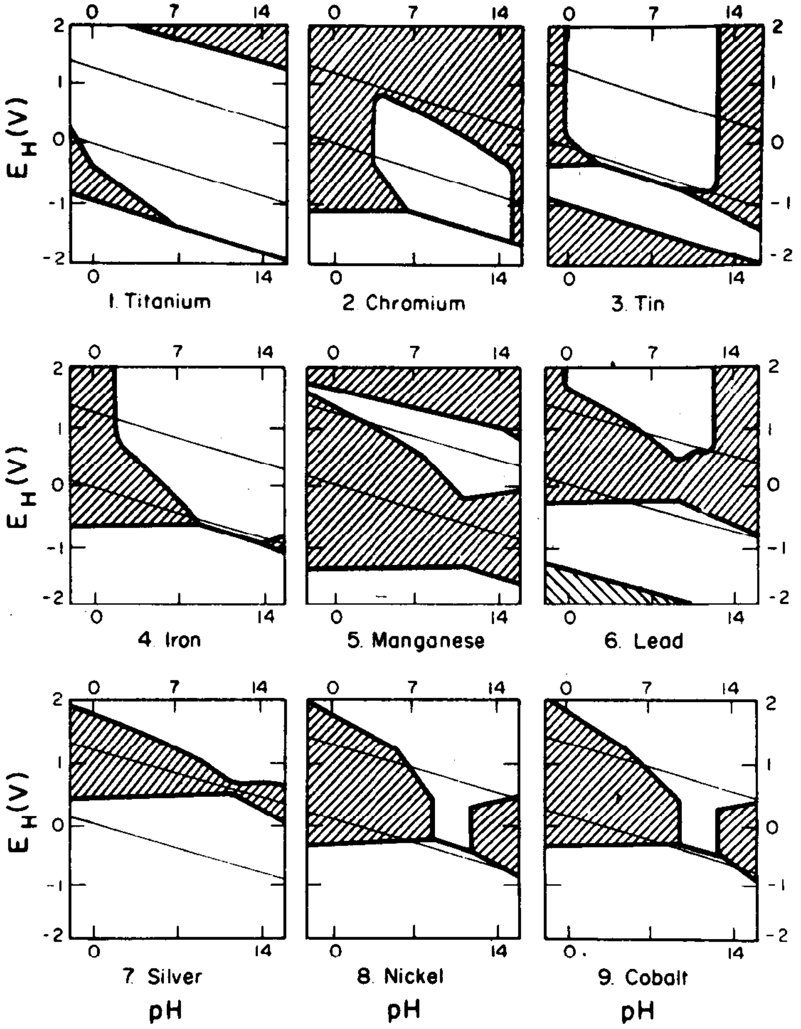

1. Titanium
2. Chromium
3. Tin
4. Iron
5. Manganese
6. Lead
7. Silver
8. Nickel
9. Cobalt

Figure 15. Passive and active metals (after M. Pourbaix[33,34]).

By order of decreasing passivation ability, these are Ti, Cr, Sn, Fe, Mn, Pb, Ag, Ni, and Co (Figure 15).

For titanium, chromium, and tin, whose lower limit of passivation is situated either totally or partially below the stability of water, passivation is theoretically easy and can be realized spontaneously, even in the absence of an oxidizer.

For iron, passivation requires an oxidizing action, slight for a pH between 9 and 13, strong for other pH values.

Passivation of manganese, lead, silver,† nickel, and cobalt can be achieved only by an energetic oxidizing action. Nickel, and perhaps cobalt, will often passivate at electrode potentials inferior to those foreseen by the binary E–pH diagram of Figure 15.

Hoar(145) explains this premature passivation ability of nickel by the fact that, as the electrode potential of nickel increases in the corrosion area, the reaction of dissolution could become more difficult kinetically. Thus as soon as the potential corresponding to the prolonging of the Ni–$Ni(OH)_2$ equilibrium is reached, *nickelous hydroxide,* $Ni(OH)_2$, *is formed in metastable conditions.* This is valid with porous layers, where the pH of the electrode is the same as that of the solution. This is shown in the Fe-saturated solution of the $FeCl_2$ system studied by Sathler.(70)

However, when there is a tight formation, as, for instance, in the case of the Pb/H_2SO_4 system (Ruetschi and Angstadt(181)), the pH at the interface electrode–passivating layer becomes higher than the pH of the solution through the diffusion of OH^- anions. Hence the interpretation of Hoar cannot be applied.

Conversely, once titanium, chromium, and tin are passivated, they can be activated only with difficulty. They generally remain passive even after the cessation of the oxidizing action.

Iron between a pH level of 9 and 13 can also be activated only with difficulty, but easily outside these values.

The five other metals (Mn, Pb, Ag, Ni, and Co) are easily activated. Activation will always produce corrosion in manganese, a non-noble metal whose domain of immunity exists only at low electrode potentials. Activation of the other four metals produces corrosion only if there remains a strong oxidizing action, at varying intensities depending on the metal, which maintains the electrode potential in the corrosion domain.

6.3. Efficiency of Oxidizing Inhibitors of Corrosion

Thermodynamic guides can also be applied to the study of theoretical conditions of the efficiency of oxidizing inhibitors. These inhibitors act through the elevation of the electrode potential of the metal so that it is preserved from corrosion in the domain of passivation. Oxidization implies a reduction of the oxidizer, so the protective action of an oxidizing inhibitor can be efficient if it is likely to be reduced with the formation of a solid derivative. By depositing itself on the weak points of the metal surface, this solid body is able to produce passivation or improve the protective power of the preexisting oxide layer. However, if the solid derivatives are not protective, passivation is not perfect and will lead to localized corrosion with intensified corrosion on unprotected surfaces. When derivates stemming from reduction of oxidizing inhibitor are soluble, there will be an accelerated attack on the metal by corrosion.

---

† Despite difficult passivation, silver resists corrosion because of the extent of its immunity.

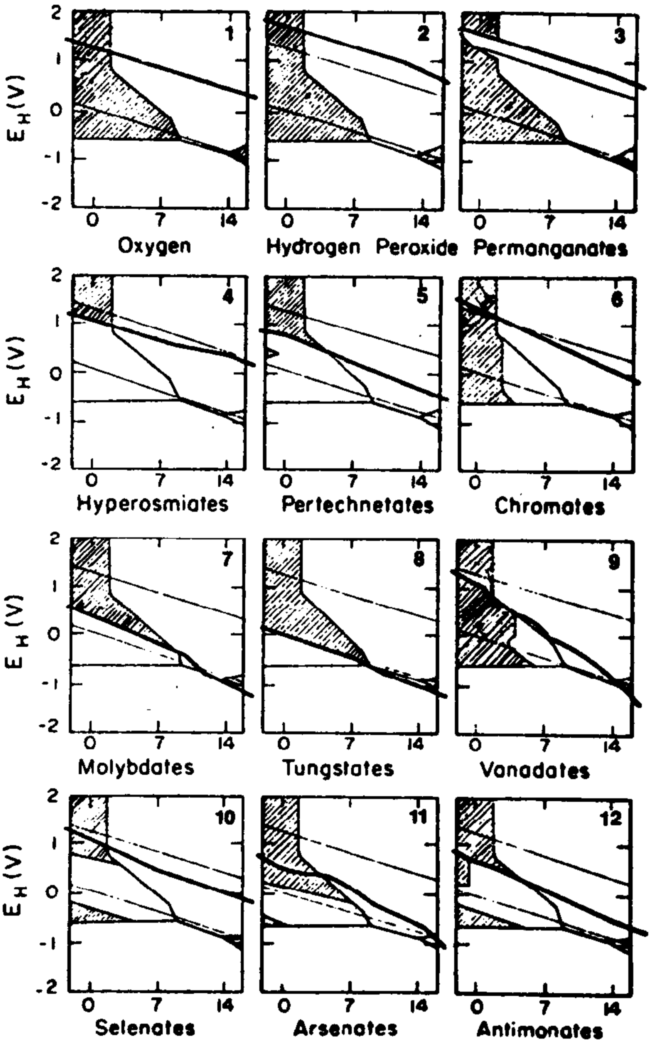

Figure 16. Oxidizing corrosion inhibitors (after M. Pourbaix[(33,34)]).

In the case of a perfect protective passivation, the electrode potential of the metal will rise to the reduction potential of the inhibitor.† When this reaction is reversible, the equilibrium potential of the reaction is dealt with.

---

† Van Rysselberghe calls "reduction potential" the electrode potential above which the reaction takes place with considerable speed (i.e., 10^{-8} A cm^{-2}) in the direction of reduction. "Oxidation potential" is the potential above which the reaction takes place with noticeable speed in the direction of oxidation. In the case of a perfect reversible reaction, where the speed is noticeable as soon as the electrode potential deviates from the equilibrium value, the reduction and oxidation potentials take the same basic value. This is the "oxidoreduction potential," which is identified with the "equilibrium potential of the reaction."

Pourbaix(3,8,33,34,146) has shown that the study of the efficiency of oxidizing inhibitors can be carried out by superimposing theoretical corrosion–immunity–passivation diagrams of the metal to be protected onto the diagrams of E-pH equilibria *indicating the stability of these substances and the solid* bodies likely to be generated by their reduction. The application of this method to 12 oxidizing substances (oxygen, oxygenated water, permanganate, hyperosmiate, pertechnétate, chromate, molybdate, tungstate, vandate, selenate, arsenate, and antimonate) has led Pourbaix to the composite diagrams of Figure 16. The broad lines indicate the potentials above which the oxidizing inhibitor can be reduced. Cross-hatching indicates the parts of the corrosion domain of iron where reduction products of the oxidizer are not solid bodies (i.e., $CrO_4^{2-} \rightarrow Cr^{3+}$ and Cr^{2+}, $TeO_4^- \rightarrow Te^{2+}$, etc.). White indicates theoretical stability of solid bodies. If the reaction of the reduction of oxidizers is reversible and the solid bodies are providing a protective coating, the cross-hatched zones indicate the theoretical conditions of corrosion, and the noncrosshatched zones the theoretical domains of noncorrosion (immunity and protective passivation combined).

The examination of the diagrams of Figure 16 leads to the following conclusions:

6.3.1. Influence of Oxygen (Figure 16, Part 1)

In the case of solutions free from chloride and other substances harmful to the protective action of the iron oxide films, the oxygen can only be passivating at a pH close to 9–13. At other pH values, it can be passivating or activating.

6.3.2. Influence of Oxygenated Water (Figure 16, Part 2)

The presence of weak quantities of oxygenated water (0.3 g liter^{-1}) in water (pH ~ 6) provokes a strong intensification of corrosion. In the presence of an aqueous solution containing a sufficiently strong quantity of oxygenated water (3 g liter^{-1}, pH 3–4), iron is passivated. In the first case, the corrosion of iron is produced through a reduction of oxygenated water to water. In the second case, the passivated iron provokes a catalytic decomposition of oxygenated water to water and oxygen. Because of this decomposition, the content in oxygenated water decreases quickly, and the passivating action of the oxygenated water with a strong dose can only be temporary.

6.3.3. Influence of Permanganate (Figure 16, Part 3)

In the presence of water containing small quantities of permanganate (0.3 g liter^{-1}, pH ~ 7), there is a strong intensification of corrosion. In the presence of water containing larger quantities of permanganate, the metal is passivated.

In the first case, the corrosion of iron is produced because of the reduction of the permanganate ion MnO_4^- into manganous ion Mn^{2+}. In the second case, a deposition of bioxide of manganese is produced on the metal, which forms on weak points of the passivating film of iron oxide and improves its protective qualities. The action of large quantities of permanganate is permanent.

6.3.4. Influence of Hyperosmiates and Pertechnetates (Figure 16, Parts 4 and 5)

Hyperosmiates, OsO_4^{2-}, and pertechnetates, TeO_4^-, efficiently inhibit corrosion of iron, because of the inclusion in the iron oxide layer of depositions of oxide OsO_2 and osmium or of oxide TeO_2, which is particularly stable at all pHs, and of technétium. The conclusion concerning the inhibiting efficiency of the pertechnetates agrees with the experimental observations of Cartledge.(147,148)

6.3.5. Influence of Chromates (Figure 16, Part 6)

Although less efficient than the hyperosmiates and pertechnetates, chromates are efficient inhibitors, if the solution is free of chloride and the pH is higher than 3–4. This efficiency is connected to the incorporation of Cr_2O_3 diversely hydrated into the layer of iron oxide, γ-Fe_2O_3, as verified by Hoar and Evans(149) and systematically by Brasher.(150)

6.3.6. Influence of Molybdates, Tungstates, and Vanadates (Figure 16, Parts 7–9)

Molybdates and tungstates are less efficient than their homologous chromates, but they can be passivating in a weak oxidizing environment (even very acid), which is in harmony with the experimental results obtained by Kodama and Ambrose(151) in regard to molybdates. Vanadates are only slightly efficient, if at all.

6.3.7. Influence of Selenates, Arsenates, and Antimonates (Figure 16, Parts 10–12)

These substances have a protective action in weak or nonoxidizing environment, even very acid arsenates which normally corrode with a release of hydrogen. HCl, H_2SO_4 and H_3PO_4 retard corrosion of iron and steel in the presence of acid minerals. The protective action of selenates, arsenates, and antimonates results from depositing cement on the metal, formed by Se, As, and Sb, respectively. Regarding As, the predictions are in harmony with experimental results reported by Conroy,(152) Poutilova,(153) and Pourbaix *et al.*(154) In the case of Sb, the inhibiting action of the antimonates has been studied by Piontelli and Fagnani(155) and Burns and Bradley.(156)

6.4. Localized Corrosion of Copper and Iron

6.4.1. Localized Corrosion of Copper in Presence of Water

Copper pipes used for cold water distribution sometimes experience severe pittings, first studied by Campbell(168) and May.(169) The pits contained white cuprous chloride CuCl or nantokite and red cuprous oxide Cu_2O or

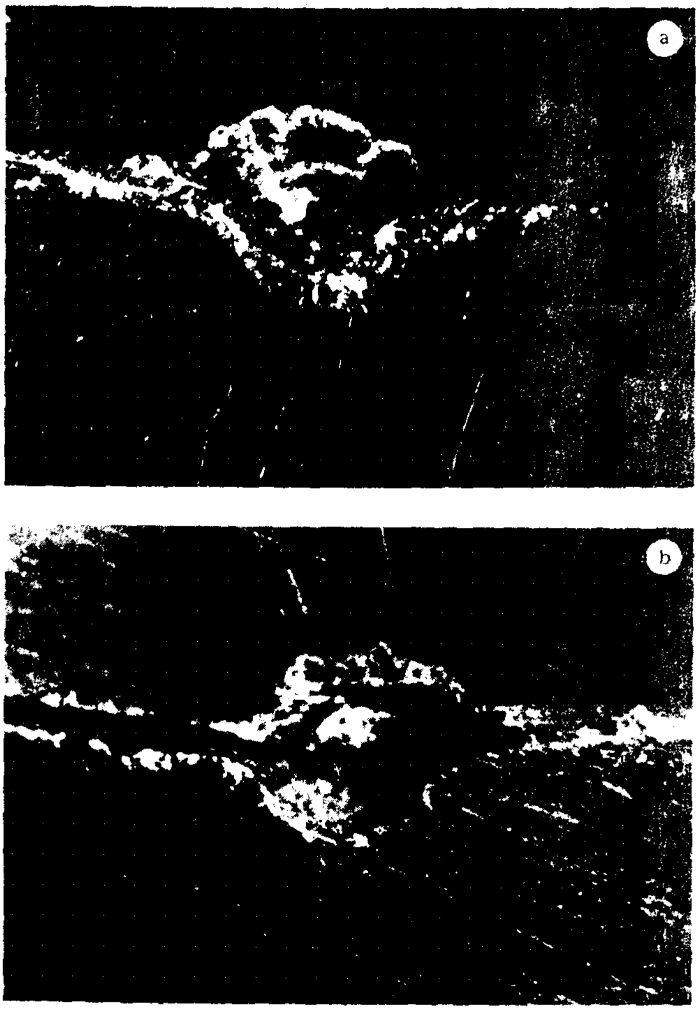

Figure 17. Cross section in a copper corrosion pit. (a) Presence of red Cu_2O and white CuCl under a dome of green malachite (30×); (b) after elimination of the loose deposit of red Cu_2O (30×). (Reproduced at 75%.)

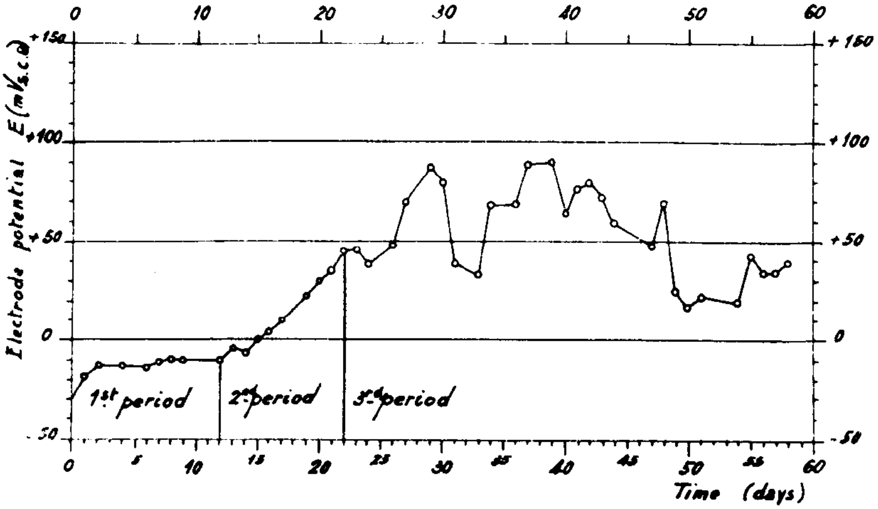

Figure 18. Influence of the immersion time on the electrcde potential of electrolytic copper vertically immerse in continuously flowing Brussels water.

cuprite. In the presence of water, such as that distributed by the city of Brussels,† they are covered by a sediment containing green malachite $CuCO_3 \cdot Cu(OH)_2$ and white calcium carbonate (Figure 17). Figure 18 shows the manner in which, as a function of time, the electrode potential of a sample of copper initially H_3PO_4-pickled and placed vertically in the city water, flowing at 20 mm sec^{-1}, evolves. During a first period of incubation, the electrode potential of the copper stayed relatively low and constant (−30 to −10 mV_{sce}) and the metal was covered with a red sediment of Cu_2O. During the second ten-day period, a progressive increase in the potential was produced until ~+50 mv_{sce} with the appearance of a green layer of malachite, containing white calcium carbonate. In the third period, alternate rising and falling of the potential appeared, which revealed ruptures of the somewhat protective layer formed on the copper. Numerous experiments carried out on samples of copper of different origins showing different initial states of surface, uncoupled and coupled with different metals (Au, Pt, Rd, Ag, Sn, C), have shown that corrosion pits develop or do not develop according to whather the electrode potential of the metal is higher or lower than a critical value, depending upon the form of the surface. This potential is +170 mV_{sce} (+415 mV_{she}) for the concave internal surface of pipes, and +100 mV_{sce} (+345 mV_{she}) for the convex surface of small wire (0.2-mm diameter). The interpretation of these experimental results can be obtained by a study of appropriate E–pH diagrams of electrochemical equilibria. Figure 19 is the E–pH diagram of the binary

---

† The essential characteristics of this water are as follows: pH = 7.90; resistivity, 1750 Ω cm; anions: Cl^-, 21.9 ppm, SO_4^{2-}, 55.9 ppm, HCO_3^{2-}, 317 ppm; cations: Ca^{2+}, 104.4 ppm, Mg^{2+}, 18.8 ppm, Na^+, 10.6 ppm.

$Cu-H_2O$ system at 25°C. It indicates that the stable forms of copper, in the presence of water with a pH equal to 8, are successively: copper if oxygen is present, copper oxide CuO in the presence of oxygen, and red copper oxide Cu_2O in the intermediary condition of aeration. Figure 20 concerns the ternary $Cu-Cl-H_2O$ system for solutions containing 10^{-2} g · ion Cl^-/liter (355 ppm), that of the water of Brussels free of oxygen and saturated with CuCl. Figure 21 is the E-pH diagram of the five-component system $Cu-Cl-SO_2-CO_2-H_2O$ at 25°C, which are the contents existing in the water of Brussels. Figures 20 and

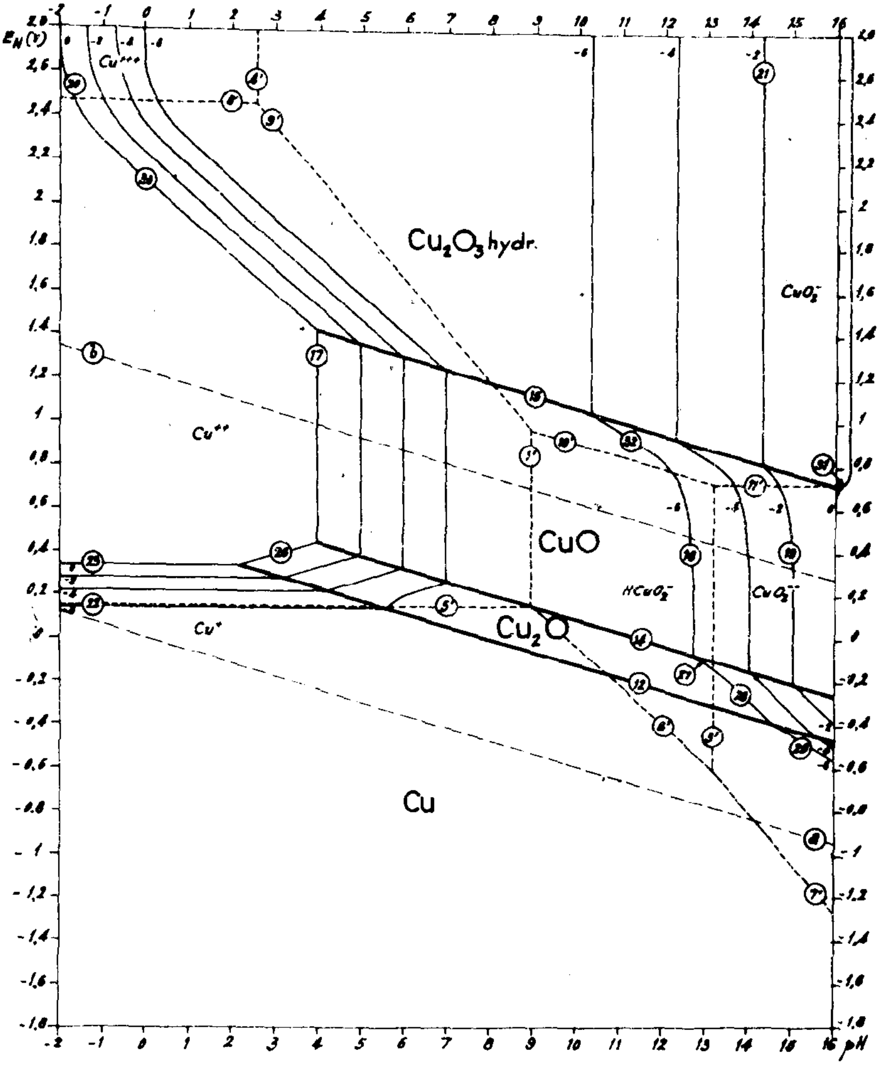

Figure 19. Potential–pH equilibrium diagram for the copper–water system at 25°C.

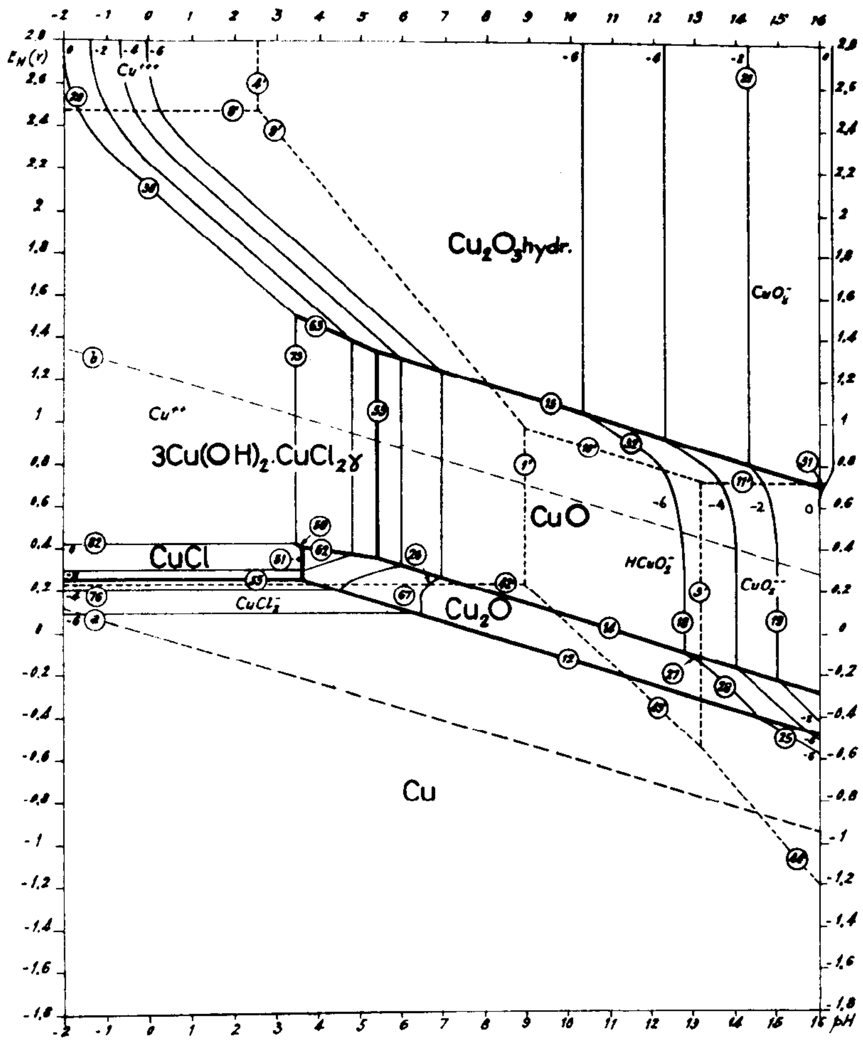

Figure 20. Potential–pH equilibrium diagram for the three-component system Cu–Cl–H_2O, for solutions containing 255 ppm Cl^- (10^{-2} g · ion/liter).

21 show that the derivate of copper which is thermodynamically stable in the presence of water, practically free of oxygen, is copper oxide, Cu_2O. The ions Cu^+ and Cu^{2+}, as well as copper chloride CuCl, are unstable in these conditions. If they are formed, they tend to hydrolyze with a formation of Cu_2O and hydrochloric acid, according to the following acidifying reactions:

$$2Cu^+ + H_2O \rightarrow Cu_2O + 2H^+ \qquad (88)$$

$$2CuCl + H_2O \rightarrow Cu_2O + 2H^+ + 2Cl^- \qquad (89)$$

$$2Cu^{2+} + H_2O \rightarrow Cu_2O + 2H^+ + 2e^- \qquad (90)$$

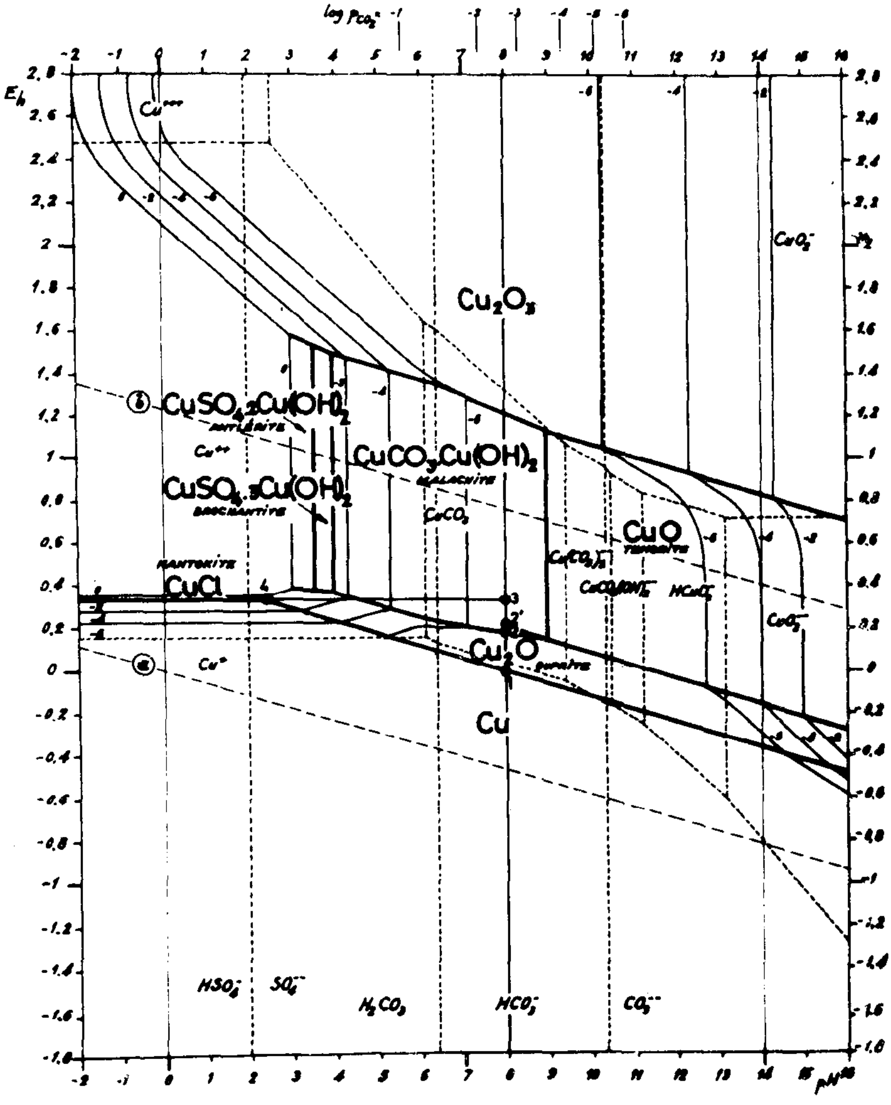

Figure 21. Potential-pH equilibrium diagram for the five-component system Cu–Cl–CO_2–SO_3–H_2O at 25°C, for solutions containing 229 ppm CO_2 ($10^{-2.28}$ g · ion/liter), 46 ppm SO_3 ($10^{-3.24}$ g · ion/liter) and 22 ppm Cl ($10^{-3.21}$ g · ion/liter).

This evolution, produced during the first period of Figure 18, is represented schematically in Figure 22a. During the second period of Figure 18, the red sediment of cuprite is progressively covered with green malachite. This layer forms a protective film between Cu_2O and the bulk of the water (Figure 22b). It passivates the metal with an elevation of its electrode potential and gradually traps the hydrochloric acid into the forming cavity. This leads to the formation

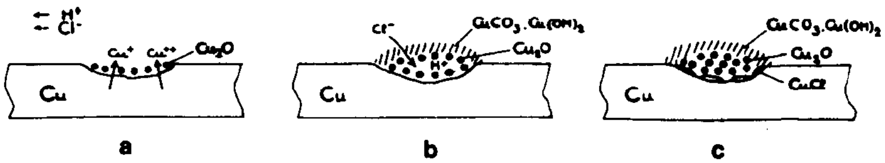

Figure 22. Initiation and evolution of a copper corrosion pit in the presence of water containing chloride. (a) First period: formation of Cu_2O and HCl by hydrolysis of Cu^+, Cu^{2+}, and CuCl. $2Cu^+ + H_2O \rightarrow Cu_2O + 2H^+$; $2Cu^{2+} + H_2O \rightarrow Cu_2O + 2H^+ + 2e^-$; $2CuCl + H_2O \rightarrow Cu_2O + 2H^+ + 2Cl^-$. (b) Second period: covering of Cu_2O with a layer of malachite, and acidification of the so-closed cavity. (c) Third period: formation of stable CuCl inside the active cavity [solution about 0.0074 M in copper and 0.0078 M in chlorine (470 ppm Cu and 277 ppm Cl)] $E = +270\ \mathrm{mV_{she}}$; pH = 3.5.

of cavities under the layer of malachite, containing a solution of growing acidity until the third stage (Figure 22c). The cavity solution becomes saturated with copper chloride, which, as it cannot hydrolyze further, is deposited on the metal. Then at the bottom of the cavity the three solid phases of copper, Cu, Cu_2O, and CuCl, coexist. The characteristics of the electrode potential, pH, and copper and chloride content totally dissolved are, respectively,

$$\begin{aligned} E &= +265\ \mathrm{mV}\ (+20\ \mathrm{mV_{sce}}) \\ \mathrm{pH} &= 3.5 \\ (\mathrm{Cu})_{\mathrm{aq.total}} &= 250\ \mathrm{ppm}\ (10^{-2.4}\ M) \\ (\mathrm{Cl^-})_{\mathrm{aq.total}} &= 277\ \mathrm{ppm}\ (10^{-2.11}\ M) \end{aligned} \tag{91}$$

In such a solution, the reaction of dissolving copper, $Cu \leftrightarrows Cu^{2+} + 2e^-$, is reversible. There is corrosion as soon as the electrode potential of the metal becomes higher than the equilibrium potential of the system, +265 mV (+20 $\mathrm{mV_{sce}}$) and deposition of copper as soon as the electrode potential becomes lower than the value of equilibrium. This is the criterion which governs the problem of copper pitting in the presence of water containing chloride. It follows that the pitting of the copper will develop (by dissolution of copper) or it will be stopped (by deposition of copper), according to whether the potential in the interior of the pit is higher or lower than +265 mV (+20 $\mathrm{mV_{sce}}$). This potential has to be measured as indicated in Figure 23a, with the help of a reference electrode reaching into the center of the pit, which in actual practice cannot usually be done. Generally, the electrode potential can only be measured as indicated in Figure 23b, with the help of a reference electrode installed at the exterior of the cavity. From this results an error due to the diffusion potential and to an ohmic drop across the malachite layer and calcium carbonate. The critical values of the external potentials indicated above, therefore, correspond to the same internal equilibrium potential of +265 mV. The "error" due to the practical position of the reference electrode is, therefore, of 150 and 80 mV, respectively.

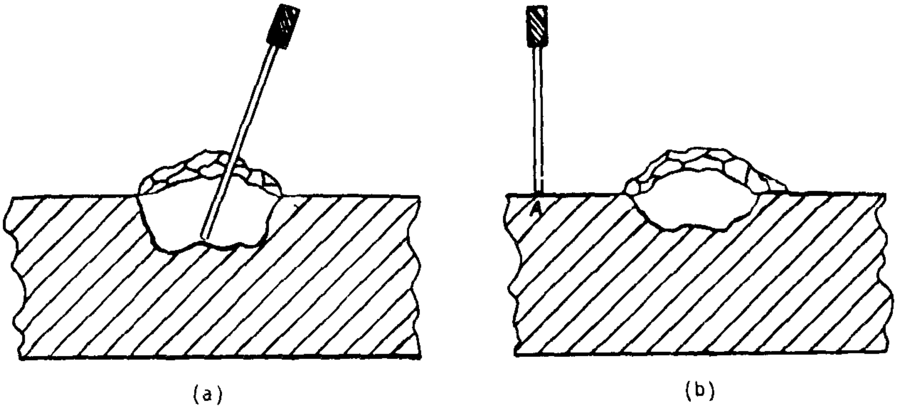

(a)

(b)

Figure 23. The electrode potential of pitted copper (a) as measured within the pit, (b) as measured outside the pit, giving the "mixed potential."

Figure 24 represents, beyond the theoretical circumstances of corrosion, immunity and passivation of copper, the conditions of pH and potential existing in the pits of corrosion of this metal and also the interval of the possible values of external electrode potential according to the conditions of the surface state and content in dissolved oxygen. Thus it can be seen that the protection potential against pitting of copper is situated between two extreme values, 0 and +600 mV, and that pitting of copper can be activated or stopped. The difference in electrode potential between the outer surface and

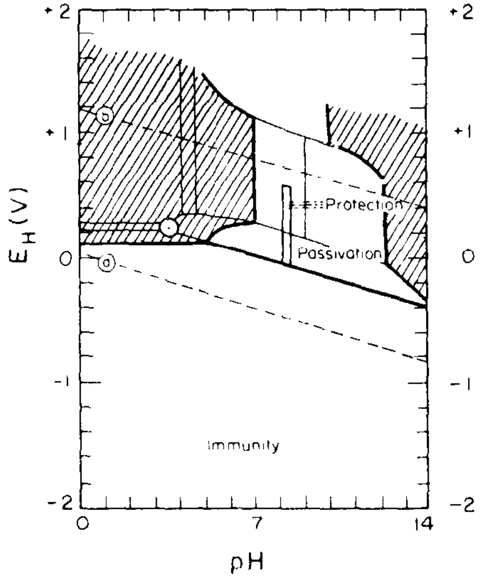

Figure 24. Copper in Brussels water. pH and electrode potential conditions inside pits in equilibrium: pH = 3.5, E = +270 mV_{she}. Possible electrode potentials outside pits at pH = 8: $E = 0$ to +600 mV_{she}. Protection potential against localized corrosion: about +350 to +420 mV_{she}.

the inner point of the corrosion cavity measures the affinity of the differential aeration cell, bringing a correction due to the existence of a diffusion potential and an ohmic drop between the aerated zone and the nonaerated cavity. If the outer potential is higher than the protection potential, the affinity is positive and the pit develops with dissolution of copper. If the outer potential is lower than the protection potential, the affinity is negative, the direction of cell function is reversed, and the pit is stifled with deposition of metallic copper.

This interpretation can explain some observations made by May,(169) where the corrosion current circulating between the outer cathodic regions and the internal anodic cavities was sometimes flowing for unknown reasons in the wrong direction. Thus the cavity occasionally became cathodic instead of remaining anodic.

Simulating a system of localized copper corrosion, LeCointre, Plichon, Berge, and LeGrand(170) utilized an electrochemical cell with two compartments, one of which contained a passivated copper wire dipped in an aerated and agitated solution of sea water, pH = 8.2, and the other a cleaned copper wire dipped into a solution of nonaerated sea water, pH = 3.5, containing copper. The possibility of direction inversion has been confirmed in copper corrosion pits, which conforms to the above interpretation. The above authors have also provided an explanation for the efficiency of the protection procedure for copper alloys condenser tubes by addition of ferrous sulfate in water. This procedure had not been elucidated, since the addition of iron sulfate is supposed to be permanent. The protection is due to the presence of Fe^{2+} ions, which, oxidizing to ferric oxide, confer to the metal uninjured zones (aerated outer surfaces) an electrode potential lower than that taken by the copper in the corrosion pits. The pits then become the seat of a cathodic reaction of deposition of copper ("reversal of the polarity of the corrosion cell"). However, this protective action is effective only when there are iron ions to be oxidized, which necessitates a permanent introduction of $FeSO_4$ to obtain a durable protection.

6.4.2. *Localized Corrosion of Iron in Presence of Chlorinated Solutions*

The general principles applied to copper are valid also for iron, with one important difference. Iron, unlike copper, cannot be thermodynamically stable in the presence of water under the usual conditions of temperature and pressure. In a corrosion cavity of iron, a state of thermodynamic equilibrium cannot be brought about. There is always a corrosion of the metal with a release of hydrogen produced.

The acidification of localized corrosion sites heretofore described in the case of the pitting of copper is a fairly general phenomenon. As indicated by Baylis,(174) Hoar,(175) Evans,(176) Edeleanu and Evans,(177) and Rosenfeld and Marchakov,(178) the solutions existing in the interior of corrosion pits of numerous metals are acidic, following a hydrolysis of the primary products of corrosion. This is so in all cases where corrosion is produced in more or less occluded cavities with restricted contact with the bulk of the solution: pitting corrosion, crevice corrosion, corrosion below depositions, intergranular corrosion, stress corrosion cracking. Even when the environment contains small quantities of chlorides, the solution which settles in the "occluded corrosion cells" (name proposed by Brown$^{(179)}$) is a hydrochloric acid solution.

By experimentally simulating a corrosion cavern (Figure 25), evolution of pH and electrode potential conditions in the interior of active crevices were examined under conditions of differential aeration on iron and steel in the presence of slightly chlorinated and strongly alkaline solution (10^{-3} M NaCl + 10^{-3} M NaOH), pH ~ 11.

The condition of pH and electrode potential of aerated "cathodic" outer surfaces and nonaerated "anodic" inner surfaces is better understood when analyzed on the basis of E–pH electrochemical equilibria diagrams. In Figure 26, representing an E–pH diagram of the Fe–H_2O system at 25°C, the evolution of these characteristics in the artificial cavity of Figure 25 is indicated from initial conditions 1 (aerated alkaline solution) to the final condition 2, or,

initial conditions: pH = 11, $E_{Fe} = -100$ to 0 mV

final conditions: pH = 2.7–4.7, $E_{Fe} = -430$ to -300 mV

While the pH and electrode potential conditions outside the cavity remain constant, in the area of passivation, they evolve in the cavity toward the area of active dissolution of iron with a possible release of hydrogen. Thus it is

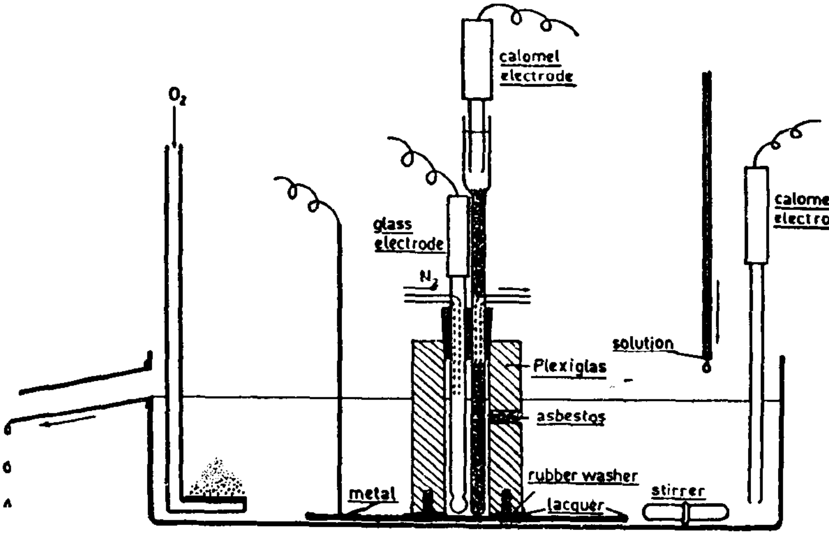

Figure 25. Device for studying crevice corrosion.

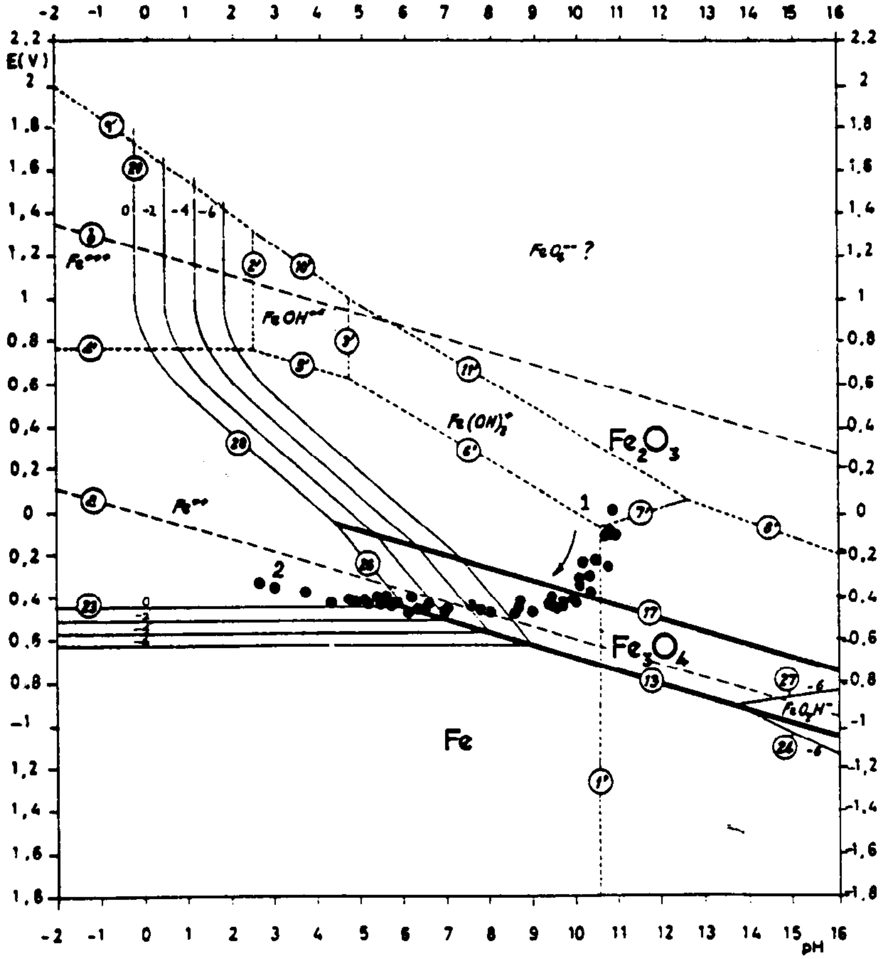

Figure 26. Evolution of the potential and pH conditions in an artificial iron crevice in chloride-containing solution, with a potential–pH diagram for the Fe–H_2O system, at 25°C, as background. 1: Initial conditions; 2: final conditions.

theoretically possible that a corrosion cavern may be maintained without reduction on the outer passive surface.

Based on a concept by Pourbaix,(162) the solutions in the center of localized corrosion cavities have a tendency to become acid due to simple or oxidizing hydrolysis and to become saturated, according to the solution, in the salt of the metal of least solubility. Fujii(180) examined the electrode potential of iron and the pH of the saturated solution of $FeCl_2 \cdot 4H_2O$ and Fe_3O_4, in the presence of pulverized iron and no oxygen. At equilibrium, the pH was found to be close to 3.8 and the electrode potential close to −330 mV.

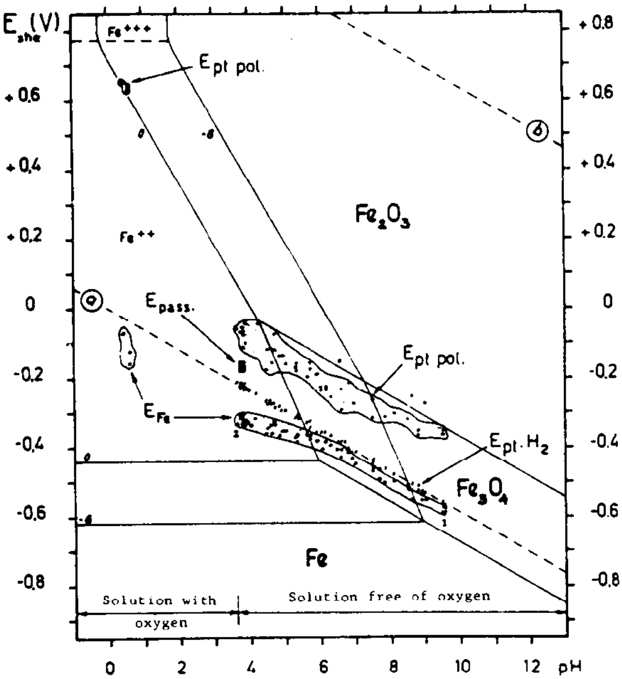

Figure 27. Effect of a concentration increase of a $FeCl_2 \cdot 4H_2O$ stirred solution containing iron and free from oxygen on the evolution of the solution pH and of the potentials of iron, of polished platinum, and of platinized platinum. Effect of oxygen on these characteristics in conditions of saturation in $FeCl_2 \cdot 4H_2O$. (After L. Sathler.(70))

Starting from the same concept, Sathler(70) carried out a thorough thermodynamic and electrochemical study of the $Fe-Cl^--H_2O$ system at 25°C to determine chemical and electrochemical characteristics of the occluded corrosion cells of iron in the presence of chlorinated solutions. The pH of the $FeCl_2 \cdot 4H_2O$ solutions of different concentrations was precisely determined in the presence of pulverized iron and no oxygen, at 25°C, as well as the electrode potential of the iron in these solutions (Figure 27).

In the presence of the saturated solution of $FeCl_2 \cdot 4H_2O$, free of oxygen, the following was found†:

$$\begin{aligned} \mathrm{pH} &= 3.8 \pm 0.1 \\ E_{\mathrm{Fe}} &= -322 \pm 12\ \mathrm{mV} \end{aligned} \tag{92}$$

---

† Chemical and thermodynamic characteristics of the saturated solution of $FeCl_2 \cdot 4H_2O$ at 25°C in the presence of pulverized iron and no oxygen obtained by Sathler(70) are as follows (page numbers in parentheses denote pages in Ref. 70): activity of the water, $a_{H_2O} = 0.597$ (p. 62); concentration of $FeCl_2$, 4.50 ± 0.05 M (p. 100), 5.15 ± 0.05 m (p. 53); mean activity coefficient $y_\pm$: 2.58 (molarity scale) (p. 58); $\gamma_\pm$: 2.26 (molarity scale) (p. 67).

Sathler has also shown that the introduction of oxygen in this solution leads to a modification of these values as follows:

$$\begin{aligned} \mathrm{pH} &= 0.6 \pm 0.2 \\ E_{\mathrm{Fe}} &= -125 \pm 40\ \mathrm{mV} \end{aligned} \tag{93}$$

with no possibility of passivation by oxidation.

There is no reason why, for a given metal under corrosion, the conditions existing in the interior of occluded pits should be different from the conditions existing in the interior of crevices, cracks, or any other kinds of corrosion with restricted diffusion. Therefore, it can be stated that the pits appeared on a passive surface of iron due to the overstepping of the critical pitting potential in a chlorinated solution, creating the appearance, in the system under consideration, of occluded acid sites where the conditions of pH and electrode potential are identical with those of point 2 of Figures 26 and 27.

Figure 28 shows the influence of a progressive decrease in electrode potential of the aerated outer surface on electrochemical characteristics of

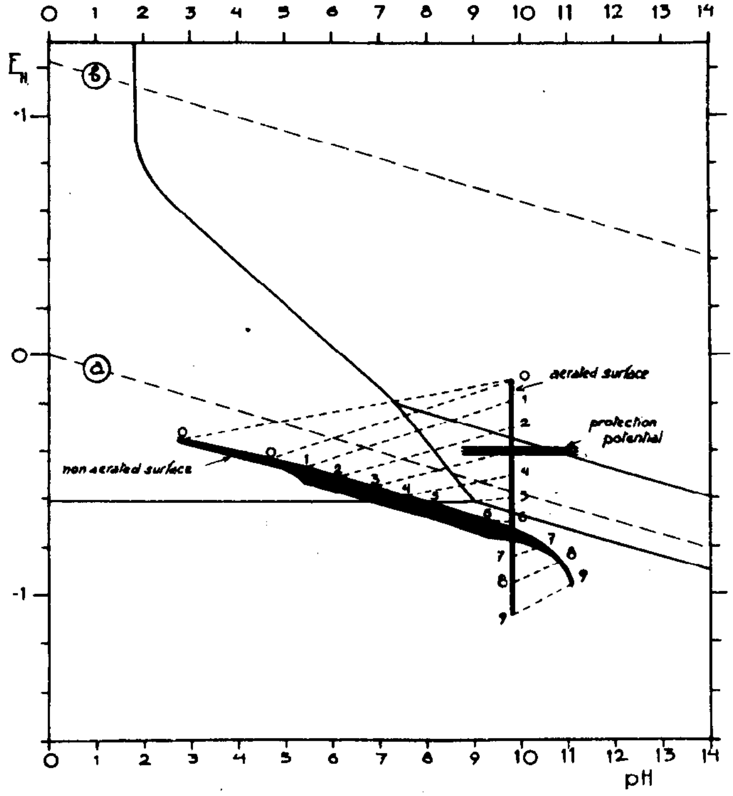

Figure 28. Influence of a slow cathodic polarization on the potential and pH conditions inside a crevice (mild steel with an aerated solution of 0.001 *M* NaOH and 0.001 *M* NaCl).

localized corrosion, simulated in Figure 25. Points marked 0 indicate conditions existing when no electric current is applied to the outer surface (about −50 mV and pH = 10 for the outer surface, and about −350 to −430 mV and pH = 2.7–4.7 for the inner cavity corroded by differential aeration). By cathodically polarizing the outer surface through the passage of electric currents of increasing intensities between this surface and an auxiliary anode of platin (points 1–9), the following can be observed:

i. When the protection potential is reached on the outer surface (point 3), the solution in the cavity is no longer acid and the iron is in the state of immunity. A release of hydrogen remains possible, for the potential of the iron is lower than line *a*.

ii. An elevation of the potential of the outer surface on the iron, above the potential for protection, causes the solution in the cavity to acidify with an increase in the speed of dissolution of the iron and maintaining the release of hydrogen.

iii. When the outer potential is lowered below the protection potential, the solution in the cavity becomes alkaline and hydrogen is released without dissolution of iron (except if the electrode potential should be situated in the little triangle of corrosion for strong alkaline and reducing solutions).

Utilizing a similar experimental arrangement, modified to allow a separate measurement of electric current intensities passing between thè outer and inner surfaces, A. Pourbaix(182) made a kinetic study of these phenomena, with conclusions in agreement with the above facts.

The scientific significance of the concept of "protection potential against localized corrosion," to be brief, "protection potential, E_{PP}," which was not obvious when it was introduced in 1962 for stainless steel (Pourbaix(183)), for copper in 1963 (Van Muylder *et al.*(184)), and in 1969 for iron and common steels (Pourbaix(171,172,185)), is well illustrated by these results.

This protection potential under which the active corrosion pits become inactive and harmless, and which depends little on pH and chloride content of the solution, is sensitively equal to the potential at point 3 in the interior of these pits, i.e., to the immunity potential of the metal, eventually increased by an ohmic drop and/or a diffusion potential across the oxidation and/or salts layer covering these pits.

The credit for having experimentally shown and confirmed the validity of this mechanism in the crucial field of stress corrosion cracking is given to Brown.(186–188) Figure 29 indicates, on the basis of a *E*–pH diagram, the characteristics of pH and electrode potential inside stress corrosion cracks of some high strength steels exposed to a 3% NaCl solution, as well as the rate of propagation of these cracks as a function of the electrode potential. By lowering the electrode potential to negative values, the pH in the center of the crack is raised. At −600 mV, the speed of cracking is minimal and there is no more dissolution of the metal. At lower electrode potentials, the cracking speed increases again without dissolution of metal.

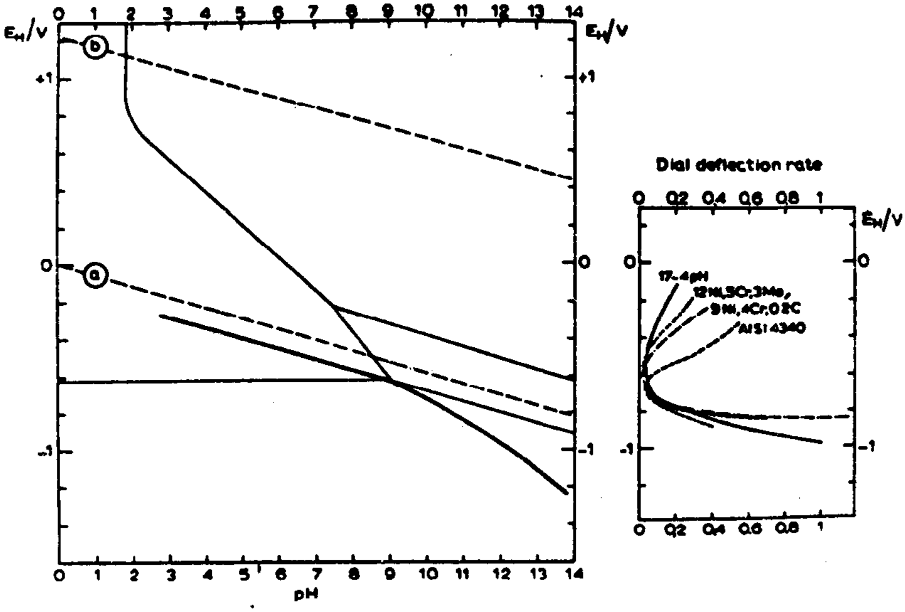

Figure 29. Influence of a cathodic polarization on the electrochemical characteristics and propagation rate of a stress corrosion crack (chromium steel AISI 4340 in contact with 3.5% NaCl solution) (after B. F. Brown(186–188)).

A comparison of Figures 28 and 29 shows a striking similarity in pH and electrode potential existing in stress corrosion cracks and in crevices, caverns, and other corrosion cavities, as well as in the evolution of these characteristics when the metal is submitted to a cathodic polarization. In each case, a lowering of the outer potential below the "protection potential" suppresses the corrosion by dissolution, but it may lead to an increase of hydrogen evolution. If the metal is sensitive to hydrogen, fragility may occur. This is generally the case for high-strength low-alloy steels. According to Smith, Peterson, and Brown(189) the propagation of corrosion cracks in these types of steel is favored by reduction of H^+ protons at the tip of the crack, where hydrogen is partially absorbed and partially released. This is confirmed by experiments of Pickering and Frankenthal.(190)

Parrish *et al.*(191) have also confirmed this. Figure 30 represents an experimental potential–pH diagram of the Fe–H_2O system at 25°C, a black circle representing the initial circumstances of pH and electrode potential in the bulk of the solution and in the artificial corrosion cavities, and a black square represents the final circumstances of pH and electrode potential in these cavities. This was observed while examining the behavior of a low-alloy high-strength steel in the presence of 0.10 *M* NaCl solutions with pH between 2.1 and 8.1. When the initial pH is higher than 5 (points 3–9), the final potential in the cavities is always lower than the potential of equilibrium of the hydrogen

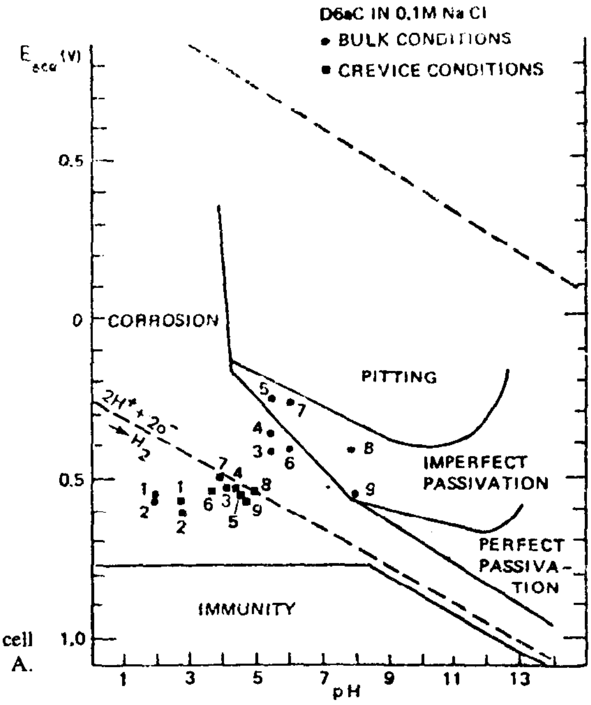

Figure 30. Artificial crevice cell results, pH 2.1–8.1 (after P. A. Parrish *et al.*[191]).

electrode and the pH is always considerably decreased (3.8–5). The influence of these characteristics on the fracture toughness under corrosion and on the absorption of hydrogen by the metal lowers the threshold stress-intensity factor K_{ISCC} from 320 to 40 kg mm$^{-3/2}$. The absorbed hydrogen will then be 3–10 times higher than the latent content (baseline). The presence of oxidizing inhibitors ($Na_2Cr_2O_7$, N_2H_4) keeps the electrode potential above the equilibrium potential of the hydrogen, raises the value of K_{ISCC} and suppresses the absorption of hydrogen.

7. Electrode Potential Measurements in Corrosion Studies

7.1. General Statements

Haber[39,192] seems to be the first who recognized the significance of electrode potential on electrochemical reactions. The majority of the study methods and corrosion experiments are presently based on the measurement of electrode potential.

Diagrams of *E*–pH electrochemical equilibria show the conditions of thermodynamic stability of each constituent of a system in specific aqueous solutions depend on the value of the electrode potential. This specific property of electrode potential is connected with the stability conditions of all bodies in aqueous solutions, and this gives rise to different electrochemical essays of corrosion called "intensiostatic and intensiokinetic, potentiostatic and potentiokinetic." The electrode potential is thus artificially run through an entire interval of values continuously, in an increasing or decreasing direction. This freely causes reactions of corrosion or other reactions which cause the system to evolve toward a thermodynamically stable state, depending on the electrode potential imposed.

Now by electrolysis operations in an agitated solution, it is generally easy to run through the entire scale of possible values of the potential of the electrodes utilized, maintaining the equilibrium potential E_0 of the reactions fairly constant. Then, on the basis of

(a) the equation

$$(E - E_0) \times i \geq 0 \tag{39}$$

which is a general expression of the second principle of electrochemical thermodynamics and according to which a given electrochemical reaction can be carried out only in the direction of oxidation ($i > 0$) or reduction ($i < 0$), depending on whether the electrode potential E is higher or lower than the equilibrium potential E_0, or it cannot be accomplished with any noticeable rate ($i = 0$),

and

(b) the "principle of superposability of the polarization curves" introduced by Wagner and Traud,(193) according to which the intensity of a current crossing an electrode during electrolysis is equal to the algebraic sum of the intensities of reaction currents relative to individual electrochemical reactions produced at the electrode:

$$I = \sum i \tag{94}$$

it follows that the experimental determination of polarization curves, realized in conditions where the equilibrium potential E_0 of all the different possible electrochemical reactions is known, can help elucidate the meaning of the intensity of the current and establish whether corrosion, passivation, activation, and other reactions are effectively produced. If so, then the velocities for the values of the electrode potential can be established.

However, the major difficulty with this is the resolution of the global intensity of the electrolysis current I in its diverse individual components i and the determination of which are relevant to the problem studies. Such an analysis requires knowledge of thermodynamics and kinetics of the reaction in question.

This fact is illustrated by Pourbaix,(3,8,194) in the case where iron is partially covered by "air oxide," Fe_2O_3, and exposed to a neutral aqueous solution at 25°C, containing less than 10^{-6} g-at. of total iron dissolved per liter.

Figure 31 indicates the theoretical conditions of the corrosion, immunity, and passivation of iron, beyond the circumstances of stability of water and its

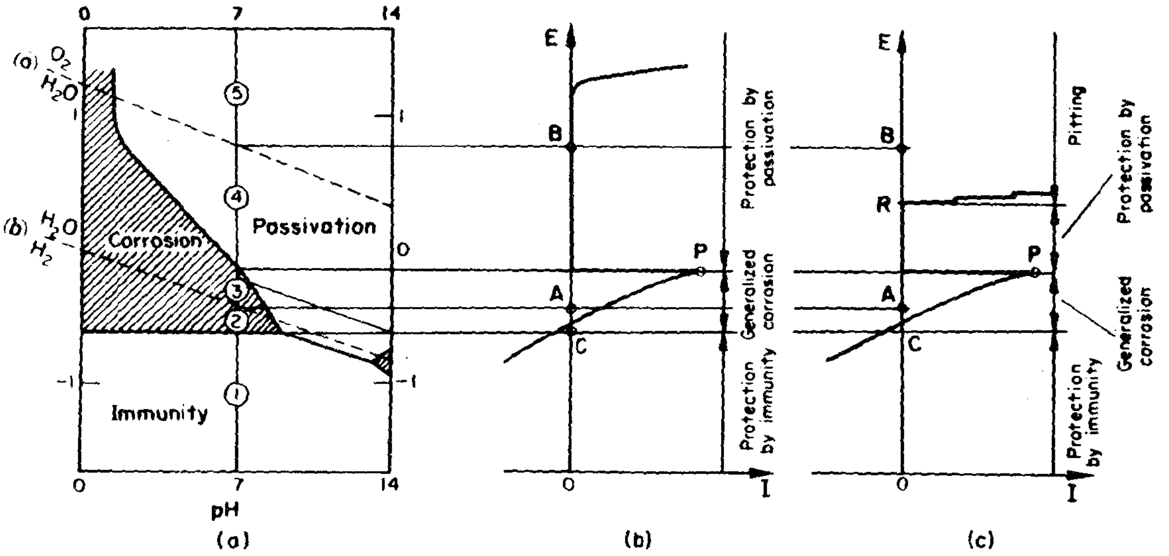

Figure 31. Theoretical and experimental predetermination of the conditions of *noncorrosion*, of generalized corrosion, and of localized corrosion (pitting) for iron in solution pH = 7. (a) Theoretical conditions of corrosion, immunity, and passivation; (b) potential–current curve obtained potentiokinetically, in the case of a perfectly protective oxide film (conditions of protection and of generalized corrosion); (c) potential–current curve obtained potentiokinetically in the case of a nonperfectly protective oxide film (conditions of protection, of generalized corrosion, and of pitting).

Table 2

Relation between the Value of Electrode Potential and the Direction of Electrochemical Reactions, in the Case of Solutions of pH = 7 Containing 0.06 ppm of Iron

	Region	$Fe–Fe^{2+}$ $Fe = Fe^{2+} + 2e^-$	$H_2–H_2O$ $H_2 = 2H^+ + 2e^-$	$Fe^{2+}–Fe_2O_3$ $Fe^{2+} + 3H_2O$ $= Fe_2O_3 + 6H^+ + 2e^-$	$H_2O–O_2$ $2H_2O = O_2 + 4H^+ + 4e^-$
1	$E < -0.6$ V	Reduction	Reduction	Reduction	Reduction
2	$-0.6 < E < -0.4$	Oxidation	Reduction	Reduction	Reduction
3	$-0.4 < E < -0.2$	Oxidation	Oxidation	Reduction	Reduction
4	$-0.2 < E \quad +0.8$	Oxidation	Oxidation	Oxidation	Reduction
5	$+0.8 < E$	Oxidation	Oxidation	Oxidation	Oxidation

reduction product H_2 and oxidation product O_2 under atmospheric pressure. It also shows that the direction in which the four reactions (Table 2) can be accomplished varies according to the electrode potential of the iron in the following manners.

7.1.1. $E < -0.60$ V (Region 1)

The four reactions can be accomplished only in the direction of the reduction, from right to left. The iron is in a state of immunity, therefore not corroded. The Fe^{2+} ions present in the solution and the ferric oxide possible present on the metallic surface are reduced to the metal state. Water is reduced to gaseous hydrogen and eventually dissolved oxygen is reduced to water. With an input of exterior energy, a cathodic protection of the iron is produced with the liberation of hydrogen.

7.1.2. $-0.60 < E < -0.40$ V (Region 2)

The iron is corroded with a release of hydrogen. There is dissolution of ferric oxide to the state of ferrous Fe^{2+} ions and a reduction of dissolved oxygen to water. This corresponds to the normal circumstances of corrosion of iron without the input of exterior energy.

7.1.3. $-0.40 < E < -0.20$ V (Region 3)

Iron corrodes without a release of hydrogen, and the other reactions are accomplished as in Region 2, but with smaller affinity.

7.1.4. $E > -0.20$ V (Regions 4 and 5)

The iron can be covered with ferric oxide, Fe_2O_3 (passivation). If this oxide is not porous and perfectly adherent, the metal will have no contact with the solution, and will be protected by perfect passivation. However, if the oxide is porous or not adherent (i.e., in solutions rich in chlorides), the protection affects only part of the surface. Passivation is not then perfect and the metal undergoes frequently severe pitting, because of the great affinity of the corrosion reaction.

7.1.4.1. $-0.20 < E < +0.80$ V (Region 4)

In this state, passivity and pitting can be produced under action of moderately oxidizing substances (i.e., O_2, H_2O_2, CrO_4^{2-}, NO_2^-) without intervention of exterior energy.

7.1.4.2. $E > +0.80$ V (Region 5)

In this state, passivity or pitting can be established only by an oxidizing action, sufficiently energetic to oxidize water in oxygen (i.e., MnO_4^- in strong dosage, TeO_4^-, $S_2O_8^{2-}$, F_2, anodic oxidation).

7.2. Electrochemical Experiments of Corrosion

The electrochemical corrosion experiments can be divided into the following six groups:

Potentiokinetic, $I = f(E)$, where the electrode potential varies as a function of time, according to a determined program. The intensity of the electrolysis current (intensity of the general reaction current) is registered as a function of the electrode potential.

Intensiokinetic, $E = f(I)$, where the intensity of the electrolysis current varies as a function of time, according to a given program. Electrode potential is registered as a function of time.

Potentiostatic, $E = Cte$, $I = f(t)$, where the electrode potential is maintained and the temporal evolution of the intensity of the electrolysis current is registered.

Intensiostatic, $I = Cte$, $E = f(t)$, where the intensity of the electrolysis current is fixed and the temporal evolution of the electrode potential is registered.

Polarization resistance, where a difference of potential, ΔE (0–10 mV) is applied between a working and auxiliary electrode and a measurement is taken of the intensity of the resulting current. According to Stern and Geary,(195) the intensity of the corrosion current, i_{corr}, is deduced:

$$i_{\text{corr}} = 0.4343 \frac{I}{\Delta E} \frac{\beta_a \beta_c}{\beta_a + \beta_c} \tag{95}$$

where βa and βc are the slopes of the straight Tafel lines(196) of the anodic and cathodic reactions concerned. Further studies of this method can be made elsewhere.(197–203)

Zero global intensity of current, $I = 0$, where the electrode potential is registered with no polarization imposed from outside with a source of continuous or alternating current.

The following illustrates the significance of potentiokinetic corrosion experiments.

7.2.1. Potentiokinetic Experiments of Corrosion

By successively increasing and decreasing the electrode potential applied to metallic samples in a given solution, tracings of polarization curves can be obtained which will reveal the corrosion behavior of the samples.

Figure 32 shows seven characteristic tracings, whose thermodynamic interpretation (Pourbaix(204,205)) leads to the following:

Figure 32a—The only two possible reactions are a release of hydrogen at a low electrode potential and a release of oxygen at a high electrode potential. The metal cannot be corroded in a solution (i.e., Pt in numerous solutions, AISI.304 steel in an acetic solution free of chloride).

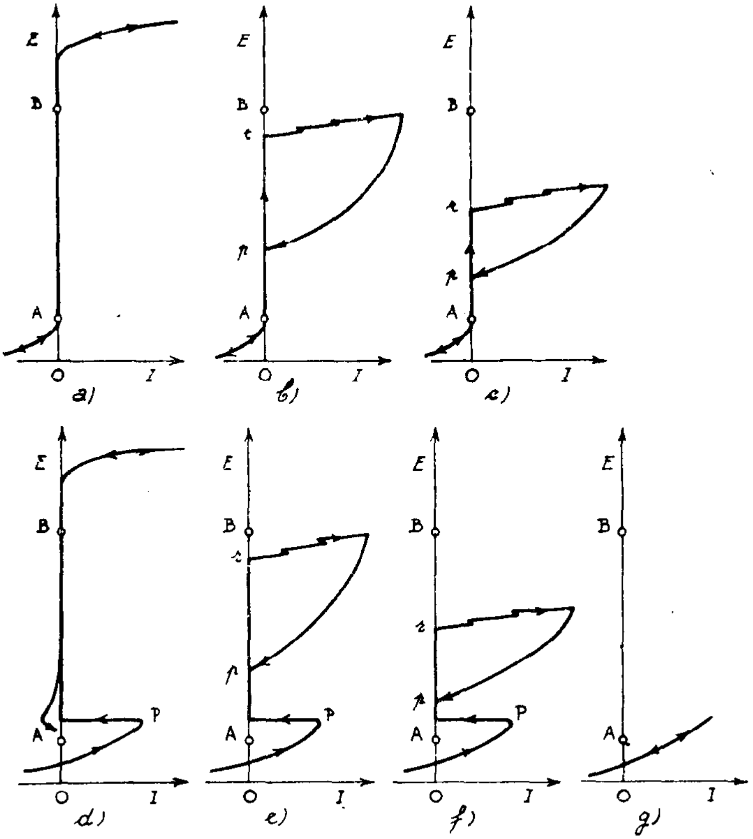

Figure 32. Types of polarization curves: (a) no corrosion; (b) no corrosion, except if stray currents are present (pitting); (c) no corrosion in absence of oxygen; pitting if oxygen or stray currents are present; (d) general corrosion in absence of oxygen; no corrosion in presence of oxygen, and crevices in case of differential aeration; (e) general corrosion in absence of oxygen; no corrosion in presence of oxygen and crevices in case of differential aeration; pitting if stray currents are present; (f) general corrosion in absence of oxygen; pitting if oxygen or stray currents are present; (g) general corrosion in absence or in presence of oxygen.

Figure 32b—A pitting can happen at relatively high elevated electrode potentials, higher than the value *B* −0.30 to −0.40 V. Oxygen is, therefore, without danger. Otherwise, there is no possibility of crevice corrosion (i.e., AISI.304 steel in an acetic solution containing a small quantity of chloride).

Figure 32c—Pitting can develop at moderately elevated potentials, lower than the value *B* −0.30 to −0,40 V. The oxygen is therefore dangerous. There is no possibility of crevice corrosion (i.e., AISI.304 steel in the presence of an acetic solution, containing a noticeable quantity of chloride).

Figure 32d—At a low electrode potential, there is generalized corrosion. There is no danger of pitting, but there is a possibility of the appearance of

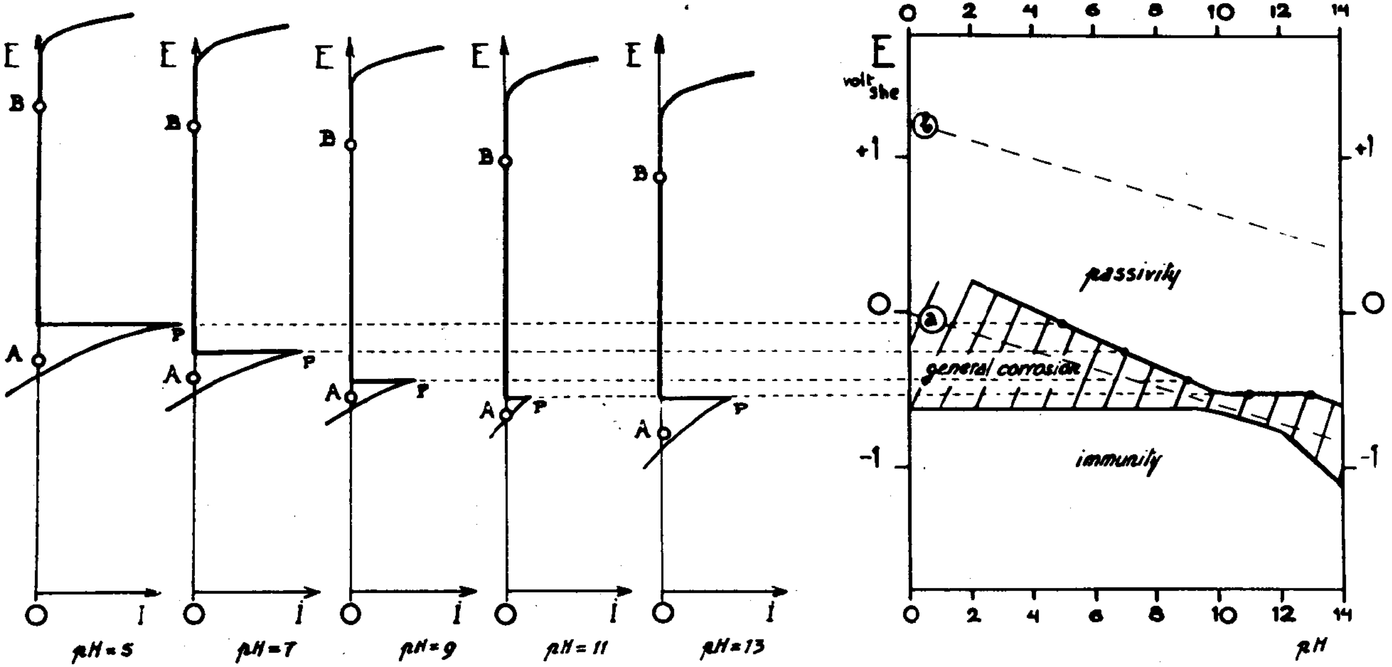

Figure 33. Behavior of iron in chloride-free solution (scheme). (Left) Polarization curves in solutions of pH 5–13; (right) experimental circumstances of immunity, general corrosion, and passivity (after M. Pourbaix[3,8,204,205]).

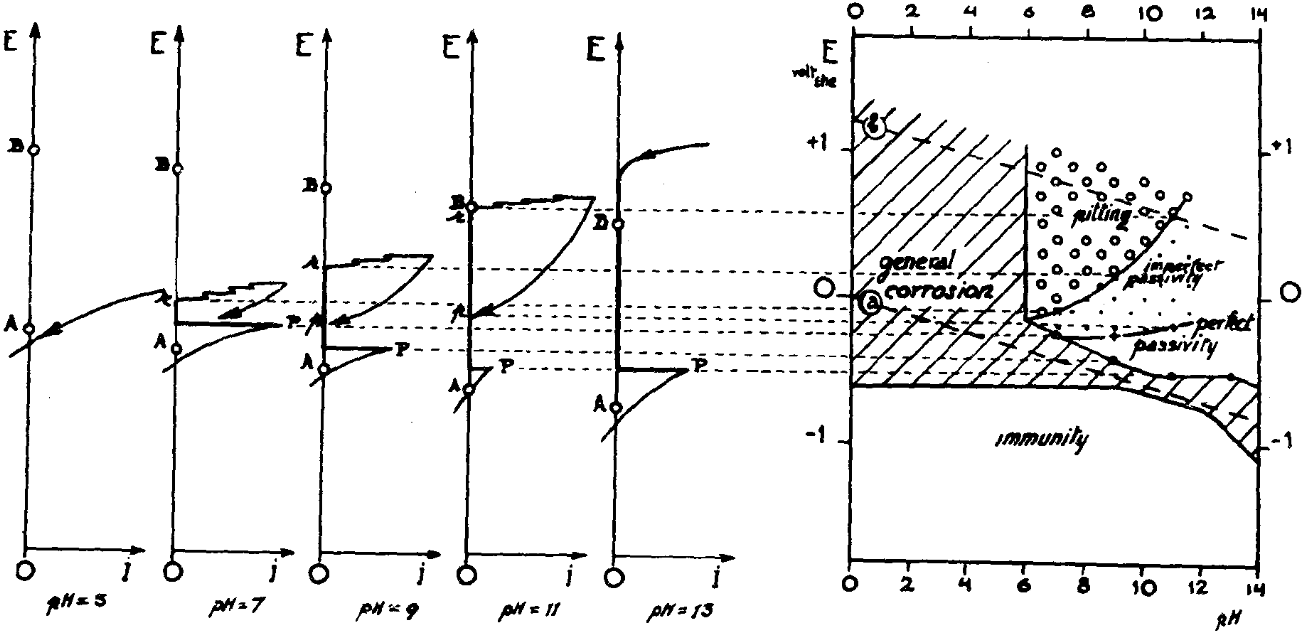
E
B
A
P
j
O
pH = 5
pH = 7
pH ≈ 9
pH = 11
pH = 13
E volt_she
+1
O
-1
0
2
4
6
8
10
12
14
pH
ⓐ
ⓑ
general corrosion
pitting
imperfect passivity
perfect passivity
immunity

Figure 34. Behavior of iron in solution containing chloride (10^{-2} g ion/liter or 355 ppm Cl^-) (scheme). (Left) Polarization curves in solutions of pH 5–13; (right) experimental circumstances of immunity, general corrosion, and perfect and nonperfect passivity, and pitting (after M. Pourbaix[3,8,204,205]).

crevice corrosion in differential aeration (i.e., iron in neutral solutions free of chloride).

Figure 32e—There is generalized corrosion at low electrode potentials. There can be pitting at relatively high electrode potentials, above the value *B* −0.30 to −0.40 V. Oxygen is, therefore, without danger here. There is a possibility of appearance of crevice corrosion in the conditions of differential aeration (i.e., iron in neutral solutions containing a small quantity of chloride).

Figure 32f—There is generalized corrosion at low electrode potentials. There can be pitting at moderately high potential, lower than the value *B* −0.30 to −0.40 V. Oxygen is therefore dangerous. There is a possibility of appearance of crevice corrosion in differential aeration (i.e., iron in neutral solutions containing a noticeable amount of chloride).

Figure 32g—There is generalized corrosion in the absence and presence of oxygen and other oxidizers, with no possibility of passivation (i.e., iron in neutral and acid solutions, rich in chloride and AISI.410 steel in the presence of seawater).

Such potentiokinetic experiments on a given metal or alloy in solutions of different pH can lead to the establishment of experimental potential–pH electrochemical diagrams, representing the experimental conditions of

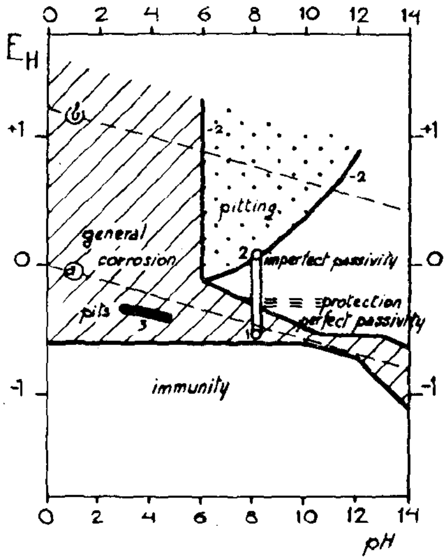

Figure 35. Potential and pH conditions for iron in presence of a solution of pH about 8. (10^{-2} *M* in Cl^-, i.e., 355 ppm Cl^-.) 1. Nonpolarized iron in oxygen-free solution: initiation of general corrosion. 2. Nonpolarized iron in solution containing oxygen: initiation of pitting. 3. Active pits and crevices (scheme).

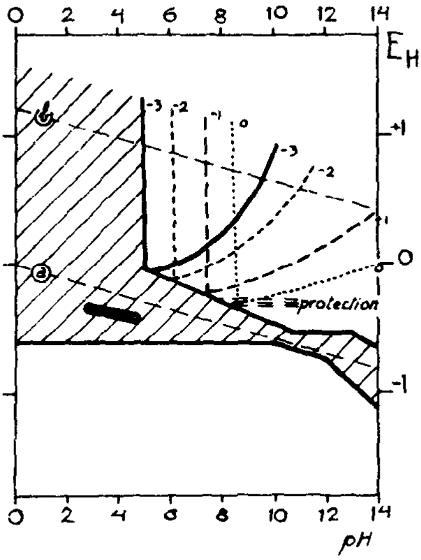

Figure 36. Influence of the chloride concentration on the rupture potential and protection potential or iron (scheme) (10^{-3}–10^{0} *M* Cl^-).

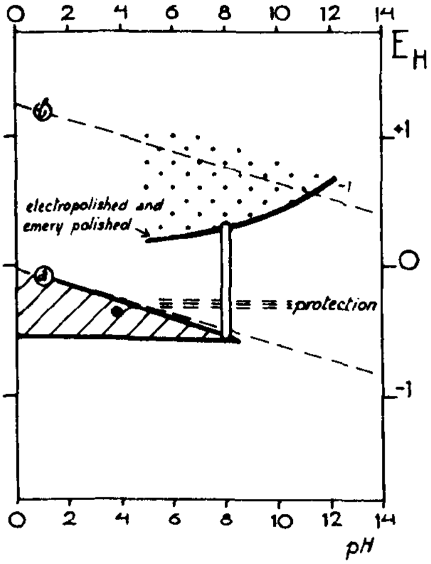
E_H
+1
0
-1
ⓑ
ⓐ
electropolished and emery polished
-1
protection
pH
0 2 4 6 8 10 12 14

Figure 37. Corrosion, immunity, passivation, and pitting conditions for chromium-steel AISI 410 (10^{-1} M Cl^-) (scheme).

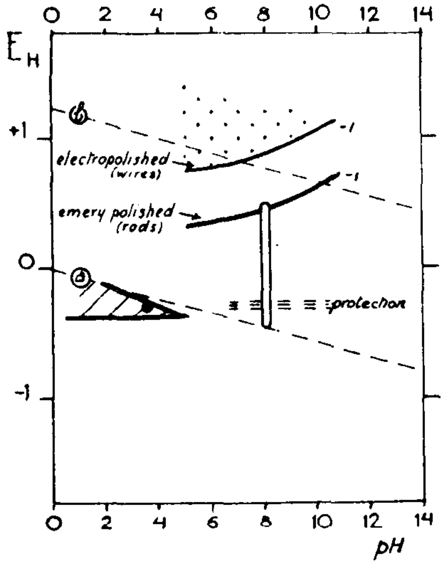
E_H
+1
0
-1
ⓑ
ⓐ
electropolished (wires)
emery polished (rods)
-1
protection
pH
0 2 4 6 8 10 12 14

Figure 38. Corrosion, immunity, passivation, and pitting conditions for chromium-nickel steel AISI 304 (10^{-1} M Cl^-) (scheme).

immunity, generalized corrosion, perfect passivation, imperfect passivation, and pitting. The principle of this method is described schematically in Figures 33 and 34, relative to solutions with and without chloride. Figure 35 represents an experimental diagram in the case of iron in a chlorinated solution

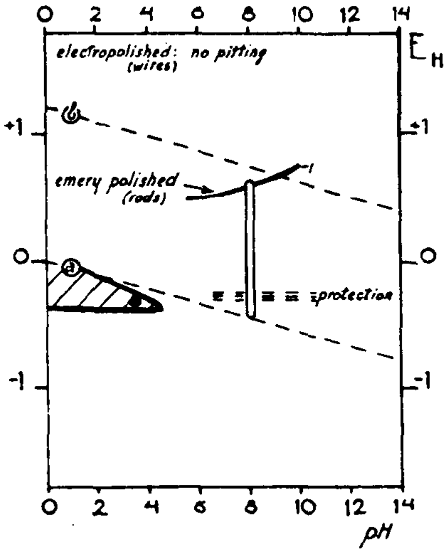
E_H
+1
0
-1
electropolished: no pitting (wires)
ⓑ
emery polished (rods)
-1
ⓐ
protection
pH
0 2 4 6 8 10 12 14

Figure 39. Corrosion, immunity, passivation, and pitting conditions for chromium-nickel-molybdenum steel AISI 316 (10^{-1} M Cl^-) (scheme).

($10^{-2} M\,\mathrm{Cl}^-$, or 355 ppm). Conditions of electrode potential are indicated which can exist at a pH close to 8, according to the aeration conditions of the solution and the conditions of pH and electrode potential in the center of the corrosion caverns. The effect of the chloride content on the pitting potentials, E_R, and on the potentials of protection, E_{pp}, is shown in Figure 36. The potential of pitting depends on the pH and chloride content. However, these two factors only slightly modify the protection potential, which is basically equal to the potential in the corrosion cavities, or -0.30 to -0.40 V.

Figures 37–39 are experimental E–pH diagrams established in chlorinated solutions and relating, respectively, to a chrome steel, AISI.410, a chrome–nickel steel, AISI.304, and a chrome–nickel–molybdenum steel, AISI.316.(205,206)

There are two critical electrode potentials, characteristic for pitting corrosion, the pitting or rupture potential, E_R, where corrosion can begin only at electrode potentials above this but can continue at potentials below pitting potential, and second, the protection potential, E_{pp} (against localized corrosion) which is the limit potential of perfect passivation, lower than the preceding one and below which the pits cannot develop.

The pitting potential is a magnitude characteristic for pitting corrosion, useful in comparing metallic materials (state of surface, thermic treatments, degrees of hammer hardening, etc.). The protection potential establishes a separation between a domain of safe utilization and a domain of contingent utilization where localized corrosion may progress if already begun.

The different electrochemical methods in determining these two magnitudes has been analyzed by Sklarska-Smialowska and Janik-Czachor.(207) The methods to measure these potentials have been reviewed by A. Pourbaix.(208)

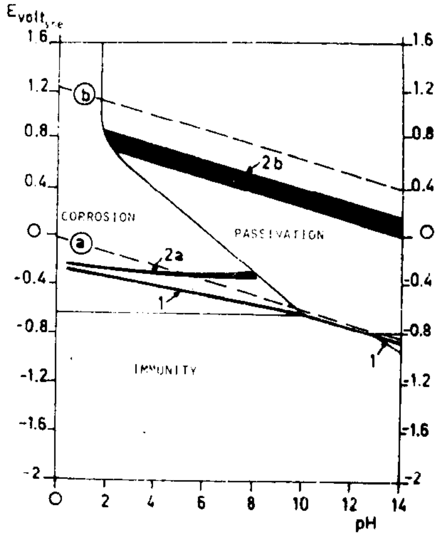

Figure 40. Conditions of immunity, of general corrosion, and of perfect passivation of iron, in the absence of oxygen (line 1) and in the presence of oxygen (lines 2a and 2b).

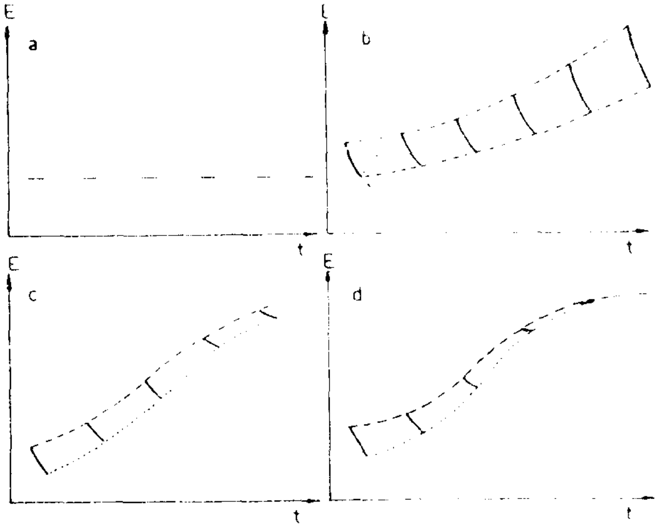

Figure 41. Evolution of the electrode potential during alternate actions of wetting and of drying. (a) General corrosion without formation of passivating deposits; (b) localized corrosion with formation of nonprotective deposits; (c) localized corrosion with formation of deposits becoming progressively highly protective; (d) localized corrosion with formation of deposits becoming progressively perfectly protective. (After M. Pourbaix.[209])

7.2.2. Atmospheric Corrosion

Figure 40 represents on the basis of a E–pH diagram for iron, at 25°C, the experimental behavior of iron electrically isolated in solutions free of chloride, with no dissolved oxygen (line 1), and containing oxygen dissolved under atmospheric pressure (lines 2a and 2b), respectively.[3,8,205,209] This indicates that in the absence of oxygen the iron is always active, while in the presence of oxygen, it can, according to the pH of the solution, exist in an active state or a passive state. In the last condition, the higher the potential of the iron is, the more protective the layer of the passivating oxide is. When protection is sufficient, the electrode potential of the iron is established at 250–500 mV below line b (equilibrium H_2O–O_2). It is a fact of general observation that the electrode potentials of perfectly passivated metals and alloys in oxygen-saturated solutions are stably established in zone 2b.† These potentials are the potentials of a reduction of oxygen. They exist for all metals and alloys and depend, to a certain degree, on the nature of the metallic material. For iron and non- or low-alloy steels, in the presence of water with a pH of 7, these electrode potentials are situated between +300 and +550 mV.

---

† In the case of noncorrodable metals with an overvoltage of reduction of oxygen which is relatively weak, which is not passivated by an oxide film in presence of oxygen but preserves a metallic surface in the state of immunity, zone 2b is higher, 50–150 mV below the potentials indicated by line b (equilibrium H_2O–O_2).

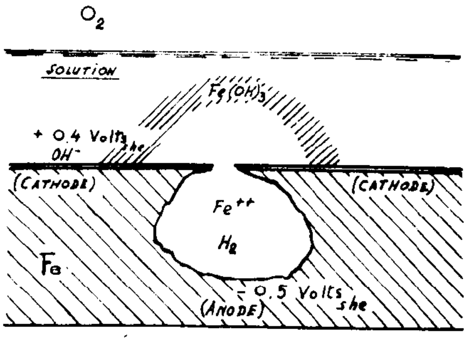

Figure 42. Crevice corrosion of iron in the presence of aerated water.

When a metallic material is exposed to alternating actions of wetting by an electrolyte and drying with or without heating, the evolution of its electrode potential from the successive contacts with the electrolyte is connected with the mechanism of formation of the products of corrosion on the metal as well as their protective character. In this respect, according to Pourbaix,(209) the four types of behavior can be considered (Figure 41), where each trait represents the potential evolution in immersion, and two successive traits are observed with two consecutive immersions. The electrolyte is water similar to rain water, dew, or spray in the presence of which the behavior of the metal or alloy is examined.

Figure 41a shows the case of steel without protective oxide and suffering generalized corrosion. The electrode potential is constantly situated in the domain of corrosion, conforming with line 1a of Figure 40. Figure 41b indicates the electrode potential at the beginning of immersion rising progressively (sign of the formation of a passivating oxide), but sinking rapidly during immersion (sign of imperfect passivation). The metal has, with the beginning of immersions, nonaerated or anodic zones, with low electrode potential, where the metal is corroded, and aerated or cathodic zones with high electrode potential, where oxygen is reduced on the passivated metal (Figure 42). This potential measured experimentally is a "mixed potential," between the potential of the local anodes and that of the local cathodes. Lowering this in immersion shows that the anodes with a low potential develop to the detriment of local cathodes. Thus, the oxide layer which develops during the drying phase

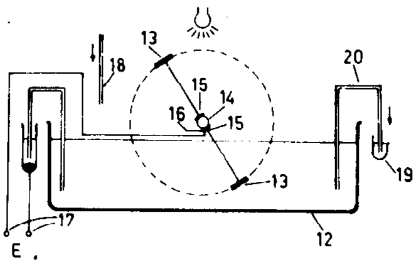

Figure 43. Rotating device for studying the atmospheric corrosion of metals and alloys.

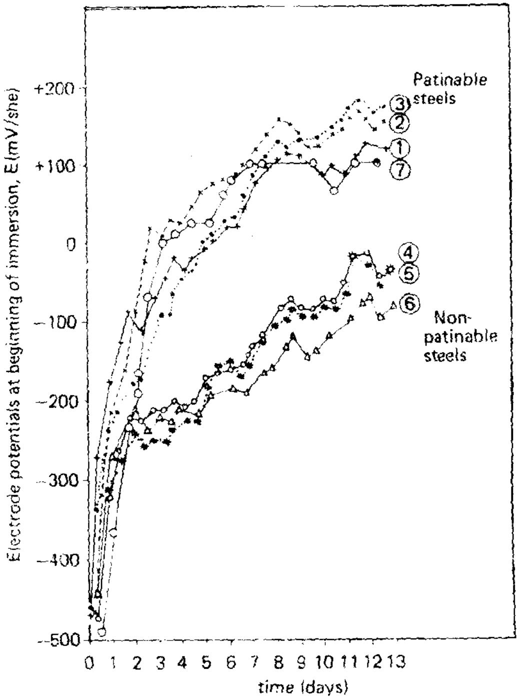

Figure 44 Differentiation between weathering and nonweathering steels.

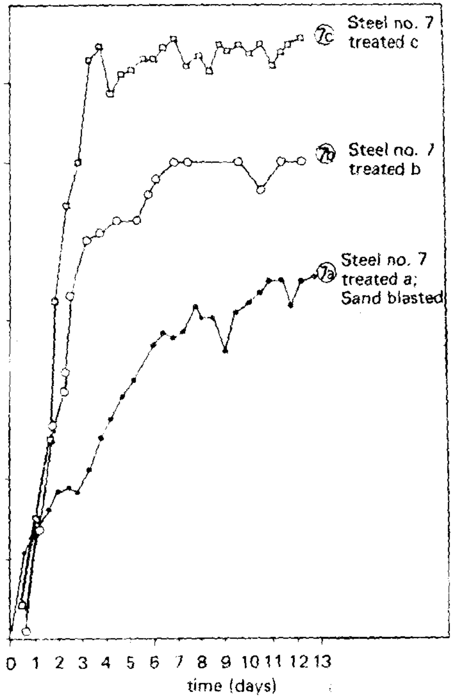

Figure 45 Influence of surface pretreatments on the weathering rate of a same steel.

is not protective. Figure 41c shows the elevation of the potential being stronger and the regression in immersion as weaker. This reveals a progressive improvement of the protective power of the solid corrosion products formed. In Figure 41d, the electrode potential stabilizes rapidly at elevated values and there is no fall in immersion. The mixed potential is barely influenced by the existences of anodes with low potential and remains constantly equal to that of the cathodes with high potential. This is a sign of the formation of a protective layer of corrosion products. It is at these values that the electrode potential of a steel perfectly "patined" by nature is stabilized.

There is, therefore, a procedure of treatment capable of producing solid corrosion products similar to that formed by nature. There is also a criterion of appreciation of the aptitude for passivation and the protective quality of corrosion products. The measurement of the electrode potential during immersion allows the quick prediction of whether the metal is or is not

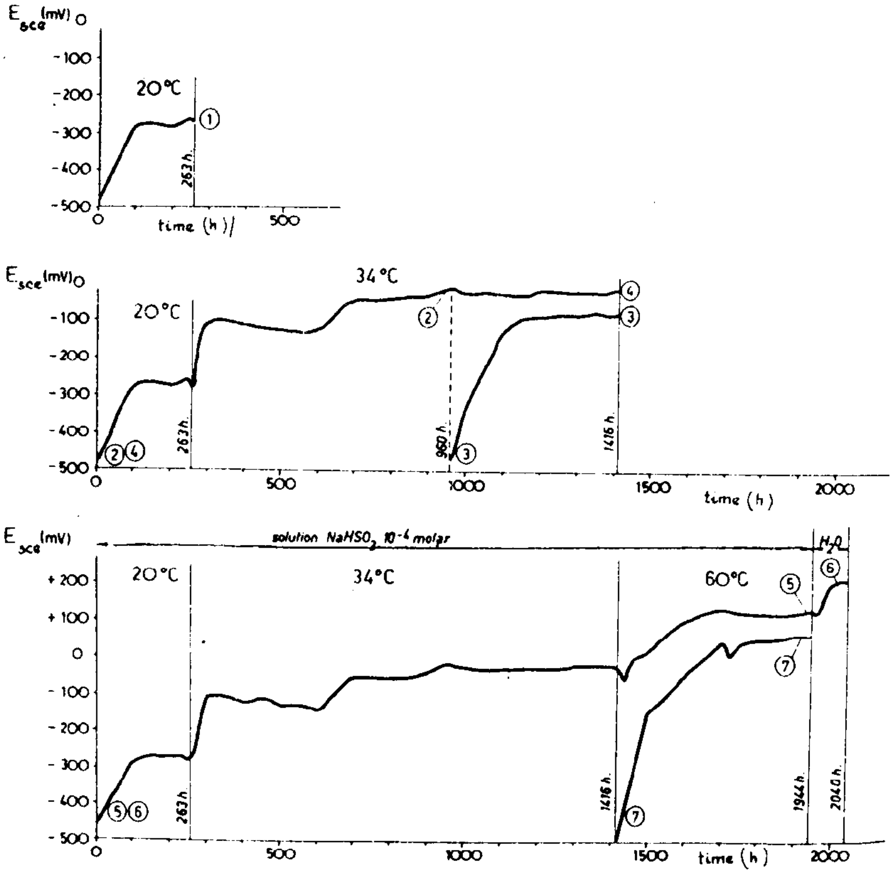

Figure 46. Effect of the temperature on potential–time curves (after L. de Miranda[47,211]).

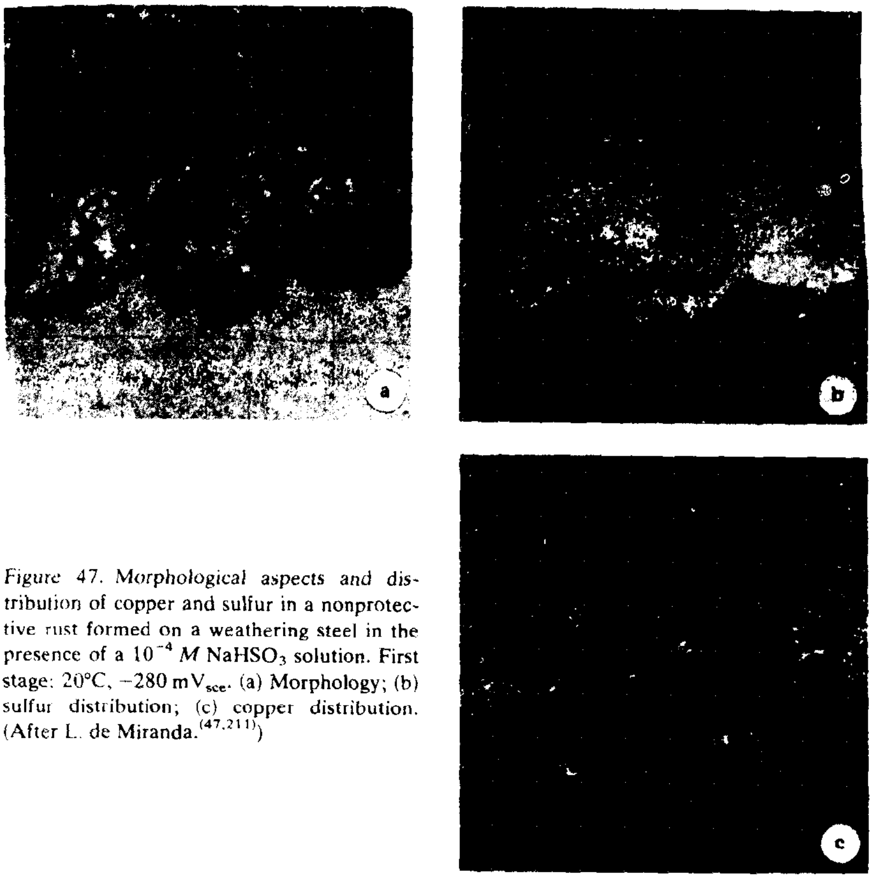

Figure 47. Morphological aspects and distribution of copper and sulfur in a nonprotective rust formed on a weathering steel in the presence of a 10^{-4} M $NaHSO_3$ solution. First stage: 20°C, -280 mV_{sce}. (a) Morphology; (b) sulfur distribution; (c) copper distribution. (After L. de Miranda.[47,211])

patinable. This experimental method (see Figure 43) is based on the fact that samples of types of steel to be examined are exposed to a cycle of immersion in a water representing rain water or dew then measuring the electrode potential during the immersion periods.

Figures 44 and 45 illustrate examples of application of the method with the utilization of a rotating apparatus turning at a speed of one turn in 53.5 min in pure aerated water, according to a cycle containing 13 min of immersion (25%) and 40.5 min of emersion (75%). The question was to establish if the three types of steel, numbered 1, 2, and 4, should be regarded as patinable or nonpatinable. Previous examinations of steel for industry have shown that, for the same surface treatment, the evolution curves of the electrode potential of the types of steel recognized to be patinable (Nos. 3 and 7) are situated distinctly above the corresponding curves of steel types recognized as being nonpatinable (Nos. 5 and 6). Two of the three types of steel examined have to

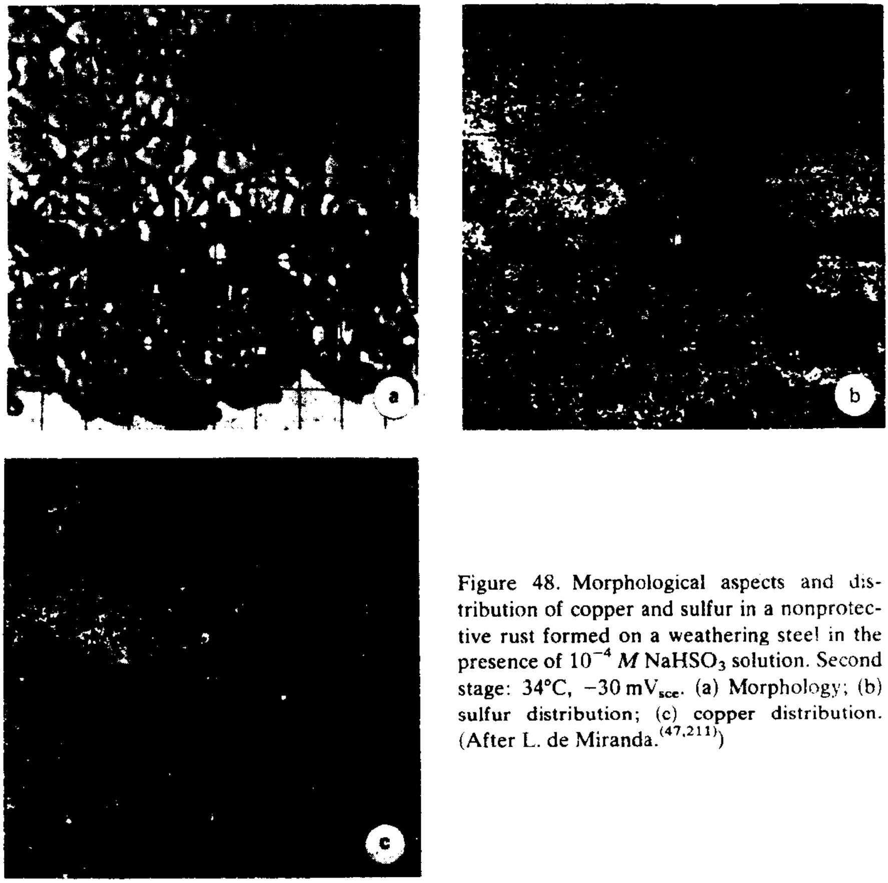

Figure 48. Morphological aspects and distribution of copper and sulfur in a nonprotective rust formed on a weathering steel in the presence of 10^{-4} M $\mathrm{NaHSO_3}$ solution. Second stage: 34°C, $-30\ \mathrm{mV_{sce}}$. (a) Morphology; (b) sulfur distribution; (c) copper distribution. (After L. de Miranda.$^{(47,211)}$)

be considered patinable (Nos. 1 and 2) and the third is not (No. 4). Figure 45 shows that the formation of patina on steel No. 7, generally used industrially sanded white, can be accelerated and improved by other surface treatments.

Figure 46 indicates, according to de Miranda,$^{(47,211)}$ the influence of different insolation periods (simulated in the case of the time covered, by the absence of heating of the samples between two consecutive immersions, or in the case of more or less insolated periods, by a more or less strong heating) on the evolution of the electrode potential of a slightly alloyed steel (weatherable)† in experiments of accelerated atmospheric corrosion utilizing a solution of 10^{-4} M $\mathrm{NaHSO_3}$ (pH = 4.6) simulating rain water of a climate polluted by $\mathrm{SO_2}$ (2×10^{-7} atm $\mathrm{SO_2}$, 530 μg $\mathrm{SO_2}$ $\mathrm{m^{-3}}$, at 25°C). Without heating the samples during emersion (20°C), a stabilization of electrode potential can be observed at relatively low values, $-230\ \mathrm{mV_{sce}}$. Heating to 34°C, the potential is established at about $-20\ \mathrm{mV_{sce}}$. Heating to 60°C, it is about $+130\ \mathrm{mV_{sce}}$.

---

† C, 0.13%; Mn, 0.65%; P, 0.10%; S, 0.038%; Si, 0.56%; Ni, 0.04%; Cr, 0.73%; Cu, 0.31%.

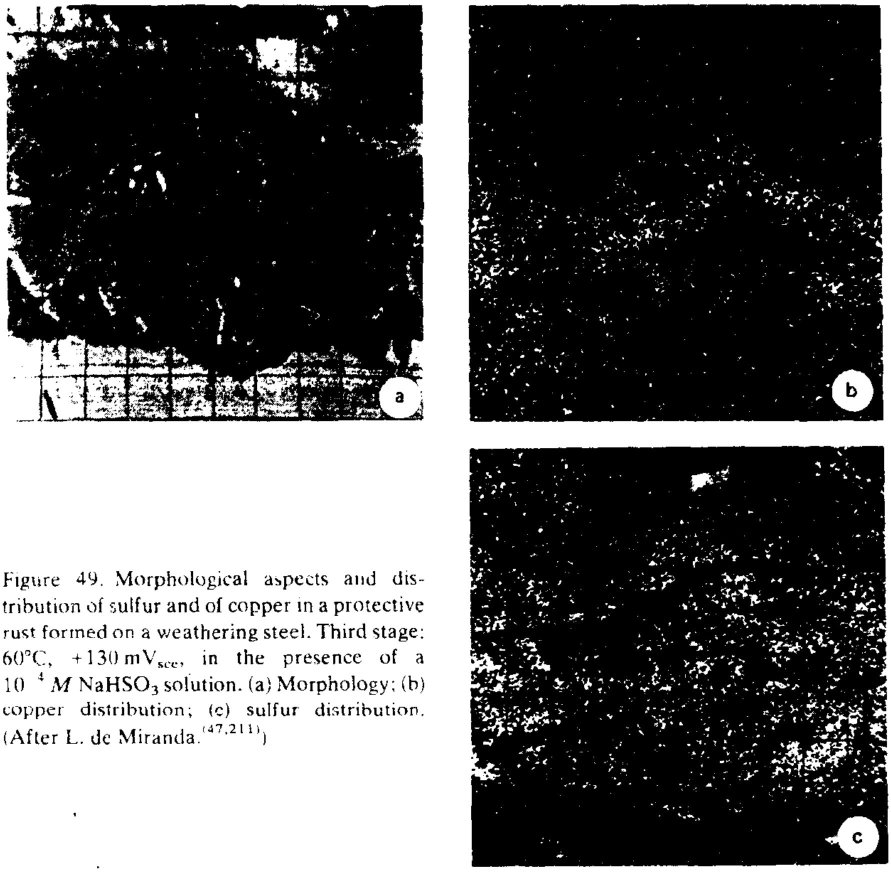

Figure 49. Morphological aspects and distribution of sulfur and of copper in a protective rust formed on a weathering steel. Third stage: 60°C, +130 mV$_{sce}$, in the presence of a 10^{-4} *M* NaHSO$_3$ solution. (a) Morphology; (b) copper distribution; (c) sulfur distribution. (After L. de Miranda.[47,211])

After 34 days of the experiment, the sodium bisulfite solution was replaced by pure aerated water (pH = 6.0) which had the effect of lifting the electrode potential from +130 to +200 mV$_{sce}$.

Figure 47 presents a morphological aspect of the corrosion layer when the potential is −280 mV$_{sce}$—longitudinal and transversal cracks, large cavities at the metal–oxide interface. The sulfur is concentrated closely to the metal–oxide interface and close to the cavity. Copper invades the metal–oxide interface and the region of the cavity.

As shown in Figure 48, the elevation of the electrode potential from −280 to −30 mV$_{sce}$ does not eliminate the crack or the cavities within the rust layer, but it has the effect of strongly reducing the localization of sulfur and favoring a regular distribution of it. The tendency toward homogenization of distribution is also noticeable in the case of copper.

When the electrode potential reaches +130 mV$_{sce}$ (Figure 49), there remain some longitudinal and transversal cracks. The distribution of sulfur in

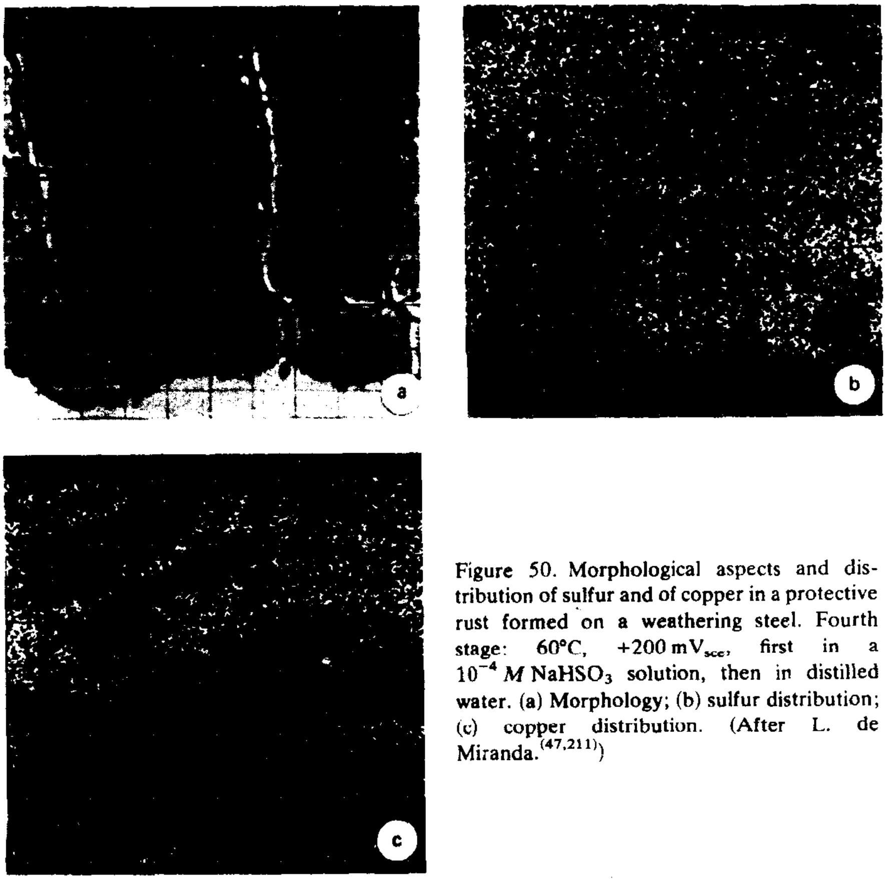

Figure 50. Morphological aspects and distribution of sulfur and of copper in a protective rust formed on a weathering steel. Fourth stage: 60°C, $+200\ \mathrm{mV_{sce}}$, first in a $10^{-4}\ M\ \mathrm{NaHSO_3}$ solution, then in distilled water. (a) Morphology; (b) sulfur distribution; (c) copper distribution. (After L. de Miranda.[47,211])

the rust layer is homogeneous. Copper does not spray above the higher longitudinal crack.

The final treatment in pure aerated water, which allowed the electrode potential to reach $+200\ \mathrm{mV_{sce}}$, has lead to rust without cavities and a more compact homogenous repartition of sulfur in the rust layer and of copper in the part above this (Figure 50).

In comparison, Figure 51 concerns a low-alloy steel exposed 30 months on the roof of a building of the Free University of Brussels, placed there during the winter. The electrode potential was about $-100\ \mathrm{mV_{sce}}$, corresponding to a nonprotective rust cover 100–150 μm thick.

The rising of the electrode potential with zero current is thus one of the best indications of the improvement of the protective quality of a patina. This elevation of the potential is connected not only to the disappearance or dying out of corrosion caverns (a necessary, but not sufficient, condition), but also with the absence of a local accumulation of sulfur (sulfur-containing "nests" or "bands").

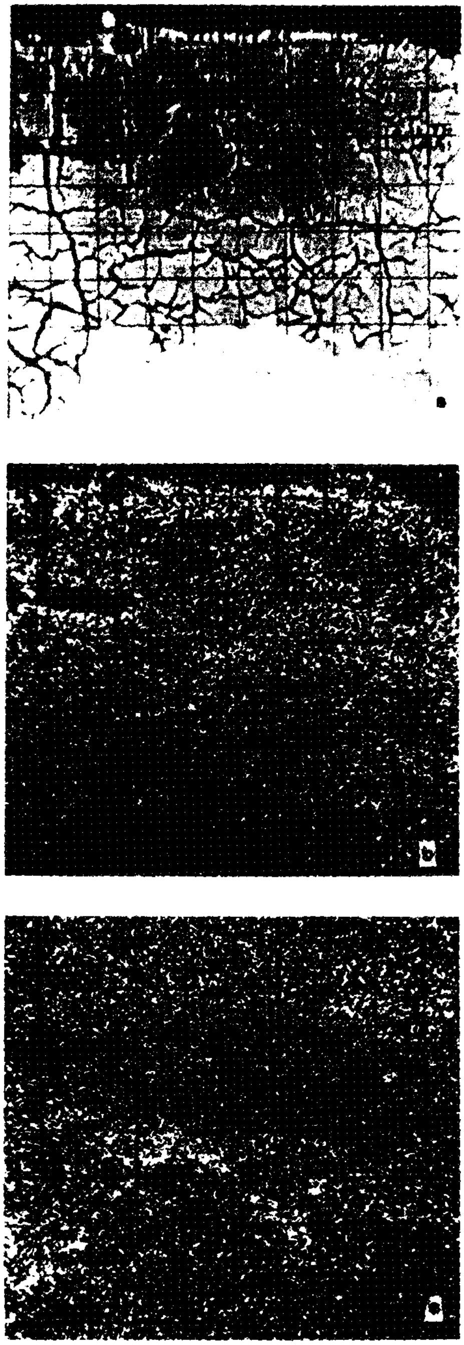

Figure 51. Weathering steel submitted to atmospheric corrosion in Brussels. 30 months. Pretreatment with solutions of 1 M $NaHSO_3$ and 0.1 M $CuSO_4$. $E = -100\ mV_{sce}$. (a) Morphology; (b) sulfur distribution; (c) copper distribution. (After L. de Miranda.(47,211))

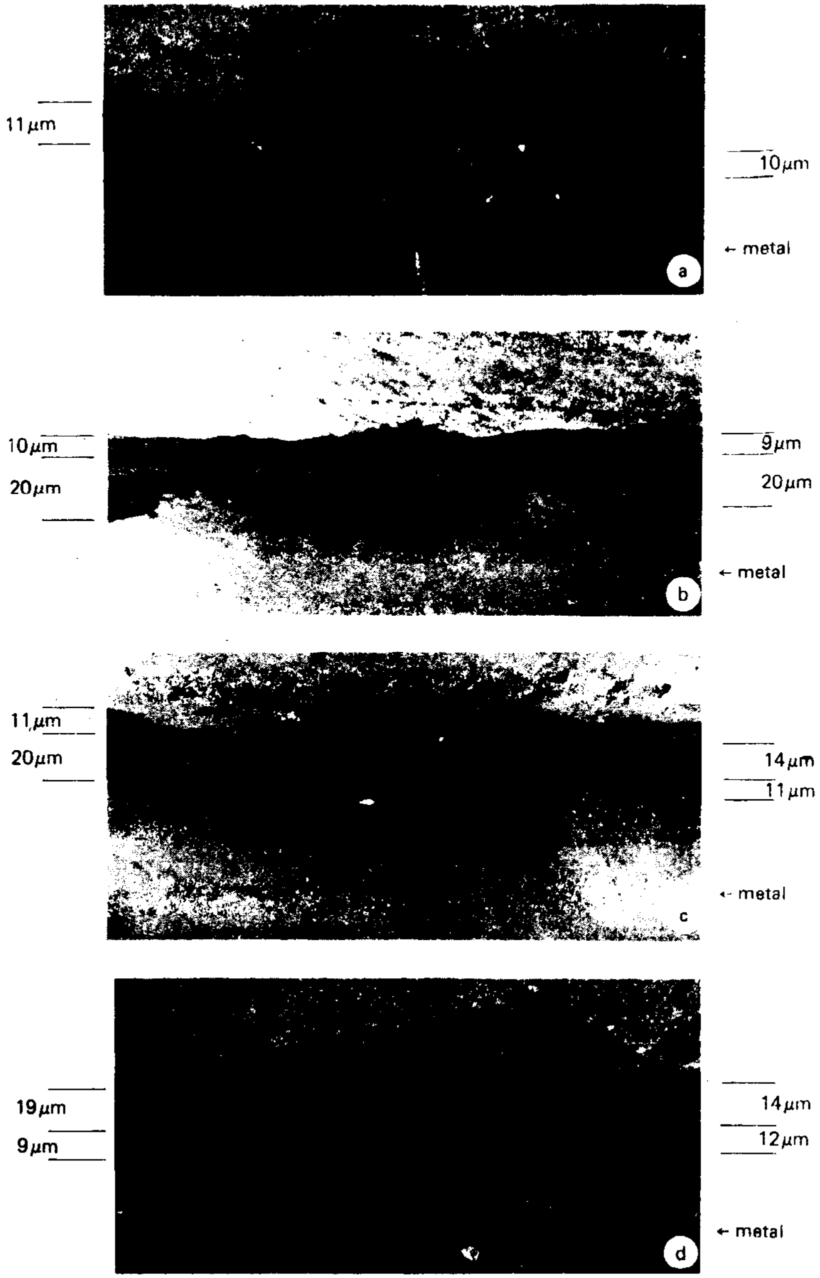
11 μm
10 μm
← metal
a
10 μm
20 μm
9 μm
20 μm
← metal
b
11 μm
20 μm
14 μm
11 μm
← metal
c
19 μm
9 μm
14 μm
12 μm
← metal
d

Figure 52. Morphological aspects of rusts examined under polarized light (a) Specimen No. 1: ($-280\ \text{mV}_{\text{sce}}$); (b) specimen No. 2: ($-125\ \text{mV}_{\text{sce}}$); (c) specimen No. 3: ($-125\ \text{mV}_{\text{sce}}$); (d) specimen No. 4: ($+220\ \text{mV}_{\text{sce}}$).

Furthermore, the observation in polarized light of the rust layers studied above has allowed de Miranda$^{(47)}$ to show their twin nature (Figure 52):

(i) Toward $-300\ \text{mV}_{\text{sce}}$: presence of a reddish layer of 10–15 μm directly above the metal. Birth of a thin gray layer of 1–2 μm.
(ii) Toward $-125\ \text{mV}_{\text{sce}}$: noticeable thickening of the grayish layer (10–30 μm). Thickness of the external reddish layer remains basically constant (10–20 μm).
(iii) Toward $+125\ \text{mV}_{\text{sce}}$: consolidation of the gray layer by thickening and improving the distribution at the metal–rust interface. The reddish layer preserves the same thickness (10–20 μm).
(iv) Toward $+220\ \text{mV}_{\text{sce}}$: identical morphological aspect, but with reinforcement of the gray layer.

de Miranda$^{(47)}$ has shown that the internal layer, gray in polarized light, whose thickness grows and distribution improves as the electrode potential rises, is effectively responsible for the protective qualities of the rust layers of weathering steels. This internal layer consists of goethite or α-FeOOH. The outer layer, reddish in polarized light, consists of lepidocrocite or γ-FeOOH, which is nonprotective.

Auxiliary Notation

H	enthalpy
G	free energy (or Gibbs free energy)
S	entropy
μ	chemical molar potential
c_p	specific heat at constant pressure
h°	standard enthalpy of formation
g°	standard free energy of formation
μ°	standard chemical potential
s°	standard entropy
c_p°	specific molar heat at constant pressure
ΔH°	standard enthalpy of reaction
ΔG°	standard free energy of reaction
ΔS°	standard entropy of reaction
ΔC_p°	specific molar heat of reaction at constant pressure
K_T	equilibrium constant
E	electrode potential (or reaction potential)
E_0	equilibrium potential of electrochemical reaction
E_0°	standard equilibrium potential of electrochemical reaction
she	standard hydrogen electrode
sce	saturated calomel electrode
a_M	activity of the constituent M
(M)	activity of the constituent M (in the equation)
c_M	concentration of the constituent M
φ_M	fugacity of the constituent M
f_M	activity coefficient of the constituent M
p	pressure (atm)
T	absolute temperature (0°C = 273.15 K)
R	constant of perfect gases = 1.98717 ± 0.00029 cal $\text{deg}^{-1}\ \text{mol}^{-1}$
F	Faraday constant = 96,487.0 ± 16 C equiv^{-1}, 23,060.9 ± 0.4 C $\text{equiv}^{-1}\ \text{V}^{-1}$
cal	thermochemical calorie = 4.1840 J
η	overvoltage = $(E - E_0)$
A	affinity = $-\Delta G = -\Sigma\nu\mu$
r	stoichiometric coefficient of reaction bodies
n	stoichiometric coefficient of reaction electrons
z	ionic charge

T277 A 5

References

1. W. E. Bardgett and J. F. Stanners, The Delhi pillar: a study of the corrosion aspects, *J. Iron Steel Inst.* **201**, 3–10 (1963).
2. G. Wranglen, The "rustless" iron pillar at Delhi, *Corros. Sci.* **10**, 761–770 (1970).
3. M. Pourbaix, *Leçons en Corrosion Electrochimique*, 2nd ed., Cebelcor, Brussels (1975).
4. Société Shell, *Exposition de la Corrosion*, organisée par la Société Shell de Belgique, sous le patronage de la Commission Belge pour l'Etude de la Corrosion, Brussels, 1937.
5. H. H. Uhlig, Cost of corrosion in the United States, *Corrosion* **6**, 29–33 (1950).
6. S. Liechtenstein, The many faces of corrosion, *Technical News* STR-3454, National Bureau of Standards NBS, Washington, D.C. (1966).
7. S. Liechtenstein, Corrosion costs $10 billions per year, *Materials Protect.* **16**, 24 (1967).
8. M. Pourbaix, *Lectures on Electrochemical Corrosion*, Plenum Press, New York and Cebelcor, Brussels (1973).
9. T. P. Hoar, The cost of corrosion and protection of metals in U.K.: a review, *Inst. Corros. Technol.* **32**, 19–22 (1972).
10. U. R. Evans, The electrochemical character of corrosion, *J. Inst. Metals* **30**, 263–267 (1923).
11. M. Pourbaix, Corrosion et protection de toitures en zinc, *Publication CEBELCOR* F.11 (1951).
12. M. Pourbaix, Deux expériences de cours en thermodynamique électrochimique, *Proceedings of the 2nd CITCE Meeting, Milan*, 1950, Tamburini, Milan (1951), pp. 371–378.
13. M. Pourbaix and J. Feron, Potentiels de passivation et d'activation du fer. Corrosion cathodique du fer en présence d'oxygène, *Proceedings of the 3rd CITCE Meeting, Bern*, 1951, Manfredi, Milan (1952), pp. 128–134.
14. J. Van Muylder and M. Pourbaix, Corrosion et protection cathodiques du fer. Expérience de démonstration, *Rapports Techniques CEBELCOR* **11**, RT.11 (1953).
15. M. Dodero, Sur la corrosion cathodique du fer et la formation anodique de ferrite cristallisée par l'électrolyse de la soude fondue, *J. Chim. Phys.* **49C**, 210–213 (1952).
16. R. K. Freier, Thermodynamik der Schutzschichtbildung bei niedrigen Temperaturen. Betriebliche Erfahrungen, *Allianz-Berichte* **16**, 8–13 (1971).
17. U. R. Evans, *An Introduction to Metallic Corrosion*, Arnold, London (1948), pp. VII, XX.
18. I. Prigogine and R. Defay, *Thermodynamique Chimique*, Desoer, Liège, Vol. I (1944), Vol. II (1946).
19. I. Prigogine and R. Defay, *Thermodynamique Chimique*, Desoer, Liège (1950).
20. G. N. Lewis and M. Randall, *Thermodynamics*, 2nd ed., McGraw-Hill, New York (1961).
21. H. S. Harned and B. B. Owen, *The Physical Chemistry of Electrolytic Solutions*, 3rd ed., Reinhold, New York (1958).
22. Th. De Donder, *L'Affinité* (*Rédaction nouvelle par P. van Rysselberghe*), Gauthier Villars, Paris (1936).
23. M. Pourbaix, *Thermodynamique des Solutions Aqueuses Diluées. Représentation Graphique du Rôle du pH et du Potentiel*, Thèse Delft (October 1945), Ch. Béranger, Paris et Liége (1945), CEBELCOR (new edition, 1963).
24. D. D. Wagman, W. H. Evans, V. B. Parker, I. Halows, S. M. Bailey, and R. M. Schumm, Selected values of chemical thermodynamic properties, *Nat. Bur. Stand.* (*U.S.*) *Tech. Note* **270-3** (1968), **4** (1969), **5** (1971).
25. D. R. Stull and H. Prophet, JANAF Thermodynamical Tables, *NRDS-NBS* **37** (June 1970), Reference data Service, National Bureau of Standards, Washington, D.C.
26. N. W. Chase, J. L. Curnutt, A. T. Hu, H. Prophet, A. N. Syverud, and L. C. Walker, JANAF Thermodynamical Tables, 1974 Supplement, Reprint No. 50, *J. Phys. Chem. Ref. Data* 3(2), 311–480 (1974).
27. Cebelcor, Enthalpies libres de formation standard, à 25°C, *Rapports Techniques CEBELCOR* **72**, RT.87 (1960).

28. C. E. Wicks and F. E. Block, Thermodynamic Properties of 65 Elements. Their oxides, halides, carbides and nitrides, Bulletin 605, Bureau of Mines, Department of the Interior, Washington, D.C.
29. G. B. Naoumov, B. N. Rijenko, and I. L. Khodakovski, *Handbook of Thermodynamic Data*, transl. G. J. Soleimani, U.S. Geological Survey P.B. 226722, NTIS U.S. Department of Commerce (1974).
30. R. K. Freier, *Aqueous Solutions. Data for Inorganic and Organic Compounds*, Walter de Gruyter, Berlin, Vol. 1 (1976), Vol. 2 (1978).
31. W. M. Latimer, *The Oxidation States of the Elements and their Potentials in Aqueous Solutions*, Prentice-Hall, New York (1952).
32. R. M. Garrels and C. L. Christ, *Solutions, Minerals and Equilibria*, Harper and Row, New York (1965).
33. M. Pourbaix, *Atlas d'Equilibres Electrochimiques à 25°C*, Gauthier-Villars, Paris and Cebelcor, Brussels (1963).
34. M. Pourbaix, *Atlas of Electrochemical Equilibria in Aqueous Solutions*, Pergamon Press, London and Cebelcor, Brussels (1965).
35. G. Charlot, *Les réactions chimiques en solution. L'analyse qualitative minérale*, 6th ed., Masson & Cie, Paris (1969).
36. L. G. Sillen and A. E. Martell, Stability constants of metal–ion complexes, Special Publication No. 17, The Chemical Society, London (1964) and Supplement No. 1, Special Publication No. 25 (1971).
37. W. Nernst, Die elektromtorische Wirksamheit des Ionen, *Z. Phys. Chem.* (*Leipzig*) **4**, 129–181 (1889).
38. F. Haber, Über die elektrische Reduktion von Nichtelektrolyten, *Z. Phys. Chem.* (*Leipzig*) **32**, 193–270 (1900).
39. R. Piontelli *et al.*, Etudes sur les méthodes de mesure des tensions de polarisation, *Proceedings of the IIIrd CITCE Meeting, Bern*, 1951, Manfredi, Milan (1952).
40. A. J. de Béthune and N. A. Swendeman Loud, *Standard Aqueous Electrode Potentials and Temperature Coefficients at 25°C*, Clifford A. Hampel, Illinois (1964).
41. J. A. Christiansen and M. Pourbaix, Conventions concernant les signes des forces électromotrices et des potentiels d'électrode, *Proceedings of the 17th Conference International Union of Pure and Applied Chemistry*, Stockholm (1953), pp. 82–85.
42. J. Detournay, L. de Miranda, R. Derie, and M. Ghodsi, "Rouille Verte II." Enthalpie libre de formation et domaine de stabilité dans le diagramme d'équilibres tension–pH du fer, *Rapports Techniques CEBELCOR* **123**, RT.215 (January 1974).
43. M. Pourbaix, Quelques applications de la thermodynamique électrochimique, *Proceedings of the 2° Convegno Nazionale, Associazione Italiana di Metallurgia, Milano, 1948.*
44. M. Pourbaix, Bases thermodynamiques de la théorie de la corrosion, *Association Belge pour l'Etude, l'Essai et l'Emploi des matériaux, ABEM, P.V. 13ème séance*, Brussels, 20 April 1945.
45. M. Pourbaix, Thermodynamique et corrosion, *Mét. Corros.* **13**(159), 189–193 (1938).
46. M. Pourbaix, Potential–pH equilibrium diagrams for the iron–water system, at 25°C, and their applications to the study of the passivation of iron, *Rapports Techniques CEBELCOR* **13**, RT.226 (May 1975).
47. L. de Miranda, Les aspects électrochimiques de la corrosion atmosphérique des aciers patinables, *Thèse Bruxelles* (October 1974), *Rapports Techniques CEBELCOR* **125**, RT.221 (October 1974).
48. J. E. O. Mayne and M. J. Pryor, The mechanism of inhibitors of corrosion of iron; I. By chromic acid and potassium chromate, *J. Chem. Soc.* 1831–1835 (1949).
49. M. Nagayama and M. Cohen, The anodic oxidation of iron in neutral solution, *J. Electrochem. Soc.* **109**, 781–790 (1962); **110**, 670–680 (1963), **114**, 994–1001 (1967).
50. M. C. Bloom and L. Goldenberg, Fe_2O_3 and the passivity of iron, *Corros. Sci.* **5**, 623–630 (1965).

51. C. L. Foley, J. Kruger, and C. J. Bechtoldt, Electron diffraction studies on active, passive and transpassive oxide films formed on iron, *J. Electrochem. Soc.* **114**, 994–1001 (1967).
52. H. T. Yolken, J. Kruger, and J. P. Calvert, Hydrogen in passive films on Fe, *Corros. Sci.* **8**, 103–108 (1968).
53. M. Pourbaix, Corrosion, passivité et passivation du fer. Le rôle du pH et du potentiel, *Thèse Bruxelles* (1945), *Mémoires Soc. Royale Belge des Ingénieurs et Industriels* No. 1 (March 1951).
54. N. Feitknecht and P. Schindler, *Löslickkeitskonstanten von Metalloxide, -hydroxiden, -und -hydroxidzalen in wässerigen Lösungen*, Butterworths, London (1963).
55. N. de Zoubov, J. Van Muylder, P. Van Laer, and M. Pourbaix, Sur le comportement de cuivre en présence de solutions de bicarbonate de sodium, *Rapports Techniques CEBELCOR* **101**, RT.133 (August 1965).
56. J. Van Muylder, N. de Zoubov, and M. Pourbaix, Diagrammes d'équilibres tension–pH des systèmes $Cu-H_2O$ et $Cu-Cl^--H_2O$, à 25°C, *Rapports Techniques CEBELCOR* **85**, RT.101 (July 1972).
57. CEBELCOR's Rapports Techniques on *potential–pH diagrams of binary metal/water systems.* (a) *In French*: Cd (RT.3, 1953); Ti (RT.4, 1953); CN (RT.5, 1953); Co (RT.6, 1954); Fe (RT.7, 1954); Mn (RT.18, 1954); Ni (RT.23, 1955); Sn (RT.25, 1955); Ge (RT.27, 1955); V (RT.29, 1956); U (RT.31, 1956); W (RT.32, 1956); Te (RT.33, 1956); Mo (RT.35, 1956); Mg (RT.39, 1956); Cr (RT.41, 1956); Al (RT.42, 1956); Cl (RT.44, 1957); Zr (RT.45, 1957); As (RT.46, 1957); B (RT.47, 1957); Bi (RT.48, 1957); Te (RT.50, 1957); Re (RT.51, 1957); Ta (RT.52, 1957); Nb (RT.53, 1957); Sb (RT.55, 1957); Ru (RT.58, 1958); Rh (RT.59, 1959); Pd (RT.60, 1958); Os (RT.61, 1958); Ir (RT.62, 1958); Pt (RT.63, 1958); H (RT.69, 1958); Li, Na, K, Rb, Cs (RT.70, 1958); Be (RT.71, 1958); Ca, Sr, Ba (RT.72, 1958); Ra (RT. 73, 1958); Ga (RT.74, 1958); In (RT.75, 1958); Tl (RT.76, 1958); Cu (RT.100, 1962); Ti (RT.146, 1968). Some reports have also been published in French in the Proceedings of CITCE meetings: *CITCE 2* (Milan, 1950): Pb, 15–28; Ag, 34–41; O and H_2O_2, 42–50; *CITCE 3* (Bern, 1951): Al, As, Au, Be, Cd, Co, Hg, Se, Sn, Ti, Tl, 15–29; *CITCE 8* (Madrid, 1956): Mg, 218–237; Mo, 238–249; W, 250–257; U, 258–269; *CITCE 9* (Paris, 1957): As, 20–31; Sb, 32–46; Bi, 47–56; Tc, 57–65; Re, 66–76; Nb, 77–83; Ta, 84–91; Zr, 92–101; B, 102–116; Al, 117–129; Cl, 130–154. (b) *In English*, Proceedings of CITCE meetings: *CITCE 6* (Poitiers, 1954): Fe, 118–123; Cd, 133–137; CN, 138–152; Co, 153–166; Ti, 167–179; Mn, 390–409; Pb, 334–341, 342–350; *CITCE* 7 (Lindau, 1955): Ni, 193–215; Sn, 216–239.
58. CEBELCOR's Rapports Techniques on *Potential/pH diagrams of ternary systems in the presence of water, at 25°C.* (a) *In French*: $Fe-CO_2$ (RT.8, 1954); $Pb-CO_2$ and $Pb-SO_3$ (RT.13, 1953); $Mg-CO_2$ and $Mg-H_3PO_4$ (RT.39, 1956); Cu–Cl (RT.101, 1962); $Cu-CO_2$ (RT.133, 1965); Cu–S (RT.221, 1974); Fe–S (RT.221, 1974); $Fe-SO_3$ (RT.215 and 221, 1972). (b) *In English*: Proceedings of CITCE meetings. *CITCE 6* (Poitiers, 1954) $Fe-CO_2$, 124–132; $Pb-CO_2$, 334–341.
59. J. P. Gabano and J. P. Brenet, Quelques vérifications expérimentales du diagramme tension–pH du manganèse, *Electrochim. Acta* **1**, 242–245 (1959).
60. J. P. Brenet, J. P. Gabano, and J. Reynaud, Compléments apportés au diagramme tension–pH du manganèse, *Electrochim. Acta* **8**, 207–216 (1963).
61. T. S. de Gromobov and L. L. Shreir, The formation of nickel oxides during the passivation of nickel in relation to potential–pH diagram, *Electrochim. Acta* **11**, 895–904 (1966).
62. G. Valensi, Phénomènes de corrosion par le soufre, *Corros. Anticorros.* **2**, 189–200, 246–251 (1954).
63. G. Valensi, Comportement électrochimique du soufre. Diagrammes d'équilibres tension–pH du système $S-H_2O$, à 25°C et 1 atmosphère, *Rapports Techniques CEBELCOR* **121**, RT.207 (1973).

64. T. R. Beck, Stress corrosion cracking of titanium alloys: electrochemistry of freshly generated titanium surfaces, *Q. Prog. Rep.* No. 9 (period 1 July 1968 to 30 September 1968), contract NBS 7-489.
65. F. Letowski and J. Niemiec, Diagrammes d'équilibres électrochimiques du système U-CO_2-H_2O, à 25°C (in Polish), *Nukleonica* **11** (1966).
66. P. Duby, The thermodynamic properties of aqueous inorganic copper systems, *International Copper Research Association INCRA, Monograph* **IV**, N.S.R.D.S., N.B.S. (June 1977).
67. F. Letowski, J. Serkies, and J. Niemiec, Application of potential-pH diagrams for determination of the occurrence forms of trace elements in some economic mineral deposits, *Econ. Geol.* **61**, 1272–1279 (1966).
68. K. Post and R. G. Robins, Thermodynamic diagrams for the vanadium-water system at 298.15 K, *Electrochim. Acta* **21**, 401–405 (1976).
69. T. Misawa, The thermodynamic consideration for Fe–H_2O system at 25°C, *Corros. Sci.* **13**(9), 659–676 (1973).
70. L. Sathler, Contribution à l'étude du comportement électrochimique du fer en présence de solutions de chlorure ferreux, en liaison avec la corrosion localisée, Thèse de Doctorat, Université Libre de Bruxelles (June 1978). L. Sathler, J. Van Muylder, R. Winand, and M. Pourbaix, Electrochemical behaviour of iron in localized corrosion cells in the presence of chloride, *Proc. 7th Int. Cong. Metal Corr., Rio de Janeiro (Brazil)* **2**, 705–717 (1979).
71. M. H. Froning, M. E. Shanley, and E. D. Verink, An improved method for calculation of potential-pH diagrams of metal–ion–water systems by computer, *Corros. Sci.* **16**(6), 371–377 (1976).
72. E. Mattsson, Stress corrosion in brass considered against the background of potential–pH diagram, *Electrochim. Acta* **3**, 279–291 (1961); Diagramme tension–pH pour l'étude de la corrosion avec exemples de calculs relatifs au système Cu–Cl–H_2O (in Swedish), *Svensk Kemisk Tidskrif* **74**(2), 76–88 (1962).
73. G. Bianchi and P. Longhi, Copper in sea-water. Potential–pH diagrams, *Corros. Sci.* **13**(11), 853–864 (1973).
74. J. Horvath and M. Novak, Electrochemical studies on the corrosion of copper in aqueous hydrogen sulphide environments. I. Interpretation of electrode-potential and polarization data on the basis of the potential–pH equilibrium diagram of the ternary system Cu–S–H_2O, *Acta Chim. Acad. Sci. Hung.* **34**(4), 455–467 (1962).
75. J. Horvath and M. Novak, Potential–pH equilibrium diagrams of some Me–S–H_2O ternary systems and their interpretation from the point of view of metallic corrosion, *Corros. Sci.* **4**, 159–178 (1964).
76. J. Horvath and L. Häckl, Check of the potential–pH equilibrium diagrams of different metal–sulphur–water ternary systems by intermittent galvanostatic polarization method, *Corros. Sci.* **5**, 525–538 (1965).
77. J. Horvath, L. Häckl, and A. Rauscher, Investigation of the possibilities of corrosion inhibition in metal–sulphur–water ternary systems on the basis of potential–pH equilibrium diagrams, *Proceedings of the 2nd Symposium on Corrosion Inhibitors, Ferrara*, 1965 (1966), pp. 477–505.
78. J. Bouet and J. P. Brenet, Contribution à l'étude du diagramme tension–pH du fer en milieux sulfurés, *Corros. Sci.* **3**, 51–63 (1963).
79. A. Bustorff and J. Van Muylder, Comportement électrochimique du cuivre en solutions sulfuriques. Diagrammes d'équilibres tension–pH du système Cu–SO_4H_2–H_2O, à 25°C, *Electrochim. Acta* **9**, 607–612 (1964).
80. P. Delahay, M. Pourbaix, and P. van Rysselberghe, Some potential–pH diagrams and applications (Pb, Ag, Zn), *J. Electrochem. Soc.* **98**, 57–64, 65–67, 101–105 (1951).
81. J. M. Sluyters, H. O. Wijnen, and H. J. van den Hul, The potential–pH diagram of silver in aqueous ammonium-salt solution, *Electrochim. Acta* **5**, 72–78 (1961).

82. H. E. Hömig and G. Glass, Pourbaix-Diagramme für Kupfer in ammoniakhaltigen Lösungen, *Vereinigung Grosskessel Besitzer VGB, Speisewasser Tagung,* 1966 (1966), pp. 31–37.
83. Ph. Brouillet and F. Jolas, Problèmes concernant les anodes dans les cellules primaires, *Electrochim. Acta* **1**, 246–260 (1959).
84. F. Letowski and J. Niemiec, Diagrams of electrochemical equilibria *E*–pH at 25°C. Part I. $Cu-H_2O-NH_3-H_2SO_4$ system, *Roczmiki Chemii. Ann. Soc. Chim. Polonorum* **40**, 1149 (1966).
85. F. Letowski and J. Niemiec, Diagrams of electrochemical equilibria *E*–pH at 25°C. Part II. $Ni-H_2O-NH_3-H_2SO_4$ system, *Roczniki Chemii. Ann. Soc. Chim. Polonorum* **40**, 1159 (1966).
86. F. Letowski and J. Niemiec, Diagrams of electrochemical equilibria *E*–pH at 25°C. Part III. $Ag-H_2O-NH_3-H_2SO_4$ system, *Roczniki Chemii. Ann. Soc. Chim. Polonorum* **41**, 1483–1490 (1967).
87. F. Letowski and J. Niemiec, Diagrams of electrochemical equilibria *E*–pH at 25°C. Part IV. $Co-H_2O-NH_3-H_2SO_4$ system, *Roczniki Chemii. Ann. Soc. Chim. Polonorum* **43**, 281–290 (1969).
88. F. Letowski and B. Kozlowska-Kolodziej, Diagrams of electrochemical equilibria *E*–pH at 25°C. Part V. $Zn-H_2O-NH_3-H_2SO_4$ system, *Roczniki Chemii Ann. Soc. Chim. Polonorum* **47**, 1593–1601 (1973).
89. B. Kozlowska-Kolodziej and F. Letowski, Diagrams of electrochemical equilibria *E*–pH at 25°C. Part VI. $Cd-H_2O-NH_3-H_2SO_4$ system, *Roczniki Chemii Ann. Soc. Chim. Polonorum* **47**, 1603–1610 (1973).
90. J. Niemiec, F. Letowski, W. Charewicz, and W. Wojar, Die Herstellung von Kupfer- und Nickelpulver durch Wassestoffdruckreduktion der Kupfer-Nickel-Elektrolyte, *Freiberg. Forschungsh.* **B128**, 19–24 (1968).
91. R. Bartonicek and M. Lukasovska, A potential–pH diagram for the system $Cu-NH_3-Cl-H_2O$, *Corros. Sci.* **9**, 35–42 (1969).
92. J. van Muylder *et al.*, Fundamental research on the electrochemical behaviour and the corrosion of copper, Final Report to the INCRA (period 1 September 1962 to 31 July 1963), *Publication CEBELCOR* E.53 (1964).
93. J. Serkies, F. Letowski, and J. Niemiec, Application of the potential–pH diagrams to characteristics of some Zechstein copper deposits, *Econ. Geol.* **61**, 1266–1271 (1966).
94. P. Delahay, M. Pourbaix, and P. van Rysselberghe, Potential–pH diagrams, *J. Chem. Educ.* **27**, 683–688 (1950).
95. A. G. Guy and F. N. Rhines, Pourbaix diagrams. A firm basis for understanding corrosion, *Met. Treat. Drop Forg.* **29**, 45–54 (1962); Technical Paper No. 277, University of Florida, *Eng. Prog.* **28**(1), (1964).
96. J. A. Campbell and R. A. Whiteker, A periodic table based on potential–pH diagrams, *J. Chem. Educ.* **46**, 90–92 (1969).
97. K. Kovacs, Das periodische System in Hinsicht auf Korrosion, *Forschungsinstitut für Chemische Schwerindustrie* (November 1974) (Hungary).
98. J. Horvath and M. Novak, (a) Contributions to the mechanism of anaerobic, microbiological corrosion. II. Correlation between pH-values, oxidation–reduction potentials and the composition of solid corrosion products, *Acta Chim. Acad. Scientas. Hung. I,* **25**, 65 (1960); *II,* **33**(2), 221–225 (1962).
99. C. M. Criss and J. W. Cobble, The thermodynamic properties of high temperature aqueous solutions. IV. Entropies of the ions up to 200°C and the correspondence principle, *J. Am. Chem. Soc.* **86**, 5385–5390 (1964); V. The calculation of ionic heat capacities up to 200°C. Entropies and heat capacities above 200°C, *J. Am. Chem. Soc.* **86**, 5390–5393 (1964).
100. J. W. Cobble, The thermodynamic properties of high temperature aqueous solutions. VI. Applications of entropy correspondence to thermodynamics and kinetics, *J. Am. Chem. Soc.* **86**, 5394–5401 (1964).

101. I. L. Khodakovski, B. N. Ryzhenko, and G. B. Naumov, Thermodynamics of aqueous electrolyte solutions at elevated temperatures (temperature dependence of the heat capacities of ions in aqueous solution), *Geochem. Internat.* **5**, 1200–1219 (1968), translated from *Geokhimia* No. 12, 1486–1503 (1968).

102. I. L. Khodakovski, Thermodynamics of aqueous solutions of electrolytes at elevated temperatures (entropies of ions in aqueous solutions at elevated temperatures), *Geochem. Internat.* **6**, 29–34 (1969), translated from *Geokhimia* No. 1, 57–63 (1969).

103. A. J. de Béthune, T. S. Licht, and N. Swendeman, The temperature coefficients of electrode potentials. The isothermal and thermal coefficients. The standard ionic entropy of electrochemical transport of the hydrogen ion, *J. Electrochem. Soc.* **106**(7), 616–625 (1959).

104. G. R. Salvi and A. J. de Béthune, The temperature coefficients of electrode potentials. II. The second isothermal temperature coefficient, *J. Electrochem. Soc.* **108**(7), 672–676 (1961).

105. G. D. Manning and J. Melling, Potential Eh–pH diagrams at elevated temperatures. A survey, Warren Spring Laboratory, LR.128 (ME) (1971).

106. R. T. Lowson, Potential–pH diagrams at temperatures above 298.16°K. Part I. Theoretical background, *Aust. AEC AAEC/E* [*Rep.*] **AAEC/E219** (July 1971).

107. P. Duby, Graphical representation of equilibria in aqueous systems at elevated temperatures, Internal Report H, Krumb School of Mines, Columbia University, New York (1973?).

108. H. L. Barnes and G. Kullerod, Equilibria in sulphur-containing aqueous solutions in the system Fe–S–O, and their correlation during redeposition, *Econ. Geol.* **56**, 648–688 (1961).

109. R. J. Biernat and R. G. Robins, High-temperature potential–pH diagrams for the sulphur–water system, *Electrochim. Acta* **14**, 809–820 (1969).

110. H. C. Helgeson, Thermodynamics of complex dissociation in aqueous solution at elevated temperatures, *J. Phys. Chem.* **71**, 3121–3136 (1967).

111. H. C. Helgeson, Thermodynamics of hydrothermal systems at elevated temperatures and pressures, *Am. J. Sci.* **267**, 729–804 (1969).

112. D. Lewis, Studies of redox equilibria at elevated temperatures. I. The estimation of equilibrium constants and standard potentials for aqueous systems up to 374°C, *K. Sven. Vetenskapsakad. Arkiv. Kemi* **32**, No. 32 (1971).

113. D. Lewis, Theoretical studies of aqueous systems above 25°C. 1. Fundamental concepts for equilibrium diagrams and some general features of the water system, *Ab. Atomenergi Stockholm* [*Rapp.*] **AE-431** (1971).

114. D. Lewis, Theoretical studies of aqueous systems above 25°C. I. The illustration of data in aqueous equilibria and equilibrium data for the system $O_2(g)$–$H_2O(l)$–$H_2(g)$, *Chem. Scr.* **6**, 49 (1974).

115. R. T. Lowson, Potential–pH diagrams at temperatures above 298.16°K. Part 2. Potential–pH diagrams of water for the temperature range 298.16–573.16°K, *Aust. AEC AAEC/E* [*Rep.*] **AAEC/219** (1972).

116. D. D. MacDonald, G. R. Shierman, and P. Butler, The thermodynamics of metal–water systems at elevated temperatures. Part 1: The water and copper–water systems, *At. Energ. Can. Ltd. AECL* [*Rep.*] **4136** (December 1972).

117. R. G. Robins, The application of potential–pH diagrams to the prediction of reactions in pressure. Hydrothermal processes, Wasser Spring Laboratory, LR.80 (MST) (1968).

118. H. E. Townsend, Potential–pH diagrams at elevated temperature for the system Fe–H_2O, *Corros. Sci.* **10**, 343–358 (1970); *Proceedings of the 4th International Congress on Metallic Corrosion, Amsterdam*, September 7–14, 1969, NACE, Houston (1970), pp. 477–487.

119. V. Ashworth and P. J. Boden, Potential–pH diagrams at elevated temperatures, *Corros. Sci.* **10**, 709–718 (1970).

120. D. Lewis, Theoretical studies of aqueous systems above 25°C. 2. The iron–water system, *A. Atomenergi Stockholm* [*Rapp.*] **AE-432** (1971).

121. D. Lewis, Some aspects of electrochemical thermodynamics and equilibrium diagrams for aqueous systems at elevated temperatures and for simple molten salt systems, *J. Inorg. Nucl. Chem.* **33**, 2121–2140 (1971).

122. D. Lewis, The hydrolysis of iron (III) and iron (II) ions between 25°C and 375°C, *Trans. R. Inst. Technol. Sweden*, No. 252, *Pure Appl. Chem.* **34**, 59–67 (1972).
123. P. A. Brook, Potential–pH diagrams at elevated temperatures, *Corros. Sci.* **12**, 297–306 (1972).
124. E. Bardal, pH and potential measurements on mild steel and cast iron during periodic cathodic polarization at 20° and 90°C, *Corros. Sci.* **11**, 371–382 (1971).
125. R. J. Biernat and R. G. Robins, High temperature potential–pH diagrams for the iron–water and iron–water–sulphur systems, *Electrochim. Acta* **17**, 1261–1283 (1972).
126. D. D. MacDonald, G. R. Shierman, and P. Butler, The thermodynamics of metal–water systems at elevated temperatures. Part 2. The iron–water system, *At. Energ. Can. Ltd. AECL* [*Rep.*] **4137** (December 1972).
127. J. T. Harrison and C. J. Mason, Electrode potential/pH diagrams for the iron–water system at elevated temperatures, Central Electricity Research Laboratories CERL, Laboratory note No. RD/L/N 71/66 (July 1966).
128. R. L. Cowan and R. W. Staehle, The thermodynamics and electrode kinetic behavior of nickel in acid solution in the temperature range 25° to 300°C, *J. Electrochem. Soc.* **118**, 557–567 (1971).
129. D. D. MacDonald, The thermodynamics of metal–water systems at elevated temperatures. 4. The nickel–water system, *At. Energ. Can. Ltd. AECL* [*Rep.*] **4139** (1972).
130. D. D. MacDonald, G. R. Shierman, and P. Butler, The thermodynamics of metal–water systems at elevated temperatures. 3. The cobalt–water system, *At. Energ. Can. Ltd. AECL* [*Rep.*] **4138** (1972).
131. D. D. MacDonald, The thermodynamics and theoretical corrosion behavior of manganese in aqueous systems at elevated temperatures, *Corros. Sci.* **16**, 461–482 (1976).
132. R. T. Lowson, Aluminum corrosion studies. I. Potential–pH–temperature diagrams for aluminum, *Aust. J. Chem.* **27**, 105–127 (1974).
133. R. T. Lowson, Potential–pH diagrams at temperatures above 298.16°K. Part 3. Potential–pH diagrams of aluminium for the temperature range 298.16–573.16°K, *Aust. AEC AAEC/E* [*Rep.*] **219** (October 1972).
134. D. D. MacDonald and P. Butler, The thermodynamics of the aluminum–water system at elevated temperatures, *Corros. Sci.* **13**, 259–274 (1973).
135. I. E. Diachkova and I. L. Khodakovski, Thermodynamic equilibria in the systems S–H_2O, Se–H_2O and Te–H_2O in the 25–300°C temperature range and their geochemical interpretations, *Geochem. Int.* **5**(6), 1108–1125 (1968).
136. H. Magima and E. Peters, Oxidation rates of sulphide minerals by aqueous oxidation at elevated temperatures, *Trans. Met. Soc. AIME* **236**, 1409–1413 (1966).
137. R. C. H. Ferreira, High Temperature *E*–pH diagrams for the systems S–H_2O, Cu–S–H_2O and Fe–S–H_2O, *Leaching and Reduction in Hydrometallurgy*, A. R. Birkin, ed., Institute of Mining and Metallurgy (1975).
138. E. F. Sergeieva and I. L. Khodakovski, Physico-chemical conditions of formation of native arsenic in hydrothermal deposits, *Geochem. Int.* **6**(4), 681–694 (1969).
139. O. J. Kwok and R. G. Robins, Thermal precipitation in aqueous solutions, *Proceedings of the International Symposium on Hydrometallurgy, Chicago, 1973, AIMMPE*, New York, Evans and Shoemaker, New York (1973).
140. H. Kametani and A. Aoki, Potential–pH diagram of the Cu–Cl–H_2O system at 90°C, *Denki Kagaku* **40**(10), 720–723 (1972).
141. F. Baratin, E. Peters, and M. Morris, *E*–pH diagrams for the Pb–S–Cl–H_2O system at various temperatures (University of British Columbia, Vancouver, Canada), Chloride Metallurgy, international symposium organized by Benelux Metallurgie, Brussels, 26–28 September 1977 (not published in the proceedings).
142. H. E. Townsend, The importance of heat capacity in the construction of potential–pH diagrams at elevated temperatures, *Corros. Sci.* **13**, 311–314 (1973).
143. D. Lewis, Discussion of Cowan and Staehle, *J. Electrochem. Soc.* **118**, 557–567 (1971); *J. Electrochem. Soc.* **118** (12), 1968–1969 (1971).

144. H. Gräfen, Die Ergebnisse elektrochemischer Untersuchungsverfahren der Spannungsrisskorrosion und ihre praktische Anwendung, *Corros. Sci.* 7(4), 177–196 (1967).

145. T. P. Hoar, Electrochemical principles of the corrosion and protection of metals, *J. Appl. Chem.* **11**, 121–130 (1961).

146. M. Pourbaix, Prédétermination théorique et expérimentale des circonstances d'efficacité d'inhibiteurs de corrosion, *Rapports Techniques CEBELCOR* **73**, RT.88 (1960); *Proceedings of the European Symposium on Corrosion Inhibitors, Ferrara (Italy)*, 28 September–1 October 1960, Univ. degli Studi di Ferrara, Ferrara (1961).

147. G. H. Cartledge, The pertechnetate ion as an inhibitor of the corrosion of iron and steel, *Corrosion (Houston)* **11**, 335t–342t (1955).

148. G. H. Cartledge, Action of the XO_4 inhibitors, *Corrosion (Houston)* **15**, 469t–472t (1959).

149. T. P. Hoar and U. R. Evans, The passivity of metals. Part VII. The specific function of chromates, *J. Chem. Soc.* 2476–2481 (1932).

150. D. M. Brasher and E. R. Stove, The use of radioactive tracers in the study of the mechanism of action of corrosion inhibitors, *Chem. Ind. (London)*, 171–172 (1952).

151. T. Kodama and J. R. Ambrose, Effect of molybdate ion on the repassivation kinetics of iron in solutions containing chloride ions, *Rapports Techniques CEBELCOR* **128**, RT.231 (February 1976).

152. J. T. Conroy, The rate of dissolution of iron in hydrochloric acid, *J. Soc. Chem. Ind.* **20**, 316–320 (1901).

153. I. N. Poutilova, *Metallic Corrosion Inhibitors*, Pergamon Press, London (1960) (translated from Russian).

154. M. Pourbaix *et al.*, Sur le comportement d'aciers inoxydables en solution sulfurique, *Rapports Techniques CEBELCOR* **90**, RT.106 (1962).

155. R. Piontelli and L. Fagnani, Untersuchungen über die Reaktionen zwirschen Metallen und Elektrolyten. VI. Über die Sparbeizwirkung des Antimons bei der Auflösung von Eisen, *Korros. Metallschutz* **19**, 259–263 (1943).

156. R. M. Burns and W. W. Bradley, *Protective Coatings for Metals*, 2nd ed., Reinhold, New York (1955), p. 274.

157. M. Pourbaix, J. Van Muylder, and P. Van Laer, Sur la tension d'électrode du cuivre en présence d'eau de Bruxelles. Influence de la lumière et des conditions de circulation de l'eau, *Rapports Techniques CEBELCOR* **100**, RT.125 (May 1965); *Corros. Sci.* **7**, 795–806 (1967).

158. J. Van Muylder, M. Pourbaix, P. Van Laer, and N. de Zoubov, Relation entre la tension d'électrode et les circonstances de corrosion de cuivre electrolytique en présence d'eau de Bruxelles. Influence de l'état de surface du cuivre, des circonstances de circulation de l'eau, de traitements de l'eau et d'un contact du cuivre avec du graphite ou avec du platine, *Rapports Techniques CEBELCOR* **100**, RT.126 (May 1965).

159. J. Van Muylder, M. Pourbaix, and P. Van Laer, Caractéristiques électrochimiques de piqûres de corrosion du cuivre en présence d'eaux et de solutions aqueuses chlorurées, *Rapports Techniques CEBELCOR* **100**, RT.127 (May 1965).

160. P. Van Laer, J. Van Muylder, N. de Zoubov, and M. Pourbaix, Méthodes accélérées d'appréciation du risque de piqûration du cuivre en présence d'eaux. Application à l'étude de l'influence d'un contact du cuivre avec un autre métal ou avec du graphite, *Rapports Techniques CEBELCOR* **100**, RT.128 (May 1965).

161. N. de Zoubov, J. Van Muylder, P. Van Laer, and M. Pourbaix, Sur le comportement du cuivre en présence de solutions de bicarbonate de sodium, *Rapports Techniques CEBELCOR* **101**, RT.133 (August 1965).

162. M. Pourbaix, (a) Electrochemical aspects of stress corrosion cracking, *Proceedings of the NATO Science Committee, Research Evaluation Conference "The Theory of Stress Corrosion Cracking in Alloys,"* J. C. Scully, ed., NATO, Brussels (1971), pp. 17–63; (b) Les facteurs electrochmiques de la corrosion sans tension, *Rapports Techniques CEBELCOR* **118**, RT.199 (August 1971).

163. J. Van Muylder and M. Pourbaix, Test de susceptibilité du cuivre à la corrosion par piqûres en

présence d'eau de distribution froide, *Rapports Techniques CEBELCOR* **119**, RT.201 (January 1972).

164. M. Pourbaix, J. Van Muylder, E. D. Verink, and A. Pourbaix, Etudes électrochimiques concernant les corrosions en cellules occluses C.C.O. et protection contre ces corrosions: corrosion par piqûres, corrosion caverneuse, corrosion fissurante sous tension, corrosion sélective d'alliages. Applications au fer et aux aciers, au cuivre, au cupronickels et aux laitons, *Rapports Techniques CEBELCOR* **123**, RT.214 (September 1973).
165. M. Pourbaix, Inhibition des phénomènes de corrosion localisée, *C.R. 4th European Symposium on Corrosion Inhibitors, Ferrara (Italy)*, 15–19 September 1975, Univ. degli Studi di Ferrara, Ferrara (1975), pp. 674–691.
166. M. Pourbaix, Some applications of potential–pH diagrams for the study of localized corrosion, *J. Electrochem. Soc.* **123**(2), 25C–36C (1976).
167. J. Van Muylder, Corrosion par piqûres de tubes de cuivre pour distribution d'eau urbaine, *La Tribune du Cebedeau (Centre Belge d'Etude et de Documentation des Eaux)*, No. 397 (December 1976), pp. 429–439.
168. H. S. Campbell, (a) Pitting corrosion in copper water pipes caused by films of carbonaceous material produced during manufacture, *J. Inst. Met.* **77**, 345–346 (1950); (b) The influence of the composition of supply waters, and especially of traces of natural inhibitor, on pitting corrosion of copper water pipes, *Proc. Soc. Water Treat. Exam.* **3**, 110–115 (1954); (c) Pitting corrosion of copper water pipes, *Proceedings of the 2nd International Congress on Metallic Corrosion, New York*, 1963, pp. 237–243, NACE, Houston (1966).
169. R. May, Some observations on the mechanisms of pitting corrosion, *J. Inst. Met.* **32**, 65–74 (1953).
170. G. Lecointe, V. Plichon, Ph. Berge, and J. Legrand, Protection des condenseurs en alliage cuivreux par addition de sels ferreux dans l'eau de mer en circulation, *Mét. Corros.-Ind.* **52**, 123–131 (1977).
171. M. Pourbaix, Recherches en corrosion. Résultats de travaux récents. Voyages aux Etats-Unis d'Amérique, *Rapports Techniques CEBELCOR* **109**, RT.157 (June 1969).
172. M. Pourbaix, Bases fondamentales de la protection cathodique et applications, *Rapports Techniques CEBELCOR* **111**, RT.166 (October 1969).
173. M. Pourbaix, Aspects électrochimiques de la corrosion aqueuse, *Rapports Techniques CEBELCOR* **120**, RT.204 (August 1972).
174. J. R. Baylis, Natural water corrosion and H-ion concentration, *Met. Chem. Eng.* **32**, 874–875 (1925); *J. Am. W. W. Assoc.* **15**, 606 (1926).
175. T. P. Hoar, The corrosion of tin in nearly neutral solutions, *Trans. Faraday Soc.* **33**, 1152 (1937).
176. U. R. Evans (a) *The Corrosion and Oxidation of Metals*, Arnold, London (1960); (b) *An Introduction to Metallic Corrosion*, 2nd ed., Arnold, London (1963).
177. C. Edeleanu and U. R. Evans, *Trans. Faraday Soc.* **47**, 1121 (1951).
178. I. L. Rosenfeld and I. K. Marchakov, Mechanism of crevice corrosion, *Corrosion (Houston)* **20**, 115t–125t (1964).
179. B. F. Brown, The concept of the occluded corrosion cell, *Corrosion (Houston)* **26**, 249–250 (1970).
180. C. T. Fujii, Electrochemical and chemical aspects of localized corrosion, *Rapports Techniques CEBELCOR* **123**, RT.213 (January 1974).
181. P. Ruetschi and R. T. Anstadt, Anodic oxidation of lead at constant potential, *J. Electrochem. Soc.* **111**(12), 1323–1330 (1964).
182. A. Pourbaix, Etude de la corrosion localisée de l'acier en solutions chlorurées, *Rapports Techniques CEBELCOR* **118**, RT.198 (August 1971); Characteristics of localized corrosion of steel in chloride solutions, *Corrosion (Houston)* **27**, 449–454 (1971).
183. M. Pourbaix *et al.*, Etudes potentiocinétiques et corrosimétriques sur le comportement d'aciers alliés, *Rapports Techniques CEBELCOR* **96**, RT.120 (September 1962).

184. M. Pourbaix, J. Van Muylder, P. Van Laer, *et al.*, On the pitting corrosion of copper water pipes, *Report CEBELCOR* No. 879 (December 1973).
185. N. Verheulpen-Heymans, Etude de l'influence des chlorures sur le comportement anodique du fer, Mémoire de fin d'études, Free University of Brussels, U.L.B., Faculty of Applied Sciences (Belgium, June 1969).
186. B. F. Brown (a) Cracking of martensitic type 410 stainless steel in corrosive environments, *NRL Prog. Rep.*, 40–42 (May 1958); (b) Stress corrosion cracking and related phenomena in high-strength steels, *N.R.L. Report* 6041 (November 1961); (c) Stress corrosion cracking and corrosion fatigue in high-strength steels, *DMIC Report* 210, Battelle Memorial Institute (1964).
187. B. F. Brown, C. T. Fujii, and E. Ph. Dahlberg, Methods for studying the solution chemistry within stress corrosion cracks, *J. Electrochem. Soc.* **116**, 218–219 (1969).
188. B. F. Brown (a) On the electrochemistry of stress corrosion cracking of high strength steels, CEBELCOR's Publication E.76 (1969); (b) The role of the occluded corrosion cell in stress corrosion cracking of high-strength steels, *Rapports Techniques CEBELCOR* **112**, RT.170 (January 1970).
189. J. A. Smith, M. H. Peterson, and B. F. Brown, Electrochemical conditions at the tip of an advancing stress corrosion crack in AISI 4340 steel, *Corrosion* (*Houston*) **26**, 539–542 (1970).
190. H. W. Pickering and R. P. Frankenthal, On the mechanism of localized corrosion of iron and stainless steel, *J. Electrochem. Soc.* **119**, 1297–1304 (1972).
191. P. A. Parrish, C. M. Cohen, and E. D. Verink, The retardation of crack propagation for D6A6 high-strength, low-alloy steel in aqueous media by addition of some inhibitors, *Proceedings of the ASTM Meeting, Montreal, Canada, June 1975, "Symposium on Stress Corrosion—New Approaches,"* STP 610 (1976).
192. F. Haber, Über stufenweise Reduktion des Nitrobenzols mit begsentzem Kathodenpotential, *Z. Elektrochem.* **4**, 506–514 (1898).
193. C. Wagner and W. Traud, Über die Deutung von Korrosionsvorgängen durch Überlagerung von elektrochemischen Teilvorgängen und über die Potentialbildung an Mischelektroden, *Z. Elektrochem.* **44**, 391–402 (1938).
194. M. Pourbaix, Méthodes électrochimiques de mesure de la corrosion des métaux, *Rev. Tech. Luxemb.* **57**, 9–27 (1965).
195. M. Stern and A. Geary, Electrochemical polarization. I. A theoretical analysis of the shape of polarization curves, *J. Electrochem. Soc.* **104**, 56–63 (1957).
196. J. Tafel, Über die Polarisation bei Kathodischer Wasserstoffentwicklung, *Z. Phys. Chem.* **50**, 641–712 (1905).
197. M. Pourbaix, Note concernant les méthodes d'appréciation de la vitesse de corrosion par mesure de la résistance de polarisation, *Rapports Techniques CEBELCOR* **108**, RT.156 (March 1969).
198. L. Clerbois, Détermination de la vitesse de corrosion par mesure de la résistance de polarisation, *Rapports Techniques CEBELCOR* **108**, RT.155 (March 1969); Méthodes de mesure de la résistance de polarisation et leur validité pratique, *Rapports Techniques CEBELCOR* **122**, RT 209.1 (April 1973).
199. S. Uneri, The utility of linear polarization method for the determination of the corrosion rate, *Commun. Fac. Sci. Univ. Ankara Ser. B* **16B**, 37–61 (1969).
200. A. Pourbaix, Détermination de la vitesse instantanée de corrosion par la mesure de la résistance de polarisation, ou de corrodance, *Rapports Techniques CEBELCOR* **124**, RT.219 (April 1974).
201. I. Epelboin, M. Keddam, and H. Tekanouti, Use of impedance measurements for the determination of the instant corrosion rate of metal corrosion, *J. Appl. Chem.* **2**, 71–79 (1972)

202. M. Prajak, Über die Abhängigkeiten zwischen Polarisationswiderstand und Korrosionsgeschwindigkeit des Metalle, *Werkst. Korros.* **19**(10), 845–848 (1969).

203. E. Röschenblech, Die Abhägigkeit der Korrosionsgeschwindigkeit von Polarisationswiderstand und pH-Wert, *Metalloberflaeche* **16**, 38–42, 65–69 (1962).

204. M. Pourbaix, Sur l'interprétation thermodynamique des courbes de polarisation, *Rapports Techniques CEBELCOR* **1**, RT.1 (1952).

205. M. Pourbaix, (a) Theoretical and experimental considerations in corrosion testing, *Rapports Techniques CEBELCOR* **116**, RT.196 (January 1971); (b) Potential–pH diagrams and metallic corrosion, *Handbook on Corrosion Testing and Evaluation*, W. H. Ailor, ed. John Wiley & Sons, New York (1971), No. 26, pp. 661–687.

206. E. D. Verink and M. Pourbaix, Use of potentiokinetic methods at successively increasing and decreasing electrode potentials in developing alloys for saline exposure, *Rapports Techniques CEBELCOR* **117**, RT.191 (June 1971).

207. Z. Sklarska-Smialowska and M. Janik-Czachor, The analysis of electrochemical methods for the determination of characteristic potentials of pitting corrosion, *Corros. Sci.* **11**(12), 901–914 (1971).

208. A. Pourbaix, Signification et détermination des potentiels de rupture et de protection, *Rapports Techniques CEBELCOR* **122**, RT.210.1 (April 1973).

209. M. Pourbaix, Une méthode électrochimique rapide de prédétermination de la corrosion atmosphérique, *Rapports Techniques CEBELCOR* **109**, RT.160 (August 1969).

210. L. de Miranda and M. Pourbaix, Sur la corrosion atmosphérique des aciers non alliés en atmosphère sulfureuse, *Rapports Techniques CEBELCOR* **119**, RT.200 (January 1972); M. Pourbaix, Sur le mécanisme de la corrosion atmosphérique, *Rapports Techniques CEBELCOR* **119**, RT.200 (January 1972) (Discussion).

211. L. de Miranda, J. Van Muylder, and M. Pourbaix, Sur la corrosion atmosphérique des aciers patinables en atmosphère sulfureuse, *Rapports Techniques CEBELCOR* **121**, RT.206 (April 1973).

212. CEBELCOR's Patents: Belgium No. 726,964; France No. 1,600,155; Germany No. P.1901.8601; Italy No. 806,082; Japan No. 764,830; Luxembourg No. 55,296; Sweden No. 347,773, United Kingdom No. 1,261,544.

213. J. Van Muylder and M. Pourbaix, (a) Influence des facteurs climatiques et polluants sur la corrosion atmosphérique de l'acier. Prédétermination en laboratoire, *Rapports Techniques CEBELCOR* **130a**, RT.235a (December 1976); (b) On the influence of climatic and polluting factors on the atmospheric corrosion of steels. Predetermination in the laboratory, *Proc. 7th Int. Cong. Metal. Corr., Rio de Janeiro (Brazil), Oct. 1978* **3**, 1177–1180 (1979).

214. P. B. Linkson, D. M. Nobbs, and I. A. Lake, Recovery of copper from leach solutions with sulphur dioxide, *Adv. Extr. Met., Int. Symp., 3rd,* 111–121 (1977).

215. D. D. MacDonald, B. C. Syrett, and S. S. Wing, The use of potential–pH diagrams for the interpretation of corrosion phenomena in high salinity geothermal brines, *Corrosion (Houston)* **35**, 1–11 (1979).

216. R. J. Thibeau, C. W. Brown, A. Z. Goldfarb, and R. H. Heidersbach, Raman and infrared spectroscopy of aqueous corrosion films on lead in 0.1 *M* chloride solutions, *J. Electrochem. Soc.* **127**, 1702–1706 (1980).

217. S. C. Barnes and R. J. Mathieson, in A. C. Simon's chapter in *Batteries 2*, D. H. Collins, ed., Pergamon Press, New York (1965), p. 41.

218. M. Pourbaix and Yang Xi-Zhen, Diagrams of chemical and electrochemical equilibria in the presence of a gaseous phase. 6. Iron–oxygen–hydrogen, *Rapports Techniques CEBELCOR* **138**, RT. 256 (September 1980).

219. C. J. Cron, J. H. Payer, and R. W. Staehle, Dissolution behavior of Fe–Fe_3 structures as a function of pH, potential, and anion—An electron microscope study, *Corrosion (Houston)* **27**, 1–25 (1971).

2

Electrochemistry and Corrosion on Homogeneous and Heterogeneous Metal Surfaces

WILLIAM H. SMYRL

1. Thermodynamics

The driving force for a reaction is the change in Gibbs free energy, ΔG, for reactants to products. Mathematically this may be expressed by

$$\Delta G = \sum_{\text{products}} G - \sum_{\text{reactants}} G \tag{1}$$

The summation signs are used as a general notation to indicate that all reactants and products are included in the calculation. From the nature of the free energy function, this calculation applies to initial (reactants) and final (product) states, and is independent of intervening states. The reaction may be investigated under controlled reversible conditions such as in an electrochemical cell, or under irreversible conditions such as in corrosion, and the same total free energy change (ΔG) will be appropriate. A quite general predictive capability may be applied to specific corrosion reactions since all the available thermodynamic data may be used for corrosion calculations directly. This enables the

---

WILLIAM H. SMYRL • Sandia Laboratories, Albuquerque, New Mexico 87185. This work was supported by United States Department of Energy (DOE) under contract DE-AC04-76-DP00789. Sandia Laboratories is a DOE facility.

position of final equilibrium of the corrosion system to be established. The thermodynamic calculations have the limitation that no information of the *rate* of the reaction is provided, only what the final state will be for the process. Another limitation of the thermodynamic treatment is found when there are multiple reactions in a corrosion system but none are dominant, so that the final state is not well known. The limitations will not be described further here, but the influence of kinetics on corrosion behavior is significant and is the subject of the remaining sections. However, this section will briefly describe the sources of thermodynamic data and procedures for using it, since this remains a powerful resource despite the limitations.

The free energy, G, of a reactant or product in a reaction is a function of the temperature and pressure of the system, and of the chemical composition as well when solutions or mixtures are involved. The difference in free energy, ΔG, is the thermodynamically significant quantity, and it is not necessary to fix the absolute value of G in any one state. It is convenient, however, to adopt an arbitrary standard state for chemical elements, and to assign values to other thermodynamic states relative to this standard state. This standard state for each element and for a pure chemical compound is the stable state at a particular temperature, and at 1 atm pressure.

The value of ΔG for reactions of elements to form a compound, all in their standard states at a particular temperature, is known as the standard free energy of formation of the compound, $\Delta G^\circ_{f,T}$. Here, the subscript T denotes the temperature. The free energy change for other conditions can be calculated from $\Delta G^\circ_{f,T}$ plus terms to evaluate the departure from the standard state. Description of the detailed calculations are beyond the scope of this chapter, but several excellent textbooks are available.(1,2) The free energy changes to be described below will be restricted to standard state calculations, except as noted for pH effects on corrosion.

The free energy change of a corrosion process such as the reaction of iron with water,

$$\mathrm{Fe(s)} + 2\mathrm{H_2O(l)} \rightarrow \mathrm{Fe(OH)_2(s)} + \mathrm{H_2(g)}$$

is, from Eq. (1),

$$\Delta G^\circ_T = G^\circ_{\mathrm{Fe(OH)_2},T} + G^\circ_{\mathrm{H_2},T} - G^\circ_{\mathrm{Fe},T} - 2G^\circ_{\mathrm{H_2O},T} \tag{2}$$

Equation (2) is equivalent to

$$\Delta G^\circ_T = \Delta G^\circ_{f,\mathrm{Fe(OH)_2},T} - 2\Delta G^\circ_{f,\mathrm{H_2O},T} \tag{3}$$

Either equation may be used for free energy calculations from tabulated data.

The most extensive tabulations of thermochemical data for chemical compounds in their standard state at 25°C are in a series of National Bureau of Standards publications.(3) These are NBS Technical Notes 270-3, 270-4, and 270-5, which supersede the older NBS Circular 500 for the elements they cover. The values of $\Delta G^\circ_{f,289\,\mathrm{K}}$, as well as enthalpies of formation, entropies, and heat capacities, are given for compounds which have reliable data available. These tabulations also update the older data of Latimer.[4] The book by Latimer[4] remains a valuable reference because of the description of techniques to estimate thermodynamic quantities where reliable data are sparse.

Lewis, Randall, Pitzer, and Brewer[2] also tabulated thermodynamic data for the elements and a large number of chemical compounds, in a form closely related to Eq. (2). Data are given also for aqueous solutions of a number of electrolytic solutions which are valuable for corrosion calculations. The quantities tabulated are[†] $-(F^\circ - H^\circ_{298})/T$ for elements and compounds, along with $\Delta H^\circ_{f,298}$. There is some overlap between this tabulation and the JANAF Thermochemical Tables,[5] but the latter also tabulate the standard enthalpy and free energy of formation of chemical compounds at several temperatures, along with $-(G^\circ - H^\circ_{298})/T$. The primary advantage offered by the tabulations in references 2 and 5 is the ability to make calculations at temperatures other than 298 K. Interpolation of the function $-(G^\circ - H^\circ_{298})/T$ is straightforward, so that calculations may be carried out at temperatures intermediate to those tabulated.

The calculation of the standard free energy change for the reaction of iron with water, at temperature T, is

$$G^\circ_T = T\left[\frac{(G^\circ - H^\circ_{298})}{T}\right]_{\mathrm{Fe(OH)_2}} + T\left[\frac{(G^\circ - H^\circ_{298})}{T}\right]_{\mathrm{H_2O}} - T\left[\frac{(G^\circ - H^\circ_{298})}{T}\right]_{\mathrm{Fe}}$$
$$- 2T\left[\frac{(G^\circ - H^\circ_{298})}{T}\right]_{\mathrm{H_2O}} + \Delta H^\circ_{\mathrm{Fe(OH)_2},298} - 2\Delta H^\circ_{\mathrm{H_2O},298} \qquad (4)$$

These values are tabulated[2,5] and the calculation yields, at 298 K,

$$\Delta G^\circ_{298} = -4.22 \text{ kcal} \qquad (5)$$

By comparison, copper is stable in deoxygenated water at room temperature. ΔG°_T for the reaction

$$\mathrm{Cu(s) + 2H_2O(l) \rightarrow Cu(OH)_2(s) + H_2(g)}$$

is found to be, at room temperature,

$$\Delta G^\circ_{298} = +28.4 \text{ kcal} \qquad (6)$$

The comparison with the negative value of ΔG° for the corresponding iron reaction provides an absolute measure of the relative stability of the two metals in water.

Comparison of the stability of a series of metals with a common reactant on the basis of the reaction free energy is very general. If the common reactant is a solvent, such as water in the calculations above, the free energy of the reaction is also a measure of the reduction stability of the solvent. In the case of water the reduction limit is the displacement of hydrogen. The reaction with the solvent is the base line for corrosion of a metal, and other oxidants in the solvent may cause reactions which are superimposed on the basic solvent–metal interaction. Because it determines base line behavior, reduction of the solvent is identified as the most important reaction in the metal–solvent system. For the molten salt LiCl–KCl, the reduction limit is the deposition of lithium.(6) Most metals are thermodynamically stable in the pure melt because they cannot displace lithium, i.e., the value of ΔG_T° is positive. These metals may be corroded in LiCl–KCl only if there are dissolved oxidants such as oxygen. By comparison, only a few metals are thermodynamically stable in water, and the ΔG_T° for hydrogen displacement is negative.

[†] F is used for Gibbs free energy in reference 2, and this is equivalent to the symbol G used here.

Corrosion in a given solvent will be influenced by complexation and solubility. Complexation reactions stabilize the dissolved metal species, and the driving force for corrosion is increased. Copper corrosion may be used as an example. The standard free energy of the reaction

$$\mathrm{Cu(s)} + 4\mathrm{CN^-(soln)} + \mathrm{H_2O(1)} \rightarrow \mathrm{Cu(CN)_4{}^{3-}(soln)} + 1/2\mathrm{H_2(g)} + \mathrm{OH^-(soln)}$$

is calculated to be

$$\Delta G_{298}^\circ = -10.3\ \mathrm{kcal} \tag{7}$$

Experimentally, copper is observed to corrode freely in aqueous cyanide in marked contrast to the behavior in pure water.(7) Complexation may also influence the corrosion *rate*, but the effect of interest in this section is on the thermodynamics. Solubility on the other hand, may affect corrosion behavior through the kinetics of the process. This is illustrated in principle for the unstable iron–water system. If the reaction products were soluble iron species, the only factor limiting corrosion would be the shift of the equilibrium due to concentration effects, or the availability of reactants. When solubility limits are exceeded, precipitation of a film on the metal surface may cause passivation. Passivity will not be discussed here, but it should be noted that the solubility effect is the most important factor which limits corrosion and allows many metals to be used in inherently unstable systems. Other kinetic factors which influence corrosion will be discussed in subsequent sections.

Oxide and hydroxide solubility is strongly influenced by the pH of the aqueous phase. Pourbaix recognized this and summarized the thermodynamic stability of metal–aqueous systems by the use of potential–pH diagrams.(8) The thermodynamic data tabulations already quoted(2–5) should be utilized for detailed calculations, however.

2. Kinetics of Corrosion Reactions

2.1. Corrosion and Fundamental Electrode Kinetics

Usually, when studying corrosion one is not concerned with the conditions for thermodynamic stability, but rather with the rate of attack and how it may be altered in basically unstable conditions. This comes about because of the very limited number of systems that have absolute or thermodynamic stability. As a practical matter it is necessary to accept some rate of corrosion and/or to control or mitigate the rate of attack. Thus *kinetic* stability is always relative and subject to interruption if control is not maintained. Controlling the rate of degradation may be accomplished, for example, by the use of cathodic or anodic protection, the use of inhibitors, the maintenance of protective surface films, or buffering the composition of an otherwise aggressive solution. All these techniques are widely used effectively to extend the life of metallic structures.

Corrosion reactions that are electrochemical in nature are to be described further here. Degradation reactions that are not electrochemical are outside the scope of this contribution and will not be treated (for example, high-temperature oxidation). Corrosion by "chemical" reactions has been suggested to be the dominant mode of attack on some film covered surfaces in solution,(9) but this will not be discussed here. The kinetics of the corrosion reactions are then related to the kinetics of the *electrochemical* reactions that occur during the corrosion process. Fundamental studies of electrode kinetics have application in corrosion, although the occurrence of several (at least two) simultaneous reactions makes the application complex. For help in identification of mechanisms and stoichiometry in a specific system, one may draw on the large literature for many individual electrode reactions.

The discussion to follow will briefly describe some of the principles of electrode kinetics, and the application of the principles to the specific system of copper corrosion in acids. The ideas will be introduced that are essential to treat electrochemical reactions in corrosion. This leads to the final major section, which treats the models of nonuniform corrosive attack on heterogeneous surfaces. There detailed knowledge of corrosion kinetics is used to define boundary conditions for the models.

2.2. Basic Concepts of Electrode Kinetics

Several references may be consulted for detailed discussion of the basics of electrode kinetics and mechanisms. These include books,(10–12) reference works,(13,14) and reviews.(15) References are also available for specific systems such as the hydrogen electrode reactions,(16,17) and the oxygen electrode reactions,(18–20) which are important in aqueous corrosion studies. In this section it will be assumed that a corrosion system may be separated into a treatment of the metal reactions and a treatment of the reactions of the oxidizing agent or agents. Coupling of the two reactions will be discussed in the next section. Such an approach emphasizes the importance that the basic electrode kinetic studies have for corrosion kinetics applications.

The overall reaction process determines the stoichiometric numbers for the reaction. For the general reaction involving an n-electron transfer process,

$$fA \rightleftarrows bB + ne^-$$

the stoichiometric numbers are f and b. For an elementary, one-electron transfer process, the stoichiometry also gives the reaction order. The order of a reaction with respect to a particular species is the dependence of the rate of the reaction on the concentration of that species. For the process

$$\mathrm{M(s)} \rightleftarrows \mathrm{M^+(soln)} + e^-$$

the cathodic reaction is first order in $\mathrm{M^+}$, and the cathodic rate is a linear function of the concentration of $\mathrm{M^+}$. The anodic process could also be considered first order with respect to M, but the metal concentration does not change during the reaction and is absorbed in the rate constant for convenience.

For more complex, multistep reactions the stoichiometry and the reaction order of a species are different in general. The reaction may involve steps which are dependent on the concentration of a species such that it cancels out in the overall stoichiometry, but does not cancel out in the rate expression. Thus the order may be nonzero.

The rate of an electrochemical reaction may be written, for the elementary anodic reaction

$$\mathrm{M(s)} \rightarrow \mathrm{M^+} + e^-$$

as a current density

$$i_a = F\bar{k}_a \tag{8}$$

The rate of the backwards (cathodic) reaction may also be written as a current density,† i.e.,

$$i_c = -F\bar{k}_c C_{\mathrm{M^+}} \tag{9}$$

The quantities $\bar{k}_a$ and $\bar{k}_c$ are heterogeneous electrochemical rate constants which are dependent on the electrical potential. Anodic currents are taken to be positive, and cathodic currents are negative. The potential dependence of each of the rate constants is defined to be

$$\bar{k}_a = k_a \exp\left(\frac{\alpha_a F}{RT}\phi\right) \tag{10}$$

$$\bar{k}_c = k_c \exp\left(\frac{-\alpha_c F}{RT}\phi\right) \tag{11}$$

where the potential is taken with respect to the standard hydrogen electrode. The constants k_a and k_c are the fundamental heterogeneous rate constants which are independent of potential (but depend in an arbitrary way on the choice of the standard hydrogen electrode as the reference potential). The parameters α_a and α_c are intrinsic kinetic parameters of the system, and usually have the value of 1/2 for elementary one-electron transfer reactions. With these definitions the anodic and cathodic reactions may be written

---

† Concentrations of reactants and products will be used throughout rather than activities.

$$i_a = Fk_a \exp\left(\frac{\alpha_a F}{RT}\phi\right) \tag{12}$$

$$i_c = -F(k_c C_{\mathrm{M}^+}) \exp\left(\frac{-\alpha_c F}{RT}\phi\right) \tag{13}$$

The net current density for the reaction will be

$$i = i_a + i_c \tag{14}$$

or

$$\frac{i}{F} = k_a \exp\left(\frac{\alpha_a F}{RT}\phi\right) - (k_c C_{\mathrm{M}^+}) \exp\left(\frac{-\alpha_c F}{RT}\phi\right) \tag{15}$$

At equilibrium, the net current is zero so that

$$k_a \exp\left(\frac{\alpha_a F}{RT}\phi^\circ\right) = k_c C_{\mathrm{M}^+} \exp\left(\frac{-\alpha_c F}{RT}\phi^\circ\right) \tag{16}$$

The equilibrium potential ϕ° (with respect to the standard hydrogen electrode) is therefore

$$\phi^\circ = \frac{RT}{F(\alpha_a + \alpha_c)} \ln \frac{k_c C_{\mathrm{M}^+}}{k_a} \tag{17}$$

Defining a quantity called the exchange current density

$$i_0 = Fk_a\left(\frac{k_c C_{\mathrm{M}^+}}{k_a}\right)^{\alpha_a/(\alpha_a+\alpha_c)} \tag{18}$$

the net current density is now given by

$$i = i_0\left\{\exp\left[\frac{\alpha_a F}{RT}(\phi - \phi^\circ)\right] - \exp\left[\frac{-\alpha_c F}{RT}(\phi - \phi^\circ)\right]\right\} \tag{19}$$

One may further define the surface overpotential, η_s, as the quantity

$$\eta_s = \phi - \phi^\circ \tag{20}$$

and obtain

$$i = i_0\left[\exp\left(\frac{\alpha_a F}{RT}\eta_s\right) - \exp\left(\frac{-\alpha_c F}{RT}\eta_s\right)\right] \tag{21}$$

This equation is the Butler–Volmer expression for the electrode kinetics of the single step.

Expressing the net rate of an electrode reaction in terms of the exchange current density and overpotential is equivalent to expressing it in terms of the heterogeneous rate constants and the potential. The same information is contained in each. Stoichiometry and reaction order dependence is given more explicitly when the heterogeneous rate constant form is used. The equivalence between the two forms is preserved for more complex, multistep reactions, but the specific systems to be given below will be treated in terms of heterogeneous rate constants. The parameters α_a and α_c, sometimes called transfer coefficients, are not expected to be equal to 1/2 in general unless they refer to an elementary step. These coefficients are important for determining the mechanism of the reaction, and have characteristic values which depend, in general, on the reaction model.

2.3. Coupled Reactions

The single one-electron transfer reaction treated above for a hypothetical metal is the basis for discussing more complex reactions. An electrode reaction encountered in practice usually consists of several steps *in series* or *in sequence*. Some of these may be electron transfer reactions while others may be simple chemical reactions. The overall rate of the reaction is limited by the step in the sequence which has the smallest rate. At steady state, the rate of each step is equal to that of all the other steps, both preceding and following. Expressed as the current density of the individual steps this is

$$i_1 = i_2 = i_3 = \cdots = i_j = i$$

The reactions are coupled chemically since the product of one step in the sequence is a reactant in the next step.

Mathematical treatment of the reaction system is simplified by assuming that all steps except the rate-determining step are in equilibrium. This is equivalent to assuming that all rate constants of all the equilibrated steps are much larger than the rate constant of the rate-determining step. The number of independent species concentrations that have to be specified in the overall rate equation (or its equivalent Butler–Volmer expression) is minimized, the other concentrations being eliminated through the equilibrium constants for individual steps. The order of the reaction with respect to the independent concentrations is given in the derived rate equation. The reaction sequence mechanism may be verified by comparing the derived order against measured values. Small differences between proposed mechanism reaction orders and those measured may be the result of the assumption of equilibrium, i.e., not all steps have rate constants that are much larger than for the rate-determining step.

Corrosion reactions involve not one but at least two electron transfer reactions, and the reactions are not in series but are in parallel. The introduction to kinetics given above was discussed in terms of a one-electron transfer reaction for dissolution of a hypothetical metal. This reaction occurs in a corrosion situation, but in parallel with a simultaneous cathodic reaction.

Dissolution of an isolated metal produces an excess of electrons on the metal surface and the reaction can proceed only to an infinitesimal extent unless a second reaction occurs which consumes the electrons generated. The electrical forces generated by the charge separation of the first reaction are large and act to return the system to its original state. If the cathodic second reaction is simply redeposition of the metal cations from solution, there is no net change in the isolated metal. This is in fact the picture of equilibrium, where the exchange of material between the electrode and solution occurs at the rate measured by the exchange current density, but the net change is zero. If the backward metal reaction is suppressed, and replaced by wmer cathodic reaction, the electrical state of the isolated metal will have a kind of kinetic stability (see below), but corrosion is produced.

Coupling of *parallel or simultaneous* reactions is essential to the corrosion process. Each of the simultaneous processes may consist of multiple steps, respectively, as described above, but the simultaneous, independent reactions are coupled electrically. The independent reactions occur on the same surface at the same time, but also at the same potential. The reactions may be coupled chemically as well, e.g., through pH effects, but this is not essential. The specific relation that defines the coupling of simultaneous corrosion reactions on an isolated metal surface is

$$\sum_{\text{anodic}} I_a = -\sum_{\text{cathodic}} I_c \tag{22}$$

There will then be zero net current to the corroding metal electrode. The relationship is written in terms of currents rather than current densities, for reasons which will be discussed below. The potential at which the balance is satisfied is the mixed or corrosion potential. It is determined by the *rates* of the simultaneous reactions, and is not defined by the state of the system in a thermodynamic sense. The corrosion potential always lies between the equilibrium potentials of the anodic and cathodic processes, respectively.

Coupled simultaneous reactions in corrosion cause the corrosion potential to be controlled by the process with the largest rate. That is, the corrosion potential will be nearest the potential of the fastest of the two coupled processes. This will be discussed in more detail in a later section, but an example will help to establish the point here.

Copper corrodes in oxygen-free, nonoxidizing acids very slowly. The driving force for corrosion is small because of the thermodynamic stability of the system, and the coupling produces only a small corrosion rate. Upon dissolving oxygen in the acidic solution, a second simultaneous cathodic reaction becomes important. The rate of oxygen reduction is larger than hydrogen reduction at the corrosion potential, and the corrosion rate is increased. Thus coupling several simultaneous cathodic reactions with the anodic reaction produces a corrosion rate that is controlled by the cathodic reaction with the largest rate. The corrosion potential would lie nearer to the copper reversible potential than to the oxygen potential because the copper reaction is the faster of the two.

2.4. Superposition of Simultaneous Reactions

Wagner and Traud(21) were the first to discuss definitively corrosion systems as the superposition of independent, simultaneous reactions on the corroding metal surface. They refer to older work where the principle was used but not discussed in detail. Simply stated, corrosion reactions are independent, separable reactions which are superposed at each point over the entire surface of a *homogeneous* metal. That is, the balance of the anodic and cathodic reactions at the corrosion potential may be made in terms of *current density*, not total current as given above. The total anodic current must still be equal in magnitude to the total cathodic current at the corrosion potential, but the more restrictive current density relationship will be obeyed for uniform corrosion. A homogeneous metal surface is taken to be one which corrodes uniformly and has the current density balanced everywhere. A heterogeneous metal surface has nonuniform corrosion and the current density balance will not be obeyed, but the balance of total current will be observed. These two definitions are basic to the present treatment.

Wagner and Traud(21) described the principle of superposition as an average or statistical balance. Thus an anodic site on the surface one instant will then become a cathodic site at a later instant, and vice versa, so that overall uniform corrosion is produced on the entire surface. The average condition is one of uniformity and the anodic–cathodic balance is assumed to apply on a current density basis at each point on the surface. The principle is *macroscopic*, however, and may be applied in a macroscopic sense. Kaesche(22) has noted recently that the assumption of superposition allows one to develop all the usual laws of corrosion and is therefore of fundamental importance. It is basically a *model* which may be approached more or less closely in practice. Homogeneous metals which corrode uniformly, in systems where the reactants or products do not influence the coupled reactions, will obey superposition exactly. Fortunately this describes a large preponderance of practical corrosion systems.

Heterogeneous surfaces are commonly observed in corrosion situations and are of the three following general classes: (1) the inclusion of foreign metal impurities on the metal surface, (2) the nonuniform coverage of the surface by a film, usually an oxide film in aqueous solutions, and (3) nonuniform conditions in the electrolyte environment. All these are of great importance because localized, or nonuniform, corrosion of metals may be caused by any of the three. A form of galvanic corrosion is caused by the first type of heterogeneity, while crevice and pitting corrosion are produced by both (2) and (3). Nonuniform corrosion will be treated in detail in the last section of this contribution. It will be shown there that heterogeneous surfaces may be treated as a collection of homogeneous surfaces which are perturbed by the specific conditions of the system. Thus homogeneous surfaces serve as the limiting case model where the perturbations go to zero. As a final point it should be noted that heterogeneity of the third type may be produced by chemical coupling of the anodic and cathodic process. This may occur when the anodic process, for example, causes a decrease of local solution pH. More acid conditions will cause an acceleration of the cathodic hydrogen evolution. If the two processes are spatially separated, the anodic process will be increased.

2.5. Coupled Corrosion Reactions

The general relationship for current balance at the corrosion potential was given in Eq. (22). A heterogeneous surface will satisfy the overall current balance expressed in Eq. (22) although locally it is not obeyed. If the heterogeneous surface is a collection of locally homogeneous areas, A_i, on which the current density is uniform, the current balance equation is

$$\sum_{k,\text{anodic}} i_k A_k = -\sum_{j,\text{cathodic}} i_j A_j \tag{23}$$

Bockris$^{(13)}$ has suggested the term *polyelectrodes* to be applied to this system. We shall see in the final section that assumption of a locally uniform but heterogeneous surface described by Eq. (23) has only limited usefulness. The current density distribution is expected in general to be nonuniform on the individual areas.

Attention will be given now to homogeneous surfaces which satisfy the current density balance at each point on the surface, i.e.,

$$\sum_{k,\text{anodic}} i_k = -\sum_{j,\text{cathodic}} i_j \tag{24}$$

For the special case of a single metal dissolution reaction coupled with a single cathodic reaction (cf. Bockris$^{(13)}$)

$$i_a = -i_c = i_{\text{corr}} \tag{25}$$

The last relationship identifies the corrosion current. Substituting the Butler–Volmer equation for each reaction,

$$\begin{aligned} i_{0a}\left\{\exp\left[\frac{\alpha_{aa}F}{RT}(\phi^* - \phi_a^\circ)\right] - \exp\left[\frac{-\alpha_{ac}F}{RT}(\phi^* - \phi_a^\circ)\right]\right\} \\ = -i_{0c}\left\{\exp\left[\frac{\alpha_{ca}F}{RT}(\phi^* - \phi_c^\circ)\right] - \exp\left[\frac{-\alpha_{cc}F}{RT}(\phi^* - \phi_c^\circ)\right]\right\} \end{aligned} \tag{26}$$

The potential, ϕ^*, is the corrosion potential, and it lies between ϕ_a° and ϕ_c°. An example of a corrosion couple of this sort is provided by zinc corrosion in deaerated acid solutions, where the cathodic reaction is hydrogen evolution. As shown by Wagner and Traud,$^{(21)}$ the anodic zinc reaction is very fast compared to the hydrogen reaction, and the corrosion potential was found to be near the zinc reversible potential.

Given the α values, and the values of i_{0a}, i_{0c}, and ϕ_a°, ϕ_c°, one may calculate the corrosion potential. A closed form solution can be found when the α values are all equivalent, i.e.,

$$\alpha_{aa} = \alpha_{cc} = \alpha_{ac} = \alpha_{ca}$$

Additionally, if all the α values are equal to 1/2, Eq. (26) may be rearranged to give ϕ^*

$$\phi^* = \frac{RT}{F} \ln \left[\frac{(i_{0a} \exp (F/2RT)\phi_a^\circ + i_{0c} \exp (F/2RT)\phi_c^\circ)}{(i_{0a} \exp (-F/RT)\phi_a^\circ + i_{0c} \exp (-F/2RT)\phi_c^\circ)} \right] \tag{27}$$

When the equilibrium potentials for the two reactions are widely separated, the back reaction for either or both reactions may be negligible. Stern$^{(23)}$ and Stern and Geary$^{(24)}$ first treated this superposition for metal dissolution and hydrogen evolution, and obtained

$$i_{\text{corr}} = i_{0a} \exp \left(\frac{\alpha_{aa}F}{RT} \right) (\phi^* - \phi_a^\circ) = i_{0c} \exp \left(\frac{-\alpha_{cc}F}{RT} \right) (\phi^* - \phi_c^\circ) \tag{28}$$

The corrosion potential may be shown to be

$$(\alpha_{aa} + \alpha_{cc})\phi^* = \frac{RT}{F} \ln \left(\frac{i_{0c}}{i_{0a}} \right) + \alpha_{cc}\phi_c^\circ + \alpha_{aa}\phi_a^\circ \tag{29}$$

Introducing the definition for the current density [Eq. (28)] and corrosion potential [Eq. (29)], the total current density is given by (cf. Stern$^{(23)}$)

$$i_T = i_a + i_c = i_{\text{corr}} \left[\exp \left(\frac{\alpha_{aa}F}{RT} \right) (\phi - \phi^*) - \exp \left(\frac{-\alpha_{cc}F}{RT} \right) (\phi - \phi^*) \right] \tag{30}$$

This equation resembles the Butler–Volmer equation for a single reaction, where the corrosion potential and corrosion current density have replaced the equilibrium potential and exchange current density. The primary justification for writing the equation in this form is to describe the corrosion kinetics concisely and economically. It is not meant to suggest that the corrosion potential is characteristic of a thermodynamic or reference state, and it may be unstable if the rates of the participating reactions vary with time.

Neglect of the back reactions is valid for large positive potentials (with respect to the equilibrium potential) for the anodic reaction or for large negative potentials (with respect to the equilibrium potential) for the cathodic reaction. At the corrosion potential both conditions are assumed to be fulfilled simultaneously for the Stern treatment, and each reaction is said to be under Tafel control. This is shown graphically in Figure 1. The dotted lines represent the two individual current–voltage curves, and the solid line is the *net* current measured at each potential. At potentials which are large and positive with

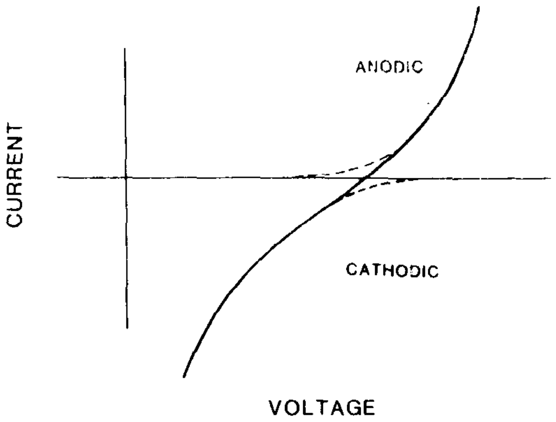

Figure 1. Schematic plot of current density–voltage behavior of superposed corroding couple with Tafel control of each reaction.

respect to the corrosion potential, the current is due solely to anodic dissolution. The cathodic reaction dominates the current at large negative potentials with respect to the corrosion potential. Figure 2 demonstrates the same thing, but now the plot has a Tafel format, i.e., log *i* vs. potential. The dotted lines are the extrapolated Tafel curves for the anodic and cathodic reactions, respectively, and the net measured current is given by solid lines.

The neglected back reactions are proportional to the solution concentration of metal ions and dissolved hydrogen, respectively, where the cathodic process is hydrogen evolution. The contribution of the back reactions to the overall current density will be small when the respective concentrations are small—a condition usually satisfied in corrosion. The neglect of the back

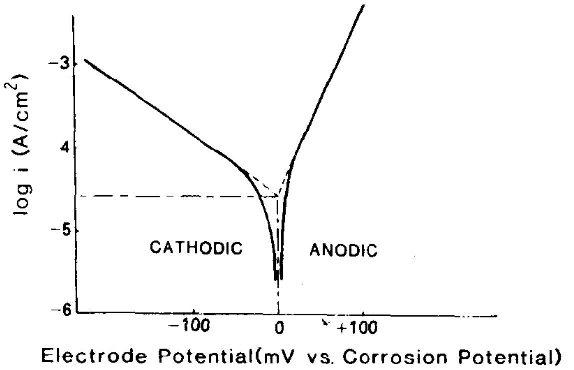

Figure 2. Current density–overpotential curves for a metal–hydrogen corrosion couple emphasizing the Tafel kinetics for each reaction.

reaction as compared to the dominant reactions is then an excellent approximation in corrosion.

The hydrogen evolution reaction or the anodic dissolution reaction occurs alone at the two (Tafel) extremes, respectively, so the principle of superposition is not needed there. It is only near the corrosion potential that both reactions occur simultaneously, and there superposition is relevant. Stated another way, the entire electrode surface is involved in either the metal dissolution or hydrogen evolution reaction under anodic or cathodic Tafel conditions respectively. The surface is homogeneous under these conditions.

Returning to a discussion of Eq. (30), it is assumed that the corrosion potential is stable and reproducible. The corrosion current density may be determined by (1) extrapolation of Tafel measurements, and (2) linear polarization measurements. These will be discussed in turn below.

2.5.1. Tafel Polarization

Figure 2 shows a schematic plot of Eq. (31) i vs. $(\phi - \phi^*)$. The value of the cathodic Tafel slope

$$\frac{d(\phi - \phi^*)}{d \log i} = \frac{2.303RT}{\alpha_{cc}F} \tag{31}$$

was drawn with a 120 mV/decade value, characteristic of hydrogen evolution, where

$$\alpha_{cc} = 1/2$$
$$T = 298\text{ K}$$

The anodic Tafel slope

$$\frac{d(\phi - \phi^*)}{d \log i} = \frac{2.303RT}{\alpha_{aa}F}, \tag{32}$$

was drawn with a 40 mV/decade value, characteristic of

$$\alpha_{aa} = 3/2$$
$$T = 298\text{ K}$$

Several divalent metals have this value of α_{aa}.

Extrapolation of the Tafel branches to their interaction at the corrosion potential gives the corrosion current density, i_{corr}. The extrapolation is shown by the dotted lines in Figure 2. The actual, measured current would follow the solid lines and the deviation from the extrapolated (dotted) curves indicates the increased importance of the other, superposed, reaction as the corrosion potential is approached from either Tafel extreme.

The Tafel extrapolation technique for measurement of corrosion kinetic parameters was introduced by Stern(23) and Stern and Geary.(24) The technique may be used to determine the anodic and cathodic Tafel slopes as well as the corrosion current density. It has been widely used for the investigation of corrosion kinetics, with the most success in acidic solutions and other systems in which there are soluble reaction products.

Aside from limitations caused by the precipitation of insulating and protective films, the Tafel technique has limitations caused by ohmic and mass transfer effects. Kinetic measurements in the Tafel region must be made at current densities much larger (absolute magnitude) than the corrosion current density. At high current densities, solution ohmic resistance may become important and this will cause deviations from Tafel behavior. If the aggressive solution of interest is of low conductivity, the deviation may be so severe that it is not possible to obtain Tafel behavior for determination of the kinetic parameters. Mass transfer effects will also cause deviations from Tafel behavior by limiting the supply of the electroactive species. Increasing the electrode potential would not produce a higher current, and a limiting current plateau would be observed.

2.5.2. Linear Polarization

The exponentials in Eq. (30) may be expanded and higher terms neglected where

$$|i| \ll i_{\text{corr}}$$

so that one obtains

$$i = i_{\text{corr}} \frac{(\alpha_{aa} + \alpha_{cc})F}{RT}(\phi - \phi^*) \tag{33}$$

The kinetic parameters are combined as the product $i_{\text{corr}}(\alpha_{aa} + \alpha_{cc})$ and may not be separately determined by measurements in the linear domain. Calculation of the corrosion current density requires a separate determination of the α values, α_{aa} and α_{cc}, from measurements in the Tafel region. The linear polarization method is then not an independent technique to evaluate corrosion kinetics.

The linear behavior given by Eq. (33) is restricted to about ±15 mV with respect to the corrosion potential where $|i| \ll i_{\text{corr}}$. The technique is highly sensitive to drift of the corrosion potential, which in many cases can amount to several millivolts. Measurements in such a restricted region are also susceptible to errors from ohmic effects. Despite these limitations, however, the method is the most widely used electrochemical technique for determining corrosion rates in industrial applications.

Stern[(23)] first introduced the linear polarization method, and described the limitations carefully and accurately. A recent review by Mansfeld[(25)] gives a detailed account of both fundamental and applied work which has been performed to evaluate the technique in many systems. The review[(25)] also describes industrial practice and the specialized instrumentation which is available to make linear polarization measurements, both in a manual and in a semiautomatic mode. Also described are the results obtained for several metals in a wide range of environments.

2.5.3. Ohmic Effects

Ohmic effects were mentioned briefly in both sections above. These effects may be manifested in two ways. The first is the deviation from predicted kinetic behavior. The deviation is worse at high current densities and/or low electrolyte conductivities.

The second way in which ohmic resistance is important is in nonuniform current and potential distributions. This is a macroscopic effect and is strongly dependent on geometry.[(26)] Geometries such as concentric spheres, or concentric cylinders (neglecting end effects), would be expected to have uniform current on the electrodes even if the current–voltage behavior is completely dominated by ohmic resistance. On the other hand, most geometries met in practice have nonuniform ohmic distributions (also called primary distributions), which lead to nonuniform corrosive attack. This is an important aspect of galvanic corrosion caused by coupling dissimilar metals.

The relative importance of ohmic resistance and interfacial kinetic polarization resistance may be made by calculation of the dimensionless numbers,[(27,28)]

$$J = \frac{(\alpha_{aa} + \alpha_{cc})FL}{\kappa RT} i_{\text{corr}} \qquad \text{(linear polarization)} \qquad (34)$$

$$\delta = \frac{\alpha_{aa}FL}{\kappa RT} i_{\text{avg}} \qquad \text{(anodic Tafel polarization)} \qquad (35)$$

with a similar expression for cathodic Tafel polarization. L is a characteristic dimension for the system, and κ is the electrolyte conductivity. For small values of J, kinetic factors dominate in linear polarization measurements, and the macroscopic current distribution will be uniform. For large J values the ohmic effects dominate and the current distribution may be very nonuniform, depending on the geometry. The magnitude of δ depends on the level of current, and reflects the increased importance of ohmic effects at high current densities in Tafel polarization measurements.

The discussion will return to current and potential distributions in a later section. The dimensionless parameters J and δ will be used extensively in discussion of galvanic and localized corrosion.

2.6. Corrosion with Soluble Products

2.6.1. Anodic Reactions

Even complex multistep anodic reactions have kinetic behavior which can be described in rather simple mathematical relationships. For example, Bockris(29) and Kelly(30) have discussed the iron dissolution kinetics in sulfuric acid solutions and have described the complex mechanism in terms of heterogeneous rate constants. Nobe and co-workers(31) have made extensive measurements on iron in chloride solutions. Kelly(30) has recently described in a very elegant series of papers the complex kinetics of dissolution of titanium as well.

It is at the point where the reaction products are insoluble that the present approach begins to have limited application. The insoluble products introduce nonuniform surface conditions, and only the uncovered part of such surfaces may be treated as homogeneous. Furthermore, the cathodic reaction will also have altered kinetics on the film covered part of the surface, which leads to very complex behavior. In acidic aqueous solutions, and in some fused salts where the surface films are fluxed off, metals behave in a homogeneous manner. These represent the most successful application of electrode kinetic principles to corrosion, and the model behavior is approached closely in these systems.

2.6.2. Cathodic Reactions

As stated previously, the cathodic reactions that couple with the anodic reaction in aqueous solutions are usually (1) the hydrogen evolution reaction, or (2) the reduction of dissolved oxygen. These will be described individually here because of their importance in aqueous corrosion, but details may be found elsewhere.

The kinetics of the hydrogen evolution reaction have been studied by many workers, and several excellent reviews are available.(11-17) In acid solution, the reaction for hydrogen evolution is

$$2H_3O^+(\text{soln}) + 2e^- \rightarrow 2H_2O(l) + H_2(g)$$

The reduction is accomplished in several steps. Vetter(11) describes the reduction in terms of two systems of reactions, i.e., either

$$H_3O^+(\text{soln}) + e^- \rightarrow H_2O(l) + H(\text{adsorbed})$$

$$H(\text{adsorbed}) + H(\text{adsorbed}) \rightarrow H_2(g)$$

or

$$H_3O^+(\text{soln}) + e^- \rightarrow H_2O(l) + H(\text{adsorbed})$$

$$H_3O^+(\text{soln}) + H(\text{adsorbed}) + e^- \rightarrow H_2(g) + H_2O(l)$$

The first step is common to both mechanisms. The second step of the first mechanism is purely chemical (i.e., no charge transfer occurs), but the corresponding step in the second mechanism is electrochemical. The stability of atomic hydrogen adsorbed on the surface, and the fraction of the surface covered are important in determining the rate of the second step for both reactions. For most metals the first step is rate determining. The first mechanism is identified(11) as the Volmer–Tafel mechanism, and the second is the Volmer–Heyrovsky mechanism.

The overall Butler–Volmer relationship for both mechanisms with the first step (i.e., hydrogen ion discharge) rate determining is

$$i_c = i_{0c}\left[\exp\left(\frac{\alpha_{ca}F}{RT}\right)(\phi_c - \phi_c^\circ) - \exp\left(\frac{-\alpha_{cc}F}{RT}\right)(\phi_c - \phi_c^\circ)\right] \qquad (36)$$

For both sequences, it can be shown (cf. Bockris and Reddy(12)) that $\alpha_{cc} = 1/2$. Both the derived Butler–Volmer relationship and the value of 1/2 for α_{cc} are appropriate for conditions such that the surface coverage by atomic hydrogen is very small. The same value of α_{cc} is also found for the situation when the two steps of the second mechanism are of equal rate. Further, for rate control by the Heyrovsky reaction α_{cc} may also be 1/2. This value of 1/2 for α_{cc} is found experimentally for a large number of metals. Any exceptions will be due to rate control by the chemical desorption step of the first mechanism (cf. Vetter(11)). Vetter has collected the Tafel polarization data for hydrogen evolution on a large number of metals.(11) Uhlig(32) has tabulated the cathodic hydrogen Tafel slopes for a number of metals as measured in corrosion investigations. Bockris(13) has summarized the mechanisms which have been observed on several metals.

The reduction of dissolved oxygen in aqueous solution is very complex and the subject of continued investigation. Vetter(11) and Hoar(18,19) have described the kinetic information that is known for several metals. In acid solutions oxygen may be reduced to water in an overall two-step sequence:

$$O_2(\text{soln}) + 2e^- + 2H_3O^+ \rightarrow 3H_2O_2(\text{soln})$$

$$H_2O_2(\text{soln}) + 2e^- + 2H_3O^+ \rightarrow 4H_2O$$

A second mechanism is an overall four-electron sequence which does not involve peroxide. Detailed discussion of the reduction process is described by Bockris.(13) For the purposes of the discussion in the next section, the peroxide mechanism will be used for copper corrosion. Peroxide is known to be generated on copper surfaces in corroding(33) and noncorroding situations.(11)

3. Corrosion of Copper in Acidic Aqueous Solutions

Application of the general principles of the previous sections will now be made to the copper corrosion system. In acid solution, the corrosion products of copper are soluble. Hydrogen ion reduction will drive the dissolution reaction at a very low rate, even at low pH.(34) Dissolved oxygen may be reduced on copper and this strongly accelerates the corrosive attack. Rigorous treatment of the corrosion of copper in oxygenated acidic solutions would require that the two cathodic reactions be considered as simultaneous. It will be shown that neglect of the hydrogen evolution reaction is an excellent approximation near the corrosion potential in the presence of oxygen. Extension to other systems where both cathodic reactions are superposed is straightforward, but some caution is advised because there may be chemical coupling through pH effects.

3.1. Copper Dissolution Kinetics and Corrosion

The electrochemistry of copper has been reviewed recently by Bertocci.(35) An earlier paper by Bertocci(36) is an excellent reference which describes much of the general nature of copper corrosion in some aqueous solutions. Several other references(37–40) also describe corrosion investigations on copper, but with conflicting results, as to the influence of convective diffusion on corrosion in oxygenated solutions. The investigation of copper corrosion by Smyrl(41) follows closely the treatment of copper electrode kinetics by Newman,(28) and by Bockris *et al.*,(42) and presents results of impedance measurements, as determined by the digital Faradaic impedance at multiple, simultaneous frequencies. This technique gives a very detailed and rapid measure of electrode kinetics over a time scale limited only by the lowest frequency of the existing spectrum.

Bockris *et al.*(42) found for copper dissolution–deposition processes in acidic sulfate solutions that two, one-electron transfer reactions are important (written here for dissolution):

$$\mathrm{Cu(s)} \underset{k_{1c}}{\overset{k_{1a}}{\rightleftharpoons}} \mathrm{Cu^{+}(surface)} + e^{-} \qquad \text{(fast)} \tag{37}$$

$$\mathrm{Cu^{+}(surface)} \underset{k_{2c}}{\overset{k_{2a}}{\rightleftharpoons}} \mathrm{Cu^{2+}(soln)} + e^{-} \qquad \text{(slow)} \tag{38}$$

It was concluded that the first step was much faster than the second in sulfate solutions.

Development of the mathematical treatment of this two-step reaction was given(42) (see also Newman(28)), and the two steps were taken to be sequential in the steady state. The intermediate cuprous species concentration was determined by the first, fast step which was assumed to be in equilibrium. This accounted for the experimental observations very well, and there was no evidence for the loss of cuprous species from the surface. That is, the cuprous species was assumed to be an interfacial species, perhaps adsorbed, and none was lost into the bulk solution. If the two reactions are treated as simultaneous, with the cuprous species an interfacial species, the resulting mathematical relationships are similar.

For copper dissolution in media where there is complexation and stabilization of the cuprous species, e.g., in chloride solutions, the second reaction may not be important. Subsequent formation of cupric ions would be accomplished at higher potentials in a clearly separated reaction, or by homogeneous reaction with an oxidant in solution. The latter reaction is important for corrosion in oxygenated chloride solutions.

The anodic dissolution of copper will be given first for acidic sulfate media, followed by the kinetic treatment for acidic chloride solutions. A brief description of coupling these reactions with the cathodic reduction of hydrogen ions will follow; these combinations produce quite low rates of corrosion. Next, the corrosion in oxygenated solutions will be described. Corrosion in oxygenated, acidic chlorides will be treated first because it is found to be simpler. The complexity arising from the chemical reaction of cuprous ions with oxygen is not important for these solutions. In acidic sulfate solutions, the presence of oxygen causes the corrosion kinetics to be quite complex, and this will be treated last. It is believed that the latter case may be more general, and may illustrate a class of systems where superposition may not be valid. In these systems an intermediate species may directly react with an oxidant in solution rather than react in a following electrode reaction.

3.2. Copper Dissolution Kinetics in H_2SO_4

Copper dissolution kinetics in deaerated sulfate solutions is a two-step process [Eqs. (37) and (38)], in which the second step is rate limiting. The material balance on the intermediate cuprous species is simple since it is an interfacial species in this system. The total dissolution current density for the two-step reaction is

$$\frac{i_T}{2F} = \frac{k_{1a}\exp\left[\dfrac{(\alpha_{1a}+\alpha_{1c}+\alpha_{2a})F}{RT}V\right]}{\exp\left[\dfrac{(\alpha_{1c}+\alpha_{2a})F}{RT}V\right] + \dfrac{k_{1c}}{k_{2a}} + \dfrac{k_{1c}k_{2c}}{k_{2a}}\left(\dfrac{\delta}{D_{\mathrm{Cu}^{2+}}}\right)\exp\left[\dfrac{-\alpha_{2c}F}{RT}V\right]} \tag{39}$$

where V is discussed in the paragraph following Eq. (44). This equation assumes dissolution into a cupric-free sulfate solution. Diffusion of cupric ions is responsible for the third term in the denominator, where δ is the diffusion layer thickness and $D_{\mathrm{Cu}^{2+}}$ is the diffusion coefficient of the cupric species. When diffusion effects are negligible, e.g., for solutions containing cupric ions, Eq. (39) is transformed to the usual equation for copper electrode kinetics (cf. Newman(28)).

Copper dissolution into sulfuric acid solution is found to have a Tafel slope of 37 mV/decade,(43) in agreement with results in copper sulfate–sulfuric systems.[42] This result is consistent with Eq. (39) when the first term in the denominator is small compared to the second and third terms. With this approximation, Eq. (39) may be written

$$\frac{i_T}{2F} = \frac{k_{1a} \exp\{[(\alpha_{1a} + \alpha_{1c} + \alpha_{2a})F/RT]V\}}{(k_{1c}/k_{2a})\{1 + k_{2c}(\delta/D_{\mathrm{Cu}^{2+}}) \exp[(-\alpha_{2c}F/RT)V]\}} \tag{40}$$

The anodic Tafel slope ($dV/d \log i_T$) would be between the two limits

$$\frac{2.303\, RT}{(\alpha_{1a} + \alpha_{1c} + \alpha_{2a})F} \tag{41}$$

or

$$\frac{2.303\, RT}{(\alpha_{1a} + \alpha_{1c} + \alpha_{2a} + \alpha_{2c})F} \tag{42}$$

depending on whether the first or second term of the denominator is dominant, respectively. For the condition that (41) is valid in the limit

$$1 \gg k_{2c}\left(\frac{\delta}{D_{\mathrm{Cu}^{2+}}}\right) \exp\left(\frac{-\alpha_{2c}F}{RT}\, V\right) \tag{43}$$

the anodic Tafel slope would be 40 mV/decade and the anodic current would have no dependence on the diffusion of cupric ions. This slope was calculated at 25 °C and for all the α values to equal to 1/2. In the other extreme, where (42) gives the anodic Tafel slope of 30 mV/decade, diffusion would be dominant. It has been found experimentally[43] that the Tafel slope is 37 mV/decade and diffusion is important but not dominant. Both terms should then be retained in the denominator of Eq. (40), and this will be followed in the treatment of dissolution in corrosion in a subsequent section.

The first term of the denominator in Eq. (39), i.e., $\exp\{[(\alpha_{1c} + \alpha_{2a})F/RT]V\}$ may not be neglected at large values of the potential, where in fact it becomes the dominant term (cf. Newman[28]). Under such conditions, the anodic Tafel slope becomes

$$\frac{2.303\, RT}{\alpha_{1a}F} \tag{44}$$

which has a value of 120 mV/decade at 25°C for an α_{1a} value of 1/2.

It will be noted that the equations in this section are written in terms of a potential, V. The potential is taken to be the copper electrode potential versus a reference electrode potential. The reference electrode potential is considered to be constant throughout and serves as an arbitrary standard. The choice of the standard hydrogen electrode would be the most obvious, but another could be used just as well. The slope of the current–voltage curves would not be affected by different choices of the reference electrode, when measurements are made at the same current density. The choice will affect the absolute values of the rate constants, but both the anodic reaction and the coupled cathodic reaction (under corrosion conditions) will be influenced so that the *corrosion current* will not depend on the choice of the reference potential. The alternative is to describe the anodic process in terms of the reversible potential of the process and an overpotential which accounts for departure from the reversible potential. Electrode kinetics are normally described this way because the reversible situation is achieved when products and reactants are both present everywhere in the system and there are no concentration gradients. In corrosion, however, the metal dissolution occurs in a solution which normally contains none of the product metal ion. The reversible potential would not be defined in this case, and the awkward situation can be relieved only partially by insisting that any solution will contain a trace of the metal ion of interest. This may be a harmless procedure since the choice of the fictitious solution concentration is later canceled out when the anodic and cathodic corrosion processes are superimposed, and both processes are brought to a common potential scale. The use of overpotentials will be avoided here for the individual processes, as has been done above for copper dissolution, but a "corrosion overpotential" will be used below when the corrosion potential is well defined and stable. The corrosion overpotential measures the departure of the potential of the corroding surface from the corrosion potential.

3.3. Copper Dissolution in Acidic Chloride Solutions

In the absence of oxygen, copper dissolves anodically in dilute hydrochloric acid to form $CuCl_2^-$ as the dominant species. The reaction may be written

$$\mathrm{Cu(s)} + \mathrm{Cl^-(soln)} \underset{k_c}{\overset{k_a}{\rightleftharpoons}} \mathrm{CuCl_2^-(soln)} + e^- \tag{45}$$

Other complexed species may be formed at high concentrations of Cl^-. A recent study(44) of copper dissolution in chlorides has described some of the chloro complexes that are important in concentrated chloride solutions.

The steady state current–voltage relationship for the electrode reaction (45) is

$$\frac{i_1}{F} = k_a \exp\left(\frac{\alpha_a F}{RT} V\right) - k_c(C^\circ_{\mathrm{Cu^+}}) \exp\left(\frac{-\alpha_c F}{RT} V\right) \tag{46}$$

$C^\circ_{\mathrm{Cu^+}}$ is the concentration of the cuprous ion at the surface. This concentration also obeys the equilibrium relationship for complexation

$$K_c = \frac{[\mathrm{CuCl_2^-}]}{[\mathrm{Cu^+}][\mathrm{Cl^-}]^2} \tag{47}$$

The concentration of the complex species $C_{\mathrm{CuCl_2^-}}$ (given below with a subscript *c*) which appears in the equilibrium relationship has a mass balance given by

$$N_c = -\frac{D_c(C_c^{\infty} - C_c^{\circ})}{\delta} = \frac{i_1}{F} \tag{48}$$

The first part of (48) relates the flux of $CuCl_2^-$ normal to the electrode surface to the rate at which it is transported to the surface by convective diffusion. This flux is equivalent to the current at the electrode (divided by F) for a single electrode section [reaction (45)]. D_c, C_c^{∞}, and C_c° are the diffusion coefficient, bulk concentration, and interfacial concentration, respectively, of $CuCl_2^-$. The diffusion layer thickness is δ.

Equation (48) is the approximate mass balance when there is an excess of supporting electrolyte (HCl in this case) and convective diffusion is approximated by a Nernst diffusion layer treatment. A more complete description would use the total flux expression for an ion (cf. Newman[(28)]):

$$\frac{i_1}{F} = N_c = -D_c C_c \frac{F}{RT}\frac{d\Phi}{dx} - D_c \frac{dC_c}{dx} + C_c v \tag{49}$$

The first term accounts for the migration of the ion in an electric field, and becomes negligible for a species whose concentration is small compared to the concentration of a supporting electrolyte. The small concentration ratio causes the transference number (which is roughly the fraction of current carried by an ionic species) of the minor species to be negligible. Consequently, the electric field does not influence the transport of the minor species. The last two terms of Eq. (49) are the diffusion and convection contributions to the flux. The two contributions are accounted for in the Nernst diffusion layer treatment [Eq. (48)] by a diffusion flux across a layer of thickness δ, which is a function of convection conditions.

Adopting (48) for the mass balance (with $C_c^{\infty} = 0$ and $C_{Cl^-}^{\circ} = C_{Cl^-}$) and (47), the current equation [Eq. (15)] becomes

$$\frac{i_1}{F} = k_a \exp\left(\frac{\alpha_a F}{RT} V\right) - k_c \frac{i_1}{F}\frac{\delta}{D_c K_c (C_{Cl^-})^2} \exp\left(\frac{-\alpha_c F}{RT} V\right) \tag{50}$$

Solving for i_1/F,

$$\frac{i_1}{F} = \frac{k_a \exp[(\alpha_a F/RT)V]}{1 + k_c[\delta/D_c K_c (C_{Cl^-})^2]\exp[(-\alpha_c F/RT)V]} \tag{51}$$

The importance of diffusion of the cuprous complex is measured by the relative magnitude of the two terms in the denominator of (51). For the limiting case,

$$k_c \frac{\delta}{D_c K_c (C_{Cl^-})^2} \exp\left(\frac{-\alpha_c F}{RT} V\right) \gg 1 \tag{52}$$

the equation for the net current becomes

$$\frac{i_1}{F}=\frac{k_a}{k_c}\frac{D_cK_cC^2_{\mathrm{Cl}^-}}{\delta}\exp\left(\frac{(\alpha_a+\alpha_c)F}{RT}V\right) \tag{53}$$

For the limit expressed by the reverse of (52), the current is

$$\frac{i_1}{F}=k_a\exp\left(\frac{\alpha_aF}{RT}V\right) \tag{54}$$

Equation (53) would be expected to describe copper dissolution where both forward and backward reactions are fast, i.e., faster than the diffusion rate of $CuCl_2^-$. Equation (54) would be appropriate at high anodic currents and large potentials, where the forward reaction is dominant. Hurlen$^{(45)}$ and Braun and Nobe$^{(46)}$ found the dissolution current to be proportional to $(C_{\mathrm{Cl}^-})^2$, in agreement with Eq. (53). The anodic Tafel slope from (51) is

$$\frac{dV}{d(\log i)}=\frac{2.303\{1+k_c(\delta/D_cK_cC^2_{\mathrm{Cl}^-})\exp[(-\alpha_cF/RT)V]\}}{(\alpha_aF/RT)+[(\alpha_a+\alpha_c)F/RT](k_c\delta/D_cK_cC^2_{\mathrm{Cl}^-})\exp[(-\alpha_cF/RT)V]} \tag{55}$$

In the limit expressed by (52), the anodic Tafel slope becomes

$$\frac{dV}{d(\log i)}=\frac{2.303\,RT}{(\alpha_a+\alpha_c)F} \tag{56}$$

Equation (56) gives 60 mV/decade at 25°C with both α values of 1/2.

Hurlen,$^{(45)}$ Braun and Nobe,$^{(46)}$ Miller,$^{(47)}$ and Baccarella *et al.*,$^{(48)}$ have all observed Tafel slopes in agreement with Eq. (56). The experimental values are best described with $\alpha_a=\alpha_c=1/2$ at all the temperatures and chloride concentrations studied, as well as at each of the convection conditions. Equation (56) has no dependence on convection (through δ), although the current density is inversely proportional to δ in Eq. (53). Some workers have described the copper dissolution to be "mass transport controlled" since the approximation (52) leads to (53) and (56). A better terminology might be "mass transport–kinetic control" to emphasize the importance of both influences on the dissolution process. The limit which leads to (54) is purely kinetically controlled, but this is not important in corrosion conditions where the dissolution rates are low.

Braun and Nobe$^{(46)}$ found the mass transport–kinetic limit to be a good description of the Tafel slope for dissolution in chloride media, but to be less satisfactory for describing the convection effects on the current density at a particular potential. A rotating copper disk electrode was used for these studies,$^{(46)}$ and convection effects are given by the dependence of the diffusion layer thickness, δ, on the rotation rate as (cf. Homsy and Newman$^{(49)}$)

$$\delta_{(\text{rotating disk})}=\Gamma(\tfrac{4}{3})\left(\frac{\nu}{\Omega}\right)^{1/2}\left(\frac{3D}{\alpha\nu}\right)^{1/3} \tag{57}$$

where Γ is the gamma function $[\Gamma(\frac{4}{3}) = 0.89298]$, ν the kinematic viscosity, Ω the disk rotation rate, D the diffusion coefficient, and α is a constant = 0.5103. This equation leads to the prediction that the current density (53) should be proportional to $(\Omega)^{1/2}$, but Braun and Nobe(46) were unable to confirm this dependence. Recent results by the author(43) in 0.1 N HCl show a closer fit to the expected $(\Omega)^{1/2}$ dependence. The deviations, which are minor, indicate that Eq. (53) may not be strictly valid at all rotation rates, and (51) should be used at very high rotation rates.

Except for the minor deviations noted, Eq. (53) describes the current–voltage behavior for dissolution in chloride solutions below 1 M. At higher concentrations, the presence of other chloro complexes must be taken into account.(44) The Tafel slope will be given by Eq. (56). These two relationships will be used below to describe the anodic portion of copper corrosion in chlorides.

3.4. Copper Corrosion in Deoxygenated H_2SO_4 and HCl

The calculations in the thermodynamics section showed that there is a small driving force for copper corrosion in both sulfuric and hydrochloric acid solutions which are free of oxygen. For 0.1 N HCl with 1 atm of hydrogen gas, and the redox potential of 0.263 V, the calculation for the reaction

$$H_3O^+(\text{soln}) + 2Cl^-(\text{soln}) + Cu(s) \rightleftarrows \tfrac{1}{2}H_2(g) + H_2O(l) + CuCl_2^-(\text{soln}) \quad (58)$$

gives the equilibrium concentration of $CuCl_2^-$ of

$$[CuCl_2^-] = 10^{-7}\ \text{mol/l}$$

This equilibrium concentration of the cuprous species is small and could almost be expected as a trace impurity in the solution—very little corrosion would be required to produce it. Increasing the Cl^- concentration and/or decreasing the pH would lead to a larger driving force for corrosion, i.e., a higher concentration of $CuCl_2^-$ would be necessary to achieve equilibrium. The equivalent calculation in sulfuric acid for the reaction

$$2H_3O^+(\text{soln}) + Cu(s) \rightleftarrows Cu^{2+}(\text{soln}) + H_2(g) + H_2O(l) \quad (59)$$

yields the equilibrium concentration

$$[Cu^{2+}] = 10^{-14}\ \text{mol/l}$$

at 1 atm of H_2 and 0.1 N H_2SO_4. This is indeed small, and little corrosion would be required to reach equilibrium.

3.4.1. Sulfuric Acid

Superposition of copper dissolution in H_2SO_4 [Eq. (40)] with the cathodic hydrogen ion reduction yields equations for the corrosion potential, corrosion current density, and current–voltage relationship in the vicinity of the corrosion potential.

These equations are as follows:

(1) For the corrosion potential, V^*

$$\frac{2k_{2a}k_{1a}}{k_{\mathrm{CH}}k_{1c}}\exp\left[\frac{(\alpha_{1a}+\alpha_{1c}+\alpha_{2a}+\alpha_{\mathrm{CH}})F}{RT}V^*\right] - k_{2c}\frac{\delta}{2D_{\mathrm{Cu}^{2+}}}\exp\left(\frac{-\alpha_{2c}F}{RT}V^*\right) = 1 \tag{60}$$

(2) For the corrosion current density,

$$\frac{2k_{2a}k_{1a}}{k_{\mathrm{CH}}k_{1c}}\left(\frac{i_{\mathrm{corr}}}{k_{\mathrm{CH}}}\right)^{(\alpha_{\mathrm{CH}}+\alpha_{1a}+\alpha_{1c}+\alpha_{2a})/\alpha_{\mathrm{CH}}} - \frac{k_{2c}}{2D_{\mathrm{Cu}^{2+}}}\left(\frac{i_{\mathrm{corr}}}{k_{\mathrm{CH}}}\right)^{\alpha_{2a}/\alpha_{\mathrm{CH}}} = 1 \tag{61}$$

The quantities k_{CH} and α_{CH} are kinetic parameters for the hydrogen reaction, where a Tafel expression has been used to derive the two equations above, i.e.,

$$\frac{i_{\mathrm{H}}}{F} = -k_{\mathrm{CH}}\exp\left(\frac{-\alpha_{\mathrm{CH}}F}{RT}\phi_c\right) \tag{62}$$

(here $\phi_c = V^*$). ϕ_c and the potential V^* used throughout the remainder of this section are taken with respect to the standard hydrogen electrode.

As described in Section 3.2, anodic dissolution for copper as described by Eq. (40) and used above lies between two limiting cases. For the limiting condition expressed in (43), the corrosion potential and corrosion current density are

$$V^* = \frac{RT}{\alpha_{1a}+\alpha_{1c}+\alpha_{2a}+\alpha_{\mathrm{CH}}}\log_e\left(\frac{k_{\mathrm{CH}}k_{1c}}{2k_{1a}k_{2a}}\right) \tag{63}$$

$$i_{\mathrm{corr}} = k_{\mathrm{CH}}\left(\frac{2k_{1a}k_{2c}}{k_{\mathrm{CH}}k_{1c}}\right)^{\alpha_{\mathrm{CH}}/(\alpha_{1a}+\alpha_{1c}+\alpha_{2a}+\alpha_{\mathrm{CH}})} \tag{64}$$

In the other limit, where the inequality in (43) is reversed, the corrosion potential and corrosion current density are

$$V^* = \frac{RT}{F(\alpha_{1a}+\alpha_{2a}+\alpha_{1c}+\alpha_{2c}+\alpha_{\mathrm{CH}})}\log_e\left(k_{2c}\frac{\delta}{2D_{\mathrm{Cu}^{2+}}}\frac{k_{\mathrm{CH}}k_{1c}}{2k_{2a}k_{1a}}\right) \tag{65}$$

$$i_{\mathrm{corr}} = k_{\mathrm{CH}}\left(\frac{4D_{\mathrm{Cu}^{2+}}k_{2a}k_{1a}}{k_{2c}k_{\mathrm{CH}}k_{1c}\delta}\right)^{\alpha_{2a}/(\alpha_{1a}+\alpha_{2a}+\alpha_{1c}+\alpha_{2c}+\alpha_{\mathrm{CH}})} \tag{66}$$

Equations (63) and (64) have no dependence on convection (purely kinetically controlled), but convective diffusion is dominant for (65) and (66) and there is a weak dependence on δ. For a rotating disk with δ inversely proportional to the square root of rotation rate [see Eq. (57), and all the α values in Eqs. (65) and (66) equal to 1/2], the corrosion potential and corrosion current density would obey the following relationships:

$$V^* = \frac{RT}{2.5F}\left[-\frac{1}{2}\log_e \Omega + \log_e\left(A\frac{k_{2c}k_{CH}k_{1c}}{4k_{2a}k_{1a}D_{Cu^{2+}}}\right)\right] \tag{67}$$

$$i_{corr} = k_{CH}\left(\frac{4D_{Cu^{2+}}k_{2a}k_{1a}}{k_{2c}k_{1c}k_{CH}A}\right)^{1/5}\Omega^{1/10} \tag{68}$$

The proportionality constant A comes from the general equation (57) for δ. Equations (67) and (68) give the maximum rotation rate effects which could be observed for copper corrosion in deoxygenated H_2SO_4. The measured rotation effect would be expected to be lower than this. Unpublished data[(43)] confirms the weak but discernible rotation effects on copper corrosion in deoxygenated H_2SO_4.

Tafel plots from unpublished data[(43)] for hydrogen ion discharge and copper dissolution in 0.1 N H_2SO_4 saturated with hydrogen gas is shown in Figure 3. Data were obtained between 10^{-3} and 10^{-6} A/cm^2 for each branch of the curve on a rotating copper disk electrode (area = 0.694 cm^2). Lines have been drawn here, and the complete set of data will be published elsewhere. The anodic dissolution currents varied with Ω in a complex way, approximately as given in (40). The cathodic branch had a 110-mV/decade Tafel slope.

Extrapolation of the anodic and cathodic branches to intersection gives a predicted corrosion current density of about 2×10^{-9} A/cm^2, for a 1000 rpm (104.72 rad/sec) rotation rate. The corrosion current density for 3000 rpm (314.16 rad/sec) was only slightly but discernibly different,[(43)] i.e., 2.2×10^{-9} A/cm^2. These very low corrosion current densities would be difficult to

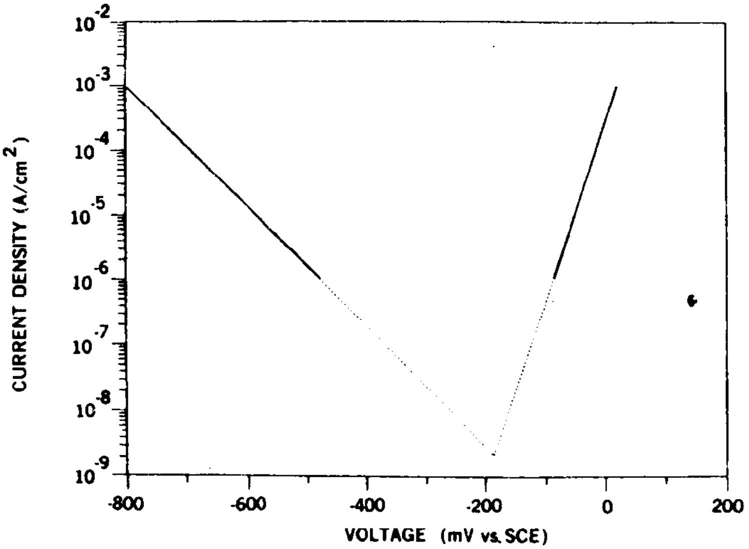

Figure 3. Corrosion kinetics of a copper disk in oxygen-free 0.1 N H_2SO_4, at 25°C.

measure in any way except by the Tafel extrapolation technique used here. Small quantities of dissolved oxygen or other impurities would completely obscure the determination by the linear technique. Weight loss measurements for such slow rates would be very difficult to make as well. Further discussion will follow the treatment of corrosion in 0.1 *N* HCl.

3.4.2. Hydrochloric Acid

In HCl solutions, the copper anodic current density equation was given by (53) when the dissolution was governed by mass transport and kinetics. The cathodic hydrogen ion discharge is of the general form of (62), although the heterogeneous rate constant k_{CH} would be expected to be different in general in HCl as compared to that in H_2SO_4. At the corrosion potential, V^*,

$$i_1(\text{anodic}) = -i_{\text{H}}(\text{cathodic}) = i_{\text{corr}} \tag{69}$$

which leads to the relationship

$$k_{\text{CH}} \exp\left(\frac{-\alpha_{\text{CH}}F}{RT}V^*\right) \equiv \frac{k_a}{k_c}\left\{\frac{D_cK_cC^2_{\text{Cl}^-}}{\delta}\exp\left[\frac{(\alpha + \alpha_c)F}{RT}V^*\right]\right\} \tag{70}$$

Solving for V^* gives

$$V^* = \frac{RT}{F(\alpha_a + \alpha_c + \alpha_{\text{CH}})}\left(\log_e \frac{k_{\text{CH}}k_c}{k_a}\frac{\delta}{D_cK_cC^2_{\text{Cl}^-}}\right) \tag{71}$$

As with the sulfuric acid system, the relationship for the corrosion potential V^* displays the dependence on the parameters for both reactions of the corrosion couple. The equation for the corrosion current density is obtained by substitution of (71) into (69). The result is

$$i_{\text{corr}} = \left[(k_{\text{CH}})^{\alpha_a+\alpha_c}\left(\frac{k_a}{k_c}\right)^{\alpha_{\text{CH}}}\right]^{1/(\alpha_a+\alpha_c+\alpha_{\text{CH}})}\left(\frac{D_cK_cC^2_{\text{Cl}^-}}{\delta}\right)^{\alpha_{\text{CH}}/(\alpha_a+\alpha_c+\alpha_{\text{CH}})} \tag{72}$$

For $\alpha_{\text{CH}} = \frac{1}{2}$, the corrosion current density is predicted to be proportional to $[\text{Cl}^-]^{2/3}$ and $\delta^{-1/3}$. The latter dependence leads to the expectation that the corrosion current density would be proportional to $\Omega^{1/6}$ for a rotating disk. The derivative $dV^*/d \log \Omega$ would be, from (71),

$$\frac{dV^*}{d \log_e \Omega} = \frac{-2.303\,RT}{2F(\alpha_a + \alpha_c + \alpha_{\text{CH}})} \tag{73}$$

This would give a value of −19.7 in mV/(decade rotation rate) at 298 K and $\alpha_a = \alpha_c = \alpha_{\text{CH}} = 1/2$. That is, the corrosion potential would decrease (i.e., become more negative) with an increase in rotation rate. This is a larger effect than the *maximum* expected for the sulfuric acid system [see Eq. (67)] which is −11.8 mV/(decade rotation rate). However, the result is again a decrease of the corrosion potential with an increase of rotation rate. Both effects are the result of diffusion of the species produced by the electrode reaction.

The general current density–voltage behavior in the vicinity of the corrosion potential may be obtained in terms of the corrosion potential and current density as follows. The total current to a corroding copper electrode is

$$i_T = i_{\text{anodic}} + i_{\text{cathodic}}$$

and for the copper–hydrogen couple one has

$$i_T = \frac{k_a}{k_c} D_c K_c C^2_{\text{Cl}^-} \exp\left[\frac{(\alpha_a + \alpha_c)F}{RT} V\right] - k_{\text{CH}} \exp\left(\frac{-\alpha_{\text{CH}}F}{RT} V\right) \tag{74}$$

Substitution of (71) and (72) into this equation yields

$$i_T = i_{\text{corr}}\left\{\exp\left[\frac{(\alpha_a + \alpha_c)F}{RT}(V - V^*)\right] - \exp\left[\frac{-\alpha_{\text{CH}}F}{RT}(V - V^*)\right]\right\} \tag{75}$$

which has the form of the Butler–Volmer equation for electrode kinetics.

Experimental results(43) for anodic dissolution and hydrogen discharge in the Tafel regions for each, respectively, are shown in Figure 4. The Tafel cathodic slope has a 120 mV/decade slope in agreement with Bockris and Pentland.(50) The anodic Tafel slope is 60 mV/decade as predicted from Eq. (53). These anodic results agree with the findings of Braun and Nobe,(46) Miller and Bellavance,(47) Baccarella and Griess,(48) Bonfiglio *et al.*,(51) and Turner and Brook,(52) in acid chloride solutions of higher concentration. The anodic

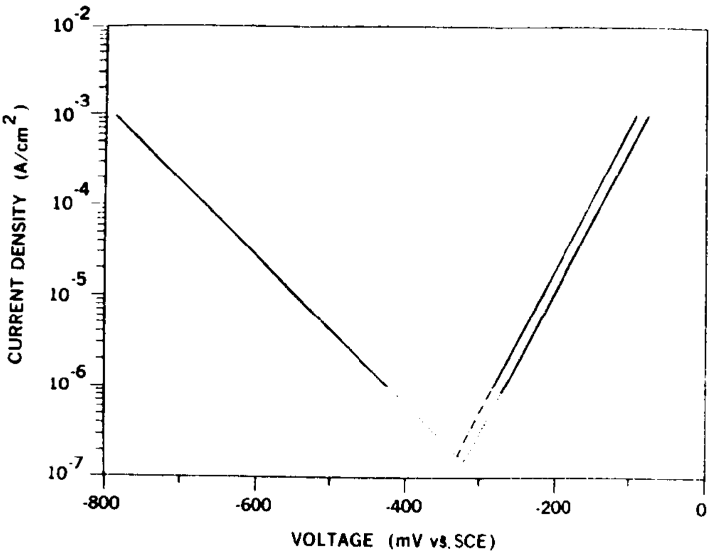

Figure 4. Corrosion kinetics of a copper rotating disk in oxygen-free 0.1 *N* HCl, at 25°C.

current density at a particular potential was found to depend on $(\Omega)^{1/2}$ as expected from (53).

Extrapolation of the two branches to their intersection, in Figure 4, gives a corrosion current density of 1.5×10^{-7} A/cm^2 at 1000 rpm (104.72 rad/sec). This rate is larger than for the sulfuric acid system, but again quite low. In both solutions, the stability of copper is assured both by the thermodynamic stability and by the kinetic stability as measured by the corrosion current densities.

This section demonstrates the low corrosion rates of copper in dilute nonoxidizing acids. The corrosion rate is higher in more acidic solutions (cathodic effect), higher stirring rates (anodic effect), and higher concentrations of Cl^- in chloride media (anodic effect). The corrosion rate would also be higher in solutions which complex the product ions more strongly than for chloride solutions above.

The general approach illustrated here demonstrates the importance of obtaining data on the individual reactions that make up the corrosion couple, when this is possible. The emphasis is on the basic electrode kinetics, but it is often found that mass transfer effects in the *anodic* reaction are also important in corrosion systems. This may be a dominant influence for fast reactions as shown for the chloride system, or of minor importance as in the sulfuric acid system. The emphasis has been on obtaining mathematical relationships that describe the corrosion coupling, to compare to experimental data. The same approach will now be extended to a system of another degree of complexity—copper corrosion in oxygenated acid solutions.

3.5. Copper Corrosion in Oxygenated HCl and H_2SO_4

Addition of oxygen to acid solutions increases the corrosion rate of copper. The reduction of oxygen occurs simultaneously with the reduction of hydrogen ions, and can exceed the hydrogen-driven corrosion in some hydrochloric and sulfuric acid solutions. The maximum rate of oxygen reduction is limited by the rate of transport of oxygen to the surface by convective diffusion. The diffusion-limited oxygen reduction current density may be estimated from the equation

$$i_L = nFN_{O_2} = nF\left[\frac{-D_{O_2}(C^{\infty}_{O_2} - C^{\circ}_{O_2})}{\delta}\right]$$

Here the number of electrons in the reaction is noted by n, and the flux of oxygen, N_{O_2}, is approximately given by the Nernst diffusion layer value, i.e., the terms inside the brackets. At the diffusion-limited rate, $C^{\circ}_{O_2}$ is zero, and

$$i_L = 2 \times 10^{-3} \text{ A/cm}^2 \tag{76}$$

for an oxygen concentration of 10^{-6} mol/cm^3, diffusion coefficient of 10^{-5} cm^2/sec, and $n = 2$ (i.e., oxygen to peroxide reaction). The hydrogen discharge current density driving copper corrosion in dilute H_2SO_4 and HCl, as described in the previous section, is negligible as compared to i_L from (76). Although the oxygen reduction described below does not attain the diffusion limited value, the treatment will assume the hydrogen discharge rate to be negligible by comparison. This assumption will be found to be justified except at low oxygen concentrations.

The treatment will start with corrosion of copper in oxygenated 0.1 *N* HCl because it is simpler than the sulfuric acid system. Superposition is found to give a good description of the corrosion reaction system in HCl, but not in H_2SO_4. Reaction between oxygen and cuprous intermediate in H_2SO_4 perturbs the corrosion system and the corrosion current density is larger than would be expected from superposition of the individual electrode reactions.

3.5.1. Hydrochloric Acid

Copper corrosion in oxygenated, 0.1 *N* HCl occurs at rates lower than the mass transfer limited oxygen diffusion rate at short exposure times (i.e., minutes).(43) The oxygen reduction reaction to peroxide is the dominant cathodic process. Below the limiting current, the highly irreversible oxygen reaction is described by the equation

$$\frac{i_{\text{ox}}}{2F} = k_{ao} C_p^\circ \exp\left(\frac{\alpha_{ao} F}{RT} V\right) - k_{co} C_o^\circ \exp\left(\frac{-\alpha_{co} F}{RT} V\right) \tag{77}$$

C_p° and C_o° denote interfacial concentrations for peroxide and oxygen, respectively. The first term for peroxide oxidation is to be neglected. Coupling this equation with Eq. (53) for copper dissolution for the condition

$$i_{\text{anodic}} = -i_{\text{cathodic}} = i_{\text{corr}}$$

yields relationships for the corrosion potential and corrosion current. For the corrosion potential V^*,

$$V^* = \frac{RT}{F(\alpha_a + \alpha_c + \alpha_{co})} \log_e \left(\frac{2k_c k_{co}}{k_a} \frac{\delta C_o^\infty}{D_c K_c C_{\text{Cl}^-}^2}\right) \tag{78}$$

where the subscripts a and c refer to the copper dissolution process, and D_c is the diffusion coefficient of $CuCl_2^-$. It is assumed that oxygen reduction is kinetically controlled, and the bulk and interfacial concentrations are equal and denoted by C_o^∞. The relationship for the corrosion current density is

$$i_{\text{corr}} = \frac{k_a}{k_c} \frac{D_c K_c C_{\text{Cl}^-}^2}{\delta} \left(\frac{2k_c k_{co} C_o^\infty}{k_a} \frac{\delta}{D_c K_c C_{\text{Cl}^-}^2}\right)^{(\alpha_a + \alpha_c)/(\alpha_a + \alpha_c + \alpha_{c0})} \tag{79}$$

If the α values (including α_{co} for oxygen reduction) are all equal to 1/2, the corrosion current density would depend on the dissolved oxygen concentration as $(C_o^\infty)^{2/3}$, on chloride concentration as $(C_{\text{Cl}^-})^{2/3}$, and on the diffusion layer thickness as $(\delta)^{-1/3}$. The experimental data in 0.1 *N* HCl (Reference 43)

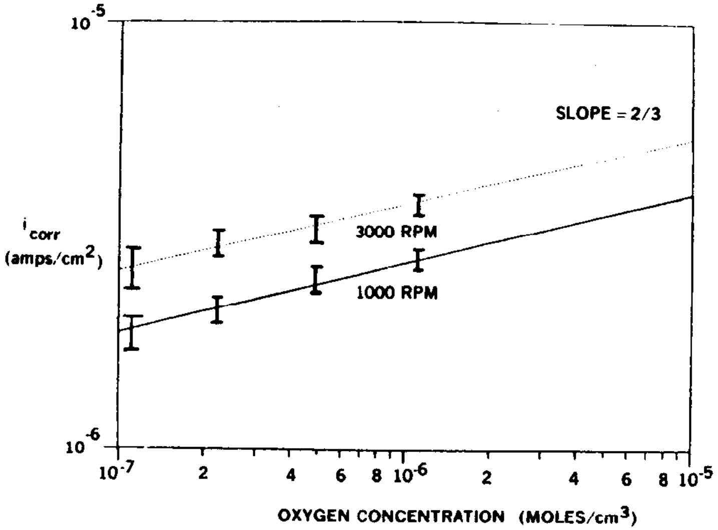

Figure 5. Corrosion current density of copper in oxygenated 0.1 *N* HCl at several rotation rates, at 25°C.

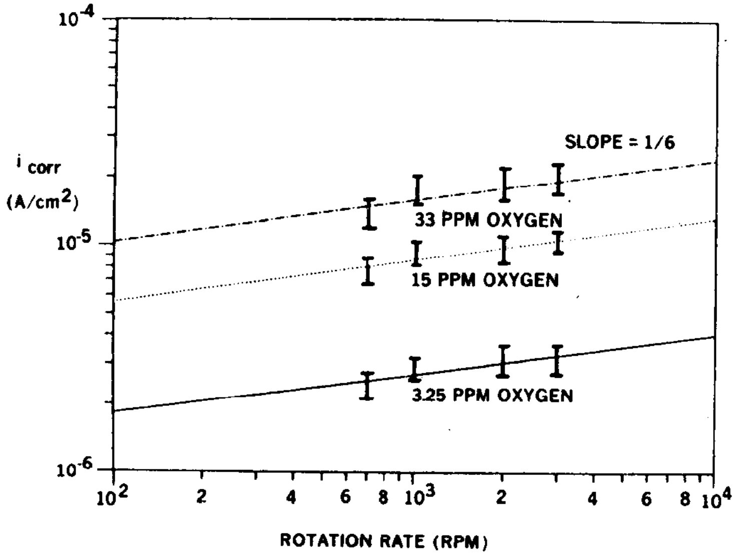

Figure 6. Corrosion current density of copper in oxygenated 0.1 *N* HCl as a function of rotation rate.

support the oxygen concentration dependence, as shown in Figure 5. For a rotating disk electrode, the corrosion current would depend on rotation rate as $\Omega^{1/6}$, and experimental data(43) support this prediction as shown in Figure 6 for 0.1 N HCl. Corrosion rates are shown to be larger than for hydrogen coupling in the previous section.

Bertocci(35) has given a recent review of much of the literature on copper and copper alloy corrosion. Miller and Bellavance(47) have reported results of rotating ring–disk studies on corroding copper and copper-30 zinc in oxygenated 0.1 M HCl–1 M NaCl. Their work(47) is consistent with the description given above in the following ways: (1) Oxygen is reduced to peroxide, with no further reduction to water; (2) the corrosion at times up to an hour occurs at rates much lower than the diffusion-limited rate given by the dissolved oxygen concentration; (3) the product ion, $CuCl_2^-$, is not oxidized by oxygen (or peroxide) at the electrode surface, but this does not preclude a slow homogeneous reaction in the bulk; (4) the corrosion rate is higher by about an order of magnitude than the data reported in Figures 5 and 6, reflecting the higher chloride concentration in Reference 47; (5) by replotting their data for rotation rate dependence, it may be shown that the corrosion rate varies approximately as $\Omega^{1/6}$ as found above. In addition, Miller and Bellavance(47) found that the corrosion rate, measured directly by a ring–disk technique, was exactly the anodic current density measured in deaerated solutions at the potential equal to the corrosion potential. This directly confirms the validity of superposition for the system.

Faita *et al.*(53) describe results for dissolution and corrosion studies in NaCl solutions at several pH values. It was concluded that corrosion occurs at rates lower than diffusion control by oxygen, but corrosion rates were not reported. Tracy(34) reviewed the older literature on corrosion of copper, including data in oxygenated and deoxygenated HCl. The data given by Tracy(34) show a higher corrosion rate than the corrosion rates obtained from Figures 5 and 6, which may be explained in part because of the more concentrated Cl^- solution in his tabulation. Equation (79) predicts the corrosion current density to increase with Cl^- concentration as $(C_{Cl^-})^{2/3}$. Decreased pH, to the values of Tracy,(34) would also cause the corrosion rate to increase. This has not been discussed, but the heterogeneous rate constant k_{co} used above contains a dependence on the pH, approximately as

$$k_{co} = (C_{H^+})^2 \bar{k}_{co} \tag{80}$$

The corrosion current density, Eq. (79) would depend on the hydrogen in concentration as $(C_{H^+})^{4/3}$. Finally, Tracy(34) quotes data that were determined at long times, and it is known(43,47) that the corrosion rate in chloride solutions changes with time. The data in the figures above were determined at short times.(43) The agreement between the two sets of data appears to be satisfactory.

It is concluded that the data given in Figures 5 and 6, and the data in the literature, are consistent with the mathematical description given here. The dependence on oxygen concentration and rotation rate fit the predictions very well, and the chloride concentration dependence is in general agreement. Superposition of the reduction and anodic dissolution reactions is valid for this system. The assumption of superposition may be checked by comparing the corrosion current density with the anodic current density measured at the same potential (corrosion potential) in the separated system. This was briefly described above. That is, in oxygenated hydrochloric acid solution, the corrosion current density was 1.5 (±0.2) $\times 10^{-5}$ A/cm^2, at a corrosion potential of −195 mV (vs. SCE), a rotation rate of 1000 rpm (104.72 rad/sec), and with the oxygen concentration of 33.5 ppm (see Figure 5). In deoxygenated HCl, at this rotation rate and potential, the anodic dissolution was found (Figure 4) to be 1.5×10^{-5} A/cm^2. This close check is repeated for the other data reported in Figures 4–6, which will be published in detail elsewhere. Superposition is verified for these systems, and the technique may be applied in any other system as a check.

3.5.2. Sulfuric Acid

The general section on corrosion with soluble products is concluded with copper corrosion in oxygenated H_2SO_4. The previous sections have described the fundamentals of treating corrosion systems. The emphasis has been placed on using the data for the electrode kinetics of the individual anodic and cathodic reactions and superimposing the processes. Superposition in this manner assumes the anodic and cathodic processes are coupled only electrically, and do not influence one another chemically. The two overall processes are balanced locally for homogeneous surfaces. The general approach described here has been very successful in application to a wide range of corrosion systems. The success has been so good that superposition may almost be taken for granted in treating new systems. However, there are possible corrosion processes that have coupling which is not only electrical, but chemical as well, and superposition may not be applied. Anderson *et al.*(33) were the first to recognize this limitation for copper corroding in oxygenated H_2SO_4.

The dissolution kinetics of copper in sulfuric acid has been described in a previous section to go through two steps:

$$\mathrm{Cu} \overset{\text{fast}}{\rightleftharpoons} \mathrm{Cu}^+ + e^- \qquad \text{(I)}$$

$$\mathrm{Cu}^+ \overset{\text{slow}}{\rightleftharpoons} \mathrm{Cu}^{2+} + e^- \qquad \text{(II)}$$

The cuprous ion is in equilibrium through the first reaction, but apparently remains on the surface and does not diffuse into solution. When the dissolution process is coupled with oxygen reduction on the copper surface, the direct oxidation of cuprous ion in a chemical reaction might be expected to compete with the second electrochemical step to produce cupric ions. The chemical reaction is

$$2Cu^{+}(\text{surface}) + O_2 + 2H_3O^{+} \rightarrow 2Cu^{2+} + H_2O_2 + 2H_2O$$

and this is taken to occur on the corroding metal surface, since there is no evidence that the cuprous ions exist in solution under the corrosion conditions. If the rate of this reaction is equal to or greater than the electrochemical oxidation rate, the overall corrosion process is not given by superposition. Electrical coupling still yields the relationship

$$i_{\text{anodic}} = -i_{\text{cathodic}}$$

but the total anodic current is no longer a measure of the corrosion rate. The total anodic current could be called the "balance" current perhaps, but it is not simply related to the net rate of dissolution of copper to the cuprous state which is the corrosion rate. The extent to which the chemical reaction competes for oxidation of the cuprous species is a measure of the disparity between the "balance" current and the corrosion current. These ideas will be made quantitative in the following treatment.

The current density equations for the two copper reactions are

$$\frac{i_1}{F} = k_{1a} \exp\left(\frac{\alpha_{1a}F}{RT} V\right) - k_{1c}C_s^{\circ} \exp\left(\frac{-\alpha_{1c}F}{RT} V\right) \tag{81}$$

$$\frac{i_2}{F} = k_{2a}C_s^{\circ} \exp\left(\frac{\alpha_{2a}F}{RT} V\right) - k_{2c}C_c^{\circ} \exp\left(\frac{-\alpha_{2c}F}{RT} V\right) \tag{82}$$

The s and c subscripts on the interfacial concentrations refer to the cuprous and cupric species, respectively. The kinetic equation for oxygen reduction is

$$\frac{i_3}{2F} = -k_{co}C_o^{\circ} \exp\left(\frac{-\alpha_{co}F}{RT} V\right) \tag{83}$$

The mass balance for the cuprous ions must account for the chemical reaction. The amount of cuprous ions produced is proportional to i_1, and that consumed in the second electrode reaction is proportional to i_2. The difference is the amount lost through the heterogeneous chemical reaction with oxygen. The quantity $(i_1 - i_2)/F$ has the units of flux, and satisfies the relationship

$$\frac{i_1 - i_2}{2F} = \frac{D_o(C_o^{\infty} - C_o^{\circ})}{\delta} + \frac{i_3}{2F} \tag{84}$$

The stoichiometry of the chemical reaction has been accounted for in this equation. If no chemical reaction occurs, the left hand side of Eq. (84) is zero.

The equation for conservation of cupric ions is

$$\frac{i_2}{F} + \frac{i_1 - i_2}{F} = \frac{D_c C_c^{\circ}}{\delta} \tag{85}$$

The first term is the electrochemical production of cupric ions and the second is that from the chemical reaction. Cupric ions generated by the two reactions diffuses into the solution. The solution is taken to be copper free (i.e., $C_c^\infty = 0$).

The material balance for peroxide does not affect the control of the corrosion system since it has been assumed that peroxide is neither oxidized back to oxygen nor reduced to water, but simply diffuses from the corroding surface into the solution. This should be included in a general treatment.

The final relationship that must be satisfied at the corrosion potential,

$$\frac{i_1 + i_2}{F} = i_{\text{anodic}} = \frac{-i_3}{F} = i_{\text{balance}} \tag{86}$$

also defines the "balance" current. The balance current density is equivalent to twice the corrosion current density i_1 *only* if $(i_1 - i_2)/F$ is zero.

Oxygen, dissolved in the solution, drives the corrosion system. The cathodic reduction of oxygen supplies the current density i_3 which balances the net anodic current density $i_1 + i_2$, and it drives the chemical oxidation of cuprous ions as well. These two reactions are dynamically coupled because the total oxygen flux and interfacial concentration are important for each. If the rate of the heterogeneous chemical reaction were too large, the interfacial concentration of oxygen would be driven to a low value. However, this would slow the electrochemical reduction, and the net anodic current would have to drop as well. The potential of the corroding metal would have to shift to reduce the anodic current and the interfacial concentration of cuprous ions would be decreased. A decreased interfacial concentration of cuprous ions would reduce the rate of the chemical reaction and the balance condition would be restored. The coupling of all the reactions is dynamic, and the balance point is determined by the rate constants, dissolved oxygen concentration, and convection conditions for a solution of given pH and temperature.

For the purposes of this section, the simplest treatment is sought which will give useful results, and a general treatment will be given elsewhere. It is assumed that the rate of oxygen reduction is far below the limiting current, as experimentally observed for short times(43) (see below also). Equation (83) becomes

$$\frac{i_3}{2F} = -k_{co} C_o^\infty \exp\left(\frac{-\alpha_{co} F}{RT} V\right) \tag{87}$$

since the surface concentration of oxygen is now equal to the bulk concentration. The material balance for cuprous ions [Eq. (84)] becomes

$$\frac{i_1 - i_2}{F} = \text{rate of cuprous–oxygen reaction, expressed as a flux}$$

$$= k_{\text{HC}}(C_s^0)(C_{\text{O}_2}^\infty) \tag{88}$$

k_{HC} is a heterogeneous rate constant for the direct *chemical* reaction between cuprous and dissolved oxygen. In (88) the interfacial concentration of oxygen is again taken to be equal to that in the bulk. It is seen that when the rate of this reaction becomes small, oxygen couples only through the electrical balance and superposition is obeyed.

Elimination of the cuprous concentration between Eqs. (82) and (88) yields

$$\begin{aligned}\frac{i_1}{F}\left\{\frac{1}{k_{\mathrm{HC}}C_o^\infty}-\left(\frac{k_{2c}(\delta/D_c)}{k_{2a}}\right)\exp\left[\frac{-(\alpha_{2a}+\alpha_{2c})F}{RT}V\right]\right\}\\ =\frac{i_2}{F}\left[\frac{1}{k_{\mathrm{HC}}C_o^\infty}+\frac{1}{k_{2a}}\exp\left(\frac{-\alpha_{2a}F}{RT}V\right)\right]\end{aligned}\tag{89}$$

A similar process of elimination of cuprous concentration between Eqs. (81) and (82) yields

$$\begin{aligned}\frac{i_1}{F}\left\{1+\frac{\delta}{D_c}\frac{k_{1c}k_{2c}}{k_{2a}}\exp\left[\frac{-(\alpha_{1c}+\alpha_{2c}+\alpha_{2a})F}{RT}V\right]\right\}\\ =k_{1a}\exp\left(\frac{\alpha_{1a}F}{RT}V\right)-\frac{i_2}{F}\frac{k_{1c}}{k_{2a}}\exp\left[\frac{-(\alpha_{1c}+\alpha_{2a})F}{RT}V\right]\end{aligned}\tag{90}$$

An equation for i_1/F may be obtained from (89) and (90), i.e.,

$$\frac{i_1}{F}=\frac{Ak_{1a}\exp\left[(\alpha_{1a}F/RT)V\right]}{\{A+(B/k_{2a})\exp\left[(-\alpha_{2a}F/RT)V\right]\}}\tag{91}$$

where

$$A=1+\frac{k_{\mathrm{HC}}C_o^\infty}{k_{2a}}\exp\left(\frac{-\alpha_{2a}F}{RT}V\right)\tag{92}$$

$$B=k_{1c}\exp\left(\frac{-\alpha_{1c}F}{RT}V\right)\left[1+\frac{\delta k_{2c}}{D_c}\exp\left(\frac{-\alpha_{2c}F}{RT}V\right)\right]\tag{93}$$

The equation for i_2/F is obtained similarly, i.e.,

$$\frac{i_2}{F}=\frac{k_{1a}\exp\left[\frac{\alpha_{1a}F}{RT}V\right]\left\{1-\left(\frac{C_o^\infty\delta k_{2c}k_{\mathrm{CH}}}{D_ck_{2a}}\right)\exp\left[\frac{-(\alpha_{2c}+\alpha_{2a})F}{RT}V\right]\right\}}{A+\left(\frac{B}{k_{2a}}\right)\exp\left[\frac{-\alpha_{2a}F}{RT}V\right]}\tag{94}$$

The corrosion current density divided by F is i_1/F evaluated at the corrosion potential ($V = V^*$):

$$\left(\frac{i_1}{F}\right)_{V^*}=\frac{Ak_{1a}\exp\left[(\alpha_{1a}F/RT)V^*\right]}{A+(B/k_{2a})\exp\left[(-\alpha_{2a}F/RT)V^*\right]}\tag{95}$$

The total anodic current density $[(i_1+i_2)/F]_{V^*}$ at the corrosion potential is

T21/A 1

equal to $-(i_3/F)_{V^*}$, i.e., the total current density from the electrochemical reduction of oxygen, and is denoted the balance current in (86). From (94) and (95),

$$\left(\frac{i_b}{F}\right)_{V^*} = \frac{k_{1a}\exp\left[\dfrac{\alpha_{1a}F}{RT}V^*\right]\left\{A+1-\dfrac{\delta k_{2c}k_{\mathrm{CH}}C_o^\infty}{D_c k_{2a}}\exp\left[\dfrac{-(\alpha_{2c}+\alpha_{2a})F}{RT}V^*\right]\right\}}{A+\left(\dfrac{B}{k_{2a}}\right)\exp\left[\dfrac{-\alpha_{2a}F}{RT}V^*\right]} \tag{96}$$

Introducing equation (87) yields a complex expression for the corrosion potential, i.e.,

$$\exp\left[\frac{-(\alpha_{co}+\alpha_{1a})F}{RT}V^*\right] = \frac{\dfrac{-k_{1a}}{2k_{co}C_o}\left\{A+1-\dfrac{\delta k_{\mathrm{HC}}k_{2c}C_o^\infty}{D_c k_{2a}}\exp\left[\dfrac{-(\alpha_{2c}+\alpha_{2a})F}{RT}V^*\right]\right\}}{A+\dfrac{B}{k_{2a}}\exp\left[\dfrac{-\alpha_{2a}F}{RT}V^*\right]} \tag{97}$$

and (96) for the balance current may be written

$$\begin{aligned}\left(\frac{i_b}{F}\right)_{V^*} &= \frac{k_{1a}(i_b/F)_{V^*}^{-(\alpha_{1a}/\alpha_{c0})}}{(2k_{co}C_o)^{-(\alpha_{1a}/\alpha_{c0})}}\\ &\times\left(2+\frac{k_{\mathrm{HC}}C_o^\infty}{k_{2a}}\left[\frac{(i_b/F)_{V^*}}{2k_{co}C_o}\right]^{\alpha_{2a}/\alpha_{c0}}\left\{1-\frac{\delta k_{2c}}{D_c}\left[\frac{(i_b/F)_{V^*}}{2k_{co}C_o}\right]^{\alpha_{2c}/\alpha_{c0}}\right\}\right)\\ &\times\left\{1+\frac{k_{\mathrm{HC}}C_o}{k_{2a}}\left[\frac{(i_b/F)_{V^*}}{2k_{co}C_o}\right]^{\alpha_{2a}/\alpha_{c0}}+\left[\frac{(i_b/F)_{V^*}}{2k_{co}C_o}\right]^{\alpha_{2a}/\alpha_{c0}}\right.\\ &\times\left\{k_{c1}\left[\frac{(i_b/F)_{V^*}}{2k_{co}C_o}\right]^{\alpha_{1c}/\alpha_{c0}}+\frac{\delta}{D_c}k_{1c}k_{2c}\left[\frac{(i_b/F)_{V^*}}{2k_{co}C_o}\right]^{(\alpha_{1c}+\alpha_{2c})/\alpha_{c0}}\right\}^{-1}\end{aligned} \tag{98}$$

In the limit that C_o^∞ approaches zero, i_1/F at $V = V^*$ is

$$\left(\frac{i_1}{F}\right)_{V^*,C_o^\infty=0} = \frac{k_{1a}\exp[(\alpha_{1a}F/RT)V^*]}{1+(B/k_{2a})\exp[(-\alpha_{2a}F/RT)V^*]} \tag{99}$$

since A approaches unity at this limit [cf. Eq. (92)]. Equation (99) is the anodic current density due to the copper–cuprous reaction in the absence of oxygen, and this is equivalent to the expression given in (40), as expected. Equation (99) is also the limit for $(i_1/F)_{V^*}$ when k_{HC} goes to zero. The total anodic current density at $V = V^*$, in the absence of oxygen is given by $2(i_1/F)_{V^*}$ from equation (99), and this is related to the balance current by the expression

$$\frac{(i_b/F)_{V^*}}{(2i_1/F)_{V^*,C_o^\infty=0}}=\frac{1+(B/k_{2a})\exp[(-\alpha_{2a}F/RT)V^*]}{2\{A+(B/k_{2a})\exp[(-\alpha_{2a}F/RT)V^*]\}}\times\left\{A+1-\frac{k_{2c}k_{\mathrm{HC}}C_o^\infty}{D_ck_{2a}}\exp\left[\frac{-(\alpha_{2c}+\alpha_{2a})F}{RT}V^*\right]\right\} \tag{100}$$

This ratio is always greater than or equal to unity and has the limiting behavior

$$\frac{(i_b/F)_{V^*}}{(2i_1/F)_{V^*,C_o^\infty=0}}\to 1 \quad \text{as} \quad \frac{k_{\mathrm{HC}}C_o^\infty}{k_{2a}}\to 0 \tag{101}$$

Also, when

$$\frac{B}{k_{2a}}\exp\left(\frac{-\alpha_{2a}F}{RT}V^*\right)\gg 1 \tag{102}$$

and

$$\frac{B}{k_{2a}}\exp\left(\frac{-\alpha_{2a}F}{RT}V^*\right)\gg A \tag{103}$$

then

$$\frac{(i_b/F)_{V^*}}{(2i_1/F)_{V^*,C_o^\infty=0}}\approx 1+\left[\frac{k_{\mathrm{HC}}C_o}{2k_{2a}}\exp\left(\frac{-\alpha_{2a}F}{RT}V^*\right)\right]\left[1-\frac{k_{2c}}{D_c}\exp\left(\frac{-\alpha_{2c}F}{RT}V^*\right)\right] \tag{104}$$

Superposition is obeyed when the ratio is given by (101). The perturbation caused by the chemical reaction results in an increase in the total anodic current density.

The corrosion current density is also increased by the chemical reaction, as measured by the relationship

$$\frac{(i_1/F)_{V^*}}{(i_1/F)_{V^*,C_o=0}}=A\frac{1+(B/k_{2a})\exp[(-\alpha_{2a}F/RT)V^*]}{A+(B/k_{2a})\exp[(-\alpha_{2a}F/RT)V^*]} \tag{105}$$

This measure of the departure from the superposition approximation approaches unity as the chemical reaction becomes negligible, i.e.,

$$\frac{(i_1/F)_{V^*}}{(i_1/F)_{V^*,C_o^\infty=0}}\to 1 \quad \text{as} \quad \frac{k_{\mathrm{HC}}C_o^\infty}{k_{2a}}\to 0 \tag{106}$$

When the inequalities expressed in (102) and (103) are obeyed,

$$\frac{(i_1/F)_{V^*}}{(i_1/F)_{V^*,C_o^\infty=0}}\approx A$$

Anderson and Eyring[33] found oxygen to accelerate the corrosion rate in 2 M H_2SO_4, and superposition was not obeyed. The acceleration of corrosion rate was an order of magnitude when the solution was saturated with O_2 at one atmosphere pressure. The results were obtained for long corrosion times, of the order of 40 hr. Other recent results(43) show the acceleration to be small (approximately a factor of 2) in 0.1 N H_2SO_4 at short exposure times. This section is concluded with the note that the corrosion current density and corrosion potential have very complex behavior when superposition is not obeyed. A more rigorous treatment than that given here would include both terms in (83) for the oxygen reduction, as well as the possible further reduction of peroxide to water. However, Anderson and Eyring(33) found peroxide to be formed in stoichiometric amounts during corrosion, with no further reduction to water. A more general treatment could also be given to the mass transport effects on the cupric ions. Further work should be done on the accelerating effect of cupric ions on the oxygen reduction reaction, where the rate of corrosion increases with time as Cu^{2+} accumulates in a closed system. A more rigorous treatment which will cover at least some of these items will be published elsewhere.

4. Nonuniform Corrosion and Heterogeneous Systems

Attention is now to be turned from uniform corrosion on a homogeneous surface to nonuniform corrosion. Nonuniform attack of two distinct types will be described: (1) nonuniform attack on a homogeneous surface caused by nonuniform solution composition or a nonuniform potential distribution across the surface, or (2) corrosion driven by coupling dissimilar metals, i.e., galvanic corrosion. Both types of localized attack are considered here in a macroscopic sense. A third cause of nonuniform attack is a variable surface film, but it will not be discussed here because active–passive corrosion kinetics are involved. Such a discussion is outside the scope of the present chapter. Other references may be consulted for recent work in the fiel.(11,22,54,55)

Locally variable solution composition may cause a varied corrosion rate across a surface through modification of the anodic reaction directly or indirectly through the cathodic reaction. Of the examples described in Section 3, a nonuniform Cl^- concentration would cause nonuniform anodic dissolution of copper in HCl solutions. A nonuniform surface concentration of Cu^{2+} ions in sulfuric acid would introduce a variable anodic dissolution rate, although this would be a small effect in most cases. The cathodic rate would be equally sensitive to composition variations, e.g., a nonuniform concentration of O_2 across the surface would cause the reduction current density for O_2 to vary locally (and thereby the anodic reaction would be varied as well).

The nonuniform corrosion on a homogeneous surface causes a nonuniform potential distribution across the surface. This is the potential in the solution phase, just outside the metal. The metal is equipotential at the surface, inside the metal phase. The variation of potential in the solution will cause current to flow, and this destroys the local balance of anodic and cathodic current densities at the corrosion potential. The total anodic and cathodic currents on the surface will still be balanced, however. Therefore, local variability of composition causes differences of corrosion rates, and associated differences of potential in the solution phase at the surface. Current flows through the solution between the two surface points of unequal potential, and passes into the equipotential metal surface at one point, and out at the other so that electroneutrality is preserved. This resembles galvanic corrosion, which will be discussed later, but here the nonuniform potential distribution is directly related to inhomogeneous solution composition rather than heterogeneous metal composition.

The remainder of this section will consider the modeling investigations which have made the ideas on localized corrosion more quantitative. The emphasis will be on the general insight which is gained from such activities, and the mathematics will be described only to the extent necessary for understanding the results. This will serve as a review of the literature on mathematical modeling of nonuniform corrosion of homogeneous, single metals, and galvanic corrosion of coupled, dissimilar metals. Most of the literature work has been on galvanic corrosion.

4.1. Mathematics of Modeling Corrosion Systems

Corrosion kinetics is a major factor in modeling, as a description of the interfacial or boundary behavior. This connects the present section to the previous sections. The kinetics information is required in the form of the Butler–Volmer equation for the corrosion reaction or reactions [Eq. (30)], but over the concentration range expected across the surface. The weakest part of the final model is usually caused by inadequate information on the concentration dependence of the kinetics.

The modeling of diffusion, migration, and convection in solution is described by the four relationships$^{(28,56)}$:

1. The flux equation for a charged species [see Eq. (49)],

$$\mathbf{N}_i = \frac{-z_i D_i C_i F}{RT} \nabla \Phi - D_i \nabla C_i + C_i \mathbf{v}$$

2. The current equation in solution,

$$\mathbf{i} = F \sum_i z_i \mathbf{N}_i \tag{107}$$

3. The material balance,

$$\frac{\partial C_i}{\partial t} = -\nabla \cdot \mathbf{N}_i + R_i \tag{108}$$

(R_i accounts for production of species i by homogeneous reaction in solution.)

4. The equation of electroneutrality,

$$\sum_i z_i C_i = 0 \tag{109}$$

The equations are written in general, partial differential form, although simplifications are generally employed for modeling.

The surface corrosion kinetics and solution transport are linked through the stoichiometry of the electrode reaction. That is, for a corrosion reaction involving species i with the stoichiometric number S_i, the flux at the surface of the electrode, and normal to it, is given by

$$\mathbf{N}_{in} = \frac{-S_i}{nF}\mathbf{i}_n \tag{110}$$

Here n is the number of electrons transferred in the reaction, and $\mathbf{i}_n$ is the normal component of the current density, from the electrode kinetics, for the reaction.

Solution of the above equations is sought subject to the restrictions of geometry, solution composition, and for corrosion, a balance of the total anodic and total cathodic currents. The relative importance of different factors is measured by dimensionless parameters for the system. The parameters are identified by dimensional analysis, but physical intuition may help. It has been found that the parameters that are most useful are the dimensionless "polarization parameters" J and δ identified in an earlier section [see Eqs. (34) and (35)]. J and δ will be used below to discuss galvanic corrosion modeling, where concentration effects are neglected and interfacial kinetics and solution ohmic factors are dominant.

Before describing results of modeling of nonuniform corrosion, it is worthwhile to note that electrochemical measurements of corrosion kinetics may be guided by consideration of the parameters J and δ for the system as well. Measurements by the linear polarization technique may be checked by calculation of the parameter J, and similarly for Tafel polarization with the parameter δ. A large value of J (i.e., $J \geq 10$) may be found for large electrodes, low conductivity, and large i_{corr} and is characteristic of ohmic control. The current distribution will approach the primary (ohmic) distribution as J increases. The system behaves in a similar fashion for large δ values in Tafel polarization. For an electrode system with a nonuniform primary distribution, conditions must be sought to minimize the nonuniformity of the distribution in order to determine the kinetic parameters. This means small J or δ values. Calculation of J from the experimental values of i_{corr} and the solution conductivity [see Eq. (34)] will identify whether the experiments were carried out for uniform current densities. Discrepancies between i_{corr} (assuming uniform current distribution), and the actual value, for kinetic control, will increase with the magnitude of J. Similar errors in the calculation of i_{avg} may be expected at large values of δ. As an example, for copper corrosion in deoxygenated 0.1 N

HCl, it was found (see Section 3.4) that the corrosion current density was 1.5×10^{-7} A/cm^2 at 1000 rpm. The corresponding J value is 3×10^{-4} at 298 K, with a rotating disk of radius 0.5 cm, and a conductivity of $3.9 \times 10^{-2}\ \Omega^{-1}\ \mathrm{cm}^{-1}$.(57) The small value of J confirms that the current distribution was quite uniform for currents near the corrosion current density. A similar calculation for deoxygenated 0.1 N sulfuric acid ($i_{\mathrm{corr}} = 2.2 \times 10^{-9}$) yields

$$J = 10^{-6}$$

where the conductivity is $2.5 \times 10^{-2}\ \Omega^{-1}\ \mathrm{cm}^{-1}$.(57) The value of δ for 0.1 N HCl, with the same parameters as above, and an average current density of 1 mA/cm^2, is found to be about 3. The current distribution would be somewhat nonuniform for this value of imposed average current density. Deviations from Tafel behavior for both anodic and cathodic branches due to the ohmic effect became apparent at currents between 10^{-2} and 10^{-3} A/cm^2 for the Cu–0.1 N HCl system.(43)

Current distribution is also important in cathodic protection. If the current distribution is nonuniform, one part of the surface may be adequately protected and another part "overprotected" with excessive current density. Even worse is the possibility that only part of the surface may be protected. Wagner(58) has discussed current distribution effects in cathodic protection, and has used dimensionless parameters similar to J and δ to describe the relative importance of ohmic and kinetic influences. Newman(59) has briefly considered cathodic protection. Smyrl and Newman(60) have described the potential distribution across a surface (inside the solution) for a uniform current distribution. There is a maximum size of the surface that may be maintained at uniform current density before the nonuniform potential induces other reactions at parts of the surface.(60) Cathodic protection control would be lost at these sites on the surface.

4.2. Modeling of Composition-Driven Nonuniform Corrosion

Modeling in this area has not progressed to the same extent as has modeling of galvanic corrosion. The complexity of treating a corrosion situation with the effects of composition gradients superimposed on ohmic and kinetic influences makes the undertaking formidable. The principles of such investigations are well known, however,(28) and the use of large-scale computers eases the management of the complex calculations. The greatest barrier to further work is the lack of fundamental corrosion kinetics information over the range of composition required in the model.

4.2.1. Oxidant Mass Transfer

Corrosion of metals may be caused by the rate of transfer of an oxidant (e.g., dissolved oxygen) to the surface. For a uniformly accessible surface, the corrosion is uniform. The rotating disk electrode is a uniformly accessible surface for mass transfer,(61) and concentric rotating cylinders are as well. Ellison *et al.*(62) were able to show, however, that nonuniform corrosion on a copper disk could be observed when the outer edge of the disk developed turbulent flow. Turbulent flow increases the mass transfer rate, and is observed only for Reynolds numbers for the disk above about 10^5. The Reynolds number varies with disk radius as

$$\mathrm{Re} = r^2\Omega/\nu \tag{111}$$

and the transition to turbulent flow occurs at large radii first for a given rotation rate Ω, and solution viscosity, ν. This satisfactorily explains the results of LaQue,(63) who found that large copper disks corrode preferentially at the outer edge when rotating above a certain velocity in oxygenated seawater. Newman(59) has discussed other examples of flow-related nonuniform corrosion involving transport of oxygen as well. For these systems the detailed knowledge of anodic dissolution kinetics is usually not required. One knows the local corrosion rate is given by the flux of the cathodic reactant, and this is calculated for the geometry, composition, and convection conditions of the system. Details for mass transfer calculations for several geometries are available in the literature.(28,61,64)

4.2.2. Crevice Corrosion

Another type of nonuniform corrosion which is controlled by composition is less direct. Restrictions of geometry, e.g., in crevices and corners prevent mixing of solutions everywhere, and local buildup of reaction products, or the exhaustion of an oxidant may occur. The local kinetics will be relatively independent of that in other regions except for electrical current flow. This may lead to nonuniform corrosion, and the most important example is that where the buildup of products increases the aggressiveness of the local solution. In this case, corrosion will be most severe, not where the concentration or flux of the bulk solution oxidant is highest but where it is lowest. Crevice corrosion is considered to be an example of this type of attack, and the aggressive solution within a crevice or pit is one which is more acid than the external solution.

Anodic dissolution plus hydrolysis of the product metal ion can cause an increase of hydrogen ion concentration. On the other hand, reduction of either hydrogen ions or dissolved oxygen reduces the hydrogen ion concentration. If the net corrosion reaction plus hydrolysis would lead to an increase of hydrogen ion concentration, the process may occur independently of any other process and would accelerate with time to some steady state where diffusion out of the occluded region would limit the buildup. If the corrosion reaction plus hydrolysis leads to no net change in H^+ concentration, an acid solution in a crevice or pit could only be created by separation of the anodic and cathodic regions. Concentrating the cathodic reaction on the outer surface would occur naturally if dissolved oxygen, for example, were the primary bulk oxidant. Coupling this with a net anodic reaction (plus hydrolysis) in the inner region for an overall current balance, would lead to a steady state crevice or pit.

In order for separation to occur as described above, a quite general condition on the corrosion kinetics must be obeyed. The outside surface must support a cathodic reaction, and it must be supported *at a potential which is positive of the potential of the anodic reaction in the crevice.* The direction of current flow through the solution establishes this criterion. A qualitative laboratory test may be used to identify metal solution combinations which could cause localized attack by the mechanism described above. The test involves the corrosion kinetics on the metal of interest. Cathodic currents must be observed on the metal in the exterior solution at potentials which are *positive* of the anodic region for the crevice conditions, or the separated reactions will not support increased anodic dissolution in the isolated region. This is a very definitive test, and very few metal–environment combinations match the criterion.

Quantitative modeling of crevice corrosion has been reported recently.(65) Mass transfer has been treated as described above, but an idealized model of active–passive kinetics was assumed for the metal. Experimental work was also performed. The model yielded distributions of current, voltage, and composition in the crevice and nearby. The results indicate that the approach shows promise, especially in predicting crevice gap/depth ratios that are the most critical for localized attack. More progress can be anticipated as actual corrosion kinetic data are used for the modeling work.

Porous electrode theory(66) can also be used to predict the depth at which the anodic reaction may be driven by an external cathodic current. Ohmic drop restricts the penetration of current into a small-gap, occluded region. This causes the anodic reaction to be distributed over a relatively small region which concentrates the attack. At greater depths in the gap, the metal is isolated from the external surface reactions. Newman(59) has calculated the depth to which a reaction may penetrate inside a pipe, in this case a cathodic protection reaction. The reaction is concentrated near the opening.

4.2.3. Pitting and Differential Aeration Corrosion

Composition gradients are considered to be important for pitting and differential aeration corrosion as well. For pitting corrosion, similar conditions to those for crevice corrosion are considered important. Pits may be initiated in ways which are different from crevice corrosion, e.g., at foreign metal inclusions. However, the propagation of pits depends largely on a locally aggressive solution. Stirring to eliminate concentration effects will stop the growth of pits. Alkire *et al.*(67) have treated mass transfer and kinetics in a pit, for a particular set of kinetic boundary conditions. References to experimental work are also included. Newman *et al.*(68) published work for the current and potential distributions both inside and outside a hemispherical pit, but with no mass transfer. The author has calculated these distributions also.(69) Differential aeration effects are due to oxygen concentration differences. This is a cathodic reaction effect, and may be related in some systems to crevice corrosion as described above. Differential aeration could also drive corrosion at locally variable rates under an electrolyte film of nonuniform thickness. The diffusion-limited flux of oxygen through the film would be directly proportional to the film thickness. If the local corrosion rate is limited by the oxygen flux, the attack will be most severe at low film thicknesses. Alkire *et al.*(70) have treated this system with an assumed model of electrode kinetics. Further progress will be made as actual corrosion kinetic data become available.

4.3. Modeling of Galvanic Corrosion

Coupling two dissimilar metals in an electrolytic solution may cause one to suffer anodic attack, while the other supports a cathodic reaction. The corrosion potential of the couple will be between the corrosion potentials of the separate metals. The anodic kinetics on one and the cathodic kinetics on the other will determine (along with other factors to be described below) the extent of the reactions. Aluminum and copper couples in aqueous solution show extensive, accelerated attack on aluminum. At the corrosion potential aluminum dissolution will occur at a rate which is balanced by the cathodic reduction of hydrogen ions and oxygen on copper. An iron–titanium couple, on the other hand, will show negligible galvanic corrosion effects in neutral electrolytes, even though the two have different corrosion potentials. The enhanced anodic attack of iron, which would be expected from the corrosion potentials, is absent because titanium *will not support a cathodic current at potentials which are anodic for iron.* When the two are coupled, the corrosion potential is identical to the corrosion potential for iron. Iron behaves as if it were not coupled.

Modeling the current and potential distributions for galvanic corrosion will be described here where ohmic and kinetic influences dominate the behavior. In the absence of composition gradients, the flux equation [Eq. (49)] becomes

$$\mathbf{N}_i = \frac{-z_i D_i F C_i}{RT} \nabla\Phi + C_i \mathbf{v} \tag{112}$$

The current equation is now

$$\mathbf{i} = -\sum_i \frac{z_i^2 F^2 D_i C_i}{RT} \nabla\Phi + \mathbf{v} \sum_i z_i C_i \tag{113}$$

and the last term is zero because of electroneutrality [Eq. (109)]. Since(56)

$$\kappa = \sum_i \frac{z_i^2 F^2 D_i C_i}{RT} \tag{114}$$

Eq. (113) is Ohm's law for the electrolytic solution. Equations (113), (114), and the equation of continuity [Eq. (108)] may be combined at steady state to yield Laplace's equation, i.e.,

$$\nabla^2\Phi = 0 \tag{115}$$

For galvanic corrosion, solution of (115) is sought subject to boundary conditions that are appropriate for electrode kinetics on the two metals. The aim is to obtain the current and potential distributions on both metals. Two forms of the electrode kinetics have been used for modeling studies. The first is the linear form of the Butler–Volmer equation for corrosion kinetics [Eq. (33)],

$$i = i_{\text{corr}} \frac{(\alpha_{aa} + \alpha_{cc})F}{RT}(V - V^*) \tag{116}$$

written in terms of an arbitrary reference electrode. The second boundary condition which is used is the Tafel form for either the anodic or cathodic branch of the kinetics as appropriate, written here for the anodic reaction

$$i = i_{\text{corr}} \exp\left[\frac{\alpha_{aa}F}{RT}(V - V^*)\right] \tag{117}$$

Equation (116) is used for potentials near the corrosion potential, and $i \ll i_{\text{corr}}$. For potentials far from the corrosion potential, and

$$|i| \gg i_{\text{corr}}$$

the Tafel equation should be utilized.

Particularly simple results are obtained for kinetic control. If both metals are in the linear region [Eq. (116)], the J parameters would be small for each metal. Similarly, δ would be small for Tafel polarization on each. The current distribution on each metal would be uniform and the total current on each would be simply related to the current density and electrode kinetics. For linear kinetics on each metal, the relationship between the anodic current on metal 1 to the cathodic current on metal 2 is

$$I_{\text{anodic}} = -I_{\text{cathodic}}$$

This yields the equation for the corrosion potential of the couple, V^{**}:

$$V^{**} = \frac{A_1 i_{\text{corr}_1}(\alpha_{aa} + \alpha_{cc})_1 V_1^* - A_2 i_{\text{corr}_2}(\alpha_{aa} + \alpha_{cc})_2 V_2^*}{A_1 i_{\text{corr}_1}(\alpha_{aa} + \alpha_{cc})_1 - A_2 i_{\text{corr}_2}(\alpha_{aa} + \alpha_{cc})_2} \tag{118}$$

The corrosion potential of the couple will lie between the corrosion potentials of the separate metals. The galvanic corrosion current, I_g, may be calculated at this potential, and is

$$\frac{I_g}{A_1} = i_{\text{corr}_1}(\alpha_{aa} + \alpha_{cc})_1 \frac{F}{RT} \frac{A_2 i_{\text{corr}_2}(\alpha_{aa} + \alpha_{cc})_2 |V_1^* - V_2^*|}{A_1 i_{\text{corr}_1}(\alpha_{aa} + \alpha_{cc})_2 - A_2 i_{\text{corr}_2}(\alpha_{aa} + \alpha_{cc})_2} \tag{119}$$

I_g has the two limits,

$$I_g \to 0 \qquad \text{as} \quad \frac{A_1}{A_2} \to \infty$$

or

$$I_g \to 0 \qquad \text{as} \quad A_1 \to 0$$

and is a maximum at $A_1 = A_2$.

Stern[(71)] has calculated the galvanic corrosion potential, galvanic corrosion current, and corrosion rate for *Tafel* polarization on the metals, and for kinetic control (i.e., δ is small for both metals). As for the case above, the corrosion rate is maximized on the anode when the area ratio A_1/A_2 is small. The total galvanic corrosion current is largest when A_1 is equal to A_2.

Oldham and Mansfeld[(72)] treated galvanic corrosion with uniform current densities on each metal, but with more general reactions. Analytical (closed-form) results were obtained for several cases.

Analytical results have been calculated for several other simple, but important cases. Levich and Frumkin[(73)] considered a single circular anodic disk in a cathodic plane of infinite extent. The current density on the disk was uniform (J_d or δ_d small), and the plane was reversible, i.e., J'_p large. The disk may be assured of uniform current density if it is of small size. Note that there is no parameter δ for an electrode of infinite extent unless the current density is uniform everywhere, and J'_p is defined by

$$J'_p = \frac{(\alpha_{ap} + \alpha_{cp})Fr_d}{\kappa RT}\, i_{\text{corr},p} \tag{120}$$

The length used to calculate J'_p is the disk radius. The absolute value of the current density on the plane is nonuniform approaching infinity at the edge intersection with the disk, and equal to

$$|i_p| = \frac{2i_d}{3\pi}\left[\left(\frac{r}{r_d}\right)^2 - 1\right]^{-3/2} \tag{121}$$

at large distances from the disk. Newman treated the extreme case of a disk in an insulating plane.[(74)] Nanis and Kesselman[(75)] obtained results for both these cases. Wagner[(58)] has considered the cathodic protection of a disk in a plane.

In an extensive series of papers, Waber *et al.*[(76–80)] solved Laplace's equation for strip electrodes in a plane. These papers use numerical methods with the Fourier series solution to Laplace's equation to calculate the current and potential distributions on both anode and cathode strips. The electrode kinetics on each were assumed to be in the linear region, and results obtained as a function of dimensionless polarization parameters of the anode and cathode. The dimensionless polarization parameters used there are very similar to the J and δ parameters utilized here. One of the interesting cases considered was that for galvanic corrosion of two adjacent coplanar metals under a thin film of electrolyte. As the layer of electrolyte decreases in thickness, the galvanic current is restricted to areas just adjacent to the metal–metal joint. Areas of the metals far from the intersection are not important for determining the corrosion behavior in this case. Simmons *et al.*(81) used similar numerical techniques for concentric, coplanar rectangular galvanic couples. Doig and Flewitt(82) recently obtained results for coplanar electrodes, with one of infinite extent.

Circular disks on a plane were treated with the same technique as above, and linear kinetics, by McCafferty(83) and by Gal-Or *et al.*(84) Smyrl and Newman(85) treated a disk in a plane with the full Butler–Volmer equation on each as well as with the Tafel expression in the extreme. This represents the first time the full Butler–Volmer expression or Tafel kinetics have been used for galvanic corrosion with nonuniform current densities. The results were compared to those of Levich *et al.*(73) as a limiting case. The calculation technique was the method of finite differences using a digital computer. These authors also derived an expression for the corrosion potential of an array of anodic disks on a cathodic surface. The corrosion potential was found to depend linearly on the area ratio of anode/cathode for these conditions rather than *logarithmically* as found by Stern(71) for kinetic control. Further work has been presented(86) on the comparison of the two calculations of corrosion potential for several values of the dimensionless polarization parameters. The corrosion potential of a disk coupled to a finite plane is shown on Figure 7,(86) and compared to results calculated according to Stern.(71) The two approach

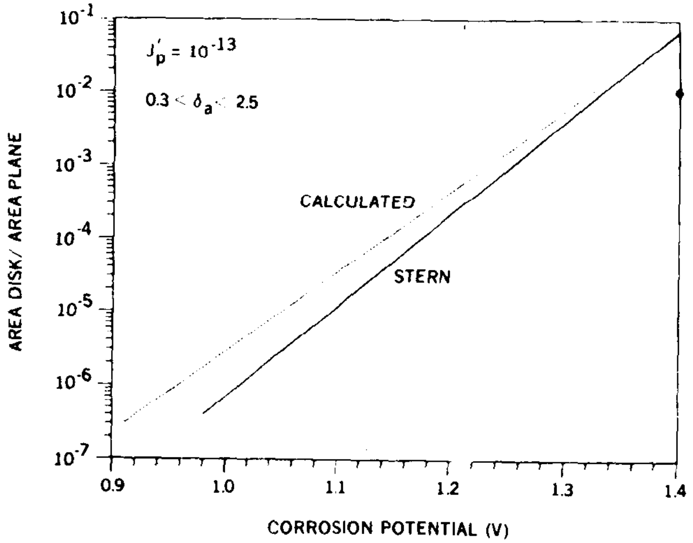

Figure 7. Corrosion potential as a function of area ratio of a disk–plane galvanic couple calculated for small polarization parameters.

one another as expected as uniform current densities are achieved on both surfaces. What is surprising is the departure from kinetic behavior at values of J_d and J'_p which are still quite small. At the extreme where the plane size becomes large, the corrosion potential is a *linear* function of the area ratio,(86) as shown by Smyrl and Newman.(85)

It has been popular to "linearize" Tafel kinetics about some average current density for electroplating applications. The same technique was used to linearize Tafel kinetics for galvanic corrosion, and the results compared to the full Tafel expression,(86) as shown on Figure 8. It may be seen that the linearized Tafel approximation is not accurate for some values of the polarization parameters. The surface is large enough to have current densities and potential that depart significantly from the average value used for linearization. This result suggests that some of the earlier work mentioned above, which shows large changes in the current distribution across the surface, may be in error because linearized Tafel boundary conditions were used for the calculation. The numerical technique introduced by Smyrl and Newman(85) should be used instead in some cases, because the full Butler–Volmer kinetic expression may be used for the boundaries. This goes over to the Tafel extreme or the linear behavior on each surface of the couple automatically, and no change of kinetic expression is required.

Doig and Flewitt(82) recently treated radially symmetric galvanic couples with an approximate technique and Tafel kinetics. They were critical of the above work,(85) because equal values of α for the anodic and cathodic Tafel

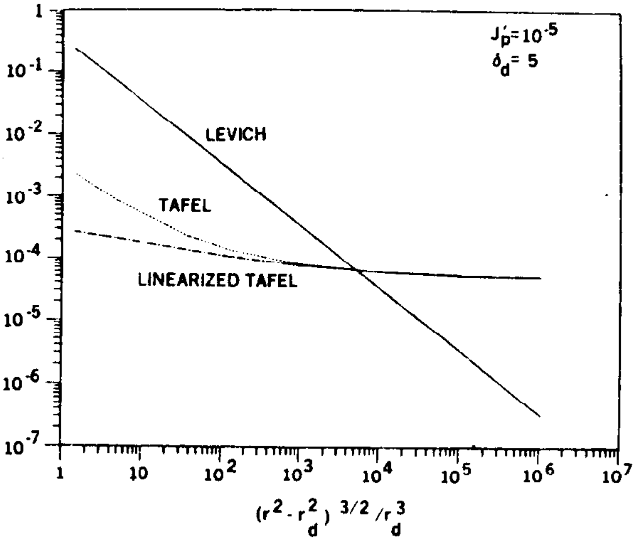

Figure 8. Current density to the plane for a disk–plane galvanic couple calculated for Tafel kinetics and compared to linearized Tafel kinetics and to the Levich treatment.

expressions were used, apparently without realizing the nature of dimensionless parameters. Although specifically stating that the calculations were made for equal α values, the results in fact are independent of the values of α.(85) The results are shown in the form of the dimensionless polarization parameters which are either J_D or δ_D and J'_p. From the definition above for these parameters, the results depend on the *total* combined effects of ohmic and kinetic influences, and not just on α. To evaluate how a particular system behaves from the results,(85) it would be necessary to use the appropriate value of α.

5. Summary

Fundamental electrode kinetics are an essential element for the understanding of the reactions which are coupled in corrosion systems. Superposition of the individual, simultaneous reactions on a homogeneous metal surface is a good approximation for many corrosion processes. The corrosion of copper in hydrochloric acid has been used to illustrate the superposition approximation, and there are many other systems which could be used. Limitations to the approximation arise when chemical coupling also occurs, as the copper-oxygenated sulfuric acid system demonstrates.

The corrosion of heterogeneous metal surfaces involves current flow through solution and nonuniform composition in solution. Modeling of localized corrosion on heterogeneous and homogeneous metals reveals the relative importance of the factors that influence behavior. The kinetics of the electrode reaction describes the boundary, and this is matched with the mass transfer and ohmic influences of the solution for the calculation of corrosion reaction, potential, and composition distributions. The principles of modeling calculations are well established for electrochemical systems, and their extension to corrosion has been accomplished for simple processes. This has revealed the necessity for more complete descriptions of the electrode kinetics at all the compositions across the heterogeneous surface. Further work may then be performed to describe both the initiation and propagation of localized processes.

References

1. E. A. Guggenheim, *Thermodynamics*, North-Holland, Amsterdam (1959).
2. G. N. Lewis and M. Randall, *Thermodynamics*, revised by K. S. Pitzer and L. Brewer, McGraw-Hill, New York (1961).
3. NBS Technical Notes 270-3, 270-4, 270-5, U.S. Government Printing Office (1968–1971).
4. W. M. Latimer, *Oxidation Potentials*, Prentice-Hall, Englewood Cliffs, New Jersey (1952).
5. JANAF Thermochemical Tables, NSRDS-NBS 37, U.S. Government Printing Office (1971).
6. J. A. Plambeck, *Fused Salt Systems, Encyclopedia of Electrochemistry of the Elements*, Vol. X, A. J. Bard, ed., Marcel Dekker, New York (1976).

7. H. Leidheiser, Jr., *The Corrosion of Copper, Tin, and Their Alloys*, John Wiley and Sons, New York (1971).
8. M. Pourbaix, *Atlas of Potential/pH Diagrams*, Pergamon, Oxford (1962).
9. G. M. Florianovich and Ya. M. Kolotyrkin, *Dokl. Akad. Nauk SSSR.* **157**, 422 (1964).
10. P. Delahay, *Double Layer and Electrode Kinetics*, Interscience, New York (1966).
11. K. J. Vetter, *Electrochemical Kinetics*, Academic Press, New York (1967).
12. J. O'M. Bockris and A. K. N. Reddy, *Modern Electrochemistry*, Plenum Press, New York (1970).
13. J. O'M. Bockris, in *Modern Aspects of Electrochemistry*, Vol. 1, J. O'M. Bockris, ed., Butterworths, London (1954).
14. T. N. Anderson and H. Eyring, *Physical Chemistry*, H. Eyring, D. Henderson, W. Jost, eds., Academic Press, New York (1970).
15. N. Tanaka and R. Tamamushi, *Electrochim. Acta* **9**, 963 (1964).
16. A. N. Frumkin, *Advances in Electrochemistry and Electrochemical Engineering*, Vol. 1, P. Delahay and C. W. Tobias, eds., Interscience, New York (1961).
17. A. N. Frumkin, *Advances in Electrochemistry and Electrochemical Engineering*, Vol. III, P. Delahay and C. W. Tobias, eds., Interscience, New York (1963).
18. J. P. Hoare, *Advances in Electrochemistry and Electrochemical Engineering*, Vol. VI, P. Delahay and C. W. Tobias, eds., Interscience, New York (1967).
19. J. P. Hoare, *The Electrochemistry of Oxygen*, Interscience, New York (1968).
20. A. Damjanovic, *Modern Aspects of Electrochemistry*, Vol. 5, J. O'M. Bockris and B. E. Conway, eds., Plenum Press, New York (1969).
21. C. Wagner and W. Traud, *Z. Electrochem.* **44**, 391 (1938).
22. H. Kaesche, *Z. Metallk.* **61**, 94 (1970).
23. M. Stern, *Corrosion* (*Houston*) **14**, 440t (1958).
24. M. Stern and A. L. Geary, *J. Electrochem. Soc.* **104**, 56 (1957).
25. F. Mansfeld, *Advances in Corrosion Science and Corrosion Engineering*, Vol. 8, M. Fontana and R. Staehle eds., Plenum Press, New York (1978).
26. C. Wagner, *J. Electrochem. Soc.* **98**, 116 (1951).
27. J. Newman, *J. Electrochem. Soc.* **113**, 1235 (1966).
28. J. S. Newman, *Electrochemical Systems*, Prentice-Hall, Englewood Cliffs, New Jersey (1973).
29. J. O'M. Bockris, D. Drazic, and A. R. Despic, *Electrochim. Acta* **4**, 325 (1961).
30. E. J. Kelly, *J. Electrochem. Soc.* **112**, 124 (1965).
31. S. Asakura and K. Nobe, *J. Electrochem. Soc.* **118**, 13 (1971); S. Asakura and K. Nobe, *J. Electrochem. Soc.* **118**, 19 (1971); R. J. Chin and K. Nobe, *J. Electrochem. Soc.* **119**, 1457 (1972); H. C. Kuo and K. Nobe, **125**, 853 (1978).
32. H. A. Uhlig, *Corrosion and Corrosion Control*, (New York: John Wiley and Sons, New York (1971).
33. T. N. Anderson, M. H. Ghandehari, and H. Eyring, *J. Electrochem. Soc.* **122**, 1580 (1975).
34. A. W. Tracy, in *Corrosion Resistance of Metals and Alloys*, F. L. LaQue and H. R. Copson, eds., Reinhold, New York (1963).
35. U. Bertocci, *Encyclopedia of Electrochemistry of the Elements*, Vol. II, A. J. Bard, ed., Marcel Dekker, New York (1974).
36. U. Bertocci, *Electrochim. Acta* **11**, 1261 (1966).
37. B. C. Y. Lu and W. F. Graydon, *Can. J. Chem.* **32**, 153 (1954).
38. D. P. Gregory and A. C. Riddiford, *J. Electrochem. Soc.* **107**, 950 (1960).
39. I. Cornet, E. A. Barrington, and G. U. Behrsing, *J. Electrochem. Soc.* **108**, 947 (1961).
40. G. Demedts and A. P. van Peteghem, *Corros. Sci.* **18**, 1041 (1978).
41. W. H. Smyrl, in *Electrochemical Techniques for Corrosion Investigations*, F. Mansfeld and U. Bertocci, eds., American Society for Testing Materials, Philadelphia (1980).
42. E. Mattson and J. O'M. Bockris, *Trans. Faraday Soc.* **55**, 1586 (1959).
43. W. H. Smyrl, unpublished data.
44. R. K. Astakhova and B. S. Krasikov, *Zh. Prikl. Khim.* **44**, 363 (1972).

45. T. Hurlen, *Acta Chem. Scand.* **15**, 1231 (1961).
46. M. Braun and K. Nobe, *J. Electrochem. Soc.* **126**, 1666 (1979).
47. B. Miller and M. I. Bellavance, *J. Electrochem. Soc.* **119**, 1510 (1972).
48. A. L. Baccarella and J. C. Griess, Jr., *J. Electrochem. Soc.* **120**, 459 (1973)
49. R. V. Homsy and J. Newman, *J. Electrochem. Soc.* **121**, 521 (1974).
50. J. O'M. Bockris and N. Pentland, *Trans. Faraday Soc.* **48**, 833 (1952).
51. C. H. Bonfiglio, H. C. Albaya, and O. A. Cobo, *Corros. Sci.* **13**, 717 (1973).
52. M. Turner and P. A. Brock, *Corros. Sci.* **13**, 973 (1973).
53. G. Faita, G. Fiori, and D. Salvadore, *Corros. Sci.* **15**, 383 (1975).
54. R. P. Frankenthal and J. Kruger, eds., *Proceedings of the Fourth International Symposium on Passivity*, The Electrochemistry Society, Princeton, New Jersey (1978).
55. *Proceedings of the Fifth International Congress on Metallic Corrosion*, NACE, Houston (1974).
56. J. Newman, in *Advances in Electrochemistry and Electrochemical Engineering*, Vol. 5, P. Delahay and C. W. Tobias eds., Interscience, New York (1967).
57. R. A. Robinson and R. H. Stokes, *Electrolyte Solutions*, Butterworths, London (1959).
58. C. Wagner, *J. Electrochem. Soc*, **99**, 1 (1952).
59. J. Newman, in *Localized Corrosion*, R. Staehle, ed., NACE, Houston (1974).
60. W. H. Smyrl and J. Newman, *J. Electrochem. Soc.* **119**, 208 (1972).
61. V. G. Levich, *Physicochemical Hydrodynamics*, Prentice-Hall, Englewood Cliffs, New Jersey (1962).
62. B. T. Ellison and I. Cornet, *J. Electrochem. Soc.* **118**, 68 (1971).
63. F. L. LaQue, *Corrosion* (*Houston*) **13**, 303t (1957).
64. J. R. Selman and C. W. Tobias, in *Advances in Chemical Engineering*, Vol. 10, T. B. Drew, G. R. Cokelet, J. W. Hoopes, Jr., and T. Vermeulen, eds., Academic Press, New York (1978).
65. D. W. Siitari and R. C. Alkire, paper 238 presented at the Electrochemical Society Meeting, Los Angeles, October 1979.
66. J. Newman and W. Tiedeman, in *Advances in Electrochemistry and Electrochemical Engineering*, Vol. II, H. Gerischer and C. W. Tobias, eds., Wiley Interscience, New York (1978).
67. R. C. Alkire and D. W. Siitari, *J. Electrochemical Soc.* **126**, 15 (1979).
68. J. Newman, D. N. Hanson, and K. Vetter, *Electrochim. Acta* **22**, 829 (1977).
69. W. H. Smyrl, unpublished data.
70. R. C. Alkire and G. Nicolaides, *J. Electrochem. Soc.* **121**, 183 (1974).
71. M. Stern, *Corrosion* (*Houston*) **14**, 329t (1958).
72. K. B. Oldham and F. Mansfeld, *J. Appl. Electrochem.* **2**, 183 (1972).
73. V. G. Levich and A. Frumkin, *Acta Physicochim. URSS* **18**, 1 (1943).
74. J. Newman, *J. Electrochem. Soc.* **113**, 501 (1966).
75. L. Nanis and W. Kesselman, *J. Electrochem. Soc.* **118**, 454 (1971).
76. J. T. Waber, *J. Electrochem. Soc.* **101**, 271 (1954).
77. J. T. Waber and M. Rosenbluth, *J. Electrochem. Soc.* **102**, 344 (1955).
78. J. T. Waber, *J. Electrochem. Soc.* **102**, 420 (1955).
79. J. T. Waber, J. Morrissey, and J. Ruth, *J. Electrochem. Soc* **103**, 138 (1956).
80. J. T. Waber, *J. Electrochem. Soc.* **103**, 567 (1956).
81. J. A. Simmons, S. R. Coriell, and F. Ogburn, *J. Electrochem. Soc.* **114**, 782 (1967).
82. P. Doig and P. E. J. Flewitt, *Philos. Mag. B* **38**, 27 (1978); *Br. Corros. J.* **13**, 118 (1978).
83. E. McCafferty, *J. Electrochem. Soc.* **124**, 1869 (1977).
84. L. Gal-Or, Y. Raz, and J. Yahalom, *J. Electrochem. Soc.* **120**, 598 (1973).
85. W. H. Smyrl and J. Newman, *J. Electrochem. Soc.* **123**, 1423 (1976).
86. W. H. Smyrl, unpublished data.

3

The Study of the Passivation Process by the Electrode Impedance Analysis

ISRAËL EPELBOIN, CLAUDE GABRIELLI, MICHEL KEDDAM, and HISASI TAKENOUTI

1. Introduction

The passivity of metals has been known for a long time and an enormous amount of work has been done to characterize the nature of the passive state. An historical survey of the problem has been recently published(1) and modern contributions to the field can be found in the four International Symposia on Passivity(2–5) and in other meetings devoted to related topics.(6,7) In the course of the last decade, surface spectroscopy and optical techniques have improved our knowledge of the passive layer.(8) During the same period, advanced electrochemical techniques become applicable to the solid electrode–electrolyte interface and were successfully introduced in the study of the anodic behavior of metals including the passivity phenomenon.(9) Among these techniques, the present chapter deals with ac impedance measurements,(10) extended to the subacoustic frequency range, which provide information about the kinetics of the passivation process.

ISRAËL EPELBOIN, CLAUDE GABRIELLI, MICHEL KEDDAM, and HISASI TAKENOUTI • Groupe de Recherche No. 4 du C.N.R.S. "Physique des Liquides et Electrochimie," associé à l'Université Pierre et Marie Curie, 75230 Paris Cedex 05, France.

So-called passivation can be defined as the transition from the active to the passive state which usually takes place over a few hundreds of millivolts. In spite of its outstanding kinetic importance in the formation of the passive film, the passivation range has been scarcely analyzed in acidic media.(11) This is not surprising if one considers that in most cases, the passivation range gives rise to oscillations or aperiodic transitions instead of a stable steady state.(12) In some cases, a hysteresis cycle with two steep transitions may occur.(13) Instability and hysteresis behavior can be shown to arise from the interaction between the polarization device used to control the interface and the electrical properties of the latter. Therefore a stable and continuous transition from activity to passivity may be obtained by using a regulating device with suitable characteristics. The important problem of compatibility and stability of the interface-regulation pair will be dealt with in the present chapter (Section 2). Its solution provides a key to understanding many of archetypal features of the passivity phenomenon, e.g., at the iron–nitric acid interface.

Non-steady-state techniques are normally used when the overall process is supposed to occur in more than one elementary step. In principle, multistep processes can be analyzed and the kinetic parameters estimated on the basis of the time or frequency dependence of the system when subjected to an external perturbation. Non-steady-state techniques can be classified into large perturbation techniques and small signal techniques.(14) In small signal techniques, because of the vanishingly small amplitude of the perturbation (e.g., order of millivolts), only the first-order terms are considered in the response (i.e., linearization). Regardless of the signal shape, linear system theory shows that the dynamic behavior of the interface is completely defined by either its impedance shown in the frequency domain or its transient response in the time domain; the frequency and time domains being related by the well-known Fourier or Laplace functional transformations. Pulse, stepwise, ramp, or multiplex signals, white noise, etc. can be used but frequency-by-frequency measurements by means of correlation techniques provide highly accurate results and excellent noise-rejection capacity. It is worth emphasizing that the ac impedance approach to the study of an electrode process involves, in addition to the frequency dependence of the impedance, its variations with dc potential change and relevant physicochemical parameters (pH, concentration of reacting species, temperature, etc.).

In the present chapter, first the literature on passivation and passivity studies using ac signals will be briefly reviewed. Then a basic definition of the electrode impedance will be given and the general features of impedance data associated with a phenomenological passivation process will be shown. The next section is devoted to the measuring techniques, including aspects such as accessibility to the steady state polarization curve, stability of the regulation-interface system and finally signal processing in the digital transfer function analyzer allowing efficient rejection of noise. Applications of ac impedance data to passivation studies will be exemplified by many systems such as titanium, nickel, and iron in acidic media. In the case of iron, the important role of mass transport phenomena will also be considered.

1.1. Brief Review of the Literature

Ac impedance techniques have developed rapidly as an important field in electrochemical kinetics studies over the last 30 years in connection with the extraordinary progress of electronics for regulating dc and ac polarizations and measuring the impedance. A complete analysis of this material is far beyond the scope of the present contribution and the literature review will be focused on the specific passivity problem.

In the early 1950s, the state of the art can be found in the excellent paper by D. C. Grahame.(15) The impedances resulting from several electrode processes in addition to the double-layer contribution are considered, namely: linear semi-infinite diffusion known as Warburg's impedance,(16) charge transfer in a fast redox process at and near equilibrium(17) (Randle's impedance), charge transfer coupled to a homogeneous chemical reaction,(18) and film-forming process. However, none of these elementary electrode processes was able to account for the most important features of the impedance at dissolving and passivating anodes such as inductive effects and negative resistance. The modern interpretation of these impedances in terms of multistep heterogeneous reaction with adsorbed intermediate relies entirely on the model elaborated by Gerischer and Mehl for describing the non-steady-state behavior of the hydrogen evolution reaction.(19) This approach has been extended to the passivation process.(20) More and more intricate mechanisms have been treated, mostly by means of computer techniques, since the early paper by Epelboin and Keddam on the consecutive mechanism of the iron dissolution in a sulfuric acid medium.(21)

As a first approximation, it can be said that in the audio-frequency range the non-faradaic contribution from the double layer and from surface films, if any, is predominant. Faradaic effects are mostly detected at low and very low frequencies where slow phenomena such as diffusion, chemisorption, and film-forming processes are allowed to relax.

1.1.1. Passive State and Impedance at Audio Frequencies

Since the pioneering work of Finkelstein,(22) many authors have dealt with the impedance of passive electrodes. Most of them(23-25) use ac impedance bridge measurements or Lissajous figures(26) at frequencies ranging between tens of kilohertz and tens of hertz; current-step(27-30) or potential-step(26,) techniques have also been used giving a value for impedance roughly in the kilohertz frequency range. The use of wide-band, high-gain amplifiers in the design of modern potentiostats allows a full dc to megahertz potential control to be performed.(32) Recent integrated operational amplifier technology makes the task even easier.(33)

These measurements disclose a capacitive behavior. When the frequency is varied, parallel RC representation can be adopted mainly due to the form in which the data are provided by the bridge. Electrolyte resistance R_e measured in series with the interfacial impedance may be neglected when discussing the results. Increasing values of R and C with decreasing frequency are generally reported. Qualitatively, a similar behavior is observed within this frequency range for either a passive material (except in the case of thick anodic films) or a film-free noble metal surface where electron transfer takes place. As pointed out by Finkelstein,(22) in both cases C is of the same order, i.e. 50–100 μF cm^{-2}. This value is usually ascribed to the electrical double layer so that the capacitance of passive electrodes cannot be readily attributed to the passive film. The situation is somewhat clarified by investigating the potential dependence of C at a given frequency. The current and C variations with respect to the potential E are found roughly similar to each other, in the whole potential range between active dissolution and oxygen evolution.(23,31) In the full passive domain, at these frequencies, linear $1/C$ vs. E relationships are obtained(23,26,31,34) consistent with the capacitance of a dielectric film(10) whose thickness, as shown for that of the passive layer,(35) increases linearly with increasing potential. Correlation to the film thickness is usually found, but in fact in the equation of the parallel plate capacitor, thickness, dielectric constant of the passive film, and roughness factor, if any, are unknown.(26,31) By correlating C measurements to thickness determination by cathodic charging curves, reasonable values are found for the dielectric constant,(29) but in turn they depend closely on the reduction reaction assumed. The capacitance of the passive film has also been investigated during its growth(31) or removal,(30,36–38) but up to now no clear conclusion has been drawn.

The capacitance can also be interpreted in terms of the semiconductor properties of a passive layer on chromium.(39) Schultze *et al.*(40) distinguished three potential ranges: in the full passive range where C is inversely proportional to the layer thickness, at high anodic potentials where C is dependent on the degree of occupation of the valency band at the oxide surface, and in the passivation range where C obeys the Schottky–Mott law. However, the exact origin of the high capacitance value preceding the passivation is still a matter of discussion. It could be attributed to an adsorption–desorption process.(41–43)

The origin of the resistance of the passive surface is also controversial. The passive layer must be considered as a good electronic conductor and a poor ionic conductor,(26,44) whereas its dielectric properties are determinant in the thickness dependence of C. This contradiction could be resolved by assuming the tunnel effect.(45) The measurement of the impedance at frequencies as low as 10^{-3} Hz by Lissajous figure techniques have been made, and the film resistivity in the order of 10^{12} Ω cm was estimated for the passive material on a stainless steel surface.(46) On the contrary, a redox process such as ferri–ferro cyanide takes place easily on the passive surface. The impedance of these kinds of system was interpreted as a parallel arrangement of the impedance of the passive surface and that of the redox reaction.(47)

1.1.2. Passivation and Impedance at Low Frequencies

In most cases, the variables such as coverages and layer properties determining the steady state are governed by slow processes. Consequently, impedances must be measured at very low frequencies, usually far below 1 Hz, in order to get meaningful faradaic information. At frequencies low enough with regard to the rate at which the interface reaches its steady state, the impedance tends towards a pure resistance equal to the slope (dE/dJ) of the steady state polarization curve. Therefore low-frequency impedance measurements, if performed in a transition range from activity to passivity, should reveal a negative resistance and the associated relaxation of the passivating process. This was verified by an early measurement(48) by means of Lissajous figures. The passivation process contributes largely to the impedance measured in a very wide frequency range at many electrodes, e.g., chromium,(48-50) nickel,(48,51-54) iron,(48,55-59) titanium,(60-62) ferritic iron–chromium alloys,(63,64) and spontaneous passivation of iron in a concentrated nitric acid medium.(65,66)

Related processes can be mentioned for those systems such as In(III)–In or Zn(II)–Zn on mercury electrode in a SCN^- containing medium, which exhibit a negative slope region in their current–potential curve.(67-69) In order to explain negative values in in-phase and in out-of-phase components of the ac polarogram, a negative transfer coefficient was invoked.(70) A potential-dependent coverage of the electrode such as in the case of passivation could be a far more realistic explanation if the transfer resistance was assumed to be very small.

1.2. Electrochemical Impedance

As the electrochemical system is essentially nonlinear, the electrode impedance is an electrical impedance defined only about a particular dc polarization point (E_0, J_0). The electrode impedance can thus be measured only by using a perturbation signal of sufficiently small amplitude that it is no longer dependent on the amplitude.

In Figure 1a, the steady state polarization curve (E, J) is schematically drawn. A low-amplitude sine wave potential signal $\Delta E = |\Delta E| \exp(j\omega t)$ is superimposed on the dc polarization (E_0, J_0) where $\omega = 2\pi f$, f being the frequency in Hz and $|\Delta E|$ the amplitude. The current response is then analyzed. If $|\Delta E|$ is sufficiently small, i.e., if the perturbation of the electrochemical system does not extend out of the linear regime, the response is also a sine wave but with a phase shift ψ, $\Delta J = |\Delta J| \exp[j(\omega t + \psi)]$. $|\Delta J|$ is proportional to $|\Delta E|$

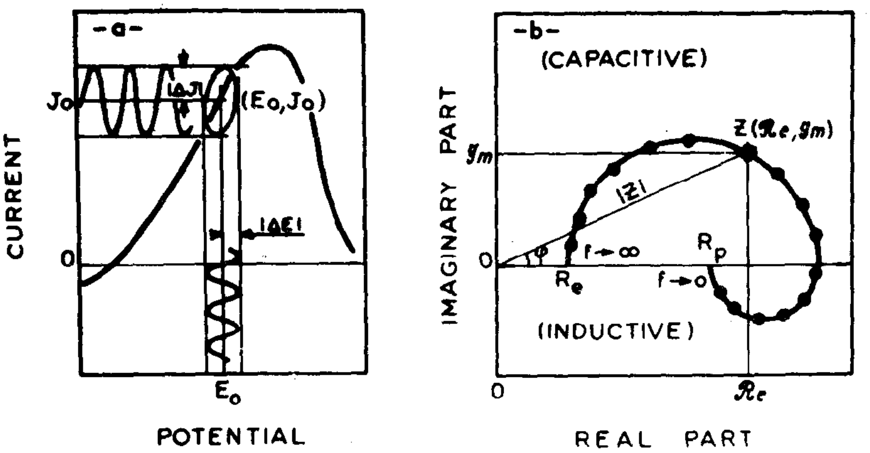

Figure 1. (a) Schematic polarization curve and superimposed measuring signal $\Delta E = |\Delta E| \exp(j\omega t)$ and its response $\Delta J = |\Delta J| \exp(j\omega t + \psi)$. (b) Impedance diagram, locus of $Z(\omega) = \Delta E/\Delta J = \text{Re} - j\,\text{Im}$ in a complex plane. The capacitive impedance is plotted in $\text{Im} > 0$.

for a given frequency. The impedance $Z(\omega)$ is defined by

$$Z(\omega) = \frac{\Delta E}{\Delta J} = \frac{|\Delta E| \exp(j\omega t)}{|\Delta J| \exp[j(\omega t + \psi)]} = |Z(\omega)| \exp(-j\psi) \tag{1}$$

where $|Z|\omega = |Z(\omega)| = |\Delta E|/|\Delta J|$. $Z(\omega)$ can be plotted in the complex plane either in polar coordinates [magnitude $|Z(\omega)|$ and phase shift ψ] or in rectangular coordinates (real part Re and imaginary part Im):

$$Z(\omega) = \text{Re} - j\,\text{Im} \tag{2}$$

In electrochemistry, the capacitive impedances are plotted above the real axis of the complex plane. The locus of $Z(\omega)$ in a wide frequency domain gives the impedance diagram for the chosen polarization point (E_0, J_0). Because of the inherent nonlinearity of the electrochemical system the diagram is characteristic of this point only. The low-frequency limit of the impedance, i.e., the polarization resistance R_p, is equal to the slope of the steady state polarization curve. The high-frequency limit of the impedance is, often, equal to the electrolyte resistance. Hence, in order to analyze the electrochemical processes thoroughly, it is necessary to measure the impedance over a large domain of potential and a large frequency range (namely, 10^{-3}–10^{5} Hz).

1.3. Formal Model of the Passivation Process Impedance

The faradaic impedance Z_F can be calculated following the formalism proposed by Gerischer and Mehl.(19) A more general presentation is given here without any assumption on the type of the passivation process. During the transition between the activity and the passivity, dissolution (Ia), and passivation (Ib) reactions occur simultaneously on the electrode surface following the mechanism

$$\mathrm{M} \rightleftarrows \mathrm{S} + ne^- \tag{Ia}$$

$$\mathrm{M} \rightleftarrows \mathrm{P} + me \tag{Ib}$$

where M is the metal, S the soluble dissolution product, and P the passivating species.

The reaction model formed by the processes (Ia) and (Ib) will now be transcribed into mathematical expressions. x represents the influence of P on the kinetics. If P is an adsorbed species (adsorption theory of passivity), x is the fractional coverage of the surface(71,72) or the fraction of the active sites blocked.(73) If P is the species involved in the passive film (oxide layer theory), x is the thickness or the resistance of the film. As the formation of P needs certain quantity of electricity, the rate of variation of x, i.e., mass balance of P, depends on both the potential E and the value of x:

$$\frac{dx}{dt} = g(E, x) \tag{3}$$

The current J passing through the interface also depends on E and x, hence

$$J = f(E, x) \tag{4}$$

When the potential E is only slightly perturbed, the current response is calculated using a Taylor expansion:

$$\frac{dJ}{dE} = \left(\frac{\partial f}{\partial E}\right)_x + \left(\frac{\partial f}{\partial x}\right)_E \frac{dx}{dE} \tag{5}$$

From Eq. (3), one can write

$$\frac{d\delta x}{dt} = \left(\frac{\partial g}{\partial x}\right)_E \delta x + \left(\frac{\partial g}{\partial E}\right)_x \delta E \tag{6}$$

Since the variation about the steady state is considered in a simple case,

$$\frac{d\delta x}{dt} = a\delta x + b\delta E \tag{7}$$

where a and b are only potential dependent. When the variation of the potential δE is a sine wave, $|\delta E| \exp(j\omega t)$, its induced response δx is also a sine wave provided that the perturbation amplitude is sufficiently small:

$$\delta x = |\delta x| \exp[j(\omega t + \phi)] \tag{8}$$

where $|\delta x|$ is the amplitude and ϕ the phase difference with the perturbating

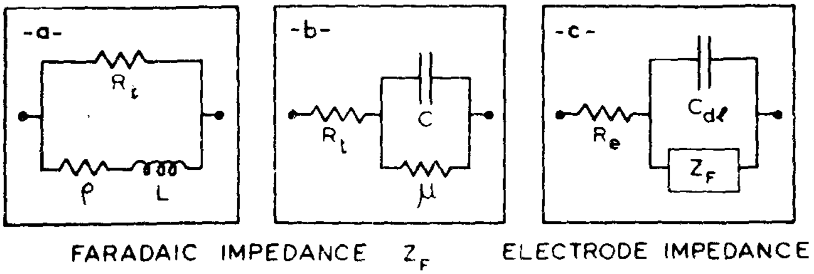

Figure 2. Equivalent circuit of faradaic impedance according to (a) Eq. (13) and (b) Eq. (14); (c) overall electrode impedance.

signal δE. Hence

$$\begin{aligned} \frac{d\delta x}{dt} &= j\omega\delta x = a\delta x + b\delta E \\ \frac{dx}{dE} &= \frac{b}{j\omega - a} \end{aligned} \tag{9}$$

Hence the time constant related to the x variation is, from Eq. (9), $\tau_x = -1/a$.

Substituting Eq. (9) in Eq. (5), one gets the faradaic impedance:

$$\frac{1}{Z_F} = \frac{dJ}{dE} = \frac{1}{R_t} + \frac{b}{j\omega - a} f'_E, \qquad \text{where } f'_E = \left(\frac{\partial f}{\partial x}\right)_E \tag{10}$$

For a sufficiently high frequency, $\omega \gg 1/\tau_x$, $[b/(j\omega - a)]f'_E$ tends to zero. The perturbation rate of the interface is such that x cannot follow the δE variation and x remains equal to its steady state value. The current change with respect to the potential perturbation is governed only by the change of electron transfer, according to Eq. (5), hence the definition of the charge transfer resistance R_t:

$$\left(\frac{1}{Z_F}\right)_{f\to 0} = \left(\frac{\partial f}{\partial E}\right)_x = \frac{1}{R_t} \tag{11}$$

For a very low frequency, $\omega \ll 1/\tau_x$, x follows the δE variation exactly. Hence the current varies along the steady state polarization curve, the slope of which is defined as the polarization resistance R_p:

$$\left(\frac{1}{Z_F}\right)_{f\to 0} = \frac{1}{R_p} = \frac{1}{R_t} + \frac{1}{\rho}, \qquad \text{where } \frac{1}{\rho} = -\frac{b}{a} f'_E \tag{12}$$

For a positive value of ρ, the faradaic impedance can be represented by an equivalent circuit such as that depicted in Figure 2a. The value of the self-inductance is linked to the time constant of x relaxation by

$$L = \frac{\rho}{\tau_x} = bf'_E \tag{13}$$

If ρ has a negative value, the faradaic impedance can be represented by an equivalent circuit such as that depicted in Figure 2b, and instead of having negative L and ρ, one has

$$\mu = -\frac{(R_t)^2}{R_t + \rho} \quad \text{and} \quad C = -\frac{\rho \tau_x}{(R_t)^2} \qquad (14)$$

The steady state expression, Eq. (9), is equal to $dx/dE = b\tau_x$, and if x is chosen as the parameter which increases when the passivation advances (for example, if x is the area covered by P or the resistance of the passive film), then $dx/dE > 0$, hence b is positive. For the same reason, f'_E, which is the ratio of the current variation over x variation at a given potential [see Eq. (10)], is negative. Hence in the passivation process ρ is always negative and Z_F can be represented by the scheme drawn in Figure 2b.

To obtain the measured electrochemical impedance from the faradaic impedance Z_F, it is necessary to take into account the double-layer capacity C_{dl} and the electrolyte resistance R_e (see Section 1.2). The equivalent circuit shown in Figure 2c is then obtained.

The polarization curve (E, J) of a passivation process is schematically plotted in Figure 3a. The extrapolated curve PQ corresponds to reaction (Ia) without passivation process (Ib). Hence the deviation between PQ and $PABCR$ shows the contribution of the parameter x. In the impedance plot, this deviation is shown by a capacitive loop. At point A, the polarization resistance, i.e., the slope of the steady state polarization curve, is positive. The corresponding diagram is drawn in Figure 3b. x relaxation appears in the low-frequency loop. At the maximum of the current, i.e., at point B, R_p goes to infinity. The relaxation process appears purely capacitive because $\mu = \infty$ or $R_t + \rho = 0$ (see curve B in Figure 3b). If $|\rho|$ increases still, R_p becomes negative, e.g., point C, and the diagram shows the capacitive loop bending

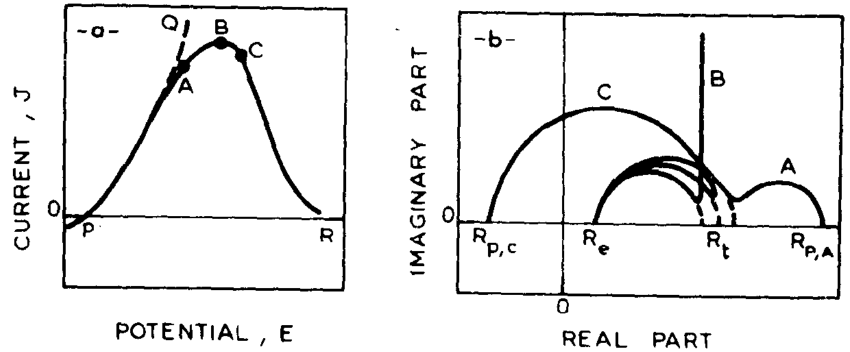

Figure 3. (a) Polarization curve showing the passivation process. PQ corresponds to the process (Ia) without the passivation process (Ib). (b) Impedance diagrams. Curves A, B, and C correspond, respectively, to those plotted at the steady state polarization points A, B, and C on curve a.

towards the negative real part associated with a resistance of negative value (see curve C in Figure 3b). This change of the shapes of the impedance diagrams, from A to C, is characteristic of a simple passivation process.

2. Plotting of the Polarization Curve and Impedance Measurement

The electrochemical impedance is measured about a steady state polarization point (E_0, J_0). In a few cases, instability phenomena are observed during the passivation process and the impedance measurement is no longer possible. Therefore before describing the impedance measurement technique (Section 2.3), some generalities on the accessibility of the nonlinear electrical properties of the electrode interface with the regulating device (Section 2.1) and on the stability of the electrochemical system (Section 2.2) will be given.

2.1. Accessibility of the Steady State

The metal–electrolyte interface is characterized by a relationship, $f(E, J) = 0$, between the current J and the potential E. The regulating device which is used to polarize the electrochemical system is characterized by another relationship called the load line (see Figure 4a):

$$E = E_s - R_o J \tag{15}$$

where E_s is the voltage source value and R_o is the output resistance. If $R_o = 0$, $E = E_s$ and thus defines a potentiostatic regulation. Equation (15) can be

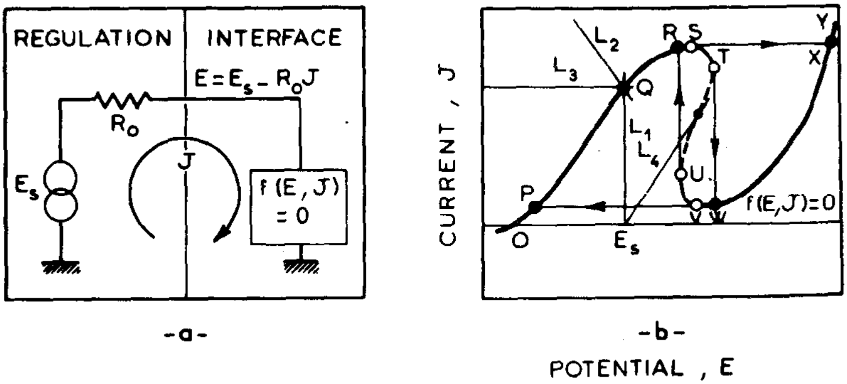

Figure 4. (a) Characteristic of a regulating device having a voltage source E_s and the output resistance R_o. (b) Interface characteristic $f(E,J) = 0$ and that of regulating device shown by the load lines L.

depicted by the load line L_1 as shown in Figure 4b. $R_o > 0$ defines a potentiometric regulation with a load line such as L_2 and $R_o = \infty$ defines a current regulation (galvanostat) with a load line such as L_3.

If the electrochemical system has a current–potential relationship $f(E, J) = 0$, such as that plotted in Figure 4b, this Z-shaped curve shows three different currents for a given potential in *RSTUVW* range, or in other words, this overhanging curve shows the multiplicity of the steady states.

When the electrode is immersed in an electrolytic solution without connection to an external current source, the electrode finds its rest potential or the open-circuit corrosion potential (the point O in Figure 4b). When the electrode is connected to a galvanostat and the current increased, the continuous branch *OS* from the point O up to the maximum of the current S is obtained. However, at the point S, the load line L_3 of the galvanostatic regulation device becomes tangent to the electrochemical characteristic curve $f(E, J) = 0$ and a potential jump is observed up to another polarization point X. If the current is further increased, the *XY* branch is obtained. When the current is decreased, the imposed polarization point goes from Y up to V (the current minimum of the interface characteristic), where L_3 is tangent to the polarization curve and another potential jump occurs, up to the point P. Hence a hysteresis cycle *SXVP* is observed. It can be remarked that in studies on passivity before the invention of the potentiostat, the onset of the passive state was defined by the potential jump *SX*.

In a potentiostatic mode, the load line L_1 is tangent to the electrochemical characteristic curve at the points T and U. Thus a hysteresis cycle *TWUR* is observed. Hence in either galvanostatic or potentiostatic modes, the *TU* range is not accessible. A device imposing a load line such as L_4 allows access to the *TU* domain. L_4 corresponds to a negative value for R_o in Eq. (15). Such a characteristic can be synthesized by means of a negative impedance converter. Hence using such a negative output resistance regulation allows one to plot the entire multiple-steady-state curve such as that described in Figure 4b.(13) Of course, a polarization curve, such as shown in Figure 3a, which is a bell-shaped curve without an overhanging part, can be plotted using a conventional potentiostat. Other details on the technique can be found in another volume of this treatise.(10)

This approach to the problem of the accessibility of the system in the steady state is not sufficient and the dynamic features are also very important. Within this point of view, the stability analysis is involved and will be described in the next paragraph.

2.2. Stability of the Electrochemical Interface(55)

Two types of stability can be distinguished: If, after a small perturbation of a system, its response vanishes with time, the system is called asymptotically stable, and if the response remains constant and does not vanish, e.g., an oscillation is maintained, the system is called stable.(74) In order to study a process by classical electrochemical techniques (polarization curve, impedance) it is necessary that it be asymptotically stable, although the stable system can be studied too (see Sections 5 and 8).

The first step of a stability analysis is a study of stability against a small perturbation. Thus the linear system, hence the electrode impedance, approximating the nonlinear electrochemical system about the polarization point studied, is considered. Only in the case of stable or unstable systems need the nonlinear features be taken into account.

The electrochemical impedance can be defined by $Z(p)$, where p is the Laplace parameter ($p = \sigma + j\omega$). When $p = j\omega$ then $Z(p = j\omega) = Z(\omega)$ as defined in Section 2.1. The current flowing through an electrochemical system with impedance $Z(p)$ polarized by means of a regulating device equivalent to a voltage source E_s in series with an output resistance R_o (Figure 4a) is

$$J(p) = \frac{E_s}{R_o + Z(p)} \tag{16}$$

In the same way, if the electrochemical interface is polarized by means of a current source J in parallel with a conductance G_o, the potential across the cell is

$$E(p) = \frac{J}{G_o + 1/Z(p)} \tag{17}$$

It is well established that the whole cell-regulation system is asymptotically stable if the poles of $J(p)$ in Eq. (16) in the potentiostatic mode [poles of $E(p)$ in Eq. (17) in galvanostatic mode] have negative real parts. For example, for an electrochemical system with only one time constant, the response to a perturbation can be written by $A \exp(\sigma t/\tau)$. Hence the response vanishes with time when $\sigma < 0$. If $\sigma = 0$, the system is stable and an onset of an oscillation can be observed. This value gives the asymptotic stability limit for the system. If $\sigma > 0$, the response increases with time and the system is unstable. Beyond the onset of an oscillation or an unstability, the subsequent behavior will depend on the higher-order terms in the current–potential relationship, the consideration of linear behavior being no longer sufficient.

Two particular cases arise when $\omega \to \infty$ and when $\omega \to 0$. In the first case ($\omega \to \infty$) the high-frequency limit of the impedance is generally the electrolyte resistance R_e. Hence if R_o is equal to $-R_e$, i.e., the ohmic drop is entirely compensated, the cell-regulation system undergoes an oscillation. In other words, the ohmic drop can only be partially compensated if this is included in the regulation loop.

In the second case, $\omega \to 0$, Eq. (16) gives the limit of stability:

$$R_o + R_p = 0 \tag{18}$$

where R_p, the polarization resistance, is such as $Z(\omega = 0) = R_p$. Equation (18) shows that a stability break arises when the load line whose slope is $1/R_o$ is tangent to the polarization curve [its slope $(dJ/dE) = 1/R_p$]. This analysis confirms the steady state condition which leads to a potential jump as shown in the preceding paragraph.

The general analysis ($\omega \neq 0$) with σ, is not easy. However, the system stability can be analyzed by means of the Nyquist plot, i.e., the impedance plotted in the $-\infty$ to $+\infty$ frequency range. The usual impedance is measured in 0 to $+\infty$ frequency range and the $-\infty$ to 0 frequency variations of the impedance are obtained by plotting the diagram symmetrically with respect to the real axis. The number of turns of the Nyquist plot about the origin, T, is positive if the Nyquist plot turns in clockwise when the frequency increases and is negative if it turns in the anticlockwise direction (see Table 1). The number of poles P with a positive real part is given by the number of turns in the clockwise direction. The number of zeros, with a negative real part is given by

$$N = P - T \tag{19}$$

The analysis is related to the unformal mapping and can be found with full details elsewhere.(55,74) The consideration is summarized in Table 1. As an example, the cell-regulation system will be asymptotically stable if $N = 0$ in the potentiostatic mode ($R_o = 0$) and $P = 0$ in the galvanostatic mode ($G_o = 0$).

In Figure 5, the various cases, where the interface relaxes with only one time constant, are analyzed, in addition to that related to the double-layer capacity-transfer resistance, in potentiostatic and galvanostatic modes. This figure shows that conditions 2 and 8 are characteristic of an unstable situation in both types of regulation modes. However, if a regulating device having a negative output resistance is used with a suitable value of R_o, diagram 2 can be transformed into diagram 1 by increasing $|R_o|$. The system is then said to be stabilized with potential regulation.

2.3. Impedance Measurement

As seen in Section 1.2, the electrochemical impedance can be determined by $\Delta E/\Delta J$ in the sine wave regime. These two signals, ΔE and ΔJ can be plotted simultaneously in order to measure the ratio of the amplitudes

Table 1
Graphical Determination of Numbers of T, P, and N

Diagram turns *n* times	*T*		*P*	*N*
	Around origin	Not around it		
↻	*n*	0	*n*	0
↺	−*n*	0	0	*n*

($|\Delta E|/|\Delta J|$) = $|Z|$ and the phase difference which give the modulus and the phase shift of the impedance. Plotting of these two sine waves on X–Y recorder, or on oscilloscope, leads to a Lissajous ellipse as can be seen in Figure 1a, and the impedance can be measured. For more accurate measurements, bridges are used, but their use is limited to the audio-frequency range, whereas faradaic relaxation often appears in the very low frequency range, e.g., less than 1 Hz.

As the measurement has to be performed in the linear domain, very low amplitude signals (typically $\Delta E < 5$ mV) have to be used and spurious noise can degrade the accuracy considerably. In order to obtain accurate measurements, synchronous detection can be used. Analog instruments allow measurement only down to 1 Hz. Hence digital equipment is required for measuring electrochemical impedances in the whole frequency range (e.g., 10^5–10^{-3} Hz). Digital transfer function analyzers are the most convenient instruments for these experiments. In Figure 6, an experimental arrangement is depicted. It allows the measurement of electrochemical impedance in the galvanostatic mode with a transfer function analyzer (frequency response analyzer, Solartron, Schlumberger type 1174) containing a sine wave voltage generator and a correlator. The operational amplifiers G_J and G_E remove the dc component J_0 and E_0 and amplify the signals of interest ΔJ and ΔE. The

N°	Z(ω) with capacitance	T	P	N	<E>	<J>	N°	Z(ω) with inductance	T	P	N	<E>	<J>
1	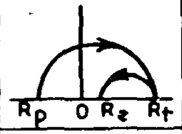	1	1	0	+	-	5	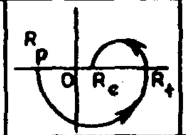	1	0	1	-	+
2	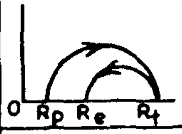	0	1	1	-	-	6	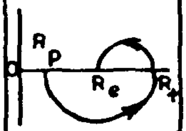	0	0	0	+	+
3	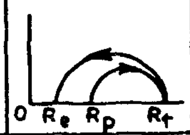	0	0	0	+	+	7	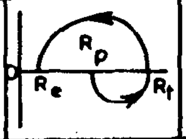	0	0	0	+	+
4	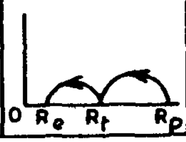	0	0	0	+	+	8	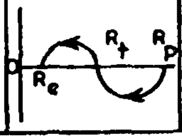	0	1	1	-	-

Figure 5. System stability with one faradaic time constant. ⟨E⟩ and ⟨J⟩ are, respectively, the regulations under a potential and current supply. +, asymptotically stable; −, unstable.

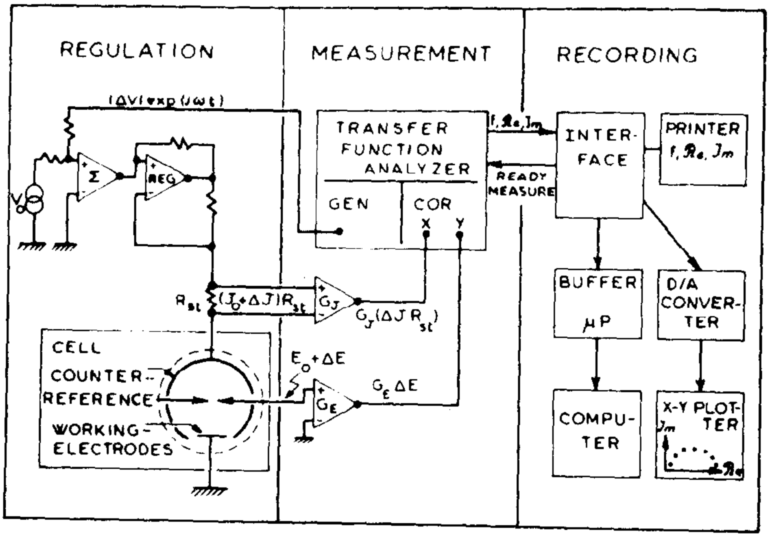
REGULATION
MEASUREMENT
RECORDING
|ΔV| exp (jωt)
Σ
REG
V_0
R_{st}
$(J_0+\Delta J)R_{st}$
G_J
$G_J(\Delta J\,R_{st})$
CELL
COUNTER-
REFERENCE
WORKING-
ELECTRODES
$E_0+\Delta E$
G_E
$G_E\,\Delta E$
TRANSFER FUNCTION ANALYZER
GEN
COR
X
Y
f, $\mathfrak{R}_e$, $\mathfrak{J}_m$
READY MEASURE
INTER-FACE
PRINTER f, $\mathfrak{R}_e$, $\mathfrak{J}_m$
BUFFER μP
D/A CONVER-TER
COMPU-TER
X-Y PLOT-TER
$\mathfrak{J}_m$
$\mathfrak{R}_e$

Figure 6. Experimental setup for the impedance measurements using a transfer function analyzer ($10^{-4} \sim 10^6$ Hz, Solartron 1174); Σ, adder circuit; REG, current regulation device; R_{st}, low inductive standard resistance; G_J and G_E, current and potential signal amplifiers including dc offsets; μP, microprocessor with buffer memories.

input signal on the Y channel is $G_E|\Delta E|\sin(\omega t+\phi_1)$, where ϕ_1 is the phase shift of the voltage signal compared with the perturbating signal imposed by the generator. The input signal on the X channel is $G_J|\Delta J|R_{st}\sin(\omega t+\phi_2)$, where ϕ_2 is the phase shift of the input signal compared with the output signal of the generator and R_{st} is a standard resistor. The correlator calculates the real and imaginary component for each channel. For instance, on the Y channel,

$$\int_0^{NT} G_E|\Delta E|\sin(\omega t+\phi_1)\sin(\omega t)\,dt = G_E|\Delta E|\cos(\phi_1)$$

$$\int_0^{NT} G_E|\Delta E|\sin(\omega t+\phi_1)\cos(\omega t)\,dt = G_E|\Delta E|\sin(\phi_1)$$

$$Y(\omega) = G_E|\Delta E|\exp(j\phi_1)$$

where $Y(\omega)$ is the result of correlation calculation on the Y-channel signal and NT is N integer periods of the signal. Through this calculation, the spurious noise can be eliminated. The transfer function analyzer then calculates the ratio $Y(\omega)/X(\omega)$, where $X(\omega)$ is the result of correlation calculation on the X channel. As $\phi_2-\phi_1$ is equal to the phase shift in the electrochemical cell, this calculation gives directly the real and the imaginary part of the impedance:

$$\frac{Y(\omega)}{X(\omega)} = \frac{G_E}{G_J}\frac{1}{R_{st}}Z(\omega) \tag{20}$$

If G_E has been chosen equal to G_J, $R_{vt}Y(\omega)/X(\omega)$ is equal to the impedance value. The results can be registered on a printer or plotted directly on a X–Y recorder as an impedance diagram when a programmable frequency sweep is used. Numerical data can be transferred to a computer for subsequent processing.

3. Passivation of Iron in a Weakly Acid Medium

The dissolution of iron and its passivity have been widely studied in sulfuric acid medium but the passivation process itself, the transition between activity and passivity, has been scarcely studied in this medium in spite of its outstanding importance for understanding the early stage of the passive layer formation. This is due essentially to the fact that the transition between these two states takes place abruptly, describing a hysteresis cycle in the polarization curve. The electrochemical process is very intricate as will be shown later (see Section 7). On the contrary, in a weakly acidified sulfate medium, the current simply decreases gradually with electrode potential.

3.1. Experimental Results

Figure 7a shows the steady state polarization curve plotted for the iron electrode immersed in 1 M Na_2SO_4 acidified to pH 5 by the addition of 1 M H_2SO_4. The solution is buffered by 4 mM CH_3COONa. The curve shows two current maxima. It can be divided into various reaction domains, labeled on the figure in the same manner as for Fe–Cr alloys(64) for the sake of simplicity.

The impedance diagrams were plotted around maximum II. The low-frequency capacitive loop begins to appear by $E = -0.8\,V_{SSE}$ and its diameter increases when the dc polarization point at which the electrode impedance is measured approaches maximum II, as can be seen on diagrams A and B. At point C, the capacitive loop bends towards the negative real part corresponding to the negative polarization resistance ($dJ/dE < 0$). The change of the impedance diagrams with potential verifies the formal model developed in Section 1.3.

3.2. Reaction Model

Since two current maxima were observed experimentally, the reaction model of iron dissolution in a weakly acidic medium should include at least two dissolution paths. Very recently, the mechanism of iron dissolution was studied(75) within a very wide pH range (0–5) in sulfate media and in a relatively wide current density domain (up to 0.1 A cm^{-2}). By analyzing the steady state polarization curves and the electrode impedances, a general model covering a

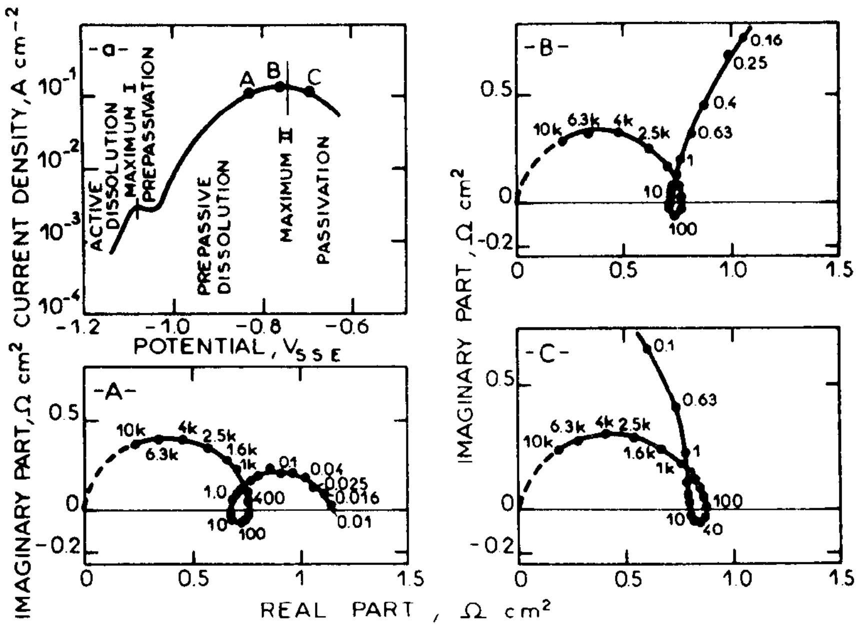

Figure 7. Polarization curves of Fe (Johnson–Matthey) disk (Φ = 3 mm) in 1 *M* Na_2SO_4 acidified by addition of 1 *M* H_2SO_4, buffered by 4 m*M* CH_3COONa, 25 ± 0.2°C deoxygenated by Ar bubbling. $\Omega = 1600 \text{ rev min}^{-1}$. (a) Steady state polarization curve. The impedance diagrams (A), (B), and (C) plotted at points *A*, *B*, and *C* respectively, on curve *a*. Parameter is frequency in hertz.

large range of experimental conditions was proposed and verified by computer simulation. The electrode process can be shown by the reaction scheme (II) given below:

$$\begin{tikzcd}
 & \mathrm{Fe^*(I)_{ad}} \arrow[d, shift left] \arrow[dr] & & \\
\mathrm{Fe} \arrow[r] & \mathrm{Fe(I)_{ad}} \arrow[u, shift left] \arrow[r] \arrow[dr, shift left] & \mathrm{Fe(II)_{sol}} & \\
 & & \mathrm{Fe^*(II)_{ad}} \arrow[u] \arrow[ul, shift left] \arrow[r, shift left] & \mathrm{Fe(II)_{ad}} \arrow[l, shift left]
\end{tikzcd} \tag{II}$$

The subscripts "ad" and "sol" indicate, respectively, species adsorbed at the electrode surface and those dissolved in the solution bulk. The reaction scheme shows three dissolution paths with three reaction intermediates and one divalent passivation species. The case in which a divalent passivating species is considered will be discussed in Section 6.

The iron dissolution through $\mathrm{Fe(I)_{ad}} \rightarrow \mathrm{Fe(II)_{sol}}$ corresponds to the dissolution mechanism proposed by Bockris, Despic, and Drazic.[76] This reaction path is the main process in the active dissolution range. This process is predominant also in a low-pH solution and at current densities where the iron mechanism is usually studied. In the prepassive dissolution range, the iron dissolution through $Fe^*(II)_{ad} \rightarrow Fe(II)_{sol}$ determines the overall reaction rate. This dissolution path can be related to that proposed by Lorenz *et al.* for a weakly acidic medium.(77)

The inductive loop observed in diagrams A, B, and C is related to the relaxation of surface coverage by $Fe^*(II)_{ad}$. The passivation process is described by the chemical transformation of this latter species into nondissolving species $Fe(II)_{ad}$. This process is potential dependent and may be related to the place-exchange mechanism(78) for passivation film growth.(79) The prepassivation process was related to the surface coverage by $Fe^*(I)_{ad}$ which makes the surface coverage by $Fe(I)_{ad}$ decrease. As a whole, the dissolution through $Fe(I)_{ad} \rightarrow Fe(II)_{sol}$ lessens as $Fe(I)_{ad}$ coverage transforms into $Fe^*(I)_{ad}$ coverage.

4. Passivation of Titanium

As for many valve metals, the passivation and the passivity of titanium occur up to very high anodic potential without oxygen gas evolution. In this chapter, only the passivation process is of interest. Thus it is limited to a low anodic potential range.

4.1. Experimental Results

The titanium electrode shows the activation–passivation transition with a bell-shaped polarization curve in a relatively concentrated sulfuric acid solution. Figure 8a shows such a curve plotted in $10\,M\ H_2SO_4$ solution.(60) The partial dissolution current was determined by the ring-disk electrode. Diagrams A and B are plotted at the corresponding polarization points marked on curve *a*. The impedance was measured by an ac bridge in the frequency range between 10 kHz and 70 Hz and by a X–Y recorder in the low-frequency range (1 Hz–0.01 Hz). The passivation process can be seen by a low-frequency capacitive loop which bends towards the negative real part on diagram B.

Curve 1 in Figure 9 shows the steady state polarization curve of a titanium electrode immersed in a fluoride sulfate medium.(61) Curve 2 shows the apparent dissolution valency determined by weight loss measurements and the quantity of electricity passed through the electrode interface. At the open-circuit corrosion potential, the overall current is 0. Hence the apparent valency is also 0. This explains the decrease of the apparent valency for $E < -0.9\,V_{SCE}$ (see curve 2). It can also be seen that the apparent valency changes from 3 to 4 when the polarization potential reaches the region of passivity. The high-frequency capacitive loop is due to the double-layer capacitance and the transfer resistance R_t.(60) The product of R_t times the dc current J is shown by curve 3. The variation of R_tJ is similar to that of the apparent valency.

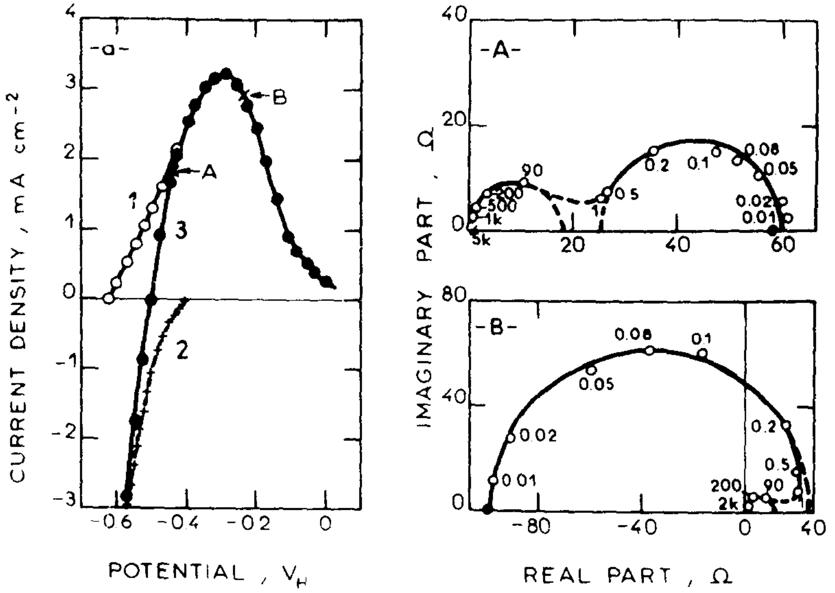

Figure 8. Ti disk electrode (Φ = 6.5 mm) in 10 M H_2SO_4; 25 ± 2°C, deoxygenated. V_H, hydrogen electrode in the same solution. (a) Steady state polarization curve with partial anodic (1), cathodic currents (2), and overall current (3). (A) and (B), impedance diagrams plotted respectively at points A and B on curve a. The parameter is frequency in hertz (curves from Reference 60).

4.2. Reaction Model

The change of apparent dissolution valency indicates the existence of two dissolution paths, the one in the active dissolution range through valency 3 and the other in the passive range through valency 4. On the other hand, for a chain reaction formed by nonreversible elementary steps, R_tJ is constant. The change of R_tJ corroborates the change of the reaction paths. As the passive current is almost independent of the electrode potential, the dissolution in the passive range may be reasonably considered as a chemical reaction. The impedance diagrams plotted for a fluoride sulfate medium showed clearly four time constants in addition to the high-frequency capacitive loop due to the double layer and the transfer resistance.[61] Thus four intermediate species can be considered to be involved in the reaction scheme. The simplest reaction scheme can be written as

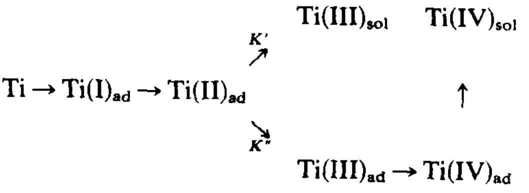

$$\begin{tikzcd}
 & & & \mathrm{Ti(III)_{sol}} & \mathrm{Ti(IV)_{sol}} \\
\mathrm{Ti} \arrow[r] & \mathrm{Ti(I)_{ad}} \arrow[r] & \mathrm{Ti(II)_{ad}} \arrow[ur, "K'"] \arrow[dr, "K''"'] & & \\
 & & & \mathrm{Ti(III)_{ad}} \arrow[r] & \mathrm{Ti(IV)_{ad}} \arrow[uu]
\end{tikzcd} \qquad \text{(III)}$$

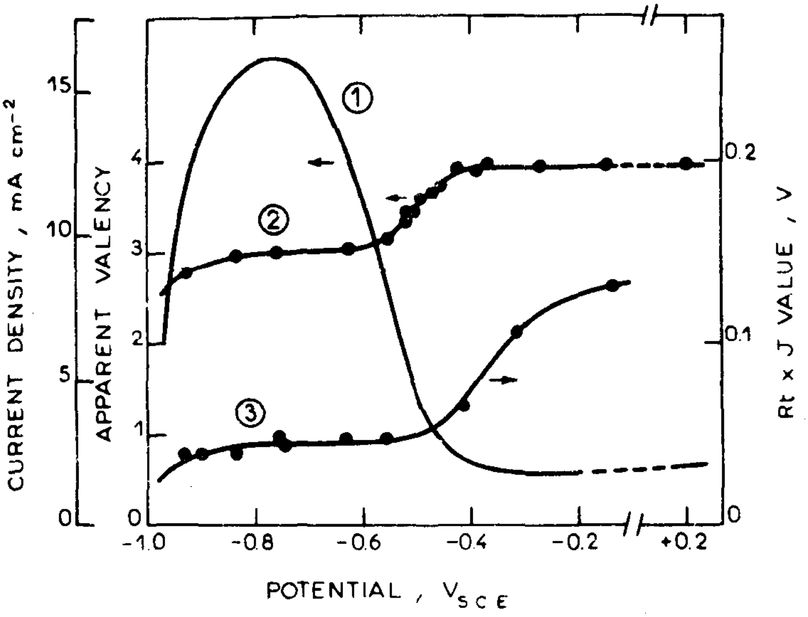

Figure 9. Ti disk (Φ = 5 mm) in 0.1 M H_2SO_4 + 0.5 M K_2SO_4 + 0.05 M HF; 28°C, deoxygenated by Ar bubbling. (1) Polarization curve, (2) apparent valency, (3) the value of R_tJ (curves from Reference 61).

K'/K'' determines, at steady state, the weight of each reaction path,$^{(61)}$ thus the apparent valency z can be calculated by

$$\frac{K''}{K'} = \frac{z-3}{4-z} \tag{21}$$

From the experimental results of z values, K''/K' was evaluated:

$$\frac{K''}{K'} = (1.84 \pm 0.8) \times 10^4 \exp\left[(21.7 \pm 0.9)E\right] \tag{22}$$

That is to say, K' and K'' follow the Tafel law in the range where z changes.

In the case of titanium dissolution in a concentrated HCl medium, the variation of the apparent dissolution valency and that of R_tJ were also observed.$^{(62)}$ But in this system a change in $(z-3)/(4-z)$ cannot be represented by an exponential law with respect to the potential. Furthermore, z and R_tJ values do not change within the same potential range. These results were interpreted by the reaction scheme including multiple branching.

5. Transpassivity of Nickel

The nickel electrode in a sulfuric acid solution shows transpassive dissolution through Ni(II). This dissolution takes place in the potential range more anodic to the passivity range. It is known that the transpassive dissolution depends on acid anions, e.g., the iron does not show such dissolution in a sulfuric acid solution but a small amount of $HClO_4$ added leads to the transpassive dissolution of this metal.(80)

5.1. Experimental Results

The steady state polarization curye of nickel electrode immersed in 1 M H_2SO_4 is shown in Figure 10a. In this figure, three ranges—transpassive dissolution, secondary passivity, and oxygen evolution range—are marked. At more anodic potentials, it is reported that the nickel dissolves in higher valency state.(81) Figure 10b shows the impedance plotted in the vicinity of 1.35 V_{SCE}. It can be seen that for $E \geq 1.36$ V, the impedance shows the negative resistance (negative real part), i.e., a passivation process appears at a potential less anodic to the current maximum. The negative resistance was forecast by Osterwald(82) since this interface shows a voltage oscillation under a current regulation. The impedance diagrams shows, on the other hand, for $E \leq 1.35$ V, that the interface corresponds to a damped oscillation circuit, whereas for $E \geq 1.36$ V, it corresponds to a sustained oscillation circuit.(83) In fact, the theory of stability (see Section 2.2) showed the capacitive loop bending to the right-hand side as

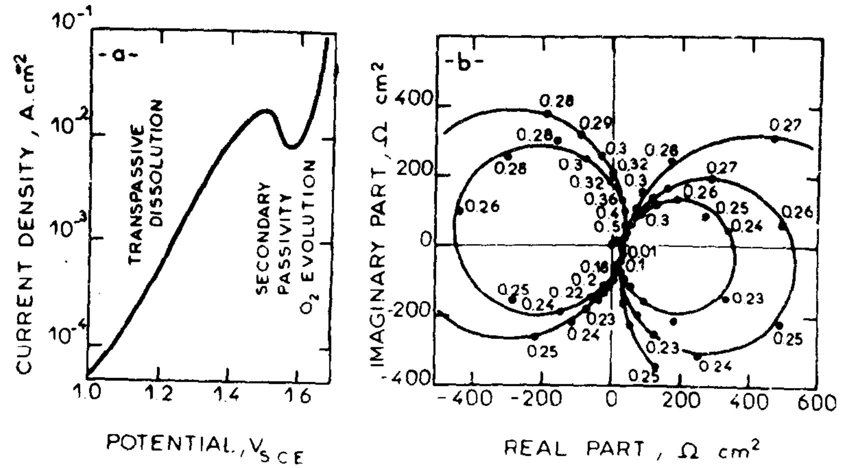

Figure 10. Ni (Johnson-Matthey) disk ($\Phi = 5$ mm) in 1 M H_2SO_4; 25 ± 0.1°C, Ω = 2000 rev min^{-1}. (a) Polarization curve, (b) impedance diagrams, potential is marked beside each curve. The parameter is frequency in hertz.

asymptotically stable, whereas that bending to the left is unstable under a current regulation.(84)

5.2. Reaction Model

The impedance diagrams showed two time constants in addition to the high-frequency capacitive loop. Provided that these two time constants originate from the relaxation of surface coverage by reaction intermediates, one can write

$$J = f(E, \theta_1, \theta_2) \tag{23}$$

The Taylor expansion of Eq. (23) gives the expression of faradaic impedance:

$$\frac{1}{Z_F} = \frac{dJ}{dE} = \frac{1}{R_t} + \left(\frac{\partial f}{\partial \theta_1}\right)_{E,\theta_2} \frac{d\theta_1}{dE} + \left(\frac{\partial f}{\partial \theta_2}\right)_{E,\theta_1} \frac{d\theta_2}{dE} \tag{24}$$

As the electrochemical process considered takes place at the potential range far from its open-circuit potential, $\bar{\theta}_1 + \bar{\theta}_2 \simeq 1$. Thus

$$\frac{d\bar{\theta}_1}{dE} + \frac{d\bar{\theta}_2}{dE} \simeq 0 \tag{25}$$

The symbol $\bar{\theta}$ indicates its steady state value. In the diagram, it can also be seen that $R_t \simeq R_p$. Thus $Z_F(\omega \to 0) = R_p = R_t$, so the following expression should be valid:

$$\left(\frac{\partial f}{\partial \theta_1}\right)_{E,\theta_2} \frac{d\bar{\theta}_1}{dE} + \left(\frac{\partial f}{\partial \theta_2}\right)_{E,\theta_1} \frac{d\bar{\theta}_2}{dE} \simeq 0$$

Thus

$$\left(\frac{\partial f}{\partial \theta_1}\right)_{E,\theta_2} \simeq -\left(\frac{\partial f}{\partial \theta_2}\right)_{E,\theta_1} \tag{26}$$

Equation (26) shows that the coverages by θ_1 and θ_2 have similar effects on the overall current J. One of these cases can be shown by the reaction scheme such as

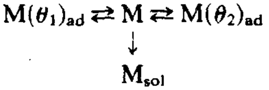

$$\begin{array}{c} M(\theta_1)_{ad} \rightleftarrows M \rightleftarrows M(\theta_2)_{ad} \\ \downarrow \\ M_{sol} \end{array} \tag{IV}$$

For instance, $M(\theta_1)$ and $M(\theta_2)$ may be attributed, respectively, to the species relating to the primary and to the secondary passivity. $M \to M_{sol}$ represents the transpassive dissolution.

The transpassive dissolution depends on the acid anion A^-. If the same reaction nature as OH^- is attributed to A^-, the general reaction scheme of the nickel electrode in HA medium can be written as shown by the following reaction scheme(53):

$$\begin{tikzcd}
 & {} & & {} & \\
\mathrm{Ni(OH)A} \arrow[d] & \mathrm{NiA} \arrow[l] \arrow[u] \arrow[d] \arrow[dl, shift left] \arrow[drr] & \mathrm{Ni} \arrow[l] \arrow[r] & \mathrm{Ni(OH)} \arrow[u] \arrow[d] \arrow[r] \arrow[dl] \arrow[dr, shift left] & \mathrm{Ni(OH)_2} \arrow[d] \\
\mathrm{Ni(OH)_2A} \arrow[ur, shift left] & \mathrm{NiAOH} \arrow[l] & \mathrm{Ni^{2+}} & \mathrm{NiAOH} \arrow[r] & \mathrm{Ni(OH)_2A} \arrow[ul, shift left]
\end{tikzcd} \qquad \text{(Va)}$$

This model covers active dissolution, primary passivity, transpassivity, secondary passivity, and oxygen evolution.

In the case of a fluoride medium, no passivity was observed. Hence NiF_{ad} plays a peculiar role.(54) In the case of a sulfate medium, the scheme is limited to the right-hand side of scheme (Va), i.e., all intermediates stem from Ni(OH). Nevertheless, by the same authors,(53) the transpassive dissolution takes place through the reduction of $Ni(OH)_2$ into NiA preceding the dissolution reaction into $Ni(A^+)_{sol}$. This reaction scheme is given in (Vb):

$$\begin{tikzcd}
 & \mathrm{Ni(OH)_2} \arrow[dl, shift left] \\
\mathrm{NiA} \arrow[r, shift left] \arrow[ur, shift left] \arrow[dr] & \mathrm{Ni(OH)A} \arrow[l, shift left] \\
 & \mathrm{Ni(A^+)_{sol}}
\end{tikzcd} \qquad \text{(Vb)}$$

This reaction scheme can be identified with the reaction scheme (IV). Thus the model can be used to interpret the diagrams shown in Figure 10b if suitable kinetic constants are determined.

6. Passivity of Iron in 1 M H_2SO_4

The passivity of iron, as defined in this chapter, is the potential range where the electrode interface can be suitably regulated by a potentiostat up to the oxygen evolution range, i.e., between the Flade potential $E = -0.17$ and the onset of the oxygen evolution $E \simeq 0.9\,V_{SSE}$.

6.1. Experimental Results

In Figure 11, the steady state polarization curve in the passivity range is shown. From the Flade potential -0.17 V to 0.2 V, the current decreases and gradually reaches the passivity current. This current is independent of the potential. Reproducible results for the passive current for a disk electrode are relatively difficult to obtain. This seems to be due to a very slight infiltration of electrolyte between the metal and the sample holder limiting the electrode surface, inducing a significant increase of the current.(85) The impedance diagrams plotted at various potentials marked by A to D on the polarization curve are also shown in the same figure. Diagrams A and B show the capacitive loop bending toward the negative real part corresponding to the passivation

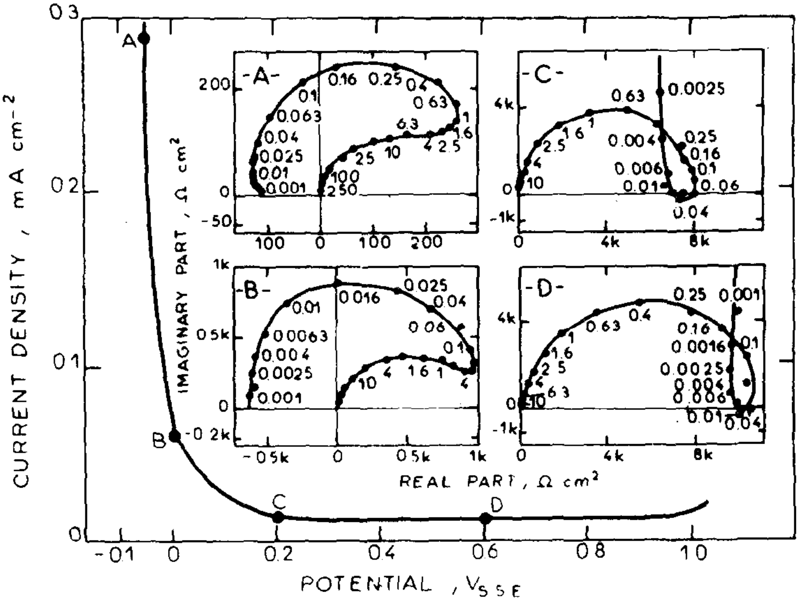

Figure 11. Fe (Johnson-Matthey) disk ($\Phi = 5$ mm) in 1 M H_2SO_4; 25 ± 0.1°C, $\Omega =$ 1600 rev min^{-1}. Polarization curve and impedance diagrams. A to D correspond to the steady state points A to D marked on the polarization curve at which the impedance was measured. The parameter is frequency in hertz.

process (cf. Figure 3b). In diagram A, two capacitive loops in addition to that of the high-frequency capacitive loop can be seen.

In diagrams C and D, the inductive loop near 0.04 Hz is observed. This inductive impedance is only observed when the passive current is low enough for this iron electrode. In our earlier work, the passive current was several times greater and the inductive loop was not revealed.(59) It can also be seen the high-frequency capacitive loop increases when the potential becomes more anodic though the passive current remains constant. The diameter of this loop can thus hardly be related to the transfer resistance (see Section 4).

6.2. Reaction Model

Diagram A indicates that the passivation process is taking place through two steps. At potentials very close to the Flade potential, only one passivating capacitive loop was observed.(59) Thus the lowest frequency capacitive loop is attributed to the relaxation of Fe(III)-adsorbed passivating species. Since this capacitive loop was observed once the current density approached several mA cm^{-2}, the main passivating species is considered to be an Fe(II)-adsorbed species. The relaxation of this species can be seen by the capacitive loop bending towards the negative real part in diagram A. The decrease of current density from more than a few A cm^{-2} observed in the active dissolution to a few mA cm^{-2} is thus due to the ferrous passivating species.(59) This consideration can be corroborated by the fact that the change of dissolution valency, from 2 to 3, occurs at the very foot of the current decrease.(86)

It is known that in the full passivity range, the ferric oxide passive film is formed and grows beyond the monomolecular thickness. Since at this potential range, the electrode impedance does not reflect various dissolution paths (see Section 3), no intermediates are considered. The simplest reaction scheme can be written as

$$\begin{tikzcd}
 & \mathrm{Fe(II)}_{sol} & \mathrm{Fe(III)}_{sol} \\
\mathrm{Fe} \arrow[ur, "K_2"] \arrow[r, shift left, "K_3"] & \mathrm{Fe(II)}_{ad} \arrow[l, shift left, "K_{-3}"] \arrow[r, shift left, "K_4"] & \mathrm{Fe(III)}_{ad} \arrow[l, shift left, "K_{-4}"] \arrow[u, "K_5"'] \arrow[d, shift left, "K_{-6}"] \\
 & & \mathrm{Fe(III)\text{-}oxide} \arrow[u, shift left, "K_6"]
\end{tikzcd} \qquad (\mathrm{V})$$

In order to perform a computer simulation according to this model, the reaction rate K of the elementary steps is considered to follow the Tafel law. But the reaction rate for the oxide formation process should be somewhat different.

1. Fe(III)–oxide is considered to form upon $\mathrm{Fe(III)}_{ad}$, whereas $\mathrm{Fe(II)}_{ad}$ and $\mathrm{Fe(III)}_{ad}$ share the electrode surface to cover.

2. The rate law describing the K_6 reaction. If the place exchange model is assumed(78):

$$K_6 = k_6 \frac{\exp(BE)}{\exp(C\delta_f)} \tag{27}$$

where δ_f is the film thickness, and k_6, B, and C are constant. If the strong electrical field theory governs the film growth, which is usually verified for valve metals,(87,88)

$$K_6 = k_6' \exp\left(\frac{B'E}{\delta_f}\right) \tag{28}$$

where E/δ_f gives the electrical field in the passive film. The electrode impedance is calculated with a small potential change and dK_6/dE for Eqs. (27) and (28) shows the same analytical form. Therefore from the electrode impedance one cannot distinguish between these two models of film growth. Notice the parallel with the usual methods using a large amplitude electrical signal.(89)

The film thickness increases roughly by 5 nm V^{-1} and the monolayer thickness corresponds to 1.5 nm. The set of experimental results, the steady

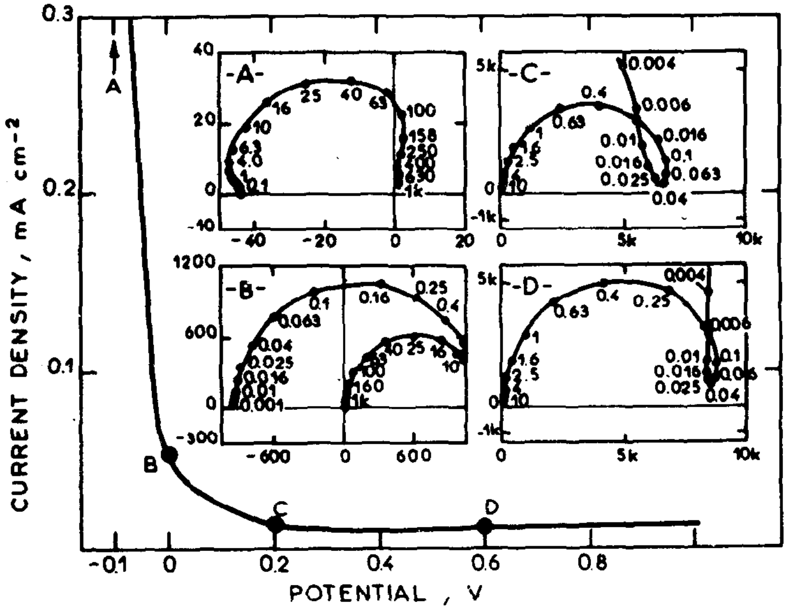

Figure 12. Simulation curves; see Figure 11. $K_2 = 4 \times 10^{-4} \exp(10E)$; $K_3 = 5 \times 10^{-5} \exp(26.4E)$; $K_{-3} = 3 \times 10^{-11} \exp(-12E)$; $K_4 = 8 \times 10^{-10} \exp(4E)$; $K_{-4} = 2 \times 10^{-9} \exp(-34E)$; $K_5 = 4 \times 10^{-11}$; $K_6 = 2 \times 10^{-16} \exp[34.2(E - E_F)/\theta_4]$; $K_{-6} = 1.8 \times 10^{-11}$; $\beta_2 = \beta_3 = \beta_4 = 1 \times 10^{-8}$, $C_{dl} = 10^{-4}$. The parameter is frequency in hertz.

state polarization curve and the impedance diagrams were computer simulated. If the ohmic drop through the passive film is taken into consideration, in the electrical field model so that the potential beneath the passive film is constant, the film resistance R_f increases by 8 kΩ cm^2 per 0.1 V for the passive current equal to 12 μA cm^{-2}. Since the capacitance of the film C_f should be of microfarad order with a reasonable value of the dielectric constant for the passive film, the R_f–C_f contribution, if it exists, can be seen on the impedance diagram. The comparison of the diagrams C and D in Figure 11 indicates the absence of such a contribution. In order to overcome this difficulty in the model, the passive film having a good electrical conductance was considered.(90) The results of simulation calculations are shown in Figure 12. With Eq. (27), we were unable to simulate the diagrams C and D suitably with the same set of rate constants. It may be concluded that in the case of iron passivity, neither the place exchange model nor the electrical field model is able to describe entirely the growth law of the passive film.

Based on the same model, the potential decay curve was also simulated.(59) That is to say, the potential arrest was not related to the thermodynamic equilibrium potential,(91) but interpreted by the nature of the kinetics. Fairly good results can be obtained by the computer simulation.(59) It is found, on the basis of the model, that the electrode potential can reach the open-circuit corrosion potential even though the oxide covers a large part of the electrode surface. These results from the model are in agreement with the experimental observation on the nickel electrode.(92)

7. Passivation of Iron in 1 M H_2SO_4

The passivation range is defined in this chapter as the transition range from the activity to the passivity. In the previous section, the passivity range was defined. Thus the passivation range in a strongly acidic medium corresponds to the electrode characteristic accessible neither with a potentiostat nor with a galvanostat.

7.1. Experimental Results

Figure 13a shows the steady state polarization curve of an iron disk electrode, $\Omega = 750\,\text{rev min}^{-1}$, in 1 *M* H_2SO_4, plotted by a potentiostat. The electrode potential is indicated as it was measured without correction of ohmic drop due to the electrolyte resistance. According to the direction of potential change, the steep current change from the activity to the passivity $D \rightarrow F$, or from the passivity to the activity $H \rightarrow B$, is observed. Thus the polarization curve reveals a hysteresis cycle *BDFH*. For the stationary electrode, the potential difference between *H* and *F* is very narrow and under certain

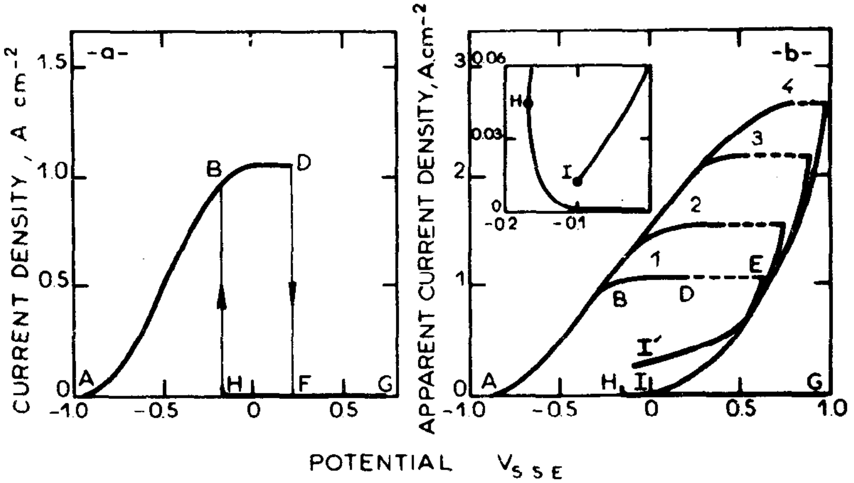

Figure 13. Polarization curve of Fe (Johnson-Matthey) disk ($\Phi = 5$ mm) in 1 *M* H_2SO_4; 25 ± 0.2°C, deoxygenated by Ar bubbling. Ω = (1) 750, (2) 1600, (3) 3000, and (4) 4500 rev min^{-1}. (a) With a potentiostat, (b) with a regulating device having a negative output resistance.

conditions, aperiodic oscillation between two states can be seen near the Flade potential.(12,93)

Figure 13b shows the steady state polarization curves plotted by a regulating device having a negative output resistance for various rotation speeds. The current plateau observed changes proportionally to $\Omega^{1/2}$; thus this current is limited by mass transport through convective diffusion. Curve *ABDEI* was plotted at the same conditions as figure *a*. Under this regulation, beyond the point *D*, the current changes considerably around the limiting current and is indicated by dashes. At the point *E*, the current stabilizes again and one obtains the *EI* curve. This branch has, thus, the passivation characteristic. The branch *EI* is a steady state and no hysteresis cycle can be seen. On the contrary, the transition between *I* and *H* is not continuous. The insert shows the polarization curve with enlarged current and potential scales. In this figure, it can be seen that point *H* corresponds to the point at which its tangent is parallel to the current axis. The steep change of current under the voltage regulation can thus be explained in the terms of the stability of the system (cf. Sections 2.1 and 2.2). Point *H*, thus, defines the Flade potential.

It was observed that in the passivation range, only a well-defined zone of the disk electrode dissolves.(13) The most general feature of the dissolution profile is a ring shape on the disk. The remaining parts of the surface are passive. If the center of the disk and the axis of rotation of electrode are not coincident, this latter determines the center of the ring; thus the concentration field determines for the border of dissolving–passive transition on the electrode surface. The ring shape and the outer and inner diameters are dependent on the rotation speed and the observed current. The current density is calculated for the observed current on the whole disk electrode surface in Figure 13b, thus yielding an apparent value. The curve *EI'* is that relative to the actually dissolving area. The true current density decreases when the observed current decreases.

For low rotation speeds, the outer diameter of the dissolving ring area is identical to that of the disk electrode; thus the electrode is divided into a passive inner disk and the dissolving outer ring. In this case, the ring shape is determined by the potential distribution.(13) At high rotation rate and high current densities, the inner diameter of the ring is so small that only the dissolving inner disk can be seen. The passivation characteristics of various rotation speeds are identical when they are plotted against the apparent current density, though they are quite different when plotted against the true current density.(57)

Figure 14 shows the impedance diagrams plotted in the passivation range. Diagram A is obtained from the disk electrode and the dissolving area is located at the outer ring part of the disk electrode. Diagram B corresponds to the case where the passive inner disk of the former case is replaced by an insulating material (epoxy resin). The whole ring surface is dissolving. The essential difference between these two cases lies in the fact that in diagram A

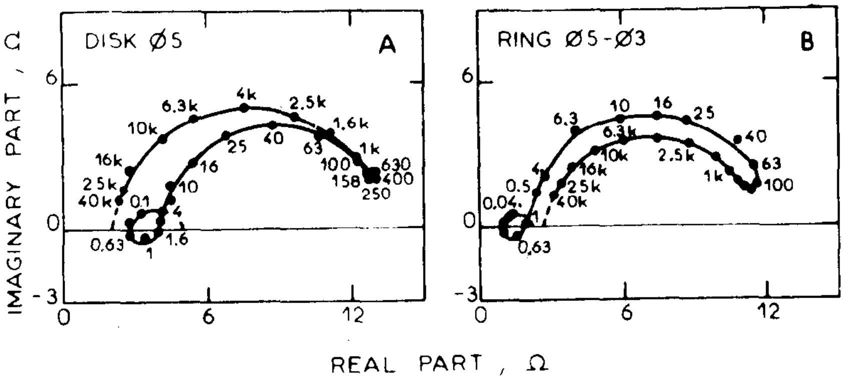

Figure 14. Impedance diagrams; for conditions see Figure 13. $\Omega = 1600\ \text{rev min}^{-1}$. (A) Disk electrode ($\Phi = 5$ mm), $E = 0.40\,V_{\text{ESS}}$, $I = 75$ mA ($J = 0.57\ \text{A cm}^{-2}$); (B) ring electrode ($\phi = 5$–3 mm), $E = 0.38\,V_{\text{ESS}}$, $I = 72$ mA ($J = 0.57\ \text{A cm}^{-2}$). The parameter is frequency in hertz.

(disk) there is a border of dissolving-passive transition on the electrode and in diagram B no border is present. It can be seen in diagram A that the polarization resistance, the impedance at the zero frequency limit, is noticeably greater than the electrolyte resistance, corresponding to the positive slope of the polarization curve even when the ohmic drop is corrected. On the contrary, in diagram B, the polarization resistance is smaller than the electrolyte resistance and the ohmic-drop-corrected polarization curve may have a negative slope. In general, the high-frequency limit of the electrode impedance is equal to the electrolyte resistance. However, in diagram A, this value (ca. 2 Ω) is significantly smaller than that found for the usual case where no border of dissolving-passive areas is present. The high-frequency limit of diagram B corresponds well to the electrolyte resistance.

The most peculiar feature of the passivation characteristic of the iron electrode in a strongly acidic medium is the Z-shaped polarization curve. Two models giving rise to such a feature are shown below.

7.2. Models of Z-Shaped Curve

The Z-shaped polarization curve shows the multiplicity of steady states, three steady state currents for a given potential. The appearance of such states is known in the thermodynamics of far-from-equilibrium process.(94) In such a system, a distribution of states often occurs in time or in space. In the case of iron passivation, either the dissolving and passive states are distributed in space by the ring-shaped dissolving profile or the aperiodic oscillation between the activity and the passivity(12,93) shows the distribution in time. The appearance of a multiplicity of steady states requires an autocatalytic process.(94) The following two models do not include an autocatalytic process in their elementary steps but are autocatalytic overall.

7.2.1. Ohmic Drop Contribution

If the ohmic drop is important, e.g., high electrolyte resistance or high current density, the faradaic model giving rise to the bell-shaped polarization curve can show the multiplicity of the steady states(57) but its shape is very different from those shown in Figure 13b. However, if both the potential distribution on the electrode surface and the local polarization curve having a steep transition between the activity and the passivity were considered, very similar polarization curves could be computer simulated.(95)

The current dependence on potential at any point of the electrode such as Figure 15a is considered. The curve is given here by the dimensionless current. The branch *AB* corresponds to the active dissolution following the Tafel law, *BD* the limiting current, *DE* the steep passivation, and *EF* the passive current. By calculating the potential distribution with the local polarization curve, the overall polarization curves were calculated for the various limiting currents by Law and Newman.(95) These curves are strikingly similar to the experimental curves. When the current decreases by the passivation process, the electrode potential becomes more anodic since the ohmic drop lessens. The passivation process thus advances further. The reaction is overall autocatalytic. This model is advantageous, compared to the trivial model, which involves adding the ohmic drop term on the faradaic bell-shaped curve, but it differs from the experimetal observations of two points:

1. In the model, the current decrease in the passivation range is due to the decrease of surface area, whereas the reaction rate is limited by convective diffusion. The true current density does not decrease contrary to experiment.

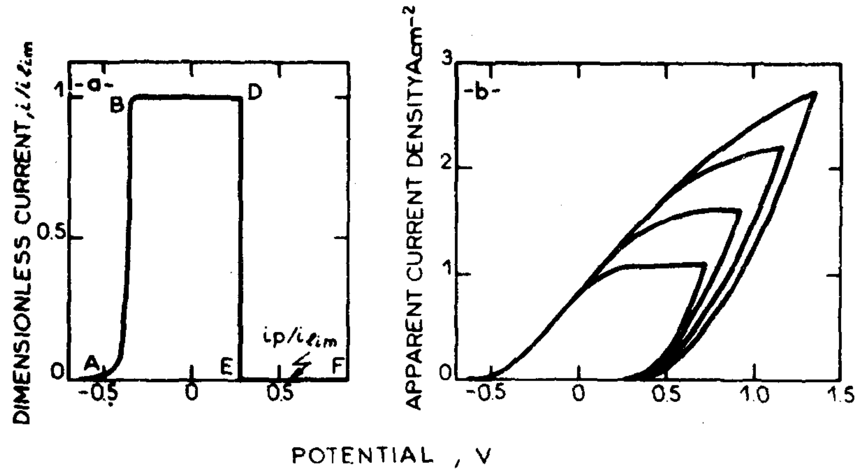

Figure 15. (a) Local polarization curve, (b) computer-calculated overall polarization curve for different diffusion limiting currents. The reaction order for the limiting current is equal to unity. (Curves from Reference 95.)

1/27 B 9

2. The model considers only the case where the dissolving area is located in the dissolving inner disk. Experimentally this form depends on the concentration profile and not on the potential distribution.(13)

Even if the electrolyte resistance is calculated according to the primary distribution(96) for the electrode whose form corresponds to the dissolving area, the correction of the ohmic drop is not enough to make the multiplicity of the steady states disappear (see Figure 16a). It can be seen that in the case of an Fe–5Cr electrode in 1 M H_2SO_4, the appearance of the multiplicity of steady states is essentially due to the change of the dissolving area with current, and that the dissolving profile is the inner disk.(97)

The authors wish to emphasize that the ohmic drop plays a most important role for the appearance of the multiplicity of steady states and that these remarks were made to indicate that the problem is more complex.

7.2.2. Kinetic Model

Another model, explaining multiplicity of steady states, calls upon the coupling of activation–passivation process through diffusion.(57) These two processes can be written more explicitly than (Ia) and (Ib) in Section 1.3:

$$\mathrm{M} + \mathrm{A} \xrightarrow{K_1} \mathrm{S} + ne^- \qquad \text{(I'a)}$$

$$\mathrm{M} + 2\mathrm{A} \underset{K_{-2}}{\overset{K_2}{\rightleftharpoons}} \mathrm{P} + me^- \qquad \text{(I'b)}$$

In this model, it is essential that the two processes have the same reacting species A and that the reaction order with respect to A be higher in the passivation process. Provided that P covers the fraction θ of the electrode surface (the same discussion can be made for other origins for passivation as discussed in Section 1.3). The current flowing through the interface can be calculated by the charge balance of processes (I'a) and (I'b), more explicitly than Eq. (4):

$$\frac{J}{F} = [nK_1(A)_0 + mK_2(A)_0^2](1-\theta) - mK_{-2}\theta \qquad (4')$$

J is expressed in A cm^{-2} and F the Faraday constant, thus K has the dimension of mol sec^{-1} cm^{-2}. $(A)_0$ is the concentration of A at the electrode interface. The material balance of P can be written more explicitly than Eq. (3):

$$\beta\frac{d\theta}{dt} = K_2(A)_0^2(1-\theta) - K_{-2}\theta \qquad (3')$$

where β is the constant linking the surface concentration and the fractional surface coverage. At steady state, no θ change should be occurring, thus

F2/1 A 6

$(d\theta/dt) = 0$:

$$\bar{\theta} = \frac{(A)_0^2K_2}{(A)_0^2K_2 + K_{-2}} \quad \text{and} \quad \bar{J} = nF(A)_0K_1(1-\bar{\theta}) \tag{29}$$

The current is also expressed by the flux of A. If the Nernst diffusion layer whose thickness is δ_N is assumed one can write

$$\bar{J} = nF\frac{D}{\delta_N}[(A)_0 - (A)_\infty] \tag{30}$$

where D is the diffusion coefficient and $(A)_\infty$ the concentration of A in the solution bulk. The quantity of flux of charge and that of A are equal, and thus

$$K_2(A)_0^3 - K_2(A)_\infty(A)_0^2 + \left(\frac{\delta_N}{D}K_1 + 1\right)K_{-2}(A)_0 - K_{-2}(A)_\infty = 0 \tag{31}$$

Equation (31) can have, if certain conditions are fulfilled,[98] three real roots between 0 and $(A)_\infty$. That is to say, three steady state currents can be observed for given K_i values, thus for a given potential. If D/δ_N is very large, $(A)_0 \simeq (A)_\infty$ and the polarization curve shows the usual bell shape.

Figure 16a shows the experimental polarization curves plotted with respect to the true current density and the potential corrected for ohmic drop (R_e value is determined by the dissolution profile). Figure 16b is relative to the calculated results. The reaction scheme is somewhat more elaborate than (Ia) and (Ib):

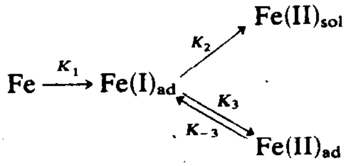

(VI)

The reactions relating to K_1 and K_3/K_{-3} imply the species A of which the flux may be limited by the convective diffusion. $(A)_\infty$ is determined in order that the limiting current be close to the experimental value for reasonable D and δ_N values. The species A is difficult to identify, but since at the current plateau the electrolyte close to the electrode is essentially saturated $FeSO_4$, H_2O is a very plausible species.[56]

The agreement between experiments and model is not perfect. The model explains, nevertheless, the appearance of the multiplicity of the steady states without the ohmic drop contribution. Furthermore, experimentally, the appearance of such states is always related to the presence of a diffusion-limiting plateau. This model explains successfully the pit propagation effected by an artificial pit.[57,58]

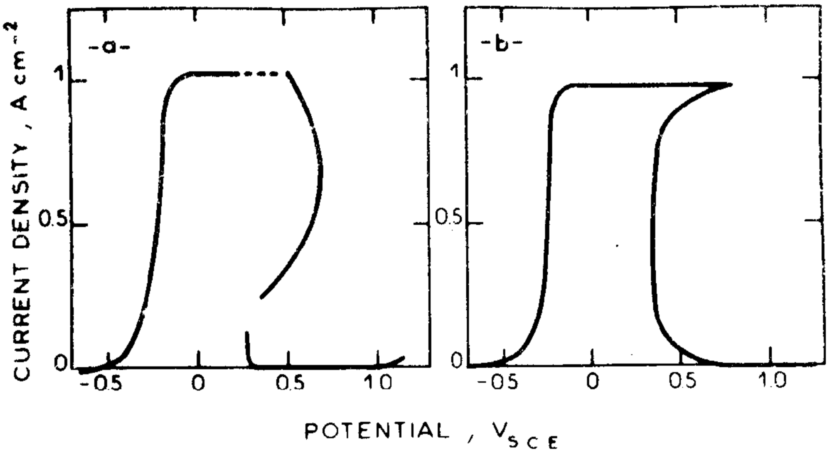

Figure 16. (a) Polarization curve of Fe–1 M H_2SO_4; for conditions see Figure 13b. $\Omega = 750$ rev min^{-1}. Corrected for ohmic drop and relative to the current density for actually dissolving area. (b) Calculated curve; $K_1 = 8 \times 10^3 \exp(36E)$, $K_2 = 5 \times 10^{-5} \exp(10E)$, $K_3 = 5 \times 10^{-4} \exp(12E)$, and $K_{-3} = 9 \times 10^{-8} \exp(-5E)$. $(A)_\infty = 10^{-4}$ and $\delta_N/D = 20$.

The high-frequency limit of the electrode impedance of the disk, Figure 14a, significantly smaller than the electrolyte resistance, was explained by the change of actually dissolving area with apparent current.(84) However, the difference in R_p values between the disk and the ring indicates clearly that neither the ohmic-drop model nor the kinetic model shown here is enough. Since the multiplicity of the steady states is related to an autocatalytic reaction, one may consider such a process as the faradaic process itself, as was already postulated.(99)

8. Iron in HNO_3 Solutions

It is well known that the iron immersed in a concentrated nitric acid solution passivates spontaneously, whereas in a dilute acid, the metal dissolves rapidly by active dissolution. NO_3^- reduction plays an outstanding role in the difference of the interface behavior but relatively few studies from the viewpoint of electrochemical kinetics have been reported. As will be shown below, the study of this system requires the use of a regulating device having a negative output resistance.(66)

8.1. Experimental Results

Figure 17a shows the steady state polarization curves obtained in 1 N HNO_3 at various rotation speeds of an iron disk electrode. The fine traces with

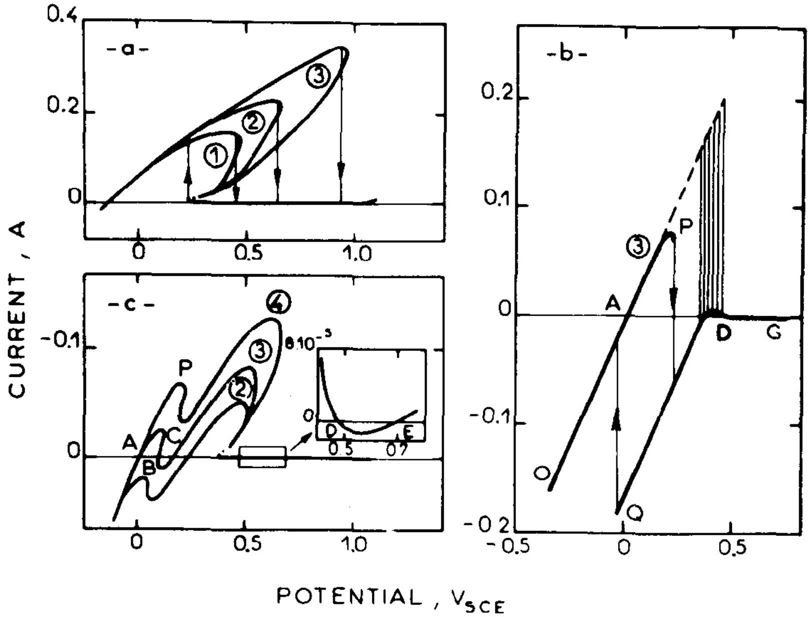

Figure 17. Fe (Johnson–Matthey) disk ($\Phi = 5$ mm); the potential and current as measured. Ω = (1) 100, (2) 400, (3) 900, and (4) 1600 rev min^{-1}. (a) In 1 *N* HNO_3 thin traces with arrow indicate the steep transition observed under potential regulation, the bold lines with a regulating device having a negative output resistance. (b) 12 *N* HNO_3 with potentiostat. Near point *D* the aperiodic oscillation was observed and is marked by thin lines. (c) 12 *N* HNO_3 with a regulating device having a negative output resistance. The insert indicates the expanded current scale in the cathodic loop range. (Curves from reference 66.)

an arrow indicate a steep transition observed under potential regulation. The bold lines are obtained by using a regulating device having a negative output resistance. Thus can be seen, in this figure, the multiplicity of the steady states. The maximum current depends on the rotation speed although no current plateau was observed.

Figures 17b and 17c show the curves plotted in 12 *N* HNO_3. The stationary electrode passivates spontaneously in this medium but if the rotation speed is high enough ($\Omega > 600$ rev min^{-1}), fast active corrosion occurs on the iron electrode. Figure 17b is relative to a potentiostatic curve. In the *OAP* branch, the metal dissolves even when the overall current is cathodic, whereas in the *QFG* branch, the metal is passive. The slope of these two branches corresponds nearly to the electrolyte resistance, i.e., the overall reaction rate is limited by the conductivity of the electrolyte. Near point *D*, aperiodic oscillations were observed. Figure 17c shows the curves observed with a regulating device having a negative output resistance. Two current maxima can be seen, whereas the *QFG* branch is absent on these curves. The characteristic linking points *P* and *D* cannot be observed by potential regulation nor by current regulation. It can also be remarked that the maximum J, located at less anodic potential, is positive as well as negative according to the rotation speed. The polarization curves show a small cathodic loop in the passivity range as shown in the insert. Thus for $\Omega < 600$ rev min^{-1}, the polarization curve crosses the potential axis (overall current $J = 0$) three times, for $600 < \Omega < 1100$ five times and for $\Omega > 1200$ as the current minimum becomes positive, again three times. As the spontaneous behavior occurs at $J = 0$, these points are very important for understanding it. For $\Omega < 600$ rev min^{-1}, the electrode is spontaneously passivated and the potential is found at point E. For higher rotation speed, the electrode potential is found at point A and undergoes active corrosion. The electrode impedances at these five points ($\Omega = 900$ rev min^{-1}) are shown in Figure 18.$^{(65)}$

The anodic behavior of the Fe–HNO$_3$ interface is profoundly modified by addition of para-nitroaniline (pna). pna is a strong reducing agent and decomposes HNO$_2$, which is spontaneously present in nitric acid in equilibrium with HNO$_3$. HNO$_2$ plays a catalytic role in the oxidation of Fe(II)$_{sol}$ into Fe(III)$_{sol}$ in the homogeneous process.$^{(100)}$ In the presence of excess pna, the polarization curves of iron in 12 N HNO$_3$ are very similar to those in a sulfuric acid medium. By measuring the anodic current contribution to an overall current J, the very strong interaction between the dissolution reaction and the cathodic reaction

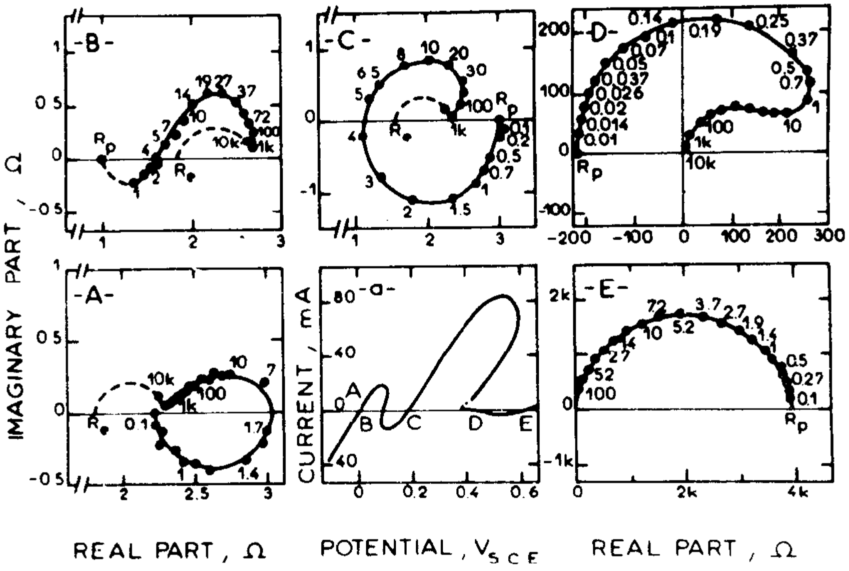

Figure 18. Impedance diagram; for conditions see Figure 17c. $\Omega = 900$ rev min^{-1}, plotted at the overall current $J = 0$ and schematically shown on the polarization curve a; R_e, electrolyte resistance; R_p, the polarization resistance determined by the steady state polarization curve. Parameter is frequency in hertz. (Curves from Reference 65.)

was seen in the absence of pna, whereas their interaction lessens considerably in its presence.[(66)]

8.2. Reaction Model

As was described in Section 2.2, the analysis of the number of poles and of zeros allows examination of the stability of the system. The results of this analysis on diagrams A to E of Figure 18 are summarized in Table 2. Points *A*, *D*, and *E* are asymptotically stable under potential regulation and were actually observed under this regulation device (see Figure 17b). Under current regulation, only points *A* and *E* are asymptotically stable and the open-circuit electrode showed only these two points. If point *A* does exist on the steady state polarization curve, high rotation speed of the disk electrode, the metal undergoes fast active corrosion. If the maximum *J* is located below the potential axis, the metal is protected from corrosion by the passivity. Diagrams B and C are stable with neither potential nor current regulation. These points were obtained only by using a regulating device having a negative output resistance.

If HNO_2 is absent by virtue of the addition of pna, the anodic behavior of the iron in nitric medium is very similar to that observed in a sulfuric medium. Thus one can write roughly

$$Fe \rightarrow Fe(I)_{ad} \rightarrow Fe(II)_{sol}$$

The reduction of HNO_3 on the iron can be written

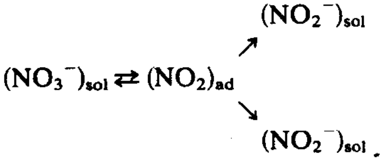

$$(NO_3^-)_{sol} \rightleftarrows (NO_2)_{ad} \begin{array}{l} \nearrow (NO_2^-)_{sol} \\ \searrow (NO_2^-)_{sol} \end{array}$$

Table 2
Analysis of Impedance Diagrams of Fe–12 N HNO_3 at $j = 0$

Diagram	T^a	P^b	N^c	$\langle E\rangle^d$	$\langle J\rangle^d$
A	0	0	0	$+^e$	+
B	0	1	1	$-^f$	−
C	0	1	1	−	−
D	1	1	0	+	−
E	0	0	0	+	+

[a] *T*, number of turns.
[b] *P*, number of poles.
[c] *N*, number of zeros.
[d] $\langle E\rangle$ and $\langle J\rangle$, potential and current regulation.
[e] +, asymptotically stable.
[f] −, unstable.

One of the $(\mathrm{NO_2})_{ad}$ reductions is such that

$$(\mathrm{NO_2})_{ad} + e^- \rightarrow \mathrm{NO_2}^-$$

and the other reduction process in the presence of $\mathrm{Fe(II)}_{sol}$ is

$$(\mathrm{NO_2})_{ad} + \mathrm{Fe(II)}_{sol} \rightarrow \mathrm{Fe(III)}_{sol} + \mathrm{NO_2}^-$$

In the absence of pna, an autocatalytic reduction of $\mathrm{HNO_3}$ may be taking place:

$$\mathrm{HNO_2} + \mathrm{HNO_3} + 2\mathrm{H}^+ + 2e^- \rightarrow 2\mathrm{HNO_2} + \mathrm{H_2O}$$

This reaction, forming $\mathrm{H_2O}$ at the vicinity of the electrode, accelerates the iron dissolution reaction[56] and the current becomes higher than the diffusion-limiting current as was observed experimentally. $\mathrm{Fe(II)}_{sol}$ thus formed promotes further the reduction of $(\mathrm{NO_2})_{ad}$. A very strong interaction is thus built up. In the presence of pna, the $\mathrm{HNO_2}$ concentration is very low and thus no strong interaction can occur. The model predicts qualitatively the experimental results. These reactions are summarized in the following reaction scheme:

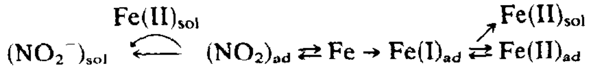

$$(\mathrm{NO_2^-})_{sol} \xleftarrow{\mathrm{Fe(II)}_{sol}} (\mathrm{NO_2})_{ad} \rightleftarrows \mathrm{Fe} \rightarrow \mathrm{Fe(I)}_{ad} \overset{\nearrow\,\mathrm{Fe(II)}_{sol}}{\rightleftarrows} \mathrm{Fe(II)}_{ad} \qquad \text{(VII)}$$

The surface coverages by $\mathrm{Fe(II)}_{ad}$ and $(\mathrm{NO_2})_{ad}$ form the reaction scheme similar to model (IV) shown in Section 5. Diagrams such as 18A and 18C can thus be explained.

Auxiliary Notation

A	reacting species
$(A)_0$	concentration of A at the electrode surface (mol cm^{-2})
$(A)_\infty$	concentration of A at the solution bulk (M)
A^-	anion of an acid HA
ac	alternating current, in particular sine wave signal
ad	"subscript" species adsorbed on the electrode surface
C	capacitance (F)
C_{dl}	double-layer capacitance (F)
D	diffusion coefficient (cm^2 sec^{-1})
dc	direct current, in particular steady state E or J value
E	electrode potential (V)
ΔE	ac voltage signal for impedance determination (V)
$\lvert\Delta E\rvert$	amplitude of ΔE
e^-	charge of electron
F	Faraday constant (96,500 C)
f	frequency (Hz)
Im	imaginary component of Z; $Z = \mathrm{Re} - j\,\mathrm{Im}$ (Ω)
J	current density (A cm^{-2})
$\bar{J}$	steady state value of J (A cm^{-2})
ΔJ	ac current signal for impedance determination (A)
$\lvert\Delta J\rvert$	amplitude of ΔJ (A)
j	$\sqrt{-1}$
K	rate constant for a unit surface area (mol sec^{-1} cm^{-2})
K_i	K for forward process i
K_{-i}	K for backward process i
L	inductance (H)
M	metal atom
N	number of zeros
P	passivating product
P	number of poles
p	Laplace parameter; $p = \sigma + j\omega$ (sec^{-1})

R_e	electrolyte resistance (Ω)
R_p	polarization resistance (Ω)
R_{st}	low inductive standard resistor
R_t	charge transfer resistance (Ω)
R	resistance (Ω)
Re	real component of Z; $Z = \mathrm{Re} - j\,\mathrm{Im}\ (\Omega)$
S	soluble dissolution product
sol	"subscript" species dissolved in the solution bulk
T	number of turns
t	time parameter
V_{SCE}	potential E with respect to KCl-saturated calomel electrode (V)
V_{SSE}	potential E with respect to K_2SO_4-saturated mercurous sulfate electrode (V)
x	parameter affecting the passivation process
Z	electrode impedance (Ω)
$Z(\omega)$	Z at frequency ω (Ω)
$\|Z\|$	modulus of Z; $Z = \|Z\| \exp(j\psi)$ (Ω)
Z_F	faradaic component in Z (Ω)
z	apparent dissolution valency (dimensionless)
β	coefficient linking the surface concentration and the fractional surface coverage (mol cm^{-2})
δ_f	thickness of passive film (nm)
δ_N	thickness of the Nernst diffusion layer (cm)
θ	fractional surface coverage (dimensionless)
$\bar{\theta}$	steady state value of θ
σ	real component of the Laplace parameter p (sec^{-1})
τ	relaxation time constant (sec)
Φ	diameter of disk electrode
ϕ	phase difference between two signals (rad)
ψ	phase shift between ΔE and ΔJ signal (rad)
Ω	rotation speed of disk electrode (rev min^{-1})
ω	angular frequency; $\omega = 2\pi f$ (rad sec^{-1})

References

1. H. H. Uhlig, Passivity of metals and alloys, *Corros. Sci.* **19**, 777–792 (1979); History of passivity, experiments and theories, in *Passivity of Metals*, R. P. Frankenthal and J. Kruger, eds., pp. 1–28, The Electrochemical Society of America, Princeton, New Jersey (1978).
2. First International Symposium on the Passivity of Metals, Heiligenberg near Darmstadt, Germany, 1957, proceedings in *Z. Elektrochem.* **62**, No. 6/7 (1958).
3. Second International Symposium on the Passivity of Metals, Toronto, Canada, 1962, contribution papers in *J. Electrochem. Soc.* **111** (1964).
4. Third International Symposium on the Passivity of Metals, Cambridge, England, 1970, contribution papers in *Electrochim. Acta* **17**, No. 2 (1972).
5. Fourth International Symposium on the Passivity of Metals, Warrenton, Virginia, 1976, *Passivity of Metals*, Corrosion Monograph Series, R. P. Frankenthal and J. Kruger, eds., The Electrochemical Society of America, Princeton, New Jersey (1978).
6. USA-Japan Seminar, Hawaii, 1975, *Passivity and Its Breakdown on Iron and Iron Base Alloys*, R. W. Staehle and H. Okada, eds., NACE, Houston (1976).
7. *Proceedings of the First Soviet-Japanese Seminar on Corrosion and Protection of Metals, Moscow*, 1977, Ya. M. Kolotyrkin, ed., Nauka, Moscow (1979).
8. A. T. Fromhold Jr., Ionic transport in passive layers, in *Passivity of Metals*, R. P. Frankenthal and J. Kruger, eds., The Electrochemical Society of America, Princeton, New Jersey (1978), pp. 57–81.
9. I. Epelboin and M. Keddam, Electrochemical techniques for studying passivity and its breakdown, in *Passivity of Metals*, R. P. Frankenthal and J. Kruger, eds., The Electrochemical Society of America, Princeton, New Jersey (1978), pp. 184–222.

10. I. Epelboin, Ç. Gabrielli, and M. Keddam, Non-steady-state techniques, Chapter 3 in a forthcoming volume of *Comprehensive Treatise of Electrochemistry*, S. Sarangapani *et al.*, eds., Plenum Press, New York.
11. R. P. Frankenthal, On passivity of iron and its alloys, in *Passivity and Its Breakdown on Iron and Iron Base Alloys*, R. W. Staehle and H. Okada, eds., NACE, Houston (1976), pp. 10–18.
12. U. F. Franck and R. Fitzhugh, Periodische Elektrodenprozesse und ihre Beschreibung durch ein mathematische Modell, *Z. Elektrochem.* **65**, 156–168 (1961).
13. I. Epelboin, C. Gabrielli, M. Keddam, J.-C. Lestrade, and H. Takenouti, The passivation of iron in a sulfuric acid medium, *J. Electrochem. Soc.* **119**, 1632–1637 (1972).
14. D. D. Macdonald, *Transient Techniques in Electrochemistry*, Plenum Press, New York (1977).
15. D. C. Grahame, Mathematical theory of the faradaic admittance (pseudocapacity and polarization resistance), *J. Electrochem. Soc.* **99**, 370C–385C (1952).
16. E. Warburg, Ueber das Verhalten sogennter impolarisirebarer Elektroden gegen Wechselstrom, *Ann. Phys. Chem.* (*Wiedermann*) **67**, 493–499 (1899).
17. J. E. B. Randles, Kinetics of rapid electrode reactions, *Disc. Faraday Soc.* **1**, 11–19 (1947).
18. H. Gerischer, Wechselstrompolarisation von Electroden mit einem potential bestimmenden Schritt beim gleichgewichtspotential, *Z. Phys. Chem.* **198**, 286–313 (1951).
19. H. Gerischer and W. Mehl, Zum Mechanismus der kathodischen Wasserstoffabscheidung an Quecksilber, Silber und Kupher, *Z. Elektrochem.* **59**, 1049–1059 (1955).
20. R. D. Armstrong and K. Edmonson, The impedance of metals in the passive and transpassive region, *Electrochim. Acta* **18**, 937–943 (1973).
21. I. Epelboin and M. Keddam, Faradaic impedance: diffusion impedance and reaction impedance, *J. Electrochem. Soc.* **117**, 1052–1056 (1970).
22. A. Finkelstein, Über passives Eisen, *Z. Phys. Chem.* **39**, 91–110 (1902).
23. J. L. Ord and J. H. Bartlett, Electrochemical behavior of passive iron, *J. Electrochem. Soc.* **112**, 160–161 (1965).
24. M. Pražák, V. Pražák, and V. L. Čfhal, Über den Aufbau der Passivschicht auf Chromstählen, *Z. Elektrochem.* **62**, 739–745 (1958).
25. N. Sato and G. Okamoto, Kinetics of the anodic dissolution of nickel in sulfuric acid solutions, *J. Electrochem. Soc.* **111**, 897–903 (1964).
26. H. J. Engell and B. Ilschner, Wechselstrom- und Impulsmessungen an passivieren Eisen electroden, *Z. Elektrochem.* **59**, 716–722 (1955).
27. N. E. Wisdom and N. Hackerman, Surface studies on passive iron, *J. Electrochem. Soc.* **110**, 318–325 (1963).
28. J. L. Ord, Measurement of overpotential parameters on passive electrodes, *J. Electrochem. Soc.* **112**, 46–49 (1965).
29. G. Arnowitz and N. Hackerman, The passivity of iron–chromium alloys, *J. Electrochem. Soc.* **110**, 633–640 (1963).
30. G. M. Schmidt and N. Hackerman, Electrical double layer capacity of iron during forced cathodic decay of passivity, *J. Electrochem. Soc.* **109**, 1096–1099 (1962).
31. R. V. Moshtev, Capacitance studies of passive iron in neutral solution by potentiostatic pulse method, *Ber. Bunsenges. Phys. Chem.* **72**, 452–459 (1968).
32. M. L. Boyer, I. Epelboin, and M. Keddam, Une nouvelle méthode potentiocinétique d'étude des processus électrochimiques rapides, *Electrochim. Acta* **11**, 221–235 (1966).
33. C. Gabrielli and M. Keddam, Progrès récents dans la mesure des impédances électrochimiques en régime sinusoïdal, *Electrochim. Acta* **19**, 355–362 (1974).
34. R. D. Giles, A. Hampson, N. A. Marshall, and R. J. Latham, The electrode impedance of iron in a borate buffer solution, *J. Electroanal. Chem.* **47**, 535–538 (1973).
35. K. G. Weil, Die Beziehung zwischen Ionenstrom und Spannung Innerhalb des Oxydschicht auf passivem Eisen, *Z. Elektrochem.* **59**, 711–715 (1955).
36. A. M. Sukhotin and K. M. Kartashova, Study of the passive iron electrode by dynamic measurement of its capacitance, *Russ. J. Phys. Chem.* **33**, 562–564 (1959).

37. R. R. Sayano and K. Nobe, Capacitance measurements during activation of passive nickel, *Corrosion NACE* **23**, 27–28 (1967).
38. A. M. Sukhotin and K. M. Kartashova, The passivity of iron in acid and alkaline solutions, *Corros. Sci.* **5**, 393–407 (1965).
39. B. Lovreček and J. Sefaja, Semiconducting aspects of the passive layer on chromium, *Electrochim. Acta* **17**, 1151–1155 (1972).
40. U. Stimming and J. W. Schultze, The capacity of passivated iron electrodes and the band structure of the passive layer, *Ber. Bunsenges. Phys. Chem.* **80**, 1297–1302 (1976).
41. T. Murakawa, T. Kato, and S. Nagaura, Differential capacity curves of iron in perchloric acid in the presence of anions, *Corros. Sci.* **7**, 657–664 (1967).
42. C. D. Kim and B. E. Wilde, Analog bridge method for differential capacitive measurements during the passivation of stainless steel in halide media, *Corrosion* (*Houston*) **28**, 26–29 (1972).
43. K. Sugimoto and Y. Sawada, Interfacial impedance of stainless steel under anodic polarization, *Boshoku-Gijutsu* **23**, 63–67 (1974).
44. K. J. Vetter, Über den Zustand des passiven Eisens, insbesondere in Salpetersäure, *Z. Elektrochem.* **55**, 274–280 (1951).
45. J. W. Schultze and U. Stimming, Tunnelprozess an passivierten Eisenelectroden, *Z. Phys. Chem.*, N.F., **98**, 285–302 (1975).
46. N. Hara, K. Sugimoto, and Y. Sawada, Impedance diagram of 18-8 stainless steel in passive and transpassive states in Na_2SO_4 solutions, *Bul. Met. Soc. Japan* **40**, 1304–1310 (1976).
47. S. Haruyama and T. Tsuru, Impedance characteristics of passive iron, in *Passivity of Metals*, R. P. Frankenthal and J. Kruger, eds., The Electrochemical Society of America, Princeton, New Jersey (1978), pp. 564–585.
48. I. Epelboin, M. Keddam, and Ph. Morel, Evidence of multistep reactions on iron, nickel and chromium electrodes immersed in a sulfuric acid solution, in *Proceedings of the Third International Congress on Metallic Corrosion*, MIR Publishers, Moscow (1966), pp. 110–118.
49. R. D. Armstrong, M. Henderson, and H. R. Thirsk, Impedance of chromium in the active–passive transition, *J. Electroanal. Chem.* **35**, 119–128 (1972).
50. R. D. Armstrong and M. Henderson, Impedance of transpassive chromium, *J. Electroanal. Chem.* **40**, 121–131 (1972).
51. R. D. Armstrong and M. Henderson, Active–passive transition of nickel in sulfuric acid, *J. Electroanal. Chem.* **39**, 222–224 (1972).
52. I. Epelboin and M. Keddam, Kinetics of formation of primary and secondary passivity in sulfuric aqueous media, *Electrochim. Acta* **17**, 177–186 (1972).
53. A. Jouanneau, M. Keddam, and M.-C. Petit, A general model of the anodic behavior of nickel in acidic media, *Electrochim. Acta* **21**, 287–292 (1976).
54. M. Cid, A. Jouanneau, D. Nganga, and M.-C. Petit, Comparison between the dissolution and passivity of nickel in sulfuric and hydrochloric acids, *Electrochim. Acta* **23**, 945–951 (1978).
55. C. Gabrielli, Régulation et analyse de systèmes à états stationnaires multiples: application à l'identification des processus de passivation électrochimique du fer, Thèse d'Etat, No. C.N.R.S., AO 8060 Paris (1973); *Métaux, Corrosion, Industrie*, Nos. 573, 574, 577, and 578 (1973).
56. I. Epelboin, C. Gabrielli, M. Keddam, and H. Takenouti, Model of the anodic behavior of iron in sulfuric acid medium, *Electrochim. Acta* **20**, 913–916 (1975).
57. I. Epelboin, C. Gabrielli, M. Keddam, and H. Takenouti, A coupling between charge transfer and mass transport leading to multi-steady states: application to localized corrosion, *Z. Phys. Chem.*, N.F., **98**, 215–232 (1975).
58. I. Epelboin, C. Gabrielli, and M. Keddam, Rôle de la diffusion dans les phénomènes de passivation et de corrosion localisée du fer en milieu acide, *Corros. Sci.* **15**, 155–171 (1975).
59. M. Baddi, C. Gabrielli, M. Keddam, and H. Takenouti, Kinetic interpretation of open-circuit potential decay curve of iron electrode in sulfuric acid medium, in *Passivity of Metals*, R. P. Frankenthal and J. Kruger, eds., The Electrochemical Society of America, Princeton, New Jersey (1978), pp. 625–645.

60. R. D. Armstrong and R. E. Firman, Impedance of titanium in the active–passive transition, *J. Electroanal. Chem.* **34**, 391–397 (1972).

61. A. Caprani, I. Epelboin, and Ph. Morel, Valence de dissolution du titane en milieu sulfurique fluoré, *J. Electroanal. Chem.* **43**, App. 2-9 (1973).

62. A. Caprani and J. P. Frayret, Behaviour of titanium in concentrated hydrochloric acid; dissolution–passivation mechanism, *Electrochim. Acta* **24**, 835–842 (1979).

63. I. Epelboin, M. Keddam, O. R. Mattos, and H. Takenouti, The application of the impedance method to the study of corrosion: the passivation of iron and Fe–Cr alloys, in *Proceedings of Seventh International Congress on the Metallic Corrosion*, Abraco, Rio de Janeiro (1979), pp. 1977–1988.

64. I. Epelboin, M. Keddam, O. R. Mattos, and H. Takenouti, The dissolution and passivation of Fe and Fe–Cr alloys in acidified sulfate medium: influence of pH and Cr content, *Corros. Sci.* **19**, 1105–1112 (1979).

65. C. Gabrielli, M. Keddam, and H. Takenouti, Interprétation phénoménologique de la passivation spontanée du fer en milieu nitrique concentré, *J. Electroanal. Chem.* **61**, 367–371 (1975).

66. C. Gabrielli, M. Keddam, E. Stupnišek-Lisac, and H. Takenouti, Etude du comportement anodique de l'interface fer–acide nitrique à l'aide d'une régulation à résistance négative, *Electrochim. Acta* **21**, 757–766 (1976).

67. H. Shirai, A-c polarography study; 4. the minimum wave of nickel, indium and copper (in Japanese), *J. Chem. Soc. Japan* **81**, 1248–1253 (1960).

68. N. Tanaka, T. Takeuchi, and R. Tamamushi, The reduction of indium(III) in thiocyanate solutions at the dropping mercury electrode, *Bull. Chem. Soc. Japan* **37**, 1435–1439 (1964).

69. G. Salié, Zur Deutung von Impedanzen mit negativen Realteil bei elektrochemischen Phasengrenzreactionen, *Z. Phys. Chem.* **253**, 406–410 (1973).

70. R. de Levie and A. A. Husovsky, On the negative faradaic admittance in the region of the polarographic minimum of In(III) in aqueous NaSCN solution, *J. Electroanal. Chem.* **22**, 29–48 (1969).

71. P. F. King and H. H. Uhlig, Passivity in iron–chromium binary alloys, *J. Phys. Chem.* **63**, 2026–2032 (1959).

72. Ya. M. Kolotyrkin, Electrochemical behaviour and anodic passivity mechanism of certain metals in electrolyte solution, *Z. Elektrochem.* **62**, 664–669 (1958).

73. R. P. Frankenthal, On the passivity of iron–chromium alloys, *J. Electrochem. Soc.* **114**, 542–547 (1967).

74. R. D. Parmentier, Neutristor analysis techniques for non-linear distributed electronic systems, *Proc. IEEE* **58**, 1829–1837 (1970).

75. M. Keddam, O. R. Mattos and H. Takenouti, Reaction model for iron dissolution studies by electrode impedance, *J. Electrochem. Soc.* **128**, 257–274 (1981).

76. J. O'M. Bockris, D. Dràzic, and A. R. Despic, The electrode kinetics of the deposition and dissolution of iron, *Electrochim. Acta* **4**, 325–361 (1961).

77. A. A. El Miligy, D. Geana, and W. J. Lorenz, A theoretical treatment of the kinetics of iron dissolution and passivation, *Electrochim. Acta* **20**, 273–281 (1975).

78. N. Sato and M. Cohen, The kinetics of anodic oxidation of iron in neutral solution, *J. Electrochem. Soc.* **111**, 512–522 (1964).

79. H. Wroblowa, V. Brusic, and J. O'M. Bockris, Ellipsometric investigation of anodic film growth on iron in neutral solution; the passive film, *J. Phys. Chem.* **75**, 2823–2829 (1971).

80. Ph. Morel, Contribution à l'étude des mécanismes de dissolution du fer, du nickel et du chrome, par l'analyse des courbes de polarisation anodique, Thèse d'Etat, No. C.N.R.S. AO 2346, Paris (1968).

81. N. Sato, K. Kudo, and M. Miki, Anodic passivation behaviour of nickel in neutral solutions, *Bull. Japan. Inst. Met.* **35**, 1007–1016 (1971).

82. J. Osterwald, Die Stromspannungskurve des Eisens in Schwefelsäure beim Übergang von aktiven in des passiven Zustand, *Z. Elektrochem.* **66**, 401–406 (1962).

83. I. Epelboin, M. Keddam, and J.-C. Lestrade, Faradaic impedances and intermediates in electrochemical reactions, *Disc. Faraday Soc.* **56**, 264–275 (1973).
84. I. Epelboin, C. Gabrielli, M. Keddam, and H. Takenouti, Oscillatory and non-oscillatory phenomena connected with passivity of metals, in *Kinetics of Physicochemical Oscillations*, U. F. Franck, ed., preprint II (1979), pp. 297–306.
85. K. J. Vetter and F. Gorn, Die instationäre Korrosion des passiven Eisens in saurer Lösung, *Werst. Korros.* **21**, 703–711 (1970).
86. K. E. Heusler, Untersuchung des Auflösung des passiven Eisens in Schwefelsäure mit des rotierenden Scheiben-Ring Elektrodes, *Ber. Bunsenges. Phys. Chem.* **72**, 1197–1205 (1968).
87. N. Cabrera and N. F. Mott, Theory of the oxidation of metals, *Rep. Prog. Phys.* **12**, 163–184 (1948).
88. L. Young, *Anodic Oxide Films*, Academic Press, New York (1960).
89. D. J. Wheeler, A-c electromodulated spectroscopy and its application to the study of passive layers on iron, Ph.D., Case Western Reserve University, Cleveland, Ohio (1976).
90. M. Keddam, P. Mirebeau, and H. Takenouti, An a-c impedance approach of the passive behavior of crystalline Fe and amorphous $Fe_{80}B_{18}Mo_2$ in sulfuric medium, in *Extended Abstracts of the Fall Meeting of the Electrochemical Society of America*, Los Angeles, 1979, paper No. 262, Electrochemical Society of America, Princeton, New Jersey (1979), pp. 675–678.
91. K. J. Vetter, *Electrochemical Kinetics*, Academic Press, New York (1967).
92. B. MacDougall and M. Cohen, Mechanism of the anodic oxidation of nickel, *J. Electrochem. Soc.* **123**, 1783–1789 (1976).
93. J. J. Podestá, R. C. V. Piatti, and A. J. Arvía, The potentiostat current oscillations at iron–sulfuric acid solution interface, *J. Electrochem. Soc.* **126**, 1363–1367 (1979); Discussions by M. Keddam, C. Gabrielli, and H. Takenouti, *J. Electrochem. Soc.* **127**, 2648–2649 (1980).
94. P. Glansdorff and I. Prigogine, *Structure, Stabilité et Fluctuations*, Masson, Paris (1971).
95. C. G. Law and J. Newman, A model for the anodic dissolution of iron in sulfuric acid, *J. Electrochem. Soc.* **126**, 2150–2155 (1979).
96. J. J. Miksis and J. Newman, Primary resistances for ring-disk electrodes, *J. Electrochem. Soc.* **123**, 1030–1036 (1976).
97. M. Keddam, O. R. Mattos, and H. Takenouti, Ohmic drop and multiplicity of the steady-states: Case of Fe-5Cr in 1 *M* H_2SO_4, *Electrochim. Acta* **24**, 103–105 (1979).
98. C. Gabrielli and M. Keddam, Réactions hétérogènes couplées par la diffusion: Etats stationnaires multiples, impédance et stabilité, *J. Electroanal. Chem.* **45**, 267–277 (1973).
99. K. F. Bonhoeffer, Über periodische chemische Reaktionen, *Z. Elektrochem.* **51**, 24–37 (1948).
100. M. Karšulin, M. Stepinac-Gatin, and E. Stupnišek-Lisac, 22nd Meeting of ISE, Dubrovnik, Yugoslavia, 1970; E. Stupnišek-Lisac, Oksidacija željezo/II/-iona u dušičoj Kiselini, Dissertation, University of Zagreb, Zagreb, 1975.

4

Electrochemical Passivation of Metals

NORIO SATO and GO OKAMOTO

1. Introduction

It is common knowledge that metallic iron and nickel placed in acidic solutions corrode with evolution of hydrogen gas. In concentrated nitric acid, however, they suddenly become protected against corrosion some time after violent metal dissolution and gas evolution have occurred. A sudden decrease of metal dissolution is also observed when they are anodically polarized in acid and neutral solutions. The unstable surface of actively corroding metals in aqueous solutions can thus sometimes be made stable in the presence of a strong oxidant or by polarizing the electrode potential in the anodic (positive) direction. The phenomena, which was found in the days of Faraday,(1) is called the electrochemical passivation of metals, and the corrosion-resistance state of the stable surface is called the passive state, as contrasted with the active state of the corroding surface; the term *chemical passivation* is sometimes used for the passivation caused by oxidants and the *anodic passivation* for the anodic formation of passivity.

According to Wagner,(2) the phenomenological definitions of electrochemical passivity are as follows:

NORIO SATO • Electrochemistry Laboratory, Faculty of Engineering, Hokkaido University, Sapporo, Japan. **GO OKAMOTO** • Applied Chemistry Division, Faculty of Science, Science University of Tokyo, Tokyo, Japan.

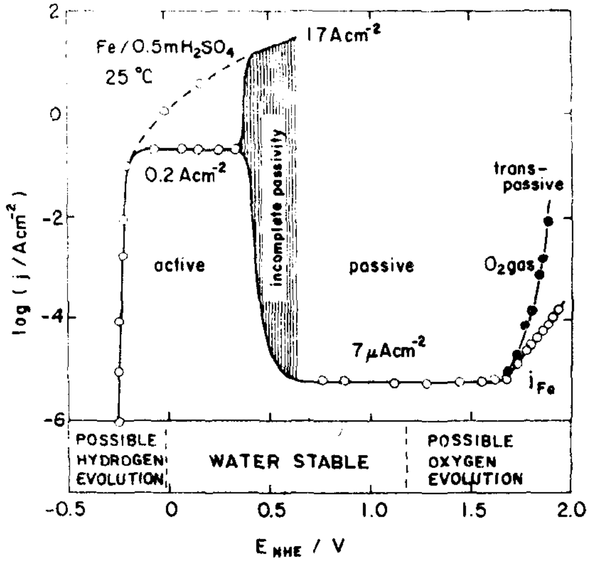

Figure 1. Potentiostatic anodic polarization curve of iron in 0.5 m H_2SO_4, showing characteristics of anodic passivation (Franck and Weil(70); Bonhoeffer(27)). J_{Fe} is the iron dissolution current density.

A metal is passive if, on increasing the electrode potential toward more noble values, the rate of anodic dissolution in a given environment under steady state conditions becomes much less than the rate at some less noble potential. Alternatively, a metal is passive if, on increasing the concentration of an oxidizing agent in an adjacent solution the corrosion rate, in the absence of external current, is much less than the rate at some lower concentration of oxidizing agent. These alternative definitions, one for the anodic passivity and the other for the chemical passivity, are in fact electrochemically equivalent to one another as described below.

Suppose an iron electrode is made anodic in† 0.5 m H_2SO_4 by using an external device called a potentiostat, which automatically adjusts electrolytic current to potential, and the potential of the iron electrode is gradually increased in the anodic direction. The resulting potentiostatic polarization curve of an iron anode is shown in Figure 1. Iron in this solution is active and corrôdes without external current producing iron(II) aqua-ion and hydrogen gas, where the electrochemical theory of corrosion applies. As the potential rises, the anodic dissolution current of iron first increases following a Tafel relation between potential and current, and then reaches a diffusion-limited current of about 200 mA/cm^2, which depends on the hydrodynamic flow of

† *Editor's note.* Although a capital M is conventionally used to stand for molarity, the author has used a lowercase m throughout.

solution. When there is no diffusion control, the true current density is estimated to be 0.2–17 A/cm^2 by short-time transient measurements. Further rise of the potential leads to a sudden decrease of the current to a value orders of magnitude lower, and a thick diffusion layer probably containing a hydrated salt film of $FeSO_4$ dissolves leaving a bright metallic surface. At this point, a very thin film called the passive film is formed on the surface, and iron becomes passive. In a potential region of incomplete passivity, the anodic current often oscillates between the active current and the passive current. The critical passivation potential is located at about +0.5 V in the normal hydrogen electrode (NHE) potential scale, and the passive current density diminishes to about 7 μA/cm^2 in the steady state. On further change of the potential, the current density remains at the low value of about 7 μA/cm^2, and the anodic dissolution product is now iron(III) aqua-ion. Water is electrochemically stable up to about +1.2 V (NHE) at which the equilibrium oxygen electrode potential is reached, but no appreciable oxygen evolution is observed until the potential exceeds +1.6 V (NHE).

Figure 2 illustrates the passivation of iron in nitric acid solution, where no external anodic current is applied. In dilute nitric acid solution iron is active, but it becomes passive above a critical HNO_3 concentration. In nitric acid nitrate ion is reduced to nitrous acid accepting electrons from the electrode:

$$NO_3^- + 3H^+ + 2e = HNO_2 + H_2O \qquad (1)$$

The iron electrode which donates electrons to the nitrate ion is thus anodically polarized producing iron ions in the acid. According to the electrochemical theory of metal corrosion, the corrosion potential is controlled by both the

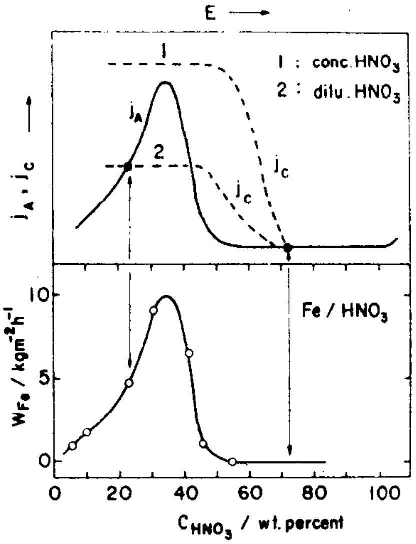

Figure 2. Corrosion rate of iron in nitric acid solution as a function of HNO_3 concentration and schematic polarization characteristics representing active corrosion and passivity (Tomashov[74]).

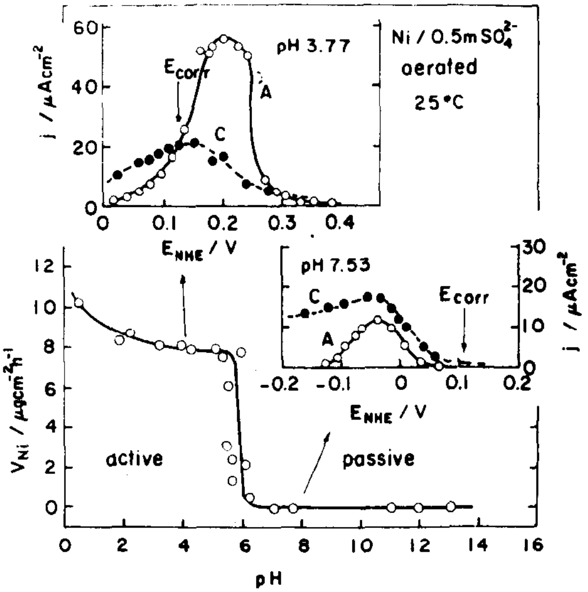

Figure 3. Corrosion rate of nickel in aerated 0.5 *m* sodium sulfate solution as a function of pH, and polarization characteristics of nickel in acidic and neutral solutions (Okamoto and Sato[(75)]). *A* is the anodic polarization curve, *C* the cathodic polarization curve.

anodic polarization curve of the metal dissolution and the cathodic polarization curve of the reduction of the oxidizing agent, as schematically shown in Figure 2. As the HNO_3 concentration is increased, the corrosion potential of iron shifts to more noble values in the active corrosion region until it reaches a critical potential above which iron passivates.

Figure 3 serves to show, as an additional example of chemical passivation, that nickel is passive in the range of neutral and alkaline pH in aerated sulfate solutions, while it is active in the acidic pH range. The active–passive transition occurs at around pH 6, above which the anodic dissolution current of nickel is smaller than the cathodic oxygen reduction current in the active potential region.

The above two illustrations demonstrate that the passivation due to an oxidizing agent is essentially equivalent to anodic passivation. In this chapter, therefore, anodic passivation of metals in aqueous solutions containing no oxidizing agent will be considered.

2. Potentiostatic Anodic Polarization Curves

2.1. General View

The form of the anodic current density–potential curve is characteristic of the transition from active to passive states showing a sharp discontinuous

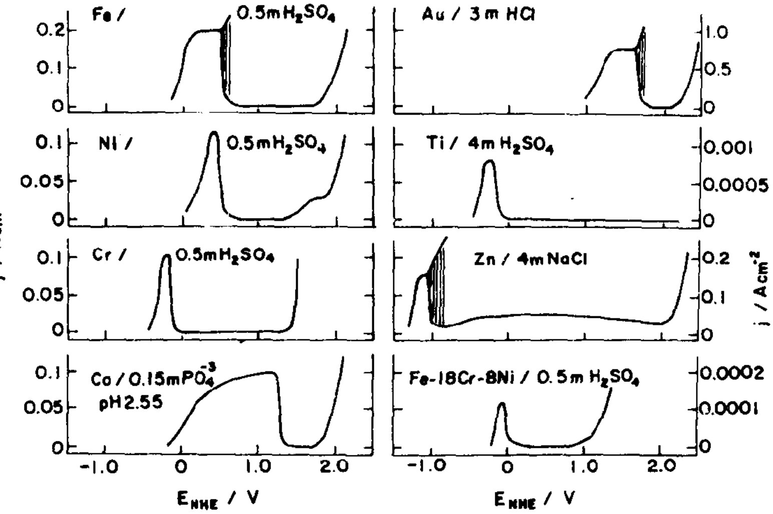

Figure 4. Potentiostatic anodic polarization curves of various passivable metals: Fe (Bonheoffer[27]), Ni (Sato and Okamoto[76]), Cr (Kolotyrkin[77]), Co (Ohtsuka[44]), Au (Franck[78]), Ti (Tomashov, Chernova, Ruskol, and Ayuyan[79]), Zn (Franck[78]), 18Cr–8Ni stainless steel (Okamoto[80]).

decrease in the anodic current density above a critical potential called the passivation potential. Figure 4 shows the anodic polarization curve for iron in acid, nickel in acid, chromium in acid, cobalt in neutral solution, gold in acid, titanium in acid, zinc in an alkaline solution, and stainless steel in acid. In the potential range of passivity, there is a small anodic dissolution current called

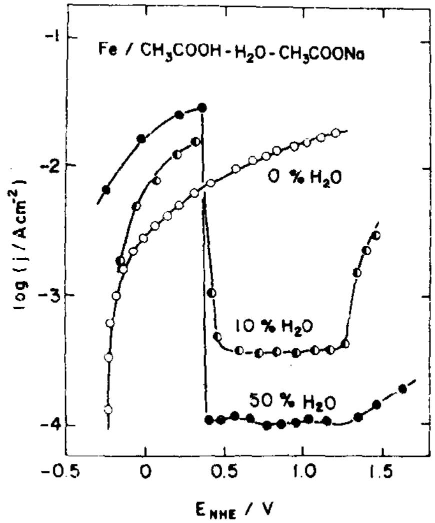

Figure 5. Effect of water on anodic polarization curve of iron in acetic acid solution (Kiss, DoNgoc, and Varsanyi[81]).

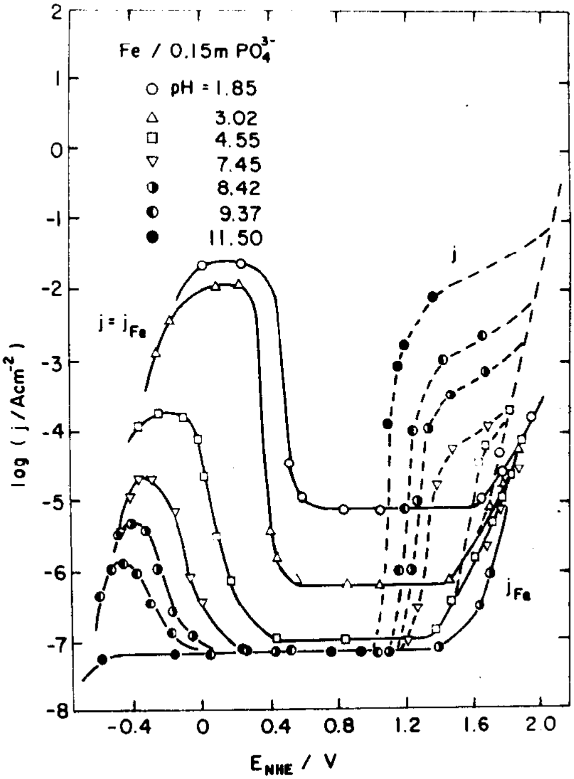

Figure 6. Potentiostatic anodic polarization curves of iron in 0.15 *m* sodium phosphate solutions of different pH values (Noda[82]).

the passive current or passivity-maintaining current, which is either potential independent or slightly potential dependent. Beyond the passive potential range, in most of passivable metals, transpassivation occurs with a potential-dependent metal dissolution current which increases to orders of magnitude larger than the passive dissolution current. In some cases, secondary passivation occurs when the potential is raised beyond the potential range of transpassivity. Furthermore, the oxygen electrode reaction takes place, if the passive film is electron conducting.

In a nonaqueous solution, the anodic polarization curve of metals is usually very much affected by the presence of a small amount of water. Metals that passivate in aqueous solutions do not necessarily passivate in nonaqueous solutions. Figure 5 shows the effect of water on the anodic polarization curve of iron in nonaqueous acidic solution. Iron passivates only in the presence of water. Similar results were also reported with iron in acidic dimethylformamid solution (Jänchen and Schwabe[3]) and chromium in acidic methanol solution (Kolotyrkin and Kossii[4]).

2.2. Iron

The potentiostatic anodic polarization curve of iron depends on the pH of the solution, as shown in Figure 6. The pH dependence of the active dissolution current j_a at constant potential, active dissolution current peak j_m, passive current j_p, and transpassive current j_{tp} are all shown in Figure 7. The positive pH dependence of j_a indicates that hydroxide ions participate in the anodic dissolution. The mechanism of this reaction was discussed by Heusler(5) and Bockris.(6) The negative pH dependence of j_m, on the other hand, indicates that the passivation of iron is facilitated by hydroxide ions in the solution. In the transpassive state where iron dissolves as iron(II) in nitrate solution (Franke, Forker, and Schultheiss(7)), the anodic dissolution current j_{tp} is nearly independent of pH; the dissolution mechanism remains to be studied. The potential-independent, passive current, j_p, also decreases as the pH is increased in an acidic pH range, indicating that the passivity is more stable in high pH solutions than in low pH solutions; the dissolution mechanism will be discussed later.

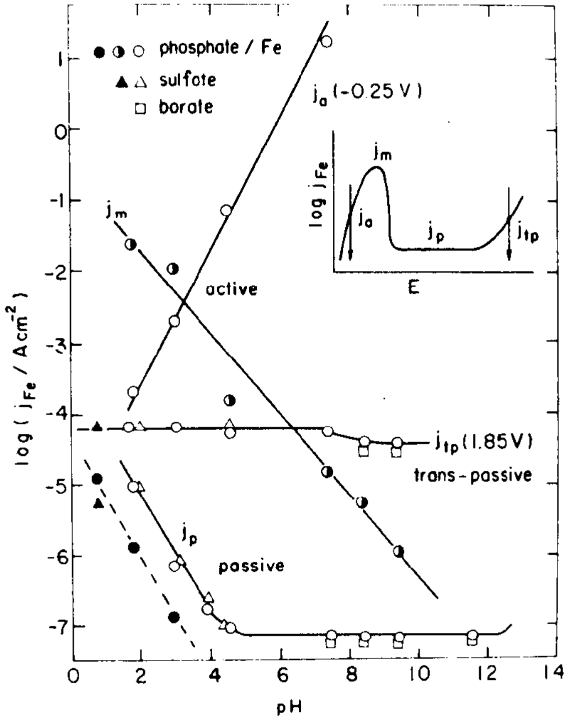

Figure 7. pH dependence of active anodic dissolution current j_a, active anodic dissolution peak current j_m, passive dissolution current j_p, and transpassive dissolution current j_{tp} in phosphate, sulfate, and borate solutions. ○, △, □, ◐: Noda(82); ▲, Franck and Weil(70); ●, Vetter.(47)

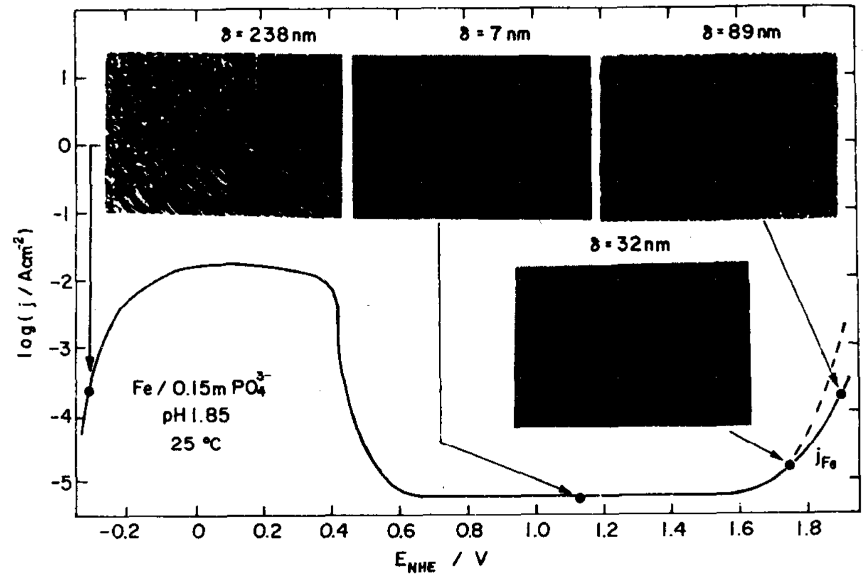

Figure 8. Microscopic appearance of iron surface anodically polarized in the active, the passive, and the transpassive potential regions (Noda[82]). δ is the surface layer thickness removed during anodic polarization.

Figure 8 shows the microscopic appearance of a surface of iron anodically polarized at different potentials in acid solution. In the active state, the etch pattern is different in different crystallographic grains, suggesting that the anodic dissolution takes place on the bare metal surface. The transpassive dissolution, on the other hand, produces a uniform etch pattern independent of the crystallographic orientation of the grains. Orientation-independent etch patterns of iron were also observed in the transpassive dissolution in nitrate

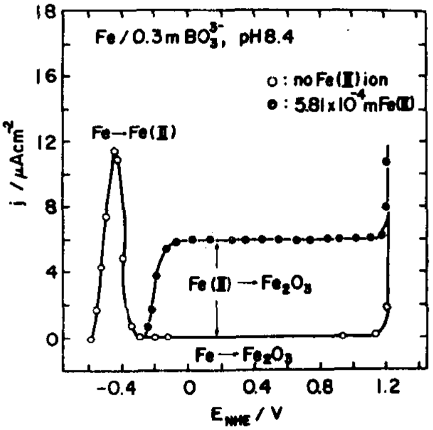

Figure 9. Potentiostatic–anodic polarization curves of iron in steady state in borate solution of pH 8.4 containing iron(II) ions (Nagayama and Cohen[83]).

solution (Franke, Forker, and Schultheiss(7)). This may provide evidence for a transpassive film existing on the surface, through which the anodic dissolution takes place.

In neutral solutions containing iron(II) ions, the anodic current in the passive potential range is much greater than the passive current and increases with increasing iron(II) ion concentration, as shown in Figure 9. This anodic current is due to the anodic oxidation of iron(II) ions to iron(III) oxyhydroxide, which precipitates to form a thick layer on the surface:

$$Fe_{aq}^{2+} + 2H_2O \rightarrow FeOOH + 3H_{aq}^{+} + e \qquad (2)$$

2.3. Nickel

Nickel is characterized by the potential-dependent transpassive dissolution current and the secondary passivation that occurs at high potentials, as shown in Figure 10. Secondary transpassive dissolution is also observed beyond the secondary passivity potential region. The dissolution valency of nickel is Ni(II) in the active, primary passive, and transpassive states, and is probably Ni(II) also in the secondary passive and transpassive region. The pH dependence of the anodic polarization curve is shown in Figure 11. Similar to iron, the anodic dissolution of nickel in the active and the passive states depends on pH, but the transpassive dissolution at more anodic potentials appears nearly independent of pH. The etch pattern observed depends on the orientation of crystallographic grains in the active state, while it is orientation-independent in the transpassive dissolution (Sato(8))

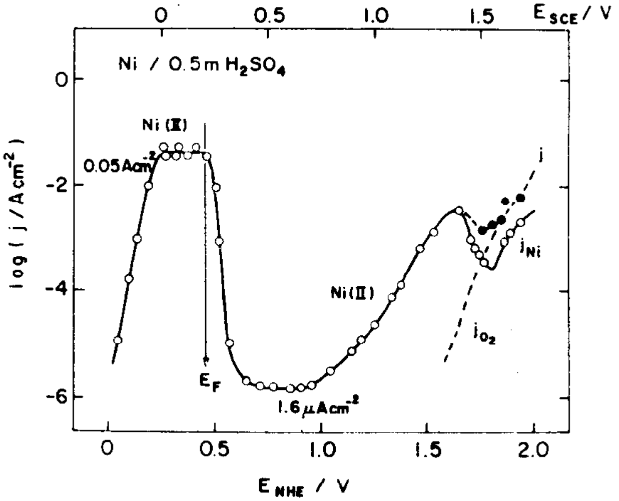

Figure 10. Potentiostatic-anodic polarization curve of nickel in 0.5 *m* H_2SO_4 solution (Sato(84); Sato and Okamoto(76); Vetter and Arnold(85)).

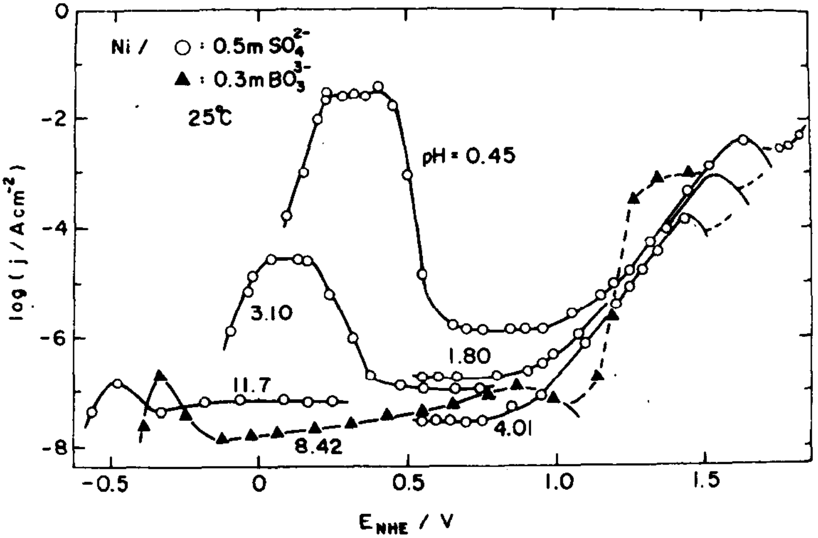

Figure 11. Anodic polarization curve of nickel in sulfate and borate solutions of pH from acid and base (Sato and Okamoto[76]; Sato and Kudo[41]).

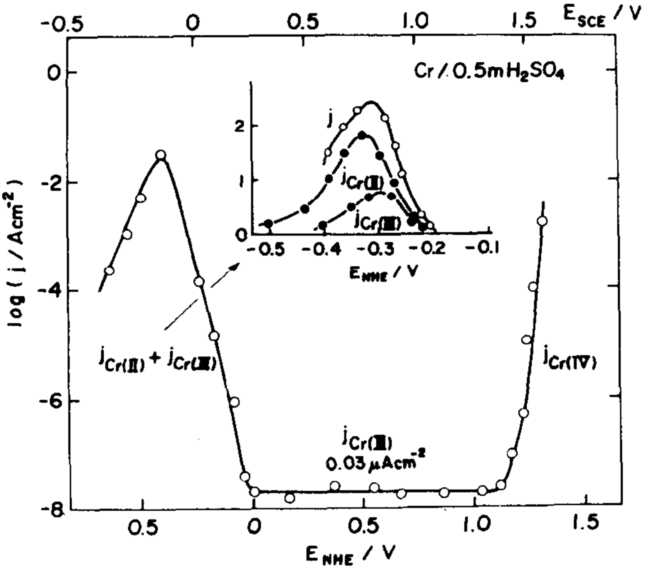

Figure 12. Anodic polarization curve of chromium in 0.5 *m* sulfuric acid (Kolotyrkin[77]) and ionic valency of dissolution in the active state (Armstrong, Henderson, and Thirsk[12]).

2.4. Chromium

Figure 12 shows the anodic polarization curve of chromium in acid solution and the dissolution valency of chromium in the active state. Chromium dissolves as Cr(II) and Cr(III) ions in the active state, as Cr(III) ions in the passive state, and as Cr(IV) ions in the transpassive state (Plieth and Vetter[9]). No oxygen evolution is usually observed on chromium because the transpassive dissolution takes place at potentials more cathodic than the anodic oxygen evolution potential.

2.5. Cobalt

Cobalt exhibits three different degrees of passivity and transpassivity in neutral solution, as shown in Figure 13. The first and second passivity region in neutral solution become the active dissolution region in an acidic solution. The

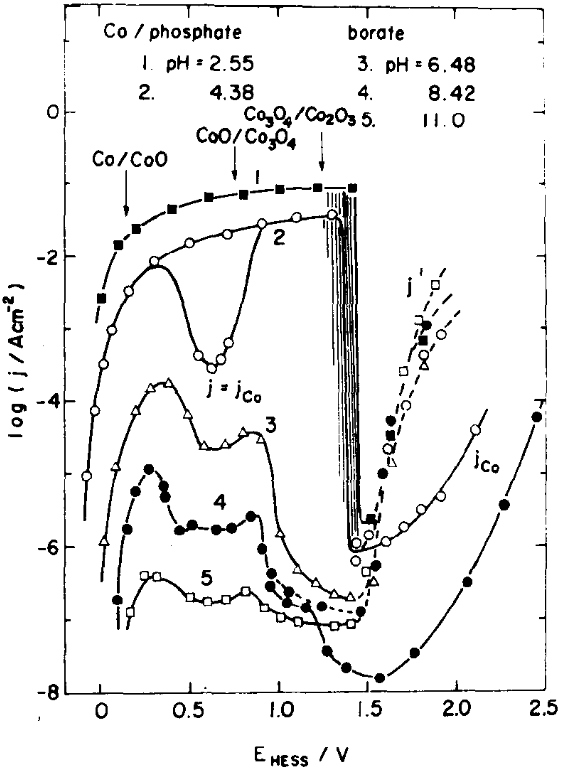

Figure 13. Potentiostatic anodic polarization curve of cobalt in 1-hr steady state in 0.15 *m* phosphate and 0.15 *m* borate solutions of pH ranging from acid to base (Ohtsuka[44]). E_{HESS} is the potential referred to the hydrogen electrode in the same solution. j_{Co} is the average dissolution current density for 1 hr.

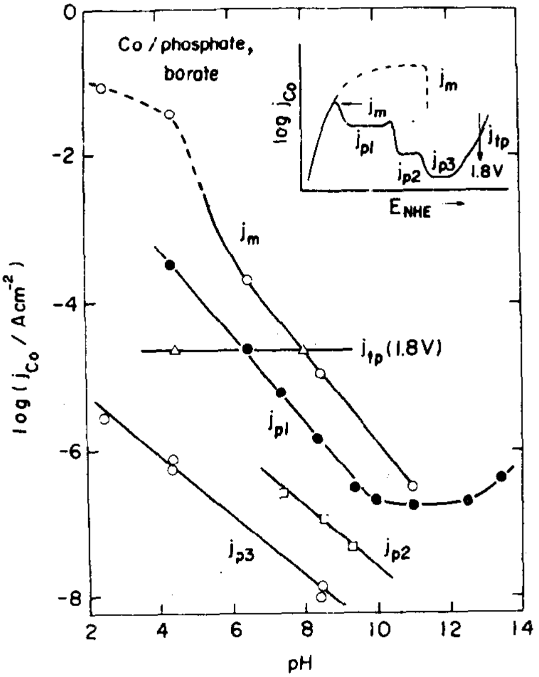

Figure 14. pH dependence of anodic active dissolution current density peak j_m, first degree passive current density j_{p1}, second degree passive current density j_{p2}, third degree passive current density j_{p3}, and transpassive current density j_{tp} for cobalt electrode in 1-hr steady state in phosphate and borate solutions (Ohtsuka(44)).

anodic active dissolution current peak, the potential-independent passive current at three different degrees of passivity, and the transpassive dissolution current at constant potential are shown in Figure 14. It can be seen that the transpassive dissolution is independent of pH, while the passive currents decrease with increasing pH.

3. Active–Passive Transition

3.1. Electrode Impedance

During the transition from active to passive states, the electrode impedance, which may provide information about the electric double layer on the metal surface, changes with potential. Figure 15 shows schematic impedance spectra of iron at different potentials in the active–passive transition potential range. In the potential range where only active dissolution occurs, the electrode impedance shows two semicircles in the complex impedance plane; semicircle 2 at low frequencies, which is a faradaic pseudo-capacitance at high current density (b) and a pseudo-self-inductance at low current density (a), can be separated from semicircle 1 at high frequencies, which represents the relaxation of the electric double layer. Epelboin and Keddam(10) ascribed the inductive and capacitive impedance at low frequencies to an intermediate

T2/7 B 10

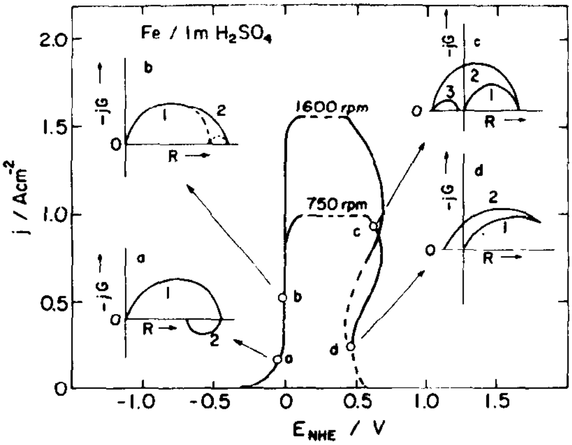

Figure 15. Steady state polarization curve in active–passive transition potential range of rotating iron electrode at two different rotation speeds in 1 *m* sulfuric acid and schematic impedance spectra at four different potentials designated: (a) active dissolution at low current, (b) active dissolution at high current, (c) passivity at high current (d) passivity at low current. With decreasing frequency from $\omega \to \infty$ to $\omega \to 0$, impedance follows semicircle 1, 2, and 3 in complex impedance plane $Z = R - JG$ (Epelboin, Gabrielli, Keddam, and Takenouchi(15)).

absorbed species $FeOH_{ads}$ which dissolves in solution as a $FeOH^+$ ion (Bockris, Drazic, and Despic(6)). In the potential range where passivation is in progress (c and d), the impedance falls on either a high-frequency circle 1 representing the electric double layer, or a low-frequency circle 2 which may be related to the relaxation of a passivating species, or a very-low-frequency circle 3 which is due to convective diffusion at high current densities. Similar results were also observed with nickel (Armstrong and Henderson(11)), chromium (Armstrong, Henderson, and Thirsk(12)), titanium (Armstrong and Firman(13)), and molybdenum (Heuman and Klimmeck(14)). Based on the impedance measurements, Epelboin, Gabrielli, Keddam, and Takenouchi(15) suggested the following reaction scheme for active dissolution and passivation of iron in acid:

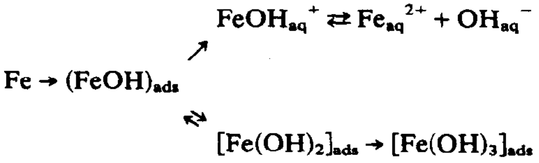

$$\begin{array}{lll} & & FeOH_{aq}^{+} \rightleftarrows Fe_{aq}^{2+} + OH_{aq}^{-} \\ & \nearrow & \\ Fe \rightarrow (FeOH)_{ads} & & \\ & \searrow\!\!\!\nwarrow & \\ & & [Fe(OH)_2]_{ads} \rightarrow [Fe(OH)_3]_{ads} \end{array} \qquad (3)$$

where $[Fe(OH)_2]_{ads}$ is a passivating species and $(FeOH)_{ad}$ an adsorbed intermediate for both active dissolution and passivation.

An infinite or very high frequencies, the surface coverage of intermediate and passivating species is frozen, so that the impedance gives the double-layer capacitance at frozen coverage of adsorbed species on the surface. Figure 16 shows the double-layer capacitance for chromium and titanium together with

T277

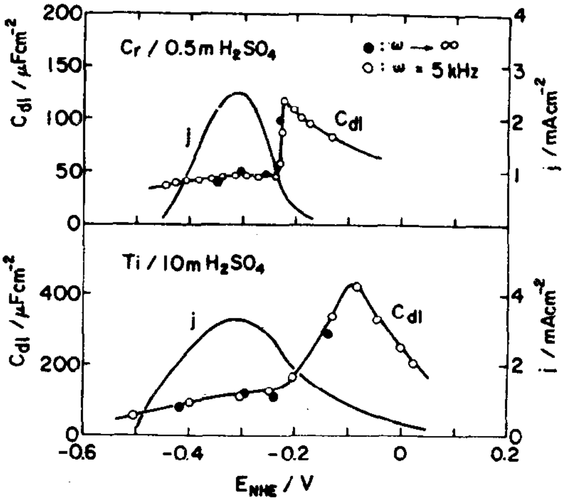

Figure 16. Electrical double-layer capacity–potential and anodic current density–potential curves in the active–passive transition potential range for chromium in 0.5 *m* sulfuric acid (Armstrong, Henderson, and Thirsk$^{(12)}$) and titanium in 10 *m* sulfuric acid (Armstrong and Firman$^{(13)}$); double-layer capacity at infinite frequency (●) and at 5 kHz (○).

their steady state polarization curves in the active–passive transition potential range. A sudden increase of the double-layer capacity is observed in the transition from the active to the passive state, indicating that passivation produces some change in structure and dielectric property of the electric double layer.

3.2. Flade Potential

When the anodic current that maintains the passivity is interrupted, passivity decays with time in the manner shown in Figure 17. The potential spontaneously decreases to an intermediate arrest potential before decaying rapidly to the active value. This arrest potential was first found by Flade$^{(16)}$ and later called the Flade potential. In the case of nickel, there are two Flade potentials corresponding to the primary and the secondary passivity.

Bonhoeffer$^{(17)}$ suggested that the Flade potential was equal to the passivation potential observed in the potentiostatic anodic polarization curve. Although agreement of the two potentials is not always clear because of a range of potential in which passivation does not come to an end, these potentials have been regarded as representing a characteristic potential for passivation.

Figure 18 shows the pH dependence of the Flade potential for iron and nickel. The Flade potential is a linear function of pH and, in most cases, is given by the relation

$$E_F = E_F^\circ - 0.059\,\mathrm{pH} \qquad (4)$$

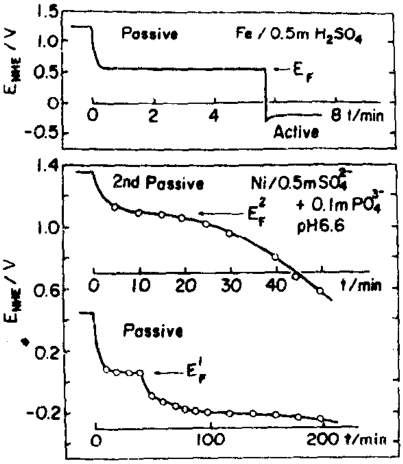

Figure 17. Spontaneous decay of passivity as a function of time, showing the Flade potential of iron in 0.5 *m* sulfuric acid (Franck and Weil(70)) and nickel in 0.5 *m*, pH 6.6 sulfate solution (Sato and Okamoto(76)).

The Flade potential and its pH dependence are characteristic of the passive film on metals, and it has been assumed that the Flade potential is the potential of an oxide-covered metal electrode. The overall reactions of this type of electrode are

$$\mathrm{Me} + n\mathrm{H_2O} \rightleftarrows \mathrm{MeO}_n + 2n\mathrm{H}^+ + 2ne \qquad (5)$$

and

$$\mathrm{MeO}_n + m\mathrm{H_2O} \rightleftarrows \mathrm{MeO}_{n+m} + 2m\mathrm{H}^+ + 2me \qquad (6)$$

Göhr and Lange(105) explained the Flade potential of iron as the equilibrium potential of the following reaction:

$$2\mathrm{Fe_3O_4} + \mathrm{H_2O} \rightleftarrows 3\gamma\text{-}\mathrm{Fe_2O_3} + 2\mathrm{H_{aq}}^+ + 2e \qquad (7)$$

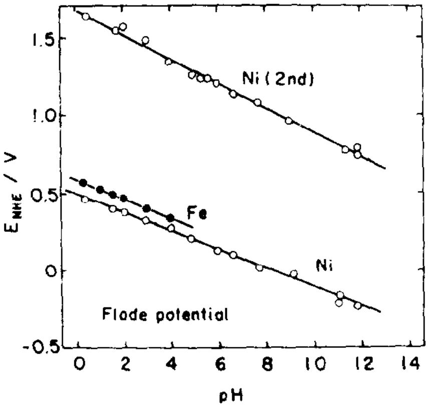

Figure 18. pH dependence of the Flade potential of iron (Franck(23)) and nickel (Sato and Okamoto(76)). E_F(iron) = +0.58–0.058 pH, E_F(nickel, primary passivity) = +0.48–0.060 pH. E_F(nickel, secondary passivity) = +1.60–0.075 pH.

Along the same line, Pryor(18) assumed the Flade potential to be determined by the reaction between excess oxygen in the passive film and hydrogen ions and electrons. Wagner(19) also described the Flade potential of iron as the potential of an iron-deficient magnetite in which excess oxygen reacts with hydrogen ions and electrons. Schottky(20) suggested that the reaction involves iron ions in the diffusion layer in solution adjacent to the metal surface:

$$2\mathrm{FeOH}_{\mathrm{aq}}^{+} + \mathrm{H_2O} \rightleftarrows \gamma\text{-}\mathrm{Fe_2O_3} + 4\mathrm{H}_{\mathrm{aq}}^{+} + 2e \tag{8}$$

Nagayama and Cohen(21) found later that, in a limited range of neutral pH, the rest potential of passive iron was a function of iron(II) ion concentration as well as pH. Another approach was made by Uhlig,(22) who assumed a chemisorbed atomic and molecular oxygen on the passive iron surface and proposed the reaction of the form

$$\mathrm{O{-}O_2(ads.\ on\ Fe)} + \mathrm{Fe} + 6\mathrm{H}_{\mathrm{aq}}^{+} + 3e \rightleftarrows \mathrm{Fe}_{\mathrm{aq}}^{3+} + 3\mathrm{H_2O} \tag{9}$$

3.3. Galvanostatic Passivation

When an anodic current density which is greater than the minimum current density j_m for passivation is applied to a metal in solution, it takes some time before the metal goes from the active to the passive state. After an induction time, τ_p, the potential rises suddenly as shown in Figure 19. This

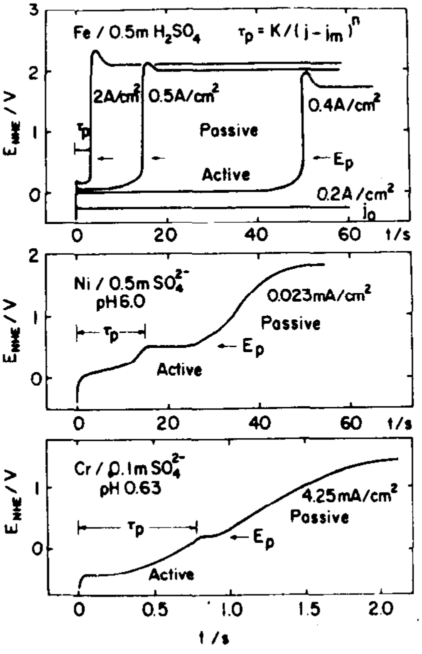

Figure 19. Potential–time curves for galvanostatic passivation of iron in 0.5 *m* sulfuric acid solution (Franck(23)), nickel in 0.5 *m* sodium sulfate solution at pH 6.0 (Sato and Okamoto(76)), and chromium in 0.1 *m* sulfuric acid solution (Heuman and Diekötter(24)).

induction time, τ_p, often called the passivation time, depends on the current density applied according to the equation of the form,

$$\tau_p = k(j - j_m)^n \tag{10}$$

where constant n has been found to be -1 for iron (Franck[23]) and chromium (Heuman and Diekötter[24]), and -2 for nickel (Landsberg and Hollnagel[25,26]). The fact that $n = -1$ indicates that a constant anodic charge is required for passivation. This amount of charge was measured to be 1700–1800 mC cm^{-2} for iron in acid and 2.3 mC cm^{-2} for chromium in acid, suggesting that a thick hydrated salt layer is deposited prior to the formation of passive film on iron, while the direct formation of a passive film is likely to occur on chromium. It is also suggested from $n = -2$ that the passivation of nickel requires some diffusing species, probably hydrogen ion, to be depleted in solution adjacent to the metal surface (Landsberg and Hollnagel[25,26]).

During galvanostatic passivation, the potential is arrested for a short time at a critical potential that separates the passive state from the active state. This anodic arrest potential (anodic Flade potential) corresponds with the cathodic arrest potential (cathodic Flade potential) that occurs during galvanostatic activation of passivated metals (Bonhoeffer and Vetter[27]).

3.4. Potentiostatic Passivation

When a metal having no surface films is subjected to anodic passivation at a passive potential, the anodic current decreases with time forming a passive film on the metal surface. Figure 20 shows the change in the anodic current and the formation of the passive film on iron in a neutral solution. The initial large current, which is dependent on the impedance of polarization circuit, seems to carry mainly the actively dissolving iron ions before the passive film starts to form. In the case of nickel in neutral solution, however, the passive film formation appears to occur first and the anodic dissolution then proceeds through the passive film, as shown in Figure 21.

Ebersbach, Schwabe and Ritter[28] proposed for the kinetics of potentiostatic passivation a competition mechanism between the active dissolution,

$$\mathrm{Me} + \mathrm{H_2O} \rightarrow \mathrm{MeOH_{aq}}^+ + \mathrm{H_{aq}}^+ + 2e \tag{11}$$

and the oxide film formation,

$$\mathrm{M} + \mathrm{H_2O} \rightarrow \mathrm{MeO} + 2\mathrm{H_{aq}}^+ + 2e \tag{12}$$

The total anodic current is then given by

$$j = (i_M + j_f)(1 - \theta) \tag{13}$$

where j_M is the current density for the active dissolution, j_f the current density due to the oxide formation, and θ the fraction of passivated portion of the

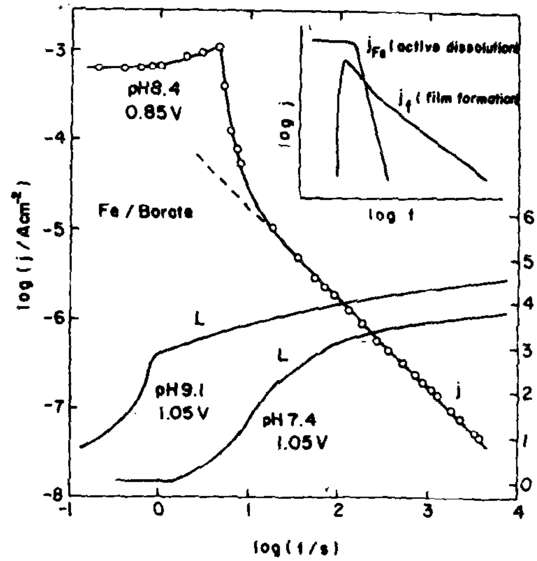

Figure 20. Change of anodic current with time (Nagayama and Cohen[83]) and initial growth of passive film (Kruger and Colvert[86]) during potentiostatic passivation of iron in borate buffer solutions, and schematic representation of active dissolution current j_{Fe} and film formation current j_f changing with time.

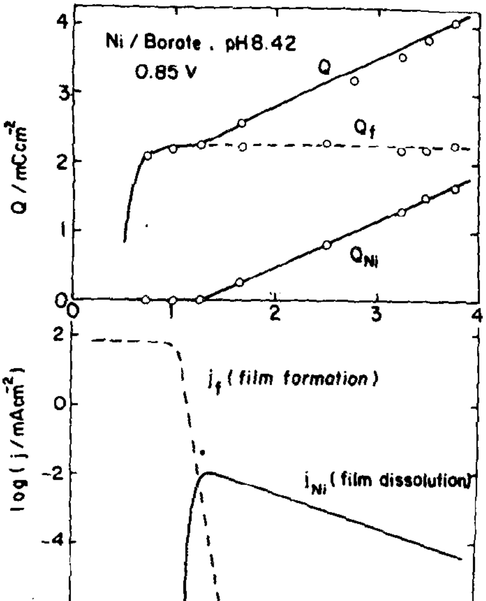

Figure 21. Change of anodic charge passed, Q, equivalent charge for dissolution, Q_{Ni}, and equivalent charge for film formation, $Q_f = Q - Q_{Ni}$, during potentiostatic passivation of nickel in borate buffer solution (Sato, Kudo, and Miki[87]) and schematic representation of film formation current j_f and dissolution current j_{Ni} changing with time.

surface. If one expresses the velocity $(\partial\theta/dt)_E$ at constant potential by

$$\left(\frac{\partial\theta}{\partial t}\right)_E = Cj_f(1-\theta) - B\theta \tag{14}$$

where C is the covered area per unit anodic charge of film formation and B is the rate of degradation of the passive film, the total anodic current becomes

$$j = (j_M + j_f)\left[1 - \frac{Cj_f}{Cj_f + B}\{1 - \exp[-(Cj_f + B)t]\}\right] \tag{15}$$

with

$$j_M = j_M^\circ \exp\left[\frac{\alpha z}{RT}(E + E_M^\circ)\right]$$

$$j_f = j_f^\circ \exp\left[\frac{\alpha' z'}{RT}(E - E_f^\circ)\right]$$

where j° denotes the exchange current density, E° the equilibrium potential, and z and z' are the numbers of electrons involved in the reactions. By assuming reasonable values for the kinetic constants in Eq. (15), the anodic current–potential curve may be calculated as a function of potentiostatic polarization time. Figure 22 shows a calculated polarization curve together with the experimental value of the active dissolution peak current density for potentiostatic 5-min polarization of nickel in 0.05 m sulfuric acid solution. Equation (15) always leads to a current peak for the active–passive transition if the following conditions are satisfied: (a) the two exchange current densities j_M° and j_f° are of a similar order of magnitude, (b) the equilibrium potentials E_M° and E_f° are not too far apart, and (c) the degradation rate B is not too great. But

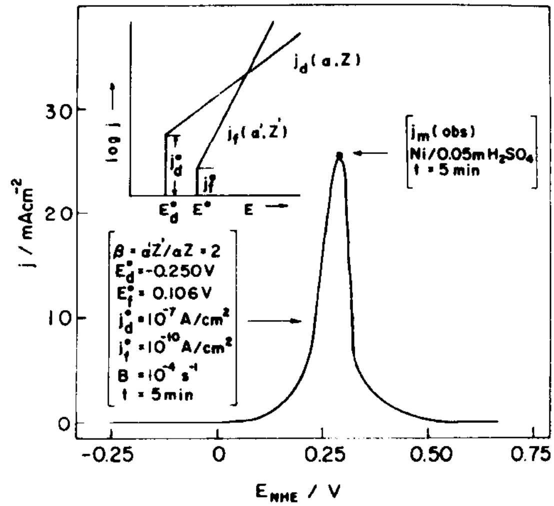

Figure 22. Potentiostatic anodic current-potential curve calculated from Eq. (15) for passivation time $t = 5$ min with reasonable values for the kinetic constants, and experimentally estimated peak current in active dissolution for nickel in 0.05 m sulfuric acid (Ebersbach, Schwabe, and Ritter[28]).

if $j^\circ_M \gg j^\circ_f$ and, moreover, if $E^\circ_M \gg E^\circ_f$, the metal dissolution reaction is predominant and a primary passivation is expected to occur only when the saturation of metal ions has been attained leading to the formation of a salt or hydrated salt layer at the surface.

3.5. Effect of Anions

In many cases of metal passivation, anions in solution exert influence on the active–passive transition. Figure 23 shows the effects of anions on the potentiostatic anodic polarization curve of iron in neutral solutions. The addition of phosphate ions in a borate solution leads to two, instead of one, stages for passivation. The primary stage probably corresponds to the formation of an insoluble iron phosphate layer and the secondary stage to the passive oxide film formation. The primary salt layer passivation is facilitated as the phosphate ion concentration increases, but it degrades above a certain potential in the presence of sulfate ions at some concentration.

Figure 24 shows a primary passivation due to the adsorption of sulfate ions on the surface of nickel in a sulfuric acid solution. The adsorbed sulfate ions are desorbed above a certain potential, and two current peaks appear in the anodic polarization curve of nickel preimmersed for 18 hr in 0.5 *m* sulfuric acid solution. When the time of preimmersion is extended to 70 hr, the first current peak disappears owing probably to the complete coverage of adsorbed sulfate ions on the surface and only the second current peak remains increasing with preimmersion time (Feller, Kesten, and Krupki[29]).

In general, anions either facilitate or retard the passivation of metals through their adsorption and salt layer formation at the metal surface. The

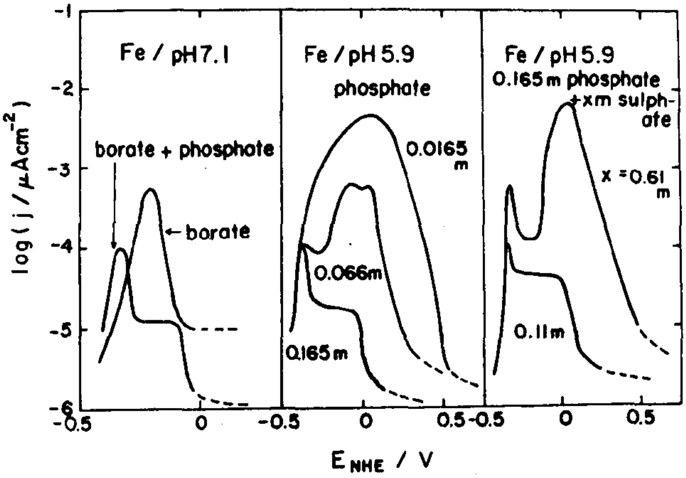

Figure 23. Effect of anions on potentiostatic anodic polarization curve for active–passive transition of ion in neutral solutions (Florianovich, Kolotyrkin, and Kononova[88]).

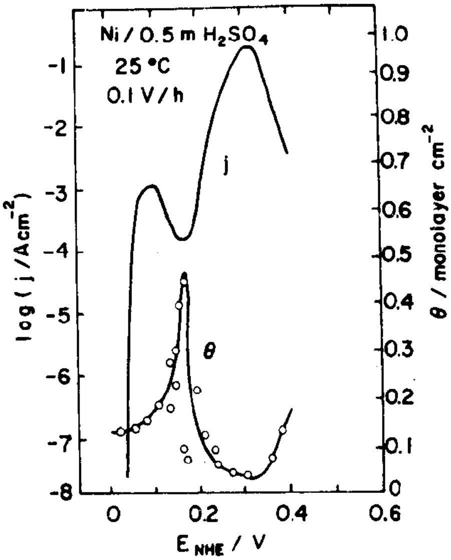

Figure 24. Anodic potential scan polarization curve and surface coverage of sulfate ions θ as a function of potential for nickel preimmerged for 18 hr in 0.5 *m* sulfuric acid (Feller, Kesten, and Krupki[29]).

reaction schema may be written as follows:

$$M + xH_2O + (1-x)A_{aq}^{-} \rightarrow \begin{bmatrix} xMOH_{ad} \\ (1-x)MA_{ad} \end{bmatrix} + 2xH_{aq}^{+} + xe \quad (16)$$

(a) Acceleration or inhibition of dissolution,

$$\begin{bmatrix} xMOH_{ad} \\ (1-x)MA_{ad} \end{bmatrix} \rightarrow xMOH_{aq}^{+} + (1-x)MA_{aq}^{+} + e \quad (17)$$

(b) Precipitation of salt or basic salt layer,

$$MA_{aq}^{+} + A_{aq}^{-} \rightarrow MA_2 \quad (18)$$

$$MA_{aq}^{+} + H_2O \rightarrow MAOH + H_{aq}^{+} \quad (19)$$

(c) Direct formation of salt layer,

$$[MA_{ad}] + A_{aq}^{-} \rightarrow MA_2 + e \quad (20)$$

4. Passive Films

4.1. Iron

Most of the present knowledge about the passive film on iron have been obtained by studying iron anodes in neutral borate buffer solutions. According to Sato, Kudo, and Nishimura,[30] the passive film on iron by potentiostatic 1-hr passivation in a borate solution at pH 8.4 has two layers, one is a barrier layer in

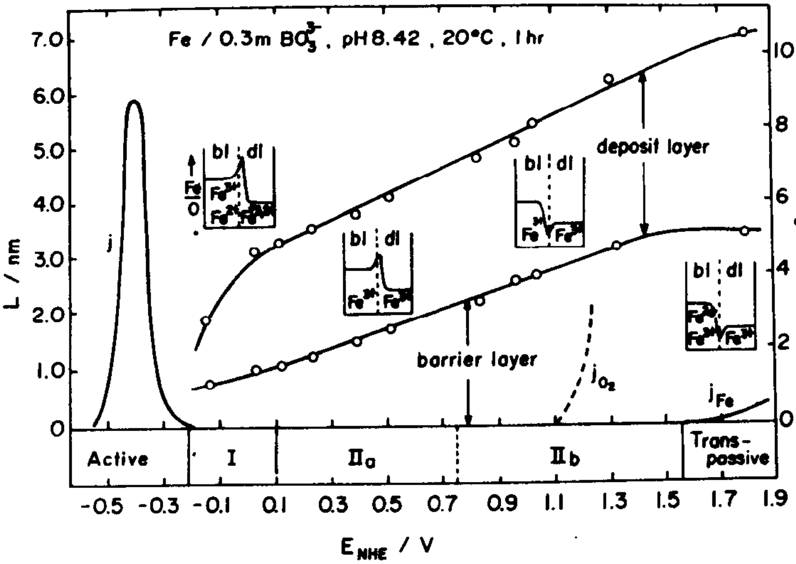

Figure 25. Film thickness–potential and anodic current–potential curves for the passive film on iron by potentiostatic 1-hr oxidation in sodium borate solution at pH 8.42. The passive film is bilayered with a barrier layer and a deposit layer, and the in-depth iron–oxygen profile change with potential exhibiting iron excess or oxygen excess at the barrier–deposit boundary (Sato, Kudo, and Nishimura(30)).

contact with the metal, and the other a deposit layer which is formed on the barrier layer. The barrier layer thickness is approximately a linear function of anodic potential with the slope of about 1.8 nm V^{-1} until it levels out in the transpassive potential region, whereas the deposit layer thickness appears almost independent of potential except in a range of low passivating potentials as shown in Figure 25. In this solution, the barrier layer is an iron(III) oxide in

Table 1
Electron Diffraction Analyses of Passive Films Formed on Iron in Acidic, Neutral, and Basic Solutions[a]

Solution	State and potential	Identification
0.5 *m* H_2SO_4	Passive, +1.4 V, +1.6 V	γ-Fe_2O_3
pH 1.1	Transpassive, +1.75 V	Fe_3O_4
0.15 *m* BO_3^{3-}	Prepassive, −0.6 V	Fe_3O_4 or α-FeOOH
pH 8.5	Passive, +0.75 V, +0.85 V	γ-Fe_2O_3
	Transpassive, +1.25 V	Fe_3O_4
0.1 *m* NaOH	Prepassive, open circuit	Fe_3O_4 or γ-Fe_2O_3
pH 11.4	Passive, +0.5 V	γ-Fe_2O_3
	Transpassive, +1.0 V	Fe_3O_4

[a] Reference 33.

the passive potential region and contains iron(II) ions to some percentage in the transpassive potential region as well as at low passivating potentials close to the active potential region (Sato, Kudo, and Nishimura(30)), while the deposit layer is a hydrated iron(III) oxide or oxyhydroxide containing a small percentage of borate ions (Sato, Kudo, and Noda(31); Seo, Sato, Lumsden, and Staehle(32)). Foley, Kruger, and Bechtoldt(33) identified by means of electron diffraction the passive film as γ-Fe_2O_3 and detected Fe_3O_4 in the active and transpassive regions, as shown in Table 1. The hydrated nature of the passive films is evident from the measurements of water in the passive film (Sato, Kudo, and Noda(31); Yolken, Kruger, and Calvert(34); Kudo, Shibata, Okamoto, and Sato;(35) Revie, Baker, and Bockris(36); O'Grady and Bockris(37)). It was also suggested from in-depth analyses of the passive film (Sato, Kudo, and Nishimura(30)) that there was either excess iron or excess oxygen at the boundary between the barrier layer and the deposit layer, as schematically shown in Figure 25.

The composition of the barrier layer was found to differ with different anions in the solution, as shown in Table 2 (Nishimura and Sato(38)). In neutral phosphate solutions the barrier layer is an iron(II)–(III) mixed oxide in contrast to an iron(III) oxide of the barrier layer formed in neutral borate solutions.

In acid solutions where the passive current of iron increases with increasing acidity, the deposit layer dissolves and only the barrier oxide layer remains on the passivated iron surface, as shown in Figures 26 and 27. Vetter and Gorn(39) suggested from their ellipsometric measurements of the passive film that the barrier layer was bilayered with an inner Fe_3O_4 layer and an outer γ-Fe_2O_3 layer. Oshe, Rosenfeld, and Doroskenko(40) measured the photoelectric polarization of iron anodes as a function of potential in sulfuric acid solution. Their results are shown in Figure 28. The negative sign of the photoresponse potential V_{pep} indicates that the surface films formed in the active and passive regions are of the *n* type. They also attributed a sudden

Table 2
Passive Films Formed on Iron at +0.845 V (NHE) for 1 hr in Phosphate and Borate Solutions at pH 8.42[a]

	Mean ionic valency of iron Z_{Fe}		Optical constant		Thickness, A		Boundary between barrier layer and deposit layer
pH = 8.42	b.l.[b]	d.l.[c]	b.l.	d.l.	b.l.	d.l.	
Phosphate sol.	2.33	2.94	2.50–0.35*i*	2.20–0.14*i*	18	32	No iron deficiency (no oxygen excess)
Boric–borate sol.	3.00	3.00	2.50–0.30*i*	2.20–0.10*i*	22	26	Iron deficiency (oxygen excess)

[a] Reference 38.
[b] Barrier layer.
[c] Deposit layer.

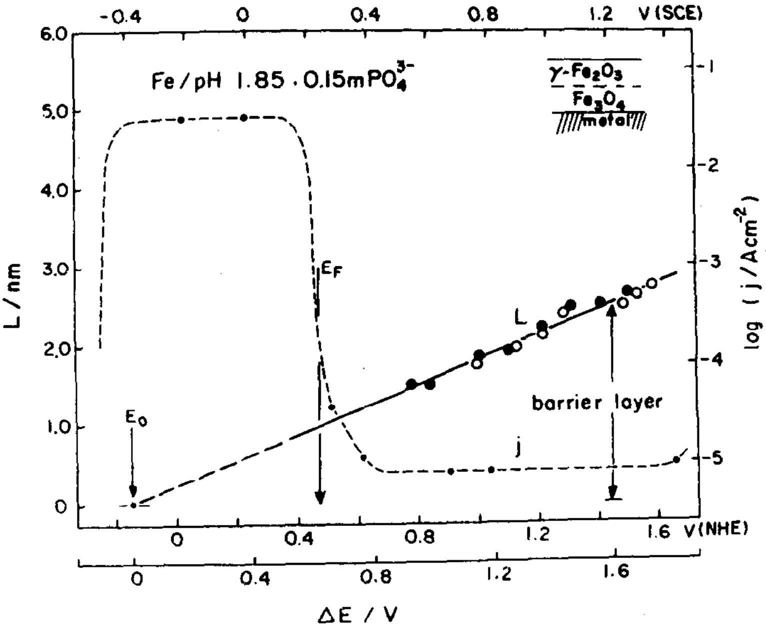

Figure 26. Film thickness–potential and anodic current–potential curves for the passive film on iron by potentiostatic 1-hr oxidation in phosphoric acid. The passive film is a barrier layer probably consisting of an inner Fe_3O_4 layer and an outer γ-Fe_2O_3 layer (Sato, Kudo, and Noda[31]).

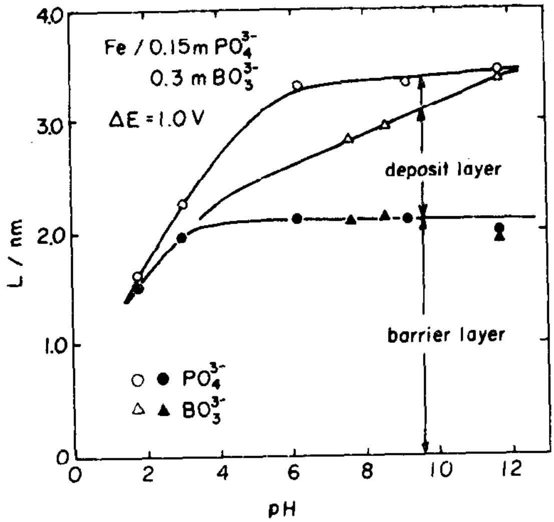

Figure 27. Effects of pH on the barrier and deposit layer thicknesses for the passive film formed on iron by potentiostatic 1-hr oxidation at a constant overpotential $\Delta E = 1.0$ V in 0.15 *m* phosphate and 0.3 *m* borate solutions (Sato, Kudo, and Noda[31]).

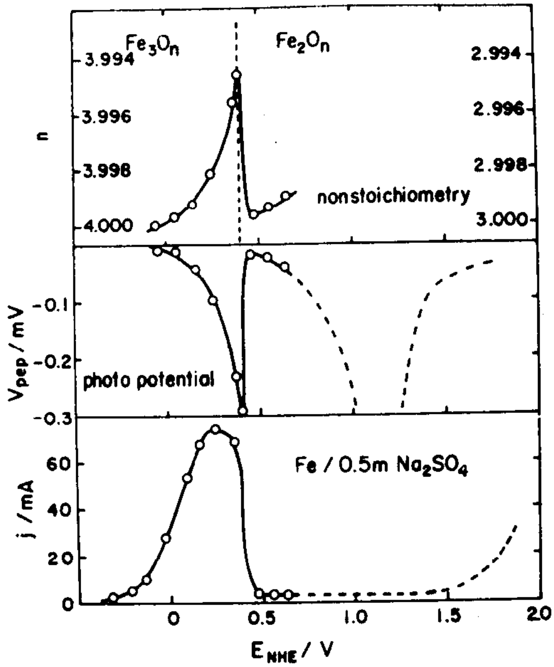

Figure 28. Anodic current density, photoelectric polarization potential V_{pep} induced by light pulses from mercury lump, and nonstoichiometric composition (iron ion vacancies) in anodic surface films estimated from V_{pep} as functions of potential for iron anode in 0.5 *m* sodium sulfate solution (Oshe, Rosenfeld, and Doroskenko[(40)]).

change of photoresponse potential at the passivation potential to the transformation of the surface film from Fe_3O_4 in the active region to Fe_2O_3 in the passive region, and estimated from the amplitude of the photoresponse the nonstoichiometric composition of these oxide films as a function of potential. The photoresponse amplitude is related to the cationic and anionic vacancy concentrations in the oxide:

$$V_{pep} = \frac{kT}{2e} \ln \frac{[V_c^{m+}]^0}{[V_A^{n-}]^0} - C \tag{21}$$

where $[V_c^{m+}]^0$ and $[V_A^{n-}]^0$ are concentrations of cationic and anionic vacancies and C is a constant.

4.2. Nickel

Compared with iron, the passive film on nickel does not grow thick but rather tends to dissolve into the solution. Figure 29 shows the anodic film thickness–potential and current density–potential curves for nickel in a borate buffer solution at pH 8.42. The passive film thickness, though increasing with potential, is not a linear function of potential and hence the film thickness for unit voltage dL/dE is not constant but decreases with potential. The minimum thickness of the film required for anodic passivation is about 0.3 nm, in

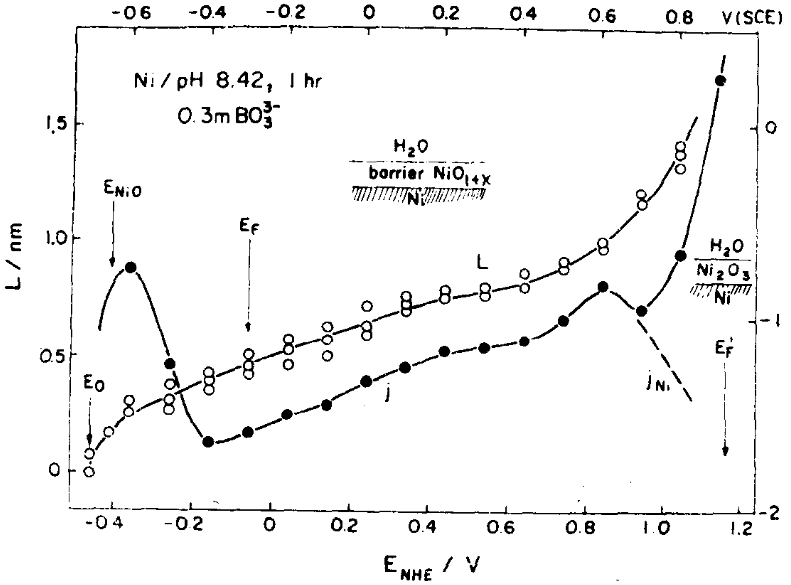

Figure 29. Passive film thickness–potential and current density–potential curves of nickel anode potentiostatically polarized for 1 hr in borate buffer solution of pH 8.42 (Sato and Kudo(41)).

agreement to the monolayer thickness of oxygen adsorption. According to Sato and Kudo,(41) the secondary passivation produces an increased film thickness levelling out at about 6 nm in the secondary passive and transpassive regions, where a higher valence nickel oxide or oxyhydroxide is formed:

$$Ni^{2+} + 2H_2O \rightarrow NiOOH + 3H_{aq}^{+} + e \qquad (22)$$

$$NiO + H_2O \rightarrow NiOOH + 2H_{aq}^{+} + 2e \qquad (23)$$

In alkaline solutions where the dissolution of nickel may be ignored, the transformation of the anodic oxide film on nickel from $Ni(OH)_2$ to NiOOH under galvanostatic oxidation conditions was observed by ellipsometry, as shown in Figure 30. Notice that the anodic oxide transformation occurs in a wide range of potential rather than at a definite transformation potential. The reflection spectroscopic measurements under potential–modulation conditions by Heusler and Schoner(42) also revealed the transformation of $Ni(OH)_2$ to NiOOH on nickel in 1 *m* NaOH solution to take place in a wide range of potential.

Gobrecht, Paatsch, and Thull(43) measured, using modulation spectroscopy, the surface film formed on nickel in the passive and transpassive regions in sulfuric acid solution, and found a layer transformation to occur in the transpassive potential region, as shown in Figure 31. With increasing anodic potential, the energy band gap for electrons in the film estimated from the spectrum of modulated reflectance changes from 4 eV, which is the energy gap

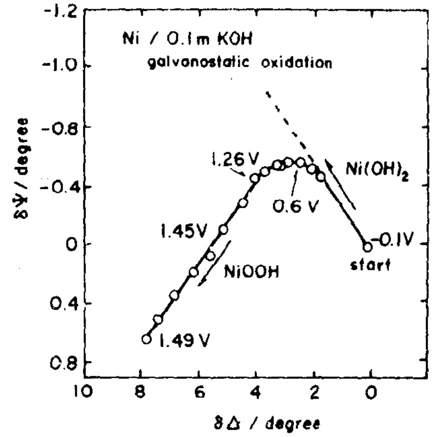

Figure 30. Anodic film growth curve as measured by ellipsometry during galvanostatic oxidation of nickel anode at 37.6 $\mu A/cm^2$ in 0.1 *m* potassium hydroxide solution; $\delta\Psi$ and $\delta\Delta$ are ellipsometric parameters (Visscher and Damjanovic[89]).

of optically stable NiO, to 4.23 eV corresponding to the energy gap of another optically stable nickel probably having an increased oxidation degree. Figure 32 illustrates the photoelectric polarization response potential as well as the anodic current density as a function of potential for nickel anodes in acidic sulfate solution. The positive sign of the photoresponse potential indicates that

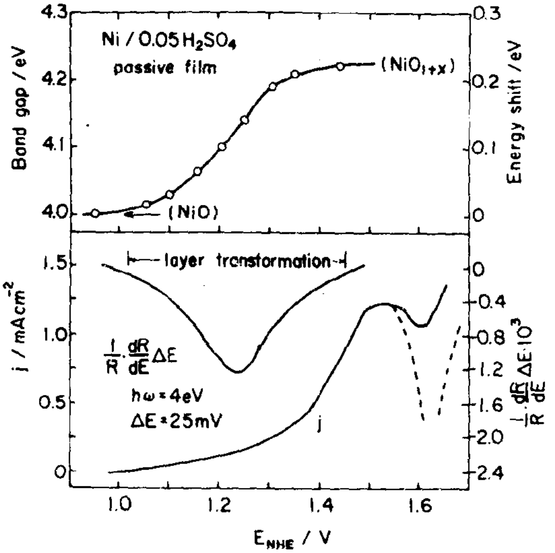

Figure 31. Anodic current density, modulated reflectance with photon energy 4 eV and potential modulation amplitude 25 mV, and electron energy gap estimated from modulated reflectance spectrum as functions of potential for the passive film on nickel anode in 0.05 *m* sulfuric acid solution (Gobrecht, Paatsch, and Thull[43]).

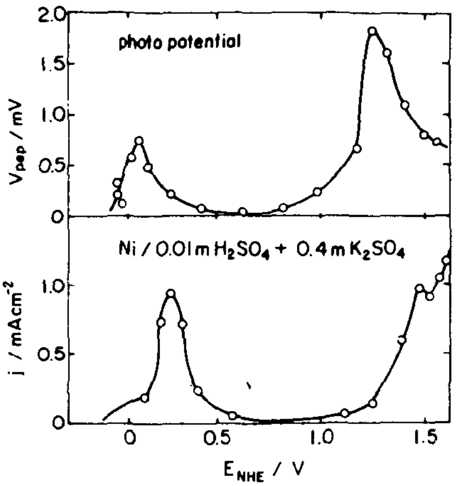

Figure 32. Photoelectric response potential and anodic current density as functions of potential for nickel anode in acidic 0.5 *m* sulfate solution (Oshe and Rosenfeld[90]).

the anodic surface film on nickel is always of *p*-type semiconductor in agreement with NiO containing excess oxygen.

4.3. Cobalt

Cobalt exhibits three degrees of passivity in neutral solutions, as shown in Figure 33. In the primary passivity region, a single layer of CoO polymer

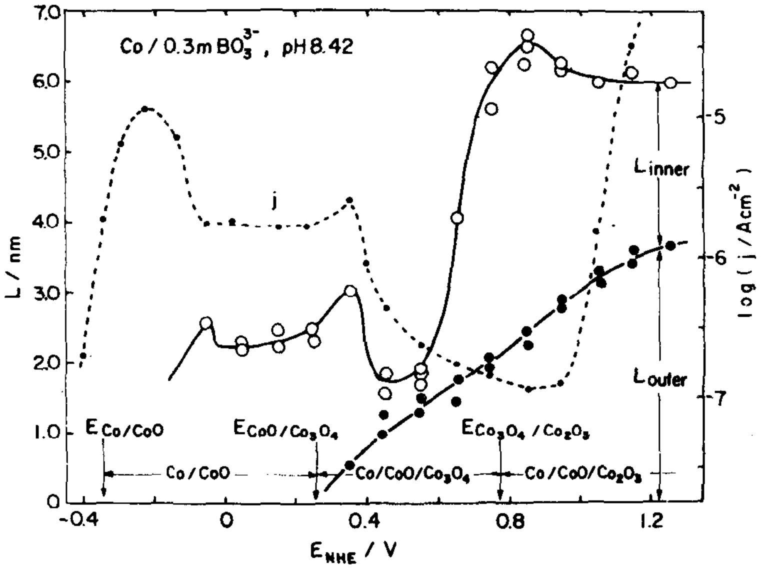

Figure 33. Passive film thickness–potential and anodic current density–thickness curves for cobalt anode in borate buffer solution at pH 8.42 (Sato[56]; Ohtsuka[44]). L_{inner} and L_{outer} are the thicknesses of the inner CoO layer and the outer Co_3O_4 or Co_2O_3 layer.

containing water is formed, the thickness of which is nearly independent of potential. The secondary passivation is due to the formation of another layer of hydrated Co_3O_4 polymer on the primary passive film, leading to a bilayered film. In the ternary passivity region, the secondary passive film of Co_3O_4 is oxidized to Co_2O_3 and the passive film turns to be a bilayered film consisting of CoO and Co_2O_3 (Ohtsuka(44)). The outer Co_3O_4 or Co_2O_3 layer thickness increases nearly linearly with increasing anodic potential, while the inner CoO layer thickness is a complicated function of potential.

Figure 34 illustrates the thickness, optical constant, and composition of the outer layer as well as the anodic current in the secondary and ternary passive potential regions, serving to show that the transformation from Co_3O_4 to Co_2O_3 takes place. Simons, Kellerman, and Leidheiser(45) identified using emission Mössbauer spectroscopy the anodic film as being in the +2 and +3 oxidation states of cobalt at low passivating potentials, primarily in the +3 oxidation state at high passivating potentials, and in the +3 and +4 oxidation states in the transpassive potential regions in a borate solution at pH 8.5.

4.4. Chromium

The passive film on chromium has been suggested to be Cr_2O_3. The film thickness is of the magnitude of adsorbed monolayer oxygen thickness at low

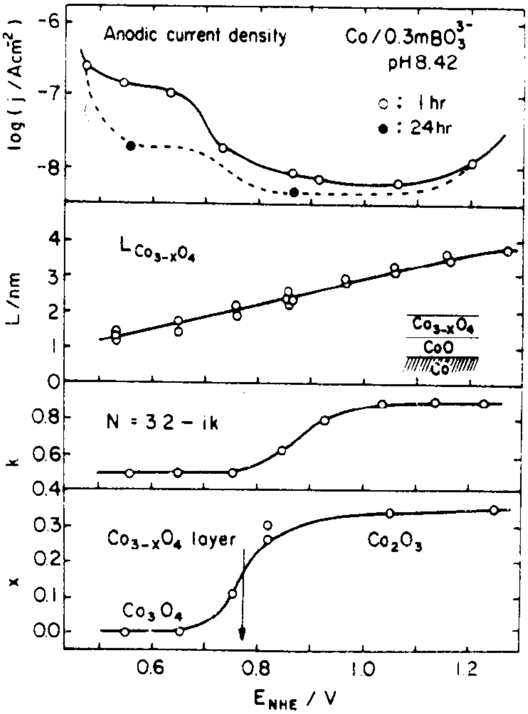

Figure 34. Anodic current density, outer layer thickness, optical constant of the outer layer, and composition of the outer layer as functions of potential for cobalt anode in borate buffer solution at pH 8.42 (Ohtsuka(44)). In 24-hr oxidation, the anodic current is equal to the dissolution current of cobalt.

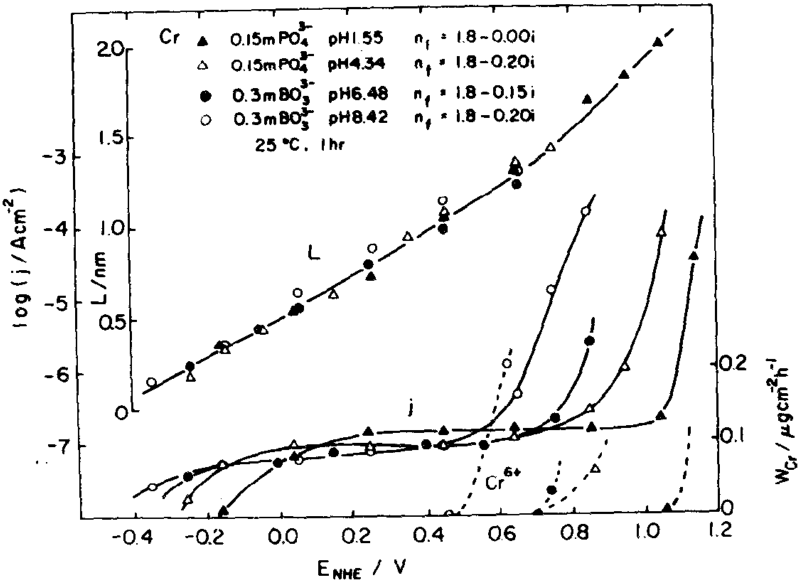

Figure 35. Passive film thickness–potential and anodic current density–potential curves for chromium anode in acidic phosphate and neutral borate solutions (Sato$^{(62)}$); n_f is the optical constant of the passive film.

passivating potentials and increases with potential to 1.5 ~ 2.0 nm before chromium goes into the transpassive region, as shown in Figure 35.

4.5. Stainless Steel

The passivity of alloys is of practical importance, and many papers in the literature have presented the effect of alloy composition on the shape of the anodic polarization curve, on the passivation potential, on the critical current density for passivation, and on the passive current density. As an example, the anodic polarization curve of austenitic 18Cr–8Ni stainless steel together with the curves for component metals is shown in Figure 36. As may be suspected from comparison of these polarization curves, the passive film is chromium rich at low passivating potentials and iron rich at high passivation potentials (Sugimoto, Kishi, Ikeda, and Sawada$^{(46)}$).

5. Dissolution of Passive Metals

5.1. Dissolution in Steady States

The dissolution of passive metals proceeds through the passive film and the reaction may be written as

$$\text{M(metal)} \rightarrow \text{M}^{2+}\text{(passive oxide film)} + ne \tag{24}$$

$$\text{M}^{n+}\text{(passive oxide film)} \rightarrow \text{M}^{n+}\text{(aq)} \tag{25}$$

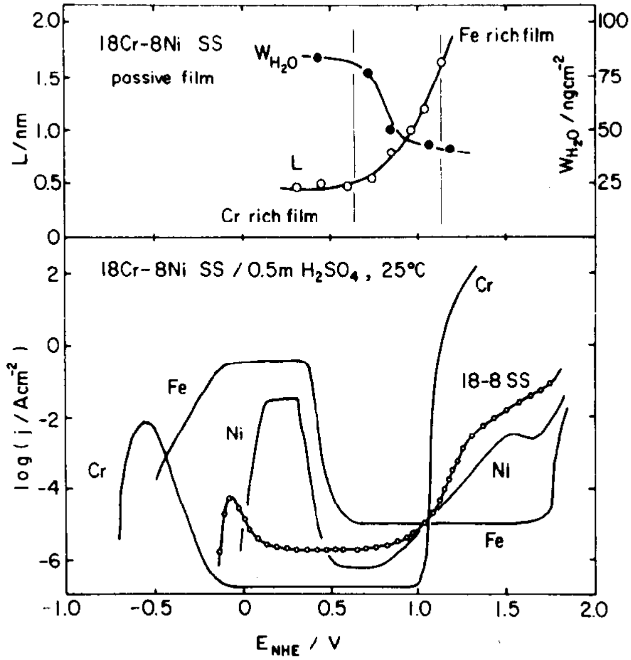

Figure 36. Potential dependence of passive film thickness and water content in the passive film, and anodic polarization curve for austenitic 18Cr–8Ni stainless steel in 0.5 *m* sulfuric acid solution (Shibata and Okamoto(91); Okamoto(80)). Polarization curves for iron, nickel, and chromium are also plotted for comparison.

In the steady state of passivity maintaining current, therefore, the ionic current through the film is equal to the dissolution current of the film. Figure 37 shows the steady passive current of iron as a function of pH in phosphate solutions. The logarithm of the passive dissolution current is a linear function of pH. According to Vetter,(47) the dissolution rate of passive films is controlled by the potential difference $\Delta\phi$ at the oxide–solution interface:

$$j_a = j_a^{\circ} \exp\left(-\frac{\alpha n F \Delta\phi}{RT}\right) \tag{26}$$

where α is the ionic charge transfer coefficient for metal ion dissolution.(25) If the potential difference at the oxide–solution interface is determined by the following electrochemical reaction,

$$H_2O(aq) = O^{2-}(ox) + 2H^+(aq) \tag{27}$$

which is in equilibrium in the steady state, the dissolution rate becomes a function of pH:

$$\log j_d = -\alpha n \ \mathrm{pH} + \mathrm{const} \tag{28}$$

in agreement with the observation for iron in acid solution (Figure 37).

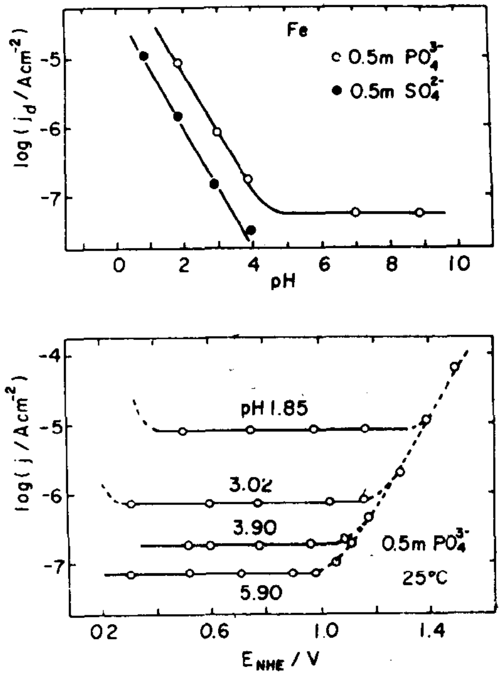

Figure 37. pH dependence of potential-independent dissolution current density of passive iron in the steady state in phosphate solutions (Noda and Sato(92)) and in sulfate solutions (Vetter(47)).

In the same way, but assuming for the passive film a nonstoichiometric oxide whose composition depends on the potential, Vetter(48) also explained the potential-dependent transpassive dissolution current of nickel. In the case where the passive oxide composition changes with potential, the potential difference at the oxide–solution interface determined by reaction (26) is no longer a simple function of pH but also depends on the nonstoichiometric composition of the passive film itself:

$$\log j_d = K \log a_{O^{2-}(ox)} - \alpha n \, \mathrm{pH} + \mathrm{const} \qquad (29)$$

where K is a constant and $a_{O^{2-}(ox)}$ is the activity of oxygen ion in the outermost layer of the passive film.

5.2. Dissolution in Non-Steady-States

The dissolution rate of passive iron in non-steady-states is not equal to that in the steady state (Novakovski and Likkackev(49)). Figure 38 serves to show that the dissolution current increases immediately after an anodic current greater than the steady state value is applied to a passive iron in sulfuric acid solution. The passive iron dissolution rate, which is potential independent in the steady state, is not always potential independent, but appears to differ with different anodic currents in the non-steady-state. In Figure 38, the difference

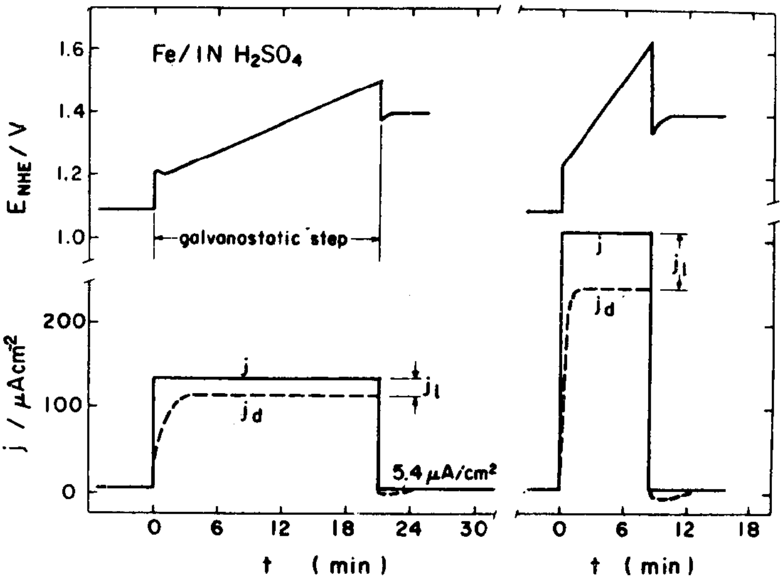

Figure 38. Dissolution current density j_d, anodic current density j, and potential of passive iron as functions of time during galvanostatic step from a steady state in 0.5 *m* sulfuric acid solution. (Vetter and Gorn(104)). $j_l = j - j_d$ is the current density for the rate of film growth.

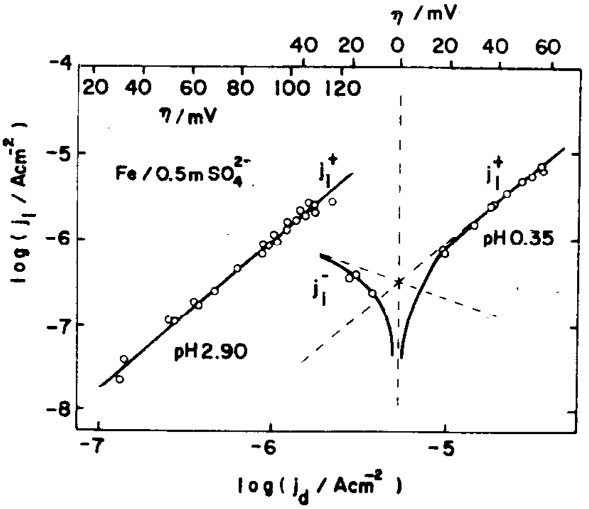

Figure 39. Relation between film growth current density j_l and film dissolution current density j_d at the the passive film–solution interface for passive iron under non-steady-state conditions in 0.5 *m* sulfate solutions at pH 0.35 and 2.90 (Vetter and Gorn(51)). j_l^+ is the film growth current density, j_l^- the film removal current density, and η the overpotential at the film–solution interface.

between the anodic current j and the dissolution current j_d is denoted by j_l, which represents the growth rate of the passive film. There are two electrochemical reactions occurring at the oxide–solution interface; one is the iron ion transfer, $Fe^{3+}(ox) \rightarrow Fe^{3+}(aq)$, and the other the oxygen ion incorporation, $H_2O(aq) \rightarrow O^{2-}(ox) + 2H^+$. From the theory of electrochemical kinetics leading to $j_d = j_d^\circ \exp(-3\alpha F\Delta\phi/RT)$ for the iron ion transfer and $j_l = j_l^\circ \exp(-2\alpha' F\Delta\phi/FT)$ for the oxygen ion incorporation, a linear relationship between $\log i_d$ and $\log j_l$ at a given $\Delta\phi$ is obtained;

$$2\alpha' \log j_d = 3\alpha \log j_l + \text{const} \tag{30}$$

The experimental results by Heusler(50) and by Vetter and Gorn,(51) are in agreement with Eq. (30), as shown in Figure 39.

5.3. Ionic Current through Passive Barrier Films

The ionic current in passive films on iron has been suggested to follow either a field-assisted ion conduction in which the activation energy is a function of the electric field in the film (Weil(52); Moshtev(53)) or a place-exchange mechanism in which the activation energy is a function not only of the electric field but also of the film thickness (Sato and Cohen(54)).

For the field assisted ion conduction,

$$\begin{aligned} j &= j_0 \exp\left(\frac{\alpha a n F}{RT}\frac{\Delta E}{L}\right) \\ &= j_0 \exp(B\Delta E/L) \end{aligned} \tag{31}$$

where α is the ionic charge transfer coefficient, a the activation distance, n the ionic valency of moving ions, and $\Delta E/L$ the electric field in the film. On the other hand, the place exchange mechanism leads to an ionic conduction equation given by

$$J = j_0' \exp(-L/B_1)\exp(B_2 E) \tag{32}$$

where B_1 is a kinetic parameter including the oxygen lattice constant and the free energy of activation for each exchange of iron ion and B_2 another kinetic parameter including the ionic charge transfer coefficient and the stoichiometric number.

6. Theory of Passivity

6.1. Passivation Processes

There are three possible mechanisms for the formation of passive film on metals; these are the direct film formation, the dissolution–precipitation, and anodic deposition mechanisms.

The direct film formation process is the reaction of the metal surface with the solution to form an oxygen adsorption film or a compact oxide film, and may be written as follows:

$$M_{metal} + H_2O_{aq} \rightarrow MO_{ad} + 2H_{aq} + 2e \qquad (33)$$

$$M_{metal} + H_2O_{aq} \rightarrow MO(ox) + 2H_{aq}^{+} + 2e \qquad (34)$$

The dissolution–precipitation process is a two-step process in which metal ions dissolved precipitate to form an oxide film on the metal surface:

$$M_{metal} \rightarrow M_{aq}^{2+} + 2e \qquad (35)$$

$$M_{aq}^{2+} + H_2O_{aq} \rightarrow MO(ox) + 2H_{aq}^{+} \qquad (36)$$

The anodic deposition process is an anodic oxidation of metal ions in solution to form an oxide film whose oxidation state is higher than that of the metal ions, for instance,

$$M_{metal} \rightarrow M_{aq}^{2+} + 2e \qquad (37)$$

$$2M_{aq}^{2+} + 3H_2O \rightarrow M_2O_3(ox) + 6H^{+} + 2e \qquad (38)$$

In general, the passive oxide film may not be a rigid oxide but may be hydrated to some extent, as suggested in the preceding sections. It is supposed that the precipitate or deposit oxide film is fully hydrated in the initial stage of formation, and that once the precipitate or deposit film is formed on the metal surface, however, dehydration of the film will proceed, particularly at the innermost layer in contact with the metal, because of high anodic electrical field.

6.2. Theory of Passivity

A number of passivity theories have been presented in the literature, all of which fall into the categories of adsorption theory and polyatomic phase oxide theory.

The anodic metal dissolution is an electrochemical reaction whose rate is controlled by the electrode potential of the metal, i.e., the potential difference between the metal and the solution. If there is no surface film on the metal, the potential difference is located across the electrical double layer (the Helmholtz layer) separating the metal surface by about 0.5 nm from the closest plane of approach of hydrated ions (the outer Helmholtz plane). The diffuse double layer extending from the outer Helmholtz plane to the bulk of solution takes a part of the total potential difference but this may be ignored in solutions of high ionic intensity.

When the metal surface is covered with a thin film of monoatomic oxygen or polyatomic oxide, the structure of the electrified double layer is altered from a single Helmholtz layer at the metal solution interface to a multilayered structure at least consisting of a thin surface film on the metal and a Helmholtz layer formed at the film–solution interface. Consequently, the metal dissolution takes place as a consecutive reaction comprising the transfer of metal ions from the metal phase to the surface film, the migration of ions through the film, and the transfer of metal ions across the Helmholtz layer at the film–solution interface. The last step is in fact the hydration of metal ions, and in the steady state its rate controls the overall rate of metal dissolution.

According to Kuznetsov and Dogonadze,(55) the pd ϕ_c across the Helmholtz layer at the interface between a thin intrinsic semiconductor film on a metal and a solution is related to the overall pd ϕ_M between the metal and the solution as follows;

$$\phi_c = \phi_M\left(1 + \frac{L}{\delta}\frac{\varepsilon_H}{\varepsilon_M}\right)^{-1} \tag{39}$$

where L is the film thickness, δ the thickness of the Helmholtz layer, and ε_F and ε_H are, respectively, the dielectric constants of the film and the Helmholtz layer. If there is no surface film, ϕ_c is equal to ϕ_M. Sato(56a) made use of this equation to propose a general theory of metal passivity.

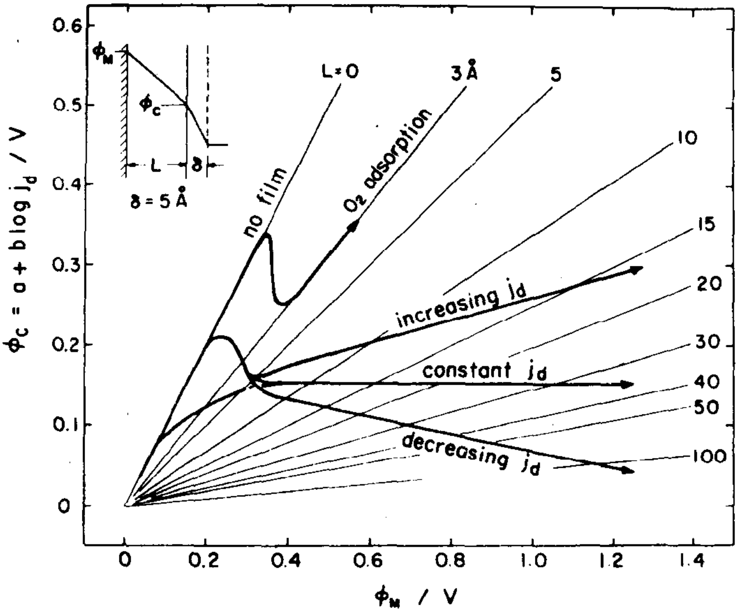

Figure 40. Potential Φ_c at the surface of a thin semiconductor film on metal electrode calculated according to Eq. (39) for various film thicknesses, and possible shapes of Φ_c vs. Φ_M curve and hence anodic polarization curve for metal dissolution (Sato(56)). Potential Φ_c and Φ_M are relative to the potential of electrolyte solution.

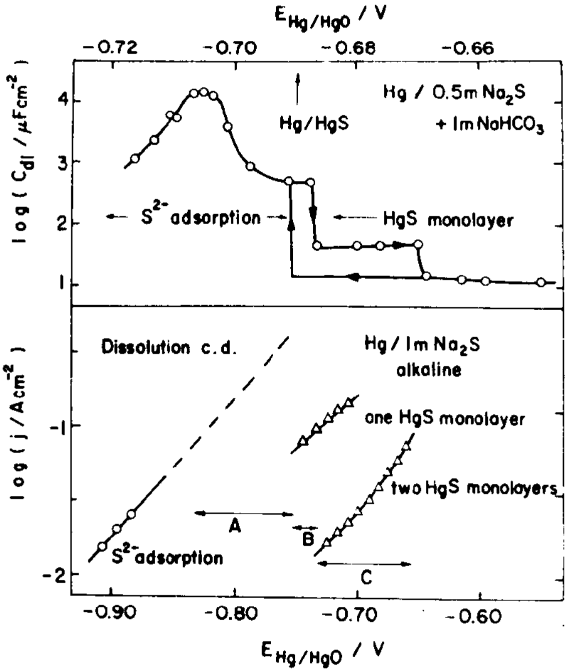

Figure 41. Potential dependence of electrode double-layer capacity C_{dl} and of anodic dissolution current density of mercury in sulfide ion solutions, showing monolayer sulfide passivity (Armstrong, Porter, and Thirsk[93]). Potential region A is of strong S^{2-} ion adsorption, B of first HgS monolayer stability, and C of stability of first and second HgS monolayers.

Since the rate of metal dissolution is controlled by the Helmholtz layer pd ϕ_c no matter whether any surface film is present or absent, the anodic polarization curve for metal dissolution in the active and passive states may be explained by the Helmholtz layer pd ϕ_c which changes as a function of the metal potential ϕ_M and the surface film thickness L. Figure 40 shows ϕ_c calculated as a function of ϕ_M for various L by assuming for the sake of simplicity $\varepsilon_H \approx \varepsilon_F$ and $\delta \approx 0.5$ nm. Several possible ϕ_c–ϕ_M curves (and hence $\log j_d$–ϕ_M curves) are also illustrated for a metal anode on which no surface film, a monoatomic oxygen film, or an oxide film growing as a function of ϕ_M at different growth rates is formed. It appears that the adsorption of monoatomic oxygen layer does decrease the potential ϕ_c and hence diminish the anodic metal dissolution rate to some extent, which may lead to passivation. The metal dissolution rate, however, will increase with increasing ϕ_M, unless the monoatomic oxygen layer does grow to a polyatomic thickness. Figure 41 shows the sulfide monolayer passivation of mercury in sulfide ion solutions, where the passive dissolution current is seen to increase with anodic potential.

It appears also that the passive dissolution current will increase, remain constant, or decrease depending on the film growth as a function of ϕ_M.

Agreement between the theory and experimental results was demonstrated for iron in acid and for nickel in a neutral solution (Sato[56a]).

7. Chemical Breakdown of Passive Films

7.1. Passivity Breakdown due to Aggressive Anions

When the solution contains aggressive anions, the passive film often locally breaks down and the pitting type of localized metal dissolution is initiated at the surface sites of film breakdown. Figure 42 shows the anodic pitting dissolution current of zirconium and stainless steel in halide-containing solutions. A steep increase of anodic current observed in the otherwise passive potential region is a result of chemical breakdown of passive films due to halide ions.

The critical potential for pit initiation is called the pitting potential. It is a function of the nature and concentration of aggressive and inhibitive anions. Generally, the pitting potential is more positive (noble) the smaller the aggressive anion concentration and the greater the inhibitive anion concentration. There is, therefore, a critical concentration of aggressive ions for a given concentration of inhibitive anions, below which no pitting occurs in the passive potential region.

Sulfate ions are inhibitive against chloride pitting of stainless steel, and shifts the pitting potential in the anodic direction. Nitrate ions are also inhibitive, and are able to inhibit completely chloride pitting to recover the

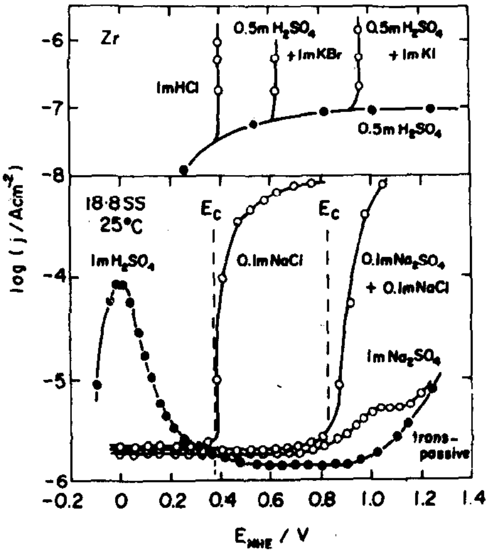

Figure 42. Anodic polarization curves of austenitic 18Cr–8Ni stainless steel in solutions of sulfuric acid, sodium chloride, sodium sulfate, and sodium sulfate containing chloride ions (Leckie and Uhlig[94]), and of zirconium in solutions of sulfuric acid, hydrochloride, sulfate containing bromide ions, and sulfate containing iodide ions (Kolotyrkin[95]), showing the critical potential of pitting dissolution in the presence of halide ions.

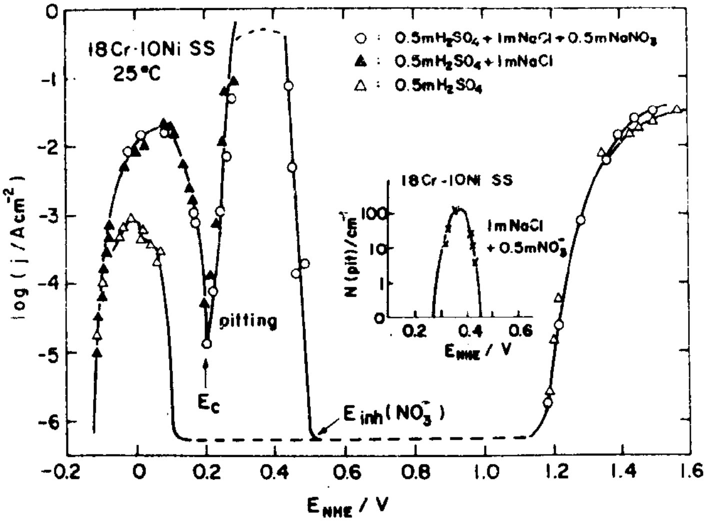

Figure 43. Anodic polarization curves of austenitic 18Cr-10Ni stainless steel in sulfuric acid solutions containing no chloride ions, chloride ions, and chloride and nitrate ions (Braus and Schwenk$^{(96)}$; Schwenk$^{(97)}$), and pit density-potential curve of 18Cr-10Ni stainless steel potentiostated for 24 hr in sodium chloride solution containing nitrate ions (Herbsleb$^{(98)}$).

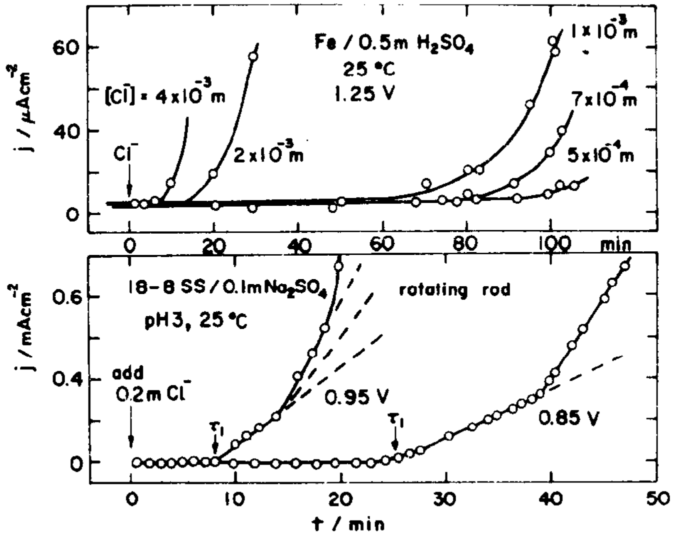

Figure 44. Anodic current density at constant potential as a function of time after addition of chloride ions for prepassivated iron in sulfuric acid (Engell and Stolica$^{(99)}$) and prepassivated 18Cr-8Ni stainless steel in sodium sulfate solution (Sato, Nakagawa, Kudo, and Sakashita$^{(100)}$), showing the incubation time for initiation of pitting dissolution.

passivity of stainless steel at more anodic passivating potentials, as shown in Figure 43.

There exists an induction period for pit initiation after introduction of chloride to prepassivated metals at constant potential anodic to the pitting potential. Figure 44 shows the change in anodic current with time after introduction of chloride for passive iron in sulfuric acid and for passive stainless steel in sulfate solution. As a general tendency, the induction period is shorter the greater the overpotential exceeding the pitting potential.

7.2. Film Breakdown

During the induction period for chloride pit initiation in passivated iron, the passive film dissolution rate oscillates irregularly around a mean value which increases with increasing chloride concentration, as shown in Figure 45. The oscillation continues to occur even after appearance of the pits. Such effects of chloride on the film dissolution does not depend on whether the potential is above or below the pitting potential. The passive film is always breaking down and repairing to a greater or lesser degree depending on the nature and concentration of anions in the solution. If the repair rate is not sufficient to prevent propagation of pits, anodic pitting takes place. The pit initiation is therefore a process in which two competitive reactions of film breakdown and repair are involved.

The observations by McBee and Kruger(56) for iron and by Paatsch(57) for nickel showed that the property of the passive film as measured optically changes in the presence of chloride, as shown in Figure 46. Although the changes are subtle and cannot be interpreted easily, it is evident that chlorides influence the passive film itself.

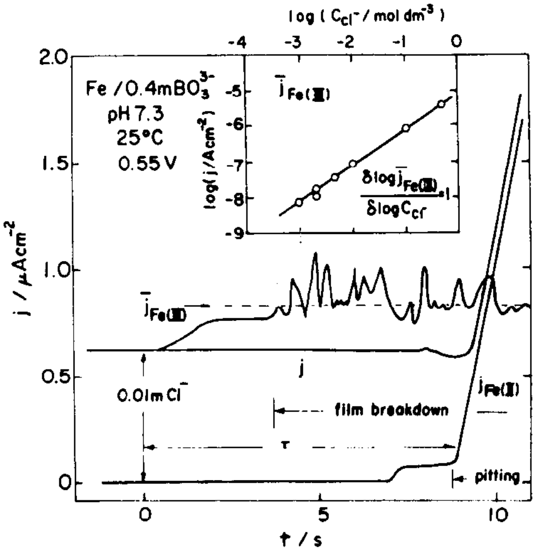

Figure 45. Changes in anodic current j, iron(III) ion dissolution current $j_{Fe(III)}$ (passive film dissolution current), and iron(II) ion dissolution current $j_{Fe(II)}$ (pitting dissolution current) for passive iron in borate solution as functions of time after introduction of chloride ions (Heusler and Fischer(101)).

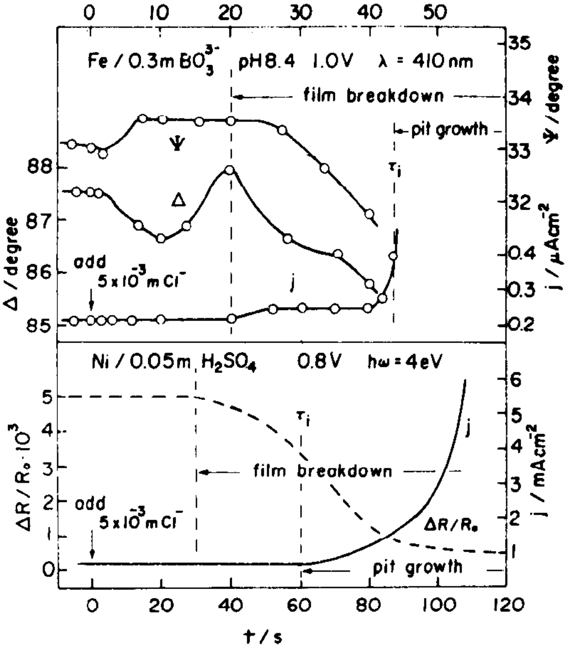

Figure 46. Ellipsometric measurements of changes in Δ and Ψ and in anodic dissolution current for passive iron at constant potential in borate solution (McBee and Kruger[56]), and measurements of changes in modulated reflectivity and anodic dissolution current for passive nickel at constant potential in sulfuric acid solution (Paatsch[57]) after introduction of chloride.

Okamoto, Tachibana, Nishiyama, and Sugita[58] measured the noise in the passive current of stainless steels in sulfuric acid solutions in the presence or absence of chloride. The noise spectra are shown in Figure 47. In the range of noise frequency from 4 to 40 Hz, the mean square of the noise current does not depend on whether chloride ions are present or absent, whereas in

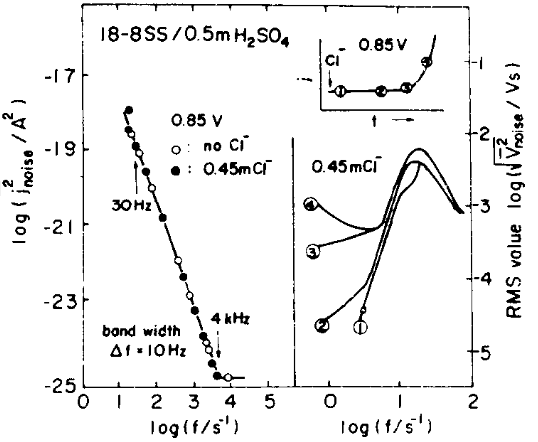

Figure 47. Noise spectra of passive current of stainless steel in 0.5 *m* sulfuric acid solution with or without chloride. The left shows the mean square of noise current versus noise frequency, and the right the root mean square of noise voltage versus noise frequency at different stages of film breakdown during induction for pitting (Okamoto, Tachibana, Nishiyama, and Sugita[58]).

the frequency range lower than 4 Hz the passive current noise represented by the root mean square values of noise voltage increases with time during the induction period of chloride-pit initiation. This is an indication of the breaking down and repairing of the passive film.

7.3. Film Breakdown Models

According to Kruger,(59) theoretical models that have been proposed to describe the events leading to passive film breakdown are classified into three groups; adsorbed ion displacement models, ion migration or penetration models and chemicomechanical models.

The first group of models predict that breakdown occurs when a more strongly adsorbing damaging anion displaces the oxygen forming the passive film or that a small number of aggressive anions jointly adsorb to form a high-energy complex on the surface of the passive film. The film of oxygen monolayer adsorption is thus locally removed at the site of anion adsorption, or the passive polyatomic phase oxide film is made thinner at the site where adsorbing damaging anions readily remove cations from the passive film lattice. When other anions are present, they can compete with the damaging anions for sites and inhibit breakdown.

The second group of models assumes that migration or penetration of aggressive anions through the passive film occurs. The processes which involve ion migration or penetration can occur in a variety of ways, such as a pore mechanism in which preexisting pores or defects provide a penetration path, and an anion or cation vacancy mechanism in which a path of high ionic conductivity is created.

The last group of models involve chemically induced mechanical disruption of the passive film. Stress in the passive film can arise for several reasons such as interfacial tension, electrostriction pressure, volume ratio of the oxide to the metal, hydration or dehydration, and impurities. According to Sato,(60) the electrostriction pressure and interfacial tension generate the pressure acting normal to the passive film as given by

$$P = \frac{\varepsilon(\varepsilon - 1)E}{8\pi} - \frac{\gamma}{L} \tag{40}$$

where ε is the dielectric constant of the film, E the electric field in the film, γ the surface tension, and L the film thickness. This film pressure could exceed the fracture strengths of the oxides and lead to the mechanical rupture of passive films.

7.4. Pit Generation Kinetics

The generation of pits in passive metals is a random phenomenon discrete in time and location on the surface, and hence may be regarded as a stochastic

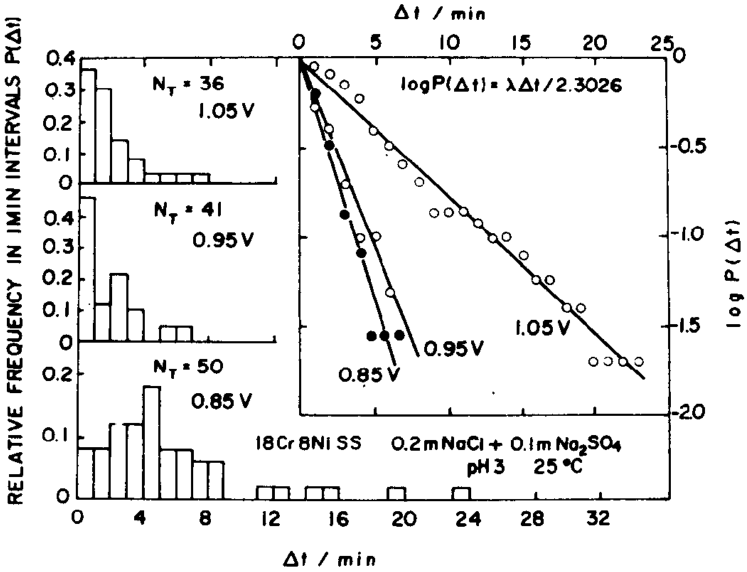

Figure 48. Frequency histogram (left) and cumulative relative frequency curve (right) of pit generation time interval Δt for chloride-pit generation in rotating 18Cr–8Ni stainless steel electrode at three different potentials in 0.2 m sodium chloride solutions containing 0.1 m sodium sulfate of pH 3 (Sato(62)).

process (Shibata and Takeyama(61)). According to Sato,(62) the time interval, Δt, for chloride pits successively breaking out in rotating stainless steel electrode scatters in such a manner as to satisfy the Markov restriction that the probability $P(\Delta t)$ for a pit to break out in a time interval greater than Δt is given by

$$dP(\Delta t)/P(\Delta t) = -\lambda\, dt \tag{41}$$

and hence by

$$d \log P(\Delta t)/dt = -\lambda/2.3026 \tag{42}$$

where λ is the pit generation intensity. Figure 48 shows the frequency histograms and cumulative relative frequency curves for Δt at three different potentials, indicating that pit initiation can be regarded as a Markov process. The pit generation intensity λ depends on the potential and the surface area.

7.5. Stability of Pitting

According to Franck,(63) the active and passive states cannot coexist stably on the same surface (all-or-nothing law). In the presence of aggressive ions, however, the active surface in growing pits is stable with the passive surface surrounding the pits. Such coexistence of two different states, from the viewpoint of irreversible thermodynamics, is possible only when certain transport processes are taking place to stabilize a heterogeneous pattern created on the surface.

Hisamatsu[64] has suggested that the mass transport between the pit inside and the bulk of solution determines the stability of a growing pit. The transport equation is given by

$$\Delta\Sigma C = \frac{j_w r}{nFD} \text{ mol/cm}^3 \tag{43}$$

where $\Delta\Sigma C = \Sigma C_{\text{pit}} - \Sigma C_{\text{out}}$ denotes the total concentration difference for all ionic species between the solution within the pit and the solution outside the pit, n the metal ion valency, D the diffusion coefficient of metal ions, j_w the anodic dissolution current density at pit wall, and r the pit mouth radius. He found experimentally that, independent of the pit radius, a growing pit was stable unless the total concentration difference $\Delta\Sigma C$ decreased below a critical value, $(\Delta\Sigma C)^*$, which was 1.8 m/cm^3 for 18Cr–8Ni stainless steel in sodium chloride solution.

Essentially the same transport equation was presented by Pickering and Frankenthal[65] and was modified by Galvele,[66] who emphasized the local acidification due to metal ion hydrolysis within the pit rather than the local concentration of salts.

Equation (43) may also be applied to describing the critical condition for pit initiation. Substituting a Tafel equation $j_w = j_w^\circ \exp(\beta E)$ in Eq. (43) leads to the critical potential for pit initiation,

$$E^* = \frac{1}{\beta} \ln \frac{nFD(\Delta\Sigma C)^*}{r^* j_w^\circ} \tag{44}$$

where r^* is the size of pit embryo, which was estimated to be about 10 ~ 20 μm for stainless steels.

8. Transpassive Dissolution

8.1. Transpassivity

There are two apparently different modes of transpassivity, as observed in the cases of nickel and chromium. Nickel dissolves as nickel(II) ions in the transpassive state, and the oxidation state of the dissolution product is the same as that in the passive state. This mode of transpassive dissolution may be classified into a group of potential-dependent passive dissolution.

In chromium, however, the dissolution product of chromium(IV) ions in the transpassive state is in the higher oxidation state than in the passive state where chromium dissolves as chromium(III) ions. This is not the same reaction as that of the passive film dissolution described before, but the oxidizing dissolution of the passive film:

$$Cr_2O_3 + 4H_2O \rightarrow Cr_2O_7^{2-} + 8H^+ + 6e \qquad (45)$$

As the transpassive dissolution rate increases, the passive film thickness of Cr_2O_3 decreases to probably less than monolayer.

8.2. Anodic Brightening

When the potential of passivated metal is raised in the anodic direction, one or more of several phenomena, such as shown in the lower half of Figure 49, may occur, among which anodic brightening is of practical use in electrochemical polishing and machining of metals. Hoar(67) has suggested that the occurrence at metal anodes of active dissolution, passivity, pitting, transpassivity, and brightening can be produced by suitable variation of potential and anion–water concentration ratio in solution. As schematically shown in the upper half of Figure 49, anodic metal brightening is more favored at more anodic potentials in more concentrated solutions. During anodic brightening, the metal surface is covered with a viscous salt layer dissolving rapidly into the solution, and it is believed that a very thin, passivelike oxide film is formed at the interface between the metal and the viscous salt layer.

Comparisons between the anodic polarization curves in dilute solutions and those in concentrated solutions are made for iron and nickel in Figure 50. In concentrated chloride solutions, the general dissolution takes place in two different potential regions corresponding to the active dissolution at lower potentials and the brightening type of dissolution at higher potentials, and the pitting occurs at the boundary between the two potential regions.

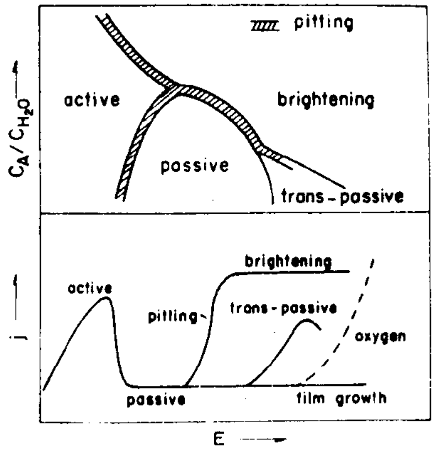

Figure 49. Scheme showing metal anode behavior at various potentials in solutions of various anion–water concentration ratios (upper) and several modes of anodic polarization curves at potentials more positive than the passive range (Hoar(67)).

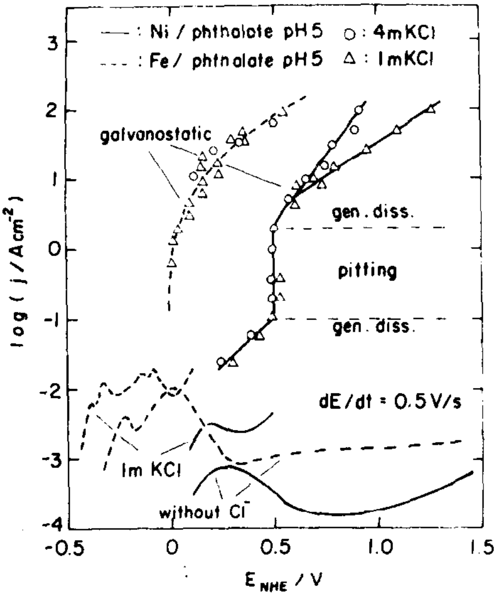

Figure 50. Galvanostatic transient polarization curves in concentrated 1 *m* and 4 *m* chloride solutions and potentiodynamic polarization curves in dilute 0.05 *m* phthalate solutions with or without chloride for iron and nickel anodes (Strehblow and Wernners(103)).

9. Electron Transfer Reactions at Passive Metal Electrodes

9.1. Oxygen Electrode Reaction

The anodic oxygen evolution reaction at passive metal electrodes requires electrons to transfer across the passive barrier film. The electron transfer may occur by the tunnel mechanism even if the passive film is an insulator. Morozumi and Moriya(68) found that, at passive zirconium electrodes, the anodic oxygen evolution took place only when the passive film was thin enough for electron tunneling. Figure 51 shows the potentiodynamic polarization curve of passive zirconium in ammonium borate solution. The oxygen current j_{O_2} appears only in the first anodic potential sweep where the passive film thickening is in progress. When the passive film thickness exceeds a certain value, the oxygen current suddenly decreases to less than the anodic current of passive film formation. Once a thick passive film is formed, the oxygen current peak no longer appears in the succeeding potential sweeps.

According to Hartman,(69) the electronic tunnel conduction is given by

$$J_e = \frac{4\pi m^* e}{h^3 C^2} \frac{\pi CkT}{\sin(\pi CkT)} \exp(-B)[1 - \exp(Ce\eta)] \tag{46}$$

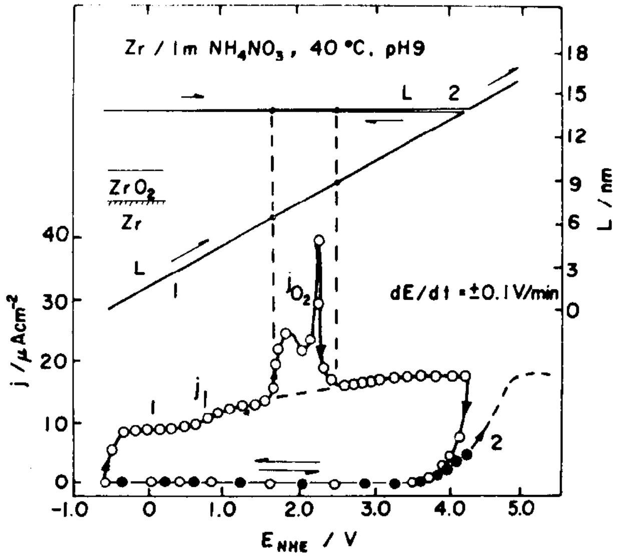

Figure 51. Anodic current-potential and film thickness-potential curves of zirconium in ammonium nitrate solution at pH 9 during anodic and cathodic potential sweep (1) followed by another anodic sweep (2) at sweep rate $dE/dt = \pm 0.1$ V/min. j_1, film formation current density. j_{O_2}, oxygen evolution current density (Morozumi and Moriya[68]).

where B and C are, for low bias voltage ($e\eta < \Phi_1$),

$$B(\eta) = 2\alpha L[(\Phi_1 - e\eta)^{3/2} - \Phi_2^{3/2}]/3(\Phi_1 - \Phi_2 - e\eta)$$

$$C(\eta) = \alpha L[(\Phi_1 - e\eta)^{1/2} - \Phi_2^{1/2}]/(\Phi_1 - \Phi_2 - e\eta)$$

and, for high bias voltage ($e\eta > \Phi_1$),

$$B(\eta) = -2\alpha L\Phi_2^{3/2}/3(\Phi_1 - \Phi_2 - e\eta)$$

$$C(\eta) = -\alpha L\Phi_2^{1/2}/(\Phi_1 - \Phi_2 - e\eta)$$

where $\alpha = 4(2m^*)^{1/2}/hL$, L is the film thickness, m^* the electron effective mass, η the overpotential (bias voltage), and h the Planck constant. Φ_1 and Φ_2 are the energy barrier heights at the metal–film interface and at the film–solution interface, as shown in the upper half of Figure 52.

For a growing passive barrier film on zirconium, comparisons were made between the electronic tunneling current calculated from Eq. (46) and the observed anodic oxygen current, and good agreement was obtained at high overpotentials where the electronic conduction was determining the rate of the oxygen electrode reaction, as shown in the lower half of Figure 52. At low overpotentials, the rate-determining step is not of the electron conduction but of the electrochemical process occurring at the film–solution interface.

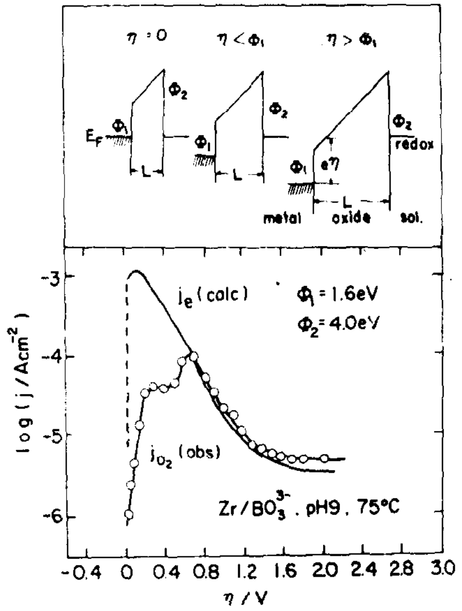

Figure 52. Schematic illustration of electron energy band model for metal–passive film–solution system and comparison between calculated tunnel electron conduction current $j_{e(cal)}$ and experimental potential sweep polarization curve at $dE/dt = 0.1$ V/min for passive zirconium electrode covered with a passive film growing with potential in saturated ammonium borate solution at 75°C. Φ_1 and Φ_2 are the energy barrier heights at the metal–film and film–solution interfaces and η the overpotential (bias voltage) for oxygen electrode reaction (Morozumi and Moriya(68)).

9.2. Redox Reactions

Redox reactions other than oxygen electrode reactions may also take place on passive metal surfaces covered with thin passive films. Actually, at passive iron electrodes, redox reactions such as Ce^{2+}–Ce^{4+} (Franck and Weil(70)), Fe^{2+}–Fe^{3+} (Makrides(71)), and $[Fe(CN)_6]^{4-}$–$[Fe(CN)_6]^{3-}$ (Moshtev(72); Schultze and Stimming(73)) were observed to occur with fairly large rates.

Figure 53 shows the magnitude of redox current densities for the redox reaction of iron(II)–(III) cyanides at passive iron electrodes as a function of the passive film thickness. The redox current density, which depends on the overpotential, decreases as the film thickness increases. This suggests that the passive film on iron is not as good an electronic conductor as metallic iron. Electrons, therefore, would have to transfer across the passive film which is more or less involved in the structure of the electrical double layer between the metal and the solution, as mentioned before (Figure 40). It is reasonable to consider that the electron transfer takes place mainly by the tunnel mechanism.

The redox current density also appears to depend on the semiconducting property of the passive film. Figure 54 shows the anodic and cathodic polarization curves of iron(II)–(III) cyanides for various passive metal electrodes, where the current density is normalized for unit concentration of iron cyanides.

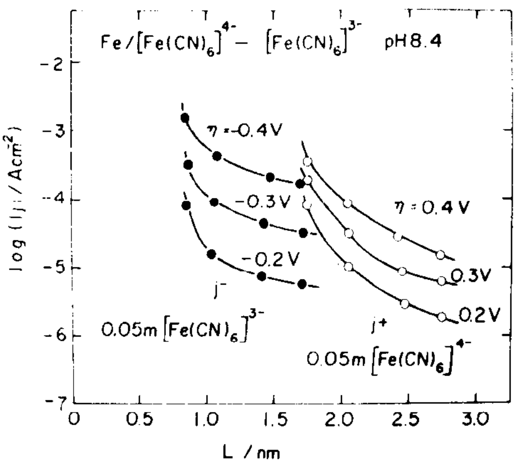

Figure 53. Anodic and cathodic current density of iron(II)-(III) cyanides redox reaction at different overpotentials on passive iron electrode as functions of the passive film thickness (Schultze and Stimming[73]).

The passive films on titanium, iron, and niobium are of *n*-type semiconductors, and allow the anodic current to flow more easily than the cathodic current, which tends to level off with increasing overpotential. This is probably due to the electronic energy band structure of the passive film, as expected from the semiconductor electrode kinetics.

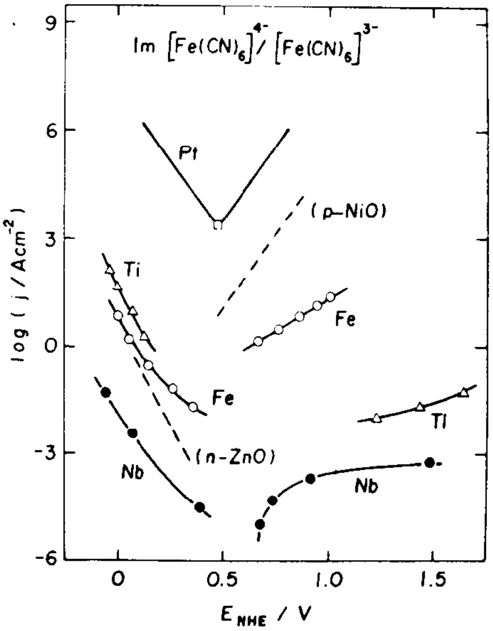

Figure 54. Anodic and cathodic polarization curve of iron(II)-(III) cyanides redox reaction at passive electrodes of platinium, titanium, iron, and niobium, and at oxide electrodes of *p*-type NiO and *n*-type ZnO. Current densities are normalized for 1 *m* iron cyanide concentration. The passive film thickness is 5.0 nm for Ti-TiO_2, 1.7 nm for Fe-γ-Fe_2O_3, and 12 nm for Nb_2O_5 (Schultze and Stimming[73]).

10. Concluding Remarks

This chapter has attempted to delineate as many of the experimental facts as possible which one can depend on to understand the phenomenon of passivity. Although a general framework has been established, it is evident that further experimental and especially theoretical analysis is required. At the present stage of experimental techniques, it is not difficult to measure the polarization curve of a metal anode in a given environmental solution from which one can determine the potential regions for stable passivity, transpassivity, and passivity breakdown. Neither experimental methods nor the experimental results, however, are sufficiently detailed or accurate to provide the reliable base for the complete understanding of the nature and function of the passive film.

It should be noted that the passive film, which has been described as an oxide in the previous sections, may not be a rigid crystalline oxide but may be a vitreous polymer oxide which contains bound water forming hydroxyl bridges in the film. Because of its thickness of the order of a nanometer, the passive film is more or less sensitive to the environmental variables. Thus one cannot make arguments about the nature and composition of the passive film without defining the history of its formation and the environment in which it has been aged.

Finally, we hope that this chapter will prove helpful in recognizing the present state of knowledge and the essential problems to be studied on the electrochemical passivity of metals, which undoubtedly is of importance in the field of metallic corrosion and electronic technology.

Acknowledgments

The authors would like to thank Mr. R. Nishimura and Miss C. Miura for help during the preparation of the manuscript. The authors are also indebted to those workers whose valuable experiments and comments have been incorporated in this chapter.

References

1. M. Faraday, *Experimental Research in Electricity*, Vol. II, University of London, London (1844), pp. 2 and 244.
2. C. Wagner, *Corros. Sci.* **5**, 751 (1963).
3. M. Jänchen and K. Schwabe, *Z. Phys. Chem. (Leipzig)* **237**, 129 (1976).
4. Ya. M. Kolotyrkin and G. G. Kossii, *Zaschtschita Metallov* **1**, 272 (1965).
5. K. E. Heusler, *Z. Elektrochem.* **62**, 582 (1958).
6. J. O'M. Bockris, D. Drazic, and A. R. Despic, *Electrochim. Acta* **4**, 315 (1961).
7. L. Franke, W. Forker, and P. Schultheiss, *Electrochim. Acta* **18**, 877 (1973).
8. N. Sato, *Trans. Japan, Inst. Metals* **6**, 63 (1965).
9. W. J. Plieth and I. J. Vetter, *Ber. Bunsenges. Phys. Chem.* **73**, 1977 (1969).

10. I. Epelboin and M. Keddam, *Electrochim. Acta* **17**, 177 (1972).
11. R. D. Armstrong and M. H. Henderson, *J. Electroanal. Chem.* **39**, 222 (1972).
12. R. D. Armstrong, M. Henderson, and H. R. Thirsk, *J. Electroanal. Chem.* **35**, 119 (1972).
13. R. D. Armstrong and R. E. Firman, *J. Electroanal. Chem.* **34**, 391 (1972).
14. T. Heuman and M. Klimmeck, in *Proceedings of 5th ICMC–Tokyo, Japan*, 1972, NACE, Houston (1975), p. 115.
15. I. Epelboin, C. Gabrielli, M. Keddam, and H. Takenouchi, *Electrochim. Acta* **20**, 913 (1975).
16. F. Flade, *Z. Phys. Chem.* **76**, 513 (1911).
17. K. R. Bonhoeffer, *Z. Metallk.* **44**, 77 (1953).
18. M. J. Pryor, *J. Electrochem. Soc.* **106**, 557 (1959).
19. C. Wagner, *Ber. Bunsenges. Phys. Chem.* **77**, 1090 (1973).
20. W. Schottky, *Halbleiter Problem II*, 233 (1958).
21. M. Nagayama and M. Cohen, *J. Electrochem. Soc.* **110**, 670 (1963).
22. H. H. Uhlig, *Z. Elektrochem.* **62**, 626 (1958).
23. U. F. Franck, *Z. Naturforsch.* **49**, 378 (1949).
24. Th. Heuman and F. W. Diekötter, *Z. Elektrochem.* **62**, 745 (1958).
25. R. Landsberg and M. Hollnagel, *Z. Elektrochem.* **58**, 680 (1954).
26. R. Landsberg and M. Hollnagel, *Z. Elektrochem.* **60**, 1098 (1956).
27. K. F. Bonhoeffer and K. J. Vetter, *Z. Phys. Chem.* **196**, 127 (1950).
28. U. Ebersbach, K. Schwabe, and K. Ritter, *Electrochim. Acta* **12**, 927 (1967).
29. H. G. Feller, M. Kesten, and J. Krupki, in *Proceedings of 5th ICMC–Tokyo, Japan*, 1972, NACE, Houston (1975), p. 155.
30. N. Sato, K. Kudo, and K. Nishimura, *J. Electrochem. Soc.* **123**, 1419 (1976).
31. N. Sato, K. Kudo, and T. Noda, *Z. Phys. Chem.* N.F. **98**, 217 (1975).
32. M. Seo, N. Sato, J. B. Lumsden, and R. W. Staehle, *Corros. Sci.* **17**, 209 (1977).
33. C. L. Foley, J. Kruger, and C. J. Bechtoldt, *J. Electrochem. Soc.* **114**, 994 (1967).
34. H. T. Yolken, J. Kruger, and J. P. Calvert, *Corros. Sci.* **8**, 103 (1968).
35. K. Kudo, T. Shibata, G. Okamoto, and N. Sato, *Corros. Sci.* **8**, 809 (1963).
36. R. W. Revie, B. G. Baker, and J. O'M. Bockris, *J. Electrochem. Soc.* **122**, 1560 (1975).
37. W. E. O'Grady and J. O'M. Bockris, *Surf. Sci.* **38**, 249 (1973).
38. R. Nishimura and N. Sato, *Boshoku Gijutsu* (Corrosion Engineering, Japan) (1977).
39. K. J. Vetter and F. Gorn, *Z. Phys. Chem.* N.F. **86**, 113 (1973a).
40. E. K. Oshe, I. L. Rosenfeld, and V. G. Doroskenko, *Dokl. Akad. Nauk SSSR* **194**, 614 (1970).
41. N. Sato and K. Kudo, *Electrochim. Acta* **16**, 447 (1971).
42. K. E. Heusler and K. Schoner, *Ber. Bunsenges Phys. Chem.* **77**, 885 (1973).
43. H. Gobrecht, W. Paatsch, and R. Thull, *Ber. Bunsenges. Phys. Chem.* **75**, 1353 (197
44. T. Ohtsuka, Dissertation, Hokkaido University, Japan, 1976.
45. G. W. Simmons, E. Kellerman, and H. Leidheiser, Jr., *J. Electrochem. Soc.* **123**, 1276 (1976).
46. K. Sugimoto, K. Kishi, S. Ikeda, and Y. Sawada, *J. Japan Inst. Metals* **38**, 54 (1974).
47. K. J. Vetter, *Z. Elektrochem.* **59**, 67 (1955).
48. K. J. Vetter, *J. Electrochem. Soc.* **110**, 597 (1963).
49. V. M. Novakovski and Y. A. Likkackev, *Electrochim. Acta* **12**, 267 (1967).
50. K. E. Heusler, *Ber. Bunsenges. Phys. Chem.* **72**, 1197 (1968).
51. K. J. Vetter and F. Gorn, *Electrochim. Acta* **18**, 321 (1973b).
52. K. G. Weil, *Z. Elektrochem.* **59**, 711 (1955).
53. R. V. Moshtev, *Ber. Bunsenges. Phys. Chem.* **71**, 1079 (1967).
54. N. Sato and M. Cohen, *J. Electrochem. Soc.* **111**, 52 (1963).
55. A. M. Kuznetsov and R. R. Dogonadze, *Izv. Akad. Nauk SSSR Ser. Him.*, No. 12, 2140 (1964); English Translation, Consultants Bureau, New York, p. 2042.
56. C. L. McBee and J. Kruger, *Localized Corrosion*, R. W. Staehle, B. F. Brown, J. Kruger, and A. Agrawal, eds., NACE, Houston (1974), p. 252.

56a. N. Sato, in *Passivity and Its Breakdown on Iron and Iron Base Alloys, USA–Japan Seminar,* 1975, R. W. Staehle and H. Okada, eds., NACE, Houston (1976), p. 1.
57. W. Paatsch, *Ber. Bunsenges. Phys. Chem.* **77**, 895 (1973).
58. G. Okamoto, K. Tachibana, S. Nishiyama, and T. Sugita, in *Passivity and Its Breakdown on Iron and Iron Base Alloys, USA–Japan Seminar,* 1975, R. W. Staehle and H. Okada, eds., NACE, Houston (1976), p. 106.
59. J. Kruger, in *Passivity and Its Breakdown on Iron and Iron Base Alloys, USA–Japan Seminar,* 1975, R. W. Staehle and H. Okada, eds., NACE, Houston (1976), p. 91.
60. N. Sato, *Electrochim. Acta* **16**, 1683 (1971).
61. T. Shibata and T. Takeyama, *Nature* **260**, 315 (1976).
62. N. Sato, *J. Electrochem. Soc.* **123**, 1197 (1976).
63. U. F. Franck, *Korrosion* **13**, 3 (1960).
64. Y. Hisamatsu, in *Passivity and Its Breakdown on Iron and Iron Base Alloys, USA–Japan Seminar,* 1975, R. W. Staehle and H. Okada, eds., NACE, Houston (1976), p. 99.
65. H. W. Pickering and R. P. Frankenthal, *J. Electrochem. Soc.* **119**, 1297 (1972).
66. J. R. Galvele, *J. Electrochem. Soc.* **123**, 464 (1976).
67. T. P. Hoar, *Corros. Sci.* **7**, 341 (1967).
68. T. Morozumi and M. Moriya, in *Proceedings of 5th ICMC–Tokyo,* 1972, NACE, Houston (1975), p. 322.
69. T. E. Hartman, *J. Appl. Phys.* **35**, 3238 (1964).
70. U. F. Franck and K. Weil, *Z. Elektrochem.* **56**, 814 (1952).
71. A. C. Makrides, *J. Electrochem. Soc.* **111**, 394 (1964).
72. R. V. Moshtev, *Electrochim. Acta* **16**, 2039 (1972).
73. J. W. Schultze and U. Stimming, *Z. Phys. Chem.* N.F. **98**, 285 (1976).
74. N. D. Tomashov, *Theory of Corrosion and Protection of Metals,* MacMillan, New York (1966), p. 325.
75. G. Okamoto and N. Sato, *J. Japan Inst. Metals* **23**, 725 (1959).
76. N. Sato and G. Okamoto, *J. Electrochem. Soc.* **110**, 605 (1963).
77. Ya. M. Kolotyrkin, *Z. Elektrochem.* **62**, 664 (1958).
78. U. F. Franck, *Werkstoffe Korr.* **9**, 504 (1958).
79. N. D. Tomashov, G. P. Chernova, Yu. S. Ruskol, and G. A. Ayuyan, in *Proceedings 5th ICMC–Tokyo, Japan,* 1972, NACE, Houston (1975), p. 248.
80. G. Okamoto, *Corros. Sci.* **13**, 471 (1973).
81. L. Kiss, L. DoNgoc, and M. L. Varsanyi, *Coll. Czech. Chem. Commun.* **36**, 914 (1971).
82. T. Noda, Dissertation, Hokkaido University, Japan, 1973; T. Noda, K. Kudo, and N. Sato, *Japan. Inst. Metals* **37**, 951, 1088 (1973).
83. M. Nagayama and M. Cohen, *J. Electrochem. Soc.* **109**, 781 (1962).
84. N. Sato, Dissertation, Hokkaido University, Japan, 1961.
85. K. J. Vetter and K. Arnold, *Z. Elektrochem.* **64**, 244 (1960).
86. J. Kruger and J. P. Colvert, *J. Electrochem. Soc.* **114**, 43 (1967).
87. N. Sato, K. Kudo, and M. Miki, *J. Japan. Inst. Metals* **35**, 1007 (1971).
88. G. M. Florianovich, Ya. M. Kolotyrkin, and D. Kononova, *Proceedings of the 4th ICMC–Amsterdam,* 1969, NACE, Houston (1972), p. 694.
89. W. Visscher and A. Damjanovic, Extended Abstracts, I.S.E. 27th Meeting, Zurich, 1976, No. 138.
90. E. K. Oshe and I. L. Rosenfeld, Extended Abstracts, 6th ICMC—Sydney, 1975, No. 1-23.
91. T. Shibata and G. Okamoto, *Boshoku Gijutsu* **21**, 263 (1972).
92. T. Noda and N. Sato, *J. Japan Inst. Metals* **28**, 1143 (1974).
93. R. D. Armstrong, D. F. Porter, and H. R. Thirsk, *J. Phys. Chem.* **72**, 2300 (1968).
94. H. P. Leckie and H. H. Uhlig, *J. Electrochem. Soc.* **113**, 1262 (1966).
95. Ya. M. Kolotyrkin, *J. Electrochem. Soc.* **108**, 209 (1961).
96. E. Brauns and W. Schwenk, *Arch. Eisenhuttenw.* 387 (1961); *Werkstoffe Korr.* **12**, 73 (1961).
97. W. Schwenk, *Corrosion (Houston)* **20**, 129t (1964).

98. G. Herbsleb, *Werkstoffe Korr.* **16**, 929 (1965).
99. H. J. Engell and N. D. Stolica, *Z. Phys. Chem.* N.F. **20**, 113 (1959).
100. N. Sato, T. Nakagawa, K. Kudo, and M. Sakashita, in *Localized Corrosion*, R. W. Staehle, B. F. Brown, J. Kruger, and A. Agarawal, eds., NACE, Houston (1974), p. 447.
101. K. E. Heusler and L. Fischer, *Werkstoffe Korr.* **27**, 551 (1976).
102. R. Saito, graduation thesis, Hokkaido University, Japan, 1976.
103. H. H. Strehblow and J. Wenners, *Z. Phys. Chem.* N.F. **98**, 199 (1975).
104. K. J. Vetter and F. Gorn, *Werkstoffe Korr.* **21**, 703 (1970).
105. H. Göhr and E. Lange, *Z. Elektrochem.* **62**, 1292 (1957).
106. N. Sato and R. Nishimura, *Boshoku Gijutsu* (*Corrosion Engineering, Japan*) **26**, 305 (1977); **27**, 457 (1978).

5

The Kinetics of the Growth of Oxides

M. J. DIGNAM

1. Introduction

1.1. The Nature of the Problem

The growth of an oxide film on a metal surface involves the transport of matter and/or charge in at least three phases, the metal, the oxide film, and the oxidizing medium. Many metals form more than one stable oxide, and some oxides exist in both amorphous and crystalline forms. The oxides may possess pores or fissures complicating the transport processes, while grain boundaries and dislocations can provide short-circuit transport paths. To this potpourri must be added surface and space charges and the ever-elusive properties of at least two interfaces and their attendant processes. The result is an overwhelming range of possible—and no doubt actual—kinetic behavior.

It is clearly impossible in a chapter of this length to either consider the kinetic consequences of all the various combinations of basic processes or review all the published data. At present, we can hope to understand only the simplest of systems, and even here, we must expect to find alternative models that will account for the available data. With this in mind, a few typical systems will be examined in some detail, and in the process, some of the fundamentals will be provided for analyzing the kinetics of many metal–oxide systems.

M. J. DIGNAM • Department of Chemistry, University of Toronto, Toronto, Canada

Much of the material omitted can be found in reviews as follows: Hoar,(1) Evans,(2) Young,(3) Burger and Young,(4) Fleischmann and Thirsk,(5) Vermilyea,(6) Bardina,(7) Hoar,(8) Goruk, Young, and Zobel,(9) Diggle, Downie and Goulding,(10) Fehlner and Mott,(11) Dell'Oca, Pulfrey, and Young,(12) Evans,(13) Ahmed,(14) Brusic,(15) Dignam,(16) Vijh,(17) Wood,(18) Fromhold,(19) and Belanger and Vijh.(20)

In Section 1.2 of this Introduction, a summary of the overall kinetics of oxide film growth is presented for a number of systems giving rise to distinct and reasonably well-characterized behavior. This is then followed in Sections 2 and 3 by analyses of some of the separate components that together comprise the growing oxide film. In the final two sections, more detailed discussion of some typical systems is presented.

1.2. Commonly Observed Kinetic Behavior

1.2.1. High-Field Conduction

A large number of metals and semiconductors, when anodically polarized in a suitable electrolyte, exhibit kinetic behavior over some range of potential, which is characteristic of the valve metals. For purposes of this chapter, valve metal or high-field conduction behavior will be defined as that in accord with

$$i \simeq A \exp(\beta E) \tag{1}$$

where i is the faradaic current associated with the metal oxidation, A and β are temperature-dependent constants, and E is the electric field strength in the film. The latter is usually set equal to either the mean field $\bar{E}$ or differential field $\tilde{E}$, defined as

$$\bar{E} = (\eta - \eta_0)/X, \qquad \tilde{E} = (\partial\eta/\partial X)_i \tag{2}$$

where η is the overpotential for the metal oxidation process and X is the film thickness. The quantity η_0 allows for the possibility that some of the overpotential appears as an interfacial potential drop. It is commonly found to be zero within experimental error,(21) and we introduce this simplification here. Since β appears as a multiplier of E in Eq. (1), it is frequently referred to as the field coefficient. It is also sometimes called the reciprocal Tafel slope, owing to the obvious similarity between the Tafel equation and the logarithmic form of Eq. (1):

$$E \simeq \beta^{-1} \ln(i/A) \tag{3}$$

We leave the microscopic origin of Eq. (1) to Section 2 and pursue now the types of kinetic behavior to which it gives rise. We warn, however, that Eq. (1) is frequently only approximately obeyed so that the derived kinetics, while qualitatively correct, will not necessarily accurately duplicate data.

1.2.2. Ideal Valve Metal Behavior

The simplest kinetics derivable from Eq. (1) are those exhibited by the so-called valve metals, principally Ta, Nb, and Al. In an electrolyte which does not act as a solvent for the oxide, when polarized anodically up to overpotentials as high as or exceeding 100 V, these metals form oxide films of essentially fixed stoichiometry and remarkable uniformity in thickness, to the exclusion of other processes, such as metal dissolution and oxygen evolution.(3) A large number of other metals, semiconductors, and alloys are alleged to approach this "ideal valve metal behavior" under certain conditions of restricted potential, etc., e.g., W, Bi, Fe, Ti, Ge, Si, Zr, Sb, InSb (3); V, Mo (22); Pt (23); Ni (24); alloys of Al with Mg, Zn, Cu, Si, Fe (25); alloys of Nb with Zr, W, Ti, V, and Mo (26); alloys of V with Nb, Ti, Ta, and Al (27); and alloys of Ta with Nb, Ti, and Zr.(27)

We examine now the basic kinetics typical of valve metals. Since all of the faradaic current goes to film formation,

$$X = X_0 + (\Omega/F)\int_0^t i\,dt \tag{4}$$

where X_0 is the film thickness at time zero, Ω is the volume per electrochemical equivalent weight of the oxide, F is Faraday's constant, and t is time. Substituting $E = \bar{E}$ from Eq. (2) and X from Eq. (4),

$$\eta \simeq \beta^{-1} \ln (i/A)\left[X_0 + (\Omega/F)\int_0^t i\,dt\right] \tag{5}$$

1.2.2.1. Galvanostatic Conditions

For galvanostatic conditions, differentiating Eq. (5) with t,

$$\left(\frac{\partial \eta}{\partial t}\right)_i \simeq \frac{\Omega}{\beta F} i \ln \frac{i}{A} \tag{6}$$

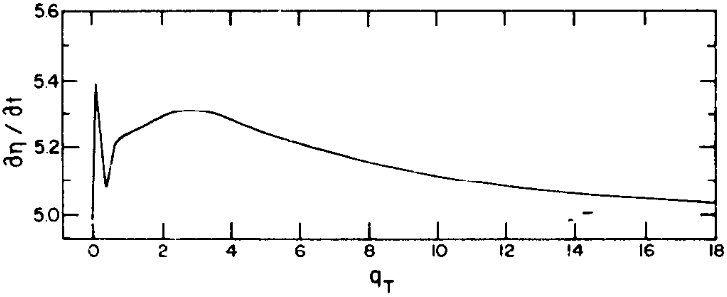

Figure 1. $\partial\eta/\partial t$ in arbitrary units versus total charge passed, q_T (in mC/cm^2) for Al anodically oxidized under galvanostatic conditions in a glycol borate electrolyte (1 mC/cm^2 ~ 5.5 Å; data according to Dignam and Ryan(28)).

Since $i \ggg A$, a factor of 10 increase in i typically results in only a few percent increase in ln (i/A).(3) Thus Eq. (6) predicts that η will increase linearly with time, the slope being approximately proportional to i. Figure 1 shows data obtained for Al anodically oxidized under galvanostatic conditions in a glycol borate electrolyte, with $\partial\eta/\partial t$ determined by electronic differentiation.(28) For $X \gtrsim 100$ Å, $\partial\eta/\partial t$ appears to be more or less constant.

1.2.2.2. Potentiodynamic Conditions

Since galvanostatic conditions establish a linear ramp potential, application of a linear ramp potential must ultimately establish a constant current density. Such a current–time or potentiodynamic plot for a freshly anodized Al specimen is shown in Figure 2. The form of the current step is obtained by substituting $\eta = (d\eta/dt)t = \dot{\eta}t$ into Eq. (5) and eliminating the integral by differentiation, which gives

$$\frac{dy}{y \ln y} + \frac{dy}{(\beta\dot{\eta}F/A\Omega) - y \ln y} \simeq \frac{dt}{t} \tag{7}$$

where $y = i/A$. Setting $y_s = i_s/A$, where i_s is the final steady state current density, it follows from Eq. (6) that

$$y_s \ln y_s = \beta\dot{\eta}F/A\Omega \tag{8}$$

Substituting for $\beta\dot{\eta}F/A\Omega$ from Eq. (8), Eq. (7) becomes, after integrating and taking antilogarithms,

$$t \simeq \frac{X_0}{\beta\dot{\eta}}(\ln y)\exp\left(\int_1^y \frac{dy}{y_s \ln y_s - y \ln y}\right) \tag{9}$$

where the boundary conditions $y = 1$ at $t = 0$, and $(t/\ln y) \to X_0/\beta\dot{\eta}$ as $t \to 0$ have been used [Eq. (5)].

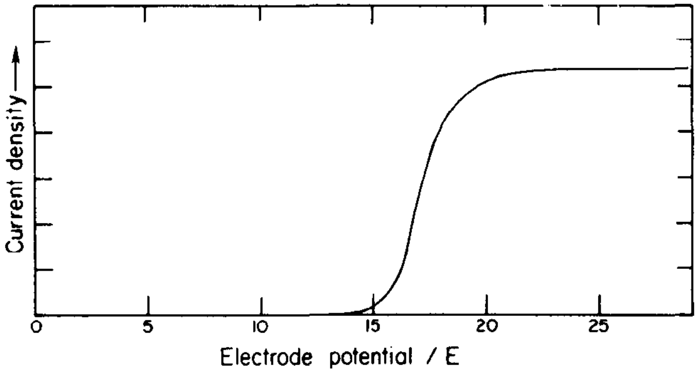

Figure 2. Potentiodynamic plot for Al anodically oxidized to ~14 V in aqueous 2 M boric acid neutralized to pH 6.0 with NH_4OH. (Measurement made at $\partial\eta/\partial t = 0.1$ V/sec in the same electrolyte; data according to Dignam.(29))

Since $\ln y$ varies slowly with y, as noted previously, an excellent approximation to the integral in Eq. (8) is obtained on replacing $\ln y$ by $\ln y_s$ to give

$$\eta \simeq (X_0/\beta)[\ln (i/A)](1 - i/i_s)^{-1/\ln(i_s/A)} \tag{10}$$

The error introduced by this approximation is less than 0.1% for $\ln (i_s/A) \sim 33$.

The data in Figure 2 are well represented by Eq. (10). Potentiodynamic curves for valve metals are sensitive to film history, however, and do not always lead to curves of this form.

1.2.2.3. Potentiostatic Conditions

The form of the kinetics predicted from Eq. (5) for potentiostatic conditions is obtained on differentiating it by t to eliminate the integral, as before, but this time treating η as a constant,

$$\left[\frac{\partial(1/i)}{\partial t}\right]_\eta \simeq \frac{\Omega[\ln (i/A)]^2}{F\beta\eta} = \frac{\Omega\beta E}{FX} \tag{11}$$

where the final expression makes use of Eq. (3). Thus $1/i$ is predicted to be approximately a linear function of t. The approximation is, in fact, remarkably good. In Figure 3, data covering a wide range in i for the anodic oxidation of Al are plotted according to Eq. (11). The decrease in slope as i decreases can be seen, but for data which are less accurate, or cover the narrower range of i often dictated by the presence of "leakage currents" (currents associated with the

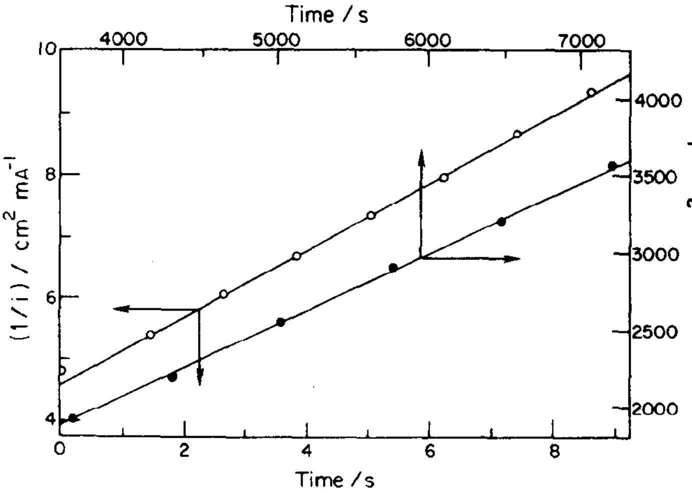

Figure 3. Plot of $1/i$ vs. t for first few seconds and after several hours for Al under potentiostatic conditions in a glycol borate electrolyte. The electrode was anodically oxidized at $i = 0.21$ mA/cm^2 to $\eta = 27.6$ V, after which η was held constant and i measured. The data are according to Dignam and Goad.(30)

oxidation of solution species or with metal or film dissolution), the departure from linearity would be undetectable.

Since

$$dX/dt = i\Omega/F \tag{12}$$

the rate equation $d(1/i)/dt = \text{const}$ is equivalent to the so-called direct logarithmic rate equation$^{(31)}$:

$$X = X_0 + A_l \ln (t/\Upsilon + 1) \tag{13}$$

Comparison of Eqs. (11) and (13), using Eq. (12) and the approximation $\partial(E/X)/\partial t \simeq 0$, gives

$$A_l = X/\beta E, \qquad \Upsilon = FX/i_0\Omega\beta E$$

where i_0 is the value of i at $t = 0$. Making no approximations, Eq. (1) leads to Mott–Cabrera growth kinetics,$^{(32)}$

$$\frac{dX}{dt} = A' \exp\left(\frac{B}{X}\right) \tag{14}$$

where $A' = A\Omega/F$ and $B = \beta\eta$. An approximate integrated form of this, called the inverse logarithmic law, is

$$\frac{1}{X} \simeq \frac{1}{X_0} - A_{il} \ln (t/\Upsilon + 1) \tag{15}$$

where $A_{il} = B^{-1}$, $\Upsilon = X^2/A'B \exp (B/X_0)$.

Under certain circumstances, the direct, not inverse, logarithmic growth law better represents kinetics in accord with the Mott–Cabrera model.$^{(33)}$ More often, the fractional change in thickness during a run is too small to distinguish between the two laws.

1.2.3. Limited Valve Metal Behavior

1.2.3.1. Oxygen Evolution

Oxides which are electronic conductors show departure from "ideal" valve metal behavior with the onset of a reaction in which solution species are oxidized at the oxide–electrolyte interface, e.g., oxygen evolution. This prevents further significant growth of the film, since the electronic current density in the film, responsible for O_2 evolution, say, ultimately becomes much larger than the ionic current density i. For example, if O_2 evolution is controlled at the oxide–electrolyte interface, and obeys a Tafel relation, then for $\eta_t > \eta_{O_2}$ the total faradaic current density, i_T, will be given by

$$i_T = i + i_e \simeq A \exp (\beta\eta/X) + A'' \exp (\eta_{O_2}/b_T) \tag{16}$$

where A'' and b_T are the exchange current density and base e Tafel slope, and

η_{O_2} the overpotential for O_2 evolution. At a constant potential greater than that required for O_2 evolution, i falls off rapidly with time, due to the resulting increase in X, while i_e remains constant. A large η cannot now be established because of the resulting large i_e. The situation is similar if electronic conduction in the film is rate controlling. A proper treatment of this topic requires an analysis of electrode reactions at semiconductor surfaces,(17) including space charge effects.

1.2.3.2. Oxide Dissolution

In electrolytes that act as solvents for the metal oxide, several kinds of behavior that relate to Eq. (1) can arise. Which of these takes place depends on details of the kinetics and mechanism of dissolution and of film growth. For the purpose of illustrating how the different kinds of behavior can arise, the oxide dissolution, expressed as a current density, i_d, will be represented by the equation

$$i_d = A_d \exp(\beta_d E) \qquad (17)$$

where E is the field in the film. For $\beta_d = 0$, Eq. (17) represents chemical dissolution of the oxide (i_d independent of E and η). For $\beta_d > 0$, on the other hand, it corresponds to potential assisted dissolution of the oxide with the oxide–electrolyte double-layer potential assumed to be proportional to the field in the film. The net rate of film formation, expressed as a current density, is given by

$$i - i_d = i[1 - (A_d/A)\exp(\beta_d - \beta)E] \qquad (18)$$

where we have used Eqs. (1) and (17), and have excluded film formation by a dissolution precipitation mechanism. The condition for a steady state film thickness, X_s, to be established is that $i = i_d$, so that from Eq. (18)

$$X_s/\eta = (\beta - \beta_d)/\ln(A_d/A) = E_s^{-1} \qquad (19)$$

We consider in turn the four cases arising from $\beta/\beta_d > 1$ or <1, and $A/A_d > 1$ or <1.

For $\beta > \beta_d$ and $A > A_d$, no steady state exists, i.e., X_s/η is negative. The film continues to grow indefinitely at a rate given by Eq. (18). The result is very nearly ideal valve metal behavior, with passivity achieved at the outset.

For $\beta > \beta_d$ and $A < A_d$, Eq. (19) represents a stable and physically attainable steady state. The corresponding steady state dissolution current density is given by Eq. (1) with $E = E_s$. If film growth occurs entirely at the oxide–electrolyte interface, then a film of uniform thickness should be established, since thin spots in the film will grow faster than they dissolve, etc. If, however, some or all of the newly formed oxide appears at the metal–oxide interface, then conditions are right for porous film formation, such as occurs on Al in aqueous sulfuric acid. Thus dissolution will take place most rapidly where the film is thinnest, while the entire film can grow at the metal–oxide interface

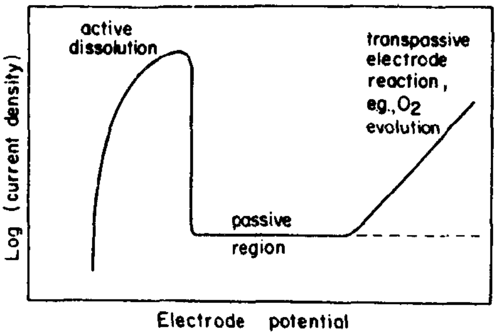

Figure 4. Active–passive behavior typical of that displayed by many metals, e.g., Fe in 1 *M* H_2SO_4, using a slow potentiodynamic anodic sweep. Metals forming oxides which are electronic insulators do not display a transpassive reaction.

via current confined to the thin spots or pores. For the Al system, the steady state thickness of the film at the pore bases is proportional to η, while the overall thickness increases at a constant rate, determined by i.

For $\beta < \beta_d$ and $A > A_d$, Eq. (19) has a solution for positive X_s, but the resulting steady state is an unstable one. Thus if E is increased slightly from its steady state value, the dissolution current density will exceed the film-forming current density [Eq. (18)], and the imbalance will increase as the film thins. The net result is active metal dissolution and no oxide film, except for, perhaps, one or so atomic layers, as Eq. (1) is probably invalid for such thin films. On the other hand, if E is reduced slightly from its steady state value, by the same argument, film growth continues indefinitely, ultimately in accord with Eq. (1) to a good approximation, i.e., passivity results. To achieve passivity, however, a film thickness greater than X_s must somehow form, and this clearly cannot occur by a direct mechanism if one starts with a bare metal surface or with one covered by a film of thickness less than X_s. However, as the potential is made more anodic, the metal dissolution rate will increase and ultimately establish supersaturation conditions in the electrolyte adjacent to the electrode surface, so that oxide precipitation onto the electrode can take place. If the deposition rate is high enough, a film thickness greater than X_s can be formed and hence passivity established. Most metals displaying active–passive behavior [e.g., Fe and Ni in acid electrolytes (Figure 4)] probably do so roughly in this manner, though the process is certainly more complex than indicated here.(15) As unresolved controversy surrounds the topic of passivity, and the field has been reviewed recently(15); we pursue it no further.

Finally, for $\beta < \beta_d$ and $A > A_d$, once more no steady state exists, but this time no film growth can take place beyond one or so atomic layers. Active dissolution is predicted for all conditions, thus passivity cannot be achieved. In alkaline solution, Fe appears to behave this way.(15) For such a case, film growth can still take place via a dissolution–precipitation mechanism, provided the oxide solubility is low enough, a condition that appears to be satisfied for Ag_2O formation on Ag in alkaline solution.(34)

The foregoing analysis (Section 1.2.3.2) is essentially descriptive in nature, with different kinds of behavior being conveniently classified in terms of Eqs. (1) and (17). Real systems are generally much more complex, involving films of varying stoichiometry, ionic, and electronic properties, etc.

1.2.4. Battery Metal Behavior

Not all oxide films, once having formed a complete cover on the metal, continue to grow by a high-field mechanism, although that is the general rule. Data for many systems, such as Fe, Ni, and Pt, have been analyzed in terms of the direct logarithmic and other laws, but also appear to satisfy the high-field equation within experimental error.(15) Data for the anodic oxidation of Ag, Cd, Pb, and other "battery" metals, however, clearly do not. Results for Ag anodically oxidized in alkaline solution under galvanostatic conditions are shown in Figure 5, and are typical of this group. The initiation of film growth is accompanied by a small overshoot in the potential, related no doubt to the extra overpotential required to form oxide nuclei. This is followed by a relatively constant overpotential region associated with Ag_2O formation, followed by similar regions for AgO and O_2 formation. The main characteristics of this group are the low overpotentials required for formation of quite thick films, and the frequently abrupt potential steps between successive anodic stages.

We turn now to a consideration of ion transport through oxide films, with a special emphasis on high-field transport, because of its important role in the kinetics of anodic oxide film growth.

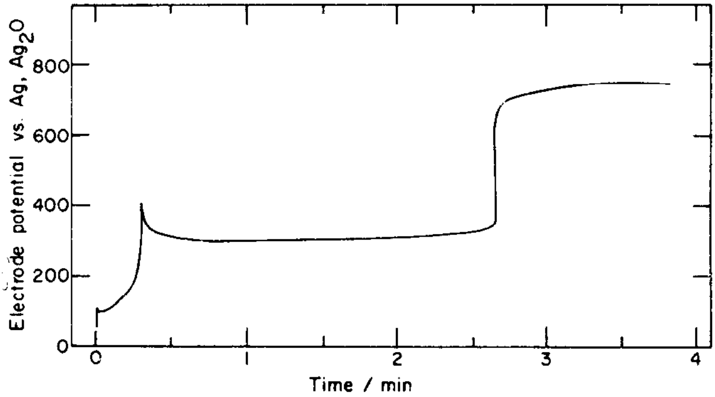

Figure 5. Galvanostatic polarization curve for electropolished Ag in 0.7 *M* aqueous NaOH, 27°C, 2.5 mA/cm^2. The data are according to Dignam, Barrett, and Nagy.(35)

2. Theory of Ionic Transport through Solids

2.1. Approximate One-Dimensional Model for Bulk Transport

Any model involving the field-assisted motion of charged species over one or more potential energy barriers can under certain circumstances lead to an equation essentially of the form of Eq. (1). The conventional model for ionic conduction in crystalline solids is presented first as the various transport equations in common use are developed from it. It consists of parallel linear arrays of symmetrical, identical, potential energy barriers oriented in the field direction, and along which ionic species of charge q are assumed to migrate. Figure 6 depicts the situation in the absence and presence of a uniform field. The net activation energy for migration over a potential energy barrier located at x is $[Q + q\psi(x) - q\psi(x - a)]$ in the positive x direction, and $[Q + q\psi(x) - q\psi(x + a)]$ in the negative x direction, where $\psi(x)$ is the electrostatic potential at position x. From elementary rate theory, the net particle flux J across this barrier is given by[3,19,36]

$$J = 2a\nu \exp(-Q/kT)[n(x-a)\exp\{q[\psi(x-a) - \psi(x)]/kT\} - n(x+a)\exp\{q[\psi(x+a) - \psi(x)]/kT\}] \tag{20}$$

where ν is the particle's attempt frequency, and $n(x)$ is the volume concentration of particles at position x. If the formalism of absolute-reaction-rate theory is employed, $\nu \simeq (kT/h)\exp(\Delta S^{\ddagger}/k)$ and $Q = \Delta H^{\ddagger}$ where $\Delta S^{\ddagger}$ and $\Delta H^{\ddagger}$ are the standard entropy and enthalpy of activation, respectively. [Equation (20) neglects the small shifts with field strength in the positions of the

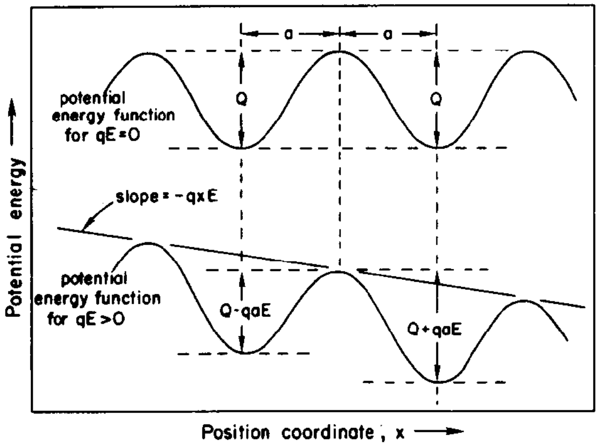
a
a
potential energy function for qE=0
Q
Q
slope = -qxE
potential energy function for qE>0
Q-qaE
Q+qaE
Potential energy
Position coordinate, x

Figure 6. Potential energy of a mobile ionic defect as a function of position in the crystalline solid; upper curve, $E = 0$; lower curve, E constant and nonzero, where E is the Maxwell field strength in the solid.

extreme in the potential energy.] The following dimensionless parameters are now introduced:

$$c = \frac{n}{N}, \qquad s = \frac{x}{a}, \qquad p = \frac{q\psi}{kT}, \qquad \varepsilon = -\frac{\partial p}{\partial s} = \frac{qaE}{kT}, \qquad j = \frac{J}{2a\nu N \exp(-Q/kT)} \tag{21}$$

where N is the concentration of sites for ionic defects in the crystal and $E = -\partial\psi/\partial x$. The particle concentration, position, potential, field strength, and flux density are now represented by c, s, p, ε, and j, respectively, and Eq. (20) becomes

$$j = -\exp[-p(s)]\{c(s+1)\exp[p(s+1)] - c(s-1)\exp[p(s-1)]\} \tag{22}$$

A Taylor series expansion of $c(s+1)\exp[p(s+1)]$ and $c(s-1)\exp[p(s-1)]$ about s ultimately reduces this to(36)

$$j = 2[\sinh(\varepsilon - \partial/\partial s)]c \tag{23}$$

where the term in brackets is an operator.

Factoring $(\varepsilon - \partial/\partial s)$ from the operator converts Eq. (23) to

$$j = 2\left[\frac{\sum_{n=0}^{\infty} (\varepsilon - \partial/\partial s)^{2n}}{(2n+1)!}\right]\left(\varepsilon c - \frac{\partial c}{\partial s}\right) \tag{24}$$

Expansion of the operator in brackets in terms of increasing order in $\partial/\partial s$ and retaining only the zeroth-order term gives

$$j = 2(\sinh\varepsilon)\left(c - \frac{1}{\varepsilon}\frac{\partial c}{\partial s}\right) \tag{25}$$

Including the first-order term requires that the right-hand side of Eq. (25) be multiplied by(36) $[1 - (1/2 + \varepsilon^{-1}\coth\varepsilon - \coth^2\varepsilon)\,\partial\varepsilon/\partial s]$, from which we conclude that neglect of the first- and presumably higher-order terms is permissible, provided that $|\partial\varepsilon/\partial s| \lesssim 1/5$, i.e., provided that the space charge concentration is sufficiently low. For ε independent of s (i.e., no space charge) Eq. (25) is the exact steady state solution of Eq. (23) and is an excellent approximation for space charge concentrations up to about 10^{20} electron charges per cm^3,(36) above which the model itself would be expected to break down. In the conventional variables, Eq. (25) becomes

$$J = -\frac{Dn}{kT}\frac{\partial\bar{\mu}}{\partial x}\frac{\sinh(qaE/kT)}{qaE/kT} \tag{26}$$

where $D = 4a^2\nu\exp(-Q/kT)$ and $\bar{\mu}$ is the electrochemical potential of the ionic species in the usual approximation,(16) i.e., $\bar{\mu} = \mu^\circ + kT\ln n + q\psi$, where

μ° is the standard chemical potential of the ionic species. For low field strengths ($qaE/kT \ll 1$), Eq. (26) reduces to

$$J = -(Dn/kT)\,\partial\bar{\mu}/\partial x = -D\,\partial n/\partial x + n\bar{v}E \qquad (27)$$

where $\bar{v} = qD/kT$. This is the well-known linear transport equation, so that D and $\bar{v}$ are the diffusion coefficient and mobility for this model. For $(\partial n/\partial x) = 0$, Eq. (26) reduces to the Mott–Cabrera conduction equation(32):

$$J = 4a\nu n \exp(-Q/kT)\sinh(qaE/kT) \qquad (28)$$

For high field strengths ($qaE/kT \gg 1$); this in turn reduces to

$$J = 2a\nu n \exp(-Q/kT)\exp(qaE/kT) \qquad (29)$$

which is of the form of Eq. (1) and corresponds to Verwey's(37) model for valve metal anodic oxidation.

2.2. Transport Rate Controlled by Defect Injection

Mott and Cabrera(32) assumed that at the high field strengths required to obtain exponential dependence of J (or j) upon E, J would be determined by the rate at which the ionic defects enter the film. We define $x = 0$ to coincide with the entrance boundary and the positive x direction as the direction of net motion of the defects. Referring to Figure 7, they assumed that the ionic defects, having surmounted the entrance barrier, would move rapidly through the film and hence, contribute a negligible space charge. The field in the film would therefore be uniform and equal to its value at $x = 0$. The rate of defect injection per unit area, or J, is thus given by

$$J = M\nu_0 \exp[-(Q_0 - qbE)/kT] \qquad (30)$$

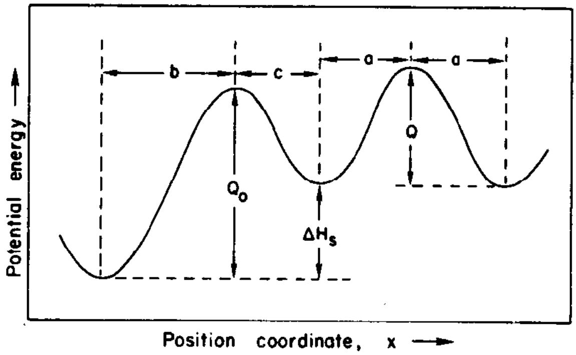

Figure 7. Potential energy of a mobile ionic defect as a function of position near the interface $x = 0$, and for $E = 0$. ΔH_s is the enthalpy change on moving the ionic species from a surface to an interior site.

where M is the surface concentration of sites for defect injection, and ν_0 the appropriate attempt frequency.

2.3. Transport Rate Controlled by Both Bulk Transport and Injection Process

Verwey's and Mott's treatments represent limiting cases of a more general one in which specific allowance is made for space charge within the films due to the mobile ionic defects, and to any compensating background space charge due to impurities. Dewald(38) was the first to treat the former, while Young(39) generalized Dewald's treatment to include a uniform background space charge.

It can be shown(16) that for high fields ($\varepsilon \gg 1$ or $qaE/kT \gg 1$), Eq. (23) or (25) reduces to Verwey's equation

$$j = c \exp \varepsilon \tag{31}$$

In unrationalized electrostatic units, Poisson's equation takes the form

$$\frac{\partial E}{\partial x} = \frac{4\pi q(n - n_\infty)}{K} \tag{32}$$

where $-qn_\infty$ is the background space charge density and K the dielectric constant of the film, assumed to be independent of x. Transforming to dimensionless variables, it becomes

$$\partial\varepsilon/\partial s = \alpha(c - c_\infty) \tag{33}$$

where $c_\infty = n_\infty/N$ and

$$\alpha = 4\pi q^2 a^2 N/KkT \tag{34}$$

Elimination of c from Eqs. (31) and (33) leads to

$$\partial\varepsilon/\partial s = \alpha(j\,e^{-\varepsilon} - c_\infty) \tag{35}$$

which can be integrated to give(16)

$$\varepsilon = \varepsilon_0 + \ln\left[e^{-\alpha c_\infty s} + (c_0/c_\infty)(1 - e^{-\alpha c_\infty s})\right] \tag{36}$$

where the boundary conditions $\varepsilon = \varepsilon_0$ and $c = c_0$ at $s = 0$ have been used. For the high-field conditions assumed here, there is negligible motion of ionic defects against the field so that c_0, ε_0, and the interfacial contribution to the potential drop at $x = 0$ are independent of total film thickness for fixed current density and temperature.(16) Neglecting any possible variation with film thickness of the interfacial potential drop at $x = X$, it can be shown that(16)

$$\tilde{E} \equiv (\partial\eta/\partial X)_i = E_X \tag{37}$$

where E_X is the field strength at $x = X$. Equation (37) implies that the increment in overpotential resulting from a small increment, δX, in film thickness appears across an element of oxide of thickness δX situated at the boundary toward which the ionic defects are moving. Transforming to conventional variables and making use of Eq. (37), Eq. (36) leads to

$$\tilde{E} = E_0 + \frac{kT}{qa}\ln\left\{\exp\left(\frac{-fn_\infty X}{kT}\right) + \frac{n_0}{n_\infty}\left[1 - \exp\left(\frac{-fn_\infty X}{kT}\right)\right]\right\} \tag{38}$$

where $f = 4\pi q^2 a/K$. To complete the model, we note that J is given by both Eqs. (29) and (30), and in particular, each applies at $x = 0$, where $E = E_0$. Eliminating E_0 from these equations gives

$$n_0 = [(M\nu_0)^{\gamma}/2a\nu]\{\exp[(Q - \gamma Q_0)/kT]\}J^{(1-\gamma)} \tag{39}$$

where $\gamma = a/b$. Furthermore, an expression for E_0 can be obtained from Eq. (29),

$$E_0 = \frac{kT}{qb}\ln\frac{J}{M\nu_0} + \frac{Q_0}{qb} \tag{40}$$

The elimination of E_0 and n_0 from Eq. (38), using Eqs. (39) and (40), gives J as a function of $\tilde{E}$ and X. As the resulting expression is rather messy, we examine certain limiting cases.

2.3.1. Low Space Charge Limit

For sufficiently thin films or low space charge concentrations, Eq. (38) reduces to

$$\tilde{E} = E_0 \qquad \text{for } f|n_0 - n_\infty|X/kT \ll 1 \tag{41}$$

so that $\tilde{E}$ and hence E are independent of x. The result, through Eq. (40), is just the Mott–Cabrera equation [Eq. (30)].

2.3.2. High Background Space Charge

For sufficiently high background space charge, on the other hand, Eq. (38) becomes

$$\tilde{E} = E_0 + (kT/qa)\ln(n_0/n_\infty) \qquad \text{for } fn_\infty X/kT \gg 1 \tag{42}$$

and once again $\tilde{E}$ and E are independent of x.

Substituting for E_0, using Eq. (29), one obtains Verwey's equation, Eq. (29), with n replaced by n_∞, so that the mobile defect concentration is controlled by the background space charge density.

2.3.3. High Space Charge Due to Mobile Species

Finally, for conditions in which the background space charge is negligible, but that due to the mobile species large, Eq. (38) reduces to

$$\tilde{E} = E_0 + (kT/qa)\ln(fn_0X/kT), \qquad fn_\infty X/kT \ll 1, \quad fn_0X/kT \gg 1 \tag{43}$$

which on substituting for E_0 from Eq. (29) gives

$$J = X^{-1}(\nu kTK/2\pi q^2)\exp(-Q/kT)\exp(\tilde{E}qa/kT),$$
$$fn_\infty X/kT \ll 1, \quad fn_0X/kT \gg 1 \quad (44)$$

Equation (44) is not precisely of the form of Eq. (1) as it predicts a dependence of $\tilde{E}$ on X for constant J (or i). Specifically, it predicts the same dependence of $\tilde{E}$ on X for fixed J as of $\tilde{E}$ on J for fixed X. Valve metals typically show a change of $\tilde{E}$ of a few percent for a factor of 10 change in i. Only very careful measurements would therefore reveal the difference between Eq. (1) and the above.

2.4. Intrinsic Ionic Conduction

In the previous section, the mobile ionic defects have been assumed to be generated entirely at one interface, with any background space charge being provided by immobile impurities. At sufficiently high temperatures, however, crystalline solids are known to give rise to equilibrium concentrations of ionic defects generated through lattice dissociation.(40) Schottky defects (cation and anion vacancies) form at free surfaces and at grain boundaries and dislocations, while Frenkel defects (cation vacancies and interstitial cations) can form at any cation lattice site. The treatment of low field ionic conduction in crystals due to Schottky or Frenkel defect pairs is well known (e.g., review by Mott and Gurney(40)). Extension of the Frenkel defect model to high fields was first presented by Bean, Fisher, and Vermilyea(41) and subsequently clarified in certain details by Dewald,(42) Young,(39) Dignam and Taylor,(16,43) and Dignam.(44)

The model involves the generation of defect pairs by lattice dissociation in the presence of a field, along with their recombination. Under conditions of constant field strength, for thick enough films, this leads ultimately to a steady state concentration of defect pairs, and no space charge in most of the film.

Employing a one-dimensional model as in Section 2.1., the rate of formation of Frenkel defects, R_f, is given by

$$R_f = (N - n_-)\nu_f\{\exp[-W_f(E)/kT] + \exp[-W_f(-E)/kT]\} \quad (45)$$

where N is the concentration of cation lattice sites, n_- the concentration of vacancies, ν_f the attempt frequency for the lattice dissociation, and $W_f(E)$ the net activation energy for the process in the presence of a field E. The two terms in Eq. (45) correspond to dissociation with and against the field, respectively. In the same approximation which led to Eqs. (26) and (30), $W_f(E)$ is given by

$$W_f(E) = Q_f - qa_fE \quad (46)$$

where Q_f is the activation energy corresponding to zero field, q is the charge on the interstitial cation, and a_f is the activation distance for the process (i.e., the distance between the minimum and maximum in the potential energy surface, analogous to a and b, defined earlier).

In the absence of significant concentration gradients, or for high enough fields,(16) the flux densities for the cationic and anionic defects, J_+ and J_-, are given by equations of the form of Eq. (28), i.e.,

$$J_+ = 2a_+\nu_+n_+\{\exp[-W_+(E)/kT] - \exp[-W_+(-E)/kT]\} \tag{47}$$

$$J_- = 2a_-\nu_-n_-\{\exp[-W_-(E)/kT] - \exp[-W_-(-E)/kT]\} \tag{48}$$

where the subscripts + and − refer to the interstitial cation and cation vacancy, respectively, and

$$W_\pm(E) = Q_\pm \mp qa_\pm E \tag{49}$$

2.4.1. Only One Defect Mobile

Bean *et al.*(41) assumed explicitly that $J_+ \gg J_-$ throughout the film, and implicitly that interstitial cations are injected at the interface $x = 0$. Making these assumptions, the rate of recombination of defect pairs is given by

$$R_r = \sigma n_-(2a_+\nu_+n_+)\{\exp[-W_+(E)/kT] + \exp[-W_+(-E)/kT]\} \tag{50}$$

where σ is the capture cross section of a vacancy for an interstitial. The two terms in Eq. (50) arise from motion of the interstitial with and against the field, respectively, both contributing positively to recombination.

For steady-state conditions in a film much thicker than the characteristic space charge and recombination lengths, throughout most of the film, both the net rate of formation of defect pairs, and the space charge density will be zero, i.e., $R_f = R_r$ and $n_+ = n_- = n_s$, leading to

$$n_s^2 = \frac{(N - n_s)\nu_f}{2a_+\sigma\nu_+}\,\frac{\exp[-W_f(E)/kT] + \exp[-W_f(-E)/kT]}{\exp[-W_+(E)/kT] + \exp[-W_+(-E)/kT]} \tag{51}$$

The steady state ion flux density, $J_s = J_+(n_+ = n_s)$ is obtained from Eqs. (47) and (51), and becomes on setting, $N - n_s \simeq N$, and using Eqs. (46) and (49),

$$J_s = 2\left(\frac{2a_+N\nu_f\nu_+}{\sigma}\right)^{1/2} \exp\left(-\frac{Q_s}{kT}\right)\left[\frac{\cosh(qa_fE/kT)}{\cosh(qa_+E/kT)}\right]^{1/2} \sinh\left(\frac{qa_+E}{kT}\right) \tag{52}$$

where $Q_s = (Q_f + Q_+)/2$.

For high fields (qa_fE and $qa_+E > 4kT$), Eq. (52) reduces to

$$J_s = \left(\frac{2a_+N\nu_f\nu_+}{\sigma}\right)^{1/2} \exp\left(-\frac{Q_s}{kT}\right) \exp\left[\frac{q(a_f + a_+)E}{2kT}\right] \tag{53}$$

which is the result obtained by Bean *et al.*(41) For low fields, Eq. (52) becomes

$$J_s = 2\left(\frac{2a_+N\nu_f\nu_+}{\sigma}\right)^{1/2} \frac{qa_+E}{kT} \exp\left(\frac{Q_s}{kT}\right) \tag{54}$$

and is equivalent to the usual linear conduction equation derived for crystals in which Frenkel defects predominate.(40)

It has been shown(16) that neither the low- nor the high-field equation derived above is likely valid when applied to films $\lesssim 10^4$ Å in thickness. The characteristic space charge length at high fields for this model is of the order of $\exp[(W_f - W_+)/2kT]$ Å, which is expected to be $\gg 10^4$ Å. For thinner films, this model leads to ionic conduction controlled at the interface $x = 0$,(44) i.e., to the Mott–Cabrera model.

2.4.2. Both Defects Mobile

There are aspects of the so-called high-field Frenkel defect model that have hitherto been missed. These develop when we drop the assumption made by Bean *et al.*(41) that $J_- = 0$. For $J_+ \neq 0 \neq J_-$, in addition to defect recombination, annihilation of defect pairs takes place through their migration to opposite interfaces. We consider here only cases arising from no defect injection at the interfaces, cases forbidden if $J_- = 0$.

In addition, we restrict our attention to high fields and negligible space charge ($\partial E/\partial x = 0$). Equations (45), (47), and (48) then become

$$R_f = N\nu_f \exp(-W_f/kT) \tag{55}$$

$$J_\pm = \pm n_\pm v_\pm \tag{56}$$

where v is the speed of the defect in question, given by

$$v_\pm = 2a_\pm \nu_\pm \exp(-W_\pm/kT) \tag{57}$$

Since for high fields the defects move only with the field, the recombination rate is given by

$$R_r = \sigma n_+ n_-(v_+ + v_-) \tag{58}$$

The continuity condition on the defect fluxes takes the form

$$\frac{\partial J_\pm}{\partial x} + \frac{\partial n_\pm}{\partial t} = R_f - R_r \tag{59}$$

For steady state conditions of constant E and J, $\partial n_\pm/\partial t = 0$, so that, on substituting for $J_\pm$ and R_r, Eq. (59) gives rise to the following:

$$\frac{dn_+}{dx} v_+ = -\frac{dn_-}{dx} v_- = R_f - \sigma n_+ n_-(v_+ + v_-) \tag{60}$$

The problem now reduces to solving Eq. (60) subject to the following boundary conditions imposed by our condition that there be no defects injected at the boundaries:

$$\begin{aligned} &\text{At } x = 0: \quad && n_+ = 0, \quad && n_- = n^\circ_-, \quad && J_+ = 0, \quad && J_- = -J \\ &\text{At } x = X: \quad && n_+ = n^X_+, \quad && n_- = 0, \quad && J_+ = J, \quad && J_- = 0 \end{aligned} \tag{61}$$

where $J = J_+ - J_-$, and is the total metal ion flux carried by the interstitials and vacancies.

The first part of Eq. (60) integrates directly to give with Eq. (61)

$$n_+v_+ + n_-v_- = n_+^X v_+ \tag{62}$$

Eliminating n_- between Eqs. (60) and (62) gives

$$\frac{dy}{ds} = 1 - 4y(Y - y) \tag{63}$$

where y and s are dimensionless concentration and position variables defined by

$$y = \tfrac{1}{2}[\sigma(v_+^{-1} + v_-^{-1})/R_f]^{1/2} v_+ n_+ \tag{64}$$

$$s = \tfrac{1}{2}[\sigma(v_+^{-1} + v_-^{-1})R_f]^{1/2} x = x/X_r \tag{65}$$

and Y is the value of y at $x = X$, or $s = S$.

Equation (63) leads to a physically meaningful solution only for $Y < 1$, which is[44]

$$\frac{1}{2(1 - Y^2)^{1/2}} \arctan \frac{2y - Y}{(1 - Y^2)^{1/2}} = s + \frac{1}{2(1 - Y^2)^{1/2}} \arctan \frac{-Y}{(1 - Y^2)^{1/2}} \tag{66}$$

where the final term is the integration constant evaluated from $y = 0$ at $s = 0$ [Eq. (61)]. From the condition $y = Y$ at $s = S$, Eq. (66) becomes on rearranging and taking the tangent

$$Y(1 - Y^2)^{-1/2} = \tan [S(1 - Y^2)^{1/2}] \tag{67}$$

We now examine the thin- and thick-film limits of Eq. (67).

2.4.2.1. Thin-Film Limit, Negligible Space Charge

For $S \ll 1$, the tangent in Eq. (67) may be replaced by its argument, giving

$$Y \simeq S(1 - Y) \simeq S \tag{68}$$

On substituting for Y and S according to their definitions [Eqs. (64) and (65)], this becomes

$$n_+^X = XR_f/v_+ \tag{69}$$

Now, from Eq. (61)

$$J = n_+^X v_+ = XR_f \tag{70}$$

which, on substituting for R_f and W_f from Eqs. (55) and (46) becomes

$$J = XN\nu_f \exp(-Q_f/kT) \exp(qa_fE/kT), \qquad X \ll X_r \tag{71}$$

Equation (70) or (71) arises from the situation in which defect recombination is negligible. Although Eq. (71) is not of the form of Eq. (1), as was the case for Eq. (44), it is difficult to distinguish experimentally between these two equations.

2.4.2.2. Thick-Film Limit, Negligible Space Charge

For $S \gg 1$, Eq. (67) leads to

$$Y \simeq 1 \tag{72}$$

Substituting for Y according to Eq. (4), this becomes

$$n_+^X = (2/v_+)[\sigma(v_+^{-1} + v_-^{-1})/R_f]^{1/2} \tag{73}$$

and $J = n_+^X n_+$ becomes

$$J = 2R_f^{1/2}/\sigma^{1/2}(v_+^{-1} + v_-^{-1})^{1/2} \tag{74}$$

Substituting for R_f, v, W_f, and W from Eqs. (55), (57), (46), and (49), and making the assumption that v_+ and v_- differ in magnitude by at least two powers of 10, Eq. (74) leads to[44]

$$J = 2\left(\frac{2aNv_f\nu}{\sigma}\right)^{1/2} \exp\left(-\frac{Q_s'}{kT}\right) \exp\left[\frac{q(a_f + a)E}{2kT}\right] \qquad \text{for } X \gg X_r \tag{75}$$

where $Q_s' = (Q_f + Q)/2$, and a, ν, Q belong to the defect having the lower speed.

Equation (75) and the Bean–Fisher–Vermilyea equation [Eq. (53)] differ formally simply by a factor of 2. The mechanisms are, however, quite different. The parameters a, ν, and Q are for the less mobile species in Eq. (75), while for the more mobile species in Eq. (53).

The characteristic recombination length, X_r, is given from Eqs. (65), (55), and (57) by

$$X_r = 2\left(\frac{2a\nu}{N\nu_f\sigma}\right)^{1/2} \exp\left[\frac{W_f - W}{2kT}\right] \tag{76}$$

Since $\nu \sim \nu_f$ and $(2a/N\sigma)^{1/2} \sim 1$ Å, $X_r \sim \exp[(W_f - W)/2kT]$ Å, so one would expect $X_c \gg 10^4$ Å. For anodic films, therefore, the thin-film approximation, Eq. (71), is much more likely to be obeyed than is the thick-film approximation, Eq. (75). In the following section, we include the effect of space charge in the thin-film case, i.e., the case of negligible defect recombination.

2.4.2.3. Thin-Film Limit Including Space Charge

In this section, we solve for J under conditions in which $\partial n_\pm/\partial t = 0$ as before, but for $R_r = 0$ and dE/dx given by Poisson's equation. An analytical solution is available only for the case $a_+ \simeq a_- \simeq a_f$. For $X \ll X_s$, the characteristic space charge length, Eq. (71), is, of course, once again obtained. For $X \gg X_s$, however,[44]

$$J = \left[\frac{N\nu_f\nu KkT}{2\pi q^2}\right]^{1/2} \exp(-Q_s'/kT) \exp(qa\bar{E}/kT) \tag{77}$$

where $Q_s' = (Q_f + Q)/2$ and the parameters Q and ν refer to the defect having the higher speed.

For the particular conditions chosen in deriving Eq. (77), the increase in J with increasing X, resulting from the homogeneous generation of defect pairs, is just compensated by the inhibiting effect of space charge buildup with increasing X. Once again, however, it is improbable that Eq. (77) is obeyed for anodic oxide films, since the high space charge condition, $X \gg X_s$, is unlikely ever to be satisfied. Thus

$$X_s = \left[\frac{KkT\nu}{4\pi Nq^2\nu_f}\right]^{1/2} \exp\left[\frac{Q_f - Q}{2kT}\right] \tag{78}$$

where Q applies to the defect of *lower* speed.(44) Reasonable values for the parameters in the preexponential term lead to $X_s \sim \exp[(Q_f - Q)/2kT]$ Å, and again one would expect $X_s \gg 10^4$ Å. Note that the characteristic recombination and space charge lengths are comparable, i.e., $X_r \sim X_s$, provided $a \simeq a_f$, where a applies to the defect of lower speed. It seems, therefore, that a proper treatment for thick films must include both defect recombination and space charge simultaneously. For thick enough films, however, the Bean–Fisher–Vermilyea equation [Eq. (53)] is once again obtained.(44)

The present analysis serves the purpose of showing that of all of the models involving homogeneous generation of defects at high fields, only that leading to Eq. (71) is likely to be applicable to anodic film formation, although the others cannot be entirely dismissed out of hand.

2.5. Second-Order Effects

2.5.1. Higher-Order Terms in the Net Activation Energy

A more careful analysis of the form of the net activation energy, $W(E)$, for a field-assisted process, shows that it is not expected to be simply a linear function of E. Furthermore, Young(45) discovered that a number of apparent anomalies concerning the anodic oxidation of Ta in dilute H_2SO_4 could be accounted for quantitatively if a quadratic field term of opposite sign to the linear term was included in $W(E)$.

The most obvious process contributing to higher-order terms in $W(E)$ has been alluded to in Section 2.1. The net activation energy was calculated there incorrectly in that the positions of maximum and minimum in the potential energy surface for a mobile ionic defect were assumed to remain stationary upon application of an electric field. If $U(x)$ is the potential energy function for $E = 0$, then $U(x) - qxE$ is the potential energy function in the presence of a uniform field E (Figure 6). The extrema in $U(x) - qxE$ are obtained from

$$\frac{\partial}{\partial x}[U(x) - qxE] = 0 \tag{79}$$

not from $\partial U(x)/\partial x = 0$, as implied by assuming that the positions of the extrema do not change with E. Representing adjacent positions of minimum and maximum in the net potential energy by x_0 and x_m, the net activation energy is given by $W(E) = U(x_m) - U(x_0) - q(x_m - x_0)E$. For example, if we chose a cosine potential energy function

$$U(x) = (Q/2)[1 - \cos(\pi x/a)] \tag{80}$$

Eq. (79) leads to[16,46]

$$\sin(\pi x/a) = 2qaE/\pi Q \tag{81}$$

Solving for x, the values of x_0 and x_m are given by the solutions that lie in the intervals $[0, a/2]$ and $[a/2, a]$, respectively. Finally, after some algebra, it can be shown that $W(E)$ is given by

$$W(E) = Q\left[1 - \left(\frac{2qaE}{\pi Q}\right)^2\right]^{1/2} - qaE + \frac{2qaE}{\pi}\arcsin\left(\frac{2qaE}{\pi Q}\right) \tag{82}$$

Expansion of the square root and arcsin terms as power series in $2qaE/\pi Q$ gives

$$W(E) = Q - qaE\left[1 - d_2\left(\frac{qaE}{Q}\right) + \cdots\right] \tag{83}$$

where $d_2 = 2/\pi^2$. Other potential functions lead to an equation of the form of (83) but with different values for d_2. Thus contacting, alternately inverted parabolas give $d_2 = 1/4$.[16] The condition that the quadratic field term from this source be important is that $qaE \sim Q$.

Other physical phenomena have been proposed as giving rise to, or contributing to, the quadratic field term. Young[47] suggested that electrostriction of the film would lead to Q decreasing approximately linearly with E^2, hence, contributing a quadratic term to $W(E)$. Ibl[48] noted that when one includes the energy of polarization of the mobile ionic defect, $-\frac{1}{2}\alpha E_L^2$, where α is the polarizability, and E_L the local field strength at the defect in question, a quadratic term appears. It arises since E_L is expected to decrease on going from a site of minimum to one of maximum potential energy.[49] Dignam and Gibbs[49] consider the effect of distortion of the potential energy barrier by the field distortion due to displacement of the lattice ions which give rise to the barrier. Again, this contributes a quadratic term, but of opposite sign to that observed.[16] None of these is likely to produce a quadratic coefficient as large as that calculated from simply treating the barrier lowering process properly.[16]

Finally, Ord *et al.*[50] have suggested a source for the quadratic term of an entirely different nature. It appears that the field to be inserted in the expression for $W(E)$ is frequently not the mean or Maxwell field strength, but rather a "local field," E_L, which is a product of E and a linear function of the dielectric constant of the film, K. If K decreases linearly with increasing field, then E_L will be a quadratic function of E, leading to a term in $W(E_L)$ proportional to E^2 and of the correct sign.

2.5.2. Consequence of Amorphous Film Structure

2.5.2.1. Form of Net Activation Energy

Amorphous films, and microcrystalline films where the crystallites are small, relative to the film thickness, can in some respects be considered together. Thus, for both, there will exist a range of values of Q, a, ν, and K. The principal effect of a local variation in the dielectric constant, K, will be to introduce spatial variations in the local field strength, which can be incorporated into an effective activation distance if we wish.(16) The net result is that if ionic conduction data are fitted to an equation of the form of Eq. (26) or any approximation to it, Q and a will be found to be functions of T and E. How strongly dependent they are on T and E is determined by the distributions of Q and a and how they are correlated.(16) Note that the analysis of Section 2.5.1 shows that in a sense Q is a linear function of E^2, and/or a a linear function of E. Neither, however, is predicted to be a function of T, in contrast to the consequences of an amorphous or microcrystalline film structure. The presence of a significant range of values of Q, a, and ν is, therefore, made apparent through the necessity of treating the net activation energy, $W(E)$, as a function of temperature.

Treating ion transport in terms of a three-dimensional rather than one-dimensional model also introduces a temperature dependence into $W(E)$, as there is now a range of paths for the ion to cross the barrier. The same effect arises in the treatment of chemical kinetics, where it leads to a temperature dependence of the activation energy.(51) One might expect amorphous film structure to lead to a larger temperature dependence than this, however.

A further possible effect of amorphous film structure on growth kinetics can arise if the film structure depends on current density and time. This will introduce conduction transients.

2.5.2.2. Network Defects

The nature of point defects responsible for ionic conduction in crystalline solids is well understood(40); anodic oxide films are frequently found to have amorphous or vitreous structure, however. A discussion of possible point defects in vitreous solids is therefore in order.

For mixed oxide glasses at high enough temperatures, such that the linear conduction equation is obeyed, the conductivity is generally found to follow the normal exponential temperature dependence characteristic of a thermally activated process. For SiO_2–B_2O_3 glasses containing Li or Na, the activation energy ~0.6 eV,(52) with the current carriers believed to be the alkali metal ions. For pure vitreous B_2O_3, on the other hand, the activation energy is about 2.2 eV.(53) Furthermore, the preexponential factor is much larger than for the glasses containing alkali ions, suggesting a conduction mechanism involving lattice dissociation, perhaps similar to the Schottky, or Frenkel models for ionic conduction in crystalline solids.(40)

In 1966, the author presented a model for the point defects responsible for ionic conduction in vitreous anodic oxide films. A summary of their properties follows:(16)

A schematic representation of the defects and their mode of formation and migration is shown in Figure 8. They are described most succinctly as ionized dangling bonds in the interior of the solid. Their main properties are deducible by considering them to be vacancylike in behavior. However, for odd valent vitreous metal oxides (e.g., B_2O_3, Ta_2O_5, etc.), they would carry a charge of

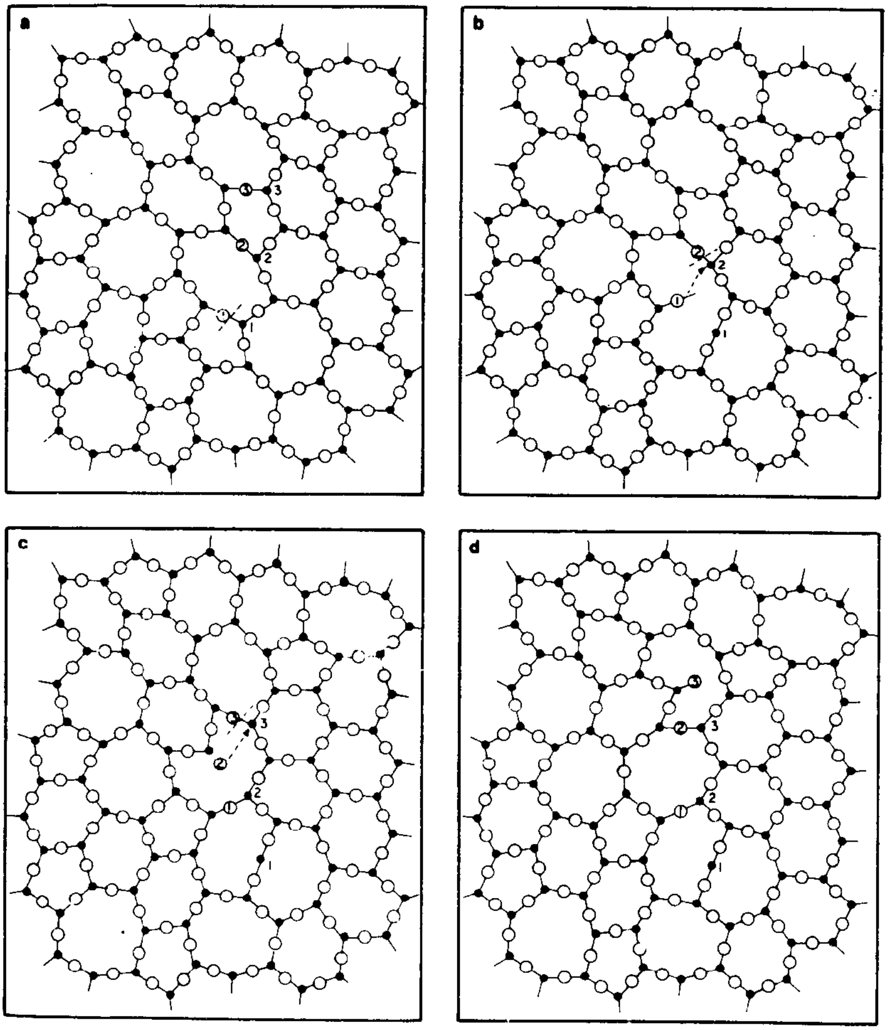

Figure 8. Random-network model for vitreous B_2O_3 showing the formation (*a* → *b*) and migration (*b* → *c* → *d*) of network defects; after Dignam.(16)

only $\pm e$, and a mass of one atom equivalent of metal and oxygen, respectively (e.g., $1/3\ B^{3+}$ and $1/2\ O^{2-}$, respectively, for B_2O_3) and must move via cooperative motion of both metal and oxide ions over an extended region of the glass. A very similar picture of the mechanism of ion transport in anodically formed Ta_2O_5 has been offered by Pringle.(54)

If such defects exist for even valent vitreous oxides (e.g., ZrO_2), they must carry a charge of $\pm 2e$, and a mass of two atom equivalents (e.g., $1/2\ Zr^{4+}$ and O^{2-}, respectively, for ZrO_2).

An estimate of the enthalpy of formation of such network defects pairs in vitreous B_2O_3 led to $\Delta H_f \simeq 2.2_8$ eV. The empirical activation energy, Q_e, for low-field ionic conduction is predicted to be $\frac{1}{2}\Delta H_f + Q$, where Q is the activation energy for migration of the defect of higher mobility. Setting $Q \simeq \frac{1}{2}\Delta H_f$, which seems reasonable, gives $Q_e \simeq 2.28$ eV, in close agreement with the experimental value, 2.16 eV.

In Figure 9, the zero field empirical activation energies for the anodic oxidation of Bi, Al, Nb, and Ta, all of which form vitreous oxides, are plotted against theoretical estimates of ΔH_f.(16) The result is a good linear correlation, represented by

$$Q_e \simeq 0.43\Delta H_f + 0.87\ \text{eV} \tag{84}$$

One cannot conclude from this that network defects are, in fact, responsible for ionic transport in these anodic films, since the correlation could be an indirect one. The relation does, however, lend credence to the idea.

2.6. Local Field Model

In Section 2.5.1., mention was made of the possibility that the field responsible for the kinetics of film growth [i.e., the field in Eq. (1)] may not be

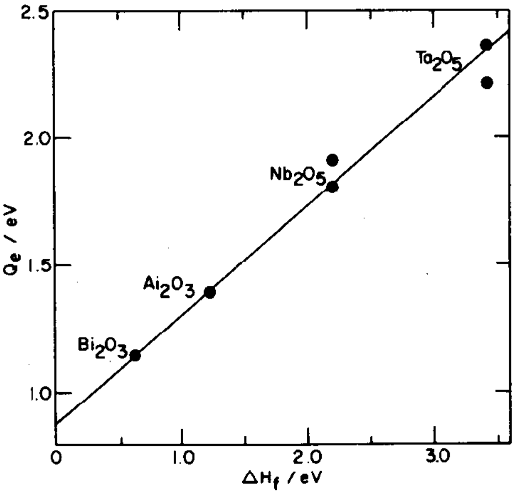

Figure 9. Graph of empirical activation energy for anodic film growth extrapolated to $E = 0$, against the calculated enthalpy of formation of network-defect pairs; after Dignam.(16)

the Maxwell field, but instead a local field of some sort, E_L. Various ways in which this could arise are now examined.

2.6.1. Internal Local Field

The distribution of the electric field strength through an inhomogeneous region of space where all free charges are confined to the surfaces, is given by the following form of Poisson's equation, written for zero space charge density, but allowing for variation of the dielectric constant, K, with position

$$\operatorname{div} \mathbf{D} = 0 \tag{85}$$

where $\mathbf{D} = K\mathbf{E}$ is the electric displacement vector. Applying this to a film of uniform thickness, and with inhomogeneity on a scale small compared to the film thickness, leads to $\mathbf{D}$ constant throughout the film, and directed normal to the boundaries. If the film is amorphous, however, microscopic regions of low mean density will in general correspond to regions of low mean K and, hence, high mean E, where the averages are introduced to eliminate fluctuations due to the atomic nature of matter. For crystalline solids, there are accordingly no fluctuations in E, except at dislocations and grain boundaries. It can be shown(16,54) that the proper field to use for ionic conduction in a perfect crystal is the Maxwell field. That is not necessarily so, however, for a vitreous solid. Thus, for the case of intrinsic ion conduction, lattice or network dissociation might well be favored at microscopic regions of low mean density, and hence, high local field strength. If, for simplicity, we regard these regions as having the shapes of ellipsoids of revolution oriented normal to the film boundaries, then the local field in these regions is given by(56)

$$E_L = E[1 + \gamma_L(K/K_L - 1)] \tag{86}$$

where K_L is the appropriate value for the dielectric constant within the local regions, and γ_L a shape factor which is zero for a long needlelike cavity, 1/3 for a spherical cavity, and 1 for a flat disklike cavity. Note that for $\gamma_L(K/K_L) \gg 1, E_L \propto (K/K_L)E$.

2.6.2. Interfacial Local Field

A similar situation can arise if ionic conduction is controlled by defect generation or injection at one of the interfaces. Suppose, for example, that the rate is controlled by an electrochemical step in the oxide–electrolyte double layer. The continuity condition on the normal component of $\mathbf{D}$ leads to(16)

$$KE = K_\delta E_\delta + 4\pi\sigma_{se} \tag{87}$$

where K_δ and E_δ are the effective dielectric constant of, and field in, the double layer, and σ_{se} the surface charge density on the oxide at the oxide–electrolyte interface. If it should happen that the oxide surface properties are such that $\sigma_{se} \simeq 0$, then again, $E_L \simeq (K/K_L)E$, where $E_L = E_\delta$ and $K_L = K_\delta$.

2.7. The Direct Logarithmic Equation

2.7.1. The Elovich Equation

The most widely used relationship for presentation of kinetic data for chemisorption of gases on solids is that commonly known as the Elovich equation, usually written

$$dq/dt = a_E \exp(-b_E q) \tag{88}$$

where q is the amount of gas adsorbed at time t, and a_E and b_E empirical constants. Although it is extremely unlikely that Eq. (88) arises from a single mechanism, it is possibly more than just an empirical formalism.(57) It is usually derived by assuming that the overall activation energy for the surface reaction is a linearly increasing function of coverage. The parameter a_E is expected to depend on gas phase (solution) concentrations, but is generally assumed to be independent of coverage. The implication is that all of the surface is available for chemisorption, including that part already covered, with only the activation energy changing. If one includes a coverage factor by replacing a_E by $(1 - q/q_s)a_E$, where q_s corresponds to saturation, the resulting equation does not lead to empirically distinguishable results, provided that $b_E(q_s - q) \gg 1$.

Ritchie(58) has shown that much chemisorption data previously believed to fit a two-stage Elovich equation, in fact fits a kinetic equation of the form

$$\frac{dq}{dt} = a_R\left(1 - \frac{q}{q_s}\right)^n \tag{89}$$

where for the systems examined, $n \simeq 2$. For $n = 1$, Eq. (89) is a simple rate equation, first order in surface sites, while for $n \gg 1$ and $q \lesssim q_s/2$, it is easily shown that it reduces to the Elovich equation with $a_E = a_R$ and $b_E = (n - 1)/q_s$.

2.7.2. The Electrochemical Elovich Equation

To adapt the Elovich equation to an electrochemical chemisorption process, we need only include the effect of the electrode potential on the rate constant in the usual way, to obtain for an anodic process

$$i = a_E \exp(V/b_T - b_E q) \tag{90}$$

where q is now interpreted as the charge passed during the electrochemical deposition, with V the electrode potential and b_T the base e Tafel slope.

2.7.3. Application to Anodic Film Formation

To ease comparison with the high-field equation we rewrite Eq. (90) in the form

$$i = a_E \exp(\eta/b_T - b'_E X) \tag{91}$$

For galvanostatic conditions, this equation, with Eq. (4), leads to

$$\left(\frac{\partial \eta}{\partial t}\right)_i = (b_T b'_E \Omega / F) i \tag{92}$$

Comparison with the corresponding result [Eq. (6)] for the high-field conduction equation shows that the two can be distinguished experimentally only if careful measurements are made over several decades in i. For potentiostatic conditions, Eq. (91) with Eq. (4) leads to

$$\left[\frac{\partial(1/i)}{\partial t}\right]_\eta = \frac{b'_E \Omega}{F} \tag{93}$$

Comparison with the corresponding result [Eq. (11)] for the high-field conduction equation shows that if a series of measurements can be made covering a large range in film thickness, the two are readily distinguishable, since Eq. (93) predicts the slope of $1/i$ vs. t to be independent of X, while Eq. (11) predicts it to be approximately proportional to $1/X$. For any single potentiostatic experiment, however, the fractional change in X during the run will generally be too small to distinguish between Eq. (11) and Eq. (93). Thus, for systems in which only very thin films can be grown (e.g., Fe and Pt), distinguishing between Eqs. (11) and (93) will be difficult.

As noted in Section 1.2.2.3, under galvanostatic conditions, Eq. (93) can be integrated to give the direct logarithmic rate equation [Eq. (13) with $A_l = 1/b'$ and $Y = F/b'\Omega i_0$].

2.8. Summary of Ionic Transport Equations

All of the limiting high-field conduction equations relevant to anodic oxide film formation under steady-state conditions may be written

$$i = AX^g \exp[-W(E_L)/kT] \tag{94}$$

where

$$W(E_L) \simeq Q_e - \mu^{\ddagger} E_L[1 - d_2(\mu^{\ddagger} E_L/Q_e)] \tag{95}$$

$$E_L \simeq E[1 + \gamma_L(K/K_L - 1)] \tag{96}$$

and $\mu^{\ddagger}$ is the low-field limit of the empirical charge, activation distance, product, and has been named the activation dipole by the author.$^{(16)}$

2.8.1. Interfacial High-Field Equations

If the rate is controlled at one interface, $g = 0$, and either $Q_e = Q_0$ and $\mu^{\ddagger} = qb$, as for the Mott–Cabrera model (Figure 7), or these parameters belong to an interfacial electrochemical step. In the latter case, and for $\sigma_{*} \simeq 0$, it is easily shown[16] that

$$\mu^{\ddagger} = kT\delta/b_T \qquad (97)$$

where δ is the effective thickness of the oxide–electrolyte double layer, and b_T the base e Tafel slope for the reaction. If the rate-controlling interfacial reaction is of the Mott–Cabrera type ($\mu^{\ddagger} = qb$) then the kinetics must follow a different equation during formation of the first atomic layer or so of oxide, possibly the Elovich equation or the conventional equation for interfacial electrochemical kinetics allowing for surface coverage.

2.8.2. Internal High-Field Equations

If the oxide growth rate is controlled by high-field bulk transport processes, then several possibilities exist.

2.8.2.1. Only One Type of Ionic Defect

In this case for thick enough films, $g = -1$, $Q_e = Q$, and $\mu^{\ddagger} = qa$ [Figure 6 and Eq. (44)]. These kinetics cannot be followed for very thin films, hence a transition in the kinetics should be observable, for example, a transition from Eq. (30) to Eq. (44) as the film thickness increases. This transition will occur for $X \sim kT/fn_0$.

2.8.2.2. Two Types of Ionic Defect, Only One Mobile

If a second immobile defect of opposite charge is present in the film, then for thick enough films, $g = 0$. If the compensating charge is provided by uniformly distributed impurities, then $Q_e = Q$, and $\mu^{\ddagger} = qa$. On the other hand, if defect pairs are generated by lattice dissociation, then $W(E_L) \simeq [W_f(E'_L) + W(E''_L)]/2$. Again, a transition in kinetics should be observable for both these cases, similar to the previous case.

2.8.2.3. Homogeneous Generation of Defect Pairs

If all the defects are generated by lattice dissociation, and none by injection at the boundaries, then for sufficiently thin films, $g = 1$, $Q = Q_f$, and $\mu^{\ddagger} = qa_f$. The resulting equation cannot be applied to the formation of the first atomic layer or so of oxide, but beyond this up to $X \gtrsim 10^4$ Å, no change in kinetics is expected.

For sufficiently thick films, on the other hand, behavior similar to that described above in Section 2.8.2.2 is expected.

2.8.3. The First One or So Atomic Layers

The kinetics of formation of the first atomic layer or so of oxide or chemisorbed oxygen have been variously described in terms of the high-field equation, the Elovich equation, the Tafel equation corrected for surface coverage, and equations developed from a model of oxide nucleation and growth.

3. The Metal–Oxide and Oxide–Electrolyte Interfaces

3.1. Introduction

A proper treatment of the kinetics of growth of anodic oxide films requires an understanding of the metal–oxide, oxide–electrolyte, and metal–electrolyte interfacial regions. The last of these has been the subject of many investigations, and although considerable progress has been made, probably still represents the central problem in electrode kinetics. The oxide–electrolyte interface has also received much attention, but mainly in connection with the surface properties of finely divided oxide powders.(14)

No generally accepted model for the oxide–electrolyte interface exists.(59) As an interim measure, we present the essential features of a model proposed by the author(60) that is in a sense a composite of the models due to Ahmed(59) and Levine and Smith.(61)

3.2. Transition Layer Model: Thermodynamic Properties

A large number of oxide electrodes that are conducting are found to obey the Nernst equation

$$\psi_M - \psi_{aq} = 2.303(kT/e)(\mathrm{pH}_{zpc}^{(M)} - \mathrm{pH}) \tag{98}$$

where ψ_M is the potential of the metal in contact with the oxide, ψ_{aq} that of the aqueous electrolyte, $\mathrm{pH}_{zpc}^{(M)}$ the pH of the electrolyte for which $\psi_M - \psi_{aq} = 0$, and e the charge on the proton. That Eq. (98) should be obeyed for insoluble oxides is rather surprising, as pointed out by Levine and Smith.(61) The model set out below was developed(60) to account quantitatively for Eq. (98), and qualitatively for capacitance data on the oxide–electrolyte interfacial region.(59)

We consider here an insoluble, cationic conducting oxide. The oxide–electrolyte interfacial region is treated as an approximately two-dimensional lattice, or net, of cation and anion site, occupied by metal ions, M^{z+}, as well as O^{2-}, H^+, OH^-, H_2O, and the counterions. The presence of H_2O and the counterions has no effect on the Nernstian behavior of the system, but can influence the distribution of potential across the oxide and the double layer.(60) If the oxide is a good enough cationic conductor, to obtain Nernstian behavior we need only find mechanisms for establishing equilibria between H^+, OH^- in the transition layer and in the electrolyte, and between M^{z+}, O^{2-} in the transition layer and adjacent to it in the oxide. The former presents no problem. The latter will be effected for M^{z+} if the activation energy for surface diffusion of M^{z+} from lattice steps on the oxide surface into plateau regions is not too large (i.e., $\lesssim 0.7$ eV for a relaxation time $\lesssim 1$ sec). The O^{2-} equilibrium can be effected in much the same way, except that effective surface migration can now take place through the electrolyte (e.g., $O^{2-}_{\mathrm{step}} + H^+_{\mathrm{aq}} \rightleftharpoons OH^-_{\mathrm{aq}} \rightleftharpoons O^{2-}_{\mathrm{plateau}} + H^+_{\mathrm{aq}}$).

In this model, thermodynamic equilibrium can be established between the oxide and aqueous ions through the good offices of the transition layer, so to speak. Extension of this model to an anionic conducting oxide involves introducing a transition layer at the metal–oxide interface. Electronic conducting oxides can be treated in much the same way.$^{(60)}$

3.3. Transition Layer Model: Distribution of Charge and Potential

Neglecting the adsorption of counterions and H_2O into the transition layer, and using Langmuir-type adsorption isotherms, leads to the following equation for the net surface charge, σ_{se}, in the oxide–electrolyte transition layer of an oxide of composition MO$^{(60)}$

$$\sigma_{se}/eM = \tfrac{1}{2}\gamma_{se} \sinh[e(\psi_{se} - \psi^*)/kT] \tag{99}$$

where

$$\Delta\psi_e \equiv 2.303(kT/e)(\mathrm{pH}^{\mathrm{OX}}_{zpc} - \mathrm{pH}) = \psi^* - \psi_{\mathrm{aq}} \tag{100}$$

where ψ_{se} is the potential of, and M the surface concentration of cation and anion sites in, the transition layer, while $\mathrm{pH}^{\mathrm{OX}}_{zpc}$ is the pH corresponding to the zero point of charge for the oxide, and γ_{se} is a dimensionless constant restricted to the range $1 \geq \gamma_{se} > 0$. If the energetics are such that the transition layer is populated almost entirely by either M^{2+} and O^{2-}, or H^+ and OH^-, then $\gamma_{se} \lll 1$. If the populations of M^{2+}, O^{2-}, and H^+, OH^- are comparable, then $\gamma_{se} \sim 1$.

For $\gamma_{se} \sim 1$, since $\sigma_{se}/eM \lll 1$, it follows from Eq. (99) that $\psi_{se} \simeq \psi^*$, hence, from Eq. (110), $\psi_{se} - \psi_{\mathrm{aq}} = \Delta\psi_e$. Thus, for $\gamma_{se} \sim 1$, the oxide–electrolyte double-layer potential, $\psi_{se} - \psi_{\mathrm{aq}}$, obeys the Nernst equation, while in order to satisfy Eq. (98), $\psi_{\mathrm{M}} - \psi_{se}$ is given by

$$\Delta\psi_m \equiv 2.303(kT/e)(\mathrm{pH}^{(\mathrm{M})}_{zpc} - \mathrm{pH}^{(\mathrm{OX})}_{zpc}) = \psi_{\mathrm{M}} - \psi_{se} \tag{101}$$

and is independent of pH. A similar analysis involving the metal–oxide transition layer$^{(34)}$ shows that in the absence of significant space charge in the oxide film, $\psi_{\mathrm{M}} - \psi_{sm} = \Delta\psi_m$, where ψ_{sm} is the potential of the oxide surface, or transition layer, at the metal–oxide interface. Thus, for $\gamma_{se} \sim 1$, $\psi_{sm} - \psi_{se} = 0$, so there is no potential drop or concentration gradients in the film.

For $\gamma_{se} \lll 1$, and negligible space charge, the situation is quite different. In the extreme, this leads to $\sigma_{se} \simeq 0$ [Eq. (99)], so that $\psi_{sm} - \psi_{\mathrm{aq}} = \Delta\psi_e$.

Furthermore, $\Delta\psi_e$ is distributed so that the electric displacement D is constant throughout the film and the Helmholtz double layer.

3.4. Consequences for Oxide Growth Kinetics

3.4.1. Case in Which $\gamma_{se} \sim 1$

For $\gamma_{se} \sim 1$, at the equilibrium potential, the field and concentration gradients in the oxide are zero, while the potential drops across the two interfaces are given by $\Delta\psi_m$ and $\Delta\psi_e$ [Eqs. (101) and (100)]. Even if the oxide film is a nonconductor, this will be the case, provided that equilibrium conditions are established within the transition layers. If the potential of the metal electrode is now displaced anodically from its equilibrium value, but not sufficiently to cause significant ionic conduction in the film, the entire overpotential will appear as an electrostatic potential drop between the two transition layers, i.e., across a region of thickness equal to the oxide film thickness to within a fraction of an atomic layer. As the potential is increased to the point where significant film growth commences, two situations can arise, depending on whether or not the transition layer equilibria are or are not essentially maintained. If they are, all of the overpotential remains as an electrostatic potential drop across the oxide film, as above; if not, the overpotential becomes distributed between the film and one or both interfaces to equalize the rates. If the former is the case, a graph of η vs. X for i constant will yield a straight line or curve which extrapolates to $\eta \simeq 0$ at $X = 0$, independent of i and pH; if the latter is the case, it will extrapolate to a positive value for η_0, which will increase as i is increased. Note that the former case, i.e., $\eta_0 \simeq 0$, can arise even if ionic conduction through the oxide is controlled at a boundary in accord with the Mott–Cabrera model. Thus the injection of a cation vacancy at the oxide–electrolyte interface will presumably involve the movement of a lattice cation from the underlying oxide plane into the transition layer, which process is not influenced by the potential drop $(\psi_{se} - \psi_{aq})$. (The above injection process is not the same as the movement of a cation from a surface step into a surface plane, the process described in Section 3.2.)

3.4.2. Case in Which $\gamma_{se} \lll 1$

For $\gamma_{se} \lll 1$, $\sigma_{se} \simeq 0$. At the equilibrium potential, $\psi_M - \psi_{sm} = \Delta\psi_m$ [Eq. (101)], while $\psi_{sm} - \psi_{aq} = \Delta\psi_e$ [Eq. (100)]. Thus the electrostatic potential drop and concentration gradient through the film are not zero at equilibrium. Under conditions of film growth in which transition layer equilibria are maintained, the field in the film and that in the double layer are related through Eq. (87) with $\sigma_{se} = 0$, from which it can be shown that$^{(34)}$

$$\eta_0 = (\delta K/K_\delta)E(0) - 2.303(kT/e)(\mathrm{pH}_{\mathrm{fb}}^{\mathrm{OX}} - \mathrm{pH}) \tag{102}$$

where δ is the thickness of the double layer, $E(0)$ is the field required to sustain the current density i in the limit $X \to 0$, and $\mathrm{pH}_{fb}^{\mathrm{OX}}$ is a temperature-dependent constant. (E is defined for $x = 0$ chosen at the metal–oxide interface.) Thus, if i is a function of E and X only, and independent of pH, η_0 should vary linearly with pH. If the overpotential intercept is defined to correspond to the point of intersection of the family of curves of η vs. X for fixed pH, then even for i a function of pH, this intercept varies linearly with pH.(34)

If equilibrium conditions are not maintained in the oxide–electrolyte transition layer, then the situation described in Section 2.6.2 can arise and the behavior of η_0 with pH is uncertain as it depends on details of the kinetic model used for the interfacial rate processes.

From the foregoing, it can be seen that analysis of the dependence of η_0 on i, pH, and the concentration of other solution species, can provide important information concerning the mechanism of anodic oxidation.

4. Kinetics of Growth of Valve Metal Oxides

4.1. Steady State Kinetics

For i a function of E only, galvanostatic control ultimately establishes steady state conditions (i and E time independent). In this section we present results so obtained, mainly for Ta, Nb, and Al.

4.1.1. Interfacial Versus Bulk Control

Most investigations have reported no detectable variation of E with X for galvanostatic conditions. However, Dignam and Ryan(28) found for Al in a glycol borate electrolyte a reproducible decrease in $\partial\eta/\partial t$ with increasing X (Figure 1). Young(62) observed a similar result for Ta, but found that it vanished when he calculated the field strength in a way intended to eliminate any effect of change in the electrode area with film growth. This he did by calculating X from $[(\int i\,dt)(1/C)]^{1/2}$, where C is the electrode capacitance measured at 1 kHz; however, see reference 44.

We conclude that valve metal anodic film formation is represented under steady state conditions by Eq. (94) with either $g \sim 0$ or $g \sim 1$.(28) In no case, however, is a transition in kinetics observed over a range of film thickness covering a few angstroms up to several thousand angstroms, where electrode sparking leads to oxide crystallization and reduced current efficiency.

Siejka, Nadai, and Amsel,(63) using nuclear methods of analysis, showed that the overpotential intercept, η_0, was zero to within ±0.1 V (corresponding to ±1 to 2 Å uncertainty in X) and independent of i for both Al and Ta anodized in a 5 wt % aqueous ammonium citrate electrolyte of pH 6. Earlier, Young found a similar result for Ta anodized in 0.2 N aqueous H_2SO_4.(21)

From this very limited data, it appears that within experimental error, η_0 is zero, independent of i and pH,(34) which suggests that for these systems, $\gamma_{se} \sim 1$ and equilibrium conditions are maintained within the transition layers during film formation. This precludes rate control within the oxide–electrolyte double layer, a model previously proposed by the author(16,64) and also within the metal–oxide double layer. Further evidence against the latter is provided by the results of Vermilyea,(65) who showed that the kinetics for Ta_2O_5 formation are not influenced by the crystallographic orientation of the metal surface. A similar result was obtained for Al by Basinska *et al.*(66)

Within the limitations provided by the accuracy of currently available data, and the scope of currently available theoretical analyses, the only two possible mechanisms are the Mott–Cabrera mechanism [Eq. (30)], as interpreted in Section 3.4.1, and the mechanism involving homogeneous generation of defect pairs with both defects mobile [Eq. (71)].

4.1.2. The Form of W(E)

As noted in Section 2.5.1, Young(45) was the first to discover that certain apparent anomalies relating to the simple high-field equation were eliminated if a quadratic field term was included in $W(E)$, as per Eq. (83). In four independent sets of measurements, by Young *et al.*, two for Ta and two for Nb, the value of d_2 was found to be the same within experimental uncertainty, namely, $d_2 = 0.29_7 \pm 0.01_0$.(16,49) Dignam and Goad showed that a quadratic term was also required to account for the steady state kinetics for Al, and obtained an estimate of d_2 of 0.2_8,(30) the uncertainty being due to lack of knowledge of the precise value for the activation energy.

Prior to Young's discovery of the quadratic field term, several investigators noted that the field coefficient, β, did not vary proportionally to $1/T$, as predicted by the simple transport equations. It was this fact that led Dewald to develop his dual-barrier model. On including the quadratic term in $W(E)$, however, this apparent anomaly is entirely eliminated.(45,46)

4.1.3. The Case for a Local Field Model

The evidence in favor of a local field model is strong. In all those experiments in which the dielectric constant K of the film can be changed, either by changing the temperature,(67) or by altering the amount of electrolyte incorporation by changing the electrolyte,(68–70) it has been found that the activation dipole (charge, activation distance, product) calculated using the Maxwell field in $W(E)$, is to a good approximation proportional to K.(3,16) Maurer(71) was the first to note such an effect in high-field conduction measurements on thin sheets of soda-lime glass, contacted by aqueous solutions 3.5 N in NaCl. When the Lorentz local field (E_L for $\gamma_L = 1/3$, $K_L = 1$) was used, the apparent temperature dependence in the activation distance was eliminated, and a constant value of about 2.5 Å obtained on setting $q = e$ (Na^+ mobile).

The activation dipoles obtained for anodic formation of Bi_2O_3, Al_2O_3, Ta_2O_5, and Nb_2O_5, on using the Lorentz local field, are given by $2.6 \pm 0.8e$ Å.(16) Assuming the mobile species to be vitreous network defects of charge $\pm e$ gives activation distances, therefore, close to that for soda-lime glass.

The precise form of the local field is unknown as forms other than that due to Lorentz would yield similar results.

4.1.4. Electrolyte Incorporation and Transport Numbers

Beginning with the work of Vermilyea,(68) then Randall, Bernard, and Wilkinson,(72) Dell'Oca and Young,(70) and others, it is now well established that during anodic formation of Ta_2O_5, electrolyte constituents (e.g., phosphate, sulfate, etc.) are incorporated in the film and reside entirely in a fraction of the film adjacent to the electrolyte, the fraction being ~1/2. Furthermore, Amsel and Samuel(73) and Pringle(74) have shown via ^{18}O labeling that the mechanism of ion transport in Al_2O_3 and Ta_2O_5 preserves the order in the oxygen sublattice. Similar experimental results obtained using radioactive tantalum labeling by Pringle,(75) show that the order in the tantalum sublattice is also largely preserved. Davies, Pringle, and co-workers(76) and Witton,(77) using noble gas markers, have obtained metal ion transport numbers for several anodic film systems, the results for Ta_2O_5 being ~0.3. For a review and interpretation of the above results as well as those of Perrier, Rigo, and Siejke(78) for the anodic oxidation of duplex films of Ta and Nb, the most recent publications by Pringle(54) should be consulted. The following, while not equivalent to Pringle's interpretation, is consistent with it, and offers the advantages associated with a better-defined, if not more exact, model.

The above phenomena are consistent with either a mechanism involving homogeneous generation of vacancy-like defect pairs with both defects mobile, or a Mott–Cabrera mechanism in which either cationic network defects are generated at the metal–oxide interface, or anion network defects at the oxide–electrolyte interface.(16) Since the proper microscopic interpretation of the transport number data is uncertain,(16) due to the fact that the films are amorphous, no decision between these two mechanisms can be made at this time. The above data, however, are inconsistent with any of the conventional mechanisms of ion transport through crystalline solids.

Data for electrolyte incorporation in other nonporous valve metal oxide films is unavailable. The noble gas marker experiments, however, give the following metal ion transport numbers(16): Al_2O_3, ~0.6; Ta_2O_5, ~0.3; Nb_2O_5, ~0.3; WO_3, ~0.3; ZrO_2, ~0.0; HfO_2, ~0.0. If the mechanism of growth of the even valent oxides, ZrO_2 and HfO_2, is by homogeneous generation of defect pairs, the defects must be oxygen ion vacancies and interstitials, respectively.

4.2. Isothermal Transient Kinetics

4.2.1. Nature of Transients

If a system is subjected to a sufficiently rapid change in current density or field, the relationship between them during the transition is not that found for steady-state conditions.

The most easily characterized transient property is the transient differential field coefficient, $\tilde{\beta}_t$, defined as

$$\tilde{\beta}_t = \lim_{(dE/dt)\text{large}} \left(\frac{\partial \ln i}{\partial E}\right)_T \tag{103}$$

and is measured by determining the change in i resulting from a sudden change in E, or vice versa, and requires correcting for the capacitive current.(16) In general, $\tilde{\beta}_t$ will be a function of the steady-state field strength present immediately before initiating the transient, as well as the field displacement from this value.(16) For comparison, the steady-state differential field coefficient is defined by

$$\tilde{\beta}_s = \lim_{(dE/dt)\to 0} \left(\frac{\partial \ln i}{\partial E}\right)_T \tag{104}$$

Each of these is found to be a linear function of E for those systems for which the data are available [Ta (reference 49) and Al (reference 79)], owing no doubt to the quadratic field term. The ratio $\tilde{\beta}_s/\tilde{\beta}_t$, however, appears to be independent of E and has a value ranging from 2.1 to 3.4 for Ta, Nb, Al, and Bi.(16)

Galvanostatic transient data have been obtained on Ta, InSb, and Al by Dewald(42) and Goad and Dignam.(80) Results for Al are shown in Figure 10 and were obtained by changing the current abruptly following the establishment of steady-state conditions. The data are presented as a logarithmic plot of the reduced excess field, $(E - E_2)/(E_1 - E_2)$ against the total charge passed, $q_T = \int_0^t I\,dt$, where I is the total current density, including charging current, and E_1 and E_2 are steady state fields corresponding to the initial and final current densities I_1 and I_2. Following the rapid rise in the excess field, associated with charging the metal oxide electrolyte capacitor, the data for different I_1, I_2 are superimposed plotted in this way. The transient is characterized by charge passed, rather than time elapsed, i.e., the larger I_2, the more rapid the transient.

Potentiostatic transient measurements have usually been performed on films which are thick enough so that the field strength may be regarded as constant during the transient. Measurements of this sort have been reported by Vermilyea,(81) Young,(82) Masing and Young,(83) Dignam and Ryan,(84) and Taylor and Dignam(64) for Nb, Al, and Bi. Data for Al obtained by rapidly reapplying a constant overpotential to a preformed electrode are shown in

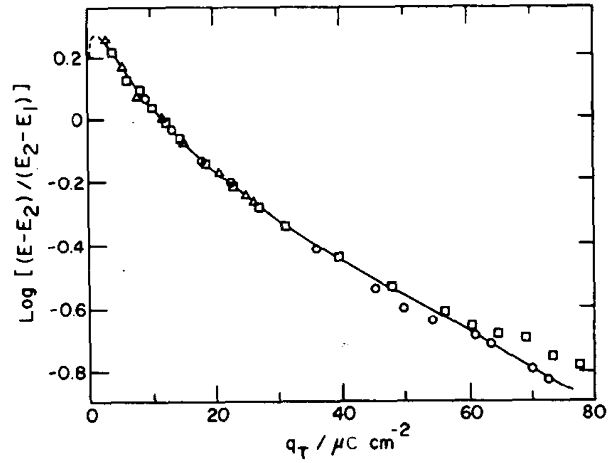

Figure 10. Decay of the reduced excess field, $(E - E_2)/(E_2 - E_1)$ following initiation of galvanostatic transients for film covered Al in a glycol borate electrolyte. The data are according to Goad and Dignam.(80)

Figure 11. The initial current spike presumably corresponds to the buildup and decay of charging current, with the final potentiostatic current rise being due to a buildup of the ionic current in the film. Again, it was found that for the region between *c* and *d* the data are characterized by charge passed, not time elapsed.(16)

Open-circuit transients, or potential decays have been employed extensively by Ord, DeSmet, and their co-workers(23,24,86–93) in measurements on Fe,

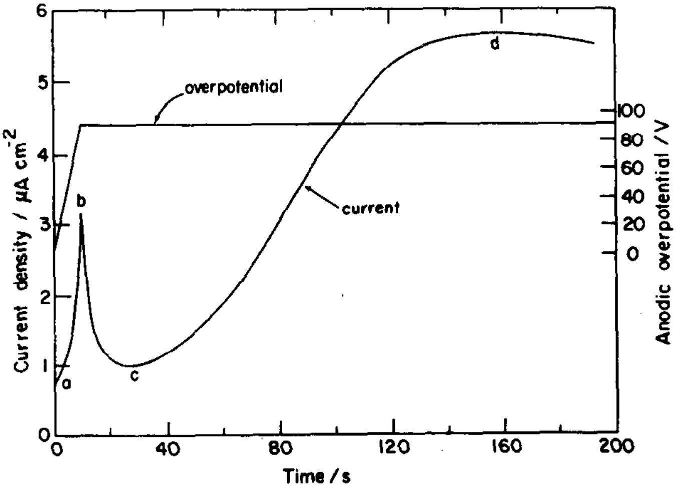

Figure 11. Time dependence of the current density on reapplication of a potential, as illustrated, to an Al electrode formed initially at 209.5 μA/cm^2 in a glycol borate electrolyte, then annealed at 60°C. The data are according to Dignam and Ryan.(84)

Ta, Nb, Bi, V, Zr, Pt, and W. Analysis of the initial portion of such decays(91) to a first approximation(95) yields values for $\tilde{\beta}_t/X$ and K/X [i.e., during the initial rapid decay, $i \,\dot{\propto}\, \exp(\tilde{\beta}_t/E)$, while the charging current density, $i_c = K\partial E/\partial t$ and $i + i_c = 0$]. Some of the above have been accompanied by ellipsometric measurements of the film optical properties, and transients in these accompanying galvanostatic current transients, results from which we refer to in the next section.

4.2.2. Explanation for Isothermal Transients

A total of five basic explanations have been offered for the transients observed, for Ta and Al primarily. Insofar as these two metals are concerned, it is the author's view that transients arise most probably as a result of time-dependent polarization phenomena.

The first quantitative attempt at explanation was due to Bean, Fisher, and Vermilyea,(41) through their high-field Frenkel defect model, outlined in Section 2.4.1. When the steady state condition ($R_f = R_r$) is dropped, the model gives rise to transients, since on changing the field rapidly, the mobile defect concentration does not adjust immediately to its new steady state value. The model accounts for the two differential field coefficients, $\tilde{\beta}_t$ and $\tilde{\beta}_s$, but not for the fact that their ratio appears to be independent of E.(16) Again, it accounts satisfactorily for the form of the galvanostatic transients,(42) but not that of the potentiostatic transients.(83,84) Finally, as already noted, the model predicts a transition in the kinetics with increasing film thickness, which is not observed.

Young(82,96) offered an explanation for the apparently "autocatalytic" buildup of current during potentiostatic transients, according to which mobile defects are generated initially at a rate proportional to i^2. Recently, Young and Smith(95,97) extended this model to provide kinetic equations capable of accounting quantitatively for the ionic current transients. They proposed a functional dependence for the rate of change of concentration of ionic current carriers, dn/dt, on E, i, and n that reproduced expressions derived earlier by the author(16) from a different model, the dielectric relaxation model. Specifically they proposed that

$$dn/dt \propto ni[\beta' E - (\ln n)] \tag{105}$$

where β' is a field coefficient of the usual form. Although an attempt was made to justify the form of Eq. (105) in terms of the vitreous nature of the oxide film, the main justification offered was the end result. As a purely phenomenological account of the transient data, it falls short of the success achieved by the dielectric relaxation model.

Young(3,12) has expanded a model due to Adams, Van Rysselberghe, and Willis according to which a Mott–Cabrera model is assumed, with the concentration of sites for defect injection varying with time on changing i, as a result of changes in the surface step concentration associated with spiral dislocations in the metal. No attempt at a quantitative application of this model has been made.

De Wit, Wijenberg, and Crevecoeur(98) proposed a model which again was designed to reproduce the author's result,(16) in which both ions are assumed to be mobile in the bulk of the oxide film. In addition, they postulated the existence of a "boundary layer" at the metal–oxide interface, a few atomic layers in thickness, that is impervious to negatively charged defects. In this model, a surface charge at the interface between the bulk oxide and the boundary layer adjusts the fields in the respective regions for equal ion current density under steady-state conditions. Since the surface charge cannot adjust immediately to a sudden change in E or I, transients result, the form of which can be made to duplicate those based on the dielectric model. Indeed, since dielectric polarization can be expressed as a surface charge, the connection between the two models is apparent. The main shortcoming of the model is that it predicts a nonzero overpotential intercept, η_0, which would also have to be a logarithmic function of the current density. As noted in Section 4.1.1, for both Ta and Al, η_0 is zero, independent of current, within about ±0.1 V, an uncertainty too small to leave room for this model to operate. Furthermore, as with Young and Smith's model, it falls short of the success achieved by the dielectric relaxation model.

The case for dielectric relaxation being responsible for the transients follows. As already noted, there is considerable evidence that the field responsible for film growth is a local one which varies approximately proportional to KE. Ord and co-workers have shown that sudden changes in i are accompanied by sudden changes in the refractive index, film thickness, and dielectric constant, K, following which relaxation in these occurs.(50) If it is assumed that under formation conditions the polarization or dielectric constant relaxes at a rate proportional to i, all the isothermal transients are reproduced with a single set of parameters.(16,64) Finally, that the polarization or dielectric constant does indeed relax as required to fit the ion current transient has been verified through charging current measurements made on the Ta system.(99)

4.2.3. The Dielectric Relaxation Model

4.2.3.1. Phenomenological Equations

Representing the local field [Eq. (96)] by

$$E_L \simeq w(KE) = w(E + 4\pi P) \tag{106}$$

where P is the polarization per unit volume, and differentiating by t gives

$$\frac{1}{w}\frac{dE_L}{dt} = K_1\frac{dE}{dt} + 4\pi\frac{\partial P}{\partial t} \tag{107}$$

where E and t are treated as independent variables, and $K_1 = 1 + 4\pi\ (\partial P/\partial E)$, the dynamic dielectric constant of the film. In accord with the foregoing account the polarization relaxation rate is represented by

$$4\pi\frac{\partial P}{\partial t} = Bi(\chi_s E - 4\pi P) \tag{108}$$

where χ_s is the steady state electric susceptibility. Equations (107) and (108), with (94) and (95), reproduce all isothermal ionic current transients quite well, though for a faithful reproduction, a second relaxation process of the form of Eq. (108) must be introduced.(16)

These equations can be derived from a somewhat different but equivalent point of view. Ord *et al.*(93) have concluded from their recent results on tungsten that K decreases approximately linearly with E when E is increased rapidly. This result may be reproduced as follows.

From Eq. (106), we get

$$\frac{1}{w}\frac{dE_L}{dt} = K_1'\frac{dE}{dt} + E\frac{\partial K}{\partial t} \tag{109}$$

where $K_1' \equiv K + E(\partial K/\partial E)$. Assuming a relaxation rate for K proportional to i gives

$$\frac{\partial K}{\partial t} = Bi(K_s - K) \tag{110}$$

where $K_s = 1 + \chi_s$ and is the steady state dielectric constant. The two sets of equations are exactly equivalent if $K_1' = K_1$. Integrating $K_1 = K + E(\partial K/\partial E)E$ for $K_1' = K_1$ = a constant, gives for t constant (E changing rapidly)

$$K = K_1 + (K_s - K_1)(E_s/E) \tag{111}$$

where E_s is the field strength for which $K = K_s$, i.e., that corresponding to steady-state conditions. For E changing rapidly and not too different from E_s, Eq. (111) leads to K decreasing approximately linearly with increasing E as required.(94)

The argument for a relaxation rate of the form of Eq. (108) or (110) is that, on passing through the amorphous oxide, the ionic defects bring about structural changes in their wake. The constant B is thus the interaction cross-sectional area for a moving defect divided by the charge on it.(16) The apparent need to include two such relaxation processes might arise from both anionic and cationic defects being mobile and/or as a result of the duplex nature of the films.

4.2.3.2. Comparison with Data

It is easily shown(16) that the dielectric relaxation model gives for the ratio of the differential field coefficients the result $\tilde{\beta}_s/\tilde{\beta}_t = K_s/K_1$.

The solid line in Figure 10 was fitted to the data presented there using the same model, and is typical of the agreement achieved for galvanostatic potentiostatic and ac impedance measurements.(16)

Assuming unit electron charge on the defects, analysis of the isothermal transients for Ta and Al yields the following values for the interaction radius, $r_0 = (eB/\pi)^{1/2}$: for Ta, 1.8_2 and 4.6_9 Å; for Al, 2.4_8 and 6.8_7 Å. As already noted, both give $K_s/K_1 \sim 3$. Details concerning the analyses can be found elsewhere.(16)

4.2.3.3. Microscopic Bases of the Equations

In Section 2.5.2, it was suggested that a possible consequence of amorphous film structure is the introduction of conduction transients as a result of a dependence of film structure on current density and time. Vermilyea(81) was in fact the first to make such a suggestion, and it is explicitly the basis of Young and Smith's model, and implicitly that of the dielectric relaxation model. One can imagine, therefore, a class of "structure models" in which transients are associated with time-dependent structural changes, leading to a time dependence in one or more of the kinetic parameters in Eq. (94) say. Thus in Young and Smith's model, structural changes are supposed to give rise to changes in A (with $A \propto n$, $g = 0$, and $E_L \propto E$) in accord with Eq. (105). Exactly the same net kinetic expressions can be obtained by postulating that they give rise to changes in the zero field activation energy, Q_e, in accord with

$$\frac{dQ_e}{dt} \propto i[(Q_e^0 - \beta'' E) - Q_e] \tag{112}$$

where Q_e^0 and β'' are constants.

In the dielectric polarization model, the structural changes give rise to polarization changes, leading therefore to changes in E_L. Clearly other possibilities exist. We now examine whether or not it is possible to make a unique choice based on experimental results.

Only a structural dependence of E_L leads inevitably to $\tilde{\beta}_1/\tilde{\beta}_s$ being field-independent, with $\tilde{\beta}_1$ and $\tilde{\beta}_s$ individually dependent on the field strength. For any other "structure model," this observed result must arise from an accidental relationship among several kinetic parameters. That this should occur for both of the systems for which the necessary data are available (Ta_2O_5 and Al_2O_3) is unlikely on general grounds.

Only a structural dependence of E_L resulting from dielectric polarization changes will give rise inevitably to dielectric charging kinetics which share common kinetic parameters with the ion-current transient kinetics. As already noted, this connection has been verified for the Ta_2O_5 system.(99) Again, one may postulate an accidental coincidence, this apparently being the position taken by Young and Smith.(97)

We examine separately the model by de Wit *et al.*(98) since it does not fit into the class of "structure models." Since it involves a time-dependent surface charge, which is phenomenologically equivalent to a polarization change, it also can lead to the observed connection between charging and ion-current transient kinetics. It does not predict the field independence of $\tilde{\beta}_1/\tilde{\beta}_s$, however, and most importantly, as already noted, it requires a dependence of the overpotential intercept on i, contrary to observation.

We are left finally with the question of precedence and physical reasonableness. While the model of de Wit *et al.* involves a number of ad hoc postulates, only one appears to be physically questionable, namely the postulate that the ratio of the current carried in the bulk of the film by the negative ions to that carried by the positive ions is proportional to the field strength. There is no precedence, nor microscopic justification, offered for this postulate. The observed transport numbers for these oxides may be otherwise explained, and on a reasonable basis (Sections 2.5.2.2 and 4.1.4).

There is likewise no precedence for Young and Smith's equation [Eq. (105)]. It implies a rate of defect formation which is proportional to the product of :n^2, the hopping frequency of a defect (an exponential function of the field), and E. While an attempt is made to justify the presence of the first two factors on mechanistic grounds, none is made for the presence of the factor E, and no mechanistic argument is offered for a defect annihilation rate proportional to $ni \ln n$.

This leaves the dielectric relaxation model, which has been challenged on similar grounds to those above. Specifically, the challenge is that the form chosen for the relaxation time in Eq. (108), namely $1/Bi$, lacks a physical basis. Such a physical basis exists, however, and has precedence.

Whether one uses Young and Smith's,(97) Pringle's(54) or the author's(16) description of the mobile defects responsible for film growth (Sections 2.5.2.2 and 4.1.4), the motion of a mobile defect involves in a formal sense the breaking of certain bonds, and the formation of others, with accompanying structural changes. These changes must arise since the order around a given mobile defect will change from one location to another due to the random components in the vitreous oxide structure. Chemical reactions can likewise be described in terms of the breaking of certain bonds and the formation of others, with accompanying structural changes. Theoretical work has been published concerning the role of chemical reactions in dielectric polarization phenomena.(100) In one domain of behavior (large reaction rate, slow thermally activated polarization rate) the polarization is predicted to relax in a simple first-order fashion, with the relaxation time having no direct temperature dependence, but rather being inversely proportional to the reaction rate per unit volume.

During ion transport through amorphous films, the bond rearrangement, or reaction rate, per unit volume will be proportional to the number of defect hops per unit volume per unit time; i.e., proportional to the current density, i, leading therefore precisely to Eq. (108) in this limit. The polarization process associated with Eq. (108) can be thought of as corresponding to fairly long-range structural rearrangements in an extremely viscous fluid.

4.2.4. Thermally Induced Transients

A number of investigators have studied the ionic conduction behaviors of valve metal systems following thermal annealing.(81,101–103) The most thorough of such studies is due to Crevecoeur and de Wit.(103) They investigated the properties of Al during reanodization following a thermal anneal in oxygen at 400°C for 15 min. Figure 12 shows potentiodynamic data for an annealed and unannealed specimen formed under identical conditions, which are in agreement with earlier data by the author.(101) Examination of the film by transmission electron microscopy, at various stages of the reanodization process, revealed the formation of dark patches ~0.1 μm in diameter which grew during the current transient until the entire film appeared uniform again. Such a phenomena was not observed for unannealed samples. Furthermore, X-ray diffraction studies revealed no structural change caused by annealing. The thermally induced potentiostatic current transients were accounted for extremely well by the following model: nuclei of conducting oxide (dark patches) increase in number linearly with time, and grow laterally at a constant rate.

We offer the following partial and tentative explanation for their data. Annealing eliminates those regions of low density in the film or at one of its

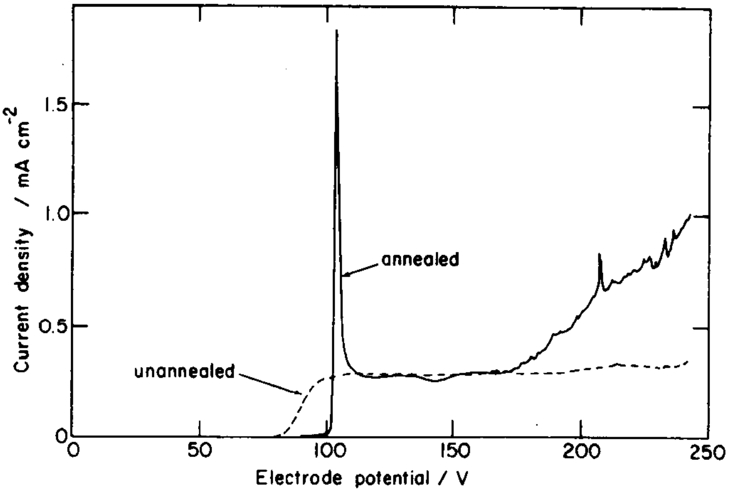

Figure 12. Potentiodynamic plot for Al electrodes anodically oxidized to 90 V in a glycol borate electrolyte. The measurements were performed for $\partial\eta/\partial t = 0.125$ V sec^{-1} in the same electrolyte for specimens both unannealed and annealed in oxygen at 400°C for 15 min. The data are according to Crevecoeur and de Wit.(103)

boundaries where the local field is high, i.e., those regions where mobile defects are formed. A higher field is, therefore, required to initiate conduction at sparsely distributed nucleation sites which then grow laterally by a mechanism analogous to the current-induced dielectric relaxation process. Measurements performed on annealed films, subsequently thinned in HF, suggest that the "nucleation and growth" process is controlled at the metal–oxide interface or within the inner one-half or so of the film. Dependence of both the growth rate constant for the nuclei, and the incubation time, on the film thickness (constant E), however, suggest a volume-controlled mechanism, such as would be expected for the ionic conduction model involving homogeneous generation of defect pairs with both defects mobile.

4.2.5. Conclusion

Although the details of the various transient phenomena are of intrinsic interest, an important lesson to be learned from them is that whenever a local field model applies, dielectric relaxation phenomena will give rise to transients, though not necessarily of the same form as those found for Al and Ta. Attempts to determine growth kinetics and mechanisms may well be confounded, therefore, by interference from these transients, transients which are not particularly diagnostic of the ionic conduction mechanism. Primary kinetic data should, therefore, be obtained under steady state conditions of constant or nearly constant i and E. Such conditions are very difficult to achieve for very thin films (a few atomic layers). Conflicting kinetics reported for metals such as Ni,(15) Fe,(15) Pt,(20) and others may well be accounted for in this way.

5. Other Metal–Oxide Systems

5.1. Porous Anodic Oxide Films—Al, Al_2O_3

Porous films can be formed on Nb, Ta, Zr, and V–Nb alloys in very aggressive electrolytes, and on Al in many acid electrolytes.(18) However, only porous alumina films have been extensively studied, owing to their commercial applications as finishes for aluminum products. The field has been reviewed recently by Wood(18); a brief summary is given here. At the same time, the simple model of Section 1.2.3.2 is used as a framework on which to hang the facts.

Under galvanostatic control, the formation voltage ultimately becomes more or less constant, and the total film thickness increases at a constant rate. Chemical dissolution of the walls of the porous oxide limits the maximum achievable film thickness. The relationship between current density and formation voltage depends upon the temperature, solution constituents, and concentration of the aqueous electrolyte, and upon stirring, owing, no doubt, to local joule heating, particularly at the pore bases.

To a good approximation, the film morphology is determined by the formation voltage alone. An idealized representation of a porous alumina film is given in Figure 13.(18) The inner "barrier layer" thickness, X_b, the cell wall thickness, X_w, the cell and pore diameters, D_c and D_p, are all found to be approximately proportional to the formation voltage, being, e.g., ~28 Å/V for D_c (Figure 13 is roughly to scale). Presumably the thickness of the barrier layer determines the other dimensions according to simple geometric considerations.

The oxide dissolution process taking place at the bases of the pores has been found to be field assisted,(104,105) so that part of the overpotential must appear across the oxide–electrolyte double layer.

Using the outer surface of the film as a marker, Dekker and Middelhoek(106) determined the metal transport number appropriate for a pore filling, reanodization of the film in a nonsolvent (boric acid) electrolyte, and obtained 0.24. Thus some film growth occurs at the metal–oxide interface, as required for the overall film thickness to increase beyond that of the barrier layer.

If we assume that the fields in the barrier layer and the double layer at the pore bases are proportional to one another when a solvent electrolyte is used (i.e., $\sigma_{se} \simeq 0$), the dissolution current density at the pore base, i_d, can presumably be represented by

$$i_d = A_d \exp(\beta_d E) \tag{113}$$

For steady state conditions, i and η are more or less constant, so that

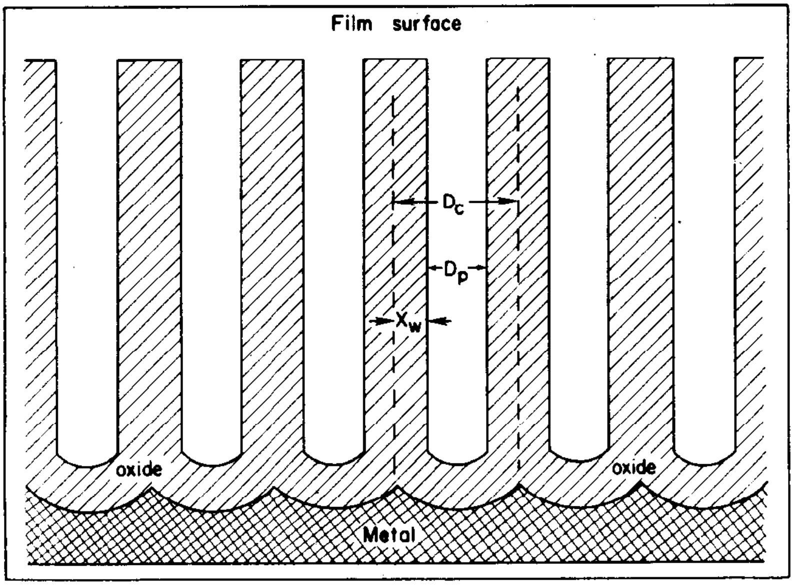

Figure 13. Cross section of an idealized model of a porous anodic film adapted from that according to Wood.(18)

$dX_b/dt = 0$ and hence

$$i_d \simeq \theta_p i \tag{114}$$

where θ_p is the fraction of the surface area corresponding to pores. Representing the ionic current density in the barrier layer by Eq. (1), then Eqs. (1), (113), and (114) lead to

$$E_s \simeq (\beta - \beta_d)^{-1} \ln (A_d/\theta_p A) \tag{115}$$

where E_s is approximately the mean steady state field in the barrier layer. Since the geometry for current flow is not linear (Figure 13) and the mechanism for ionic transport in the barrier layer uncertain, the precise interpretation of E_s is uncertain. Presumably, however, $E_s \simeq \eta/X_b$ so that Eq. (115) predicts a nearly constant Å/V ratio. Actually, it should vary linearly with $1/T$, and also somewhat with electrolyte composition primarily through A_d. To account for a forming ratio ~10 Å/V for X_b, however, requires that $\exp(\beta - \beta_d) \gg 1$ and $A_d/\theta_p A \gg 1$ and hence $\ln(A_d/\theta_p A)$ is a slowly varying function of A_d. The predicted variation of the forming ratio would, therefore, appear to fall within the range of the observations.(18)

From Eqs. (1), (114), and (115)

$$i = A(A_d/\theta_p A)^{\beta/(\beta - \beta_d)} \tag{116}$$

so that at first glance the prediction is that the formation current density be nearly independent of the formation voltage or vice versa. However, A and A_d are exponential functions of the temperature at the pore base, and hence dependent on $i\eta$ and the rate at which heat can be dissipated, leading to a complex dependence of η on i and X. Typically, η goes through a maximum during which a stable pore structure is established,(18) falling off by about 20% at longer times. The process of pore nucleation is not well understood.(18,105) To improve this situation a better understanding of the ionic transport and oxide–electrolyte double layer processes is required.

5.2. Growth of Thick Films by Dissolution, Precipitation Mechanism—Ag, Ag_2O

As noted in Section 1.2.3.2, most metals that display an active to passive transition, probably do so through a dissolution–precipitation mechanism. Such processes are, however, very difficult to follow, since once oxide precipitation begins, very little film growth occurs before passivity is achieved. This situation arises when film growth obeys either a high-field type of equation or the Elovich equation, and the overpotential is limited by the onset of oxygen evolution or some other transpassive electrode reaction. On the other hand, very thick oxide films may be formed anodically on Ag in alkaline electrolytes by a dissolution–precipitation mechanism, allowing a more complete analysis of the situation. We therefore examine this system in detail.

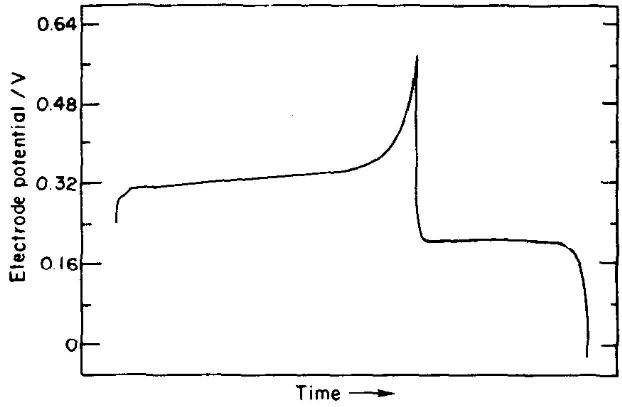

Figure 14. Galvanostatic oxidation and reduction curves for Ag_2O film formation at 27°C in 0.7 *M* NaOH under conditions of rapid electrolyte flow. During oxidation, $i = 0.33\ \mathrm{mA/cm^2}$ and duration = 7.6 min. During reduction, $i = 0.39\ \mathrm{mA/cm^2}$ and duration = 4.3 min. The data are according to Gibbs *et al.*(107)

An investigation of the kinetics and mechanism of formation of Ag_2O films on Ag is contained in a recent paper by Gibbs *et al.*(107) It is proceeded by many studies,(108,109) most of which, however, are concerned primarily with the composition of the film formed during the various potential steps, and/or with means of increasing the discharge capacity of the Ag, AgO electrode in connection with its use in storage batteries.

The studies by Gibbs *et al.*(107) were of Ag electrodes prepared by electropolishing followed by reduction in an H_2 stream at 500°C. The cell was part of a flow system designed to circulate the electrolyte (0.7 *M* NaOH) past the electrode surface at very high speeds to control the diffusion conditions at the oxide electrolyte interface.

A typical galvanostatic–reduction curve is shown in Figure 14. The turn-up at the end of the oxidation portion, if uninterrupted, rises to the AgO formation plateau (Figure 5). The maximum or limiting Ag_2O film thickness obtained in this way is shown as a function of formation current density, *i*, in Figure 15, while Figures 16 and 17 give the current efficiency for film formation and the overpotential intercept η_0 (η for $X \to 0$) as a function of *i*.

Figure 15 is of the form expected for a process which is controlled by diffusion through the film. Such is only possible if either the diffusing species carries no charge and/or the film is a good enough electronic conductor to prevent the establishment of a field in the film. In either case, there is negligible electrostatic potential drop across the film, so that the usual dilute solution form of the chemical potential gives for equilibrium boundary concentrations

$$\eta = \eta_0 + \frac{kT}{e} \ln\left(\frac{n_0}{n_0 - \Delta n}\right) \tag{117}$$

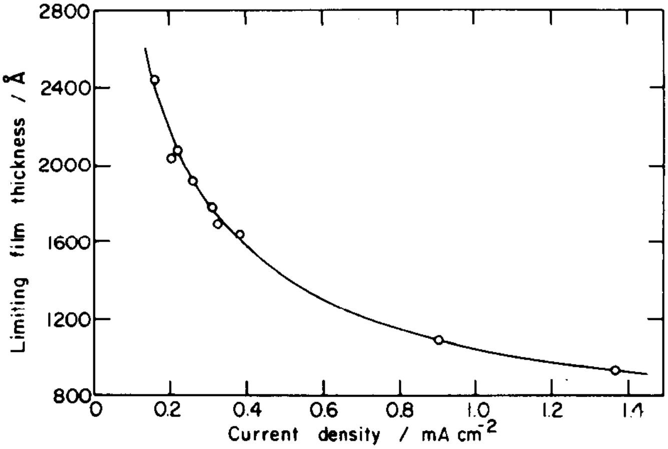

Figure 15. Limiting thickness of Ag_2O film as a function of formation current density. The data are according to Gibbs *et al.*(107)

where n_0 is the concentration of the diffusing species at the boundary where they are generated, and Δn the concentration drop across the film. The linear transport equation, Eq. (27), then gives

$$i = |qJ| = |q|D_{\mathrm{Ox}}\Delta n/X \tag{118}$$

where $\pm|q|$ is the charge associated with the diffusing species. Elimination of Δn

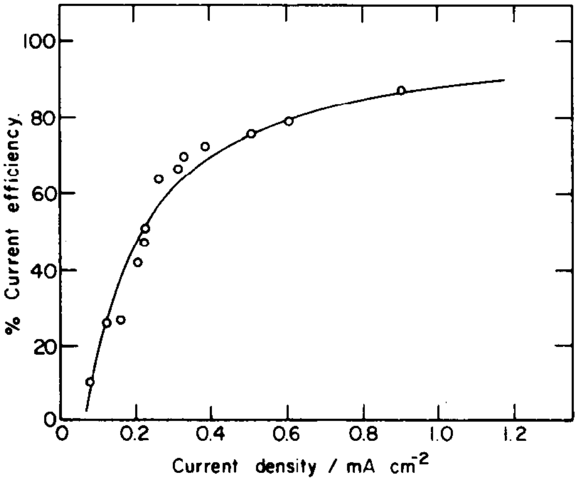

Figure 16. Current efficiency for formation of Ag_2O film as a function of formation current density. The data are according to Gibbs *et al.*(107)

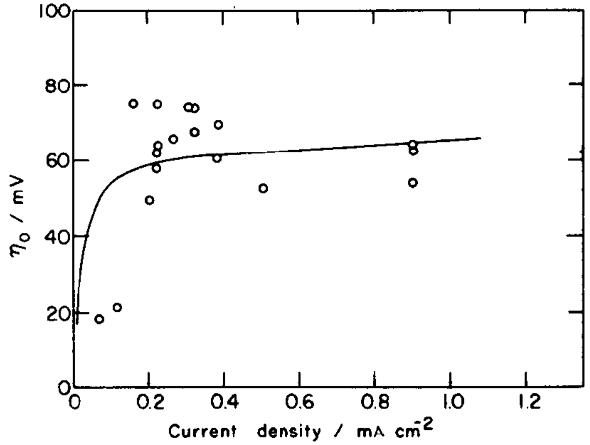

Figure 17. Overpotential intercept, η_0, as a function of formation current density. The data are according to Gibbs *et al.*$^{(107)}$

between Eqs. (117) and (118) leads to

$$\eta = \eta_0 - \frac{kT}{e}\ln\left[1 - \frac{Xi}{|q|n_0 D_{\mathrm{OX}}}\right] \tag{119}$$

where η_0, the interfacial contribution to η, is generally expected to be a function of i. The limiting film thickness, X_L, is obtained from Eq. (119) using the condition $\eta = \eta_L$, where η_L is the value of η at the inflection point (Figure 14):

$$1/X_L = i/|q|nD_{\mathrm{OX}}\{1 - \exp\left[e(\eta_L - \eta_0)/kT\right]\} \tag{120}$$

Figure 15 is of the form predicted by Eq. (119), and although $1/X_L$ was not found to be proportional to i, $1/(X_L - 695\ \text{Å})$ was. This discrepancy might have been caused by residual electrode roughness, since such roughness was found to have a significant effect on the dissolution kinetics at low current densities.

The behavior of the current efficiency (Figure 16) and η_0 (Figure 17) was accounted for as follows. Metal dissolution as $Ag(OH)_2^-$ at the oxide–electrolyte interface produced supersaturation conditions, giving rise to a dissolution current density

$$i_d = eD_{\mathrm{aq}}[n_{\mathrm{aq}}\exp(e\eta_0/kT) - n_{\mathrm{aq}}]/\delta_D \tag{121}$$

where n_{aq} is the bulk concentrate of $Ag(OH)_2^-$, D_{aq} its diffusion coefficient and δ_D the effective thickness of the boundary diffusion layer at the oxide–electrolyte interface. The film-forming current density, i_f, was assumed to have the form$^{(110)}$

$$i_f = A_f[n_{\mathrm{aq}}\exp(e\eta_0/kT)][\exp(-Q^{\ddagger}/\eta_0 kT)] \tag{122}$$

where $Q^{\ddagger}/\eta_0$ is the free energy for a nucleation process at the oxide surface.

Gibbs *et al.* assumed that this process is the nucleation of step sites for the deposition of oxide on the film.

The solid curves in Figures 16 and 17 were calculated by using Eqs. (121) and (122) and the best values for $D_{aq}n_{aq}/\delta_D$, $A_f n_{aq}$ and $Q^\ddagger$, the resulting fit being within experimental scatter. From $D_{aq}n_{aq}/\delta_D$, δ_D was estimated to be 0.008 cm, in agreement with independent values,(111) while from $Q^\ddagger$, the surface free energy of the oxide in contact with the electrolyte was estimated to be 120 erg cm^{-2}, closely matching those for ionic crystals.(112) We are skeptical of this result, however, as it should not be necessary to nucleate steps on the oxide surface, since screw dislocations terminating at the surface should provide an inexhaustible supply of these. It is more likely that the nucleation process is related to oxide deposition at the curved steps to which screw dislocation gives rise,(112) which would also lead to an equation of the form of Eq. (122), but even this seems doubtful, as the interface is expected to be highly disordered.

Electrical measurements were made on representative films via aluminum counterelectrodes formed by vacuum deposition. In general, the films displayed asymmetric electronic conduction and capacitance behavior, a result consistent with the establishment of a concentration gradient across the film during its formation. Furthermore, the thermoelectric power was found to be negative, signifying an n-type semiconductor, a surprising result. The presence of uncharged silver atoms in the film could produce this result, and might also explain the nature of the diffusing species.

Ellipsometric determination of the oxide film thickness leads to film densities in exact agreement with those for bulk Ag_2O if a roughness factor of 1.06 is assumed. Their ir absorption spectra were also in agreement. The films are, therefore, essentially compact, not porous.

There are several points of general interest contained in these results. The first is that some sort of activation process seems to be required for oxide deposition onto oxide, though the associated overpotential is small (~60 mV). Second, mass transport through the film is in accord with the linear equation [Eq. (27)] at room temperature, implying a very low value for the diffusion activation energy. This appears to be a fairly general property of silver salts. Indeed the photographic process in AgBr is dependent on a high mobility for the photolytically generated silver atoms.(113) We note here that if ion migration, rather than diffusion, were involved, η would be a linear function of X up to formation of AgO. A complete treatment of a linear transport system should proceed from the full Eq. (27), and include space charge.(16) Fromhold(19) has carried out, through computer calculations, a fairly extensive examination of this problem, which arises also in the treatment of electronic conduction in semiconductors and insulators.(114)

Finally, if the diffusion geometry within the boundary layer at the oxide–electrolyte interface is not kept simple by, e.g., electrolyte flow across a polished electrode surface, strange results can be obtained. Figure 18 presents such a case. These data by Dignam, Barrett, and Nagy(34) were obtained at very

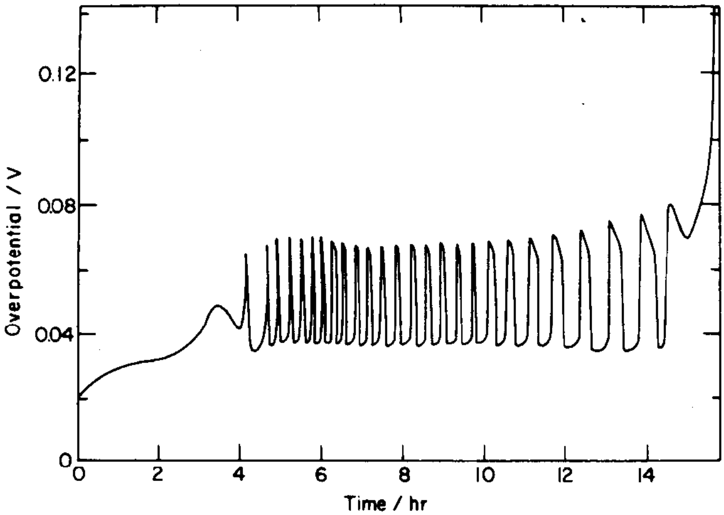

Figure 18. Galvanostatic oxidation curve for Ag_2O film formation at 27°C in 0.7 *M* NaOH under quiescent electrolyte conditions and a current density of 2.9 $\mu A/cm^2$. The data are according to Dignam, Barrett, and Nagy.(34)

low current densities in the absence of electrolyte stirring. The oxide film so formed has a very dark appearance compared to those formed under conditions of electrolyte flow, owing no doubt to high porosity. We believe the autocycling of the potential evident in Figure 18 is a result of introducing, through the complex diffusion geometry, nonlinearities in the differential equations for the rate processes. Much of the early work on the anodic oxidation of Ag was performed on cycled (repeatedly oxidized and reduced) electrodes having thereby exceedingly porous surfaces [surface roughness factors ~100 (reference 35)]. Studies on such electrodes cannot be used to elucidate the mechanism. In the author's view, cycling to reproducible behavior is in general a questionable practice in mechanistic studies and is no substitute for careful electrode preparation.

The transformation of Ag_2O to AgO in the second potential wave (Figure 5) begins with an overpotential peak, most probably associated with the free energy for nucleation of the AgO phase. Following nucleation, the transformation of Ag_2O to AgO appears to be controlled by O^{2-} migration across the Ag_2O–AgO interface.(115)

5.3. Formation and Growth of Oxide Nuclei

5.3.1. General Remarks

Only those metals which form electrochemically reducible oxide films can be used to study the nucleation and growth of films on the bare metal. The other metals react chemically with water to form very rapidly a complete film cover.

The specific free energy of a small patch of oxide differs from that of bulk oxide due to interfacial free energy contributions. If the net effect of these is to reduce the specific free energy below that of the bulk, then underpotential deposition of oxide becomes a possibility. We believe, however, that in such instances the film so formed would be better described as chemisorbed oxygen. The initial oxygen layer deposited electrochemically on Pt appears to be of this sort.

If the effect of the interfacial free energy contributions is to increase the specific free energy for a small patch of oxide above that of the bulk, then an overpotential will be required to initiate film formation. If nucleation takes place by a dissolution precipitation process, then a competition can take place between nucleation sites on the surface and in the electrolyte close to the surface.

The following four types of nucleation situations can therefore arise:

(i) Very rapid coverage of the metal surface by direct chemical reaction with the electrolyte.
(ii) Deposition (possibly underpotential) of chemisorbed OH and/or oxygen, followed by an activated transformation to bulk oxide.
(iii) Nucleation and growth of oxide patches via adsorbed intermediates or a direct interfacial electrochemical step.
(iv) Nucleation and growth of oxide patches via a dissolution–precipitation mechanism.

Reactive metals such as the valve metals (Ta, Nb, Al, etc.) act as in (i) above. Examples of the other three cases will be considered in turn.

5.3.2. Oxygen Deposition and Transformation—the Pt Electrode

It appears that anodic oxidation of the noble metals offers the only established example of this type of behavior. This field has been reviewed recently by Belanger and Vijh.(20) As Pt has been the most thoroughly studied, we present here a summary of the most recent results for bright Pt.

The initial stages of anodic film formation have been extensively investigated by Angerstein-Kozlowska, Conway, and Sharp,(116) Biegler,(117) and Goldstein, Zalkind, and Veselovskii,(118) using mainly cyclovoltametry. The data by Angerstein-Kozlowska *et al.* presented in Figure 19, were obtained using a triangular wave potential, cycling anodically to a potential short of either O_2 evolution or Pt dissolution, and cathodically, short of H_2 evolution. The curves are generally in accord with those due to Biegler, both showing three peaks in the oxygen deposition wave.

If the anodic sweep is stopped before the process responsible for the second wave commences, the film formed can be reduced reversibly.(116) If the

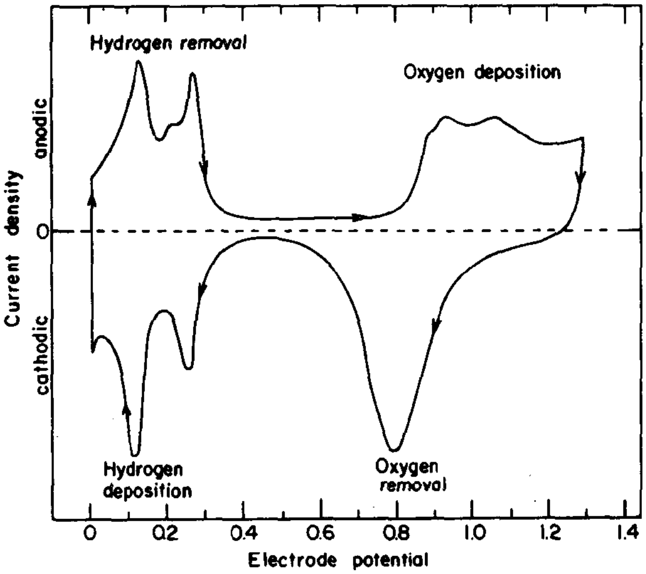

Figure 19. Cyclic voltamogram of a bright Pt electrode in 0.5 *M* H_2SO_4 at 25°C. The data are according to Angerstein-Kozlowska *et al.*,(116) and were obtained at a sweep rate of 0.1 V/sec.

potential is swept anodically beyond this point, however, reduction is irreversible, i.e., takes place at a potential more cathodic than that required for formation of the film.

Conway *et al.*(116,119) attribute the three anodic peaks to successive deposition of OH^- at sites with coordination numbers of 4, 2, and 1. This accounts for the successive charge increments to reach each peak and for the lack of dependence of the deposition curves on potential sweep rate. With appropriately chosen parameters, they were also able to generate theoretically the anodic depositon curves. Finally, they attribute the onset of irreversibility in the reduction process to a transformation of the adsorbed OH film via some sort of Pt, O or Pt, OH place exchange. Goldstein *et al.*,(118) however, found under certain formation conditions two peaks in the reduction curve which they related to a proposed two step oxidation process. In the first step OH^- is deposited, while in the second, H^+ is abstracted, leaving O^{2-} (chemically bound oxygen).

Both potentiostatic and galvanostatic kinetic measurements have been made on this system. Vetter and Schultze(120) found that for constant polarizing potentials of from 1 to 2 V (Figure 19), charge varied linearly with η and the direct logarithmic law of film growth was obeyed from 2 msec to 10^3 sec. A similar result was obtained by Gilroy and Conway.(121)

From galvanostatic studies Vetter and Schultze(122) concluded that beyond the first layer of oxide, the film is a phase oxide, rather than adsorbed layer, and grows according to a high-field transport mechanism, a conclusion shared by Visscher and Devanathan(123) and Ord and Ho.(95) On the other hand, Biegler *et al.*(124) found a limiting oxide coverage corresponding to about a monolayer of PtO_2.

If Pt is polarized at high anodic potentials for a long time, quite thick films (~10 monolayers of PtO_2) can be formed(20,125) with growth kinetics consistent with partial control by diffusion through the film,(125) as for Ag_2O formation. Whether or not such a film is formed seems to depend on the electrode pretreatment.

Finally, the behavior of the Pt electrode is further complicated by its apparent ability to absorb oxygen from the anodic film into the metal lattice.(20,126)

In summary, there appear to be several regimes of film growth, depending on the potential and elapsed time involved. It seems likely that initially OH^- is deposited, possibly at different types of sites successively, and that further oxidation involves H^+ abstraction and rearrangement of Pt, O^{2-}, and OH^- (i.e., so-called place exchange). Both this stage and further growth to coverages corresponding to the order of a monolayer of PtO_2 obey logarithmic type kinetics, the mechanistic origins of which are uncertain. Quite thick oxides can be formed, with the process apparently controlled by a combination of an interfacial process plus diffusion through the film. Mechanistic details for the other noble metals are less certain.

5.3.3. Nucleation and Growth Kinetics—Cu, Cu_2O

A full discussion of the kinetics of crystal nucleation and of crystal growth falls outside the scope of this chapter. These topics have been reviewed by Dunning(112) and by Jacobs and Tompkins(127) for chemical systems, and by Fleischmann and Thirsk(5) in connection with electrochemical processes. The transposition from chemical to electrochemical applications is straightforward.

In this section we shall confine our attention to the kinetics of formation of Cu_2O films. Only three attempts to quantify the kinetics and mechanisms for this system have been published to date, that due to Dignam and Gibbs,(128) who used an 0.05 *M* aqueous sodium borate electrolyte, that by Ashworth and Fairhurst,(129) who used various concentrations of NaOH, and that by Fletcher, Barradas, and Porter,(130) who studied Cu_2O formation on both copper and copper amalgams in 0.1 *M* LiOH. Since the borate electrolyte leads to no detectable metal dissolution, even for current densities as low as 3 $\mu A/cm^2$ (cf. Ag_2O formation) we consider these results in connection with nucleation and growth via surface species.

5.3.3.1. Involving Surface Species

In Figure 20, galvanostatic polarization curves are shown for three formation current densities. The curves terminate at the inflection point leading to

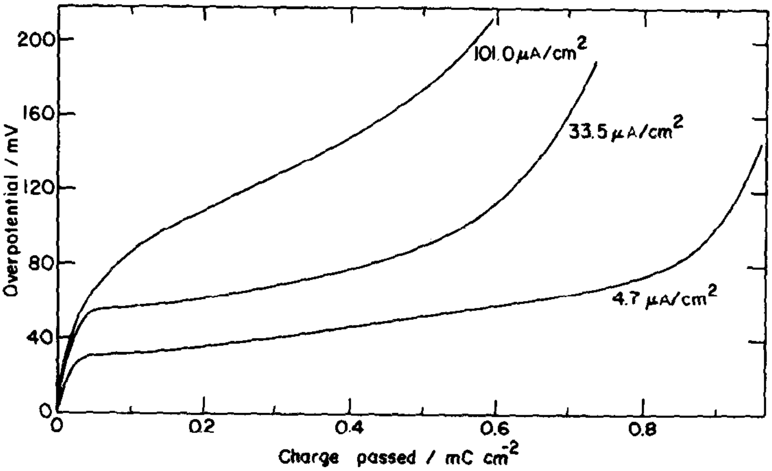

Figure 20. Galvanostatic polarization curves for Cu_2O formation in 0.05 M aqueous sodium borate. The data are according to Dignam and Gibbs.$^{(128)}$

the next oxidation plateau, presumably CuO formation. The limiting film thicknesses varied from ~15 Å at 3 μA/cm^2 to ~5 Å at 300 μA/cm^2 based on Cu_2O of bulk density. All experiments were performed on 99.999 + % purity Cu electrodes which were electropolished, reduced in flowing H_2, then introduced, oxide free, into oxygen free electrolyte.$^{(128)}$ A freshly prepared electrode was used for each oxidation run.

A quantitative account of the data, including the effect of temperature, was obtained from the following mechanism, given here in outline only.

Mobile surface species (possibly OH) are generated by an electrochemical step at the metal–electrolyte interface. When these reach a sufficient state of supersaturation, oxide nuclei form at favorable sites on the surface (lattice steps or crystal boundaries). The resulting concentration drop (overpotential drop, Figure 20) stops any further significant nucleation rate, and thereafter the nuclei grow by incorporating the surface species at their peripheries. Both linear growth (growth predominantly in one direction, e.g., along steps or grain boundaries) and two-dimensional growth (equal growth rates in the two directions in the plane) were considered, with one-dimensional growth giving both the better and an excellent fit. Termination of oxide growth occurs when the metal surface is covered with oxide.

The final equation takes the form

$$\eta = \frac{kT}{e}\left[\ln\frac{i}{i_1} + \ln\left(1 + a_1 \exp\frac{e\eta}{2kT}\right) - \ln\left(1 - \frac{q}{q_L}\right)\right] \tag{123}$$

where i_1 and a_1 are products of rate constants with the concentration of sites for nucleation and a shape factor, and are the only truly adjustable parameters; q

and q_L are the charge passed and its limiting value. The agreement achieved was within experimental scatter for all three temperatures (14, 25, and 36°C) and for all but the highest current densities, where a small discrepancy appeared.(128) From i_1 and a_1, the temperature dependence of the rate constant for the electrochemical deposition step was obtained. It gave a linear Arrhenius plot and an activation energy of 0.84 eV.

Possible variations in this type of mechanism are many. For example, under potentiostatic control the nucleation process might well follow first-order kinetics.(127) In short, a whole range of combinations of nucleation kinetics(112) and growth kinetics(127) are possible, coupled in a variety of ways through electrochemical, chemical, and surface diffusion steps.

5.3.3.2. Involving Aqueous Species

In aqueous NaOH electrolytes, some metal dissolution takes place upon polarizing Cu anodically.(129,130) Ashworth and Fairhurst,(129) using electrodes etched in alcoholic ferric chloride, observed by electron microscopy that the anodic films were of the form of small crystallites about 0.1 μm in size, with a cubic shape when 0.01–0.1 *M* NaOH was used, while a polyhedral shape when 1 *M* NaOH was used. The galvanostatic kinetic data were accounted for very well by a nucleation and growth model similar to that described in Section 5.3.3.1, except that the electrochemical rate-determining step was the dissolution of Cu at the metal–electrolyte interface, with nucleation and growth taking place at the expense of the resulting aqueous species. One might expect three-dimensional growth of the nuclei for such a case and in fact this was observed by both Ashworth and Fairhurst(129) and Fletcher *et al.*(130) for polycrystalline Cu. The galvanostatic curves were similar in appearance to those of Figure 20, but much thicker films were formed.

For an amalgam, 5 m*M* in Cu, Fletcher *et al.*(130) found that the surface became saturated at a coverage corresponding closely to a monolayer of the unit cell of Cu_2O. They suggest that the difference between the behavior of the polycrystalline Cu and the amalgam is due to the presence in the former system of "macroscopic (surface) features which persist through the unit cell layer" and act as sites for further three-dimensional growth of Cu_2O to much greater thickness.

6. Concluding Remarks

Mapping out the anodic behavior of metal and semiconducting electrodes presents an enormous task which has barely begun. Many topics have been omitted from this chapter, such as the influence of light absorption on anodic film formation.(3) It is hoped, however, that it might serve to focus attention on some of the elementary processes that combine to produce the overall kinetic and morphological results. Some of the techniques of surface science should prove helpful in this task, but there are fundamental difficulties here, since most of these require vacuum conditions. In the final analysis, there is no substitute for an experiment carefully designed to bring out a few features of the kinetic system, and suppress the others. To achieve this end, experiments must be designed with a model in mind, then modified as results are accumulated, a slow, but ultimately rewarding, process.

Auxiliary Notation

a	activation distance associated with the interior of an oxide film
a_E	constant in the Elovich equation
A	preexponential factor
b	activation distance for defect injection at an interface
b_E	a constant in the Elovich equation
B	constant of proportionality in the rate equation for ion current induced dielectric relaxation
c	dimensionless concentration, $=n/N$
d_2	dimensionless quadratic coefficient in the field expansion of the net activation energy, W
D	diffusion coefficient, electric displacement
e	charge on the proton
E	electric field strength
$\bar{E}$	mean field strength, $=(\eta-\eta_0)/X$
$\tilde{E}$	differential field strength, $=(\partial\eta/\partial X)_i$
f	a constant equal to $4\pi q^2 a/K$
g	dimensionless exponent of X in equation for high-field ionic transport
ΔH	enthalpy change
i	ionic current density
i_c	charging current density
i_d	current density associated with oxide dissolution
i_e	electronic current density
i_T	total faradaic current density, $=i+i_e$
I	total current density
J	atom or ion flux density
k	Boltzmann's constant
K	dielectric constant
K_I, K_{II}	rate constants in the direct logarithmic and inverse logarithmic equations
M	surface concentration of sites at an interface, either for defect injection or adsorption
n	volume concentration, index in Ritchie's equation
N	concentration of sites for mobile defects, or of sites for defect pair formation
p	dimensionless electrostatic potential, $=q\psi/kT$
pH_{pzc}	pH at the point of zero charge
P	dielectric polarization per unit volume
q	charge carried by the mobile ion; ionic charge passed, $=\int_0^t i\,dt$; amount of material adsorbed
q_T	total charge passed, $=\int_0^t I\,dt$
Q	activation energy for zero electrostatic field strength
R_f, R_r	rate of formation and recombination, respectively, of ionic defect pairs
s	dimensionless position coordinate
S	dimensionless film thickness
t	time
T	absolute temperature
v	speed of ionic species
$\bar{v}$	mobility of ionic species
V	electrode potential
W	net activation energy for a process involving ionic defects
x	position variable
X	film thickness
X_c	characteristic space charge length
X_r	characteristic length for defect recombination
z	oxidation number
α	dimensionless constant in the dimensionless form of Poisson's equation, $=4\pi q^2 a^2 N/KkT$
β	field coefficient
$\tilde{\beta}$	differential field coefficient

γ_{se}	dimensionless equilibrium parameter associated with the oxide–electrolyte transition layer
γ_L	dimensionless shape factor associated with local electrostatic fields
ε	dimensionless field strength, $= -\partial p/\partial s = qaE/kT$
η	overpotential
$\dot{\eta}$	$d\eta/dt$
η_0	portion of overpotential associated with one or more interfaces
$\bar{\mu}$	electrochemical potential
μ°	standard chemical potential
$\mu^\ddagger$	activation dipole for an ion transport process, $=\lvert qa\rvert$ or $\lvert qb\rvert$, etc.
ν	kinetic frequency factor
σ	capture cross section for recombination of defect pairs
σ_{se}	surface charge density at the oxide–electrolyte interface
Υ	constant with the dimensions of time appearing in the logarithmic rate equations
χ	electric susceptibility
Ω	volume per electrochemical equivalent weight of the oxide

Subscripts

aq	pertaining to the aqueous or electrolyte phase
d	associated with oxide dissolution
e	parameter having an empirical, rather than mechanistic, significance
f	associated with the formation of defect pairs
L	associated with a local electrostatic field
M	pertaining to the metal phase
OX	pertaining to the oxide phase
s	corresponding to the steady state or to saturation conditions
se, sm	pertaining to the oxide-electrolyte and metal–oxide interfaces, respectively
t	measured under transient conditions
0	evaluated at $x = 0 = s$, in X_0 and i_0, at $t = 0$

References

1. T. P. Hoar, The anodic behavior of metals, in *Modern Aspects of Electrochemistry*, Vol. 2, J. O'M. Bockris, ed., Academic Press, New York (1959).
2. U. R. Evans, *The Corrosion and Oxidation of Metals*, St. Martins, New York (1960).
3. L. Young, *Anodic Oxide Films*, Academic Press, New York (1961).
4. F. J. Burger and L. Young, Electrolytic capacitors, in *Progress in Dielectrics*, Vol. 5, Heywood, London (1962).
5. M. Fleischmann and H. R. T. Thirsk, Metal deposition and electrocrystallization, in *Advances in Electrochemistry and Electrochemical Engineering*, Vol. 3, P. Delahay and C. W. Tobias, eds., Interscience, New York (1963).
6. D. A. Vermilyea, Anodic films, in *Advances in Electrochemistry and Electrochemical Engineering*, Vol. 3, P. Delahay and C. W. Tobias, eds., Interscience, New York (1963).
7. N. G. Bardina, Anodic oxide films, *Russ. Chem. Rev.* **33**, 286 (1964).
8. T. P. Hoar, in *Encyclopedia of Electrochemistry*, C. A. Hampel, ed., Reinhold, New York (1964).
9. L. Young, W. S. Goruk, and F. G. R. Zobel, Ionic and electronic currents at high fields in anodic oxide films, in *Modern Aspects of Electrochemistry*, Vol. 4, J. O'M. Bockris, ed., Butterworths, London (1966).
10. J. W. Diggle, T. C. Downie, and C. W. Goulding, Anodic oxide films on aluminum, *Chem. Rev.* **69**, 365 (1969).
11. F. Fehlner and N. F. Mott, Low-temperature oxidation, *Oxid. Met.* **2**, 59 (1970).

12. C. J. Dell'Oca, D. J. Pulfrey, and L. Young, Anodic oxide films, in *Physics of Thin Films*, Vol. 6, Academic Press, London (1971).
13. U. R. Evans, Inhibition, passivity and resistance: a review of acceptable mechanisms, *Electrochim. Acta* **16**, 1825 (1971).
14. S. M. Ahmed, Electrocal double layer at metal oxide–solution interfaces, in *Oxides and Oxide Films*, Vol. 1, J. W. Diggle, ed., Marcel Dekker, New York (1973).
15. V. Brusic, Passivation phenomena, in *Oxides and Oxide Films*, Vol. 1, J. W. Diggle, ed., Marcel Dekker, New York (1973).
16. M. J. Dignam, Mechanisms of ionic transport through oxide films, in *Oxides and Oxide Films*, Vol. 1, J. W. Diggle, ed., Marcel Dekker, New York (1973).
17. A. K. Vijh, *Electrochemistry of Metals and Semiconductors*, Marcel Dekker, New York (1973).
18. G. C. Wood, Porous anodic films on aluminum, in *Oxides and Oxide Films*, Vol. 2, J. W. Diggle, ed., Marcel Dekker, New York (1974).
19. A. T. Fromhold, Jr., Space-charge effects on anodic film formation, in *Oxides and Oxide Films*, Vol. 3, J. W. Diggle and A. K. Vijh, eds., Marcel Dekker, New York (1976).
20. G. Belanger and A. K. Vijh, Anodic oxides on noble metals, in *Oxides and Oxide Films*, Vol. 5, A. K Vijh, ed., Marcel Dekker, New York (1977).
21. L. Young, *Trans. Faraday Soc.* **53**, 841 (1957).
22. M. R. Arora and R. Kelly, *J. Electrochem. Soc.* **124**, 1493 (1977).
23. J. L. Ord, D. J. DeSmet, and M. A. Hopper, *J. Electrochem. Soc.* **123**, 1352 (1976).
24. J. L. Ord, J. C. Clayton, and D. J. DeSmet, *J. Electrochem. Soc.* **124**, 1714 (1977).
25. G. C. Wood and A. J. Brock, *Nature* **209**, 773 (1966).
26. G. Parsons and G. C. Wood, *Corros. Sci.* **9**, 367 (1969).
27. G. C. Wood and S. W. Khoo, *J. Appl. Electrochem.* **1**, 189 (1971).
28. M. J. Dignam and P. J. Ryan, *Can. J. Chem.* **41**, 3108 (1963).
29. M. J. Dignam, unpublished data.
30. M. J. Dignam and D. Goad, *J. Electrochem. Soc.* **113**, 381 (1966).
31. D. J. Young and M. J. Dignam, *Oxid. Met.* **5**, 241 (1972).
32. N. Cabrera and N. F. Mott, *Rep. Prog. Phys.* **12**, 163 (1948).
33. D. J. Young and M. J. Dignam, *J. Phys. Chem. Solids*, **34**, 1235 (1973).
34. M. J. Dignam and R. K. Kalia, *Surface Sci.* **100**, 154 (1980).
35. M. J. Dignam, H. M. Barrett, and G. D. Nagy, *Can. J. Chem.* **47**, 4253 (1969).
36. M. J. Dignam, D. J. Young, and D. G. W. Goad, *J. Phys. Chem. Solids* **34**, 1227 (1973); M. J. Dignam, *Can. J. Chem.* **57**, 1329 (1979).
37. E. J. W. Verwey, *Physica (The Hague)* **2**, 1059 (1935).
38. J. F. Dewald, *J. Electrochem. Soc.* **102**, 1 (1955).
39. L. Young, *Can. J. Chem.* **37**, 276 (1959).
40. N. F. Mott and R. W. Gurney, *Electronic Processes in Ionic Crystals*, 2nd ed., Oxford University Press, London (1957).
41. C. P. Bean, J. C. Fisher, and D. A. Vermilyea, *Phys. Rev.* **101**, 551 (1956).
42. J. F. Dewald, *J. Phys. Chem. Solids* **2**, 55 (1957).
43. M. J. Dignam and D. F. Taylor, *Can. J. Chem.* **49**, 416 (1971).
44. M. J. Dignam, *J. Electrochem. Soc.* **126**, 2188 (1979).
45. L. Young, *Proc. R. Soc. (London) Ser. A* **258**, 496 (1960).
46. M. J. Dignam, *Can. J. Chem.* **42**, 1155 (1964).
47. L. Young, *J. Electrochem. Soc.* **110**, 589 (1963).
48. N. Ibl, *Electrochim. Acta* **14**, 1043 (1967).
49. M. J. Dignam and D. B. Gibbs, *J. Phys. Chem. Solids* **30**, 375 (1969).
50. J. L. Ord, M. A. Hopper, and W. P. Wang, *J. Electrochem. Soc.* **119**, 439 (1972).
51. J. C. Polanyi and J. L. Schreiber, in *Physical Chemistry, An Advanced Treatise*, Vol. VIA, *Kinetics of Gas Reactions*, W. Jost, ed., Academic Press, New York (1974).

52. G. W. Morey, *The Property of Glass*, Reinhold, New York (1954).
53. K. Otto, *Phys. Chem. Glasses* **7**, 29 (1966).
54. J. P. S. Pringle, *Electrochim. Acta* **25**, 1403, 1423 (1979).
55. M. J. Dignam, *J. Phys. Chem. Solids* **29**, 249 (1968).
56. A. R. Von Hippel, *Dielectrics and Waves*, Wiley, London (1954).
57. F. S. Stone, in *Chemistry of the Solid State*, W. E. Garner, ed., Butterworths, London (1955).
58. A. G. Ritchie, *J. Chem. Soc. Faraday Trans. 1* **10**, 1650 (1977).
59. S. M. Ahmed, in *Symposium on Oxide–Electrolyte Interfaces*, R. S. Alwitt, ed., The Electrochemical Society, Princeton, New Jersey (1973).
60. M. J. Dignam, *Can. J. Chem.* **56**, 595 (1978).
61. S. Levine and A. L. Smith, *Discuss. Faraday Soc.* **52**, 290 (1971).
62. L. Young, *Proc. R. Soc. London Ser. A* **244**, 41 (1958).
63. J. Siejka, J. P. Nadai, and G. Amsel, *J. Electrochem. Soc.* **118**, 727 (1971).
64. D. F. Taylor and M. J. Dignam, *J. Electrochem. Soc.* **120**, 1299 (1973).
65. D. A. Vermilyea, *J. Electrochem. Soc.* **103**, 690 (1956).
66. S. J. Basinska, J. J. Polling, and A. Charlesbry, *Acta Metall.* **2**, 313 (1954).
67. A. L. Bacerella and A. L. Sutton, *Electrochem. Technol.* **4**, 117 (1966).
68. D. A. Vermilyea, *Acta Metall.* **2**, 482 (1954).
69. P. H. G. Draper, *Electrochim. Acta* **8**, 847 (1963).
70. C. J. Dell'Oca and L. Young, *J. Electrochem. Soc.* **117**, 1545, 1548 (1970).
71. R. J. Maurer, *J. Chem. Phys.* **9**, 579 (1941).
72. J. J. Randall, W. J. Bernard, and R. R. Wilkinson, *Electrochim. Acta* **10**, 183 (1965).
73. G. Amsel and D. Samuel, *J. Phys. Chem. Solids* **23**, 1707 (1962).
74. J. P. S. Pringle, *J. Electrochem. Soc.* **120**, 1931 (1973).
75. J. P. S. Pringle, *Electrochemical Society, Extended Abstracts*, Vol. 78-1, Abstract No. 195, Seattle, Washington (May 1978).
76. J. A. Davies, J. P. S. Pringle, R. L. Graham, and F. Brown, *J. Electrochem. Soc.* **109**, 999 (1962); R. L. Graham, F. Brown, J. A. Davies, and J. P. S. Pringle, *Can. J. Chem.* **41**, 1686 (1963); J. A. Davies and B. Domeij, *J. Electrochem. Soc.* **110**, 85 (1963); J. A. Davies, B. Domeij, J. P. S. Pringle, and F. J. Brown, *J. Electrochem. Soc.* **112**, 675 (1965).
77. J. W. Whitton, *J. Electrochem. Soc.* **115**, 58 (1968).
78. J. Perriere, S. Rigo, and S. Siejka, *J. Electrochem. Soc.* **125**, 1549 (1978).
79. M. J. Dignam and P. J. Ryan, *Can. J. Chem.* **46**, 535 (1968).
80. D. G. W. Goad and M. J. Dignam, *Can. J. Chem.* **50**, 3250 (1972).
81. D. A. Vermilyea, *J. Electrochem. Soc.* **104**, 427 (1957).
82. L. Young, *Proc. R. Soc. (London)* **A263**, 395 (1961).
83. L. Masing and L. Young, *Can. J. Chem.* **40**, 903 (1962).
84. M. J. Dignam and P. J. Ryan, *Can. J. Chem.* **46**, 549 (1968).
85. D. F. Taylor and M. J. Dignam, *J. Electrochem. Soc.* **120**, 1306 (1973).
86. J. L. Ord and J. H. Bartlett, *J. Electrochem. Soc.* **112**, 160 (1965).
87. J. L. Ord, *J. Electrochem. Soc.* **113**, 213 (1966).
88. J. L. Ord and D. J. DeSmet, *J. Electrochem. Soc.* **113**, 1876 (1966); **116**, 762 (1969); **123**, 1876 (1976).
89. D. J. DeSmet and M. A. Hopper, *J. Electrochem. Soc.* **116**, 1184 (1969).
90. B. H. Ellis, M. A. Hopper, and D. J. DeSmet, *J. Electrochem. Soc.* **118**, 860 (1971).
91. M. A. Hopper, T. A. Wright, and D. J. DeSmet, *J. Electrochem. Soc.* **124**, 44 (1977).
92. J. L. Ord and F. C. Ho, *J. Electrochem. Soc.* **118**, 46 (1971).
93. J. L. Ord, J. C. Clayton, and K. Brudzewski, *J. Electrochem. Soc.* **125**(6), 908 (1978).
94. J. L. Ord, J. C. Clayton, and W. P. Wang, *J. Electrochem. Soc.* **124**, 1671 (1977).
95. L. Young and P. J. Smith, *J. Electrochem. Soc.* **126**, 1972 (1979).
96. L. Young, *Can. J. Chem.* **50**, 574 (1972).
97. L. Young and D. J. Smith, *J. Electrochem. Soc.* **126**, 765 (1979).

98. H. J. de Wit, C. Wijenberg, and C. Crevecoeur, *J. Electrochem. Soc.* **126**, 779 (1979).
99. M. J. Dignam and D. F. Taylor, *Can. J. Chem.* **48**, 1971 (1970); D. F. Taylor and M. J. Dignam, *J. Electrochem. Soc.* **120**, 1306 (1973).
100. G. Schwartz, *J. Phys. Chem.* **71**, 4021 (1967).
101. M. J. Dignam, *J. Electrochem. Soc.* **109**, 184 (1962).
102. L. Young, *J. Electrochem. Soc.* **111**, 1289 (1964).
103. C. Crevecoeur and H. J. de Wit, *J. Electrochem. Soc.* **121**, 1465 (1974).
104. J. P. O'Sullivan and G. C. Wood, *Proc. R. Soc. London Ser. A* **317**, 511 (1970).
105. C. J. Dell'Oca and P. J. Fleming, *J. Electrochem. Soc.* **123**, 1487 (1976).
106. A. Dekker and A. Middelhoek, *J. Electrochem. Soc.* **117**, 440 (1970).
107. D. B. Gibbs, B. Rao, R. A. Griffin, and M. J. Dignam, *J. Electrochem. Soc.* **122**, 1167 (1975).
108. J. A. McMillan, *Chem. Rev.* **62**, 65 (1962).
109. J. A. Allen, in *Proceedings of the First Australian Conference on Electrochemistry*, Pergamon, London (1965).
110. K. J. Vetter, *Electrochemical Kinetics*, Academic Press, New York, (1967), pp. 317–325.
111. L. L. Bircumshaw and A. C. Reddiford, *Quart. Rev.* (*London*) **6**, 157 (1952).
112. W. J. Dunning, in *Chemistry of the Solid State*, W. E. Garner, ed., Butterworths, London (1955).
113. J. W. Mitchell, in *Chemistry of the Solid State*, W. E. Garner, ed., Butterworths, London (1955).
114. G. T. Wright, *Solid State Electron.* **2**, 165 (1961).
115. R. G. Barradas and G. H. Fraser, *Can. J. Chem.* **42**, 2488 (1964).
116. H. Angerstein-Kozlowska, B. E. Conway, and W. B. A. Sharp, *J. Electroanal. Chem.* **43**, 9 (1973).
117. T. Biegler, *Aust. J. Chem.* **26**, 2571 (1973).
118. M. D. Goldstein, T. I. Zalkind, and V. I. Veselovskii, *Elektrokhim.* **10**, 1533 (1974).
119. B. V. Tilak, B. E. Conway, and H. Angerstein-Kozlowska, *J. Electronanal. Chem.* **48**, 1 (1973).
120. K. J. Vetter and J. W. Schultze, *J. Electroanal. Chem.* **34**, 131 (1972).
121. D. Gilroy and B. E. Conway, *Can. J. Chem.* **46**, 875 (1968).
122. K. J. Vetter and J. W. Schultze, *J. Electroanal. Chem.* **34**, 141 (1972).
123. W. Visscher and M. A. V. Devanathan, *J. Electroanal. Chem.* **8**, 127 (1964).
124. T. Biegler, D. A. J. Rand, and R. Woods, *J. Electroanal. Chem.* **29**, 269 (1971).
125. J. Balej and O. Spalek, *Collect. Czecho. Chem. Commun.* **47**, 499 (1972).
126. T. P. Hoare, *The Electrochemistry of Oxygen*, Interscience, New York (1968).
127. P. W. Jacobs and F. C. Tompkins, in *Chemistry of the Solid State*, W. E. Garner, eds., Butterworths, London (1955).
128. M. J. Dignam and D. B. Gibbs, *Can. J. Chem.* **48**, 1242 (1970).
129. V. Ashworth and D. Fairhurst, *J. Electrochem. Soc.* **124**, 506 (1977).
130. S. Fletcher, R. G. Barradas, and J. D. Porter, *J. Electrochem. Soc.* **125**, 1960 (1978).

6

Corrosion Inhibition

R. N. PARKINS

1. Introduction

Changes in the composition of otherwise corrosive environments to reduce or prevent the corrosion of metals and alloys is widely practiced and has resulted in an extensive literature that will not be reviewed here. The inhibition of corrosion by chemical control of the environment is frequently defined in electrochemical terms,(1) since corrosion itself is a combination of at least two electrochemical electrode reactions, involving, respectively, electron sinks at which metal dissolution occurs and electron source areas at which an electronation reaction, such as the deposition of hydrogen, occurs. It follows that if the velocities of either or both of these electrode reactions, or any of the partial steps which they may involve, can be reduced, then some degree of inhibition of the corrosion will ensue. Such a simple definition of inhibition is preferable to a chemical one, in which substances that prevent the corrosion of a particular metal are defined in terms of their chemical constitution. Thus the species that promotes inhibition may be generated *in situ*, as opposed to being added to the environment from an external source, and moreover some of those substances which may be regarded as chemical inhibitors of a particular form of corrosion may indeed stimulate other forms. For example, those carbonates, hydroxides, nitrates, phosphates, etc. that are used to prevent the general corrosion of mild steels in some circumstances can themselves promote the stress corrosion of

---

R. N. PARKINS • Department of Metallurgy and Engineering Materials, The University, Newcastle upon Tyne, England.

such steels. While then an electrochemically based definition of inhibition involving velocity reductions of the constitutive reactions is preferable, there are circumstances in which such a definition is somewhat deficient. Localized forms of corrosion (pitting, intergranular corrosion, stress corrosion, corrosion fatigue) by their very nature are frequently more objectionable in service situations than is general corrosion, in which a similar amount of metal dissolution is more widely dispersed over the exposed surfaces. Localized forms of corrosion involve a number of critically balanced features including, of course, the relative areas and sites for the dissolution reactions on the one hand and those for the electronation reactions on the other. While it is the case that reductions in the velocities of these reactions will promote inhibition to some degree, it is also the case that stimulation of corrosion can sometimes inhibit localized corrosion. Thus the intergranular stress corrosion cracking of mild steels in hot nitrate solutions can be inhibited by the addition of sufficient chloride to the solution, with an attendant change in the amount and distribution of dissolution. While it is preferable therefore to consider inhibition in electrochemical terms, it should be remembered that there are special circumstances in which stimulation can inhibit certain forms of corrosion, as well as a reduction in the velocities of any or all of the partial reactions.

2. Polarization Curves and Inhibition

A convenient graphical representation of the electrode reactions involved in corrosion is provided by polarization curves, upon which the influence of inhibitors can be interpreted. If either or both of the principal electrode reactions is inhibited, for whatever reasons, then this will be manifest as a reduction in the exchange current density, a decrease in the effective area of the electrode, or an increase in the Tafel slope for the reaction. Consequently the dissolution current density will be decreased and there may be attendant changes in the corrosion potential. Figure 1 shows the polarization curves, A and C, for the anodic and cathodic reactions, respectively, involved in the corrosion of a metal where the corrosion current density and potential are given by the point of intersection (1). If the dissolution reaction is inhibited, e.g., by the formation of a passivating oxide film at the anodes, then the polarization curve will move to A_I, with the point of intersection upon the E–I curve for the electronation reaction now at (2) and associated with a rise in potential and a decrease in current density. Alternatively, if the electronation reaction is inhibited, the cathodic polarization curve is moved to C_I, with the attendant reductions in potential and current density indicated by the point of intersection (3). The opposite directions in which the potential moves upon inhibiting the anodic and cathodic reactions is sometimes used for distinguishing the actions of inhibitors as anodic or cathodic according to which reaction they principally influence. However, there are substances that influence both

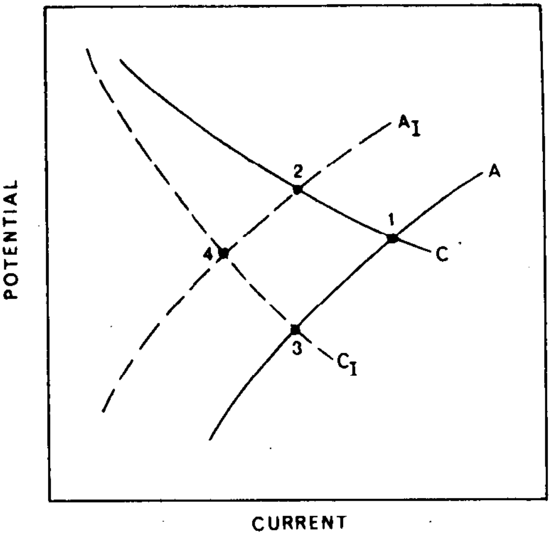

Figure 1. Anodic and cathodic polarization curves with (A_I, C_I) and without (A, C) inhibitor present.

reactions, usually by adsorption over the metal surface generally, possibly after initially reacting preferentially at electron sink or electron source areas, and such adsorption inhibitors may cause the potential to move in either direction or not at all, as represented by the point of intersection (4) for curves A_I and C_I in Figure 1.

3. The Inhibition of General Corrosion

The classification of inhibitors as anodic, cathodic, or adsorption types has some systematic merit, and will be followed here, even though the specific function of a particular substance is not always clear or agreed. Much detailed information, both of a practical nature and concerned with mechanisms of inhibition, will be found in the volumes associated with the quinquennial conferences on inhibition held at the University of Ferrara.(2)

Anodic inhibitors form sparingly soluble salts at electron sink areas to form adherent barriers that isolate the underlying metal. The films formed are frequently sufficiently thin to be invisible to the naked eye *in situ*, and they are often oxides, hydrated or not, although any other substance that has the necessary filming characteristics can be equally effective. The facts that many anodic inhibitors promote the formation of oxide films, and some are only effective if oxygen is present in the solution, may suggest that the effectiveness of anodic inhibition is related to the oxidizing power of the inhibitor, but this does not appear to be the case. Thus, while chromates and nitrites are very effective inhibitors of the general corrosion or iron, nitrates are less effective, while sulfates, chlorates and permanganates, for example, have little, if any, inhibitive action. Moreover, while chromates and nitrites are effective inhibitors in the absence of oxygen, other substances, such as benzoates, borates, carbonates, and silicates, all of which contain oxygen, are only effective in the presence of dissolved oxygen, and the latter itself can either stimulate or inhibit corrosion depending upon its concentration.

The fact that inhibitive action is not always monotonically dependent upon concentration is a matter of considerable practical importance in the use of anodic inhibitors, which may, at certain concentrations, stimulate certain forms of corrosion and has caused them to be classed as dangerous or unsafe. Figure 2 shows the effects of various anodic inhibitors at different concentrations on the corrosion of iron, from which it is apparent that carbonate, phosphate and silicate additions actually increase the corrosion rate at concentrations below those necessary for complete inhibition.(3) Possibly of even greater practical significance is the fact that, with some anodic inhibitors when present in insufficient amount, the distribution of the attack may be altered from one involving general corrosion to pitting. These effects may be understood when it is realized that in near-neutral solutions the corrosion rate of iron is effectively controlled by the electronation reaction. Thus with insufficient inhibitor, say, nitrite, present, the cathodic reduction process according to

$$NO_2^- + 8H^+ + 6e^- = NH_4^+ + 2H_2O \tag{1}$$

results in too low a current density to exceed the critical value (i_{crit}) for the

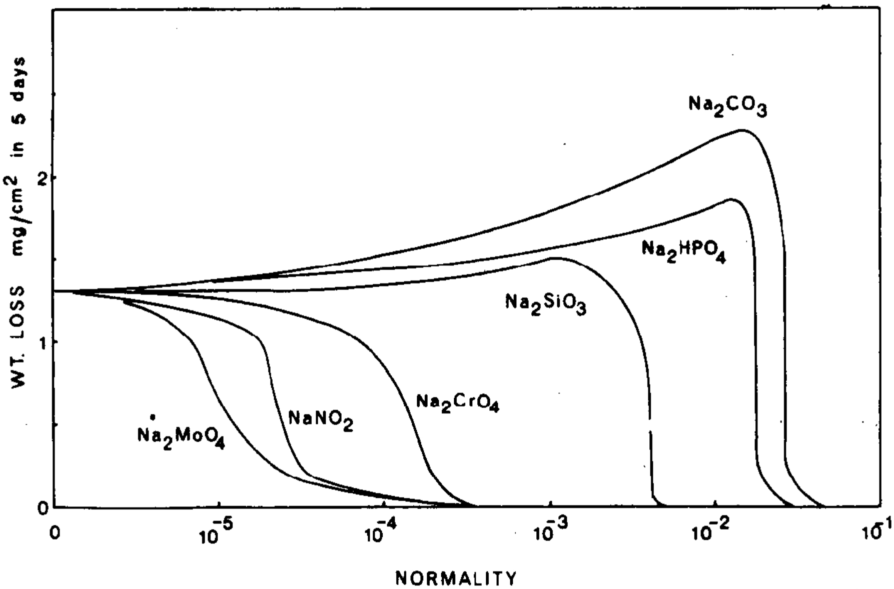

Figure 2. Effects of concentration of different inhibitors on the corrosion of iron.(3)

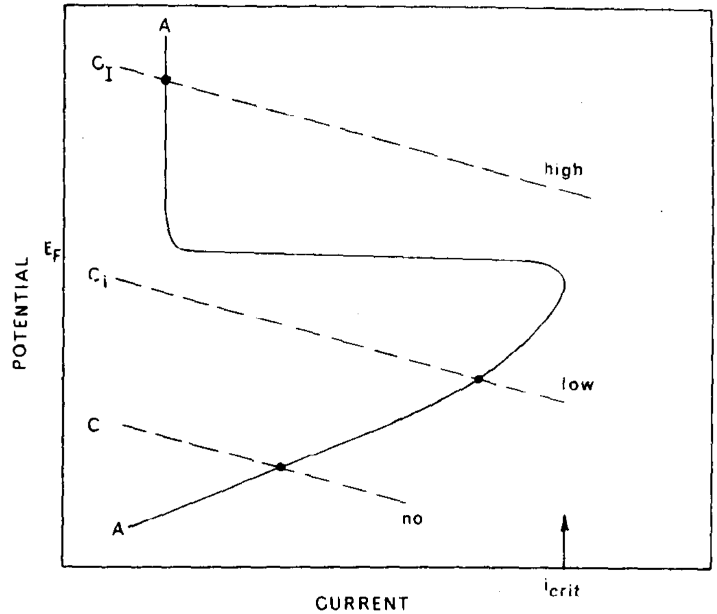

Figure 3. Schematic polarization curves at different inhibitor concentrations.

formation of a passivating film, with the result that the corrosion current density is increased even though the potential may rise, as indicated by the shift in the cathodic polarization curve from C to C_i in Figure 3. However, at higher inhibitor concentrations the limiting current density for the electronation reaction exceeds i_{crit} and a passivating film forms at E_F with an associated small current density and negligible corrosion rate at the potential where the curve C_I intersects that for the electron sink reaction represented by curve A. Now, if the initial concentration of anodic inhibitor is sufficient to cause filming at some, but not all, of the electron sink sites the intensity of the attack upon the remaining active sites will increase and pitting, rather than general, corrosion will result.

The localization of corrosion in the presence of insufficient anodic inhibitor is not restricted to pitting in a widely disseminated form, since intense attack is sometimes observed just below a stagnant water line or partially immersed surfaces in the absence of an adequate amount of inhibitor, without corrosion being visible over the remainder of the immersed surfaces. The explanation(4) of this effect appears to be related to the liquid in the meniscus acting as a trap in which the corrosion has tendencies toward autocatalysis but replenishment of inhibitor is restricted, with the result that the prevention of water line attack requires considerably higher concentrations of inhibitor for its prevention than does the prevention of corrosion at immersed surfaces below the meniscus.

Not all inhibitors that promote a rise in potential, and may therefore be classed as anodic inhibitors, promote dangerous localized corrosion if added in insufficient amount to prevent corrosion completely. Thus benzoate, silicate, and orthophosphate ions are not dangerous in that the attack with which they are associated at inadequate concentrations remains widespread. Such action appears to be due to these inhibitors not restricting their activities to electron sink sites, which may be so in the earlier stages of immersion, but later they spread their sphere of influence to electron source areas providing more general coverage of the exposed surfaces and so avoiding the dangerous combination of large cathodic and small anodic areas that result in localized attack. The safe action of these inhibitors has resulted in their use in combination with other inhibitors which, singly, may be dangerous but in combination reduce the risk of pitting. Indeed the use of two or more inhibitors together, a subject returned to later, is becoming increasingly practiced since, for reasons not always understood, the effect of using a combination of inhibitors is frequently greater than the sum of their separate effects, implying synergistic influences.

Cathodic inhibitors restrict the electronation reaction either by interfering with the hydrogen discharge reaction or by influencing the reduction of oxygen. In acid solutions, many metals evolve hydrogen gas by a two-stage reaction in which

$$H^+ + e^- = H(ads) \tag{2}$$

and

$$H^+ + H(ads) + e^- = H_2(gas) \tag{3}$$

The former is usually controlling, but the latter reaction can be influenced by the presence of the group V elements, P, As, and Sb, which can effectively prevent the formation of hydrogen molecules according to

$$AsO^+ + 2H(ads) + e^- = As + H_2O \tag{4}$$

or

$$As_2O_3 + 6H(ads) = 2As + 3H_2O \tag{5}$$

There is, however, some danger in using such an approach as a method of corrosion prevention in that the adsorbed hydrogen atoms that are prevented from escaping as a gas may diffuse into the metal lattice promoting a sensitivity towards cracking, if the metal is stressed, a point returned to later. There is no equivalent problem if the electronation reaction involves the reduction of oxygen according to

$$O_2 + 4H^+ + 4e^- = 2H_2O \tag{6}$$

or

$$O_2 + 2H_2O + 4e^- = 4OH^- \tag{7}$$

which more commonly occurs in near-neutral solutions. The control of these reactions involves restricting the access of oxygen to the metal surface, either by its removal from the system by reaction with, for example, hydrazine according to

$$2N_2H_4 + 5O_2 = 4NO_2^- + 4H^+ + 2H_2O \tag{8}$$

or by the precipitation of films that slow oxygen diffusion. Such cathodic inhibitors usually form films that are visible, gel-like, and less adherent and compact than those formed by anodic inhibitors, by comparison with which, at equivalent concentrations, they are much less efficient. For example, 10^{-1} N $ZnSO_4$ will reduce the corrosion of iron by about 80%, compared to virtually complete inhibition by 10^{-3} N Na_2CrO_4. Since the functioning of cathodic inhibitors involves their interaction at electron source areas they are usually positively charged ions, transported to cathodic sites where they adsorb or react with the products of the electronation reaction to form a precipitate. Salts of zinc and nickel, with sparingly soluble hydroxides, for example, are typical cathodic inhibitors, although polyphosphates, promoting the formation of colloidal particles of polymerized PO_3^-, are increasingly used, and the bicarbonate ion provides another example of a negatively charged cathodic inhibitor. Such anionic species acting as cathodic inhibitors arises because of secondary reactions, a mechanism that probably is also involved with certain mixed inhibitors in which organic cations stabilize adsorbed anionic layers.

The indecisiveness of some anionic species in not simply acting as anodic inhibitors, or of cationic not necessarily acting as cathodic inhibitors, has been mentioned already in the context of benzoate, silicate, and orthophosphate ions providing more general coverage of the exposed surfaces than would be required if their function was simply to inhibit the reactions at electron sink areas. Such duality of function is most marked in the third general group of inhibitors, those frequently classed as adsorption inhibitors. These are frequently organic substances, based upon amines, quinolines, or thioureas, for example, that can effectively exist as charged species, especially in acid solutions in which they are used as restrainers to inhibit partially attack upon exposed metal after scales have been removed by reaction with the acid. The effectiveness of such inhibitors may be expected to relate to the extents to which they adsorb and cover the metal surface and the influence that they exert on the anodic or cathodic reactions, or both. Some or all of these effects may be expected to be capable of relation to the chemistry or structure of the inhibitor and much effort has been expended in attempting to systematize this particular aspect of corrosion inhibition, arguably to an extent that is barely justified by the practical importance of the inhibition of acid corrosion.

The coverage, θ, of an electrode surface by an adsorbed inhibitor is frequently expressed in terms of the corrosion rates with, k_i, and without, k_0, the inhibitor present as

$$\theta = 1 - \frac{k_i}{k_0} \tag{9}$$

Not surprisingly, the coverage is observed to depend upon the concentration of inhibitor present, frequently according to the isotherm due to Frumkin,

$$\frac{\theta}{1-\theta}\exp(f\theta) = Kc \tag{10}$$

where c is the concentration of inhibitor, K is the equilibrium content for the adsorption reaction, and f is a parameter related to the variation of adsorption energy with θ. Figure 4 shows results due to Hoar and Holliday(5) for the corrosion of mild steel in sulfuric acid inhibited by quinolines or thioureas, indicating not only the effects of inhibitor concentration but also the marked variation in inhibitor efficiency at a particular concentration. The results of Hoar and Holliday also indicate that the concentration of inhibitor influences its function in the sense that the shift in potential can vary with inhibitor concentration. Figure 5 shows some of their results which suggest that quinolines are essentially anodic inhibitors, while the thioureas inhibit cathodically at low concentrations acquiring anodic tendencies as the concentration increases. West(6) has provided results confirming the tendency of a quinoline to adsorb preferentially at electron sink sites initially but for some cathodic coverage to

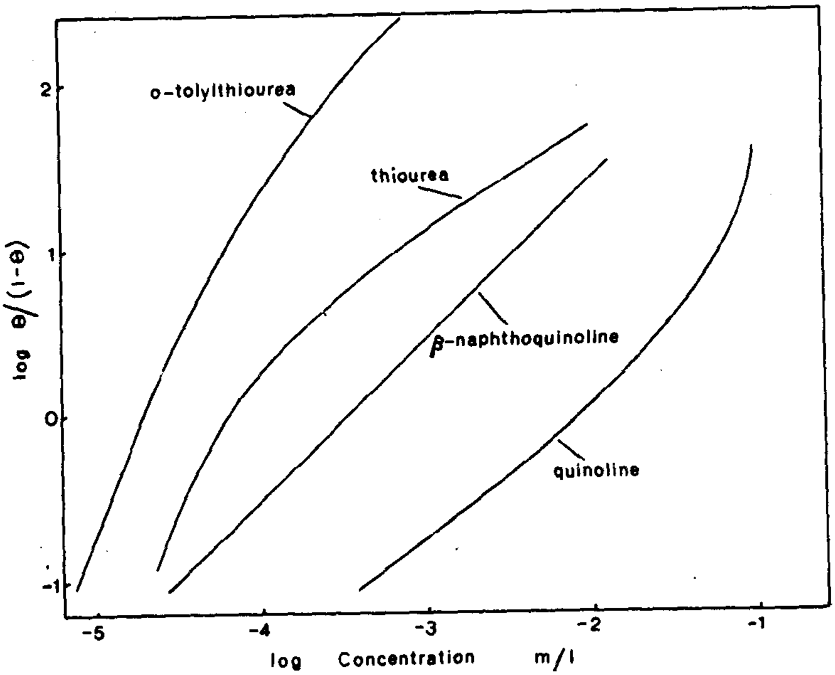

Figure 4. Relationship between degree of inhibition of mild steel, θ, and inhibitor concentration in 5% H_2SO_4 at 70°C.(5)

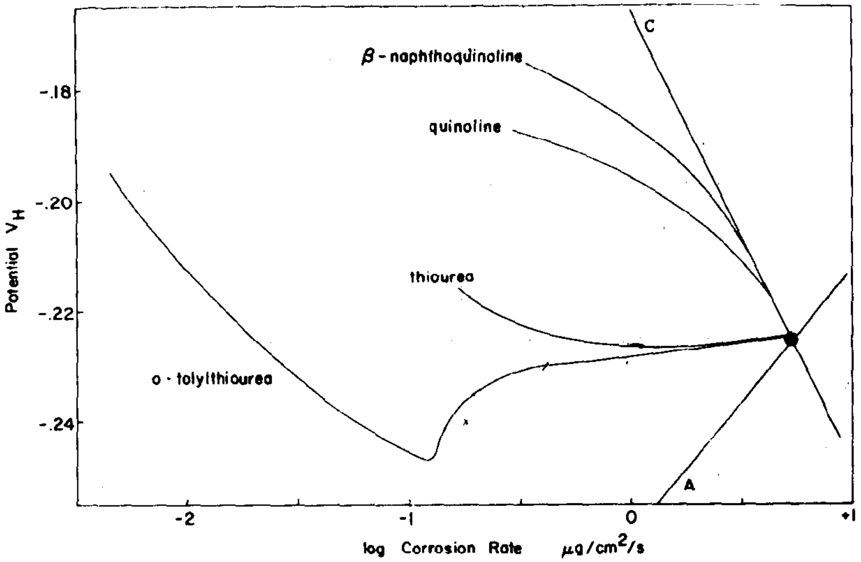

Figure 5. Relationship between corrosion potential and corrosion rate of mild steel in 5% H_2SO_4 at 70°C in the presence of various inhibitors.(5)

arise at higher inhibitor concentrations, although the relative coverage at anodic and cathodic sites by tolylthiourea added to sulfuric acid in which mild steel is immersed shows little difference until the inhibitor concentration exceeds about 0.1 m*M*, as is apparent from Figure 6. The reasons for such duality of function of some adsorption inhibitors continues to be debated, but the fact that certain molecules can influence both the anodic and cathodic reactions is beyond dispute.

The simultaneous use of a mixture of two or more inhibitors is frequently, but not always, based upon combining a cathodic with an anodic inhibitor. Thus organic substances or zinc salts are often mixed with chromates, phosphates, nitrites, or silicates, with results that are better than the sum of the separate effects of the inhibitors involved. Chromate–phosphate mixtures have provided an attractive alternative to chromate alone since the early work of Palmer(7) showed that the mixture did not suffer from the disadvantage of chromate alone, that when present in insufficient amount, pitting resulted. The reason for the safe behavior of the chromate–phosphate mixture is thought to be related to the effect of the phosphate in preventing the formation of blisterlike membranes over electron sink sites, which, if formed, prevent access of inhibitor to the underlying metal. The orthophosphates used originally have now largely been replaced by polyphosphates, which make the mixture even more effective at lower concentrations, while further improvement may be obtained by the addition of small (1–2 ppm) of zinc. The latter is also used, with calcium additions as an alternative, in combination with the polyphosphates prepared by the thermal dehydration of sodium dihydrogen phosphate and referred to as sodium hexametaphosphate or metaphosphate glass, which combinations are particularly effective in inhibiting the corrosion of mild steel in concentrated chloride solutions, moving or stagnant.(8) The dramatic effect of calcium additions to metaphosphate glass in inhibiting the corrosion of mild steel in chloride-containing solutions is shown in Figure 7, which indicates that about 100 ppm of metaphosphate, in unstirred solutions (~10 ppm in stirred solutions), is sufficient to inhibit effectively corrosion if sufficient calcium is present for the chloride content of the solution involved. Potential measurements indicate that the metaphosphate alone acts essentially as an anodic inhibitor, but in the presence of divalent metal ions its function is effectively that of a cathodic inhibitor. The mixed inhibitor therefore has the advantage of being safe at concentrations inadequate for complete protection,

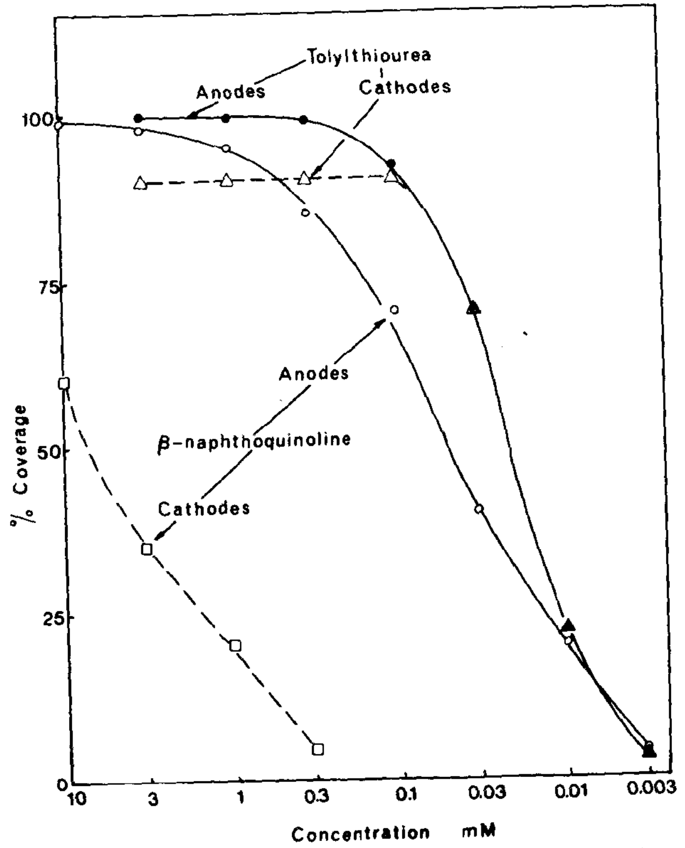

Figure 6. Coverage of anodes and cathodes on mild steel in 5% H_2SO_4 at 70°C for different inhibitors at various concentrations.(6)

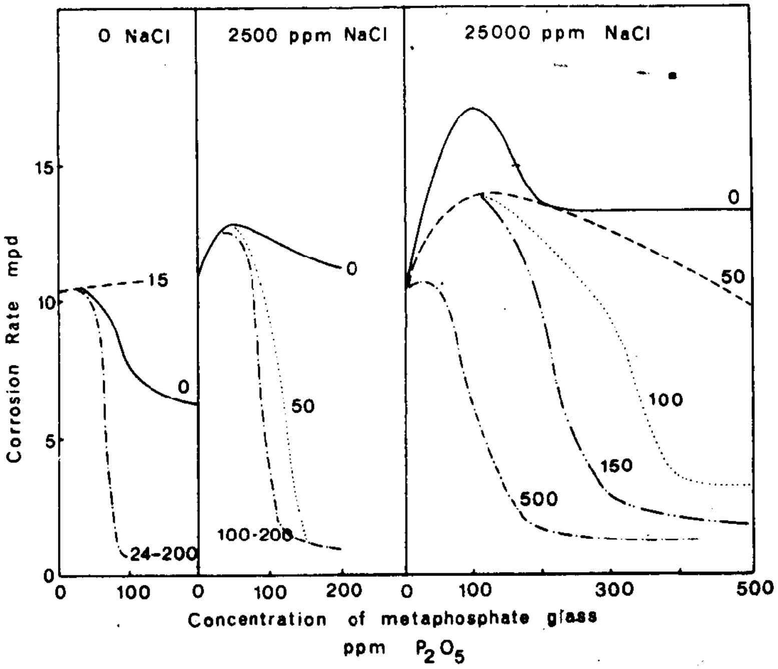

Figure 7. Influence of concentration of metaphosphate glass and calcium on the corrosion of mild steel in water and chloride solutions.(8) (The numbers appended to the curves indicate the calcium concentrations in ppm.)

with the further advantage over chromate-containing mixtures that there are no toxicity problems, so much so that it can be used in the treatment of drinking water.

4. Mechanisms of the Inhibition of General Corrosion

Attempts to systematize corrosion inhibition into a unified mechanism have not met with success, a result that is hardly surprising in view of the multitude of variables involved in the inhibition of the corrosion of different metals and alloys in various environments by diverse substances. It is usual in attempting to rationalize inhibitive actions to consider separately those situations in which the metal surface is essentially oxide free, usually associated with acidic environments, and those in which the surface is virtually covered, by oxides, hydroxides, or other salts, and which usually occur in near-neutral environments. Introduction of the pH of the environment into this distinction also introduces an additional difference in that, while the reactions at electron sink areas may be the same in acidic and neutral solutions, the electronation reactions may be very different, usually involving hydrogen reduction in acidic and oxygen reduction in neutral solutions.

In the absence of any preexisting surface film, it is clear that an inhibitor can only function if it is first adsorbed onto the metal surface, thereafter influencing the anodic or cathodic, or both, reactions. The factors that influence the adsorption of inhibitive ions on metal surfaces(9) are (a) the surface charge on the metal, (b) the functional group and structure of the inhibitor, and (c) interactions involving adsorbed inhibitor species. The charge on a metal surface may be expressed with respect to the zero charge potential (electrocapillary maximum), so that if the metal is more negative than the latter it will have negative charge and will attract positive ions, whereas at higher potentials than the zero charge potential it will attract anions. Thus iodoethylquinoline, which inhibits the dissolution of iron in acids, is no longer effective if an oxidizing agent, such as a ferric salt or chromic acid, is present. In the presence of the oxidizing agent the potential of the iron is shifted in the positive direction and adsorption of the iodoethylquinoline, an additive of the cationic type, may become small or negligible.

Apart from such electrostatic attraction, many of the organic inhibitors used in restraining acid corrosion are bonded to the metal surface by electron transfer. The S-type compounds, such as the thioureas, bond more strongly than the N- or O-type substances, because of their electronegativity, so that they adsorb more generally, interfering with both the anodic and cathodic reactions, the former by separation of the solvating water molecules from the metal surface and the latter by preventing the interaction of hydrogen atoms to form molecules. As an example of the dependence of inhibiting propensity upon electronic structure varied according to the substituent, the work of Szklarska-Smialowskà and Kaminski(10) may be cited. They studied the corrosion of mild steel in 1 N H_2SO_4 with additions of thiophene and its derivatives, observing the normalized corrosion rate to be dependent upon the constant σ in Hammett's equation

$$\log \frac{i_0}{i_R} = \rho\sigma \qquad (11)$$

where i_0 is the corrosion rate in the presence of thiophene without substituent, i_R is the corrosion rate in the presence of a substituted thiophene, ρ is the reaction constant, and σ is a measure of the polar properties of the substituent. It is apparent from Figure 8 that the substitution of a hydrogen atom by either the nucleophylic substituents 2-CH_2OH, 2-CH_3, or 3-CH_3 ($\sigma < 0$), or by the electrophylic substituents 2-Cl, 2-COOH, 3-Br, 2-$COCH_3$, 2-CHO, or 2-$COOCH_3$ ($\sigma > 0$), increases the efficiency of inhibition over that provided by thiophene itself, a poor inhibitor, by an amount that is simply proportional to σ. These and similar results by other workers studying different systems are consistent with the increased inhibition deriving from greater adsorption due to increasing strength of coordinate bonding via easier electron transfer.

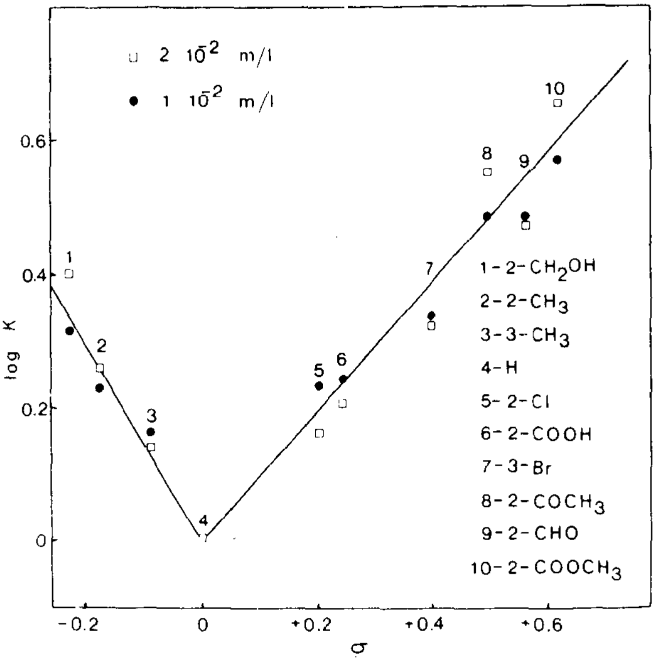

Figure 8. Log $K(=i_0/i_R)$ as a function of Hammett's constant, σ. (i_0 is the corrosion rate in the presence of thiophene and i_R is the corrosion rate in the presence of a substituted thiophene.)(10)

Adsorbed species may enter into various interactions on the surface of an electrode that may significantly influence their inhibitive propensities and the mechanism of their action. Hoar and Khera(11) have considered the significance of lateral interactions between adsorbed species which, in general terms, may be attractive or repulsive, leading to greater or lesser adsorption and hence a change in inhibitive efficiency, such interactions explaining some of the synergistic effects observed with mixed inhibitors. With some inhibitors secondary reactions after adsorption may produce products that are either more or less efficient inhibitors than the primary adsorbant. For example, Trabanelli *et al.*(12) have shown that if dibenzylsulfoxide is reduced to dibenzylsulfide there is an improvement in inhibitive efficiency. The size of the adsorbed molecule is to be expected to exert a significant effect in inhibition if for no other reason than that the extent of surface coverage may vary with the size, and orientation, but molecule size also enters into the displacement reaction involving the removal of water molecules from the electrode surface. Thus Szklarska-Smialowska and Wieczorek(13) have shown that the coefficient f in Eq. (10) changes systematically with chain length, as is apparent from Figure 9, which shows the increased efficiency of amines in inhibiting the corrosion of mild steel in 1 N H_2SO_4 as the chain length is increased.

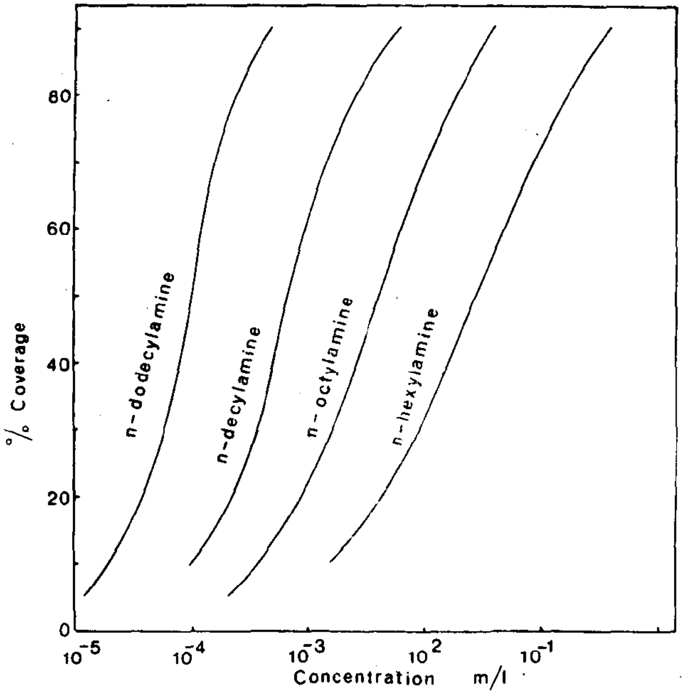

Figure 9. Adsorption isotherms for various aliphatic amines on mild steel in 1 *N* H_2SO_4 at 25°C.[13]

Once the inhibitor has been adsorbed it may influence the corrosion rate through one or more of a number of mechanisms, involving the adsorbed species in either an active role, through their influence upon the electrode reactions, or a passive role, in which they provide a physical barrier separating the reactants that would otherwise promote corrosion. Antropov[14] has provided a useful summary on these matters but it will suffice here to indicate that either the adsorbed ions may enter the electrical double layer, displacing the potential and hence influencing the electrochemical reactions, or the corrosion reactions that occur in the absence of the inhibitor, involving the formation of intermediate products, may be modified by the presence of the inhibitor, which will usually be apparent as a change in the Tafel slope for either or both of the constituent reactions. Where the role of the adsorbed species is physical rather than electrochemical such changes in the electrochemical parameters are not observed. Thus if the adsorption simply results in the blocking of the electron sink or source areas then the extent of the latter available for entering into the reactions is decreased and the average rates of the reactions are reduced in proportion. A somewhat similar response is obtained if the adsorbed inhibitor restricts diffusion of species to or from the metal surface, although such films, usually associated with very large molecules, can promote concentration or polarization resistance.

In near-neutral solutions, where the controlling reaction is usually oxygen reduction, the commoner metals can be induced to acquire a film of insoluble material that inhibits reaction at either anodic or cathodic sites. The mechanism whereby cathodic inhibitors function is simply that of providing a barrier to oxygen diffusion to the metal surface, the films themselves also usually being such poor electronic conductors that they are incapable of promoting oxygen reduction at the film–solution interface. On the other hand, anodic inhibitors, which react preferentially at electron sink sites, usually promote the formation of oxide films and discussion continues on certain aspects of mechanistic detail as to the important step in the formation of these passivating films. The commoner metals will usually have an air-formed oxide film upon their surfaces before exposure to any aqueous environment and the extent to which the latter is aggressive or inhibitive will depend upon the extent to which this initial film is impaired by reaction with the constituents of the solution. Where the initial film is stable but contains defects, the latter will need to be plugged or repaired with insoluble, diffusion-limiting, resistive films if inhibition is to be achieved, with similar protective filming requirements if there is no initial film present or the film is modified upon initial contact with the environment. The conditions under which such passivating films form are reasonably well established, but controversy surrounds the extent to which the film must thicken before it provides protection.

Figure 3 shows, for those systems to which such anodic polarization behavior is relevant, that the current density suddenly falls to a relatively low value when the potential exceeds E_F, an event achieved in the presence of sufficient anodic inhibitor. In essence there are two schools of thought as to the nature of the barrier that limits the current to such low values in the passive state. One is that it is no more than a chemisorbed layer, of monomolecular or lesser thickness, of O^{2-} or other inhibiting anions that may be preferentially adsorbed at the most reactive sites so that the exchange current density is markedly reduced. Such passivating films are so thin that they can have little effect upon diffusion processes, whereas in the alternative model the latter are limited by the presence of a relatively thick film, perhaps 1 or 2 orders thicker than the monolayer of the adsorption model. It is reasonable to assume that the formation of a relatively thick passivating film will be preceded by a layer of monomolecular dimensions, but the controversy hinges upon the stage in this growth process at which the current density falls to low values, which is the essence of passivity. There is little doubt that films of appreciable thickness exist on passive surfaces, as has been shown by a variety of techniques, and the protagonists of the thin-film hypothesis accept that, in time, a chemisorbed layer will react with the underlying metal to form detectable oxides or other substances. However, the thickness of this long-term film decreases as its potential of formation decreases towards the Flade potential, E_F, so that the observation of relatively thick films is not an unequivocal demonstration that they are the cause of the sudden fall in current at E_F. It is probable that both viewpoints are correct in the sense that for some combinations of metal and environment passivation requires the formation of only a monolayer, while in other systems current restriction is only observed when a visible film is present. Indeed it appears highly improbable that there is a single mechanism of inhibition that will explain all of the effects of different anions, with the influences of concentrations of those ions as well as of oxygen, hydrogen ions, and aggressive ions, upon the behavior of various metals. However, this does not prevent the examination of working hypotheses which are valuable from a practical viewpoint and may be typified by the inhibitive action of different anions upon iron.

Thomas and Nurse(15) have shown that the critical passivation potential for iron, E_p, varies with pH in the range 6–12 according to

$$E_{p(H)} = +0.09-0.06\ \text{pH} \qquad (12)$$

which is only slightly more positive than the potentials for oxide-forming reactions on iron. Thus, for γ-Fe_2O_3, the oxide frequently detected as present on iron in passive conditions, forming according to

$$2\text{Fe} + 3\text{H}_2\text{O} = \gamma\text{-Fe}_2\text{O}_3 + 6\text{H}^+ + 6e^- \qquad (13)$$

the potential dependence is given by

$$E_0 = -0.01-0.059\ \text{pH} \qquad (14)$$

which indicates an overpotential of about 0.1 V to initiate the passive filming process. Moreover, the critical current densities for the passivation of iron in deaerated 0.1 *M* solutions of the various anions studied increases in the order: nitrite < hydroxide < chromate < borate < hydrogen phosphate < carbonate < benzoate < bicarbonate < nitrate, which is also the order of the inhibitive efficiency and aggressiveness towards mild steel of these anions. There is in such data therefore a reasonable working hypothesis in the sense that electrochemical measurements can predict the protection potential and the efficiency of the anion in promoting passivity, yet the detailed mechanisms whereby such protection is achieved is not necessarily the same for all of these anions. For example, there is significant evidence that chromate and phosphate enter into reactions whereby they are incorporated into the passivating film, either by adsorption, by ion exchange, or simply by plugging pores in the air-formed oxide film, depending upon the solution composition, yet it appears unlikely that nitrites, for example, behave similarly. Here it is likely that the nitrite facilitates oxide formation, either by reduction to NO or by the removal of the nitrogen as NH_3. In other cases the inhibitive ion may have a buffering action, preventing a reduction in pH at pores, facilitating the precipitation of insoluble compounds, or by suppressing the adsorption of aggressive ions. However, irrespective of the details of mechanism or solution requirements for effective anodic inhibition, there is the common factor that the potential must be above that for the formation and stabilization of an insoluble film, usually of one of the oxides of the metal concerned.

5. Inhibition of Localized Corrosion

The localized forms of corrosion (e.g., pitting, crevice corrosion, selective attack, erosion, fretting, corrosion fatigue, stress corrosion cracking) are frequently more damaging in their influence upon the engineering function of structures than is general corrosion and in that sense their prevention is more important. The incidence of pitting as the result of inadequate concentrations of anodic inhibitors has already been remarked upon, although the occurrence of pitting is not confined to situations in which anodic inhibitors are incorrectly applied, since the mechanism of pitting essentially involves achieving potentials in those borderline regions between generally active and passive behavior. Indeed the latter is the essence of most localized forms of corrosion, that they only occur within restricted ranges of potential in which much of the exposed surface remains relatively inactive, while activity is restricted to localized regions. The latter may result from the local breakdown of passivity by chemical or electrochemical variations over the surface, as with pitting or crevice corrosion, by mechanical disruption of otherwise protective films, as with erosion, fretting, corrosion fatigue, or stress corrosion, or because of chemical heterogeneity in the alloy, as with intergranular corrosion. Because of the importance of physical and metallurgical factors in the incidence of some of these forms of corrosion they may sometimes best be avoided by changes in alloy composition or the adoption of appropriate engineering design features, but as with all forms of corrosion they are capable of electrochemical control, including the use of inhibitors. However, while modification of environments to prevent localized forms of corrosion can show obvious similarities with the approaches to preventing general corrosion, e.g., some of the most effective inhibitors for the latter are also effective in preventing certain localized forms of corrosion, there are some important differences to be recognized. The point is illustrated by a reminder that some of the environments that cause stress corrosion cracking of low-strength steels, namely, hydroxides, carbonates, and nitrites, are indeed all anodic inhibitors of the general corrosion of such steels, and that the thioureas that may restrain the attack by acids upon high-strength steels can induce hydrogen pickup by the latter and their failure by hydrogen embrittlement. Moreover, since localized forms of corrosion usually involve a critical balance between activity and inactivity, the disturbance of this balance in either direction may inhibit the localized form of corrosion, although additions to the environment that increase activity will promote a more general distribution of attack in limiting the localized dissolution.

In general, the concentrations of inhibitors required to prevent localized forms of corrosion are higher than those required to inhibit general corrosion, although there are exceptions as with most generalized statements. Pitting that results from an inadequate supply of anodic inhibitor obviously can be remedied by an increase in inhibitor concentration, and the not infrequent observation of corrosion in crevices in inhibited solutions that are effective in preventing corrosion of readily accessible surfaces on the same structure is another example of inadequate supply of inhibitor. That the inhibitor concentration required to prevent pitting, as with general corrosion, also needs to reflect the concentration of aggressive ions present in solution is shown clearly by the results due to Kaesche(16) indicated in Figure 10. The lower pitting potential for aluminum with increased chloride concentration of the solution obviously requires markedly higher chromate concentrations for its remedy. Where the breakdown of otherwise passive films is due to mechanical disruption, as in erosion or corrosion fatigue, relatively high concentrations of inhibitor may be necessary to maintain the passive film in good repair. This is clear from the work of Gould and Evans(17) upon the corrosion fatigue of drawn mild steel wires in KCl solutions with and without K_2CrO_4 additions. Electrode potential measurements, with and without cyclic stress applied to the specimens in various solution compositions, showed relatively sudden falls in potential at certain times, indicating breakdown of a protective film. Figure 11 shows that the lifetime of the film before breakdown increases with increasing chromate concentration, but the concentration to inhibit breakdown increases with the application of stress. That these effects are related to the lifetime of the film is apparent from Figure 12, which shows the decreased lifetime with increasing stress for a given chloride content of the solution.

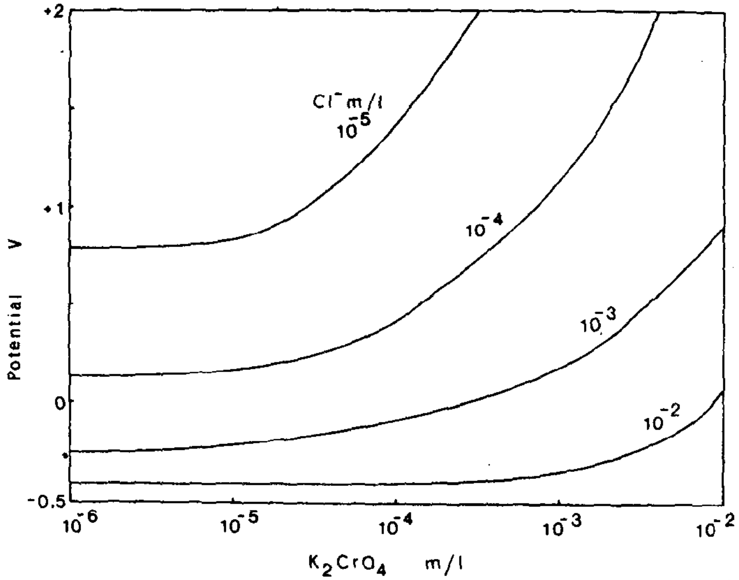

Figure 10. Dependence of the potentiokinetic breakthrough potential of aluminum on the chloride and chromate concentrations of the solution.(10)

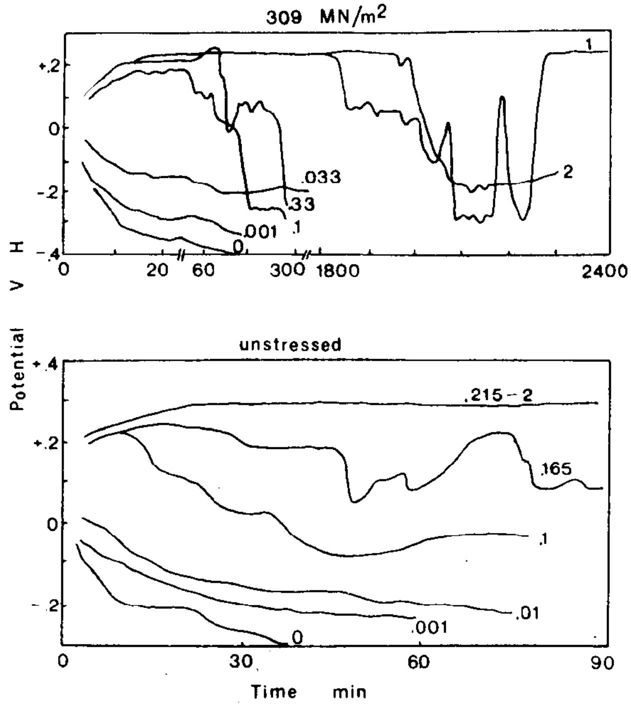

Figure 11. Potential–time curves for stressed and unstressed C–Mn steel in 0.1 *M* KCl with the additions of the molar concentrations of K_2CrO_4 shown appended to the curves.[17]

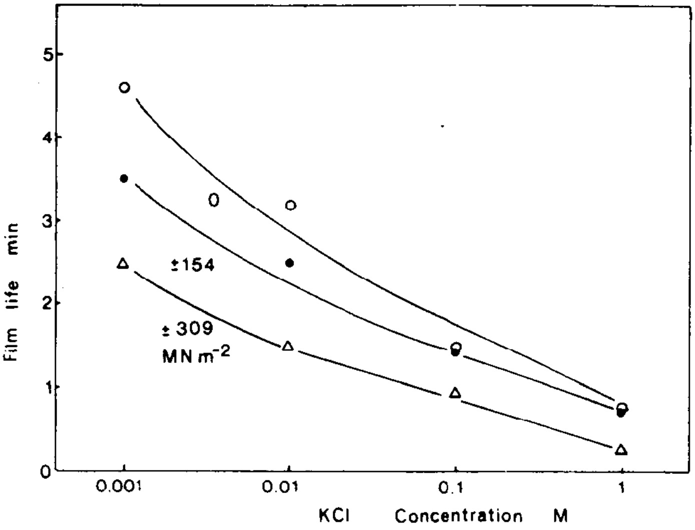

Figure 12. Influence of KCl concentration on the film life for a C–Mn steel at different stresses.[17]

It is clear from Figures 11 and 12 that the effects of increasing chromate additions to chloride solutions in inhibiting corrosion fatigue of mild steel may be due to either the increase in potential or the rate of film repair, or both. This raises important points of principle and practicality since in the latter respect particularly it raises the question as to whether inhibitors would be better chosen on the one or the other basis. That there can be quite separate effects associated with additions that change the potential or disturb the critical balance between activity and inactivity in localized corrosion processes can be illustrated by examples of inhibitive additions in the stress corrosion cracking of low-strength steels. That the latter fail in such a manner only in restricted ranges of potential, the limits of which depend upon the solution involved, is now well established. Clearly if an addition to a potent environment moves the free corrosion potential from within to without the critical potential range, cracking will be inhibited. However, those substances that prevent cracking simply by causing the rest potential to move outside the critical range may not always be "safe" inhibitors from the practical viewpoint, since other agencies that cause the potential to remain within the cracking range can promote cracking even in the presence of such additions. Thus, while raising the initial pH of nitrate solutions above a value of about 7 inhibits the cracking of mild steels at the rest potential, steels tested in even more alkaline conditions can be caused to fracture by stress corrosion quite readily if the potential is held within the cracking range. A more practical example concerns the maintenance of a $Na_2SO_4/NaOH$ ratio in excess of 2.5 in boiler waters as a means of preventing caustic cracking in boilers, a technique that is still widely practiced despite the statistical evidence that no benefit is derived. That Na_2SO_4 may cause the rest potential to fall outside the cracking range for mild steel in hydroxide solutions can be demonstrated, but if the potential is held within the cracking range then the Na_2SO_4 is without effect upon cracking susceptibility. The use of Na_2SO_4, and of $NaNO_3$ which is also sometimes used, in relation to caustic cracking in boilers should be regarded as unsafe practice, but there are some substances which may be regarded as safe in that they inhibit cracking within the range of potentials that promotes cracking in the absence of the inhibitor.

That Na_2CrO_4 additions to a $Na_2CO_3 + NaHCO_3$ solution will effectively inhibit the intergranular stress corrosion cracking that this solution produces in mild steels is apparent from Figure 13, in that the crack velocity is reduced to negligible values in the presence of Na_2CrO_4 at potentials within the normal cracking range. That this effect is due to a change in the balance between the active and passive behavior that characterize cracking conditions is readily demonstrated with the aid of current decay measurements. The rate at which the anodic current density decreases upon an initially bare metal surface can be correlated with the crack propensity,(18) since if the rate of decay is relatively slow, indicating the maintenance of active conditions, pitting is likely, while a very rapid rate of decay will prevent significant dissolution and the metal behaves in a passive manner. Between these extremes, i.e., at intermediate

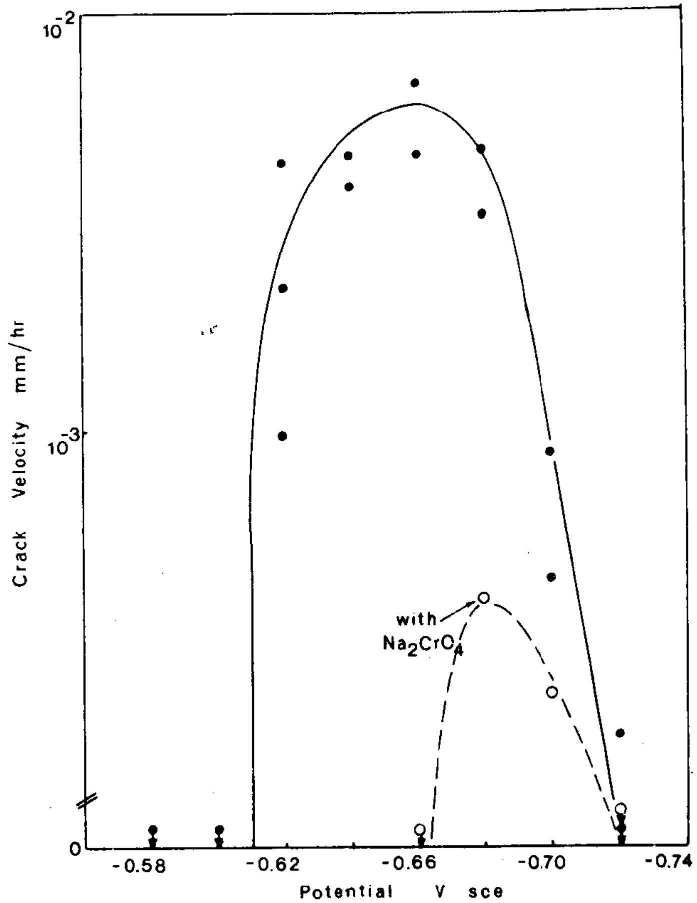

Figure 13. Stress corrosion crack velocities for C–Mn steel in 1 *N* Na_2CO_3, 1 *N* $NaHCO_3$ with and without 1% Na_2CrO_4 addition at 75°C.(19)

rates of current decay, the balance between active and inactive behavior will realize the conditions for cracking. Figure 14 shows the effect of adding 1% Na_2CrO_4 to a Na_2CO_3 + $NaHCO_3$ solution after some initial decay has occurred and clearly indicates the almost instantaneous passivation that results.

The disturbances of the critical balance between activity and inactivity that promotes cracking may not only be by the addition of inactivating substances, since an increase in activity may also disturb the balance and prevent cracking, although the latter will then be replaced by a more general form of corrosion. This happens when chloride additions in sufficient amount are made to boiling nitrate solutions, stress corrosion cracking of mild steel then being inhibited but general corrosion occurring. The cracking of Mg–Al alloys in CrO_4–Cl solutions provides a further example in that stress corrosion is most marked at

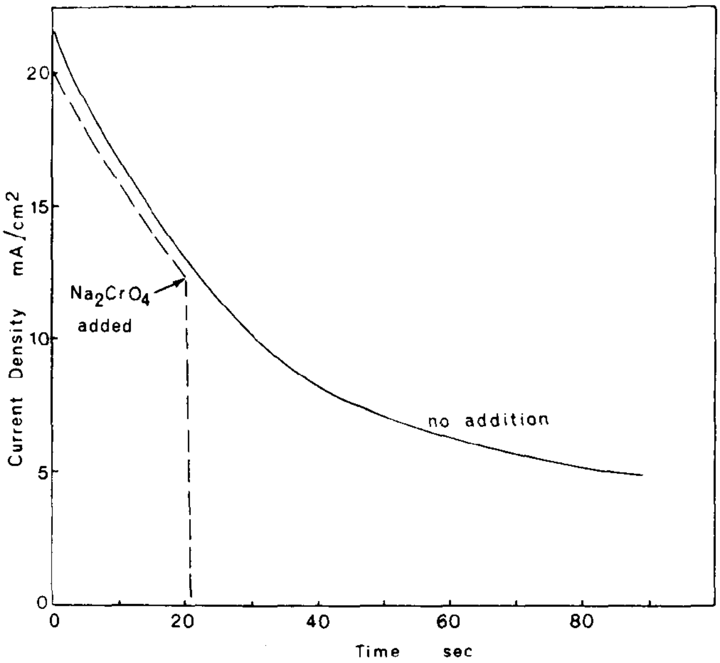

Figure 14. Current decay curve for C-Mn steel in 1 *N* Na_2CO_3 + 1 *N* $NaHCO_3$ at 75°C and effect of adding 1% Na_2CrO_4 after time shown.(19)

intermediate chromate concentrations for a given chloride content with decrease of the chromate promoting more general attack and increase of chromate producing passive behavior. This latter result raises an important point of principle in relation to the use of inhibitors in preventing environment sensitive fracture. This is that, for a given cracking environment, it is quite conceivable that intermediate amounts of inhibitor may promote cracking by facilitating the establishment of even more critical conditions than those that exist in the environment without addition, i.e., the most severe cracking conditions are not necessarily those observed with an unadulterated solution. As in the avoidance of pitting when using anodic inhibitors, the need for ensuring an adequate supply of inhibitor in avoiding environment sensitive fracture is paramount.

When localized corrosion is structurally dependent, as with intergranular corrosion or intergranular stress corrosion, the concept of solution specificity applies in that such modes of attack are markedly dependent upon solution composition. The fact that the local cell actions that are associated with these modes of failure are solution dependent implies that some inhibitive substances may be effective because they inhibit local galvanic effects, while possibly not influencing the macroscopic electrochemical behavior. Certainly there is evidence that structurally dependent attack, as with the etching of metals to reveal their microstructures, is not invariable irrespective of the electrochemical or solution conditions. Although such structurally dependent forms of corrosion have their origins in metallurgical inhomogeneity, and may therefore be avoided by modification of the structure of the alloy concerned, there is evidence that some inhibitors added to potent environments operate by disturbing the local cell action, as with NaH_2PO_4 additions to Na_2CO_3 + $NaHCO_3$ solutions in inhibiting the intergranular stress corrosion of mild steels.(19)

The effects of poisons, such as sulfur and its compounds, in facilitating the ingress of hydrogen into steels whereby the hydrogen embrittlement of the latter is enhanced is well known. It may be expected that substances which facilitate the discharge of atomic hydrogen before the latter can enter the metal will have the opposite effect, i.e., the cracking resistance will be increased. Thus the addition of chloroplatinic acid or anthraquinone in small amounts to a 0.6 *N* NaCl solution increase the cracking resistance of an 18% maraging steel over that observed in the absence of such additions.(20) The chloroplatinic acid addition results in the deposition upon the steel surface of finely divided platinum, upon which hydrogen discharge occurs, while the anthraquinone is adsorbed upon the steel surface, its quinoid component then being reduced by the hydrogen in preference to the latter entering the metal. In many instances of the failure of high-strength steels by hydrogen ingress into the metal it is probable that the cracking is initiated at and facilitated by a geometrical discontinuity, in the form of a pit, precrack, or other defect, the potential and pH conditions within which may be different from those at external surfaces and in the bulk solutions. The pH changes in particular within the crack are an important adjunct to the mechanism of cracking, so that if the pH changes are prevented, by buffer action, cracking also should be prevented. Brown(21) has shown that when sodium acetate was added to a chloride solution the cracking resistance of a high-strength steel was markedly improved as compared to that observed with the unbuffered solution.

6. Conclusions

Control of the composition of environments to avoid or retard corrosion of metals is widely practiced, involving either the removal of aggressive species from the environment or the addition of substances to the latter to counter the effects of the aggressive species. The latter is the field of inhibitors which, in general, function by promoting the formation of protective films, although in the inhibition of some of the localized forms of corrosion, involving selective attack upon structural features in the metal or cracking under nominally static or cyclic loads, inhibitors may function by other mechanisms. The details of the latter, including those involved in general corrosion, are not always fully understood, but sufficient is known, of both theory and practice, for inhibitors to be widely and effectively used. Nevertheless, there are needs for more efficient or less toxic inhibitors to be developed and the use of mixtures of inhibitors, with their possible synergistic effects, is likely to be one of the more profitable avenues for exploration in this context. Their limitations extend to their use only in closed systems where the volume of environment to be treated is not too extensive, but the incorporation of inhibitors into correctly designed coating systems can sometimes overcome this problem. Other developments, recent and continuing and not the concern of the present chapter, involve the treatment of gaseous environments to reduce corrosion, as with vapor phase inhibitors in relation to atmospheric corrosion and the use of additives to control high-temperature oxidation. In all of these areas of continuing work, improved understanding of the mechanistic aspects of inhibition is likely to result in the more rapid and efficient development of new inhibitors than the ad hoc approach that has sometimes characterized earlier work.

References

1. H. Fischer, Definition and modes of inhibition of electrochemical electrode reactions, in Proceedings of the 3rd European Symposium on Corrosion Inhibitors, Ferrara, Italy, 1970, pp. 15–21.
2. Proceedings of the 1st, 2nd, 3rd, 4th, and 5th European Symposia on Corrosion Inhibitors, Ferrara, Italy, 1960, 1965, 1970, 1975, 1980.
3. M. J. Pryor and M. Cohen, The inhibition of the corrosion of iron by some anodic inhibitors, *J. Electrochem. Soc.*, **100**, 203–215 (1973).
4. A. M. Peers and U. R. Evans, Passivity of metals, XII—Intense attack at the waterline of otherwise passive metal, *J. Chem. Soc.*, 1093–1102, 1953, Pt. II.
5. T. P. Hoar and R. D. Holliday, The inhibition by quinolines and thioureas of the acid dissolution of mild steel, *J. Appl. Chem.* **3**, 502–513 (1953).
6. J. M. West, Inhibition by organic compounds of the acid dissolution of mild steel. II. Distribution of quinolines and thioureas at the metal-acid interface, *J. Appl. Chem.* **10**, 250–256 (1960).
7. W. G. Palmer, Corrosion inhibitors for steel, *J. Iron Steel Inst.* **163**, 421–431 (1949).
8. G. Butler, Corrosion inhibition by metaphosphate glass, in Proceedings of the 3rd European Symposium on Corrosion Inhibitors, Ferrara, Italy, 1970, pp. 753–773.
9. J. G. N. Thomas, in *Mechanism of Corrosion Prevention by Inhibitors, Corrosion*, Vol. 2, L. L. Shreir, ed., Newnes-Butterworth, London (1976), pp. 18.34–18.56.
10. Z. Szklarska-Smialowska and M. Kaminski, Effect of various substitutes in thiophene on the inhibitor efficiency, in Proceedings of the 5th International Congress on Metallic Corrosion, Tokyo, Japan, Extended Abstracts, 1972, pp. 217 and 218.
11. T. P. Hoar and R. P. Khera, The inhibition by formaldehyde, pyridine, polyamines, alkanolamines and octylamines of the acid dissolution of mild steel, in Proceeding of the 1st European Symposium on Corrosion Inhibitors, Ferrara, Italy, 1960, pp. 73–93.
12. G. Trabanelli, G. L. Zucchini, F. Zucchi, and V. Carassiti, Inhibitive action of dibenzylsulphoide and dibenzylsulphide, *Brit. Corros. J.* **4**, 267–270, 1969.
13. Z. Szklarska-Smialowska and G. Wieczorek, Adsorption isotherms on mild steel in sulphuric acid solution for primary aliphatic compounds differing in length of the chain, in Proceedings of the 3rd European Symposium on Corrosion Inhibitors, Ferrara, Italy, 1970, pp. 453–470.
14. L. I. Antropov, A correlation between kinetics of corrosion and the mechanism of inhibition by organic compounds, *Corros. Sci.* **7**, 607–620 (1967).

15. J. G. N. Thomas and T. J. Nurse, The anodic passivation of iron in solutions of inhibitive ions, *Brit. Corros. J.* **2**, 13–20 (1967).
16. H. Kaesche, Pitting corrosion of aluminium and intergrannular corrosion of aluminium alloys, in Proceedings of the Conference on Localized Corrosion, NACE, Houston (1973), pp. 516–525.
17. A. J. Gould and U. R. Evans, A scientific study of corrosion fatigue. Preliminary report on experiments at Cambridge university, Second Report of the Alloy Steels Research Committee, Iron and Steel Institute, Special Report No. 24, 1939, pp. 325–342.
18. R. N. Parkins, Environmental aspects of stress corrosion cracking in low strength ferritic steels, in *Proceedings of the International Conference on Stress Corrosion Cracking and Hydrogen Embrittlement of Iron Base Alloys, Firminy, France*, NACE, Houston (1977).
19. R. N. Parkins, Inhibition of structurally-dependent localised corrosion processes, in Proceedings of the 4th European Symposium on Corrosion Inhibitors, Ferrara, Italy, 1975, pp. 595–614.
20. R. N. Parkins and I. H. Craig, Environment sensitive crack growth by dissolution and hydrogen adsorption, in *Proceedings of the Conference on Mechanics of Environment Sensitive Cracking*, Metals Society, London (1977).
21. B. F. Brown, Stress corrosion cracking of higher strength steels, in *The Theory of Stress Corrosion Cracking in Alloys*, NATO, Brussels (1971), pp. 186–204.

7

Stress Corrosion Cracking

GENADY P. CHEREPANOV

1. Introduction

"Environment–construction" systems are comparable to biological and economic systems in their complexity. Indeed, let us try to classify the processes occurring in such systems. The main factors which may prove to be decisive for the optimal projecting of a certain construction should naturally be divided into three groups: material properties, technological factors, and operational factors.

Material properties include:

- (i) chemical composition of the material, including weight-insignificant admixtures, alloying additives, etc.;
- (ii) chemical and corrosion resistance of the material;
- (iii) physical properties of the material (primarily elasticity, strength, plasticity, fracture toughness, density, material structure, thermal conductivity, electric resistance, thermal resistance, etc.).

Technological factors include:

- (i) mechanical processing (rolling, cutting, drilling, forging, punching, etc.);
- (ii) thermal processing, welding, etc.;
- (iii) surface processing, coating, protective varnishing, etc.;

GENADY P. CHEREPANOV • Tomilino (Moscow Region), 140070, USSR.

(iv) internal structural stresses, embrittled zones, structural changes, hydrogenation, and other possible aftereffects of technological operations.

Operational factors include:

(i) the shape and the dimensions of the construction;
(ii) time of operation;
(iii) the parameters of external load, its changing in time and space;
(iv) chemical composition of the environment with possible inclusion of weight-insignificant admixtures;
(v) physical properties of the environment (temperature, pressure, density, presence of radiation and electric fields, etc.).

Stress corrosion plays an important part among the branches of science which deal with the problem being discussed. This phenomenon lies at the union of chemistry, physics, and mechanics; all the factors mentioned above are essential for it. Therefore just 15 years ago it had a purely descriptive character, and a philateliclike collection of empirical qualitative data was its main aim. As to quantitative data, they did not agree even in seemingly identical experiments.

In recent years considerable progress has been achieved in the development of quantitative methods. This progress is linked, first of all, with applying methods of fracture mechanics and theoretical electrochemistry. The experiments with the precracked specimens helped to achieve far more precise description of corrosion cracking than before. At the same time these experiments stressed the fact that stress corrosion is primarily a chemical problem: even a slight change of the chemical composition of the material or the environment may lead to considerable (and sometimes, catastrophic) effects. It should be acknowledged that the progress mentioned, which demanded considerable sums for more precise experiments, was stimulated, generally, by extensive military projects with further application and development of high-strength materials.

Stress corrosion cracking of metals is dealt with in voluminous literature. Suffice it to mention the review monograph by Logan,(1) the books by N. D. Tomashov,(2) G. V. Akimov,(3) Fontana and Greene,(4) Hoar,(5) G. P. Cherepanov,(6) reviews by Johnson and Paris,(7) Brown,(8) Johnson,(9) Uhlig,(10) V. A. Marichev,(11) G. P. Cherepanov,(12) Parkins, Mazza, Royuela, and Scully,(13) Wei,(14) the collected works edited by Staehle, Brown, Kruger, and Agrawal,(15) the atlas by Pourbaix(16) of potential–pH diagrams for various metals and alloys in aqueous solutions, and the book by V. V. Romanov.(17)

Purely empirical data pertaining to the nature and mechanisms of corrosion cracking are of particular and often contradictory character. Only mathematical models of cracking processes allow one to unify different points of view and to determine their significance for concrete conditions. The nature and mechanisms of pit and crack growth can be understood only by means of

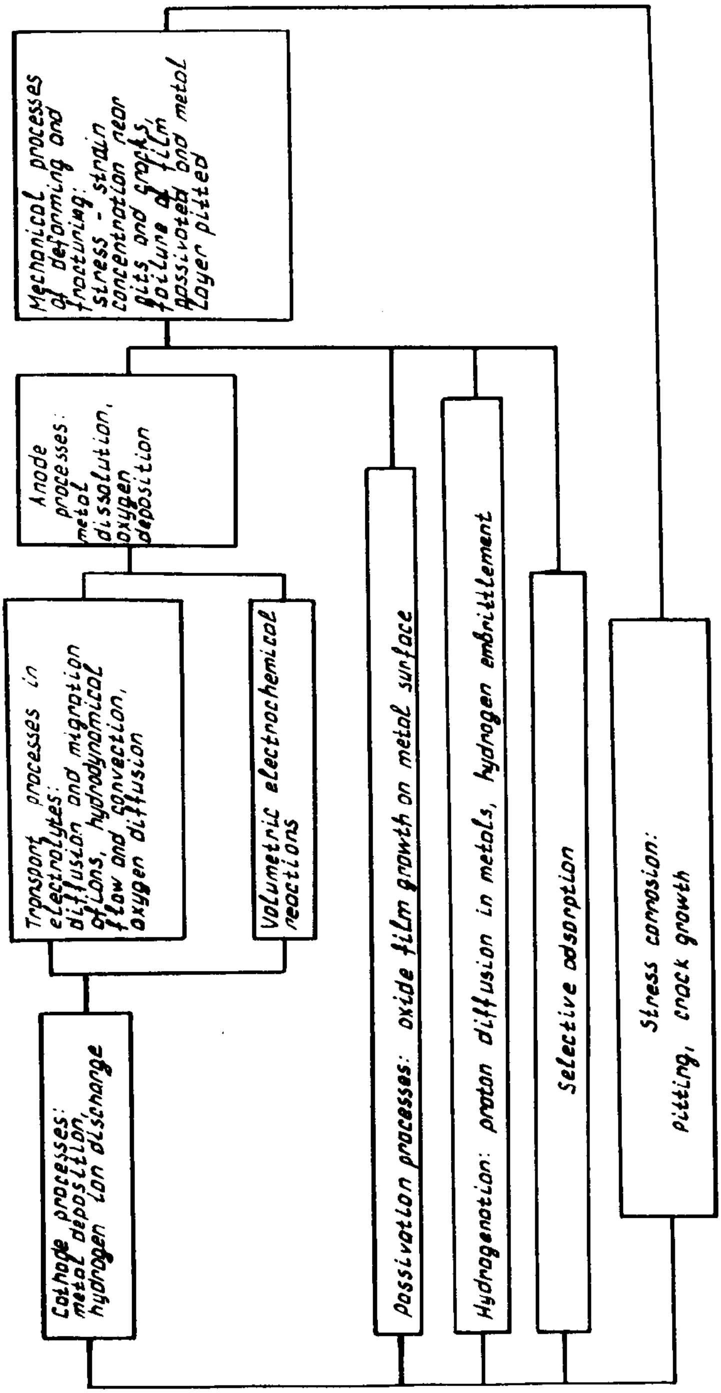
Mechanical processes of deforming and fracturing: stress - strain concentration near pits and cracks; failure of film passivated and metal layer pitted
Anode processes: metal dissolution, oxygen deposition
Transport processes in electrolytes: diffusion and migration of ions, hydrodynamical flow and convection, oxygen diffusion
Volumetric electrochemical reactions
Cathode processes: metal deposition, hydrogen ion discharge
Passivation processes: oxide film growth on metal surface
Hydrogenation: proton diffusion in metals, hydrogen embrittlement
Selective adsorption
Stress corrosion: pitting, crack growth

Figure 1. The logical block diagram of the main physicochemical processes leading to pit and crack growth in metals.

mathematical models of the phenomenon. This point of view has recently won recognition of corrosion experts.

In this chapter we deal with the principal problems of the mathematical modeling of stress corrosion cracking, while concrete information is used only to the extent necessary for construction and verification of the theory. The growth of pits (Section 2) and cracks (Sections 3–5) are considered. The logical block diagram of the main physicochemical processes proceeding in time successively or simultaneously in causing pit and crack growth in metals is presented in Figure 1. It is evident that the rate of the resulting process is governed by the rate of the slowest particular process (at the successive development of processes) and by the rate of the fastest particular process (if the processes occur simultaneously).

2. Pit Growth (Pitting)

Pitting is one of the most important processes causing the emergence of corrosion cracks in the metals which are in contact with aqueous solutions. As a rule, pitting takes up most of the time before the final fracture of smooth patterns.

All metals are subject to pitting when an external field is applied. Pitting begins at a certain critical potential of the metal (the pitting potential[(18)]). Also, there exists a protection potential below which an active pit stops growing (Pourbaix[(19)]). This protection potential is obviously less than the pitting potential. The latter depends on the pH of the solution, concentrations of ions and the inhibitor, presence of indifferent electrolyte, presence of alloying additives in the metal, etc.

It was proved experimentally (see, e.g., References 15, 18, and 20) that the solution inside a pit, a crack, or a crevice has a composition which differs from that of the main solution. In this connection some authors considered the local change in the solution composition as the cause of pitting, and attached prior importance to one or another of the components (H^+, Cl^-, etc.). According to the modern point of view (works by Vetter and Strehblow,[(21)] Pickering and Frankenthal,[(22)] Galvele,[(23)] and others) only the study of mathematical models of pit growth can give a full description of this phenomenon and explain experimental data. In models constructed by the authors mentioned, prior attention is paid to transport processes; it has been found that the latter can explain the majority of facts concerning pitting potential.

2.1. General Equations of Transport Processes

Let the solution consist of n different components. The law of conservation can be presented as the following system of differential equations:

$$\frac{\partial c_i}{\partial t} + (\mathbf{v} \cdot \operatorname{grad})c_i = D_i \Delta c_i + \frac{D_i z_i F}{RT} \operatorname{div}(c_i \operatorname{grad} \varphi) + Q_i \qquad (i = 1, 2, \dots, n) \quad (1)$$

Here Δ is Laplacian operator, c_i is the concentration of the ith component, t the time, $\mathbf{v}$ the fluid velocity, φ the electric field potential, D_i and z_i respectively, diffusion coefficients and valencies (having a sign) of ions of the ith species. Q_i is the number of moles of the ith species emerging in a unit volume per unit time at a given point of the medium due to bulk chemical reactions, T the absolute temperature, F is Faraday's constant, and R is the universal gas constant. The quantity $\mathbf{v}$ in (1) is considered to be a given function of time and coordinates; it is taken from the solution of the corresponding boundary value problem of hydrodynamics. The quantity Q_i is a certain function of concentrations of the components participating in the reaction.

In the narrow layer of the solution in the vicinity of the metal surface both concentrations and the potential undergo sharp changes in a direction normal to the surface. This layer is called the double layer.

Within the electrolyte outside the double layer the solution is electroneutral, i.e.,

$$\sum_{i=1}^{n} z_i c_i = 0 \tag{2}$$

In the double layer the solution is not electroneutral (see, e.g., Levich$^{(24)}$). By analogy with the theory of Gouy–Chapman it is natural to use the electrostatics equation for the double layer,

$$\frac{d^2\varphi}{dx^2} = -\frac{4\pi F}{\varepsilon} \sum_{i=1}^{n} z_i c_i \exp\left(-\frac{z_i F}{RT}\varphi\right) \tag{3}$$

Here x is the coordinate normal to the metal surface and ε dielectric constant of the solution.

In Eq. (3) we have neglected the gradients of potential along the surface as compared to those along the normal; the exponential factor at the right-hand side of (3) allows for the thermal motion of ions in accordance with the Boltzmann principle [the double-layer potential at the boundary with the electroneutral solution is considered to be equal to zero in (3)]. The structure and thickness of the diffuse double layer is determined from the solution of equations (3) and (1), the left-hand side of the latter being put equal to zero, and the vector operators taken with respect to x only.

Let us consider as an illustration the double layer at the electrode in a binary electrolyte at $Q_i = 0$ (e.g., in the solution of $AgNO_3$ between silver electrodes), which is placed into an indifferent electrolyte with the same anion (e.g., in the HNO_3 solution). Since the overpotential for hydrogen evolution is higher than that for silver, we can neglect hydrogen evolution at a comparatively low electrode potential, so that the current will be conducted mainly by Ag^+ ions, and in the double layer there will basically be H^+ ions. As a result, the system of Eqs. (1) and (3) will assume the form

$$\begin{aligned} &FD_1\left(\frac{dc_1}{dx}+\frac{Fc_1}{RT}\frac{d\varphi}{dx}\right)=i \\ &FD_2\left(\frac{dc_2}{dx}-\frac{Fc_2}{RT}\frac{d\varphi}{dx}\right)=0 \\ &FD_3\left(\frac{dc_3}{dx}+\frac{Fc_3}{RT}\frac{d\varphi}{dx}\right)=0 \\ &\frac{d^2\varphi}{dx^2}=-\frac{4\pi F}{\varepsilon}\left[c_3\exp\left(-\frac{F\varphi}{RT}\right)-c_2\exp\left(\frac{F\varphi}{RT}\right)\right] \end{aligned} \tag{4}$$

Here i is the density of stationary current flowing onto the electrode $x = 0$ from the solution $x > 0$; indices 1, 2, 3 refer, respectively, to Ag^+, NO_3^-, and H^+.

Solving the first three equations of (4) with respect to c_1, c_2, and c_3, one obtains

$$\begin{aligned} &c_1 = c_{10}\exp\left(-\frac{F\varphi}{RT}\right)+\frac{i}{FzD_1}\exp\left(-\frac{F\varphi}{RT}\right)\int_x^{d_l}\exp\left(\frac{F\varphi}{RT}\right)dx \\ &c_2 = c_{20}\exp\left(\frac{F\varphi}{RT}\right), \qquad c_3 = c_{30}\exp\left(-\frac{F\varphi}{RT}\right) \end{aligned} \tag{5}$$

Here c_{10}, c_{20}, and c_{30} are concentrations of the corresponding ions at the solution–double-layer boundary, and d_l the diffuse double-layer thickness.

Substituting (5) into the last equation of (4), we find

$$\frac{d^2\varphi}{dx^2}=-\frac{4\pi F}{\varepsilon}\left[c_{30}\exp\left(-\frac{2F\varphi}{RT}\right)-c_{20}\exp\left(\frac{2F\varphi}{RT}\right)\right] \tag{6}$$

Now let us integrate this equation, account being taken of the conditions $\varphi = 0$, $d\varphi/dx = 0$ at $x = d_l$. We find the potential distribution in the double layer:

$$d_l - x = \frac{1}{4F}\left(\frac{\varepsilon RT}{\pi c_{20}}\right)^{1/2}\int_1^{\exp(2F\varphi/RT)}\frac{dx}{[x(x-1)(x-c_{30}/c_{20})]^{1/2}} \tag{7}$$

Let us denote the concentration overpotential of the double layer as η. Obviously, $\varphi = \eta$ at $x = 0$. Hence, by means of (7) we find the width of the double layer as

$$d_l = \frac{1}{4F}\left(\frac{\varepsilon RT}{\pi c_{20}}\right)^{1/2}\int_1^{\exp(2F\eta/RT)}\frac{dx}{[x(x-1)(x-c_{30}/c_{20})]^{1/2}} \tag{8}$$

As we see, the value d_l grows monotonically, as η grows, tending to a certain finite value when $\eta \to \infty$ (Figure 2). In particular, we get at $\eta > 0$

$$d_l = \left(\frac{\varepsilon\eta}{2\pi F c_{10}}\right)^{1/2} \quad \text{at} \quad \frac{2F\eta}{RT} \ll 1$$

$$d_l = \frac{1}{4F}\left(\frac{\varepsilon RT}{\pi c_{20}}\right)^{1/2} \int_1^\infty \frac{dx}{[x(x-1)(x-c_{30}/c_{20})]^{1/2}} \quad \text{at} \quad \frac{2F\eta}{RT} \gg 1 \tag{9}$$

$$(c_{10} = c_{20} - c_{30},\ c_{10} \ll c_{20})$$

At $\eta < (RT/2F)\ln(c_{30}/c_{20})$ the dependence of d_l on η will be analogous (see Figure 1). In the narrow region $0 > \eta > (RT/2F)\ln(c_{30}/c_{20})$ there exists no solution, because of the neglect of the quantity c_1 on the right-hand side of the last equation (4).

The width of the diffusive double layer does not usually exceed the value of the order of 10^{-5} cm. The width of the dense (Helmholtz) part of the double layer is negligibly small as compared to this value. Therefore the Gouy–Chapman theory seems to be satisfactory for the estimation of d_l.

The knowledge of this value is extremely important for the theory of propagation of cracks and deep pits in metals. Indeed, the electrochemical mechanism of the growth of cracks and deep pits is based on assumptions concerning the existence of an electroneutral electrolyte in their cavities, which is a good conductor. Therefore current emerging from the crack or pit root is able to cover relatively long distances from the crack or pit tip through the conducting electrolyte without shorting against the sides due to the resistance of the double layer (or the passive oxide film). As soon as the thickness of the crack cavity becomes equal to the width of the double layer, the whole cavity is filled with volume charge and becomes a very bad conductor so that the electrochemical reaction is confined to a small neighborhood at the root of the crack or the pit, and the growth is arrested.

Hence it follows that (i) the threshold stress intensity factor cannot be less than the value of the factor K_I determined according to the following condition: crack opening displacement is equal to the width of the double layer for the given pair metal-electrolyte; (ii) if the inclusion of some other metal has the shape of layers or wires whose thickness is less than the double-layer width, the

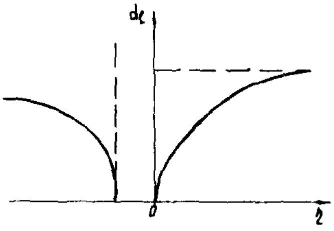

Figure 2. Double-layer overpotential dependence of the thickness of double layer [see Eq. (8)].

propagation of cracks or pits along such inclusions due to an electrochemical mechanism is impossible.

2.2. Some One-Dimensional Pitting Processes

One-dimensional models present the most convenient way for a description of pit growth. Therefore we treat here the general method of solving the system of Eqs. (1) and (2) with plane, axial, and spherical symmetry assuming that

$$\frac{\partial c_i}{\partial t} = 0, \qquad \mathbf{v} = 0, \qquad Q_i = 0 \tag{10}$$

i.e., for steady processes in a motionless electrolyte without any volume chemical reactions.

Integrating (1), we get

$$\frac{dc_i}{dr} + \frac{z_i F}{RT} c_i \frac{d\varphi}{dr} = \frac{I_i}{D_i z_i F r^{\kappa}} \tag{11}$$

Here I_i is the total intensity of the current carried by the ions of ith species, r the coordinate, and $\kappa = 0$ for plane symmetry, 1 for axial symmetry, and 2 for spherical symmetry.

Integrating (11) we find

$$\begin{aligned} c_i = {} & \exp\left[-\frac{z_i F}{RT}(\varphi - \varphi_0)\right] \\ & \times \left\{ c_{i0} + \frac{I_i}{D_i z_i F} \int_{r_0}^{r} \exp\left[\frac{z_i F}{RT}(\varphi - \varphi_0)\right] \frac{dr}{r^{\kappa}} \right\} \end{aligned} \tag{12}$$

Here $c_i = c_{i0}$, $\varphi = \varphi_0$ at $r = r_0$.

Substituting (12) into (2), we get a nonlinear integral equation for determining the potential φ. In the particular case when the entire current is carried by ions of the same species (or by different ions of the same valency) this integral equation can be presented as follows:

$$\int_{r_0}^{r} y^{z_k} r^{-\kappa}\, dr = f(y) \tag{13}$$

where

$$y = \exp\left[\frac{F(\varphi - \varphi_0)}{RT}\right], \qquad f(y) = -\frac{F y^{z_k} \sum_{i=1}^{n} (z_i c_{i0}/y^{z_i})}{\sum (I_i/D_i)}$$

Here the sum in the denominator is taken over all the current-carrying ions of the same valency z_k.

The solution of Eq. (13) has the following form:

$$\frac{F}{\sum I_k D_k^{-1}} \sum_{i=1}^{n} (z_k - z_i) c_{i0} \exp\left[-\frac{z_i F(\varphi - \varphi_0)}{RT}\right] = \begin{cases} r + \text{const} & (\kappa = 0) \\ \ln r + \text{const} & (\kappa = 1) \\ -\dfrac{1}{r} + \text{const} & (\kappa = 2) \end{cases} \tag{14}$$

The constant in (14) is determined from the condition that $\varphi = \varphi_0$ at $r = r_0$.

Formulas (12) and (14) give the distribution of the potential and concentrations with respect to r depending on the constants I_k. The latter are to be found from boundary conditions which are the equations of kinetics of electrochemical reactions on the electrodes:

$$D_i z_i F\left(\frac{dc_i}{dr} + \frac{z_i F}{RT} c_i \frac{d\varphi}{dr}\right) = f_i(c_i, \varphi) \tag{15}$$

Here on the left-hand side of the equation we have current density, and on the right-hand side the experimentally determined function of the potential and concentrations of the ions participating in the reaction on the electrodes.

A number of electrode processes are described by means of the following function resulting from the theory of delayed discharge:

$$f_i = z_i F\left\{k_1 c_i \exp\left(-\frac{\alpha z_i F\varphi}{RT}\right) - k_2 c_{iR} \exp\left[\frac{(1-\alpha) z_i F\varphi}{RT}\right]\right\}$$

(Butler–Volmer equation) (16)

Here c_i is the concentration of particles S in the solution undergoing discharge with taking on z_i electrons, c_{iR} is the concentration of particles R which emerge directly after the discharge according to the equation

$$S + z_i e \underset{k_2}{\overset{k_1}{\rightleftarrows}} R \tag{17}$$

and present in the Helmholtz part of the double layer, and α is a certain empiric number $(0 < \alpha < 1)$.

The first term in (16) describes the rate of direct discharge reaction (with constant k_1), and the second one of the reverse reaction of ionization (with constant k_2). The second term may be neglected on the cathode and the first one on the anode. The quantity φ in (16) is equal to the sum of the equilibrium potential and overpotential, i.e., it represents the potential difference of the electrode and the boundary "double-layer–electroneutral solution," if we neglect the diffusion overpotential of the double layer in comparison with the overpotential.

The Butler–Volmer equation is good enough for description of the discharge of hydrogen, deposition and dissolution of some metals, and the anode deposition of oxygen (in these cases, as a rule, the experimental data keep within some rectilinear segments on the φ–$\ln f_i$ diagram, i.e., empirical constants k_1, k_2, and α will be different on different segments).

In the general case when ions of different valencies participate in current transfer, we get the following integral equation instead of (13):

$$\sum_{i=1}^{n} \frac{z_i}{y^{z_i}}\left(c_{i0} + \frac{I_i}{D_i z_i F}\int_{r_0}^{r} y^{z_i} r^{-\kappa}\,dr\right) = 0 \tag{18}$$

This is easily solved by the following method. Let us divide the interval of the change of the independent variable (r_0, r_N) into N equal intervals of the width Δr and substitute the function y on each interval by a linear function

$$y = \exp\left[\frac{F(\varphi - \varphi_\alpha)}{RT}\right] = 1 + a_\alpha(r - r_\alpha) \qquad \text{at } r_\alpha < r < r_\alpha + \Delta r \tag{19}$$

$$(\text{at } r = r_\alpha,\ \varphi = \varphi_\alpha,\ c_i = c_{i\alpha})$$

In so doing, we substitute φ_0 by φ_α, c_{i0} by $c_{i\alpha}$, r_0 by r_α in Eq. (18), i.e., this equation is written for $r > r_\alpha$.

Substituting (19) into this equation we find

$$a_\alpha = \frac{1}{F r_\alpha^{\kappa}} \frac{\sum_{i=1}^{n} (I_i/D_i z_i)}{\sum_{i=1}^{n} z_i^2 c_{i\alpha}} \tag{20}$$

According to (12), we get similarly

$$c_{i,\alpha+1} = c_{i\alpha} + \Delta r\left(\frac{I_i}{D_i z_i F r_\alpha^{\kappa}} - c_{i\alpha} z_i a_\alpha\right) \qquad (i = 1, 2, \ldots, n) \tag{21}$$

The system of recurrent Eqs. (20) and (21) helps to easily calculate all the values of a_α and $c_{i\alpha}$. Indeed, by Eq. (20) we find a_0 in terms of the known c_{i0}, then by Eq. (21) we find c_{i1}, etc. The currents I_k, according to (15), are determined by the formula

$$I_k = r_0^{\kappa} f_i(c_{i0}, \varphi_0) \tag{22}$$

The number of steps N is chosen according to the rate of convergence by the trial and error method. It can be demonstrated that as $N \to \infty$ the solution constructed tends to the exact one. Agreement appears to be very good; practical construction of the curves of potential and concentration distribution using this method proves to be more convenient and quick even for analytical solutions (14) and (12).

Returning to pitting, we shall assume that the coordinate r_0 corresponds to the dissolved root of the pit (anode), so that in the expressions for f_i in (16) we can neglect the first term, and include the quantity c_{iR} as a constant value into the constant k_2, For pitting the coordinate r_N corresponds to the pit outlet into the external solution; we shall assume that at $r = r_N$ the potential is known and equal to the potential of the external electrolyte E, i.e.,

$$\varphi_N = E \tag{23}$$

In this case the anode potential is taken equal to zero.

The additional condition (23) serves for determining the unknown potential, φ_0 of the solution on the anode. The following method of determining φ_0 by this condition is the most convenient. At first we set at random any two values of φ_0 and carry out the calculation of the system (20)–(22) by the above-mentioned method; then we determine the two values of φ_N which correspond to them and appear not to be equal to E. Then, by these initial points on the φ_0, φ_N plane we organize the standard Newton iterative process which easily allows one to find φ_0 (only if the initial values of φ_0 were selected not too poorly).

The pit growth rate dr_0/dt is governed by the following formula:

$$\frac{dr_0}{dt} = \frac{1}{\rho F r_0^{\kappa}} \sum_{i=1}^{n} \frac{I_i(r_0)}{M_i z_i} \tag{24}$$

Here M_i is the mass of a gram-ion of ith species, ρ is the metal density, the currents I_i represent some functions of r_0 which are determined numerically by means of the above-mentioned calculation.

The differential equation (24) supplemented by the initial condition at $t = 0$, $r = r_{00}$ (where r_{00} is given; for instance, it is taken equal to zero), serves to determine the pit development in time; it is easily solved numerically using the step-by-step method as in a standard Cauchy problem.

Using this method, one can easily solve various problems of electrochemical reactions on spherical and cylindrical electrodes, as well as the problems of the growth of pits of various geometrical configuration (see, for example, Figure 3 where the surface areas covered with a passive film are shaded).

While studying pitting which occurs in the presence of an external potential, it is sufficient to restrict oneself to the reaction of metal dissolution occurring on the bare surface and hydrolysis reactions proceeding within the pit volume.(21–23) The pitting potential is likely to be equal to the potential difference necessary for breaking down the plane capacitor in which the passive film of metal and the double layer in the electrolyte serve as a gasket; it is also necessary to take the corrosion potential into account. Increasing the pH of the main solution as well as buffer anions of weak acids inhibit the process of pitting.(23) The value of the pH within the pit decreases as the pit grows, i.e., the solution, due to hydrolysis of the metal, is acidified as the pit grows.(23)

The mathematical model of the one-dimensional plane pit developed by Galvele(23) under the assumption of the solution potential constancy within the

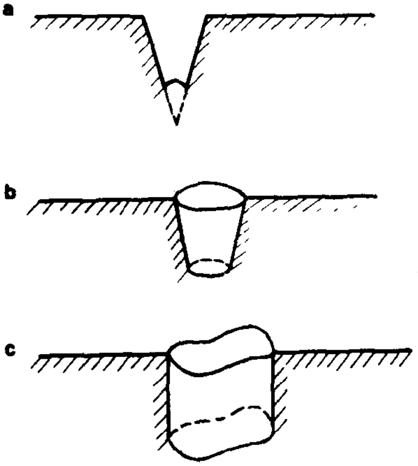

Figure 3. One-dimensional pits of various configuration: (a) wedgelike pit, (b) conelike pit, (c) cylindrical pit of arbitrary cross section.

pit attempted to explain all the main experimental facts concerning metal pitting in the presence of an indifferent electrolyte. He depicted the dependence diagrams of concentrations of metal, hydrogen and hydrolysis ions upon the pit depth and current density for a number of metals. Then he analyzed these diagrams and their corollaries, assuming that at the pit bottom the critical value of pH is realized which divides the zones of passivation and corrosion on the corresponding Pourbaix diagram. In particular, it appeared that even at the pit depth of the order of 10^{-6} cm and current density of 1 A/cm^2 the critical value of pH was attained at the pit bottom, and pitting began. The figures mentioned are characteristic of average oxide film and current density at the pitting potential, i.e., either breakdown or a crack in the film is enough for pitting to begin.

The mathematical theory developed above allows one, in particular, to extend the results of Galvele to any electrolyte and other geometrical types of pits.

While studying the corrosion pitting occurring in the absence of an external electric field, it is necessary to take into account not only the anode reaction of dissolution at the pit bottom, but also the cathode reaction (e.g., discharge of H^+) at the pit sides. This mechanism is similar to that of self-sustained growth of corrosion cracks which is considered later in Section 4.

Of interest also is the account of oxygen anode deposition at the pit root. In this case, the pit growth rate can be governed by oxygen diffusion in the pit.

The pit growth depends on the applied mechanical stress only to a small extent. However, at some critical pit depth, depending on the load and on the form and mutual position of the pits, mechanical fracture of the weakened layer takes place and a crack is originated.

The theory of pit growth allowing for cathode reactions at the pit sides is treated below, in Section 4.

3. Fracture Mechanics Approach

Fracture mechanics deals with the development of cracks in solids which is the final stage of practically any fracture process. The propagation of the crack front (i.e., the cavity in which one dimension is smaller than the other two) is determined in terms of some principal parameters describing the distribution of stresses, deformations, temperatures, potentials, etc. in the vicinity of the front.

Main efforts of researchers in the field of fracture theory are directed to the search for parameters controlling this complicated process and, as in any physical theory, to the search for corresponding universal constants. And considerable progress has been achieved in this direction during last 20 years.

3.1. General Functional Method

For example, let us consider a through open-mode crack of length l in a plate of width L_0 in the isothermal and monotonical process of increasing the external loading p applied symmetrically with respect to the crack plane (see Figure 4). The plate thickness is assumed sufficiently large, so that we can accept the conditions of plane strain. The crack front is perpendicular to the plate plane (the point O in Figure 4). As p grows, the region of plastic deformations is growing in the vicinity of the point O; the characteristic dimension of this region can be designated as d. In addition, in the course of time and with the growth of p, the length l increases, i.e., the point O moves to the right. The function $l(t)$ depends on physicomechanical properties of the material, the geometry of the specimen, environment, loading rate, temperature, etc. For all the materials and external conditions there exists some critical interval in which a sharp increase in the rate l occurs.

Suppose the following restrictions are observed:

$$d \ll l, \qquad d \ll L_0 \tag{25}$$

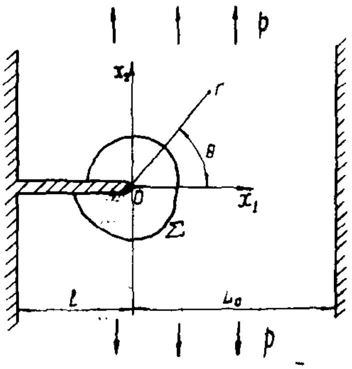

Figure 4. Edge open-mode crack in strip extended by uniform stress at infinity.

In this case for all the materials there exists a region

$$d \ll r \ll (l, L_0) \tag{26}$$

where the fields of stresses σ_{ik} and strains ε_{ik} are given by the following formulas:

$$\begin{aligned} \sigma_{ik} &= K_I(2\pi r)^{-1/2} f_{ik}(\theta, \nu_1, \nu_2, \ldots) \\ \varepsilon_{ik} &= K_I(2\pi r)^{-1/2} g_{ik}(\theta, \nu_1, \nu_2, \ldots) \end{aligned} \qquad (i, k = 1, 2, 3) \tag{27}$$

Here $r\theta$ are polar coordinates with the origin at the point O, $\nu_1, \nu_2, \ldots$ elastic constants, f_{ik} and g_{ik} certain functions calculated practically for all possible cases,(6,25) K_I is a stress intensity factor which depends only on external loadings, the crack length, the form of the body, and the crack. The normalization condition yields $f_{22} = 1$ at $\theta = 0$. The formulas (27) are the consequences of the physically evident fact that all the solids are linear elastic at sufficiently small loadings and operation times.

The formulas (27) are valid for arbitrary anisotropy and also for piecewise-homogeneous bodies when the interface coincides with the crack plane. Determining K_I in terms of external parameters is a problem of the mathematical theory of elasticity solved completely in many cases.

Asymptotic expansions like (27) in the vicinity of the crack tip were marked out in the works by Williams,(26) Sneddon,(27) and others. The role of the coefficient K_I as the controlling parameter of fracture was first understood by Irwin.(28) The proof of generality of such expansions for cracks and bodies of any form was presented by Cherepanov.(29)

The summary of formulas for stress intensity factors calculated for specimens with cracks of different configuration and loadings can be found in books, manuals, and monographs on fracture mechanics.(6,30–32) The description of the fracture mechanics experimental procedures (preparing specimens, registering cracks, measuring, etc.) can be found in many books.(33–37)

The field structure (27) testifies to the fact that any process of local fracture at the point O is controlled by external parameters only through one intermediate parameter, viz., coefficient K_I. In particular, the crack growth rate appears as some functional of $K_I(t)$:

$$\dot{l} = F\{K_I(t), t, \ldots\} \tag{28}$$

Here the dots stand for the quantities characterizing properties of the material and environment in the vicinity of the point O and responsible for local fracture at this point. This general formulation is presented by Cherepanov.(38)

If the material properties and environmental composition in the vicinity of the point O do not change in the process of crack development (or vary within the limits which do not influence the rate of local fracture at the point O), then the rate of crack growth will appear as some function of the stress intensity factor

$$\dot{l} = f\{K_I(t), \ldots\} \tag{29}$$

This assumption is far from being always valid. For instance, with considerable adsorption effect (in liquid metal–solid metal systems, etc.), with oxygen depolarization and in some other cases the local rate of fracture is limited by the rate of supplying the active chemical reagent into the crack mouth, i.e., by nonlocal transport processes. In these cases one should use the general relationship (28).

Graphic presentation of the dependence (29) in coordinates $\dot{l}$, K_I is called fracture diagram or $\dot{l}$–K_I diagram. It is a characteristic of a given material–environment system (with the exceptions mentioned) which can be determined directly from experiment. Theoretical and experimental demonstration of this fact came as the main achievement of fracture mechanics and stress corrosion. This achievement helped to present the main problem of these studies as the problem of studying the dependence of $\dot{l}$–K_I diagrams for various practical systems on material and environmental composition, temperature, and other external conditions.

Various characteristic points of this diagram can be described by means of corresponding critical values of the coefficient K_I. However, there exists a critical value of this coefficient which is independent of the environment and is called fracture toughness, K_{IC}. It characterizes sharp increases in the crack velocity up to near-sonic velocities and does not depend on the environment, because the rate of all the parallel processes of local fracture at the point O appears small compared to the rate of local mechanical fracture in vacuum or in some inert medium. Thus the quantity K_{IC} is a material constant characterizing its limiting resistance to crack development.

The K_{IC} concept, which was first put forward by Irwin(28,39) is of a universal character for all materials (if the dimensions of a specimen are sufficiently large). This concept is usually derived from energy concepts by Griffith(40) for the surface energy of solids; it should be noticed, however, that it can be deduced as well from absolutely different (and even absurd) physical assumptions, if the latter refers to the region (26) and does not depend on time. There exist a dozen constructions by different authors based on various assumptions as to the structure of the region (26) and leading to the K_{IC} concept.

In some cases (e.g., in glass–water systems, for some super-brittle steels in organic alcohols and some other systems) the velocity of environment migration and the rate of adsorption action by the environment are so high that it is practically possible to ascertain the decrease of fracture toughness under the effect of environment.

In particular, the influence of loading rate arises from these considerations: the greater it is, the less is the role of slower processes of local fracture under the effect of environment. For example, at sufficiently large loading rate in corrosion systems with branching cracks one is not likely to observe branching, and fracture occurs "prematurely" (since $K_{IC} < K_{IF}$; see Section 4 below).

The other important critical value of the stress intensity factor K_I is the so-called threshold value of the stress intensity factor K_{ISCC}, below which cracks do not propagate in a given metal–environment system. The presence of K_{ISCC} at static loadings which do not vary or slightly vary in time, was established for most corrosion systems investigated (though the results of some experiments are in question because of an insufficient test base).

In the case of cyclic loadings I know of only one work (the thesis by Linder$^{(7)}$) in which the existence of the corresponding threshold stress intensity factor was established (for aluminum alloy 2024-T3). The tests were carried out in the range of crack growth rate 10^{-10}–10^{-3} in./cycle. The corresponding threshold value proved to be about 20 times less than the value of K_C.

It seems that at cyclic and, in general, quickly changing loadings the concept of the threshold stress intensity factor is justified only for a very small number of metal–environment systems. It is always advisable to point the test base on which the threshold value was obtained. Besides, in some cases the rate of corrosion crack growth observed appears so small that during the operation period of the construction the growing crack is not dangerous. It is clear that such a material may well be considered fit for operation. All this indicates that in spite of the importance of the K_{ISCC} concept one needs detailed information about the entire $\dot{l}$–K_I diagram for final judgement of the material.

It should be noted that the emergence of cracks is, in principle, possible also at $K_I < K_{ISCC}$, for the mechanisms of crack propagation may differ from that of its origin. A similar explanation can be given to some cases observed in practice when smooth specimens do not crack, and preinflicted cracks propagate in the medium studied. (This situation is typical, to some extent, if one manages to avoid pitting corrosion on a smooth specimen whose material, however, is subject to local hydrogen embrittlement at the crack tip; see Section 5).

Catastrophic water sensitivity of some high-strength steels was almost simultaneously noticed by many researchers (Shank and his associates,$^{(41)}$ Irwin, Kies, and Bernstein,$^{(42,43)}$ Steigerwald,$^{(44)}$ and others). The same authors gave the correct explanation of this phenomenon linking it with the subcritical crack growth. Steigerwald$^{(44)}$ was the first to prove that the phenomenon was not related to the K_{IC} concept and should be studied separately. Corrosion fracture mechanics based on studying $\dot{l}$–K_I diagrams and critical stress intensity factors on precracked specimens, owes its origin to works by Johnson and Willner,$^{(45)}$ Brown and Beachem,$^{(46)}$ Hanna, Troiano, and Steigerwald,$^{(47)}$ Hancock and Johnson,$^{(48)}$ Wiederhorn,$^{(49)}$ Irwin,$^{(50)}$ Mulherin,$^{(51)}$ Peterson and associates,$^{(52)}$ Van der Sluys,$^{(53)}$ Johnson and Paris,$^{(7)}$ Smith, Piper, and Downey,$^{(54)}$ and others. By this time about a hundred works in this field have been published, and their number is growing steadily.

The fracture mechanics approach based on coefficient K_I, i.e., on the existence of linear-elastic asymptotics [Eq. (27)], is realized only if the restric-

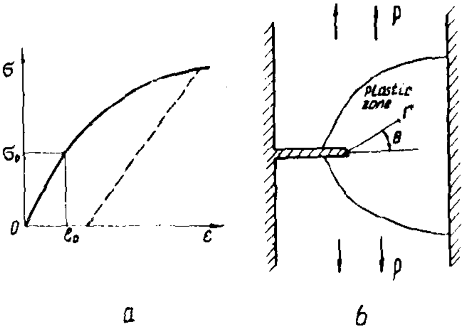

Figure 5. Uniform extension of cracked strip of nonlinear-elastic material: (a) σ–ε diagram of the material, (b) configuration of cracked strip and "plastic" zone.

tions (25) are satisfied, i.e., practically for high-strength and brittle materials. However, at cyclic or quickly varying loadings the threshold coefficient is small (or even vanishes), therefore even for low-strength and rather plastic metals the evaluation of time to failure can be carried out by means of the approach mentioned, because the main contribution to the time to failure is made by a range of low stress intensities K_I.

At stationary loading the value K_{ISCC} is rather close to K_{IC} for most low- and medium-strength alloys, and the dimensions of structural elements are such that the conditions (25) are not obeyed. The above-mentioned approach is not valid for such materials and one should apply a more general approach based on an asymptotic approach of a lower order.$^{(6)}$ For example, the following method can be applied.$^{(6)}$ The metal is considered to be incompressible up to fracture under uniform extension, and under uniaxial extension its behavior is approximated by the following nonlinearly elastic body (σ–ε diagram; see Figure 5):

$$\sigma = \begin{cases} E\varepsilon & \text{at } \varepsilon < \varepsilon_0 \\ \sigma_0 + E_\kappa(\varepsilon - \varepsilon_0)^\kappa & \text{at } \varepsilon > \varepsilon_0 \end{cases} \tag{30}$$

Here E, E_κ, σ_0, ε_0, κ are constants. These assumptions allow us to find a complete system of equations describing the behavior of homogeneous and isotropic metals of any shape and under any loading (with a certain error caused by the approximate nature of these assumptions). The exact analysis of this case shows, in particular, that near the crack tip, i.e., in the range (see Figure 4)

$$r \ll d, \qquad r \ll l, \qquad r \ll L_0 \tag{31}$$

the stress–strain field has the following form$^{(6)}$:

$$\begin{aligned} \sigma_{ik} &= k_I(2\pi r)^{-\lambda} f'_{ik}(\theta, \kappa) \\ \varepsilon_{ik} &= k_I(2\pi r)^{1+\lambda} g'_{ik}(\theta, \kappa) \\ &\left(\lambda = \frac{\kappa}{1+\kappa}\right) \end{aligned} \tag{32}$$

Here the notation is similar to that accepted in the formulas (27), d denotes a characteristic dimension of the "plastic" region where $\varepsilon > \varepsilon_0$. The quantity k_I is determined in terms of parameters of external load and dimensions of the body from the solution of the concrete boundary value problem of the nonlinear theory of elasticity (this solution, of course, is more complicated than that for the corresponding linear problem for determining K_I, but quite achievable by means of modern computing devices).

With this approach, the main problem of fracture mechanics is determining the l–k_I diagrams, and it is possible to formulate the k_{IC} concept (characterizing the beginning of unstable crack growth) and the k_{ISCC} concept (characterizing the minimal possible value of k_I at which the subcritical crack growth takes place in a given medium under stationary loading).

The values k_I and K_I are interrelated by a certain equation[6]; therefore the results of tests with large specimens can be forecast proceeding from the experimental data for small specimens [when the conditions (25) are satisfied], and vice versa.

3.2. Energy Method

Consider an arbitrary closed contour Σ, embracing the crack tip in a solid (see Figure 6). From the energy conservation law one can prove that the value Γ is independent of the contour Σ at any given time moment for any solid continuum,[6] if the physical field is steady in the reference system connected with the crack tip:

$$\begin{aligned} \Gamma &= \int_{\Sigma} [(\text{э} + \tfrac{1}{2}\rho \dot{u}_i \dot{u}_i) n_1 - \sigma_{ij} n_j u_{i,1}]\, d\Sigma \\ \text{э} &= \int \sigma_{ij}\, d\varepsilon_{ij} \qquad (i, j = 1, 2, 3) \end{aligned} \tag{33}$$

Here u_i, $\dot{u}_i$ are displacement and velocity vector components along the axes of moving Cartesian coordinates x_i connected with the crack tip; σ_{ij} and ε_{ij} are stresses and strains, ρ the density, э the deformation energy, n_i the components of unit vector, external and normal to the contour Σ. Common agreements

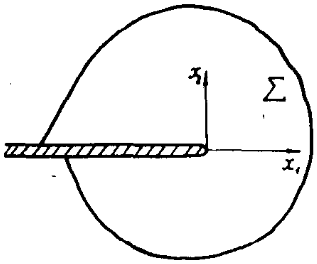

Figure 6. An arbitrary closed contour Σ embracing a crack tip in a plane solid.

concerning summation and differentiation are accepted (e.g., $\dot{u}_i\dot{u}_i = \dot{u}_1^2 + \dot{u}_2^2 + \dot{u}_3^2$, $u_{i,1} = \partial u_i/\partial x_1$, etc.).

If a closed surface Σ in a homogeneous solid contains no field singularities, the integral Γ over any such surface is equal to zero.

In a distributed physical system one can construct an infinite number of invariant Γ integrals; in particular, invariant Γ integrals were constructed for arbitrary electromagnetic deformable matter generalizing the notion of energy–momentum tensor in field theory, hydrodynamics, theory of elasticity, etc. (Cherepanov(55)). The quantity Γ is one of the three invariant Γ integrals of the first kind. For any given model of behavior of a solid it can be calculated by means of (33) from the solution of the corresponding boundary value problem. With the course of time the value Γ is, generally speaking, changing; that is why the value Γ is, in a general case, some time functional of the crack length, external loads, body configuration, etc.

The physical meaning of the invariant integral, Γ, is as follows: the quantity Γ is equal to energy dissipation per unit crack surface absorbed along the crack front.

Invariant Γ integrals of the first kind are closely related to the concept of the energy–momentum tensor put forward by Maxwell. In the theory of elasticity they first appeared in the work by Eshelby in 1951.(56) In 1967, Cherepanov obtained the Γ integral of the first kind for arbitrary continuum under small deformations, taking account of thermomechanical processes only(57); he also used it first for studying the crack growth in solids. In 1968 there appeared the famous work by Rice,(58) in which he applied the Eshelby integral to the analysis of stress and strain concentration in the vicinity of cuts and slots.†

The invariant Γ integrals technique is a powerful instrument for constructing physical theories of motion of field singular points (charges, material points, the crack front, dislocations, vortices, sources, etc.(55)).

It is natural to accept the value Γ as a parameter responsible for rectilinear crack growth. This assumption forms the basis for the energy approach. With this approach, the crack growth rate is generally represented by some functional G of $\Gamma(t)$:

$$\dot{l} = G[\Gamma(t), t, \ldots] \tag{34}$$

which is analogous to (28). The functional G degenerates into a common function, if the material properties and the environmental composition in the vicinity of the crack tip do not vary in the process of crack development (or vary, but insignificantly). In this case the $\dot{l}$–Γ diagram will be the main characteristics of the process and the material–environment system under study. Characteristic points of this diagram will be some constants for a given system. For instance, we can introduce the concept of the quantities Γ_C and Γ_{SCC} analogous to K_{IC} and K_{ISCC}. The constants Γ_C and Γ_{SCC} are the main constants characterizing resistance of the material to cracking in a given environment under stationary loads. If the conditions (25) are satisfied, or, to put it more exactly, for elastic materials, these concepts coincide, then in this case there is a simple relationship$^{(6,57)}$:

---

† Rice termed this integral "path-independent J integral." For elastic bodies the quantity $\ni$ equals specific elastic potential; in this case Γ integral Γ and J integral are identical for static case.

$$\Gamma = \frac{1-\nu^2}{E} K_I^2 \tag{35}$$

Here E is Young's modulus and ν is Poisson's ratio.

The Γ concept has a more general character because it can also be applied to nonelastic bodies when the conditions (25) are not valid. Major difficulties in its application consist in overcoming cumbersome calculations according to the formulas (33). However, with some assumptions, the value Γ in terms of the crack length and load may be determined experimentally from the load displacement diagram for a specimen with a crack, the value $\Gamma = \Gamma_i$ at the initial moment of crack motion in the process of load increase being measured (naturally, the loading rate must be large enough to neglect the subcritical crack growth during the test). In general, for elastic plastic materials the value Γ_i depends on prehistory of the initial crack formation (e.g., on the swing on K_I while growing the initial fatigue crack or on its opening displacement at the tip). But, practically, for many (even plastic) metals this dependence proved to be rather weak, which enabled one to consider the quantity Γ_i as a constant. The corresponding value K_{Ii} calculated from Γ_i by the formula (35), is accepted as fracture toughness for plastic materials whose specimens are too small for the conditions (25) to be satisfied.

To determine critical values K_{Ii} or Γ_i for real cracklike defects on laboratory specimens, it is necessary to model the structure of the defect edge.

The invariant Γ integral is also helpful in some problems as a means of calculation. Let us consider two examples of interest for pitting and branching of corrosion cracks.

3.3. Arbitrary System of Tunnels in Elastic Body

Let semispace $x_1 > 0$ have an arbitrary system of tunnels whose side surfaces are cylinders with generatrices perpendicular to the free surface of the semispace and directed along the x_1 axis (Figure 7). The bottom surface of all the tunnels will be denoted as S_B. The cross sections of the tunnels are situated on the plane x_2x_3 and are arbitrary. Let us assume that the tunnel depths are large compared to a characteristic dimension of tunnel cross section. The semi-space may undergo some uniform extension and shear in x_2x_3 plane. The surfaces and bottoms of the tunnels are free from loads. It is necessary to evaluate maximum stresses at the tunnel bottoms. Dynamic effects are neglected.

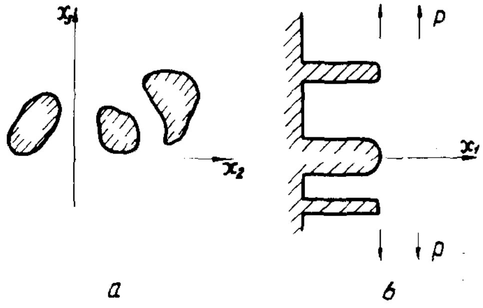

Figure 7. Arbitrary system of cylindrical pits on elastic body surface: (a) cross section of pits, (b) longitudinal section of body pitted.

As a surface Σ, let us take here the closed surface which is formed by the lateral surfaces and bottoms of the tunnels plus a cylindrical surface coaxial with the tunnels, embracing all of them and located far from them compared to their mutual spacing, plus two planes, S_+ and S_-, perpendicular to the x_1 axis. One of the planes (S_+) is in front of, and the other (S_-) behind the tunnels at a distance large compared to their mutual distance; in addition, the S_- plane should be sufficiently far from the free surface of the semispace.

In this case the invariant integral Γ is determined by the same expression (33) in which the second term may be omitted. This integral over the closed surface Σ is equal to zero, since inside this surface the body is assumed homogeneous and no singular points like crack tips, dislocations, etc. are supposed to exist. For cylindrical surfaces coaxial with x_1 all the integrals of the (33) type vanish because there $n_1 = 0$ and, besides, either $\sigma_{ij}n_j = 0$ or $u_{i,1} = 0$. Hence we come to the following relationship:

$$\int_{S_B} \ni n_1\, d\Sigma + \int_{S_+} \ni\, d\Sigma - \int_{S_-} \ni\, d\Sigma = 0 \tag{36}$$

It should be noted that in the plane S_- the medium is under the conditions of plane strain (the plane with cuts subject to a given loading at infinity, see Figure 7a).

For a model of the nonlinear-elastic body which can approximately describe metal deformations under monotonic loading, the quantity $\ni$ is equal to the specific elastic potential U which is a function of stresses or deformations at a given point. In this case we obtain

$$\int_{S_B} U n_1\, d\Sigma = \Delta U \tag{37}$$

Here ΔU is elastic energy released in the elastic plane due to the formation of the given system of holes in it (stresses at infinity are given). The value ΔU is determined from the solution of the plane problem of the theory of elasticity.

Suppose that the tunnel bottom is rounded in such a manner that at all points of S_B the value U is constant. We shall call such a bottom surface equistrong. For the equistrong bottom we obtain from (37) the following finite relationship:

$$US_B = \Delta U \tag{38}$$

Here S_B stands for the area of projection of the surface S_B upon the (x_2, x_3) plane.

In particular, if there is a small single tunnel with the cross section in the shape of a circle of radius r_0, and the linear-elastic semispace is uniformly extended in the plane (x_2, x_3) by stresses $\sigma_{22} = \sigma_{33} = p$, then we obtain

$$S_B = \pi r_0^2, \qquad \Delta U = 2\pi \frac{1-\nu^2}{E} p^2 r_0^2, \qquad U = \frac{2(1-\nu^2)}{E} p^2 \tag{39}$$

At the most dangerous point at the bottom of the circular notch there obviously takes place the uniform biaxial extension by tangential stress σ so that at this point

$$U = \frac{1-\nu}{E} \sigma^2 \tag{40}$$

Comparing this with (39), we find the stress at the most dangerous point of the equistrong notch:

$$\sigma = p[2(1+\nu)]^{1/2} \tag{41}$$

From physical considerations it is clear that for other forms of the tunnel bottom the maximum tensile stress will be larger than $p[2(1+\nu)]^{1/2}$. It should be noted for the sake of comparison that at the uniform biaxial extension of the elastic space with spherical cavity the maximum tensile stress is equal to $12p/(7-5\nu)$, and the maximum tensile stress at the sides of a circular tunnel is equal in this case to $2p$. Hence crack formation at pitting takes place owing to the rupture along the side surface of pits.

3.4. Crack Twinning

The main mode crack is twinned at some moment and then runs in two parallel branches (Figure 8a). At a sufficiently large length of the branches we come to the problem of two parallel semi-infinite cracks (Figure 8b).

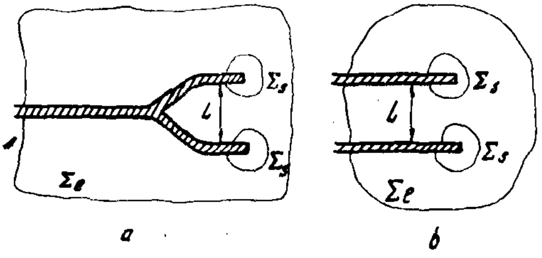

Figure 8. Forked crack: (a) contour Σ for forked crack, (b) contour Σ in the limiting case of two parallel semi-infinite cracks.

Let us consider the closed contour Σ formed by the crack banks, two small contours Σ_s embracing the tips of the branches, and the contour Σ_l embracing both branches and located at a distance from their tips large compared to their spacing L. Making use of the invariant Γ integral we find

$$\Gamma = 2\gamma_1 \tag{42}$$

Here γ_1 is the value of the invariant integral Γ for the branch tip (taken over Σ_s); the left-hand side of (42) is, as before, the corresponding value for the main crack (taken over Σ_l). It should be noted that for nonparallel cracks Eq. (42) is not valid. In particular, for an all-elastic body we find from (42)

$$k_{\mathrm{I}}^2 + k_{\mathrm{II}}^2 = \tfrac{1}{2}K_I^2 \tag{43}$$

Here k_{I} and k_{II} are stress intensity factors at the tips of the branches, K_I the corresponding value for the main crack.

If for a given material–environment system we have the unique $\dot{l}$–Γ diagram, then it follows from (42) that at $\Gamma > 2\Gamma_{SCC}$ it is possible to expect twinning of the crack and its further propagation in two branches. Moreover, if $\Gamma_C > 2\Gamma_{SCC}$, then experimental estimation of Γ_C is aggravated by branching owing to the great dispersion of this value. See it in detail below, in Section 4, where crack branching is treated from a less general point of view of the factors K_I and k_{I}.

3.5. Experimental Determination of the $\dot{l}$–Γ Diagram

The most expedient techniques of finding $\dot{l}$–Γ diagrams and, in particular, the constants Γ_{SCC} and Γ_C are the experiments with the specimens of a special form for which it is possible to calculate the value Γ theoretically. Let us dwell on one of the types of such specimens (Figure 9).

Take a plate of the material tested of thickness h_0 and make in it an edge through sharp rectilinear cut of length l_0 perpendicular to the plane of the plate and its edge. There are many technological means of carrying the last operation out. For metals a vibrator is used and the fatigue crack is grown at the lowest stresses possible from the synthetic mechanical cut. The cut length should be much greater than the plate thickness, i.e., $l_0 \gg h_0$. Then a defectless plate of thickness h_1 made of another (or of the same) material is linked with the critical plate rigidly along adjacent side planes, leaving free a strip of width h symmetrical relative to the cut trace on the side plane of the first plate (Figure 9d). To link the plates one can use diffusion welding, electric welding, gluing, and other technological operations.

The bimetal plate is then extended with the force P in the direction perpendicular to the plane of the initial cut:

$$P = (E_0h_0 + E_1h_1)\varepsilon_\infty \tag{44}$$

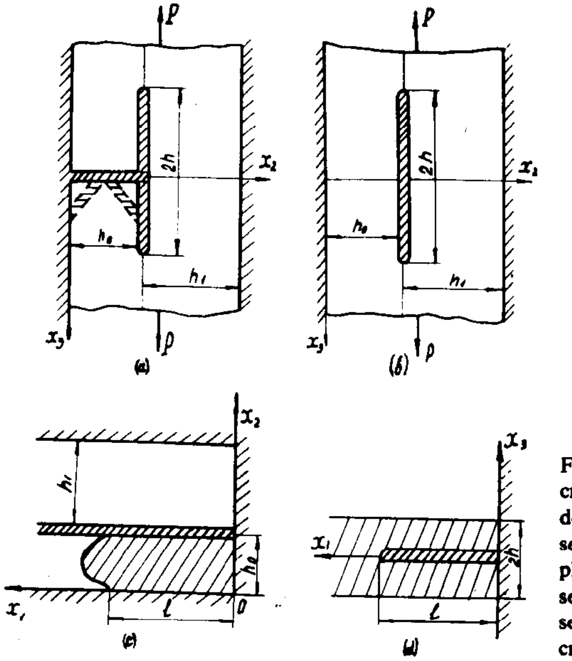

Figure 9. Configuration of a type of cracked specimens offered for determining l–Γ diagram: (a) a cross section perpendicular to crack and plate planes, (b) the same cross section without crack, (c) the cross section along crack plane, (d) a cross section parallel to plate plane.

where ε_∞ is given bimetal deformation at great distances from the crack, and E_0 and E_1 Young's moduli of the base and auxiliary materials, respectively.

Let us calculate the magnitude of the invariant Γ integral Γ at the front of the developing crack. Choose the origin of the Cartesian system of coordinates in the middle of the crack on the free bimetal plane; let the axis x_1 coincide with the direction of the crack growth, the axis x_2 lie in the plane x_1x_2 of the initial crack perpendicular to the plane of the plate with the axis x_3 perpendicular to the plane of the initial crack. In the process of crack propagation, its front is, generally speaking, curved and may protude from the initial plane, at least partially (the shear along the planes at an angle of 45° to the free surface and the initial plane). The edge of the bimetal $x_1 = 0$ is free of external loads.

Let us consider a closed surface Σ formed by intersection of the following surfaces: the plane $x_1 = 0$; the sides of the crack and of the load-free cut in the shape of a strip in the plane $x_2 = h_0$; the planes $x_2 = 0$ and $x_2 = h_0 + h_1$; the toroidal surface Σ_t of a small radius embracing the crack front; the planes $x_3 = \pm A$ and $x_1 = B$ where

$$A \gg l, \qquad B \gg l, \qquad l \gg h_0 \tag{45}$$

(l is a characteristic length of the developing crack).

The right-hand side of Eq. (33) vanishes while integrating over the surface Σ mentioned. The integrals over separate sections of this surface (except for Σ_t,

$x_1 = 0$, and $x_1 = B$) are equal to zero because of the fact that $n_1 = 0$ and $\sigma_{ij}n_j = 0$ or $u_{i,1} = 0$ on those sections.

Let us assume that the crack front propagates steadily along the axis x_1, i.e., without changing its form with time. This assumption actually arises from the general energy approach according to which the local growth of the crack is governed by the parameter, Γ. Therefore in the initial, transient period of its development the crack front rearranges itself in such a manner that Γ is the same everywhere at the front. At $x_1 = 0$ and $x_1 = B$ the material is considered to be elastic, which is not a burdensome assumption for the chosen geometry of the specimen.

Thus for the steady regime we arrive at

$$\Gamma = \frac{\Delta U}{\eta h_0} \tag{46}$$

Here ΔU is the difference of elastic energies of plates of unit thickness the plan view of which is shown in Figures 9a and 9b (the plates are in plane stress), and η is the numerical coefficient characterizing the deviation of the crack plane from the initial one (at $\eta = 1$ the crack propagates in the plane $x_3 = 0$).

The energy ΔU released owing to the crack formation is found from the solution of a standard plane problem of the theory of elasticity (see Figure 9a). It can be presented as follows:

$$\Delta U = \lambda \frac{P^2}{E_0} \tag{47}$$

where the dimensionless coefficient λ depends on E_1, E_0, h_0, h_1, ν_0, ν_1, h. The value ΔU is easily obtained directly from the experimental P–v diagrams for the corresponding specimens with and without a cut (see Figure 10 with the schematic P–v diagram where the area ΔU is shaded).

If the concept of stress intensity factor K_I is reasonable, then (46) and (35) yield, for the given pattern and the plane crack at $x_3 = 0$,

$$K_I = \left[\frac{E\Delta U}{h_0(1-\nu^2)}\right]^{1/2} \tag{48}$$

It is essential that Γ be independent of the crack length and be easily controlled by the proper choice of the force P.

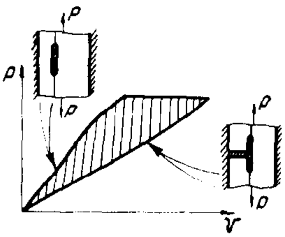

Figure 10. The P–v diagram serving to experimentally find energy released because of crack formation.

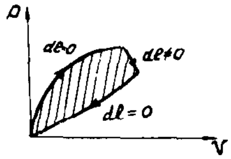

Figure 11. A schematic P–v diagram serving to determine the value Γ_c from crack initiation tests.

To study the growth of internal cracks with constrained deformation at the front, the specimen described should be changed so that the formation of "shear lips" is avoided. This can be achieved if two plates made of a much stronger and more rigid material are connected from both sides to the plate of the test material through an initial crack. As before, the quantity Γ for such a specimen is presented by the formula (46) with $\eta = 1$, because the crack will be plane in this case.

For the specimens mentioned, one can also simultaneously obtain P–v diagrams using displacement gauges, and, by measuring the area of crack growing at the moment of its starting, determine the value Γ under certain assumptions as to the material properties. For instance, it is possible, following Rice,(59) to suppose that the material behaves as a nonlinear-elastic one at the initial moment of the crack motion. With this assumption, the value Γ_C can easily be found from the shaded area in the P–v diagram (Figure 11). The comparison with the exact value of Γ_C will enable us, in particular, to judge the validity of this assumption.

In this section we have discussed, in essence, only the case of the opening mode for cracks which is of greatest practical importance. Shear cracks and cracks of the mixed type are omitted to save space.

Sometimes engineers/practitioners reproach theoreticians with their frequent neglect of many obvious properties inherent in real objects, e.g., heterogeneity and anisotropy of metals near the crack tip. However, even correct, but excessively detailed, theories often appear impractical because they require for their application equally detailed information which is difficult to obtain experimentally.

4. Electrochemical Mechanism of Crack Growth

Electrochemical processes are known to be of primary importance in corrosion embrittlement and crack growth. It is common knowledge that chemical reactions that occur on the metal–electrolyte solution interface are accompanied by the appearance of some potential difference characteristic for the given system; hence if two different metals in contact are placed into an electrolyte, then an electric current is sure to appear in the metal–electrolyte circuit (voltaic cell). In this case one of the metals (the anode) will pass into the solution as ions, thus dissolving, and another (the cathode) will be reduced. It should be noted that in most cases the corrosion-active environment is an electrolytic solution (see Table 5 of Reference 6).

Structural metals are alloys of many and diverse metals. Therefore, while in contact with an electrolytic solution, a metal surface gives rise to many microscopic voltaic cells of various kinds. This leads to dissolution of some alloy components, and, in the first place, of those components which stand higher in the electromotive series, i.e., have smaller equilibrium potential taking into account the sign. This results in the emergence of pits on the metal surface which act as stress concentrators. In the presence of external tensile loads, a crack will arise which will further develop due to electrochemical dissolution of the anodic metal at the crack root with subsequent failure of the weakened material. Below, we shall confine ourselves to considering the process of crack development only.

It is assumed that the metal is an ideal elastic-plastic body. We also need two principal assumptions: (i) anodic components are present at every point of the initial material, the newly exposed surface of the metal being considered on the average anodic as compared to the surface sections which have already undergone some environmental effect; (ii) the crack growth is continuous.

The first assumption can be explained as follows. A voltaic cell usually undergoes certain changes during its operational period, most frequently due to the deposition of hydrogen or some metals on the cathode (cathode polarization) and/or deposition of concentrated salts or oxygen on the anode (anode polarization). As a result, the potential of the microcell gradually decreases and the current stops until a newly exposed surface of fresh metal appears owing to local rupture, after which the process is resumed.

The second assumption allows us to treat the crack jumps as infinitesimal. Among all the phenomena involved in the process, the slowest stage governing the kinetics of crack growth is the electrochemical process of motion of ions in the crack cavity.

The existence of a jumping regime of the crack growth by an electrochemical mechanism (with leaps exceeding the size of the plastic zone) is hardly probable because it would require an extremely long operational period for one and the same voltaic microcell, whereas it is in fact limited by the natural processes of polarization (the cathodic at first). The phenomenon of the threshold stress intensity factor can be explained in these terms.

The estimation of the value K_{ISCC} from below is the value of the fracture toughness of the metal from whose volume all the active anodic zones causing the crack growth are mentally excluded.

Another mechanism of K_{ISCC} phenomenon is associated with the fact that at too small a magnitude of the stress intensity factor the crack opening becomes comparable to the width of the double layer, and volume charges appear in the crack cavity which hinder transport processes of ionic transfer in the solution.

4.1. Equations of Motion of Electrolyte Ions in Narrow Slits

Suppose that two metal surfaces form a narrow slit filled with an electrolytic solution. Let S denote a middle surface, i.e., the surface equidistant from the sides of the slits. The slit width is assumed small in comparison with the radius of curvature of S at any point. Let u, v be fixed orthogonal Gaussian coordinates of a point on the surface S. The solution contains ions of n species, the concentration of each specie being equal to $c_i(u, v)$.

Let h denote the part of the slit width outside the double layer in which φ as well as true concentrations may be considered as constant along the normal to the surface S (Figure 12). It is this constant value of potential that will be referred to as $\varphi(u, v)$. The value of the liquid flow velocity $\mathbf{v}(u, v)$ is assumed as known ($\mathbf{v}$ is understood as a cross section average velocity, i.e., as the volumetric flow rate vector divided by h). The double-layer thickness is negligibly small as compared to h.

Let us study the motion of ions in the layer A of thickness h (c_i includes only the ions of this layer shaded in Figure 12). Chemical reactions occur in the thin-layer metal–electrolyte between the boundaries of the layer A and the slit banks; therefore, on the boundaries of the layer A there exists a flow of ions (hence the electric current) in the direction of the normal to the surface S.

The law of mass conservation in the layer A may be expressed by the following equations on the surface S:

$$\frac{\partial c_i}{\partial t} + (\mathbf{v}\,\mathrm{grad})c_i = D_i \Delta c_i + \frac{D_i z_i F}{RT} \operatorname{div}(c_i \operatorname{grad} \varphi) - \frac{1}{h} G_i(\varphi, c_i) \qquad (i = 1, 2, \ldots, n) \tag{49}$$

Here $G_i(\varphi, c_i)$ is the number of ions of the ith species passing over into the double layer from a layer A per unit time per unit area of the middle surface; vector operations being carried out along the surface S. The functions $G_i(\varphi, c_i)$ are determined by the polarization curves which depend on the kinetics of chemical reactions and phase transitions in the double layer. In what follows we use Butler–Volmer theory for the mechanism of the hydrogen evolution reaction. Let us give the expression for the total current density at the metal–electrolyte interface:

$$j = \sum_{k=1}^{n} e z_k G_k \tag{50}$$

The first and the second terms in the right-hand side of Eq. (49) have the meaning of the rate of change of the number of particles per unit area of the

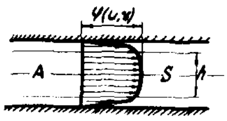

Figure 12. Structure of elastic potential in a narrow slit filled up with electrolyte.

surface S due to diffusion and migration of ions under the effect of Coulomb forces, respectively. The second term in the left-hand side of Eq. (49) gives the rate of concentration change due to the convective transfer of ions by the liquid flow.

Let us assume that the metal potential on the crack sides is equal to zero. Then $\varphi(u, v)$ represents a jump of the potential at the metal–solution boundary while passing through the double layer from the metal to the electroneutral solution. The symbol φ_0 stands for the potential of the layer A at the crack root (φ_0 is a known empirical constant of the system under consideration).† In this case we automatically take into account also the contact potential on the interface between different metals.

Equations (49) are obtained from rigorous three-dimensional equations of the electrolyte motion in the following way. In the first place, we write Eqs. (1) in the orthogonal curvilinear system of coordinates (u, v, w) so that the surface S should coincide with the surface $w = 0$. Then we introduce the following two assumptions: (i) vector $\mathbf{v}$ at any point of the layer A is independent of w, its component along the normal to the surface S being equal to zero; (ii) the derivatives $\partial\varphi/\partial u$ and $\partial\varphi/\partial v$ at any point of the layer A are independent of w. Taking these assumptions into account, the exact equations are integrated with respect to w within the layer A from $-h/2$ to $h/2$, and average concentrations over the layer thickness are introduced. The quantities G_i are equal to

$$G_i = D_i\left(\frac{z_iF}{RT}c_i\frac{\partial\varphi}{\partial w} + \frac{\partial c_i}{\partial w}\right)\Bigg|_{-h/2}^{h/2}$$

They represent the flows of the corresponding chemical reagents into the double layer (at $G_i > 0$).

Let us write one more equation assuming, as usual, that the solution in the layer A is electrically neutral:

$$\sum_{i=1}^{n} z_ic_i = 0 \tag{51}$$

Equations (49) and (51) represent a closed system with respect to the required functions $c_i(u, v)$ and $\varphi(u, v)$. The system should be supplemented with initial and boundary conditions.

At any moment the following equations of electrochemical kinetics are to be obeyed at the crack front:

$$D_i\frac{\partial c_i}{\partial n} + \frac{D_iz_iF}{RT}c_i\frac{\partial\varphi}{\partial n} = f_i(c_i, \varphi) \tag{52}$$

The crack growth rate v may be found from the mass conservation law

$$v = \frac{MD_M}{\varepsilon\rho}\left(\frac{\partial c_M}{\partial n} + \frac{z_MF}{RT}c_M\frac{\partial\varphi}{\partial n}\right) \tag{53}$$

---

† If anode polarization is neglected.

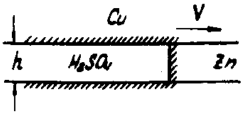

Figure 13. Dissolution of Zn plate inclusion in Cu base metal by H_2SO_4.

The following symbols are used: D_M, c_M, z_M, and M are the corresponding quantities referring to the ions of the metal being dissolved, n the direction of the normal to the crack front on the surface S; and ε the volume fraction of the metal anodic component being dissolved owing to the anode reaction at the crack root (ions of Mth species belong to one of the n species). The functions f_i are known from experiments or from the theory pertaining to the concrete anode reaction (in particular, if the flow of ions of ith species through the crack front is equal to zero, then $f_i = 0$).

The process under consideration is supposed to be isothermal; if there exist any considerable temperature gradients, the equation of heat conduction should be added to those derived:

$$\frac{\partial T}{\partial t} + (\mathbf{v}\ \mathrm{grad})T = \lambda(T - T_M) + Q \tag{54}$$

Here λ is the heat transfer coefficient at the metal–liquid boundary; T_M the temperature of the metal at the corresponding point of the surface S; and Q the portion of the total heat of reaction in the double layer associated with the solution. Because of good thermal conductivity of the metal and of the metal–solution contact, heat flows along the surface S may be neglected in comparison with the heat flow in the direction of the normal to that surface.

In the case of a plane slit and one-dimensional isothermal process the equations take the form

$$\begin{gathered}\frac{\partial c_i}{\partial t} + v_x \frac{\partial c_i}{\partial x} = D_i \frac{\partial^2 c_i}{\partial x^2} + \frac{D_i z_i F}{RT} \frac{\partial}{\partial x}\left(c_i \frac{\partial \varphi}{\partial x}\right) - \frac{G_i}{h} \\ \sum_{i=1}^{n} z_i c_i = 0\end{gathered} \tag{55}$$

For example, let the base metal (Cu) contain zinc inclusion in the shape of a thin plate of thickness h (Figure 13). In sulfuric acid this pair of metals forms a voltaic cell according to the chemical reaction

$$Zn + H_2SO_4 \rightleftarrows ZnSO_4 + H_2$$

In sulfuric acid copper is dissolved much less, so that its concentration may be neglected. In the course of time there appears a slit of width h whose front propagates at a constant rate in a steady regime.

The operation of this cell is analogous to that of the Volta cell: ions of H^+ come to the slit banks (the cathode), recombining there into molecules and neutralizing electrons ($2H^+ + 2e \rightarrow H_2$) with the formation of a gaseous layer;

SO_4^{2-} ions in solution bind Zn^{2+} ions, which pass into solution leaving their electrons on the zinc anode.

Let subscripts 1, 2, 3 refer to ions Zn^{2+}, H^+, and SO_4^{2-} respectively; the flow of Zn^{2+} and SO_4^{2-} ions to the cathode is zero, as is the flow of H^+ and SO_4^{2-} ions to the anode. Hence, in this case

$$G_1 = G_3 = 0, \qquad f_2 = f_3 = 0, \qquad f_1 = \frac{\varepsilon\rho V}{M}$$

$$z_1 = +2, \qquad z_2 = +1, \qquad z_3 = -2$$

In a steady regime the left-hand side of Eq. (55) vanishes and the crack may be regarded as semi-infinite ($x < 0$). In this case, concentration c_i and the potential φ should be given at infinity when $x \to -\infty$. The boundary value problem obtained can be solved numerically using a computer in any concrete case.

4.2. The Corrosion Crack Growth Rate

In the case of binary electrolytes the calculation can be carried out analytically. Dissolution of zinc inclusion in copper put into completely dissociated zinc sulfate may be regarded as a model of the process (Figure 14). Under the action of the emf of the voltaic cell, zinc ions pass into solution, and exactly the same number of zinc ions are discharged on copper, anodizing the silt banks. Dissolution of the copper, a nobler metal, may be neglected. In this case

$$c_1 = c_2 = c, \qquad z_1 = +2, \qquad z_2 = -2, \qquad G_2 = 0, \qquad \varepsilon = 1$$

Here subscript 1 refers to Zn^{2+} ions and subscript 2 to SO_4^{2-} ions.

For binary electrolytes the boundary value problem, according to (55), has the form

$$\begin{gathered} D_1\frac{d^2c}{dx^2} + \frac{D_1 z_1 F}{RT}\frac{d}{dx}\left(c\frac{d\varphi}{dx}\right) = \frac{1}{h}G_1(c, \varphi) \\ D_2\frac{d^2c}{dx^2} + \frac{D_2 z_2 F}{RT}\frac{d}{dx}\left(c\frac{d\varphi}{dx}\right) = 0 \\ (-\infty < x < 0) \end{gathered} \tag{56}$$

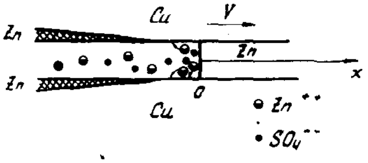

Figure 14. Transport processes in electrolyte by dissolution of Zn inclusion.

At $x = 0$, $\varphi = \varphi_0$,

$$D_2\frac{dc}{dx} + \frac{D_2 z_2 F}{RT}c\frac{d\varphi}{dx} = 0$$

At $x \to -\infty$, $c = c_\infty$ and $\varphi = \varphi_\infty$.

Here we put

$$c_1 = c, \qquad c_2 = -\frac{z_1}{z_2}c$$

Now we integrate the second equation, using the boundary conditions

$$c = c_\infty \exp\left[-\frac{z_2 F}{RT}(\varphi - \varphi_\infty)\right] \tag{57}$$

Substituting this expression for c into the first equation of (56), we get the following equation for the potential:

$$\frac{D_1 F c_\infty (z_1 - z_2)}{RT}\frac{d}{dx}\left\{\frac{d\varphi}{dx}\exp\left[-\frac{z_2 F}{RT}(\varphi - \varphi_\infty)\right]\right\} = \frac{1}{h}G_1(c, \varphi) \tag{58}$$

Let the act of discharge correspond to the equation

$$M^{+z_1} + z_1 e \to M$$

where M^{+z_1} are the particles present in solution which undergo discharge with taking on z_1 electrons, and M are the particles originated immediately after the discharge and bound to the electrode surface by adsorption (or other) forces.

Taking account of Eq. (16), one can express Eq. (58) in the form

$$\frac{d^2\phi}{dx^2} + \lambda\left(\frac{d\phi}{dx}\right)^2 = G(\phi) \qquad (0 \leq \phi \leq 1) \tag{59}$$

Here

$$\phi = \frac{\varphi - \varphi_\infty}{\varphi_0 - \varphi_\infty}, \qquad \lambda = -\frac{z_2 F(\varphi_0 - \varphi_\infty)}{RT}$$

$$G(\phi) = \frac{RT}{D_1 F c_\infty h (z_1 - z_2)(\varphi_0 - \varphi_\infty)}\exp\left(-\frac{\alpha z_1 F \varphi_\infty}{RT}\right)$$

$$\times\left\{K_1 c_\infty \exp\frac{\alpha\lambda z_1 \phi}{z_2} - k_2 c'_M \exp\left[\frac{F z_1 \varphi_\infty}{RT} - \frac{\lambda\phi}{z^2}(z_1 - \alpha z_1 + z_2)\right]\right\}$$

The quantity φ_∞ represents the equilibrium potential at the interface metal–electrolyte solution.

Denote

$$p = \frac{d\phi}{dx} \tag{60}$$

Let us transform Eq. (59) in terms of the variables p and ϕ:

$$p\frac{dp}{d\phi} + \lambda p^2 = G(\phi) \tag{61}$$

Denote

$$y = p^2 \tag{62}$$

In the variables y, ϕ the following linear equation of the first order is obtained by

$$\frac{dy}{d\phi} + 2\lambda y = 2G(\phi) \tag{63}$$

The solution of this equation satisfying the boundary condition at $\phi = 0$, $y = 0$ can be expressed in the form

$$y = 2\exp(-2\lambda\phi)\int_{\phi}^{0} G(x)\, e^{2\lambda x}\, dx \tag{64}$$

Taking (60) and (62) into account, we find the final solution of Eq. (59) satisfying the boundary condition at $x = 0$, $\phi = 1$:

$$2^{1/2}x = \int_{1}^{\phi} \frac{e^{\lambda\phi}\, d\phi}{[\int_{\phi}^{0} G(x)\, e^{2\lambda x}\, dx]^{1/2}} \tag{65}$$

By means of formulas (53), (57), and (64) we find the crack growth rate sought for:

$$\begin{aligned} V &= \frac{mD_1}{\varepsilon\rho}\left(\frac{dc}{dx} + \frac{z_1F}{RT}c\frac{d\varphi}{dx}\right)\Bigg|_{\text{at } x=0} \\ &= \frac{mD_1F(z_1 - z_2)}{\varepsilon\rho RT}\left[\int_{1}^{0} G(x)\, e^{2\lambda x}\, dx\right]^{1/2} \\ &= \frac{2^{1/2}D_1c_\infty mF(z_1 - z_2)(\varphi_0 - \varphi_\infty)}{\varepsilon\rho RT}\left[\int_{1}^{0} G(x)\, e^{2\lambda x}\, dx\right]^{1/2} \end{aligned} \tag{66}$$

In the case when ionization at the slit banks can be neglected (i.e., $k_2 = 0$), the quantity $G(\varphi)$, in accordance with (59), has the form

$$G(\phi) = \frac{k_1RT}{D_1Fh(z_1 - z_2)(\varphi_0 - \varphi_\infty)}\exp\left(\frac{\alpha\lambda z_1}{z_2}\phi - \frac{\alpha z_1F\varphi_\infty}{RT}\right) \tag{67}$$

In this case the expression (66) permits the following simplification:

$$\begin{aligned} V &= \frac{mc_\infty}{\varepsilon\rho}\exp\left(-\frac{\alpha z_1F\varphi_\infty}{2RT}\right) \\ &\quad\times\left\{\frac{2k_1D_1(z_2 - z_1)}{z_2(2 + \alpha z_1z_2^{-1})}[1 - e^{\lambda(2+\alpha z_1z_2^{-1})}]\right\}^{1/2} \end{aligned} \tag{68}$$

The value λ is negative because $\varphi_0 - \varphi_\infty < 0$. At $\varphi_0 - \varphi_\infty > 0$, when the positions of the cathode and anode are interchanged, the crack growth rate acquires an imaginary value, which is in accord with the physical meaning of the problem.

The potential difference $\varphi_0 - \varphi_\infty$ is easily found from the solution obtained and Butler–Volmer equation in the case of anode polarization by means of the following condition:

$$D_1 \frac{dc}{dx} + \frac{D_1 z_1 F}{RT} c \frac{d\varphi}{dx} = -k_{2a} \exp\left[-\frac{(1-\alpha_a) z_1 F}{RT} \varphi\right] \qquad \text{at } x = 0 \tag{69}$$

By means of (57), (64), and (69) one finds

$$\begin{aligned} &\frac{F D_1 (z_1 - z_2)(\varphi_0 - \varphi_\infty)}{RT} \left[2\, e^{-2\lambda} \int_1^0 G(x)\, e^{2\lambda x}\, dx\right]^{1/2} \\ &\qquad = -k_{2a} \exp\left[-\frac{(1-\alpha_a) z_1 F \varphi_0}{RT}\right] \end{aligned} \tag{70}$$

Thus, according to Eq. (67), the following expression is obtained:

$$\lambda = \frac{z_2}{z_1(2 - \alpha - 2\alpha_a)} \left\{\frac{z_1 F \varphi_\infty}{RT}(2 - \alpha - 2\alpha_a) + \ln\left[\frac{2 D_1 k_1 |z_1 - z_2|}{h k_{2a}^2 |2z_2 + \alpha z_1|}\right]\right\} \tag{71}$$

Hence, the potential difference $\varphi_0 - \varphi_\infty$ decreases monotonically as the crack width increases.

Substituting the latter expression for λ into (68), one obtains

$$V = \frac{m c_\infty}{\varepsilon \rho} \left[\frac{2 k_1 D_1 (z_2 - z_1)}{z_2 (2 + \alpha z_1 z_2^{-1})}\right]^{1/2} \exp\left(-\frac{\alpha z_1 F \varphi_\infty}{2RT}\right) f_0(h) \tag{72}$$

Here

$$f_0(h) = \left\{\frac{1}{h}\left[1 - \left(\frac{h}{h_0}\right)^3\right]\right\}^{1/2}$$

$$h_0 = \frac{2 k_1 D_1 |z_1 - z_2|}{k_{2a}^2 |2z_2 + \alpha z_1|} \exp\left[\frac{z_1 F \varphi_\infty}{RT}\left(2 - \alpha - 2\alpha_a\right)\right]$$

$$\zeta = -\frac{2z_2 + \alpha z_1}{z_1(2 - \alpha - 2\alpha_a)}$$

In the case of dissolving zinc inclusion in zinc sulfate (Figure 14) the crack growth rate at $\alpha = \alpha_a = 1/2$ will become, according to (72),

$$V = \frac{2 m c_\infty}{\rho} \left(\frac{2}{3} k_1 D_1\right)^{1/2} \exp\left(-\frac{F \varphi_\infty}{2RT}\right) \left\{\frac{1}{h}\left[1 - \left(\frac{h}{h_0}\right)^3\right]\right\}^{1/2} \tag{73}$$

where

$$h_0 = \frac{8 k_1 D_1}{3 k_{2a}^2} \exp\left(\frac{F \varphi_\infty}{RT}\right)$$

The formula (73) shows that the less the slit width, the greater the crack growth rate (the function f_0 decreases monotonically with the growth of h, vanishing at $h = h_0$, when the potential φ_0 becomes equal to the equilibrium potential φ_∞). The slit does not grow at $h > h_0$. Physically, this result is quite natural, since the anode current density, governing the crack growth rate, increases with decrease in the slit opening.

Now let us consider the structure of the zone in which the electrochemical reaction occurs. The width of this zone, x_0, is finite; it is easily found by means of the formula (65):

$$x_0 = \frac{1}{2^{1/2}} \int_1^0 \frac{e^{\lambda\phi}\, d\phi}{\left[\int_\phi^0 G(x)\, e^{2\lambda x}\, dx\right]^{1/2}} \tag{74}$$

Neglecting the cathode ionization, when $G(x)$ has the form of (67), we find

$$x_0 = \left[\frac{\delta D_1 h(z_2 - z_1)}{2k_1 z_2}\right]^{1/2} \exp\left(\frac{\alpha z_1 F \varphi_\infty}{2RT}\right) \int_{e^\lambda}^1 \frac{dt}{(1 - t^\delta)^{1/2}} \tag{75}$$

where

$$\delta = 2 + (\alpha z_1 / z_2)$$

It is easy to comprehend that the zone width, x_0, decreases monotonically as the dimensionless potential difference, λ, decreases, vanishing at $\varphi_0 = \varphi_\infty$. According to the formulas (57), (65), and (67), we can draw the conclusion that the electric potential and the ion concentration grow monotonically in the reaction zone with increasing x. The qualitative structure of the zone is depicted in Figure 15.

The solution obtained corresponds to the selective corrosion at $\varepsilon = 1$, when one of the alloy components, lying as a continuous layer in the base metal, is dissolved. This model may be likely applied to the propagation of intercrystaline corrosion cracks and pits when primarily intermetal compounds located between grains are exposed to dissolving. The above analysis shows that in this particular case there exists the mechanism of self-sustained propagation of cracks and pits which can lead to destruction of the body even without external load.

However, the cathode and anode reactions cannot always be considered as separated in space: very often they on the average match within the same area. Since the conditions of occurrence of electrode reactions may differ in different parts of the body surface, current irregularity appears leading to "cathodeness"

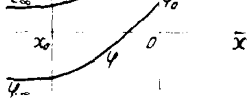

Figure 15. Structure of the zone in which electrochemical reactions occur.

or "anodeness" of some or other parts of the surface. The necessary condition for the crack propagation due to the electrochemical mechanism in the absence of external loads consists in the pronounced anodeness of its root surface with respect to its sides; in this case the reaction of ionization of the metal (or of some metal components) at the crack root must proceed simultaneously with the crack side reactions, banks serving primarily as cathodes.

In the presence of external loads when the width of the slit near its tip is approximately equal to the crack opening $2v_0$, the crack growth rate will be a monotonically decreasing function of the stress intensity factor as is seen from (72) (since $v_0 \sim K_I^2$). Such a crack grows quickly at first, while K_I is small; then, when K_I increases (under constant external loads), and the crack is dulled, its growth slows down and the crack may stop altogether (at $2v_0 \sim h_0$). This phenomenon, which at first sight seems paradoxical, was observed while experimenting with corrosion cracks under constant tensile loads (e.g., see Logan's book$^{(1)}$). Cracks of this type are characterized by simultaneous and steady development of many cracks in contrast to the common case of the monotonically increasing function $f(K_I)$ [where $\dot{l} = f(K_I)$] when only one, most dangerous, crack is primarily developed.

The most important electrode reactions in practice (alongside with ionization and deposition of metals) are hydrogen and oxygen deposition as well as metal oxidation. Aqueous media always contain extremely active ions of hydrogen and hydroxyl and besides, as a rule, some amount of dissolved oxygen. Hence, follows a very dangerous role of any aqueous media as stimuli of electrochemical corrosion.

4.3. The Tunnel Model of the Crack Growth

The model considered is easily generalized to the case when anode areas do not form a continuous layer, but are distributed in the bulk of the body uniformly, arbitrarily, and at random, causing pits (microtunnels).

At first let us derive general equations of motion of the electrolyte solutions in tunnels; the tunnel is understood as a cavity with a constant cross section; the length of this cavity is much larger than a characteristic linear dimension of the cross section (Figure 16).

Let us introduce the orthogonal coordinate system xyz so that the plane yz coincide with the plane of some cross section of the tunnel S_F (Figure 16). The following assumptions should be introduced: (i) the liquid velocity $\mathbf{v}$ at any point of the section S_F does not depend upon y and z, the components of the

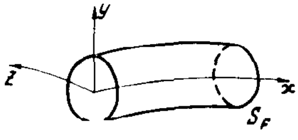

Figure 16. A curvilinear rod inclusion of dissolving metal in base one.

vector v along the axes y and z being equal to zero; (ii) the derivative $\partial\varphi/\partial x$ at any point of the section S_F is independent of y and z. Then we apply the following operator to the general equations (1):

$$\frac{1}{S_F}\iint\limits_{S_F} dy\,dz$$

where S_F stands both for the domain (the cross section) and its area.

Now let us introduce a mean concentration value averaged over the cross section:

$$\frac{1}{S_F}\iint\limits_{S_F} c_i\,dy\,dz$$

and designate as G_i the flow of ions of ith species into the double layer per unit time, per unit area of the side surface of the tunnel S_B:

$$G_i(c_i, \varphi) = \frac{1}{P_F}\oint_{P_F}\left(D_i\frac{\partial c_i}{\partial n} + \frac{D_i z_i F}{RT}c_i\frac{\partial\varphi}{\partial n}\right)ds$$

Here P_F is the closed contour of the cross section S_F and the length of this contour (its perimeter), and n the normal to the contour P_F in the cross-sectional plane. The function $G_i(c_i, \varphi)$ is supposed to be known (see Section 2).

After simple transformations using Green's formula we obtain the following equations:

$$\frac{\partial c_i}{\partial t} + v_x\frac{\partial c_i}{\partial x} = D_i\frac{\partial^2 c_i}{\partial x^2} + \frac{D_i z_i F}{RT}\frac{\partial}{\partial x}\left(c_i\frac{\partial\varphi}{\partial x}\right)$$

$$-\frac{P_F}{S_F}G_i(c_i, \varphi), \qquad \sum z_i c_i = 0 \tag{76}$$

$$[c_i = c_i(x, t), \varphi = \varphi(x, t)]$$

Here the coordinate x is reckoned along the generatrix of the tunnel lateral surface, and the mean value of concentration averaged over the cross section is denoted by c_i.

The absolute term in the equations (76) governs the cathode current magnitude; the larger this term, the larger the anode current and the tunnel growth rate. Therefore, all other things being equal, corrosion rate will increase as the ratio P_F/S_F increases.

The above solution (56)–(75) also holds for the case of tunnel development; in this case it is enough to substitute h by the ratio S_F/P_F in the corresponding formulas.

Now let us introduce the following reasonable assumption: the average value of the ratio S_F/P_F under the conditions of natural corrosion of commercial metals is a certain constant of the given system depending on the chemical composition of the metal and the electrolyte as well as on the metal structure.

It is reasonable to believe that corrosion cracks in commercial metals in the presence of aqueous media develop in accordance with the following electrochemical mechanism: (i) dissolution of anode areas and formation of microtunnels (pits) on the crack root, (ii) rupture of the pit-weakened layer on the crack root under the effect of external loads, and (iii) hydrodynamic electrolyte flow into the cavity of the crack formed. It is clear that the first, electrochemical, stage depending upon transport processes within the microtunnels (pits) represents the slowest stage of the process which governs the crack growth rate. Therefore the latter is equal to the pit growth rate.

According to assumptions formulated, Eq. (76) governing the pit growth rate does not contain any parameters associated with the crack opening displacement and crack dimensions as well as external loads.

Consequently, this model leads to the conclusion that the growth rate of corrosion cracks is a certain constant of the metal–electrolyte system under study; it is independent of external loads, and the crack length, and stress intensity factor. However, the load should be great enough to tear the metal weakened by pits in the vicinity of the crack tip (i.e., $K_I > K_{ISCC}$).

Thus, one can draw the following conclusions[6,60,61]:

i. The $\dot{l}$–K_I diagram of the electrochemical mechanism of crack development has the shape (see Figure 17)

$$\dot{l} = \begin{cases} 0 & \text{for } K_I < K_{ISCC} \\ \text{const} & \text{for } K_{ISCC} < K_I < K_{IC} \end{cases} \tag{77}$$

ii. The constant rate can be calculated if the kinetics of leading reactions and some microstructural data are known.

iii. The rate of corrosion crack growth is a thermoactivated process whose energy of activation is governed by leading electrode and transport processes.

iv. The cracks in the systems with the diagram (77) are bound to branching when the value of K_I is greater than some critical value K_{Ib}. Therefore cracks in such systems, while propagating, form characteristic treelike structures. The branching can be explained by the fact that the pitting at the crack root propagates equally well along all the anode directions (and not only in the crack plane). However, lateral corrosion crack branches, while unloading with the main crack growth, get into the region $K_I < K_{ISCC}$ and stop growing, if $K_I < K_{Ib}$.

v. The initial smooth surface of a specimen extended is covered with a lot of cracks propagating inside in the process of electrochemical corrosion. This is

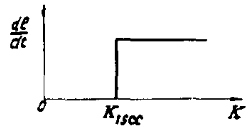

Figure 17. $\dot{l}$–K_I diagram for electrochemical mechanism of subcritical crack growth.

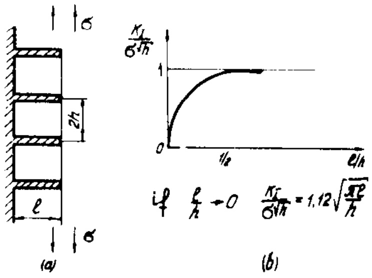
σ
2h
l
σ
(a)
$\frac{K_I}{\sigma\sqrt{h}}$
1
0
1/2
l/h
if $\frac{l}{h} \to 0$ $\frac{K_I}{\sigma\sqrt{h}} = 1{,}12\sqrt{\frac{\pi l}{h}}$
(b)

Figure 18. Extension of a half-plane with a periodical system of identical wedge cracks: (a) geometrical configuration under study, (b) crack length dependence of stress intensity factor.

obvious within the framework of our model, for the initial pitting takes place over the entire surface of the metal (and the most favorable conditions for its development are realized at the crack root). Since the crack growth rate is independent of K_I (at $K_{ISCC} < K_I < K_{IC}$), many parallel cracks may grow independently at the same rate.

Indeed, when a half-plane with a periodical system of identical cracks propagating from the free boundary is being extended, the stress intensity factor K_I equals, according to the exact solution$^{(6)}$ (see Figure 18)

$$K_I = \sigma h^{1/2} \qquad \text{at} \quad \frac{l}{h} \gtrsim 2 \tag{78}$$

i.e., it is independent of the length of the cracks. Therefore in the range $K_{ISCC} < K_I < K_{Ib}$ the growth of all the cracks is stable and autonomous. In the range $K_{Ib} < K_I < K_{IC}$ crack propagation is not stable since branching and reproduction of cracks lead to decrease in h, i.e., to decrease in K_I, according to (78). Hence we get the following estimate of the distance between corrosion cracks propagating steadily into the bulk of a smooth specimen:

$$\frac{K_{ISCC}^2}{\sigma^2} < h < \frac{K_{Ib}^2}{\sigma^2} \tag{79}$$

In particular, the greater the stress applied, the greater the number of cracks per unit surface.

It should be noted that such a character of metal surface cracking would be impossible, if the mechanism of local crack propagation at its tip depended on the external structure of the crack tip, i.e., on K_I (as is the case, for instance, for the mechanism of local hydrogen embrittlement; see below, Section 5). Indeed, in the latter case the simultaneous propagation of many parallel cracks is unstable: as soon as, owing to some casual circumstances, one of the cracks outruns the others, the stress intensity factor upon it will be greater than upon the others, and, hence, the growth rate of this crack will also increase (whereas upon neighboring cracks the intensity factor and growth rate will decrease), and the further, the greater, so that only one, the most dangerous, crack remains in the long run.

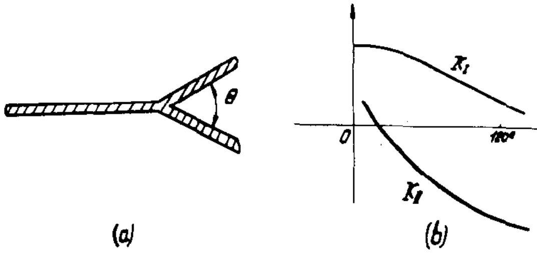

Figure 19. Forked crack: (a) configuration of semi-infinite crack, (b) branching angle dependence of super-fine stress intensity factors, k_{I} and k_{II}.

The morphological character of cracking of the surface of a smooth specimen and the crack by the electrochemical mechanism is closely similar to that in the case of the adsorption mechanism of crack growth (the theory of the latter mechanism is developed in Chapter 7, Section 4, of Reference 6; it is also shown there that the generally accepted explanation of the adsorption effect according to the Griffith theory is wrong). The most typical effect of the latter mechanism is exhibited in the liquid metal–solid metal systems. However, in adsorption systems the crack growth is governed by nonlocal transport processes of the liquid medium in the crack; therefore, a common $\dot{l}$–K_I diagram in adsorption systems does not exist. At one and the same K_I the crack growth rate may vary depending on initial conditions of liquid or gaseous medium supply to the crack tip. The adsorption effect for some high-strength steels (in isobutyl alcohol) was demonstrated by Nikiforchin.(62)

The quantity K_{Ib} may be estimated by means of the solution of the problem of a crack with two small symmetrical branches (see Figure 19). Suppose that in the area weakened by pits in the vicinity of the crack tip there appeared two identical rectilinear and symmetrically spaced rupture branches whose lengths are small compared to the crack length. The size of the plastic area at the crack tip is considered small compared to the length of branches. The main crack may be considered as semi-infinite. With these assumptions, in the vicinity of tips of the branches there appears a super-fine structure characteristic for brittle cracks and described by stress intensity factors k_{I} and k_{II}. Dimensional analysis yields

$$k_{\mathrm{I}} = K_I f_1(\theta), \qquad k_{\mathrm{II}} = K_I f_2(\theta) \tag{80}$$

where θ is the angle between branches, f_1 and f_2 some dimensionless functions of θ, K_I the stress intensity factor at the tip of the main crack (in the local situation shown in Figure 19 it describes the elastic field at infinity).

According to the solution of Reference 63, the functions $f_1(\theta)$ and $f_2(\theta)$ decrease monotonically with the growth of θ from 0 to $\theta \sim 140°$, f_1 being always positive, and f_2 vanishing at $\theta = 30° + 40°$ [at this point the value of f_1 is approximately equal to $1/(2)^{1/2}$]. It is quite natural to suppose that branches would be open-mode cracks,(16) hence the angle, θ, between different branches of a corrosion crack must be equal to 30° + 40° (the value of k_{II} being equal to 0). For the development of different branches after their formation it is necessary that the value of k_I should not be less than the value of K_{ISCC}. Hence, according to the solution mentioned, we get the following estimate:

$$K_{Ib} \approx 1.4\, K_{ISCC} \tag{81}$$

A similar estimate can be obtained based on the energy assumption by Speidel(64) for any angle of branching θ; this assumption is equivalent to Eq. (81) at $\theta = 30° + 40°$. According to Carter's experiments,(65) another correlation takes place for many high-strength steels:

$$K_{Ib} = (2\text{–}4)\, K_{ISCC} \tag{82}$$

Checking of theoretical reasoning which led to Eq. (81) shows that the latter is valid only in the limiting case when the initial perturbation (branching) is large as compared to the characteristic dimensions of the grain and plastic zone at the crack tip. Generally, a greater value of K_I is necessary for the initial ruptures of this size to appear. Therefore, Eq. (81) gives only the lower limit of K_{Ib}; the inequality

$$K_{Ib} \gtrsim 1.4\, K_{ISCC} \tag{83}$$

which is in conformity with (82), seems to be more realistic.

Certainly, the influence of microstructure (i.e., of a casual factor) and plastic deformations may lead to considerable deviations from this correlation in each particular case. At $K_I < K_{Ib}$ initial random ruptures at the crack front caused by uniform pitting and the effect of external field, do not propagate beyond the range of action of casual factors of microstructure (which is of the order of grain dimensions). That is why such fine microcracks at the crack front should not be attributed to the phenomenon of crack branching; their rise is possible at any level of external loadings and is explained by the electrochemical mechanism of the growth of pits and cracks.

It is quite obvious that the tunnel model is able to explain also the existence of two plateaus in the $\dot{l}$–K_I diagram (see Figure 20a), which were observed in Speidel's experiments(64) for certain high-strength aluminum alloys. (It should be mentioned that the crack growth rate at different plateaus varied in 10–1000 times.) For this purpose it is enough to assume that in the

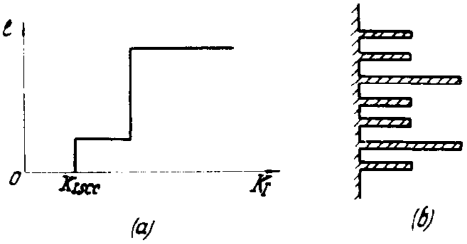

Figure 20. $\dot{l}$–K diagram with two plateaus: (a) sketch of the diagram, (b) two systems of pit corresponding to two components dissolved at crack tip.

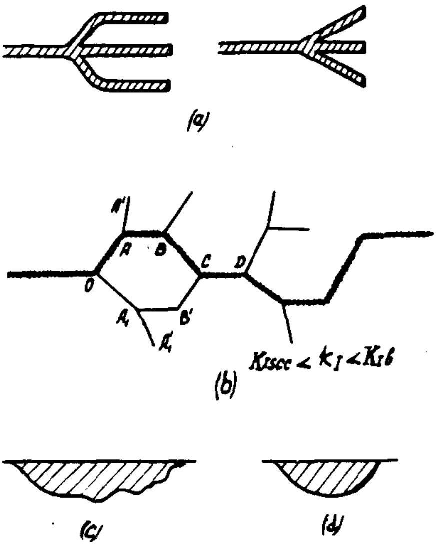

Figure 21. Morphology of corrosion cracks: (a) unstable configuration of tridentlike crack, (b) zig-zag trajectory of corrosion crack with plateau diagram, (c) uneven front of edge corrosion crack, (d) nail-form edge crack typical for fatigue and/or hydrogen-enhanced cracks.

alloy there are two soluble components, one of which dissolves very quickly, but is present in small quantities, and the other one dissolves much slower, but is present in much greater quantities (see Figure 20b).

The crack branching leads to the decrease in the local stress intensity factor k_I, and, hence, to the delay of the crack growth. Because of this fact, the brittle growth of the corrosion crack begins not at $K_I = K_{IC}$, but at $K_I = K_{IF}$ where $K_{IF} > K_{IC}$. Let us prove the following estimate for branching corrosion cracks:

$$K_{IF} \gtrsim 1.4\, K_{IC} \tag{84}$$

Indeed, the brittle propagation of the main branched crack clearly corresponds to the condition of local fracture $k_I = K_{IC}$ at the branch tip (see Figure 18).

Note that estimates (83) and (84) result also from analogous considerations for a forklike crack [see Figure 7 and formula (43)].

Let us also consider the following morphological features of corrosion cracks: (i) instability of a triple tridentlike crack (see Figure 21a), (ii) zig-zag nature of the crack trajectory (see Figure 21b), and (iii) irregular, random character of the crack front propagating into the bulk of the metal (see Figure 21c; compare it with Figure 21d in which you can see the front of an equistrong crack, characteristic for systems with monotonically increasing l–K_I diagrams).

The instability of a tridentlike configuration follows from the fact that at a small advance of the central or two lateral branches (of the order of the branch spacing) the branches fell behind unloaded almost completely and stop growing. Analogous reasoning is valid for a branched crack with three, four, etc.

branches. Thus the most stable configuration corresponds to a single crack or a branched crack with two branches.

When $K_{ISCC} < k_I < K_{Ib}$, a single crack tends to stable branching (point O in Figure 21b; the angle AOA' equals 30°–40°). Each branch emerging from the fine structure of the point O, produces, in its turn, two branches (see points A and A' in Figure 21b, angles $B'AA_1$ and $B'A'A'_1$ being equal to 30°–40°), and so on. Lateral branches $A'A'_1$ and AA_1 get into the unloaded area and do not propagate. Therefore the trajectory of the main crack has a zig-zag nature (shown approximately in bold in Figure 21b). The length of the segments OA, AB, BC, CD, etc., is, to a great extent, random, but it is obvious that with K_I increasing the length of branches must decrease tending to zero when $k_I \rightarrow K_{IB}$. The length of the segment OA and others, naturally, must be sufficiently great so that at the points A, B, etc., the condition $k_I = K_{IB}$ be satisfied. When $k_I \geq K_{IB}$, the dimension of separate zig-zags of the crack has the order of grain size ("zero" in continum approximation). Hence the estimate (84) is valid only if $k_I \leq K_{IB}$, i.e., if $K_{IF} \leq 1.4\, K_{Ib}$.

If the curve on $\dot{l}$-K_I diagram rises monotonically, the initial crack of arbitrary shape puts in line its front during subcritical growth, the stress intensity factor K_I becoming the same along the whole crack front (the concept of "equistrong" crack[(6)]). For a plateau diagram all the random irregularities of the initial crack front expand with almost no smoothing (see Figure 20c).

4.4. Analysis of Some Experimental Data

Smith, Piper, and Downey[(54)] investigated the crack growth by testing center-notched specimens of Ti–8Al–1Mo–1V alloy in 3.5% aqueous solution of NaCl. Figure 22 shows points obtained in testing the dependence of crack growth rate upon the stress intensity factor. These data indicate that titanium alloys with local stress concentrations, if kept in a chloride environment at ambient temperatures, may fail in stress corrosion. As seen from Figure 22, at $K_I < 21$ ksi(in.)$^{1/2}$ the crack growth was not observed, then with an increase of K_I the crack velocity grew rapidly up to the saturation regime.

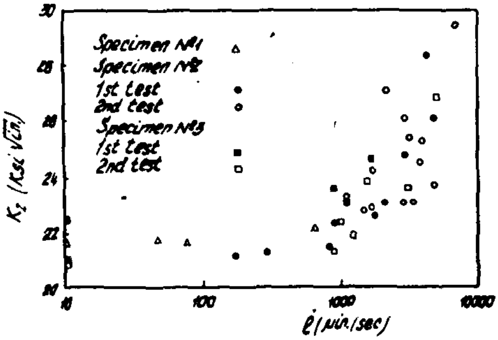

Figure 22. $\dot{l}$-K_I diagram (Ti–8Al–1Mo–1V alloy in 3.5% aqueous NaCl solution[(54)]).

Of much interest are experiments by Carter, who was the first to advance and to prove the K_{Ib} concept.(65) In a test with AISI 4340 steel containing 2.15% Si, he observed a spontaneous changing-over of the mechanism of electrochemical corrosion to hydrogen embrittlement. This happened because the simultaneous process of electrolytic-hydrogen diffusion turned to be the fastest, after the subcritical crack growth rate equaled 0.83 μin./sec and K_I approached $2K_{ISCC} = 44$ ksi(in.)$^{1/2}$. In the range of stress field intensities 18 to 44 ksi(in.)$^{1/2}$, the corrosion crack growth rate remained constant, which agrees with the tunnel model of electrochemical dissolution.

A similar phenomenon was observed by Mostovoy, Smith, Lingwall, and Rippling(66) who tested 250-grade maraging steel in 3.5% aqueous solution of NaCl. Machined specimens were austenitized at 871°C (1600°F) followed by gradual cooling. Aging at 482°C (900°F) took 3 hr. After these treatments, the yield strength $\sigma_{0.2}$ was 246 ksi. Side-grooved specimens gave a sharp rise in crack growth rate when K_I exceeded 66 ksi(in.)$^{1/2}$ (from this point, the rupture proceeded according to the mechanism of hydrogen embrittlement), even though below this level, in the range of K_I between 42 and 66 ksi(in.)$^{1/2}$, the process of rupture developed at a constant rate of crack growth of 0.52 μin./sec.

Carter also carried out a similar experiment with 250-grade maraging steel.(65) He also observed a constant growth rate of corrosion cracks, but he did not report anything on the spontaneous change-over of the growth mechanism for this material. When experimenting with the AISI 4340 steel containing (1.08% Si), Carter(65) observed a steady crack propagation at a constant rate of 0.16 μin./sec from $K_I = 31$ ksi(in.)$^{1/2}$ to the complete failure.

Mostovoy, Smith, Lingwall, and Rippling(66) tested 9Ni–4Co–0.45C alloy in 3.5% aqueous NaCl solution. The alloy was heated to 843–871°C (1550–1600°F) for 1 hr, air cooled, heated to 800–828°C (1472–1522°F) for 1 hr, quenched in salt at 236°C (457°F), held for 6 hr, and air cooled. After this heat treatment, the yield strength $\sigma_{0.2}$ was 200 ksi. The corrosion crack growth rate of 11 μin./sec proved to be greater than the value obtained by Carter for the AISI 4340 steel with (1.08% Si). This rate could be observed at all values of K_I from 23 to 80 ksi(in.)$^{1/2}$, two specimens having failed at 54 ksi(in.)$^{1/2}$, i.e., long before the maximum was reached.

Somewhat earlier, Carter(65) studied the stress corrosion of 9Ni–4Co–0.45C and 9Ni–4Co–0.3C steels after various heat treatments; the fracture proceeded at a constant rate, but the crack developed by branching. A branching of the crack was also observed(66) when 250-grade maraging steel was tested.

Notably, when the crack growth rate increases rapidly with an increase in K_I (this happens at the transition from zero to the saturation level), the side branches grow slowly and produce practically no adverse effect on the propagation of the trunk crack. This may be explained by the fact that, at small K_I, the trunk crack propagation displaces the stress field outside the zone of branching.

Carter(67) and Mostovoy *et al.*(66) explored the process of crack initiation and propagation in low-alloy 300 M steel submerged into 3.5% NaCl solution. The specimens subjected to similar heat treatments which included austenitizing at 871°C for 1 hr, oil quenching and tempering for 2 hr, plus aging at 288°C (560°F) for 2 hr to a tensile strength $\sigma_b = 302$ ksi and yield strength $\sigma_{0.2} = 253$ ksi or $\sigma_{0.2} = 233$ ksi. The dependence of the crack growth rate on stress intensity under static loads was determined by varying the value of K_I from 20 to 45 ksi(in.)$^{1/2}$. Within this range of K_I values the crack growth rate is constant, independent of K_I, and equal to 35 μin./sec. Carter's(67) measurements of corrosion crack growth rate yielded a value of 0.83 μin./sec, or 40 times smaller than those obtained by Mostovoy, Smith, Lingwall, and Rippling.(66)

Carter(68) also tested samples of 350-grade maraging steel in 3.5% solution of NaCl. The samples had been heat treated by 8 hr of aging at 482°C ($\sigma_b = 302$ ksi, $\sigma_{0.2} = 300$ ksi) or 3 hr of aging at 510°C (950°F) ($\sigma_b = 290$ ksi, $\sigma_{0.2} = 267$ ksi). The results of the experiments indicate that the samples with the highest values of yield strength were comparatively stable to stress corrosion. The crack growth rate was constant—it amounted to 0.1 μin./sec, the quantity K_{ISCC} was equal to 10 ksi(in.)$^{1/2}$.

In Reference 65 samples of 300-grade maraging steel were tested in the same environment. The metal, aged at 480°C (896°F) for 6 hr, had a yield strength of 290 ksi. The experimental points shown in Figure 23 indicate that the corrosion crack growth rate, equal to 0.042 μin./sec, does not depend on the stress intensity factor K_I in range from 33 ksi(in.)$^{1/2}$ to K_{IC}.

An investigation on Ti–11.5Mo–6Zr–4.5Sn alloy was carried out by Feeney and Blackburn.(69) Specimens with a fatigue crack propagating into the material from the top edge were loaded in cantilever bending. Aqueous solutions of 0.6 *M* KCl, 5 *M* KI, and 3.5% NaCl were used as the corrosive media, while distilled water served as a reference. The titanium alloy was austenitized for 1 hr at 871°C and aged (1) for 100 hr at 480°C or (2) for 16 hr at 629°C (1164°F). The yield strength of heat-treated specimens amounted to 218 ksi.

Specimens aged in (1) were tested in 3.5% aqueous NaCl solutions. The threshold stress intensity K_{ISCC} was 26 ksi(in.)$^{1/2}$, and the magnitude of

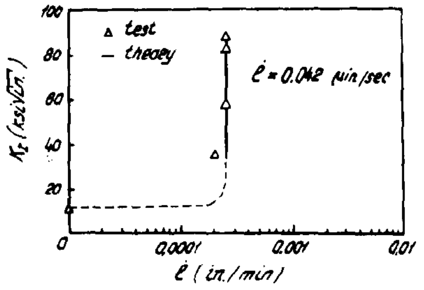

Figure 23. l-K_I diagram (300-grade maraging steel in 3.5% aqueous NaCl solution(65)).

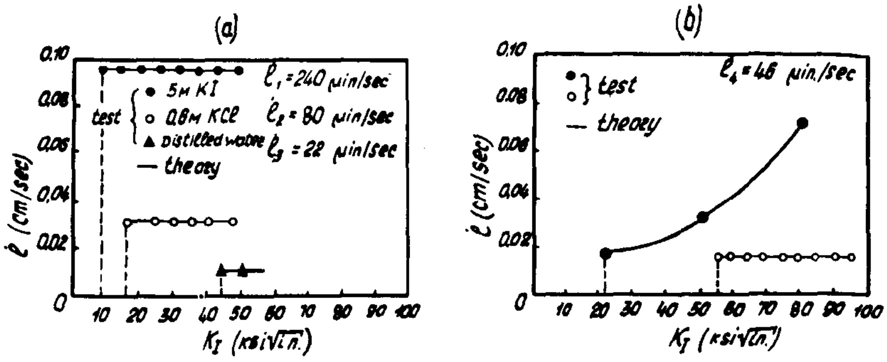

Figure 24. $\dot{l}$–K_I diagram (Ti–11.5Mo–6Zr–4.5Sn alloy in 0.6 M KCl, 5 M KI, and 3.5% NaCl solutions and in distilled water$^{(69)}$): (a) aged 100 hr at 480°C, (b) aged 16 hr at 629°C.

K_{ISCC}/K_{IC} proved to be 0.4. The rest of their experimental data are shown in Figure 24, where filled circles stand for tests in 5 M aqueous solution of KI, unfilled circles for 0.6 M KCl, and triangles for distilled water. The corresponding crack growth rates amounted to 240 μin./sec, 80 μin./sec, and 22 μin./sec. As the crack growth rate diminishes in various environments, there appears a rise in K_{ISCC}. As will be shown below in Section 5, one of the curves in Figure 24b corresponds to the hydrogen embrittlement mechanism.

The subcritical crack growth rates in the titanium alloy immersed into aqueous solutions of KCl and KI are one order below those found in 3.5% solutions of NaCl. The composition of the corrosive medium may not only affect the initiation of the crack, but also produce a considerable effect upon the rate of its growth.

The saturation regime of the crack growth in a titanium 8Al–1Mo–IV alloy was observed by Bucci and Paris.$^{(70)}$

It should be noted that Krafft and Mulherin$^{(71)}$ attributed the experimentally observed interrupted crack growth to rupture of the base material between tunnels developed due to dissolution of the anode at the crack front.

It is useful to notice the following. If the mechanism of the corrosion crack growth is due to anodic ionization of oxygen or to the growth and fracture of an oxide film on a metal surface, then, in this case, the crack growth rate would depend essentially upon the transport process of supplying oxygen into the crack mouth from the external environment. In particular, it would depend on the pressure of the environmental atmosphere and on the diffusion coefficient of oxygen; however, it would be independent of the chemical composition of the medium-filled crack cavity.

4.5. Some Models of the Tunnel Growth

The following simplification is most natural and realistic for a mathematical description of the electrochemical tunnel growth by general equations (76).

Let the cathode reaction be neglected and the indifferent electrolyte be present in the solution.[23] In this case $G_i = 0$, the potential in the tunnel and the summary current, as well as the tunnel growth rate, do not depend on its length. Moreover, in this case one can put

$$\frac{\partial}{\partial t} = 0, \qquad v_x = 0, \qquad \varphi = 0, \qquad G_i = 0$$

and the solution of the simplified equation system (76) will serve to find the concentrations of ions, current, and the tunnel rate being determined by kinetics of the anode reaction. According to the tunnel model, the rate of tunnel growth equals the subcritical crack growth rate.

However, when the ratio of tunnel (and crack) length to the diameter of tunnel cross section is sufficiently large, the cathodic reactions must be accounted for, even if they are very weak and slow. We consider here this case, accounting for ohmic electric resistance of the electrolyte and neglecting concentration gradients. This assumption is commonly taken into account while designing electrolyzers. In this case the potential in the tunnel is satisfied by the Laplace equation

$$\frac{\partial^2 \varphi}{\partial x^2} + \frac{\partial^2 \varphi}{\partial y^2} + \frac{\partial^2 \varphi}{\partial z^2} = 0 \tag{85}$$

Let us consider the tunnel development in the steady regime; in this case we can consider the tunnel to be placed at $-\infty < x < 0$ (Figure 25). According to the general kinetic theory of Volmer–Tafel for the double electric layer the boundary conditions may be formulated as follows:

At the lateral surface, S_c, of the tunnel

$$\frac{\partial \phi}{\partial n} = \eta_c \exp(\lambda_c \phi) \tag{86}$$

At the tunnel bottom for $x = 0$

$$\frac{\partial \phi}{\partial x} = -\eta_a \exp(\lambda_a \phi) \tag{87}$$

Here η_c, λ_c, η_a, λ_a are kinetic constants of the given system describing the summary cathodic reaction at S_c (mostly the discharge of hydrogen ions) and the summary anode reaction at $x = 0$ (metal ionization), respectively. The

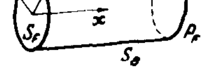

Figure 25. Semi-infinite circular cylindrical pit tunneling metal (idealized scheme).

dimensionless potential is designated as

$$\phi = \frac{\varphi - \varphi_\infty}{\varphi_0 - \varphi_\infty} \qquad (0 < \phi < 1) \tag{88}$$

where φ_∞ is the equilibrium potential at the cathode–solution contact; φ_0 is the anode potential (the metal potential is considered to equal zero). In this case the boundary condition at infinity may be expressed as follows:

$$\phi = 0 \qquad \text{at} \quad x \to -\infty \tag{89}$$

The function ϕ is evidently to satisfy the Laplace equation.

Now the operator

$$\frac{1}{S_c} \iint_{S_c} dy\, dz$$

is applied to the Laplace equation (85). For the sake of simplicity the tunnel cross section will be considered as circular with the radius r, and the function ϕ will be regarded as a constant value in each cross section of the tunnel (except for the double layer). Using Green's formula and the boundary condition (89) results in

$$\frac{d^2\phi}{dx^2} - \frac{2\eta_c}{r} \exp(\lambda_c \phi) = 0 \qquad (-\infty < x < 0) \tag{90}$$

Equation (90) physically expresses the charge balance between two infinitely close sections of the tunnel (the first term is the flow change along the axis x, the second term is the total flow to the lateral surface).

The solution of the nonlinear boundary value problems (90), (87), and (89) is quite similar to the solution of Eq. (59). Hence, we obtain

$$\left(\frac{\eta_c \lambda_c}{r}\right)^{1/2} x = \arctan (e^{\lambda_c \phi} - 1)^{1/2} - \arctan (e^{\lambda_c} - 1)^{1/2} \tag{91}$$

The boundary condition (87) allows us to find the equation determining the galvanic cell emf

$$r \lambda_c \eta_a^2 = 2\eta_c e^{-2\lambda_a} (e^{\lambda_c} - 1) \tag{92}$$

It should be remembered that according to (86) and (87) the coefficients η_a and η_c are directly proportional to $|\varphi_0 - \varphi_\infty|^{-1}$, while the coefficients λ_c and λ_a are directly proportional to $|\varphi_0 - \varphi_\infty|$.

From Eqs. (91) and (92) we find the width x_0 of the reaction zone (at $x = x_0$, $\phi = 0$)

$$x_0 = \left(\frac{r}{\lambda_c \eta_c}\right)^{1/2} \arctan (e^{\lambda_c} - 1)^{1/2} = \frac{r\eta_a}{2^{1/2}\eta_c} e^{\lambda_a} \frac{\arctan (e^{\lambda_c} - 1)^{1/2}}{(e^{\lambda_c} - 1)^{1/2}} \tag{93}$$

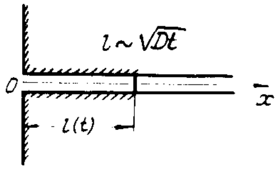

Figure 26. Diffusion dissolution of a thin rod perpendicular to the body surface undissolvable.

From Eqs. (91) and (87) the tunnel growth rate is

$$V = \frac{mD_M z_M F c_M}{\rho RT}\left(\frac{d\varphi}{dx}\right)_{x=0} = \frac{mD_M z_M F c_M \eta_a |\varphi_0 - \varphi_\infty| e^{\lambda_a}}{\rho RT} \tag{94}$$

The crack growth rate at $K_I > K_{ISCC}$ will be the same (if the curvature of anodic pathways is ignored).

Often the interaction of a solid with the environment may be described neglecting electric phenomena (e.g., if the liquid does not conduct ionically or the solid is a dielectric). In this case we can put φ = const in general equations (49); the functions $G_i(c_i)$ should be regarded as known from the kinetic equations for heterogeneous reactions at the sides of cracks or tunnels (if $G_i > 0$, the particles of the ith species pass on to a solid phase from a liquid; if $G_i < 0$, the particles of a solid dissolve in the liquid).

The propagation of cracks or tunnels in this case is possible only when the solid contains some continuously bound zones, the solubility of which in the liquid exceeds the solubility of other zones (selective solubility). Let us consider the main cases, assuming that the solution at the liquid–solid interface is saturated:

$$c = c_H \tag{95}$$

Here c is the concentration of the substance being dissolved and c_H is the concentration of the saturated solution.

Let the dissolvable component lay as a thin layer or a rod perpendicular to the body surface (Figure 26). In this case we have the following boundary value problem:

$$\begin{aligned} &\frac{\partial c}{\partial t} = D\frac{\partial^2 c}{\partial x^2} && \text{at } 0 < x < l(t) \\ &c = 0 && \text{at } x = 0 \\ &c = 0 && \text{at } t = 0 \\ &c = c_H && \text{at } x = l(t) \end{aligned} \tag{96}$$

It can be shown that the solution of the problem is of the following form

$$c = 2\rho\xi_0 e^{\xi_0^2}\int_0^{\xi} e^{-t^2}\,dt \tag{97}$$

$$l = 2\xi_0(Dt)^{1/2} \qquad \left(\xi = \frac{x}{2(Dt)^{1/2}}\right)$$

where ξ_0 is a root of the following transcendental equation:

$$\xi_0 e^{\xi_0^2}\int_0^{\xi_0} e^{-t^2}\,dt = \frac{c_H}{2\rho} \tag{98}$$

At $c_H \ll \rho$ we get $\xi_0 = (c_H/2\rho)^{1/2}$

The steady regime of crack or tunnel growth does not exist in this case. However, the steady regime becomes possible, when the particles of the substance being dissolved at the tunnel bottom can pass on to the solid phase on the lateral surface. This may occur, for instance, in cases when the liquid contains a catalyst promoting reaction between the dissolving and insoluble components of the solid with forming insoluble compositions. Let us consider the steady development of the tunnel, assuming that the coordinate $x = 0$ corresponds to the tunnel bottom (Figure 25).

The boundary value problem according to (76) is as follows:

$$D\frac{d^2c}{dx^2} = \frac{P_F}{S_F}G(c) \qquad \text{at } -\infty < x < 0 \tag{99}$$

$$c = 0 \qquad \text{at } x \to -\infty$$

$$c = c_H \qquad \text{at } x = 0$$

The function $G(c)$ is determined by kinetics of the reaction at the lateral surface ($G > 0$).

The solution of this equation, satisfying the condition at infinity, has the form

$$\left(\frac{2P_F}{DS_F}\right)^{1/2} x = \int_{c_H}^{c}\frac{dx}{\left[\int_0^x G(t)\,dt\right]^{1/2}} \tag{100}$$

The tunnel growth rate is equal to

$$V = \frac{D}{\rho}\left(\frac{dc}{dx}\right)_{x=0} = \frac{1}{\rho}\left[\frac{2DP_F}{S_F}\int_0^{c_H} G(x)\,dx\right]^{1/2} \tag{101}$$

The width of the reaction zone according to (100) is equal to

$$x_0 = \left(\frac{DS_F}{2P_F}\right)^{1/2}\int_{c_0}^{0}\frac{dx}{\left[\int_0^x G(\alpha)\,d\alpha\right]^{1/2}} \qquad \text{at } x = -x_0,\ c = 0 \tag{102}$$

In particular, if the heterogeneous reaction is of the first order, when $G = k_Bc$, we have

$$c = c_H \exp\left[x\left(\frac{k_BP_F}{DS_F}\right)^{1/2}\right], \qquad V = \frac{c_H}{\rho}\left(\frac{k_BDP_F}{S_F}\right)^{1/2} \tag{103}$$

The width of the reaction zone in this case is infinite.

The solid considered can be conceived as some "porous" structure, whose skeleton is formed by the insoluble component, and the "pores" by the dissoluble component. Numerous microtunnels developing in time according to relationships obtained appear in the surface layer of the solid under the effect of the liquid. It is natural that the value of the ratio S_F/P_F for these microtunnels is a constant for this system, dependent on the chemical composition of liquid and solid (and also on the structure of the solid), but independent of external loads and the shape of the solid. Then, the crack growth at $K_I > K_{ISCC}$ is determined by the development of microtunnels at the crack root, and the average crack growth rate does not depend on the stress intensity factor and is approximately equal to the tunnel growth rate (if curvature is neglected). Generally speaking, in this case the crack growth is interrupted; the length of a single "jump" is larger with smaller stress intensity factors. The threshold stress intensity factor K_{ISCC} is approximately equal to fracture toughness of the porous body composed by the insoluble component only.

The crack development in all the cases considered is a thermoactivated process, since the crack growth rate is proportional either to a diffusion coefficient or to a constant of the reaction rate (i.e., to thermoactivated quantities).

In the case of homogeneous dissolution, when $G_i < 0$, the liquid renders some consolidating effect, since the growth of cracks and tunnels is impossible, the tip of the initial crack getting duller due to dissolution, while its length gets smaller.

5. Crack Growth in Metals due to Local Hydrogen Embrittlement

Apart from local pitting, the mechanism of local hydrogen embrittlement is no less important for the subcritical crack growth. Hydrogen can be supplied into the metal not only by physical adsorption of molecular hydrogen at the metal surface, but also by deposition of atomic hydrogen. Besides, hydrogen can be liberated during chemical and electrochemical reactions, occurring on the metal surface (e.g., during the hydrogen discharge at the cathode). The most favorable conditions for hydrogen absorption processes exist at the crack tip, on a small area of the fresh metal surface not covered with the protective oxide film. That is why the hydrogen effect is significant in the process of subcritical crack growth; the incubative period depends, to a great extent, upon the state of the smooth specimen surface, and (when there is a cut) upon the sharpness of the cut.

Hydrogen is capable of chemisorption and diffusion in all the metals. Hydrogen is present in metals as protons. The hydrogen diffusivity in metals is greater than that of other gases and compounds. At the same time hydrogen is inferior to chlorine and, especially, to oxygen in adsorption activity. Therefore, oxygen dissolved in water can serve as a good inhibitor of the subcritical crack growth, if the growth mechanism is associated with hydrogen adsorption.

The effect of hydrogen on metals is due to the fact that protons, being intensively diffuse in dislocation cores, fill them and essentially increase the energy barrier for moving the dislocations. This effect and the embrittlement promoted are peculiar both for hydrogen and for other impurity atoms (e.g., of nitrogen). However, it is more significant for hydrogen because of its anomalously high diffusivity.

First, we treat the theory of the hydrogen effect following Refs. 6 and 72.

5.1. Theoretical Consideration

Suppose a metal is an ideally elastic-plastic body. Consider the small vicinity of the tip of an open-mode crack in that body (Figure 27). Denote the crack opening displacement at its tip as $2v_0$ and the size of the plastic range along the x axis as 2ρ. Take the crack cavity volume to be filled with a liquid or gaseous hydrogen-containing medium: hydrogen atoms penetrate the material mainly through the fresh metallic surface at the point O. The crack may be considered to be semi-infinite. At infinity, the body is subjected to static tension which can be completely described in terms of stress intensity factor K_I. Suppose now that the crack propagates in successive jumps, each time covering a distance much larger than the crack opening at its tip $2v_0$, but smaller than 2ρ. This allows the crack to be regarded as a mathematical cut (of zero thickness), the crack tip being a point source of protons in metal.

While a crack does not move, this reduces the task of determining the concentration c of protons to the following boundary value problem. If a source of protons started at $t = 0$ at the tip of a fixed semi-infinite linear cut along $y = 0$, $x < 0$, to produce protons at a constant rate Q, the value of Q being independent of time, the distribution of proton concentration in the body is found as follows:

Diffusion of protons is described by the following equation:

$$\frac{\partial c}{\partial t} = D\left(\frac{\partial^2 c}{\partial r^2} + \frac{1}{r}\frac{\partial c}{\partial r}\right) \qquad (r^2 = x^2 + y^2) \tag{104}$$

valid for $0 < r < \infty$, $0 < t < \infty$. Here D is the proton diffusion coefficient.

The mass conservation equation

$$Qt = \int_0^\infty \int_0^{2\pi} cr\,dr\,d\theta = 2\pi \int_0^\infty rc(r, t)\,dr \tag{105}$$

plays the role of the additional condition ($c \to 0$ for $r \to \infty$).

This problem has a solution, which is easy to verify, and its form is

$$c = -\frac{Q}{4\pi D} Ei\left(-\frac{r^2}{4Dt}\right) \tag{106}$$

$$Ei(x) = \int_{-\infty}^{x} t^{-1} e^t\,dt$$

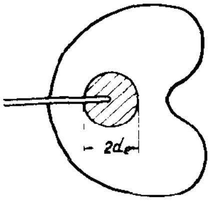

Figure 27. Scheme of the crack tip vicinity by hydrogen embrittlement.

with

$$-Ei(-x) = -\ln x + A \qquad \text{for } x \to 0$$

$$-Ei(-x) = x^{-1}e^{-x} \qquad \text{for } x \to \infty$$

($A = 0.577$ is Euler's constant).

The diffusion of protons forms a zone of embrittled metal near the crack tip. The following assumptions may be introduced.

The effect of protons on a metal is fully described by the magnitude of their local concentration. If the concentration is less than some critical value, the metal which was in a plastic state before remains plastic. If the concentration is more than this critical value the metal turns into an elastic–brittle state.

The embrittled zone, embraced by a plastic region, behaves as an elastic body. The radius d_e of the embrittled nucleus may be found from the solution (106) by the condition

$$c = c_e \quad \text{when} \quad r = d_e$$

Hence

$$\frac{4\pi D c_e}{Q} = -\mathrm{Ei}\left(-\frac{d_e^2}{4Dt}\right) \tag{107}$$

The value of c_e is a constant in this model. In the accepted model, the radius of the elastic nucleus is larger than the crack opening. At the crack tip a structure forms which is characteristic of a mathematical cut in elastic bodies. This superfine structure is described by the local stress intensity factor k_1 and is independent of the external stress field as represented by the factor K_I at distances which are large compared with the size of the plastic region.

Denote a yielding tensile strength as σ_S. The size d_e of the elastic nucleus may depend only on K_I and σ_S. Dimensional analysis yields

$$d_e = \frac{k_1^2}{\eta_1^2 \sigma_S^2} \tag{108}$$

Here η_1 is a constant (in this model, it is usually independent even of Poisson's ratio and of σ_S/E, where E is Young's modulus, and can be found in principle if the solution of the respective elastic-plastic problem is known).

According to Eq. (108), the growth of the elastic nucleus is accompanied by an increase in the local stress intensity factor k_1 until a certain limiting value

k_{IC} is reached (the fracture toughness of hydrogenized metal). Hence, the maximum size, d_{e0} of the elastic nucleus at the moment $t = \tau$ when local fracture occurs is

$$d_{e0} = \frac{k_{IC}^2}{\eta_1^2 \sigma_S^2} \tag{109}$$

The deformation opens fresh surface at the crack tip, and this surface increases proportionally to the value of opening $2v_0$. Let us introduce the following assumption:

The proton source rate, Q, is directly proportional to the crack opening displacement, the proportionality coefficient, η, is determined by concrete electrochemical reactions and transport processes in the crack cavity. The coefficient η can be considered as a constant of the metal–environment system under study.

Hence we get

$$Q = \eta v_0 \tag{110}$$

The crack opening displacement $2v_0$ is

$$2v_0 = \frac{2\eta_2 K_I^2}{E\sigma_S} \tag{111}$$

where η_2 is a certain number known in many cases (e.g., for plane strain according to the most exact calculation $\eta_2 = 0.21$).

Substituting (111) into Eq. (110) one obtains the formula

$$Q = \frac{\eta\eta_2 K_I^2}{E\sigma_S} \tag{112}$$

As can be seen from Eq. (112) the value of Q is directly proportional to the square of the stress intensity factor, K_I^2. According to Eqs. (107), (108), and (112), the mean rate of subcritical crack growth is

$$\frac{dl}{dt} = \frac{d_{e0}}{\tau} = V_0 F\left(\frac{K_I^2}{K_{I0}^2}\right) \qquad \left(K_{I0}^2 = \frac{4\pi}{\eta\eta_2} Dc_e E\sigma_S,\ V_0 = \frac{4D}{d_{e0}}\right) \tag{113}$$

Here, the function $y = F(x)$ is determined by the following relation:

$$-Ei(-y) = \frac{1}{x} \tag{114}$$

Thus the formula for the rate of subcritical crack growth under a fixed load includes only two constants characteristic of the material–environment system: K_{I0} and V_0. These constants can be found from direct experiments in subcritical crack growth. The relation described by Eq. (113) is represented graphically by Figure 28.

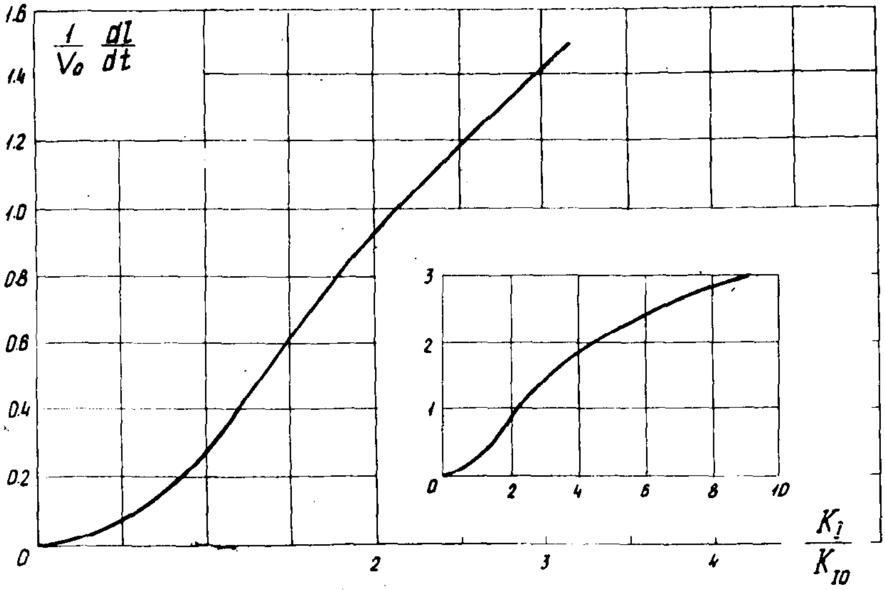

Figure 28. Theoretical dependence of the crack growth rate $\dot{l}$ on the stress intensity factor K_I ($\dot{l}$–K_I diagram) for the local hydrogen embrittlement mechanism.

An analysis of Eq. (113) determines the most important linear section that is often realized in experiments:

$$\frac{dl}{dt} = \alpha(K_I - K_0) \qquad (115)$$

The constants α and K_0 are expressed in terms of values K_{I0} and V_0 appearing in Eq. (113).

Thus, the principal regime of subcritical embrittlement appears to be as follows:

i. A crack grows by periodic jumps.

ii. While a crack stands, protons diffuse out of crack tip. The elastic–brittle circular core arises in a plastic zone, the radius of circumference increasing with time course. Simultaneously, the superfine crack tip structure forms in the brittle core.

iii. The stress intensity factor of this structure, k_{I}, depends only on core radius and on constants of yielding; it is independent of the external field because of the screen effect of the plastic zone.

iv. When k_{I} attains the fracture toughness of a hydrogenized metal, the crack tip advances instantly. The magnitude of jump equals the core radius at this moment.

It should be noted that, in principle, other mechanisms of hydrogen effect are possible.(6)

The metallurgical hydrogen diffused in the whole volume of the metal lattice after metallurgical and technological processes is concentrated in collecting traps of the type of pores, microcracks, dislocation cores, etc. It has been shown that the equilibrium pressure of molecular hydrogen in closed collectors amounts to some dozens of atmospheres.(10) The most powerful collector of metallurgical hydrogen is a crack tip. Therefore the theory treated above applies quite similarly to the last case, if we assume the crack tip to be a point outlet of protons with a flow rate equal to $-Q$. This theory may explain some unusual phenomena of subcritical crack growth in metals immersed in a dry inert gas or vacuum under constant load, which were observed in tests(9) and remain unexplained.

5.2. Analysis of Test Data

In spite of numerous experiments in stress corrosion, the mechanism of fracture has not yet been established except for a very limited number of material–environment systems. This is because exact methods of fracture mechanics and theoretical electrochemistry were applied to stress corrosion only quite recently.

The work by Johnson and Willner(45) was one of the first investigations in subcritical crack growth under static loads in which was applied the fracture mechanics approach. They studied the dependence of the rate of crack growth, $\dot{l}$, on the stress intensity factor, K_I, by loading, in tension, a plate of H-11 steel (5% Cr) with a transverse center slot immersed in water (test temperature, 27°C (81°F); yield strength $\sigma_{0.2} = 161$ kg/mm^2).

Figure 29 shows the results of their experiment under constant loads. The solid line in the same figure is the theoretical curve plotted in accordance with Eq. (113). The coincidence implies that subcritical crack development in H-11 steel in aqueous environment proceeds in conformity with the above mechanism of local hydrogen embrittlement.†

Ryder and Gallagher(73) published data on subcritical crack growth under constant and cyclic loads in SAE 4340 high-strength steel (yield strength $\sigma_{0.2} = 155$ kg/mm^2, ultimate strength $\sigma_f = 189$ kg/mm^2). Specimens were tested in distilled water (pH = 6.5–6.9) at temperatures of 5, 25, 50, and 75°C (41, 77, 122, and 167°F). Prior to testing, the samples were austenized for 1 hr in a salt bath at 870°C (1598°F), oil quenched, and tempered for 2 hr at 260°C (500°F).

Figure 30 shows the experimental points. All the four test temperatures show an increase in the crack propagation rate at higher K_I. In SAE 4340 steel containing some 2% Ni, it is natural to explain the crack growth by local hydrogen embrittlement of metal at the crack tip. Iron, whose equilibrium

---

† It should be noted that the authors of paper (45; had another viewpoint. They believed that the crack growth in this case can be described as "an electrochemical process which is allied to corrosion mechanism of iron in aqueous environments."

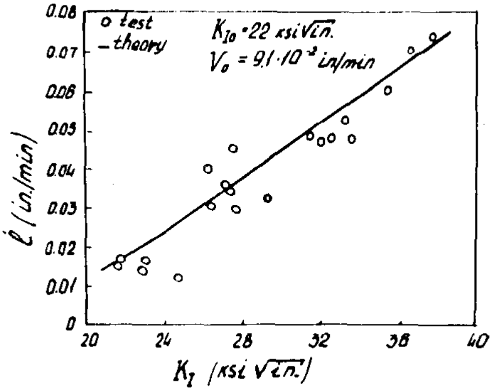

Figure 29. $\dot{l}$-K_I diagram (H-11 steel in water[45]).

potential is lower than that of nickel, probably serves as the anode, while the cathodic reactions (mostly hydrogen evolution) are concentrated on nickel inclusions. Hydrogen discharged at the crack tip diffuses in the metal.

The solid lines in Figure 30 show the results of computations by Eq. (113). Good agreement of the theoretical lines with the experimental points is achieved.

Carter[65,67,68] investigated the relationship between the crack growth rate and the stress intensity factor in high-strength steels of various grades. His papers contain a lot of test data on the behavior of specimens with artificial cracks tested in 3.5% aqueous NaCl solution.

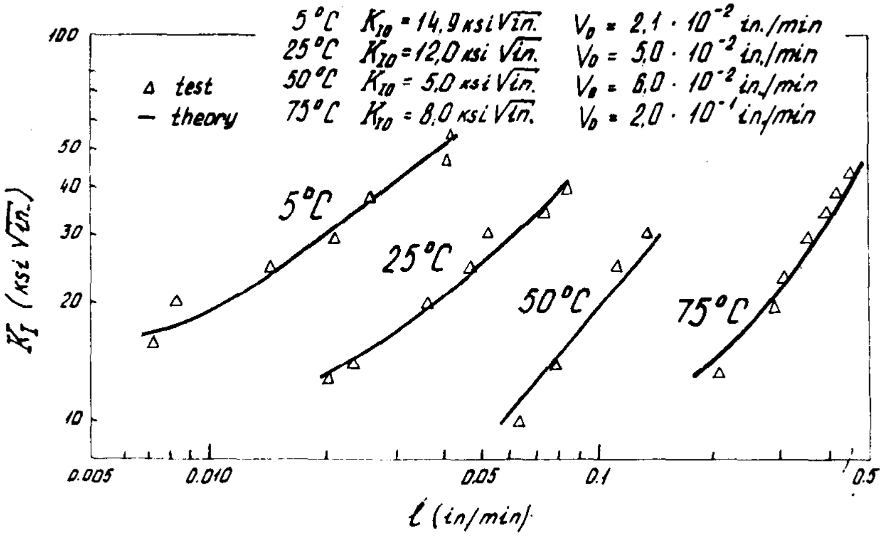

Figure 30. $\dot{l}$-K_I diagram (SAE 4340 steel in distilled water[73]).

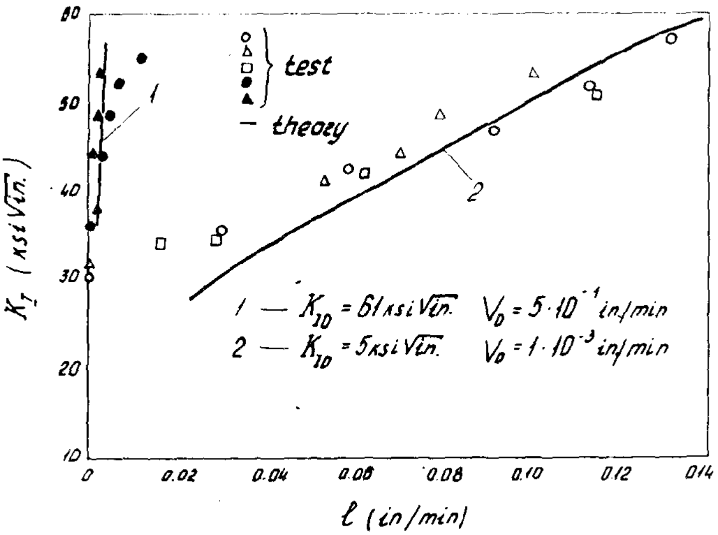

Figure 31. $\dot{l}$-K_I diagram (AISI 4340 steel with various content of silicon in 3.5% NaCl water solution[(67)]).

Maraging steels contain a high percentage (up to 18%) nickel and are rich in cobalt. AISI 4430 and 4340 steels have about 2% nickel and approximately equal percentages of manganese and chromium. The subcritical crack growth in such alloys is notably affected by the structural state of the specimens used in the experiment and by their state after heat treatment, as well as by optimum ratios between the basic components of the material and some additives, such as silicon or chromium. The experimental points obtained by Carter[(67)] are shown in Figure 31 and Table 1. The solid lines of Figure 31 were obtained from calculations according to Eq. (113).

As the silicon content exceeds 1.08% the rate of subcritical crack growth

Table 1
Mechanical Properties of Test Material

Key[a]	Silicon content, %	Tempering temperature, °C	Tensile strength, kg/mm^2	Yield strength, kg/mm^2
○	0.09	205	199	141
□	0.54	205	210	152
△	1.08	260	206	168
●	1.58	260	202	166
▲	2.15	260	204	169

[a] As used in Figure 31.

in AISI 4340 steel drops rapidly, while the increase in silicon contents from 0.09 to 0.54 and 1.08% cause similar effects upon the rate of crack growth within the scatter of the experimental point.

Note that, according to many researchers, the mechanism of hydrogen embrittlement is tangibly affected by heat treatment of steel. If the low-alloy AISI 4340 steel with a silicon content of 0.54 or 1.08% is quenched and tempered at 400–415°C (752–770°F) (Table 1), and then a similar test is carried out in the environment of 3.5% aqueous solution of NaCl, it will be found that the steel fails due to electrochemical corrosion, rather than by means of embrittlement. Moreover, there are cases when the mechanism of crack growth spontaneously changes from corrosion to hydrogen embrittlement (see Section 4).

It should be expected that change-over diagrams similar to that of Figure 32 are typical of the common type of cracks that develop by the mechanism of corrosion and hydrogen embrittlement. Probably, they may be expected in all corrosive alloys submerged in an aqueous solution of electrolytes (or in humid air).

Gerberich and Hartbower(74) tested the D6AC low-alloy steel in aqueous environment. The steel had been austenitized at 950°C (1742°F) for 30 min and tempered at 600°C (1112°F) for 2 hr. The heat-treated steel had a tensile strength σ_f of 161 kg/mm^2 and a yield strength $\sigma_{0.2}$ of 147 kg/mm^2. The experimental points showing the subcritical crack growth were widely scattered (Figure 33). The solid line in Figure 32 corresponds to Eq. (113).

Of special interest are maraging steels capable of strength in excess of 210 kg/mm^2, sometimes reaching as much as 450 kg/mm^2. Carter(68) tested 350-grade maraging steel in 3.5% aqueous NaCl solution. After aging at 415°C

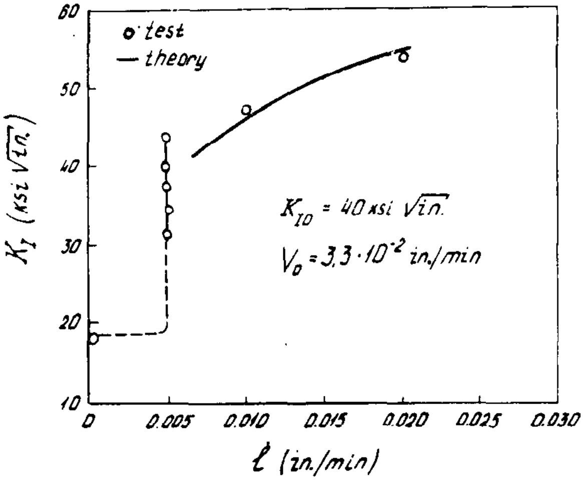

Figure 32. $\dot{l}$–K_I diagram (AISI 4340 steel with 2.15% Si in 3.5% NaCl water solution(65)).

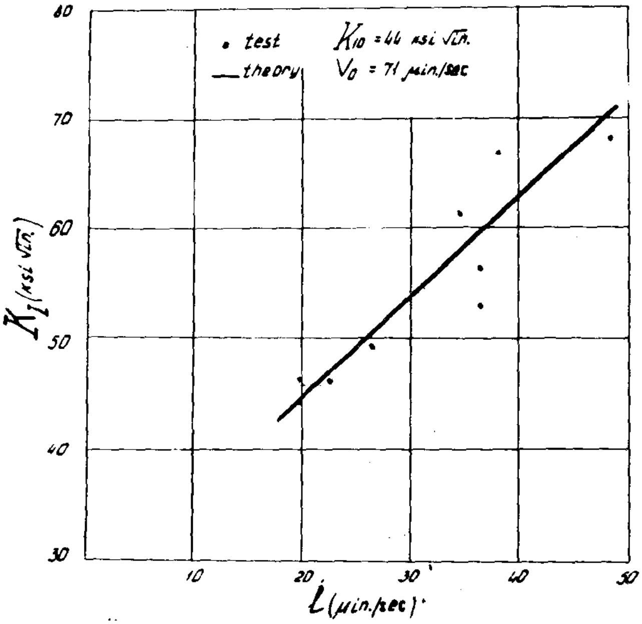

Figure 33. l-K_I diagram (D6AC steel in water$^{(74)}$).

for 8 hr, the material had a tensile strength of 212 kg/mm^2 and a yield strength of 210 kg/mm^2. His data are shown as points in Figure 34.

It must be noted that the rest of the tested maraging alloys$^{(68)}$ suggest a different mechanism of subcritical crack growth (typical for electrochemical corrosion).

McEvily, Clark, and Bond studied the subcritical crack growth under static loads in Al–5Zn–2.5Mn alloy.$^{(75)}$ Cracked plates were loaded in tension in aqueous solutions of NaCl and/or $Cr_2O_3 + NaCl + K_2Cr_2O_7$. The aluminum

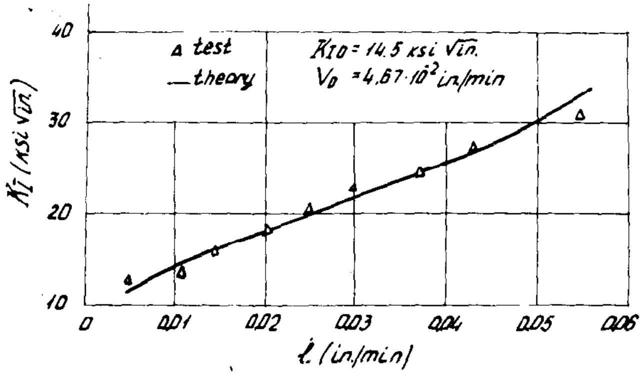

Figure 34. l-K_I diagram (350-grade steel in 3.5% NaCl water solution$^{(68)}$).

alloy specimens had been aged at 121°C (250°F) for 24 hr, after which their tensile strength was 45.2 kg/mm^2 and yield strength 42.6 kg/mm^2. The data of McEvily, Clark, and Bond as well as theoretical curves are represented in Figure 35.

The above analysis of material fracture in aqueous environments implies that hydrogen embrittlement took place in all the cases mentioned.

The model presented for subcritical crack growth due to hydrogen effects may be considered as the first approximation to the reality. It is capable of describing satisfactorily most test data on stress corrosion cracking with linear $\dot{l}$–K_I diagrams. Consequently, hydrogen embrittlement is suspected in those systems as the main cause of brittle fracture.

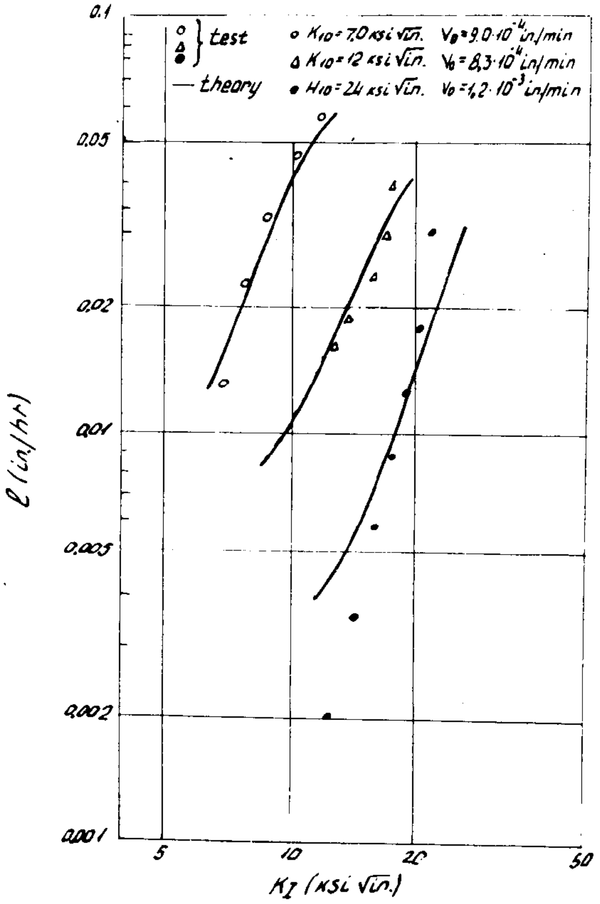

Figure 35. $\dot{l}$–K_I diagram (Al–5Zn–2.5Mn alloy in water solutions of NaCl and Cr_2O_3–NaCl–$K_2Cr_2O_7$ (75)).

5.3. Threshold Stress Intensity Factor

Let us consider two feasible mechanisms explaining the phenomenon of the threshold stress intensity factor K_{ISCC} below which no crack growth occurs. Both of them are closely related to the mathematical model of local hydrogen embrittlement described above.

The first mechanism holds for the case where the environment is a gas containing molecular hydrogen. It is obvious that the crack opening displacement, $2v_0$, and the flow of protons, Q, entering the metal decrease as the factor K_I decreases ($v_0 \sim K_I^2$, $Q \sim v_0$). When the crack opening displacement decreases, viscous forces of the gas come into effect.

Recall that the viscous gas flow rate through a plane narrow slit is directly proportional to the slit width cubed and inversely proportional to the slit length. As soon as the crack opening displacement, $2v_0$, becomes comparable to the length of the free path of environmental gas molecules, the mechanism of gas motion in the crack cavity is changed drastically (Knudsen diffusion of rarefied gas takes the place of a hydrodynamic mechanism).

It should be kept in mind that if the channel length is less than the molecular free path, the number of molecules passing through the channel per unit time varies as the reciprocal of the channel length and as the square of its width. Gas molecules move independently, the mixture components flowing as if they were alone and no other components existed. The flow is governed by the partial pressure of the corresponding component and is independent of the total pressure of the gas mixture.

This reasoning is also valid for water or humid gases if in the immediate vicinity of the crack tip there exists a gas layer followed by a liquid meniscus. Indeed, if the metal is not wettable by water, capillary force will prevent water from flowing into the narrow slit. The critical crack width is of the order of γ/p, where γ is the liquid surface tension, and p liquid pressure in the meniscus. Under normal conditions (temperature 300 K, pressure 1 atm) this parameter for water is on the order of 10^{-4} cm. In this case hydrogen is supplied to the crack tip from the gas interlayer saturated with water vapor.†

For example, in this case of H-11 steel we have, according to Figure 29,

$$K_{IC} = 140\ \text{kg/mm}^{3/2}, \qquad K_{ISCC} = 60\ \text{kg/mm}^{3/2}$$

$$(\sigma_S = 160\ \text{kg/mm}^2,\ E = 2 \times 10^4\ \text{kg/mm}^2)$$

Then one finds from Eq. (111)

$$2v_0 = 3 \times 10^{-4}\ \text{cm} \qquad \text{at } K_I = K_{IC}$$

$$2v_0 = 5 \times 10^{-5}\ \text{cm} \qquad \text{at } K_I = K_{ISCC}$$

---

† It should be noted that in the case of wettability the reverse situation is observed: the gaseous medium containing water vapor may act as common water owing to the formation of a liquid meniscus near the crack tip. This effect has been found experimentally (e.g., see the review by Johnson and Paris(7)).

Under normal conditions ($T = 300$ K, pressure $p = 1$ kg/cm^2) the calculation of the free path, λ, of hydrogen molecules (molecular diameter $s = 10^{-8}$ cm) will appear as follows:

$$(\overline{u^2})^{1/2} = (3RT/\mu)^{1/2} = 1840 \text{ m/sec}, \qquad R = 2 \text{ cal/grad mol}$$

$$n = 3p/m\overline{u^2} = 3 \times 10^{19} \text{ cm}^{-3}, \qquad \lambda = 0.2/ns^2 = 7 \times 10^{-5} \text{ cm}$$

Here μ is hydrogen's molecular weight equal to 2, and m the hydrogen molecule's mass, equal to 3.4×10^{-24} g.

As we see, the free path is found to be close to the value of the crack opening displacement at $K_I = K_{ISCC}$.

Now consider another feasible mechanism. To this end, let us first estimate the incubative period on the basis of the mathematical model of the phenomenon introduced above. Formula (107) yields the time, τ, elapsed after the moment of switching on the proton source until the first leap of the crack for a distance of d_{e0} (incubative period):

$$\tau = \frac{d_{e0}^2}{4DF(K_I^2/K_{I0}^2)} \tag{116}$$

Here the function $y = F(x)$ is determined by the relationship (114).

Since $F(x)$ decreases with decreasing x, the incubative period increases with decreasing stress intensity factor, K_{I*}, such that the crack opening displacement is large enough, when $K_I > K_{I*}$, and the gas in the crack cavity can be considered ideal; in this case the gas flow rate will be directly proportional to the crack width, and the factor η in formula (110) will be independent of the crack opening displacement and the stress intensity factor. At $K_I < K_{I*}$ the mechanism of gas motion is changed (viscous flow, Knudsen diffusion, etc.); in this regime the gas flow rate will depend on the crack width to a considerably greater extent, and the factor η will decrease with decreasing v_0 and K_I. It is seen from (116) that in the latter regime the incubative period increases quicker with decreasing K_I than in the former; e.g., in the simplest case of viscous flow we get

$$\eta \sim v_0^2 \sim K_I^4, \qquad \tau \sim 1/F(x), \qquad \text{where } x \sim K_I^6$$

Thus if the duration of the experiment is less than the incubative period, τ, the corresponding stress intensity factor will be taken as a threshold one.

In real systems the environment contains compounds capable of entering into reactions with metals and forming solid oxide films (e.g., oxygen). Therefore a competing process of the growth of an oxide passivation film at the crack tip runs parallel to the process of adsorption and diffusion of hydrogen. As soon as the film attains certain critical thickness the access of hydrogen to the metal through the crack tip stops. It takes a certain period of time to obtain a film of

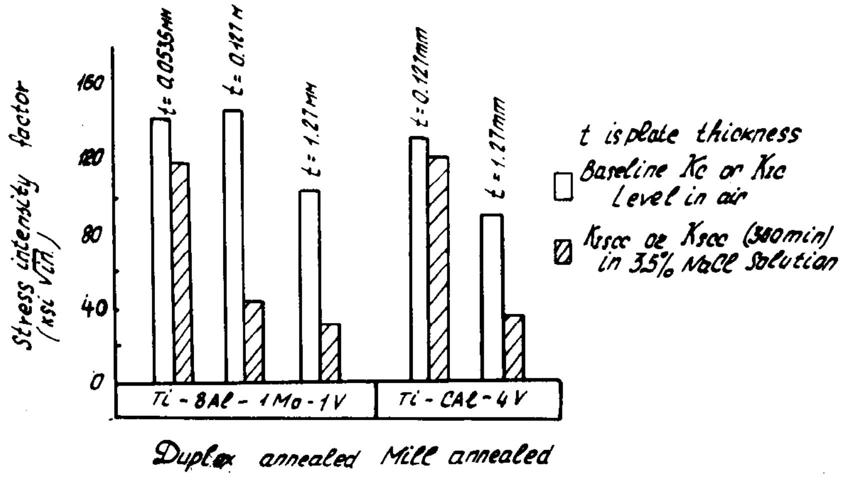

Figure 36. Threshold and unstable fracture stress intensities for two titanium alloys in different thicknesses.(7)

necessary thickness. Obviously, the more the amount of oxidizer in the environment, the shorter this period of time.†

Hence it follows that if the incubative period, τ, given by the formula (116) is longer than the time necessary for attaining the critical thickness of the passivation film, an alternative mechanism of crack propagation will take place (e.g., the crack may get overgrown with a solid film and not propagate at all). This mechanism of the appearance of a threshold stress intensity factor is, perhaps, more widely met in practice.

The effect of passivation films on crack growth was examined in the book by Cherepanov.(6)

The above considerations also lead to the understanding of the radical difference in the subcritical behavior of through cracks in thick and thin plates (see, e.g., Figure 36). Indeed, let us compare main parameters of subcritical crack growth (crack growth rate and incubative period) for the case of plane strain and a very thin plate at the same stress intensity factor.

The level of tensile stresses in the plastic area for the case of plane strain is approximately three times higher than that for plane stress (the stress σ_y at the crack tip is equal to σ_S for thin plates and approximately to $3\sigma_S$ for plane strain). Therefore external loads applied to the boundary of the circular elastic core near the crack tip will be approximately three times higher for the case of plane strain; hence the stress intensity factor k_I and the number η_1 [see Eq. (108)] for plane strain will be roughly three times as large as those for plane stress. Hence, according to the relationship (109), it follows that the constant d_{e0} for plane strain is approximately one-tenth of the corresponding constant for plane stress.

---

† The effect of the environmental oxygen diffusion on metal corrosion and subcritical crack growth is undoubtedly present when the processes mentioned depend appreciably on such factors as the depth of the test specimen submersion in water, or whether the specimen is immersed in a liquid electrolyte or else the latter is sprinkled over the metal surface. It is known that the sprinkled electrolyte is sometimes a much more active corrosion medium than the continuous one, which can be accounted for by the fact that oxygen diffusion in this case is facilitated.(13)

As is known,(6) the factor η_2 (and the constant K_{I0}^{-2}) for a thin plate is approximately twice as large as those for plane strain. Accordingly, the function $F(x)$ for plane strain will be, at least, several times less than that for the plane stress, as illustrated in Figure 28.

Taking all the above estimates into account, we come to the following conclusions making use of Eqs. (116) and (113):

a. In the case of plane stress the incubative period is at least by two or three orders of magnitude longer than in the case of plane strain.

b. Subcritical crack growth rates in comparable cases are of about the same order.

For such a (relatively) long incubative period the competing corrosion process may reduce absorption and diffusion of hydrogen into the metal through the crack tip to zero.

Thus subcritical crack growth due to hydrogen diffusion is much more dangerous for the conditions of plane strain than for through cracks in thin plates.

No less essential for the correct analysis of this phenomenon is the high adsorption activity of oxygen, which was demonstrated especially strikingly in the experiments of Hancock and Johnson,(48) dealing with the effect of minute oxygen additives into various gases upon the subcritical crack growth in H-11 steel.

6. The Environmental Growth of Fatigue Cracks

An aggressive environment may exercise substantial influence also on the crack growth at variable (in particular, cyclic) loads. Such aggressive media for metals and alloys are usually aqueous solutions of some electrolytes, sea water, moisture, humid atmosphere, etc. The intensity of environmental effect depends both on the properties of a concrete metal–environmental system and the parameters of the variable load. In a number of cases even common atmospheric humidity may lead to a many-fold increase in the growth rate of fatigue cracks in comparison with vacuum or inert gaseous medium.

According to experimental evidence presented, e.g., in References 7, 14, and 76–79, the fatigue crack growth rate for many aluminum alloys in a humid medium is approximately ten times as great as that in vacuum, and for many high-strength steels it is 20–30 times as great as that in an inert medium. In unidirectional boron–aluminum composites the growth rate of a longitudinal fatigue crack in a humid medium is approximately 200 times as high as that in an inert gas.(80) Meanwhile, some new materials exhibit amazing resistance to the action of external aggressive media and variable loads (metal glasses(81) and some composites with carbon fibres(82)).

The stress intensity factor K_I is the main parameter governing local fracture at the crack tip.† The dependence of the crack growth rate, dl/dN (where N is the number of load cycles), on the stress intensity factor K_I is the main characteristic of the given environment–material system at cyclic loading. Therefore we can judge the influence of this or that medium by comparing, for instance, (dl/dN)–ΔK_I diagrams, where $\Delta K_I = K_{I\max} - K_{I\min}$ ($K_{I\max}$ and $K_{I\min}$ are the greatest and smallest stress intensity factors during a cycle, respectively).

At cyclic loading the crack growth in metals in vacuum or an inert medium is due to local fracture as the result of finite plastic deformations near the crack tip. The theory leads to the following expression for the crack growth rate under these conditions(6,83):

$$\frac{dl}{dN} = -\beta\left(\frac{K_{I\max}^2 - K_{I\min}^2}{K_C^2} + \ln\frac{K_C^2 - K_{I\max}^2}{K_C^2 - K_{I\min}^2}\right) \tag{117}$$

where ρ and K_C are material constants. In the case of through cracks in plates they also depend on the plate thickness (the dependence; see, e.g., in Reference 6).

In particular, at $K_{I\min} = 0$ there follows the well-known empirical formula by Johnson and Paris,(7)

$$\frac{dl}{dN} = \tfrac{1}{2}\beta\left(\frac{K_{I\max}}{K_C}\right)^4 \tag{118}$$

if the high-order terms are omitted from the Taylor expansion of the logarithmic function. Formulas (117) and (118) describe the majority of data on fatigue crack subcritical growth in metals and alloys,(7,84,85) if neglect of loading frequency effect is permissible (in a certain frequency range) and if the crack growth rate under cyclic loading in some medium is greater than that under a corresponding characteristic stationary load in the same medium.

General kinetic theory‡ of the subcritical crack growth leads to the following relationship under stationary loads(38):

$$\frac{dl}{dt} = v_0 \exp\left(\frac{\zeta K_I}{RT}\right) \tag{119}$$

Here v_0 and ζ are some constants of the material–environment system. This relationship is justified experimentally for many polymers, glasses, and some metals.(6)

---

† The role of other parameters (Γ and k_I; see Section 3) essential in the presence of considerable plastic deformations before fracture is less important at cyclic loads than at stationary ones. That is why in this short presentation we shall deal only with the K_I concept.

‡ The one similar to Arrhenius' theory in chemical kinetics of Volmer's theory in electrochemistry.

If the crack growth rate under cyclic loading in some medium is close to that under corresponding characteristic stationary load in the same medium, the subcritical crack growth in such systems under any variable loads (cyclic, random, etc.) is likely to be explained and evaluated on the basis of the corresponding static l–K diagrams obtained for the environment in question. In this case the parallel mechanism of local plastic deformations is of little importance (in particular, the fatigue crack growth rate in vacuum or an inert medium is, obviously, much less than the crack rate in the medium under a characteristic stationary load).

To illustrate, let us consider the crack growth caused by hydrogen embrittlement, approximating the corresponding diagram by linear dependence (115). Let the cyclic load be sinusoidal, i.e.,

$$K_I = K_m + \Delta K \sin \omega t \tag{120}$$

where K_m, ΔK, and ω are time independent. In this case the crack increase per cycle Δl amounts to

$$\Delta l = \alpha \int_0^{2\pi/\omega} (K_I - K_0)\, dt = \frac{2\pi\alpha}{\omega}(K_m - K_0) \tag{121}$$

Hence we find the average crack growth rate under sinusoidal loading

$$\frac{dl}{dt} = \frac{\Delta l}{2\pi/\omega} = \alpha(K_m - K_0) \tag{122}$$

The same result, with the linear l–K_I diagram, clearly, holds for any form of the cycle, if by the average value K_m of the cycle is implied the ordinate value which divides the cycle into two domains of equal area.

Thus the fatigue crack growth rate at hydrogen embrittlement is equal to that under constant load, if the quantity K_I in (115) is substituted by the average value K_m in a loading cycle. By way of experimental confirmation of this result we can quote the work by Ryder and Gallagher.(73)

At hydrogen embrittlement in the linear range it is also possible to use directly the general dependence, given by Eq. (113). In this case we readily arrive at the following expression(86)

$$\begin{aligned} \frac{dl}{dN} &= V_0 F\left(\frac{K_{It}^2}{K_{I0}^2}\right) \\ K_{It} &= \frac{1}{T_e}\int_0^{T_e} (K_m + \Delta K \sin \omega t)\, dt \end{aligned} \tag{123}$$

where T_e is the time of action of tensile stress during one cycle.

Figure 37 presents the comparison of theoretical curves calculated by Eq. (123) with the experimental data of Crocker and Lange(78) obtained for specimens made of two high-strength steels 13Cr–8Ni–2Mo (triangles and the

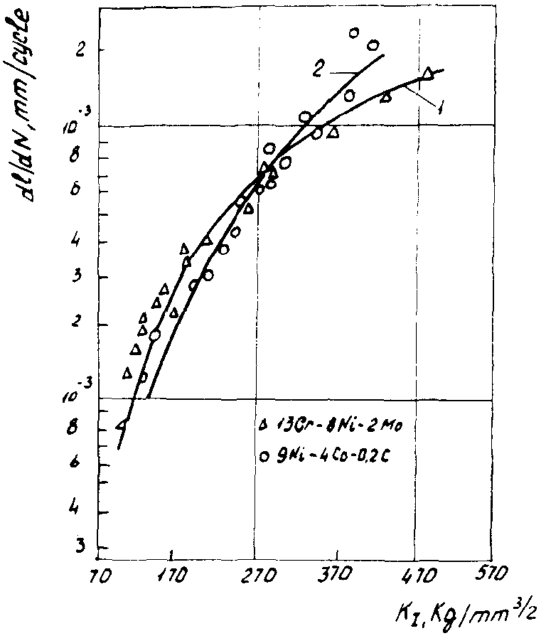

Figure 37. Comparison of the fatigue crack growth theory with experimental results by Crocker and Lange.(78)

solid curve 1 in Figure 37) and 9Ni–4Co–0.2C (circles and the solid curve 2 in the same figure) tested in salt water. The loading was a pulsating one.

The values of the constants proved to be as follows.

1. Steel alloy 13Cr–8Ni–2Mo:

$$K_{I0} = 88.5\ \text{kg/mm}^{3/2}, \qquad V_0 = 1.1 \times 10^{-2}\ \text{mm/cycle}$$

2. Steel alloy 9Ni–4Co–0.2C:

$$K_{I0} = 115\ \text{kg/mm}^{3/2}, \qquad V_0 = 1.6 \times 10^{-2}\ \text{mm/cycle}$$

In some cases of variable loading two (or, perhaps, more) different mechanisms of local fracture at the crack tip interacting with one another prove to be essential. In these cases it is natural to apply a kind of "additivity principle" assuming that the crack length increase during each loading cycle is composed of two items corresponding to the mechanisms mentioned.

For example, under simultaneous action of the mechanism of local hydrogen embrittlement, of the same order, the following formula is obtained for the crack growth rate under sinusoidal loading(86):

$$\frac{dl}{dN} = V_0 F\left(\frac{K_{It}^2}{K_{I0}^2}\right) - \beta\left(\frac{K_{I\,\max}^2 - K_{I\,\min}^2}{K_C^2} + \ln\frac{K_C^2 - K_{I\,\max}^2}{K_C^2 - K_{I\,\min}^2}\right) \qquad (124)$$

Shown in Figures 38 and 39 are the experimental data by Barsom, Imhof and Rolfe,(87) who tested two high-strength nickel steels 10Ni–Cr–Mo–Co and

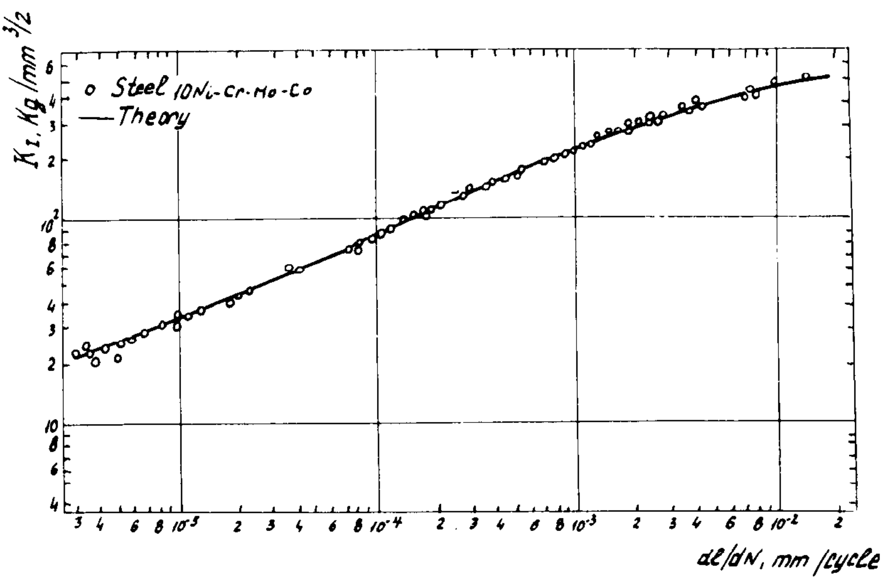

Figure 38. Theoretical curve for environment-enhanced fatigue crack growth and test data for 10Ni-Cr-Mo-Co steel alloy by Barsom, Imhof, and Rolfe.(87)

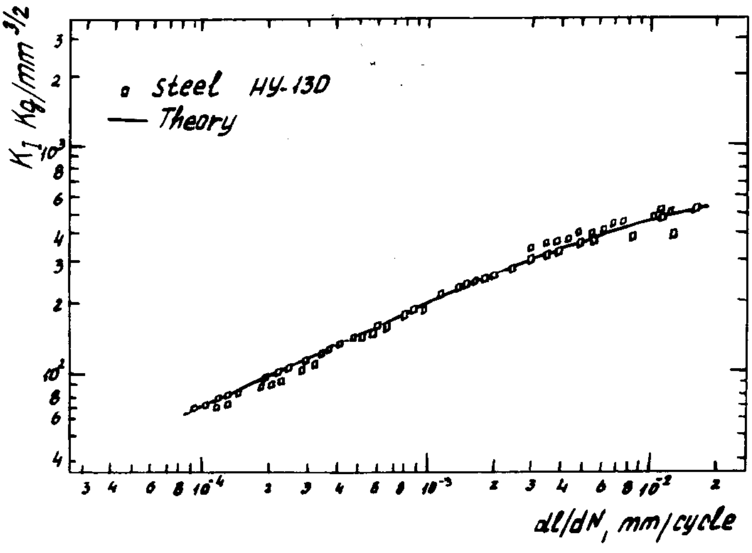

Figure 39. Comparison of the environment-enhanced fatigue crack growth theory with experimental results for HY-130 steel alloy.(87)

HY-130 at a low loading level. The experiments were carried out at room temperature in common atmosphere (the loading was pulsating). Though the authors themselves do not mark the environmental influence, in our opinion the atmospheric humidity and the related local hydrogen embrittlement had a great effect on the fatigue crack growth in these experiments.(88) This point of view finds confirmation in the excellent coincidence of experimental data and theoretical curves calculated by Eq. (123) at the following values of the constants.

i. Figure 38 (10Ni–Cr–Mo–Co steel):

$$K_{I0} = 21.2\ \mathrm{kg/mm^{3/2}}, \qquad V_0 = 1.2 \times 10^{-4}\ \mathrm{mm/cycle}$$

$$K_C = 710\ \mathrm{kg/mm^{3/2}}, \qquad \beta = 1.02 \times 10^{-1}\ \mathrm{mm/cycle}$$

ii. Figure 39 (HY-130 steel):

$$K_{I0} = 46\ \mathrm{kg/mm^{3/2}}, \qquad V_0 = 7.6 \times 10^{-4}\ \mathrm{mm/cycle}$$

$$K_C = 566\ \mathrm{kg/mm^{3/2}}, \qquad \beta = 4.6 \times 10^{-2}\ \mathrm{mm/cycle}$$

At cyclic (and, in general, variable) loading the concept of K_{ISCC} makes no sense. At a low level of loadings (less than K_{ISCC}) it is essentially impossible to find the static $\dot{l}$–K_I diagram experimentally, and the latter is necessary to estimate the contribution of the corresponding mechanism to the crack growth rate under cycling loading. Therefore, in this case an adequate theory is indispensable which would extend the experimental data into the inaccessible region.

One may expect that the relation (123) plays the role of such a theory not only for high-strength nickel steels, but also for many other metals and alloys in a humid environment and subject to hydrogen embrittlement.

It should be noted that in a large number of works dealing with metal fatigue the presence of moisture in laboratory air was neglected, and the air was considered to be a nonaggressive medium not affecting the crack growth. This approach should be creviced, and the corresponding experimental data must be rechecked for inert media.

In the case of cyclic loads, local plastic deformations at the crack tip permanently ruin the oxide passivation film preventing hydrogen adsorption and diffusion into the metal. It is this interaction of mechanisms that causes the absence of K_{ISCC} at cyclic loading. By the way, this fact provides an indirect confirmation of one of the mechanisms of K_{ISCC} presented in Section 5.

The analysis of the dependence (123) shows that the first term is most essential at the low level of loads (specifically, perhaps, at $K < K_{ISCC}$), whereas the second one is dominating when K_I is close to K_{IC}.

Consequently, the mechanism of hydrogen embrittlement is most important at low loadings, whereas at high loadings it is the plastic flow mechanism. The same dependence shows the loading frequency effect (particularly, this effect is more essential at low loadings).

For many aluminum alloys a good agreement with experiments is provided by the theory of fatigue cracks which is cased on the "additivity principle" and relies upon the common kinetic mechanism plus local plastic flow.(6,89)

A considerable body of interesting evidence on corrosion fatigue can be found in reviews(7,14) and in many papers on the subject (among the problems dealt with are the influence of chemical composition of the alloy and environment, the effect of thermal treatment, temperature, structure, plate thickness, etc.).

The fracture mechanism for some new materials subject to catastropic effect of corrosion fatigue can be understood as well on the basis of theoretical reasonings. For instance, the 200-fold acceleration of the longitudinal fatigue crack growth rate in unidirectional boron–aluminum composition in water(80) is readily explained by the theory of fatigue crack growth in aluminum alloys,(6) if one takes into account very quick longitudinal splitting of boron fibers under the direct adsorption effect of water (the latter fact was proved experimentally). For qualitative understanding of this phenomenon, it is sufficient to use formula (118). Indeed, at usual volume fraction of fibers (50%), the apparent value of $K_{I\,\max}$ in an aluminum matrix is about twice as large, because of fiber splitting, as without splitting, whereas the factor β for aluminum alloys in aqueous media becomes ten times as high as in inert media.

7. Conclusion: The Comparative Analysis of Major Mechanisms of Subcritical Crack Growth in Metals

The correct diagnosis of the causes of fracture is the fundamental base for possible applications of the theory and is, of course, indispensable for taking optimal safety measures. In some cases the analysis of fractures is quite sufficient for this purpose; however, usually (especially when the fracture cause is accounted for by the environment) this analysis is not enough. The most accurate method of fracture diagnostics is the one of the mechanics of brittle fracture which consists of studying the subcritical growth of cracks. Here the detection of the leading mechanism of the crack development causing fracture is of primary importance. It is of vital importance also for the proper judgement of the material properties as well as for its optimal projecting.

Let us enumerate the main mechanisms in the order of their practical importance†:

(1) hydrogen embrittlement,
(2) electrochemical stress corrosion,
(3) chemical stress corrosion,
(4) general kinetic mechanism,
(5) adsorption mechanism.

---

† This chapter deals only with the first and second mechanisms which are of electrochemical nature (and are of most importance). The theory of other mechanisms is developed in Reference 6.

All these mechanisms, with the exception of the adsorption one, are local, i.e., they are based upon the processes occurring at the crack tip.[†] For them the dependence of the crack growth rate upon the factor K_I and absolute temperature, T, has the thermoactivation structure

$$\frac{dl}{dt} = f(K_I) \exp\left(-\frac{U}{RT}\right) \tag{125}$$

Activation energy, U, corresponds to the rate-determining physicochemical process at the crack tip. Basically, these processes are:

(1) hydrogen diffusion in the metal,

(2) ion diffusion in the electrolyte solution, electrochemical heterogeneous reactions (the ion discharge of hydrogen and metals, metal ions hydrolysis, reduction of oxygen, ionization of metals, etc.),

(3) oxygen diffusion in the oxide film, the chemical reaction of metal oxidation, etc.,

(4) chemical decomposition of the material itself.

In reality, several different processes occur simultaneously.

The function $f(K_I)$ in (125) has substantially different forms for the mechanisms mentioned.

In the case of hydrogenation the behavior of this function when K_I is increasing is as follows: it is at first approximately proportional to K_I^2, then to K_I, and, finally, at great values of K_I, to $\ln K_I$. The saturation regime is unlikely to be practically reached. The crack growth is abrupt (spasmodic). The absence of crack propagation at $K_I < K_{ISCC}$ is accounted for by the deterioration of hydrogen supply to the crack tip and by the formation of protective oxide films owing to the competing process of metal oxidation. The transition from nonpropagation to propagation is rather smooth. As Figure 28 shows, the linearity range is most substantial; it is this range that is usually realized in experiments.

In the case of corrosion cracks the function $f(K_I)$ usually exhibits the abrupt transition from zero to the saturation level, characterized by a constant crack growth rate. The crack grows by jumps, but the jumps are smaller than in the preceding case. In contrast to other cases, corrosion cracks in the saturation regime have a tendency to branch and form branched systems.[‡]

In the case of the general kinetic mechanism the function is characterized by the absence of a saturation level as well as by the absence of a pronounced threshold of crack propagation (i.e., by the absence of the quantity K_{ISCC}). When K_I increases, $f(K_I)$ grows faster than in all other cases. This mechanism of crack propagation is of most importance for polymer materials, whereas for metals it is perhaps much less important. The crack growth is continuous.

[†] In the case of the adsorption mechanism, a common unique $\dot{l}$–K_I diagram does not exist, because the crack growth rate is then governed by transport processes due to the motion of the aggressive medium in the crack cavity. The adsorption mechanism may be assumed practically athermal.

[‡] The cracks formed by the adsorption mechanism also feature this property.

If there exist no $\dot{l}$–K_I diagrams, the curves of the dependence of the initial stress intensity factor upon the time to failure may prove extremely useful. These curves are obtained in the experiments with a man-made initial crack by merely measuring the K_I^0 value at the initial moment and time, t, to failure. For corrosion cracks these curves have a specific plateau; at hydrogenation as well as in the cases when the crack rate depends on K_I, the curves have the appearance of monotonically decreasing functions.

Thus, to diagnose fracture and to judge the material properties one should determine the following characteristics which are best suited for the purpose:

(i) $\dot{l}$–K_I diagram,
(ii) crack growth activation energy, threshold stress intensity factor, and fracture toughness,
(iii) K_I^0–t diagram.

Using the experimental results of Carter and some other authors, one can compose a table based on the analysis of the diagrams available. This table given in Reference 6 contains a brief outline of the properties of some high-strength alloys in a corrosion-active medium; the conclusions concerning the causes of local fracture are drawn there on the basis of the theory developed here.

The phenomena of fatigue crack propagation under varying loads in the range $K_I < K_{ISCC}$ are the most complicated and insufficiently known; this range is characterized by mutual superposition and strengthening of comparable plastic and corrosion effects.

With decreasing temperature, the athermal mechanism of the fatigue crack propagation plays an ever-increasing role as compared to that of thermoactivation mechanisms; beginning with some critical temperature it becomes a crucial factor governing the rate of the overall process of the fatigue crack growth. When the temperature is below some critical value, the fatigue crack growth rate is independent of the environment.

The $\dot{l}$–K_I diagrams and the system parameters K_{ISCC}, K_C, U, K_{Ib}, K_{IF}, etc., also play an important role when estimating the construction working capacity: an engineer is, in principle, capable of predicting, by the use of fracture mechanics methods, the duration of safe and reliable lifetime of structural elements. One should be aware, however, that the obtaining and application of those parameters impose heavy (sometimes practically unattainable) demands on identification of various particular material–environment systems. In some cases even minute perturbations in the system (such as the presence of alloying admixtures, or inhibitor, etc.) may lead to appreciable deviations of output parameters. Moreover, the most reasonable and complete employment of these methods for real constructions will become practical only with progress of reliable nondestructive testing techniques.

Also of great interest are direct electrochemical methods of diagnostics and study of the fracture mechanism. Among them is the investigation of crack growth rate dependence upon specimen potential. Generally speaking, anode polarization of the specimen accelerates metal dissolution and hinders hydrogen deposition, whereas anode polarization, on the contrary, accelerates hydrogen discharge and hinders the process of metal ionization. Therefore the change in specimen potential leads, in general, to effects of different sign for different mechanisms (anode polarization accelerates electrochemical crack growth and impedes crack propagation in the case of local hydrogen embrittlement; quite the reverse is the case for cathode polarization). At present, however, this simple method cannot be considered reliable if transport processes and electrochemical reactions within the crack cavity are not taken into account. Indeed, experimental and theoretical studies have demonstrated(15,23,90) that anode polarization, while accelerating metal dissolution at the crack tip, accelerates hydrolysis, pH drop, and hydrogen liberation.

Of great interest are studies of electrochemical properties of the newly formed surface and of electrolyte composition in the immediate vicinity of the growing crack tip. Such studies are directed, in essence, to modeling local conditions at the crack tip. For example, it was shown(90) that in the external neutral 3.5% NaCl solution the electrolyte acidity in a growing crack is raised to pH 3.5–3.6 for aluminum alloy and carbon steel and to pH 1.7–3.0 for titanium alloy.

This is due to the hydrolysis reaction

$$M^{+z} + nH_2O \rightleftarrows M(OH)_n^{z-n} + nH^+$$

occurring in the crack cavity. The pH value in the crack is independent of pH in the main volume of electrolyte in the range from 2 to 10.(90) On the newly formed surface the hydrogen discharge rate is ten times and anode dissolution rate (for titanium) 10^5 times as high as on the specimen surface covered with oxide films.(92)

Acknowledgments

The author would like to express his special thanks to Dr. Safrai and Mrs. Kipnis who helped him to prepare the English version of this paper.

References

1. H. L. Logan, *The Stress Corrosion of Metals*, John Wiley and Sons, New York (1967).
2. N. D. Tomashov, *The Theory of Corrosion and Protection of Metals*, USSR Academy of Science Publishing, Moscow (1959) (in Russian).

3. G. V. Akimov, *The Theory and Methods of Study of Metal Corrosion*, USSR Academy of Science Publishing, Moscow (1959) (in Russian).
4. M. G. Fontana and N. D. Greene, *Corrosion Engineering*, McGraw-Hill, New York (1967).
5. T. P. Hoar, Electrode processes, in *Modern Aspects of Electrochemistry*, Vol. 3, J. O'M. Bockris, ed., Butterworths, London (1961).
6. G. P. Cherepanov, *Mechanics of Brittle Fracture*, McGraw-Hill, New York (1978).
7. H. H. Johnson and P. C. Paris, Sub-critical flaw growth, *Eng. Fract. Mech.* **1**, 3 (1968).
8. B. F. Brown, The application of fracture mechanics to stress corrosion cracking, *Metall. Rev.* **13**, 171 (1968).
9. H. H. Johnson, Environmental cracking in high-strength materials, in *Fracture*, Vol. 3, H. Liebowitz, ed., Academic Press, New York (1971).
10. H. Uhlig, Stress corrosion cracking, in *Fracture*, Vol. 3, H. Liebowitz, ed., Academic Press, New York (1971).
11. V. A. Marichev, Environment-enhanced crack growth of high-strength materials, *Zashch. Met.* **11**, 139 (1975) (in Russian).
12. G. P. Cherepanov, Mechanics of corrosive fracture, *Physico-chem. Mech. Mater.*, No. 1 (1974) (in Russian).
13. R. N. Parkins, F. Mazza, J. J. Royuela, and J. G. Scully, Stress corrosion test methods, *Brit. Corrosion J.* **7**, 154 (1972).
14. R. P. Wei, Some aspects of environment enhanced fatigue crack growth. *Eng. Fract. Mech.* **1**, 633 (1970).
15. R. W. Staehle, B. F. Brown, J. Kruger, and A. Agrawal, eds., *Localized Corrosion*, NACE, Houston (1974).
16. M. Pourbaix, *Atlas of Electrochemical Equilibria in Aqueous Solutions*, Pergamon Press, Oxford, England (1966).
17. V. V. Romanov, *Corrosion Cracking of Metals*, Mashgiz, Moscow (1980) (in Russian).
18. Passivity and Its Breakdown on Iron and Iron Base Alloys, Japan–USA Seminar, Honolulu, Hawaii, 1975.
19. J. A. Smith, M. H. Peterson, and B. F. Brown, *Corrosion (Houston)* **26**, 539 (1970).
20. M. Pourbaix, *Corrosion (Houston)* **26**, 431 (1970).
21. K. J. Vetter and H. H. Strehblow, in *Localized Corrosion*, R. W. Staehle, ed., NACE, Houston (1974).
22. H. W. Pickering and P. R. Frankenthal, *J. Electrochem. Soc.* **119**, 1297 (1972).
23. J. R. Galvele, Transport processes and the mechanism of pitting of metals, *J. Electrochem. Soc.* **123**, 464 (1976).
24. V. G. Levich, *Physico-chemical Hydrodynamics*, Fizmatgiz, Moscow (1959) (in Russian).
25. P. C. Paris and G. C. Sih, Stress analysis of cracks, in *Fracture Toughness Testing and Its Applications*, ASTM, Philadelphia (1965).
26. M. L. Williams, Stress singularities resulting from various boundary conditions in angular corners of plates in extension, *J. Appl. Mech.* **19(4)**, 526 (1952).
27. I. N. Sneddon, The distribution of stress in the neighbourhood of a crack in an elastic solid, *Proc. R. Soc. London Ser. A* **187**, 229–260 (1946).
28. G. R. Irwin, Fracture, in *Handbuch der Physik*, Vol. 6, Springer-Verlag, Berlin (1958), pp. 551–590.
29. G. P. Cherepanov, Singular solutions in the theory of elasticity, in *Mechanics of Solids*, Sudostroenie, Leningrad (1970) (in Russian).
30. H. Liebowitz, ed., *Fracture, An Advanced Treatise*, in 7 volumes, Academic Press, New York (1968–1974).
31. G. C. Sih, ed., *Mechanics of Fracture Series*, Vol. I, Lehigh University Press, Bethlehem, Pennsylvania (1973).
32. H. Tada, P. Paris, and G. Irwin, *The Stress Analysis of Cracks Handbook*, DEL Research Corporation, Hellertown, Pennsylvania 1973.

33. Fracture toughness testing and its applications, ASTM Special Technical Publication No. 381, Chicago, 1965.
34. W. F. Brown and J. E. Srawley, Plane strain crack toughness testing of high strength metallic materials, ASTM Special Technical Publication No. 410, 1969.
35. R. S. Sharpe, ed., *Research Techniques in Nondestructive Testing*, Academic Press, London (1970).
36. Fracture toughness, ASTM Special Technical Publication No. 514, 1972.
37. Cracks and fracture, ASTM Special Technical Publication No. 601, 1976.
38. G. P. Cherepanov, Cracks in solids, *Int. J. Solids Structures*, **4**, 811–831 (1968).
39. G. R. Irwin, Analysis of stresses and strains near the end of a crack traversing a plate, *J. Appl. Mech.* **24**(3), 361 (1957).
40. A. A. Griffith, The phenomenon of rupture and flow in solids, *Philos. Trans. R. Soc. London Ser. A* **221**, 163–198 (1920).
41. M. E. Shank, C. E. Spaeth, V. W. Cooke, and J. E. Coyne, Solid-fuel rocket chambers for operation at 240.000 psi and above, *Met. Prog.* **76**, 74 (1959).
42. G. R. Irwin and J. A. Kies, Fracture theory applied to high strength steels, *Met. Prog.* **78**, 73 (1960).
43. H. Bernstein and J. A. Kies, Crack growth during static tests of rocket motor cases, *Met. Prog.* **78**, 79 (1960).
44. E. A. Steigerwald, Delayed failure of high-strength steel in liquid environments, *Proc. ASTM* **60**, 750 (1960).
45. H. H. Johnson and A. M. Willner, Moisture and stable crack growth in a high strength steel, *Appl. Mater. Res.* **4**, 34 (1965).
46. B. F. Brown and C. D. Beachem, A study of the stress factor in corrosion cracking, *Corros. Sci.* **5**, 745 (1965).
47. G. L. Hanna, A. R. Troiano, and E. A. Steigerwald, A mechanism for the embrittlement of high strength steels by aqueous environments, *ASM Trans. Q.* **57**, 658 (1964).
48. G. G. Hancock and H. H. Johnson, Hydrogen, oxygen and subcritical crack growth in a high-strength steel, *Trans. Metall. Soc. A.I.M.E.* **236**, 513 (1966).
49. S. Wiederhorn, The influence of water vapor on crack propagation in soda-lime glass, *Natl. Bur. Stand. Rep.* No. 9442 (1966).
50. G. R. Irwin, Moisture assisted slow crack extension in glass plates, *Naval. Res. Lab. Memo. Rep.* No. 1678 (1966).
51. J. H. Mulherin, Stress corrosion susceptibility of high strength steel, in relation to fracture toughness, *Trans. A.S.M.E. Ser. D* **88**, 777 (1966).
52. M. H. Peterson, B. F. Brown, R. L. Newbegin, and R. E. Groover, Stress corrosion cracking of high strength steels and titanium alloys in chloride solutions at ambient temperature, *Corrosion (Houston)* **23**, 142 (1967).
53. W. A. Van der Sluys, Effects of repeated loading and moisture on the fracture toughness of SAE 4340 steel, *J. Basic. Eng. Trans. A.S.M.E. Ser. D* **87**, 363 (1965).
54. H. R. Smith, D. E. Piper, and F. K. Downey, A study of stess–corrosion cracking by wedge-force loading, *Eng. Fracture Mech.* **1**, 123 (1968).
55. G. P. Cherepanov, Invariant Γ-integrals and some of their applications in mechanics, *Appl. Math. Mech.* **41**(3), (1977) (in Russian).
56. J. D. Eshelby, *Philos. Trans. R. Soc.* **A244**, 87 (1951).
57. G. P. Cherepanov, Crack propagation in continuous media, *J. Appl. Math. Mech.* **31**(3), 504 (1967).
58. J. R. Rice, A path independent integral and the approximate analysis of strain concentration by notches and cracks, *Trans. ASME J. Appl. Mech.* 379 (1968).
59. J. R. Rice, Mathematical analysis in the mechanics of fracture, in *Treatise on Fracture*, Vol. 2, Academic Press, New York (1968), p. 191.
60. G. P. Cherepanov, L. V. Ershov, and G. G. Kuzmin, On the growth of corrosion cracks, *Corrosion (Houston)* **27**(12) (1972).

61. G. P. Cherepanov, On the theory of electrochemical stress corrosion cracking, in Proceedings of the Third Congress on Fracture, Münich, 1973.
62. G. N. Nikiforchin, Study of crack resistance of high-strength steels under static loadings in liquids, thesis, Lvov, 1977.
63. Hideo Kitagawa, Ryoji Yuuki, and Toshiaki Ohira, Crack-morphological aspects in fracture mechanics, *Eng. Fracture Mech.* 7(3), 515 (1975).
64. M. O. Speidel, Branching of stress corrosion cracks in aluminum alloys, NATO Conference on the Theory of Stress Corrosion Cracking in Alloys, Brussels, 1971, p. 289.
65. C. S. Carter, Stress corrosion crack branching in high strength steels, *Eng. Fracture Mech.* **3**, 1 (1971).
66. S. Mostovoy, H. R. Smith, R. G. Lingwall, and E. I. Rippling, A note on stress corrosion cracking rates, *Eng. Fracture Mech.* **3**, 291 (1971).
67. C. S. Carter, The effect of silicon on the stress corrosion resistance of low alloy high strength steel, *Corrosion (Houston)* **25**, 423 (1969).
68. C. S. Carter, The effect of heat treatment on the fracture toughness and subcritical crack growth characteristics of a 350-grade maraging steel, *Metall. Trans.* **1**, 1551 (1970).
69. J. A. Feeney and M. J. Blackburn, Effect of microstructure on the strength, toughness, and SCC susceptibility of a metastable beta titanium alloy (Ti–11.5Mo–6Zr–4.5Sn), *Metall. Trans.* **1**, 3309 (1970).
70. R. J. Bucci and P. C. Paris, Observations on sustained load environmental crack growth of a titanium 8Al–IMo–IV alloy, *Corrosion (Houston)* **27**, 525 (1971).
71. J. M. Krafft and J. H. Mulherin, *Trans. ASM* **62**, 64 (1969).
72. G. P. Cherepanov, On the theory of crack growth due to hydrogen embrittlement, *Corrosion (Houston)* **28**(8), 305 (1973).
73. J. T. Ryder and J. P. Gallagher, Environmentally controlled fatigue crack-growth rates in SAE 4340 steel—temperature effects, *J. Basic Eng. Trans. ASME* **92**, 133 (1970).
74. W. W. Gerberich and C. E. Hartbower, Monitoring crack growth of hydrogen embrittlement and stress corrosion cracking by acoustic emission, in *Proceedings of the Conference on the Fundamental Aspects SCC*, September 11–15, 1967, The Ohio State University, Department of Metallurgical Engineering (1969).
75. A. J. McEvily, J. B. Clark, and A. P. Bond, Effect of thermal-mechanical processings on the fatigue and stress-corrosion properties of an Al–Zn–Mg alloy, *Trans. Metal. Soc. AIME* **60**, 661 (1967).
76. A. Hartman and J. Schijve, The effect of environment and load frequence on the crack propagation low for macro-fatigue crack growth in aluminium alloys, *Eng. Fracture Mech.* **1**, 615 (1970).
77. R. P. Wei and J. D. Landes, The effect of D_2O on fatigue crack propagation in a high-strength aluminum alloy, *Int. J. Fract. Mech.* **5**(1), (1969).
78. T. W. Crocker and E. A. Lange, Corrosion-fatigue crack propagation studies of some new high-strength structural steels, *Trans. ASME D, J. Basic Eng.* **91**, 570 (1969).
79. R. J. Dunahe, McI. H. Clark, P. Atanmo, R. Kumble, and A. J. McEvily, Crack opening displacement and the rate of fatigue crack growth, *Int. J. Fracture Mech.* **8**, 209 (1972).
80. H. H. Smith and P. Shahinian, presented at the International Conference on Corrosion Fatigue, 14–18 June 1971, Storrs, Connecticut.
81. P. Furrer and H. Warlimont, Gefüge und Eigenschaften von Aluminiumlegierungen nach rascher Erstarrung, *Z. Metallkd.* **62**(1), 12 (1971).
82. M. J. Owen, Fatigue of carbon-fiber-reinforced plastics, in *Composite Materials*, Vol. 5, *Fracture and Fatigue*, L. J. Broutman and R. H. Krock, eds., Academic Press, New York (1974), p. 342.
83. G. P. Cherepanov, On crack growth under cyclic loading, *Appl. Mech. Eng. Phys.* **6** (1968) (in Russian).
84. G. P. Cherepanov and H. Halmanov, On the theory of fatigue crack growth, *Eng. Fracture Mech.* **4**, 219 (1972).

85. R. G. Forman, V. E. Kearney, and R. M. Engle, Numerical analysis of crack propagation in cycle loaded structures, *Trans. ASME Ser. D* **89**(3) (1967).
86. G. P. Cherepanov and H. Halmanov, On the crack growth below K_{ISCC}, *Eng. Fracture Mech.* **6**(3), 551 (1974).
87. J. M. Barsom, E. J. Imhof, and S. T. Rolfe, Fatigue crack propagation in high yield strength steels, *Eng. Fracture Mech.* **2**, 301 (1971).
88. G. F. Pittinato, Hydrogen enhanced fatigue crack growth in Ti–6Al–4V ELJ weldments, *Metall. Trans.* **3**(I) (1972).
89. G. P. Cherepanov and V. D. Kuliev, Effect of loading frequence and inactive environment to the fatigue crack growth, *Strength Problems*, No. 1 (1972) (in Russian).
90. B. F. Brown, G. T. Fujü, and E. P. Dahlberg, *J. Electrochem. Soc.* **116**, 218 (1969).
91. B. F. Brown, NATO Conference on the Theory of Stress Corrosion Cracking in Alloys, Brussels, 1971, p. 186.
92. T. R. Beck, NATO Conference on the Theory of Stress Corrosion Cracking in Alloys, Brussels, 1971, p. 68.

8

Electrochemical Aspects of Hydrogen in Metals

P. K. SUBRAMANYAN

1. Introduction

The deleterious effect that hydrogen produces in metals, known popularly as hydrogen embrittlement, has been the root cause of innumerable investigations.(1-6) The hydrogen that produces embrittlement usually is of electrochemical origin such as corrosion, pickling, electrodeposition, photoelectrolysis (occurring on oxide films of Fe_2O_3, TiO_2, etc.(7-8)) and so on. Involvement of electrochemistry in the study of H in metals is a natural consequence of the origin of the damaging hydrogen. Furthermore, the electrochemical technique of measuring hydrogen permeation developed by Devanatham and Bockris(9-13) is a very convenient and rigorous method for studying fundamental properties such as the diffusion coefficient, solubility, partial molar volume (pmv), heat of solution, etc., of H in metals in the temperature range of aqueous solutions.

Cailetet in 1864 made the observation that hydrogen permeates steel during acid pickling.(14) The phenomenon of hydrogen embrittlement should be considered to have been discovered in 1871 by Johnson.(15) The interest in studying hydrogen embrittlement, however, has increased significantly only since 1926.(1) The glimpse of a world devoid of fossil fuels that we experienced in the recent past (1974) has brought about a unique and unparalleled

---

P. K. SUBRAMANYAN • Gould Laboratories, Gould, Inc., Cleveland, Ohio 44108.

importance to hydrogen–metal systems. It has become clear that hydrogen will be an important fuel in the future. This situation poses embrittlement problems with respect to transportation and storage of hydrogen. Furthermore, the study of solubility and diffusivity of hydrogen in the context of storing it as a dissolved atomic species or as a hydride has become a very important aspect of the problem. All this happened at a time when the output of scientific research on hydrogen–metal systems was leveling off or even beginning to decline.

Bockris has been arguing the case of hydrogen energy for several years.(16,17) It appears that electric power generated by fusion reactors, solar cells (photovoltaics), and from geothermal power will be used to generate hydrogen via electrolysis. Photoelectrolysis could turn out to be another important source of hydrogen when the right photosensitive material is discovered. Fuel cells will be a means for partly converting H_2 into electrical energy. Liquid H_2 is a suitable fuel for aerospace transportation. Hydrogen can be burned in internal combustion engines and used effectively as a substitute for gasoline. From several points of view, the prospects for hydrogen as a fuel look bright.

2. Experimental Study of H in Metals

A number of methods is available for investigating H in metals. These methods are as follows: (a) gas phase charging with vacuum extraction,(3) (b) electrolytic charging with vacuum extraction,(3) (c) the mass spectroscopic method,(18,19) (d) the electrochemical method,(8–12) (e) the internal friction method,(20,21) (f) the neutron scattering method,(22,23) (g) the lithium nuclear microprobe method,(24) (h) the laser pulse method,(25) and (i) the secondary ion mass spectroscopy (SIMS).(26) Of these the first four methods are suitable for studying permeation of H through metals. Most of the permeation studies in the literature have been carried out by the gas phase and electrolytic charging methods. The electrochemical technique developed by Devanatham and Bockris at the University of Pennsylvania towards the end of the 1950s is becoming a widely accepted method.(27–34) Descriptions of this method can be found in a number of publications.(35–37) The laser pulse desorption method appears to have the potential of being used to estimate the microscopic distribution of hydrogen in metals. For example, the amount of hydrogen evolved when a beam hits a defect-free region, a dislocation pile-up or a microcrack will be different. The lithium nuclear microprobe (LNM) is based on the reaction $^{7}Li\ (3.075\ meV) + H \rightarrow {}^{8}Be + (17.64\ \text{or}\ 14.74\ meV)$. It is useful for the determination of H in the superficial regions of materials as a function of depth. The usefulness of the SIMS method with respect to H in metals is not clear. It indicates the formations of species like MH_2^+, MH^+, etc. But this does not prove that such species are actually present in the metal. The intense electrical field and the high energy of the primary beam could make metals and H very reactive.

2.1. Principle of the Electrochemical Method

In this method, the metal whose permeability for H is to be studied is made to function as a bipolar membrane electrode in the permeation cell. A schematic representation of the cell and the electrical circuit involved is shown in Figure 1. Hydrogen is generated on one side of the metal membrane. Most of the discharged atomic H combines to form molecular H_2 and escapes as bubbles. But at the same time a part of it dissolves in the metal membrane and diffuses to the opposite side. At this side the potential is maintained sufficiently positive so that all the arriving H atoms are instantly oxidized to generate an equivalent electrical current. In other words, this current is equivalent to the flux of the atoms exiting at the opposite side of the membrane or the anodic side of the membrane. This current is recorded as a function of time using a suitable t–y recorder. By analyzing such current transients obtained for well-defined initial and boundary conditions, the diffusion coefficient D and the solubility C_0 of H at the given current density are obtained. Differences in permeation current densities of the order of 0.1 $\mu A/cm^2$ or even less can be measured accurately. This corresponds to a hydrogen flux of 1.036×10^{-12} g-at./cm^2 sec or less. Thus this electrochemical technique is a very sensitive one. It is also quite reliable. Of all the methods available for studying H permeation, the

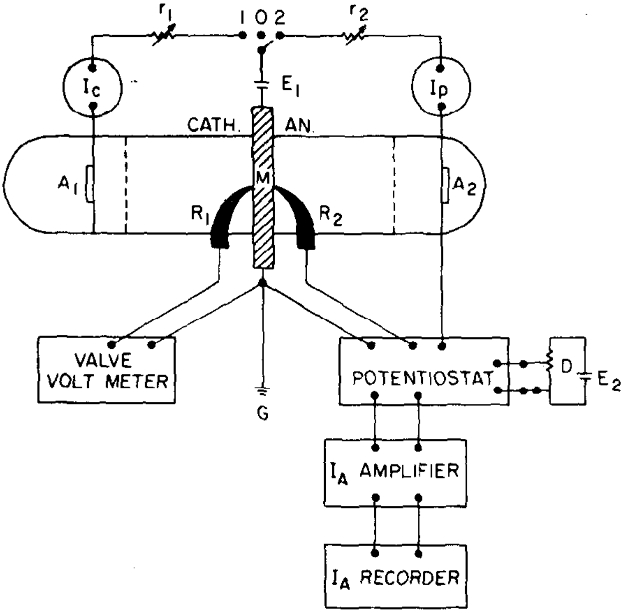

Figure 1. A schematic diagram of the experimental setup. M represents the membrane, CATH represents the cathodic side of the membrane ($x = 0$), and AN represents the anodic side of the membrane ($x = L$). R_1 and R_2 stand for reference electrodes connected through Luggin capillaries. Dashed lines represent porous partitions in the cell.

electrochemical method is the most accurate, easy to set up, and least time consuming one.

2.2. Solution of the Diffusion Equation

The relationships on which the measurements, as is common in diffusion studies, are based are the two diffusion laws of Fick, namely,

$$\frac{\partial C}{\partial t} = D\frac{\partial^2 C}{\partial X^2} \tag{1}$$

and

$$-D\frac{\partial C}{\partial X} = \frac{J}{ZF} \tag{2}$$

where C is the concentration of hydrogen at the distance X, t the time interval, and D the diffusion coefficient. In Eq. (2), the parameter J is the diffusional flux density at a distance X, Z the number of electrons involved in oxidation of the diffusing species, which is 1.0 in the case of H, and F the Faraday constant. Hydrogen diffuses in metals as atomic hydrogen. The material whose H permeability is to be studied is taken as a membrane or a plate of appropriate thickness. The following initial and boundary conditions are imposed on the test membrane: (1) $C = 0$, at $X = 0$ for $t \leq 0$; (2) $C = C_0$ at $X = 0$ and $C = 0$ at $X = L$ for $t > 0$. This is schematically shown in Figure 2. Practically, these initial and boundary conditions are attained by starting with a membrane that does not contain any dissolved H. A constant current density for generating hydrogen is maintained on the side of the membrane at $X = 0$. The potential of the side of the membrane at $X = L$ is always maintained at a sufficiently

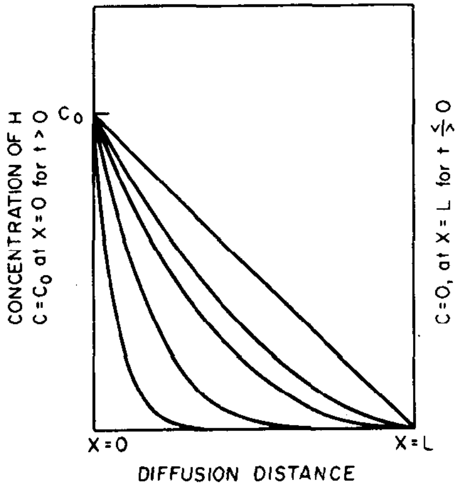

Figure 2. A schematic representation of concentration profiles of H in the permeation membrane as a function of time until the steady state is attained for the following initial and boundary conditions: $c = 0$ at $0 < x < L$ at time $t < 0$, $c = c_0$ at $x = 0$ for $t > 0$ and $c = 0$ at $x = L$ for $t \lesseqgtr 0$.

positive level so that all the H atoms arriving at $X = L$ are oxidized. The oxidation current at $X = L$ is recorded as a function of time starting from $t = 0$. This is called the permeation transient. Fick's second law, namely, Eq. (1), can be solved for the above initial and boundary conditions by the method of Laplace transform or Fourier transform. These solutions have been obtained by Devanatham *et al.*(9,10) and McBreen *et al.*(35) The Laplace transform solution of McBreen *et al.* is expressed as

$$\frac{C(X,t)}{C_0} = \sum_{n=0}^{\infty} (-1)^n \operatorname{erfc}\left(\frac{X + 2nL}{2(Dt)^{1/2}}\right) - \sum_{n=0}^{\infty} (-1)^n \operatorname{erfc}\left(\frac{2L(n+1) - X}{2(Dt)^{1/2}}\right) \tag{3}$$

The anodic current at $X = L$ which is equivalent to the flux of H diffusing out is given by Fick's first law for unit area as

$$J_t = -DZF\left(\frac{\partial C}{\partial t}\right)_{X=L} \tag{4}$$

where t represents time dependency. Hence

$$\frac{J_t}{J_\infty} = \frac{2}{\pi^{1/2}} \frac{1}{\tau^{1/2}} \sum_{n=0}^{\infty} (-1)^n \exp\left[-(2n+1)^2/4\tau\right] \tag{5}$$

where J_∞ represents the steady state permeation current and $\tau = Dt/L^2$. The first term approximation, i.e., when $n = 0$ of Eq. (5) is

$$\frac{J_t}{J_\infty} = \frac{2}{\pi^{1/2}} \frac{1}{\tau^{1/2}} \exp\left(-\frac{1}{4\tau}\right) \tag{6}$$

This approximation is valid up to $J_t = 0.965 J_\infty$. At a time when $J_t/J_\infty = 0.5$, the value of $Dt/L^2 = 0.138$. Therefore

$$D = \frac{0.138\, L^2}{t} \tag{7}$$

The time to attain 50% of the steady state value of J_∞ (or $J_t/J_\infty = 0.5$) is substituted in Eq. (7) to obtain the value of D. The solubility, C_0, of H corresponding to a given charging current density or overpotential for hydrogen evolution can be calculated from the equation for steady state permeability:

$$J_\infty = \frac{ZFDC_0}{L} \tag{8}$$

The approximate first-term solution according to Fourier transform method is obtained as

$$\frac{J_t}{J_\infty} = 1 - 2\exp(-\pi^2\tau) \tag{9}$$

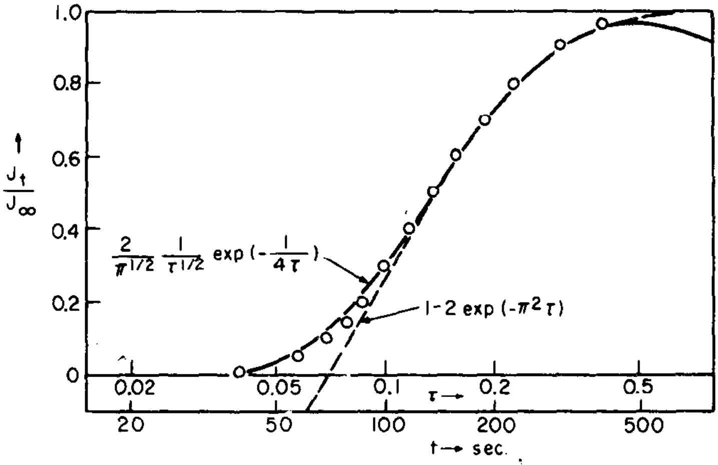

Figure 3. Graphical comparison of experimental data of buildup permeation transient (○) with the theoretically predicted buildup transients by the method of Laplace transform (——) and Fourier transform (– – –) solutions.

This solution gives erroneous values for J_t/J_∞ for $\tau < 0.1$. For $0.2 < \tau < 0.3$, the agreement between the two solutions is good. When is greater than 0.3, Eq. (9) gives better results than the Laplace transform solution.[35] These comparisons along with observed results are shown in Figure 3. A typical buildup permeation transient under the above initial and boundary conditions is shown in Figure 4.

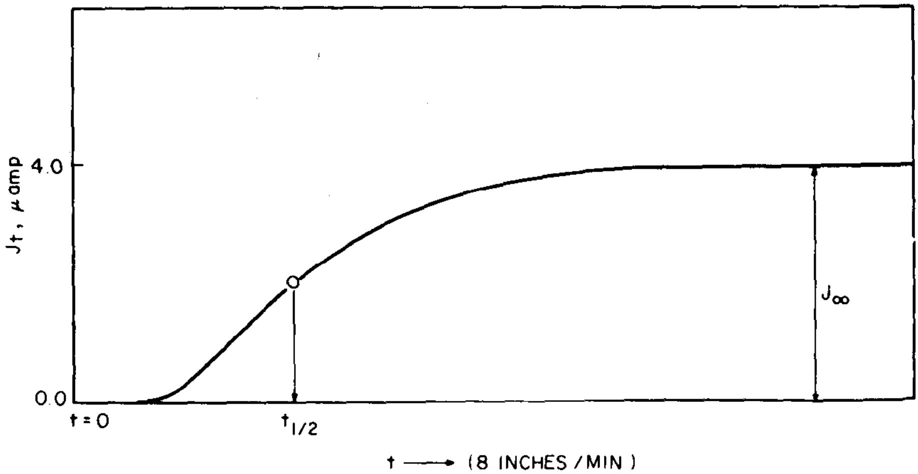

Figure 4. A laboratory record of H permeation buildup transient for Armco iron obtained under the following conditions: ambient electrolyte, 0.1 *M* NaOH; thickness of the membrane, 0.106 cm; temperature, 60°C; and cathodic current density, 10.0 mA/1.13 cm^2. The point $t = 0$ represents the time at which the cathodic current is switched on, $t_{1/2}$ the half rise time of the transient, and J_∞ the steady-state permeation current.

2.3. Solution of the Diffusion Equation when the Charging Current Is Switched Off

Suppose the cathodic current at $X = 0$ is turned off after the permeation current J_t attained steady state value. The recorder will start tracing the decay transient. A typical decay transient is shown in Figure 5. It is possible to obtain the diffusion coefficient of H by analyzing the decay transient, provided the initial and boundary conditions are known. In this particular case there is uncertainty with respect to the initial condition at $X = 0$. The following conditions may be assumed: (1) H does not exit through the surface at $X = 0$. Therefore $(\partial C/\partial t) = 0$, (2) $C = 0$ for $t > 0$ at $X = 0$, and (3) $C = C_0(1 - X/L)$ for $0 < X < L$ for $t < 0$. At $X = L$, the condition $C = 0$ for $t \gtrless 0$ prevails. McBreen *et al.*(34) deduced the solution for the conditions (1) and (3) as

$$\frac{J_t}{J_\infty} = 1 - 2 \sum_{n=0}^{\infty} (-1)^n \operatorname{erfc}\left(\frac{2n+1}{2\tau^{1/2}}\right) \tag{10}$$

For the conditions (2) and (3), the solution obtained by Nanis and Namboodhiri(38) is the following one:

$$\frac{J_t}{J_\infty} = 1 - 2 \sum_{n=0}^{\infty} \frac{1}{\pi^{1/2}} \frac{1}{\tau^{1/2}} \exp\left[\frac{-(2n+1)^2}{4\tau}\right] \tag{11}$$

The conditions assumed to prevail at $X = 0$ during decay of the permeation transient are of doubtful validity. H is mobile and reactive. Its chemical potential within the metal is higher than that corresponding to 1.0 atm of H_2.

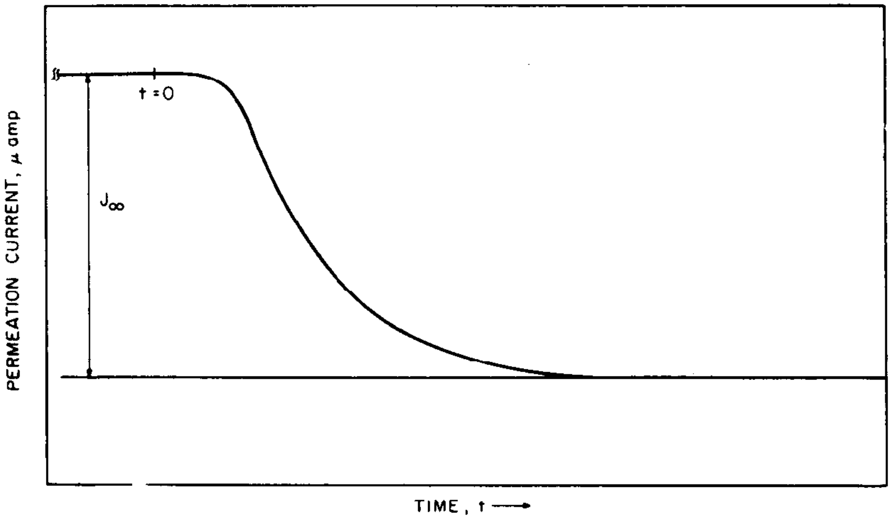

Figure 5. A typical permeation decay transient. The cathodic current is switched off at time $t = 0$. J_∞ represents the steady state permeation current before switching the cathodic current off.

Therefore it will escape through the surface at $X = 0$. However, its concentration at this surface will not be zero. The kinetics of recombination of H, namely, $2M - H \rightarrow 2M + H_2$ will not be fast enough to reduce the concentration to zero. Even if the kinetics were fast, the lowest concentration that H could attain at this surface is that which is in equilibrium with a pressure of 1 atm of H_2 unless the solution is continuously renewed by flowing fresh solution. In any case, the condition $C = 0$ at $X = 0$ is more realistic than assuming it to be an impenetrable surface.

Nanis and Namboodhiri(38) calculated the quantities of H diffusing out through the surfaces at $X = 0$ and $X = L$ under the fast-decay conditions. The concentration of H within the membrane $(0 < X < L)$ for the fast-decay conditions was deduced as

$$C = \frac{2C_0}{\pi} \sum_{n=1}^{\infty} \frac{1}{n} \sin\left(\frac{n\pi X}{L}\right) \exp\left(\frac{-n^2\pi^2 Dt}{L^2}\right) \tag{12}$$

Differentiating Eq. (12) with respect to X, substituting in Fick's first-law equation, and integrating, the quantity of H, Q_H, diffusing out was obtained as

$$Q_{H,X=0} = \tfrac{1}{3}C_0L \tag{13}$$

and

$$Q_{H,X=L} = \tfrac{1}{6}C_0L \tag{14}$$

The total quantity of H within the membrane $(Q_{H,X=0} + Q_{H,X=L})$ is equal to $(1/2)C_0L$. Hence, 1/3 of the total H diffuses out through the surface at $X = L$ and the remaining 2/3 of the total H diffuses out through the surface at $X = 0$. The equation (12) at time $t = 0$ reduces to $C = C_0(1 - X/L)$. Experimentally Nanis and Namboodhiri(34) found that the fraction of the total H diffusing out through Armco iron membrane at $X = L$ when charging was done from H_2SO_4 solution varied from 0.33 to 0.23 as the current density of charging was varied from 0.021 to 4.27 mA/cm^2. However, when H charging was carried out from NaOH solution, the value of this fraction of total hydrogen was found to be close to 0.33 in agreement with fast-decay conditions. The deviation in the case of H charging from H_2SO_4 solution was explained as a result of the diffusion coefficient increasing with the concentration of H.

As a concluding remark, it is important to point out that the most rigorous conditions for solving the diffusion equation (1) are the ones corresponding to the galvanostatic buildup transient. Potentiostating the surface at $X = 0$ as suggested by McBreen *et al.*(35) can be expected to be helpful in defining the conditions of decay transient. This should be done carefully so that the dissolved H_2 molecules in solution do not get oxidized at the surface at $X = 0$. Deluccia used a double potentiostatic circuit to study the permeation of H through β-Ti.(39) He found that unexpectedly the majority of H, namely, 94.5% exists through the cathodic surface (at $X = 0$).

2.4. Experimental Method of Studying H Permeation

The material whose H permeability is to be studied is obtained in the form of flat sheets or strips of appropriate thickness. This material is cut into suitable pieces called permeation membranes. The membranes are polished with carborundum paper down to 4/0, degreased in a Soxhlet extractor or solvent vapor degreaser. (Trichloroethylene is a good degreaser.) The membranes are then dried and annealed in purified H_2 atmosphere for about 2.0 hr at 600°C (for Fe and Ni) and allowed to cool gradually (5°C/min). When the temperature of the specimens or membranes is about 200°C, purified N_2 gas is introduced and H_2 gas is turned off. (At higher temperatures N_2 will react with Fe producing nitrides at the surface which will reduce H permeability of the membrane.) This allows all the dissolved H in the membranes to diffuse out. The specimens when cooled to room temperature are preserved in benzene.

The permeation cell shown in Figure 6 is washed thoroughly and rinsed with triple distilled water. The cell is then dried in an oven. A membrane is washed thoroughly, and etched for 20–30 sec in boiling 1.0% H_2SO_4 solution in methanol. The etched specimen is rinsed well with pure methanol and dried in air. The cell is then assembled with the membrane in position. In the case of a membrane which is subjected to anodic dissolution at the exit side, i.e., $X = L$ (such as Fe), Pd is deposited at this side as a thin layer ($\simeq 1000$ Å) from a suitable solution [for example, 0.2 *N* NaOH solution containing 10^{-5} mol/liter

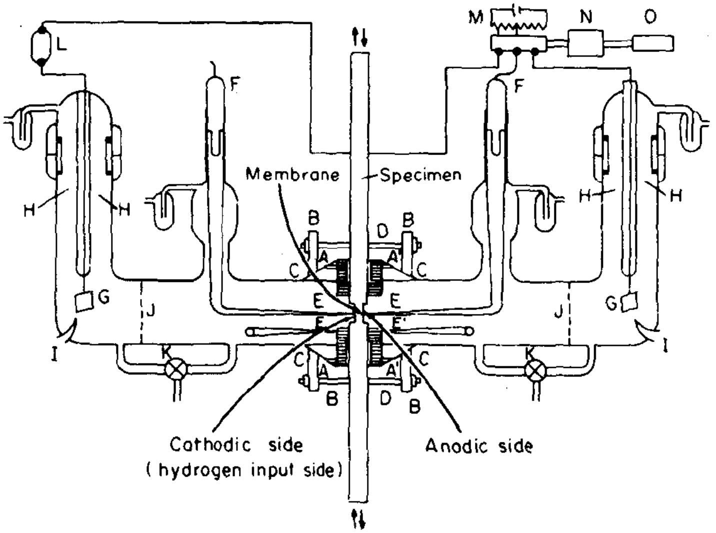

Figure 6. The cell assembly with stress permeation specimen. *A*, Teflon gasket on the cathodic side; *A'*, Teflon gasket on the anodic side; *B*, flange; *C*, Teflon washer; *D*, bolts; *E'*, Luggin capillary for bubbling gas (N_2); *F*, saturated calomel electrode; *G*, Pt counterelectrode; *H*, Teflon joint with O-ring; *J*, sintered glass partition; *K*, solution outlet; *L*, source of constant current; *M*, potentiostat; *N*, amplifier, and *O*, strip chart recorder.

palladium nitrite complex, $Na_2Pd(NO_2)_4$].(11) Deposition from the nitrite complex solution is done at 100 $\mu A/cm^2$ for 90 min. The plating solution is drained off and the anodic compartment is washed and rinsed thoroughly. It is then filled with preelectrolyzed and deoxygenated NaOH solution. The same solution or a desired solution is filled in the cathodic compartment. Purified N_2 or Ar is bubbled through both the compartments to remove all the dissolved O_2. The anodic side of the membrane is potentiostated at a sufficiently positive level so that all the H atoms diffusing out through this side will be instantly oxidized. Maintaining a potential of −0.600 V vs. SCE will ensure this condition. The background current in the anodic circuit is recorded as a function of time. When it attains a steady state value, usually less than 1 $\mu A/cm^2$ for about 1 hr, H permeation experiments can be carried out.

The recorder in the anodic circuit is set at the appropriate speed. The desired charging current is applied galvanostatically at the cathodic site of the membrane. The time of switching on the cathodic current is marked as zero on recorder chart. As the permeating H arrives at the anodic side, the anodic current rises as a transient which is recorded on the strip chart. A typical transient for Fe–Ni alloy containing 5% Ni at 60°C is shown in Figure 4. When the concentration of H in the membrane attains a steady state value, the transient correspondingly develops a steady state permeation current. When the charging current is switched off, the permeation current on the anodic side begins to decay as shown in Figure 5. This decay transient finally attains the original background current level ($<1\ \mu A/cm^2$). When this transient attains the background level, the H charging experiment can be repeated. It is desirable to start with the lowest charging current density first and then progress step by step. After the permeation studies when the cell is disassembled, the thickness of the membrane at the permeation area is measured.

2.5. Analysis of the Buildup Permeation Transient

The buildup permeation transients are analyzed to obtain the diffusion coefficient and solubility of H using the Eqs. (7) and (8). The time corresponding to $J_t/J_\infty = 0.5$, called the half rise time, is noted from the record of the transient and is substituted in Eq. (7) to obtain D. When the value of D is known, the solubility C_0 corresponding to the charging current density can be calculated from Eq. (8). The interval from time $t = 0$ up until the permeation current starts rising is called the break-through time. The half rise time includes the break-through time and the rest of the time interval up to $J_t/J_\infty = 0.5$.

When H charging is carried out at low current densities, the diffusion coefficient of H will be found to increase as current density increases. This effect arises due to the presence of an oxide film on the cathodic surface of the membrane. Initially the applied current is utilized to reduce this film before H starts permeating into the metal. The time taken for this decreases as the current density increases. When the thickness of the membrane increases, this effect decreases. In the case of Armco iron of 0.10-cm thickness in presence of NaOH ambient solution at room temperature, this effect may be noticeable up to a current density of 3.0 mA/cm^2. Beyond this current density the increase in the magnitude of D is not appreciable. The values of D obtained at low current densities should be neglected. In a similar situation, when H was charged from 0.1 N H_2SO_4 solution, Nanis and Namboodhiri(38,40) observed, in the case of Armco Fe specimens, that the diffusion coefficient of H increased from 4.84×10^{-5} to 8.45×10^{-5} cm^2/sec as the charging current density increased from 0.021 to 2.3 mA/cm^2. These investigators made the unusual conclusion that the diffusivity of H in Armco Fe increased with increasing solubility of H.

3. Solubility of H in Metals

H is discharged as atomic H on metals. Initially it is adsorbed on the metal surface. From the absorbed state H can pass on into the dissolved state by jumping into the interstitial spaces beneath the first atomic layer. From this dissolved state, H diffuses into the bulk. Most of the discharging H, however, recombines to form molecular H_2 and escapes into the solution or the atmosphere. The scheme of H permeation can be represented as

$$H^+ + e + M \rightleftarrows M - H_{\text{ads}} \rightleftarrows M - H_{\text{diss}} \xrightarrow{\text{diffusion}} M - H_{\text{diss}}$$

Here the subscripts "ads" and "diss" mean adsorbed and dissolved, respectively, and M represents the metal. Dissolution of H in the metal is a fast process. Dissolved H normally stays in the interstitial spaces available in the lattice unless larger spaces such as atomic vacancies are available. The slowest step in permeation (which includes dissolution and diffusion) is the diffusion process. This has been shown to be so by Devanathan and Stuchurski(10) and Beck *et al.*(13) Were this not so, the permeation transient would not coincide with the calculated transient based on the solutions of the diffusion equation (cf. Figure 3). Kim and Wilde experimentally determined the rate constant k of absorption of H into Ferrovac E iron by an electrochemical method.(41) The value of k was found to be 2.53 sec^{-1} at room temperature. For a rough comparison, it can be seen that $k\theta_H \gg -D(\partial C/\partial X)$ at the H entry side. The magnitude of D for Armco iron is 6.5×10^{-5} cm^2/sec. More recently, Franklin and Bayerlein deduced the value of the rate constant for H absorption into iron in presence of NaOH solution with and without the additions of NaCl, Na_2S, and NaCN.(42) In the presence of NaOH solution alone, the value of k_{abs} was found to be 1 56 sec^{-1}. Therefore absorption of H or H dissolution is a faster process than H diffusion.

The solubility of H_2 in metals varies over a wide range, for example, from 10^{-8} to 10^{-1} g-at./cm^3. On the basis of the heat of dissolution of H_2, metals are

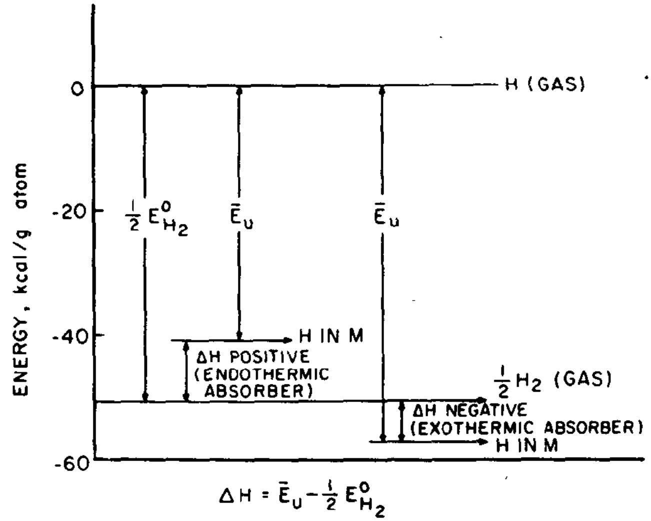
ENERGY, kcal/g atom
0
-20
-40
-60
H (GAS)
$\frac{1}{2}E^0_{H_2}$
$\bar{E}_u$
$\bar{E}_u$
H IN M
ΔH POSITIVE (ENDOTHERMIC ABSORBER)
$\frac{1}{2}H_2$ (GAS)
ΔH NEGATIVE (EXOTHERMIC ABSORBER)
H IN M
$\Delta H = \bar{E}_u - \frac{1}{2}E^0_{H_2}$

Figure 7. Schematic representation of the energy changes occurring in the process of dissolution of gaseous H_2 in metal, M.

classified as endothermic or exothermic absorbers of H_2. With respect to atomic H, all metals are exothermic absorbers. A qualitative representation of this situation is shown in Figure 7.

Many metals, for example, Li, Ti, Zr, Ca, Ba, Na, Ta, Nb, La, and so on, form binary hydrides. Iron is a metal with very low solubility for H, but it suffers the most damage due to H embrittlement. Os, Ir, Pt, Rh, W, Mo, Co, etc., also have low levels of H solubility. Normally Ni behaves as if its solubility is lower, of the order of 10^{-6} g-at./cm^3. However, it is classified sometimes as a hydride-forming metal. Pd is a special case. For a long time it was supposed to have a solubility limit of 0.55 H/Pd on the basis of *d*-band vacancy. More recently, the work of Baranowski *et al.*(43,44) have shown that it could reach as high a value as PdH under extremely high pressures of H_2, of the order of 20,000 atm.

3.1. Sievert's Law

This law relates solubility of H in metals to the pressure of H_2 gas in the ambient. It is obeyed in the lower ranges of solubility. Mathematical form of Sievert's law can be expressed as(3)

$$C_0 = kp^{1/2} \qquad (15)$$

where C_0 is the solubility of H corresponding to the pressure, P, of H_2 gas. K is the Sievert's law constant and, in magnitude, it is equal to the solubility of H in metal at a pressure of 1.0 atm of H_2. The dependence on the square root of pressure originates from the atomic nature of dissolved hydrogen. This may be shown as follows:

$$H_2 \rightleftarrows 2M{-}H_{ads} \rightleftarrows 2M{-}H_{diss}$$

The equilibrium constant of this reaction is given by $C_0^2/P = K$ or $C_0 = K^{1/2}p^{1/2} = kp^{1/2}$. Therefore the Sievert's law constant is equal to the square root of the equilibrium constant K. If K is known experimentally, the free energy change of dissolution of H in metals can be deduced through the equation $-\Delta G = RT \ln K$.

3.2. Significance of the Solubility of H Measured in Electrochemical Permeation Method

The values of solubility of H measured by the electrochemical method are values corresponding to the overpotential of H charging current from a given solution. This cannot easily be related to the pressure of H_2 gas which would give rise to the same solubility at the given temperature. The one point of

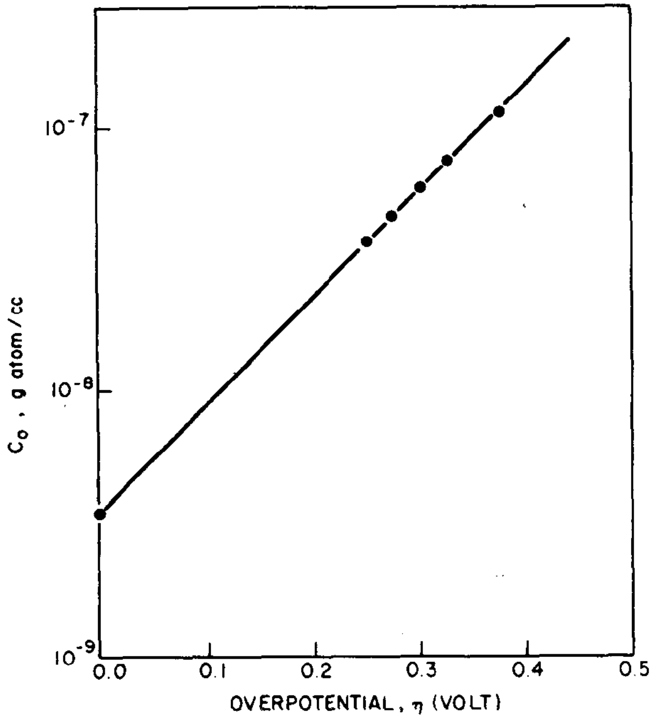

Figure 8. Hydrogen solubility–overpotential plot for Armco iron at 25°C. The value of C_0 corresponding to $\eta = 0$, corresponds to the solubility at 1.0 atm of hydrogen. Ambient electrolyte 0.1 N H_2SO_4.

correspondence is the solubility at the reversible potential for H evolution which is equivalent to the solubility at a pressure of 1 atm of H_2. Therefore a plot of the solubility, C_0, vs. the overpotential, η, can be extrapolated to $\eta = 0$ to obtain the solubility at 1 atm of H_2. The value of C_0 at the reversible potential for hydrogen evolution is independent of the ambient electrolyte. A plot of C_0 vs. η for H-charging of Armco Fe at 25°C from 0.1 N H_2SO_4 solution is shown in Figure 8.(45) The most convenient and reliable method of correlating the concentration of H in a given metal to the equilibrium pressure of H_2 gas is by obtaining the solubility at zero overpotential. This corresponds to the Sievert's law constant in magnitude. Then, for a known solubility C, the corresponding pressure can be calculated using Eq. (15). Knowledge of the equivalent pressure of H_2 is important in ascertaining the development and spreading of cracks in metals.

4. Chemical Potential of Hydrogen in Metals(46)

In traditional electrochemistry, the chemical potential of H_2 is easily related to the overpotential, η, as

$$\mu_{H_2} = \mu_{(H_2)_{rev}} + 2\eta F \tag{16}$$

From this standpoint, one could relate the chemical potential of either adsorbed or dissolved H to that of an equivalent fugacity, f_{H_2}, of H_2 given by the Nernst equation

$$\eta = -\frac{RT}{2F}\ln(f_{H_2}) \tag{17}$$

In a dynamic situation where H_2 is generated at appreciable rates, both Eqs. (16) and (17) will not be valid. The only condition under which these equations will be valid is the following: Suppose H_2 is being evolved in an electrochemical cell set up in an autoclave. Initially the pressure inside the autoclave is 1.0 atm. The cell is turned on to generate hydrogen at the cathode at a certain overpotential. The potential of the cathode is maintained constant (under potentiostatic condition). We are assuming that no oxygen is evolved on the anode. This may be accomplished by using a solution of redox couples or Na_2SO_3, with a suitable membrane. As the electrolysis proceeds, the pressure in the autoclave will rise owing to H_2 buildup. The system will attain a state in which there is no further current flow and no further increase in pressure. The state of the system as a function of time will not change anymore, provided the potential of the cathode is maintained the same and that the composition of the solution remains unchanged. The fugacity of H_2 corresponding to the pressure in the autoclave will be that given by the Nernst equation (17). With respect to the initial condition, we applied a certain overpotential η to the cathode and maintained it constant. The cell responding to this stimulus passed through a kinetic process and attained another thermodynamic (equilibrium) condition in which the reversible potential of H_2 electrode is $E_{rev}(f_{H_2}) = E_{rev}(1 \text{ atm}) + \eta$.

The Nernst equation does apply to a given system under a particular set of conditions. The experiment described in the above paragraph does not seem to have been done so far. However, there is the story of the following experiment. A long time ago, a sealed hollow sphere of iron was immersed in acid. After a certain time interval this hollow sphere exploded owing to the buildup of H_2 pressure inside.

4.1. *The Basic Relationship of the Chemical Potential of Hydrogen to the Hydrogen Evolution Kinetics*

During evolution of H_2 on a metal surface, a fraction of the total discharging H enters the metal lattice (dissolved state) from the adsorbed state. Dissolved H in the metal immediately below the surface is in equilibrium with the adsorbed H on the external surface. The basic thermodynamic equations describing this condition are

$$\mu_{H_{\text{ext surf}}} = \mu_{H_{\text{diss}}} \tag{18}$$

and

$$\mu_{H_{\text{ads}}} = \mu^{\circ}_{H_{\text{ads}}} + RT \ln\left(\frac{\theta}{1-\theta}\right) \tag{19}$$

where θ is the coverage of H on the surface. The adsorbed as well as the dissolved H can be considered to be in equilibrium with a certain unknown fugacity, f_{H_2}. Hence

$$\mu_{H_2} = \mu^{\circ}_{H_2} + RT \ln (f_{H_2}) \tag{20}$$

From these equations, the following isotherm can be obtained:

$$\frac{\theta}{1-\theta} = f_{H_2}^{1/2} \exp\left(\frac{\frac{1}{2}\mu^{\circ}_{H_2} - \mu_{H_{\text{diss}}}}{RT}\right) \tag{21}$$

From statistical mechanical considerations, the above equation can be transformed as[(46)]

$$\frac{\theta}{1-\theta} = Bf_{H_2}^{1/2} \exp\left(\frac{-u_a + \frac{1}{2}u_m}{kT}\right) \tag{22}$$

where B is a constant and the quantities u_a and u_m (the potential energies of an adsorbed H atom and of a H_2 molecule in the gas phase) are related to the heat of desorption as

$$\Delta H_{\text{diss}} = u_m - 2u_a \tag{23}$$

The quantity u_m is pressure dependent to a small extent. Neglecting this, Eq.

(22) can be modified as

$$\frac{\theta}{1-\theta} = Af_{\mathrm{H}_2}^{1/2} \exp\left(-\frac{u_a}{kT}\right) \tag{24}$$

Here A is another constant.

In the electrochemical situation, the coverage of H at the reversible potential for the hydrogen evolution reaction (h.e.r.), θ_{rev}, is equivalent to the equilibrium coverage at 1.0 atm of H_2. Therefore

$$\frac{\theta_{\mathrm{rev}}}{1-\theta_{\mathrm{rev}}} = A \exp\left(-\frac{u_a}{kT}\right) \tag{25}$$

Hence

$$f_{\mathrm{H}_2}^{1/2} = \frac{\theta}{1-\theta} \, \frac{1-\theta_{\mathrm{rev}}}{\theta_{\mathrm{rev}}} \tag{26}$$

The heat of adsorption or desorption of H is a function of coverage. For iron, the value of ΔH_{ads} varies from −32.0 to −13.0 kcal/g-at. when θ varies from 0 to 1.0 in gas phase.(47) A similar variation in presence of aqueous solution is also expected. However, the magnitude of ΔH_{ads} will be diminished in this case. Heat of adsorption usually decreases faster as θ increases beyond 0.5.

4.2. The Kinetics of Hydrogen Evolution and the Possible Pressure of Hydrogen in Internal Cracks, Cavities, or Voids in Metals

The possible pressure that could develop inside a crack in a metal when H_2 is generated electrochemically at the external surface will depend on the chemical potential of the dissolved H in the metal. Since the dissolved H is in equilibrium with the adsorbed H on the external surface, the possible pressure will depend on $\mu_{\mathrm{H}_{\mathrm{ads}}}$. Therefore the following condition prevails:

$$\mu_{\mathrm{H}_{\mathrm{ads}}\,\mathrm{ext\,surf}} = \mu_{\mathrm{H}_{\mathrm{diss}}} = \mu_{\mathrm{H}_{\mathrm{ads}}\,\mathrm{int\,surf}} = \mu_{(\mathrm{H}_2)\mathrm{crack}} \tag{27}$$

In the previous section, it was shown that if the ratio of $[\theta/(1-\theta]:[\theta_{\mathrm{rev}}/(1-\theta_{\mathrm{rev}})]$ is known, the fugacity of H_2 in the crack or void can be obtained. The equation (27) assumes that diffusion process of hydrogen in the metal is absent, i.e., there does not exist any chemical potential gradient for hydrogen in the metal. However, hydrogen evolution occurs at the external surface. It is possible to calculate $[\theta/(1-\theta)]$ as a function of the potential of h.e.r. When the potential of h.e.r. is set equal to the reversible potential, the ratio of $[\theta_{\mathrm{rev}}/(1-\theta_{\mathrm{rev}})]$ is also obtained. Thus it is possible to deduce the possible pressure of H_2 in cavities or cracks as a function of overpotential. This pressure will depend upon the mechanism of the hydrogen evolution reaction. Of the several possible mechanisms, two cases will be considered here.(46)

4.2.1. Fast-Discharge–Slow-Recombination Mechanism

According to the following mechanism,

(a) $H^+ + e^- + M \rightleftarrows M{-}H_{ads}$

(b) $M{-}H_{ads} + M{-}H_{ads} \xrightarrow{\text{rds}} 2M + H_2$

step (a) is assumed to be kinetically in equilibrium. This condition enables us to write the rate expression for h.e.r. as

$$k_a C_{H^+}(1-\theta)\exp\left(\frac{-\alpha VF}{RT}\right) = k_{-a}\theta\exp\left[\frac{(1-\alpha)VF}{RT}\right] \tag{28}$$

These quantities have their usual meanings. Rearranging the terms,

$$\frac{\theta}{1-\theta} = \frac{k_a}{k_{-a}} C_{H^+}\exp\left(-\frac{VF}{RT}\right) \tag{29}$$

Let the potential V be equal to V_{rev} for h.e.r. Hence

$$\frac{\theta_{rev}}{1-\theta_{rev}} = \frac{k_a}{k_{-a}} C_{H^+}\exp\left(-\frac{V_{rev}F}{RT}\right) \tag{30}$$

Dividing Eq. (29) by Eq. (30),

$$\frac{\theta}{1-\theta}\,\frac{1-\theta_{rev}}{\theta_{rev}} = \exp\left[\frac{(V_{rev}-V)F}{RT}\right] \tag{31}$$

Therefore, from Eq. (26), we obtain

$$f_{H_2} = \exp\left(\frac{-2\eta F}{RT}\right) \tag{32}$$

The fugacity of H_2 in this case is the same as the one given by the Nernst equation. Hence this is one mechanism that gives rise to the highest possible pressure in cracks.

4.2.2. Slow-Discharge–Fast-Electrochemical Desorption Mechanism

The slow-discharge–fast-electrochemical desorption mechanism is given as

(a) $H^+ + e^- + M \xrightarrow{\text{rds}} M{-}H_{ads}$

(b) $M{-}H_{ads} + H^+ + e^- \rightleftarrows M + H_2$

From step (b), the following equation can be derived:

$$k_b C_{H^+}\theta\exp\left(\frac{-\alpha VF}{RT}\right) = k_{-b}(1-\theta)p_{H_2}\exp\left[\frac{(1-\alpha)VF}{RT}\right] \tag{33}$$

where p_{H_2} is equal to 1.0 atm. Rearranging the terms,

$$\frac{\theta}{1-\theta}=\frac{k_{-b}}{k_b C_{H^+}}p_{H_2}\exp\left(\frac{VF}{RT}\right) \tag{34}$$

At the potential $V = V_{rev}$,

$$\frac{\theta_{rev}}{1-\theta_{rev}}=\frac{k_{-b}}{k_b C_{H^+}}p_{H_2}\exp\left(\frac{V_{rev}F}{RT}\right) \tag{35}$$

The final expression for fugacity of H_2 is obtained as

$$f_{H_2}=\exp\left(\frac{2\eta F}{RT}\right) \tag{36}$$

Since η is a negative quantity, the fugacity of H_2 in the crack or cavity will be less than 1 atm. This mechanism, therefore, is nonembrittling by the pressure mechanism.

4.2.3. Summary of the Results for the Various Probable Mechanisms

Between these two examples, there are other mechanisms which would produce the same or varying pressures. These are summarized in Table 1. It is the pressure of H_2 that is important in spreading cracks and causing embrittlement. Therefore it is necessary to relate fugacity of H_2 to sensible pressure. This is accomplished by evaluating the following thermodynamic equation of

Table 1
Summary of the Internal Pressure Calculations as a Function of the Mechanism of the h.e.r.

Mechanism	Fugacity f_{H_2}, atm	Remarks
Fast-discharge–slow combination	$\exp\left(-\frac{2\eta F}{RT}\right)$	Nernst equation valid; could be embrittling.
Slow-discharge–fast combination	1	Nonembrittling
Slow-discharge–fast electrochemical desorption	$\exp\left(\frac{2\eta F}{RT}\right)$	Nonembrittling
Fast-discharge–slow electrochemical desorption	$\exp\left(-\frac{2\eta F}{RT}\right)$	Nerst equation valid; could be embrittling.
Coupled-discharge–combination	$10^{1.5}\times\exp\left(-\frac{\eta F}{2RT}\right)$	$0 \ll 1$; could be embrittling.
Coupled-discharge–electrochemical desorption	$\exp\left(-\frac{2\eta^* F}{RT}\right)$	Only predictable exactly if η^* is known experimentally.[a]

[a] η^* represents the potential at which fast-discharge–electrochemical desorption changes to coupled-discharge–electrochemical desorption.

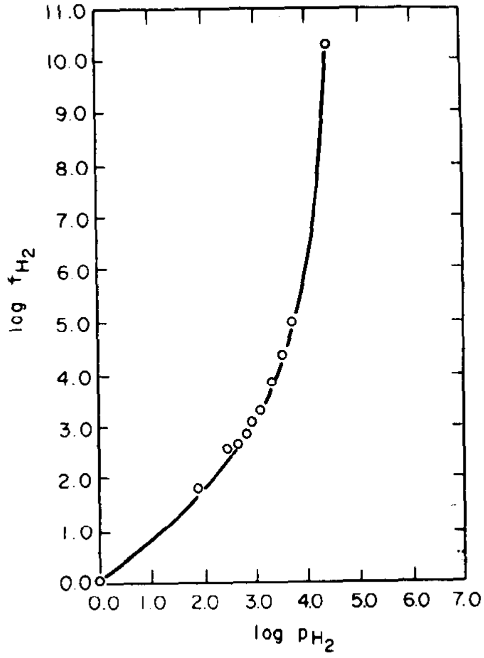

Figure 9. Fugacity–pressure relationship for H_2 at 300 K plotted from the data tabulated by Podgurski.(48) Basis of this table is the data on "Compressibility Factors and Fugacity Coefficients Calculated from Beattie–Bridgman Equation of State" by Holley *et al.*(49)

state for H_2:

$$RT \ln f = RT \ln p + \int_0^p (B + Cp + Dp^2 + \cdots) \tag{37}$$

The results are as shown in Figure 9. The fugacity of H_2 rises faster than its sensible pressure. The pressure corresponding to a fugacity of 10^{10} atm is only 10^4 atm. The maximum pressure that could be developed under severe conditions of electrolysis, according to Smialowski, is 13,000 atm.(50)

5. Permeation of H in Relationship to the Mechanism of Hydrogen Evolution Reaction

The flux of H entering a metal lattice is supposed to be proportional to the coverage on the surface. There are two basic mechanisms for h.e.r. These are as follows:

1. *Discharge–combination mechanism*

(a) $M + H^+ + e^- \rightarrow M{-}H_{ads}$

(b) $M{-}H_{ads} + M{-}H_{ads} \rightarrow 2M + H_2$

2. Discharge–electrochemical desorption mechanism

(a) $M + H^+ + e^- \rightarrow M{-}H_{ads}$

(c) $M{-}H_{ads} + H^+ + e^- \rightarrow 2M + H_2$

The adsorbed state of hydrogen is a common factor. This should be expected to be so because of the high free energy change of adsorption of atomic H on metals and the ease of availability of sites on the surface. The process of dissolution of H in metals can be represented as

(d) $M{-}H_{ads} \underset{k_{-d}}{\overset{k_d}{\rightleftharpoons}} M{-}H_{diss}$

Experimentally, it is found to be a faster process than diffusion. Therefore, it can be considered to be in equilibrium in the overall permeation process. The kinetic situation is such that

$$k_d\theta = k_{-d}C_0 \tag{38}$$

where C_0 is the solubility of H. The solubility C_0, therefore, is a parameter directly proportional to the H coverage θ:

$$C_0 = \left(\frac{k_d}{k_{-d}}\right)\theta = K\theta \tag{39}$$

where K is the equilibrium constant of reaction (d). It is known that for metals such as Fe, Ni, Pt, Pd, etc., the heat of adsorption and, therefore, the free energy of adsorption of H, decreases as the concentration of MH_{ads} increases. Further, owing to the small solubility of H in metals such as Fe, the free energy of the dissolved H should remain rather unchanged in spite of the changes in coverage on the surface. As a consequence of all this, the equilibrium constant of reaction (d) should vary continuously as θ increases. In all probability, the forward step will accelerate.

5.1. Mode of Entry of H into the Lattice

Bockris *et al.*(51) considered the case of a direct entry of H into the metal lattice as proposed by Bagotskaya and Frumkin, namely,

(e) $H^+ + e^- + M \rightarrow M{-}H_{diss}$

Their analysis showed that the steady state permeation current density in this case to be proportional to the square of the charging current density. Experimentally, J_∞ was found to be proportional to $i^{1/2}$ (cf. Figure 10). Therefore Bockris *et al.* concluded that the direct entry mechanism is inadmissible. In all probability, H enters the lattice from the adsorbed state. The exact process of entry of H is a matter for speculation. It is believed to be a diffusional jump when an appropriate fluctuation occurs. H is considered dissolved when it

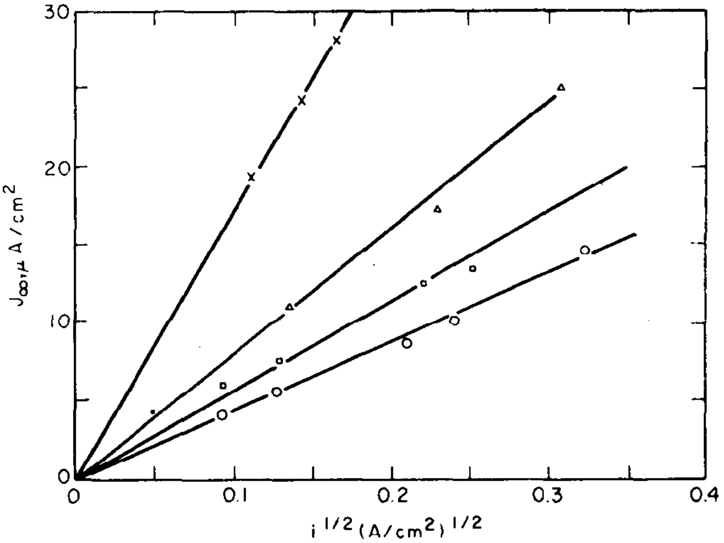

Figure 10. Hydrogen permeability vs. charging current density relationships for Armco iron. $L = 0.077$ cm at 25°C in 0.1 N H_2SO_4 with additions of KI: ○, none; □, 10^{-4} M; △, 5×10^{-4} M; ×, 5×10^{-3} M. Area = 1.0 cm².

crosses the first atomic layer. The fact that H dissolution occurs fast and attains equilibrium instantly compared to bulk diffusion is due to the following reasons: (1) The number of H atoms attempting to enter the lattice from the adsorbed state is much higher than the number of dissolved H atoms diffusing into the bulk. (2) The number of fluctuations available for diffusional jumps is much higher at the surface than in the bulk.

5.2. Dependence of Permeation Current on the Mechanism of h.e.r.

Equation (39) shows that the concentration of dissolved H is proportional to the coverage θ. The steady state permeation current density ($J_\infty = FDC_0/L$), therefore, is directly proportional to θ. Further, θ is dependent on the potential and the mechanism of h.e.r. As examples, we shall consider the following two cases: (1) coupled-discharge–recombination, (2) fast-discharge–slow-recombination.

5.2.1. Coupled-Discharge Recombination(52)

The coupled-discharge–recombination mechanism is given as

(f) $H^+ + e^- + M \xrightarrow{k_f} M - H_{ads}$

(g) $\mathrm{M{-}H_{ads} + M{-}H_{ads} \xrightarrow{k_g} 2M + H_2}$

The expression for current density in this case is

$$i = k_f C_{\mathrm{H^+}}(1-\theta)\exp\left(\frac{-\beta\eta F}{RT}\right) = k_g\theta^2 \tag{40}$$

The steady state permeation current density can be expressed as

$$J_\infty = \frac{FD}{L}\left(\frac{k_d}{k_{-d}}\right)\theta = \frac{FD}{L}\left(\frac{k_d}{k_{-d}}\right)\left(\frac{1}{k_g}\right)^{1/2} i^{1/2} \tag{41}$$

At low values of θ,

$$\theta = \left(\frac{k_f}{k_g}\right)^{1/2} C_{\mathrm{H^+}}^{1/2}\exp\left(\frac{-\beta\eta F}{RT}\right) \tag{42}$$

Hence

$$J_\infty = \frac{FD}{L}\left(\frac{k_d}{k_{-d}}\right)\left(\frac{k_f}{k_g}\right)^{1/2} C_{\mathrm{H^+}}^{1/2}\exp\left(\frac{-\beta\eta F}{2RT}\right) \tag{43}$$

Therefore

$$\frac{d\eta}{d\ln J_\infty} = -\frac{2RT}{\beta F} = \frac{d\eta}{d\ln\theta} \tag{44}$$

A plot of the overpotential of η vs. J_∞ can, thus, provide a diagnostic criterion with respect to the mechanism of h.e.r.

5.2.2. Fast-Discharge–Slow-Combination

(h) $\mathrm{H^+ + \mathit{e} + M \underset{k_{-h}}{\overset{k_h}{\rightleftarrows}} M{-}H_{ads}}$

(i) $\mathrm{M{-}H_{ads} + M{-}H_{ads} \xrightarrow{k_i} 2M + H_2}$

From the kinetic considerations of these steps,

$$k_h C_{\mathrm{H^+}}(1-\theta)\exp\left(\frac{-\beta\eta F}{RT}\right) = k_{-h}\theta\exp\left[\frac{(1-\beta)\eta F}{RT}\right] \tag{45}$$

and

$$i = k_i\theta^2 \tag{46}$$

For low values of θ, Eq. (45) reduces to

$$\theta = \frac{k_h}{k_{-h}} C_{\mathrm{H^+}}\exp\left(\frac{-\eta F}{RT}\right) \tag{47}$$

Table 2
Diagnostic Parameters for Various Mechanisms of h.e.r.

Mechanism of h.e.r.	$\frac{-\partial\eta}{\partial \log i}$			$\frac{-\partial\eta}{\partial \log J}$			$J_\infty = f(L)$		
		Temkin			Temkin			Temkin	
	Langmuir	Non-activated	Activated	Langmuir	Non-activated	Activated	Langmuir	Non-activated	Activated
Slow discharge–fast recombination	$\frac{2RT}{F}$	$\frac{2RT}{F}$	$\frac{2RT}{F}$	0	0	0	—	—	—
Slow discharge–fast electrochemical	$\frac{2RT}{F}$	$\frac{RT}{F}$	$\frac{RT}{F}$	$\frac{RT}{F}$	$\frac{RT}{F}$	$\frac{RT}{F}$	i^{-2}	i	i
Fast discharge–slow recombination	$\frac{RT}{2F}$	$\frac{RT}{2F}$	$\frac{RT}{F}$	$\frac{RT}{F}$	$\frac{RT}{F}$	$\frac{RT}{F}$	i	$i^{1/2}$	i
Fast discharge–slow electrochemical	$\frac{2RT}{3F}$	$\frac{2RT}{3F}$	$\frac{RT}{F}$	$\frac{RT}{F}$	$\frac{RT}{F}$	$\frac{RT}{F}$	$i^{2/3}$	$i^{2/3}$	i
Coupled discharge–recombination	$\frac{2RT}{F}$	$\frac{5RT}{2F}$	$\frac{3RT}{F}$	$\frac{4RT}{F}$	$\frac{5RT}{2F}$	$\frac{3RT}{2F}$	$i^{1/2}$	i	i^2
Coupled discharge–electrochemical	$\frac{2RT}{F}$	$\frac{2RT}{F}$	$\frac{2RT}{F}$	0	0	0	—	—	—

Therefore, from the variation of the steady state permeation current density as a function of η, or

$$\frac{d\eta}{d\ln J_\infty} = -\frac{RT}{F} = \frac{d\eta}{d\ln\theta} \tag{48}$$

studies of coverage–potential and i–J_∞ relationships in conjunction with current–potential relationships for h.e.r. can provide additional diagnostic parameters identifying the mechanism of h.e.r. A summary of these diagnostic parameters are given in Table 2.(52) Recently, Tilak and Conway(53) and Tilak *et al.*(54) have carried out theoretical analyses of overpotential decay behavior of h.e.r. for various probable mechanisms and deduced diagnostic criteria. The paths of h.e.r. mechanism taking place on various metals are classified as in Table 3.(55,56)

6. Influence of the Composition of the Ambient Solution on Permeation of Hydrogen in Metals

Since 1926 it has been recognized that the composition of the solution, especially, the presence of certain compounds called promotors has considerable influence on the transfer of H into metals. Reference to the earlier works can be found in the work of Radhakrishnan and Shreir.(57) The substances that usually promote the entry of H into metals are compounds of the elements As, Se, Te, S, P, Bi, Hg, and Pb. Typically, these elements could be added as $NaASO_2$, Na_2SeO_3, Na_2TeO_3, Na_2S, Ca_3P_2, etc. As a consequence of the addition of these compounds the overpotential for h.e.r. increases. A common property among these promoters of H entry, on poisons of h.e.r., is that they form hydrides of the type AsH_3, H_2Se, H_2Te, H_2S, PH_3, SbH_3, etc. The

Table 3
Mechanism of h.e.r. on Various Metals[a]

									Al		
									D		
Ti			Mn	Fe		Ni	Cu		Ga		
D			A	E, C		A	A or D		A		
	Nb	Mo			Rh	Pd	Ag	Cd		Sn	
	D	D			B	B	C or D	A		A	
	Ta	W			Ir	Pt	Au	Hg	Tl	Pb	Bi
	D	A or D			B	B	D	A	A	A	D

[a] A, slow discharge–fast recombination; B, fast discharge–slow recombination; C, slow discharge–fast electrochemical; D, fast discharge–slow electrochemical; E, coupled discharge recombination.

effectiveness of these various elements in promoting H entry has been classified by various investigators as follows: (a) $P > S > As > Se > Sb > Te > Bi$,(3,58) (b) $As > Se > Te > Sb > S > P > Bi > Hg > Pb$,(59) (c) $As > Se > Te$,(60) (d) $Se > As > Te > Sb > S > P$,(61) and (e) $As > Se > Te > S > Pb > Bi$.(58) The above classification is based on weight of the additive. Newman and Shreir(62) found that the permeation of H increases with increasing concentration of the promoter up to a certain level beyond which it levels off or decreases slightly. A recent account of the influence of promoters on H permeation is given by Fontana and Staehle.(29) Staehle and co-workers(29) observed that addition of arsenite is not effective in the low cathodic overpotential ranges in which it acts more like a H entry inhibitor. At higher overpotentials, the effect of promotion is observed. Like Smialowski,(3) these authors believe that the increase in permeation corresponds to the formation of AsH_3.

A number of theories has been put forth to account for the action of H promoters. According to Smialowski, the promoter effect arises from the formation of hydrides such as AsH_3, PH_3, etc. Shuler and Laidler consider the effect as arising from an increase in M–H bond strength.(63) Some Soviet investigators think that the colloidal particles formed during electrolysis promote the entry of H and that in presence of poisons, H enters the cathode material as protons.(64,65) According to Evans, the poisons interfere with H recombination step, thereby increasing the probability of H entry into the metal.(66)

The permeation of H through metals depends on the mechanism of evolution of hydrogen. This was pointed out by Bockris and Thacker(67) and Devanathan and Stachurski.(10) Bockris *et al.* carried out investigations on the effect of adding CN^-, I^-, naphthalene, naphthionitrile, valeronitrile, and benzonitrile.(51) Results of this study are summarized here. Additions of KI and naphthalene to H_2SO_4 increased permeability while additions of organic nitriles decreased it. The Tafel slope for h.e.r. in H_2SO_4 solution containing KI was 0.115 V/decade. The slope of the overpotential–permeability plot ($d\eta/d \ln J_\infty$) in this case was found to be 0.235 V/decade. These parameters for NaOH solutions containing the additives were 0.122 and 0.240 V/decade, respectively. In all cases, the additives increased the overpotential for h.e.r. The results for additions of KI and KCN are shown in Figure 11.

Bockris *et al.*(51) offered the following theory for accounting for the increase in permeability of H upon adding I^-, CN^-, and naphthalene. The $M–H_{ads}$ bond becomes weaker in presence of these additives. This is expected to decrease the height of the energy barrier for entry of H. In the case of iron, $Fe–H_{ads}$ species has negative charge density on H. This H^- species interacts with CN^- or I^- to produce weakening of the $Fe–H_{ads}$ bond.

It is possible to account for the increased permeability of H on grounds of interfering with the H recombination reaction by the adsorbed species such as I^-, CN^-, etc. This automatically increases the average residence time of H on

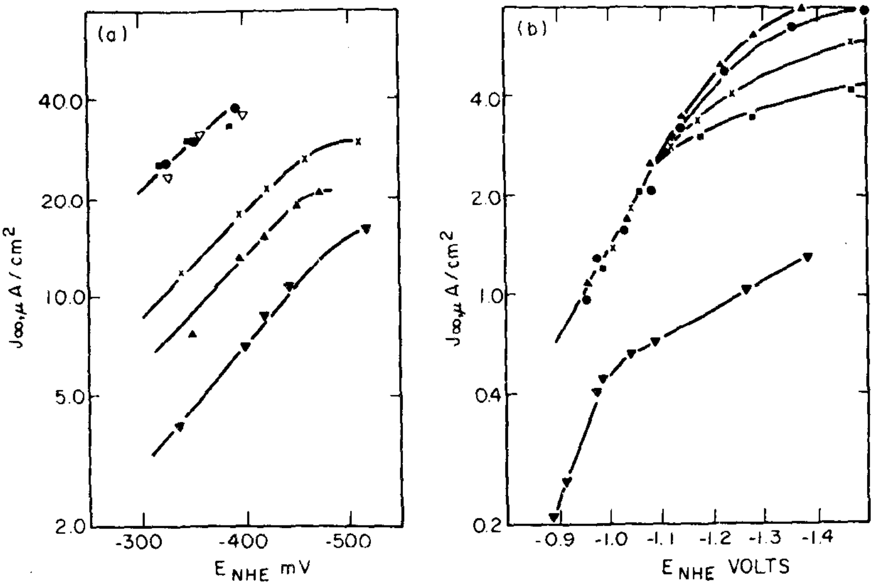

Figure 11. Effect of additives on the permeability potential relationships. (a) Permeability potential plots for Armco iron, $L = 0.077$ cm at 25° in 0.1 N H_2SO_4 solution containing various amounts of KI: ▼, none; ▲, $10^{-4}\,M$; ×, $5 \times 10^{-4}\,M$; ■, $10^{-3}\,M$; ●, $5 \times 10^{-3}\,M$; and △, $10^{-2}\,M$. (b) Permeability potential plots for Armco iron, $L = 0.077$ cm at 25°C in 0.1 N NaOH with additions of KCN as: ▼, none; ■, $1.6 \times 10^{-4}\,M$; ×, $10^{-3}\,M$; ●, $10^{-2}\,M$; and ▲, $10^{-1}\,M$. Area = 1.0 cm^2.

the surface and therefore the coverage. From the equilibrium state of the adsorption–dissolution reaction, $(k_d/k_{-d})\theta = C_0$ [cf. Eq. (38)]. Effectively, C_0 becomes large in presence of the additives. This can be either due to an increase in the magnitude of θ, or k_d/k_{-d}, or both.

7. Effect of Hydrostatic Pressure on the Kinetics of h.e.r. and Hydrogen Permeation in Iron

These effects were investigated by Nanis and Deluccia by the electrochemical method.(68) They used a special permeation cell made of Teflon, Kel-F, and Pyrex glass which could be enclosed in a pressure vessel. Hydrostatic pressure was applied on the cell by means of an air-operated, double-action pressure pump using water as the pressurizing medium. These investigators were able to vary the pressure in the range 1.0–600 atm. The aim of this study was to throw light on the mechanism of corrosion and hydrogen embrittlement of steel in deep sea conditions. The significant observations made in this study were the following: (a) permeability of H at a given charging current density increased with increasing pressure, (b) overpotential for h.e.r.

was independent of applied hydrostatic pressure, and (c) the residual permeability of H in the absence of current from the cathodic solution containing dissolved H_2, increased proportionally to the applied pressure. The last observation apparently is not in conformance with Sievert's law, which will require solubility to increase proportionately to the square root of the applied pressure. Sievert's law is a thermodynamic relationship, and therefore is applicable only in equilibrium conditions. First of all, it is not clear in the experimental conditions of Nanis and Deluccia that the catholyte was saturated with H_2. Normally, it does not become saturated with H_2 evolved at currents of the order of 1.0 mA for a few minutes (the solubility of H_2 at 25°C = 19.1 cm^3/l at 1 atm). Further, the solubility of H_2 increases as the pressure increases in accordance with Henry's law. The solubility levels of H in iron deduced by these investigators are in the range $0.34–1.56 \times 10^{-6}$ g-at./cm^3.(69) The diffusion coefficient of H in their iron specimens was 4.2×10^{-5} cm^2/sec. The solubility of H_2/cm^3 of solution was of the order of 0.8×10^{-6} mol/cm^3. The diffusion coefficient of H_2 in aqueous solution most probably is smaller than the diffusion coefficient of H in iron. Under these conditions, the permeation of H through the membrane is limited by the diffusional supply of H_2 to the surface of the membrane. Besides, in the present situation there are the adsorbed entities on the surface of the membrane. The effect of the $P\bar{V}_i$ term (where $\bar{V}_i$ is the partial molar volume of the ith species) on the adsorption of hydrogen on the surface in competition with other species also needs to be considered. Further, there is the residual corrosion of iron in the electrolyte (0.1 N H_2SO_4 + 0.01 N HCl). The situation is complicated compared to the simple gas phase hydrogen charging conditions in which Sievert's law holds true in a certain range of pressure. As long as H_2 dissolves in the metal as H, Sievert's law will be obeyed, provided the concentration of H is low in the metal. That the results of Nanis and Deluccia did not obey Sievert's law should be attributed to the inadequacies and complications in their experimental conditions.

Deluccia *et al.*(69) discussed the effect of applied hydrostatic pressure on the overpotential for h.e.r. They concluded that a kinetic overpotential for h.e.r. cannot be related to a differential pressure through the equation

$$\eta = \frac{RT}{2F} \ln \left(\frac{P_2}{P_1}\right) \tag{49}$$

because they did not find any change in η on application of stress (cf. Section 4).

8. Effect of Stress on the Chemical Potential of H in Metals

de Kazinczy appears to be the first one to study the effect of stress on H dissolved in steel.(70) He observed that a steel tube subjected to tensile stress permeates more H than the unstressed tube, when hydrogen is generated at a constant current density. Further, he noted that the effect of tensile stress was reversible, i.e., when the stress was removed the permeation level decreased to the level before application of stress. de Kazinczy, however, was not sure of the fact that the applied stress does not produce any effect on the diffusion coefficient of H in steel. Beck *et al.*(13) were the first investigators to study the effect of stress on H dissolved in iron and steel from a thermodynamic point of view and to obtain a measure of a parameter of great importance, namely, the partial molar volume (pmv) of H in metal. They deduced the pmv of H from the relationship†

$$\left(\frac{d\mu_{\mathrm{H}}}{dP}\right)_T = \frac{d \ln (C_\sigma/C_0)}{dP} = \bar{V}_{\mathrm{H}} \tag{50}$$

where C is the solubility under the applied stress and C_0 the same in the absence of stress. Beck *et al.*(13) established the fact that stress had no effect on the diffusion coefficient of H and that the effect on solubility was reversible.

The basic thermodynamic equation that we normally use to obtain the pmv of H is

$$\left(\frac{\partial\mu_{\mathrm{H}}}{\partial P}\right)_{n_1, n_2, \ldots, n_{\mathrm{H}}, \ldots, T} = \bar{V}_{\mathrm{H}} \tag{51}$$

This equation normally restricts the transfer of H between the metal and the surroundings. In any method, based on the application of pressure, whether it is electrochemical or gas phase charging, the transfer of H will take place. Therefore there is an apparent difficulty in understanding how one can use a measurement based on the application of pressure to obtain the pmv of H.

Li *et al.*(71) made a detailed thermodynamic analysis of mobile intersticial species such as H, C, N, etc., in metals. However, their approach cannot be considered rigorous from a thermodynamic standpoint. For example, they introduce the partial molar volume in a very restricted sense as the cubical effect of linear expansion in a certain direction upon adding the species. This implies that the molar or partial molar volume of the metal remains unaffected as the intersticial species is dissolved. *Prima facie*, there is no justification for such an assumption. For instance, for a two-component system of metal and H,

$$V = n_{\mathrm{M}}\bar{V}_{\mathrm{M}} + n_{\mathrm{H}}\bar{V}_{\mathrm{H}} \tag{52}$$

where V is the total volume of the system of n_{M} moles of metal and n_{H} moles of H. In the absence of H, $V_{\mathrm{M}} = \bar{V}_{\mathrm{M}}$. In the presence of H, the magnitude of $\bar{V}_{\mathrm{M}}$ could decrease, increase, or remain unchanged compared to V_{M}, the molar volume of the metal. An enlightening example in this situation is of H_2O and H_2SO_4. The resultant volume when both are mixed is less than the combined volume of the components. Secondly, there is an equilibrium with respect to the solubility of H in metals such as

---

† In the numerical evaluation of the pmv of H, Beck *et al.* made an error by dividing by the value of 2.303 instead multiplying by it.

(a) $xH_2 + nM \rightleftarrows (nM)2H_x$

When the chemical potential of the metal changes under applied stress, the solubility of H could also change. Li *et al.* ignored the major component, i.e., the metal in the analysis. Further, these authors erroneously introduced the concept that the chemical potential of an immobile component like metal in metal–hydrogen systems can only be defined at the interface and not in the bulk. This seems to have arisen from a misunderstanding of the situation considered by Gibbs in the crystallization of salt on the different faces of a nonhydrostatically stressed solid.(72)

An analysis of the metal–hydrogen system on the lines of classical thermodynamics was worked out by Bockris and Subramanyan.(73–75) A brief version of this analysis is reproduced here. The Euler equation for the metal–hydrogen system can be expressed as

$$n_M\mu_M + n_H\mu_H = E + \sigma_h V - TS - \frac{\sigma_h^2 V}{2K} \tag{53}$$

where σ_h is the hydrostatic component of the applied stress, V the volume, E the internal energy, T the temperature, and S the entropy of the system. The given amount of n_M moles of metal is supposed to be equilibrated with H_2 at a constant pressure. The hydrostatic component σ_h is defined as

$$\sigma_h = -\tfrac{1}{3}(\sigma_{xx} + \sigma_{yy} + \sigma_{zz}) \tag{54}$$

where σ_{xx}, σ_{yy}, and σ_{zz} are the components of stresses in the x, y, and z directions acting on planes normal to these directions. The right-hand side of Eq. (53) can be expressed in partial molar properties as

$$\begin{aligned} n_M\mu_M + n_H\mu_H &= (n_M\bar{E}_M + n_H\bar{E}_H) + \sigma_h(n_M\bar{V}_M + n_M\bar{V}_M) \\ &\quad - T(n_M\bar{S}_M + n_H\bar{S}_H) - \frac{\sigma_h^2}{2K}(n_M\bar{V}_M + n_H\bar{V}_H) \end{aligned} \tag{55}$$

For an isothermal reversible process of absorption of H into metal,†

$$\begin{aligned} &n_M\,d\mu_M + n_H\,d\mu_H \\ &\quad = \left(\frac{\sigma_h^2}{2K^2}n_M\bar{V}_M\,dK + n_M\bar{V}_M\,d\sigma_h - \frac{\sigma_h}{K}n_M\bar{V}_M\,d\sigma_h + n_M\mu_M\,dn'_M\right) \\ &\quad\quad + \left(\frac{\sigma_h^2}{2K^2}n_H\bar{V}_H\,dK + n_H\bar{V}_H\,d\sigma_h - \frac{\sigma_h}{k}n_H\bar{V}_H\,d\sigma_h + n_H\mu_H\,dn'_H\right) \end{aligned} \tag{56}$$

Further, imposing the condition that n_M is conserved, i.e., $dn'_M = 0$, and that the amount of dissolved hydrogen is small enough so that it does not produce any change in the bulk modulus, i.e., $dK = 0$,

---

† In Eq. (56), $n_M\,dn'_M = dn_M$ and $n_H\,dn'_H = dn_H$.

$$\begin{aligned} n_{\mathrm{M}}\left(\frac{\partial\mu_{\mathrm{M}}}{\partial\sigma_h}\right)_{n_{\mathrm{M}},K,T} &+ n_{\mathrm{H}}\left(\frac{\partial\mu_{\mathrm{H}}}{\partial\sigma_h}\right)_{n_{\mathrm{M}},K,T} \\ &= \left(1-\frac{\sigma_h}{K}\right)n_{\mathrm{M}}\bar{V}_{\mathrm{M}} + \left(1-\frac{\sigma_h}{K}\right)n_{\mathrm{H}}\bar{V}_{\mathrm{H}} + n_{\mathrm{H}}\mu_{\mathrm{H}}\frac{dn'_{\mathrm{H}}}{d\sigma_h} \qquad (57) \end{aligned}$$

Suppose the transfer of H from the system or into the system is completely restricted. Therefore

$$\begin{aligned} n_{\mathrm{M}}\left(\frac{\partial\mu_{\mathrm{M}}}{\partial\sigma_h}\right)_{n_{\mathrm{M}},n_{\mathrm{H}},K,T} + n_{\mathrm{H}}\left(\frac{\partial\mu_{\mathrm{H}}}{\partial\sigma_h}\right)_{n_{\mathrm{H}},n_{\mathrm{M}},K,T} &= \left(1-\frac{\sigma_h}{K}\right)n_{\mathrm{M}}\bar{V}_{\mathrm{M}} + \left(1-\frac{\sigma_h}{K}\right)n_{\mathrm{H}}\bar{V}_{\mathrm{H}} \\ &= \left(1-\frac{\sigma_h}{K}\right)V \qquad (58) \end{aligned}$$

In the above equation V is the total volume of the system. The pmv of the ith component is given by

$$\left(\frac{\partial\mu_i}{\partial P}\right)_{n_1,n_2,\ldots,n_i,\ldots,T} = \bar{V}_i \qquad (59)$$

In cases where the solubility of H in the metal is very small, as for example H in iron or steel, addition or removal of a small amount dn_{H} of H will leave μ_{M} unperturbed. Hence

$$\left(\frac{\partial\mu_{\mathrm{M}}}{\partial\sigma_h}\right)_{n_{\mathrm{M}},K,T} = \left(\frac{\partial\mu_{\mathrm{M}}}{\partial\sigma_h}\right)_{n_{\mathrm{M}},n_{\mathrm{H}},K,T} \qquad (60)$$

Therefore, from Eqs. (57) and (58),

$$n_{\mathrm{H}}\left(\frac{\partial\mu_{\mathrm{H}}}{\partial\sigma_h}\right)_{n_{\mathrm{M}},K,T} = \left(1-\frac{\sigma_h}{K}\right)n_{\mathrm{H}}\bar{V}_{\mathrm{H}} + n_{\mathrm{H}}\mu_{\mathrm{H}}\left(\frac{dn'_{\mathrm{H}}}{d\sigma_h}\right)_{n_{\mathrm{M}},K,T} \qquad (61)$$

When the transfer of hydrogen between the metal and surroundings is not allowed, the second term on the right-hand side of Eq. (61) reduces to zero. Hence

$$n_{\mathrm{H}}\left(\frac{\partial\mu_{\mathrm{H}}}{\partial\sigma_h}\right)_{n_{\mathrm{M}},K,T} = \left(1-\frac{\sigma_h}{K}\right)n_{\mathrm{H}}\bar{V}_{\mathrm{H}} \qquad (62)$$

which, indeed, is the basic thermodynamic equation that relates chemical potential and pressure to volume. When the exchange of hydrogen is permitted, the second term on the right-hand side of Eq. (61) makes its contribution. The changes that affect μ_{H}, namely, $d\mu_{\mathrm{H}}$ tends to zero on attaining the new equilibrium. As a result of that, the left-hand side of Eq. (61) becomes equal to zero. Thus

$$\left(1-\frac{\sigma_h}{K}\right)n_{\mathrm{H}}\bar{V}_{\mathrm{H}} = -n_{\mathrm{H}}\mu_{\mathrm{H}}\left(\frac{dn'_{\mathrm{H}}}{d\sigma_h}\right)_{\mathrm{eq.}\ n_{\mathrm{M}},K,T} \tag{63}$$

From Eq. (62),

$$n_{\mathrm{H}}\left(\frac{\partial\mu_{\mathrm{H}}}{\partial\sigma_h}\right)_{n_{\mathrm{M}},K,T} = -n_{\mathrm{H}}\mu_{\mathrm{H}}\left(\frac{dn'_{\mathrm{H}}}{d\sigma_{\mathrm{H}}}\right)_{\mathrm{eq}\ n_{\mathrm{M}},K,T} \tag{64}$$

The change in chemical potential of H on application of σ_h can be expressed as

$$\int_0^{\sigma h} d\mu_{\mathrm{H}} = RT\ln\left(\frac{C_{\mathrm{H},\sigma_h}}{C_{\mathrm{H},0}}\right) \tag{65}$$

Hence

$$-RT\left(\frac{\partial\ln\left(C_{\mathrm{H},\sigma_h}/C_{\mathrm{H},0}\right)}{\partial\sigma_h}\right)_{n_{\mathrm{M}},K,T} = -\mu_{\mathrm{H}.S}\left(\frac{\partial n'_{\mathrm{H}}}{\partial\sigma_h}\right)_{\mathrm{eq.}\ n_{\mathrm{M}},K,T} \tag{64a}$$

where $\mu_{\mathrm{H}.S}$ is the chemical potential of H on the surface where it remains unaffected by application of σ_h and the same as μ_{H} before application of σ_h. Therefore

$$-RT\left(\frac{\partial\ln\left(C_{\mathrm{H}}\sigma_h/C_{\mathrm{H},0}\right)}{\partial\sigma_h}\right)_{n_{\mathrm{M}},K,T} = \left(1-\frac{\sigma_h}{K}\right)\bar{V}_{\mathrm{H}} = \left(\frac{\partial\mu_{\mathrm{H}}}{\partial\sigma_h}\right) \tag{66}$$

For metals like iron, the maximum value of σ_h so that the metal is in the elastic range is a few orders of magnitude smaller than K. Therefore it is possible to neglect the fraction σ_h/K. In situations where the amount of H dissolved in metal is small, the bulk modulus, K, remains unchanged. The negative sign in Eq. (66) is balanced by the sign of σ_h which is negative for tensile stress and positive for compressive stress.

9. Tensile Stress and Hydrogen Pump

On application of tensile stresses (uniaxial, biaxial, or triaxial), interatomic distances in metals increase. This increase in distance can be averaged to an equivalent increase in the volume of an atom or an increase in the equivalent radius of atomic polyhedron, r_s. The radius r_s is measured in terms of the radius of hydrogen atom. For a notched or cracked specimen under tension, the volume of atoms at a small distance ahead of the notch tip or crack tip will be subjected to maximum enlargement compared to the rest of the atoms due to stress concentration. According to Tiller and Schrieffer,(76) the chemical potential of electrons in this enlarged region ahead of the crack tip is lowered, and consequently electrons flow into this region from surroundings. They calculated the magnitude of the potential change on the basis of the average energy of an electron of a monovalent metal.(76) The energy of one electron is given by the sum of kinetic (E_k), exchange (E_e), and correlation (E_c) energy terms as

$$E(r_s) = E_k(r_s) + E_e(r_s) + E_c(r_s) \tag{67}$$

According to Wigner, the various terms in Eq. (67) in the same order are:

$$E_w(r_s) = \left(\frac{2.21}{r_s^2} + \frac{0.916}{r_s} + \frac{0.88}{r_s + 7.6}\right) \text{rydbergs} \tag{68}$$

Gell-Mann and Breuchner have given the energy value in rydbergs as

$$E_{\text{G-B}}(r_s) = \frac{2.21}{r_s^2} + \frac{0.916}{r_s} + 0.062 \ln r_s + 0.096 \tag{69}$$

The calculations of Tiller and Schrieffer show that $\Delta\phi$, the difference in potential, could be about 0.8 V for 10% strain $[=(\Delta r_s/r_s) \times 100]$ for $2 < r_s < 3$. This potential is negative for tensile stress owing to the flow of electrons into the crack tip region and is sufficiently large to cause evolution of hydrogen.

More recently Tiller has improved the calculations further.(77,78) Additional energy terms have been included in the calculations. The total energy was taken as the sum of five terms as

$$E(r_s) = E_0(r_s) + E_k(r_s) + E_e(r_s) + E_c(r_s) + E_{c0}(r_s) \tag{70}$$

where E_0 is the ground state of the electron and E_{c0} is due to overlap repulsion and van der Waals attraction of the ionic cores, along with a coulomb term which is the self-potential-energy of an atomic polyhedron. The variation of E_0 as a function of r_s is larger than the sum of E_k, E_e, and E_c and is opposite in sign. However, electrons will flow from a stress-free region into a region of tension when the effects of all the terms are taken into account. But when a piece of metal is stressed in tension, its surface develops a more positive potential. This is tantamount to saying that for a clean metal surface and for zero electron redistribution, the tip of a crack would be positively charged. Sufficient redistribution of electrons may occur on the metal side of the tip to change the magnitude and sign of the potential at the tip surface. The surface potential, ϕ_S, is considered to be the sum of four terms as

$$\phi_S(S) = \phi_V + \phi_C + \phi_d + \phi_A \tag{71}$$

where S is the surface coordinate, ϕ_A is the contribution from adsorption, ϕ_d is the contribution from dislocations at surface, ϕ_C includes the effects of all terms in Eq. (67) and ϕ_V is the differential effect due to all the transferred electrons to the crack tip region. The potential of the crack tip surface, ϕ_S, could be positive or negative depending on the contributions of the various terms. However, as the load increases, it is expected that more and more electrons will flow into the crack tip region so that ϕ_S will change from positive to negative to start the hydrogen pump.(78)

A probable method of generating excess electrons needed for the stressed region is by the rejection of metal ions (M^{2+}) into the solution. This is likely to occur when the surface potential is initially positive. Since the chemical potential of electrons after redistribution is the same everywhere, it is not clear how the stressed region should develop a negative potential different from the unstressed region. Further, the electrons in the stressed region should not be any more reactive than the rest in the Fermi sea to cause hydrogen evolution selectively.

From thermodynamic calculations, Subramanyan(79) obtained two expressions for the stress-induced potential change ($\Delta\phi$) of metals as

$$\Delta\phi = \frac{5}{3}\frac{PV_0}{ZF}\left(\frac{1}{2}\beta P - \alpha T\right) \tag{72}$$

and

$$\Delta\phi = \frac{PV_0}{ZF}(1 - \alpha T) \tag{73}$$

The first equation represents the potential change in the case of an ideally polarizable electrode and the second one for a nonpolarizable electrode. In the above two equations, P stands for the hydrostatic equivalent of applied stress, V_0 the initial molar volume of metal, β the compressibility, α the coefficient of cubic expansion, and Z the number of electrons per atom of the metal. In both equations, the first term is the dominating one. These equations give only the magnitudes of potential changes. We have to assign directions to these according to the electrochemical conventions. Since a tensile stress diminishes the stability of the lattice structure and a compressive stress adds to it, the change in potential $\Delta\phi$ should be anodic in the former case and cathodic in the latter case.

10. Effect of Stress on the Solubility of H in Metals

From the theoretical considerations it was concluded that a tensile stress increases the solubility and a compressive stress decreases it. The effect of stress on solubility is reversible and the same thermodynamic equation describes it for dilative and compressive stresses. The hydrogen permeation method is suitable to study this effect because the applied stress does not alter the diffusion coefficient of hydrogen. Further, the electrochemical method of study of hydrogen permeation is particularly suitable because it is easy to maintain a well-defined chemical potential of hydrogen at the metal surface. A diagram of the setup used by Bockris *et al.* for studying the effect of compressive stress on the solubility of hydrogen in iron and steel is shown in Figure 6.(36) Results of their study using Armco iron are shown in Figure 12. These results are in good agreement with the thermodynamic theory. Partial molar volumes

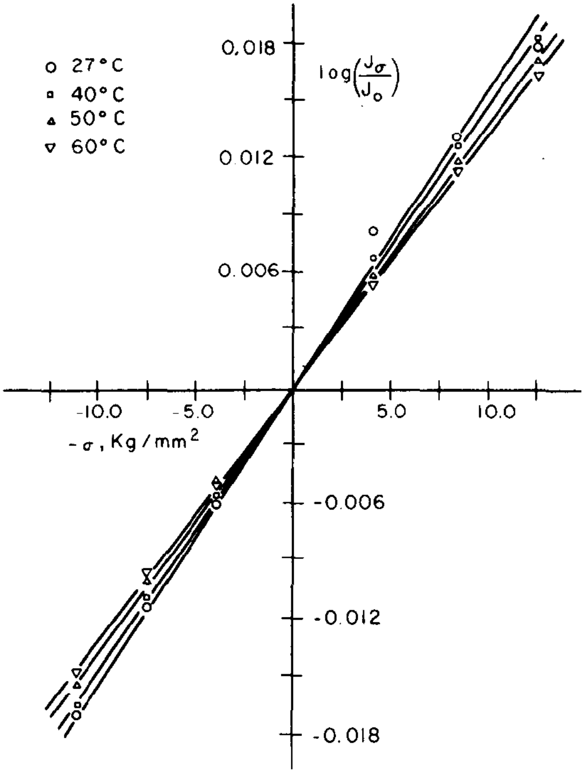

Figure 12. Hydrogen permeability–stress relationships for Armco iron at different temperatures.

Table 4
Partial Molar Volume (pmv) of Hydrogen at Different Temperatures

Material	Temperature, °C	$\bar{V}_{H3}$, cm^3 Tensile stress	Compressive stress	Average
ARMCO iron	27	2.60	2.73	2.66
ARMCO iron	40	2.69	2.74	2.72
ARMCO iron	50	2.62	2.60	2.61
ARMCO iron	60	2.52	2.61	2.56
AISI 4340 steel	27	1.84	2.08	1.96
AISI 4340 steel	60	2.03	2.40	2.06

T277 B 70

of hydrogen in Armco iron and steel (4340) deduced by these investigators are as given in Table 4.

As a corollary of the effect of stress on solubility, we should expect to find higher concentrations of hydrogen in regions of dilation and lower concentrations in regions of compression than in the unperturbed regions. Lattice dilations and compressions are associated with defects such as edge dislocations, vacancies, interstiticals, inclusions, etc. In the following section the amount of hydrogen associated with an edge dislocation which is a prominent defect in metals, is calculated.

Distribution of Hydrogen in the Stress Field of an Edge Dislocation(37)

The fundamental equation that relates solubility of H with pressure is the following:

$$\frac{\partial \ln (C_{\mathrm{H},\sigma_h}/C_{\mathrm{H},0})}{\partial \sigma_h} = \frac{\bar{V}_{\mathrm{H}}}{RT} \tag{74}$$

Upon investigation of this equation, we obtain

$$C_{\mathrm{H},\sigma_h} = C_{\mathrm{H},0} \exp\left(\frac{\sigma_h \bar{V}_{\mathrm{H}}}{RT}\right) \tag{75}$$

This is the equation that we will use to deduce the distribution of H. With respect to an edge dislocation, the hydrostatic component of the stress is expressed by(80)

$$\sigma_{rr} = \sigma_{\theta\theta} = \frac{\sigma_{zz}}{2\nu} - \frac{\tau b}{2\pi(1-\nu)}, \frac{\sin\theta}{r} \tag{76}$$

where T is the rigidity modulus, b the unit Berger's vector, ν Poisson's ratio, and θ the angle with respect to the glide plane. A schematic representation of an edge dislocation is shown in Figure 13. The average concentration of H in the stress field, $\bar{C}_{\mathrm{H},\perp}$, therefore, is

$$\bar{C}_{\mathrm{H},\perp} = \frac{\int_0^L \int_0^{2\pi} \int_{r_0}^{r_\infty} C_{\mathrm{H},0} \exp[\tau b(1+\nu)\sin\theta \bar{V}_{\mathrm{H}}/3\pi(1-\nu)rRT] r\, dr\, d\theta\, dL}{\int_0^L \int_0^{2\pi} \int_{r_0}^{r_\infty} r\, dr\, d\theta\, dL} \tag{77}$$

Substituting K' for $[\tau b(1+\nu)\sin\theta \bar{V}_{\mathrm{H}}/3\pi(1-\nu)RT]$ and x for $1/r$,

$$\bar{C}_{\mathrm{H},\perp} = -\frac{C_{\mathrm{H},0} \int_0^{2\pi} [\int_{x=0}^{x=\infty} \exp(K'x)\,(dx/x^3)]\, d\theta}{\pi(r_\infty^2 - r_0^2)} \tag{78}$$

T277 .A 20

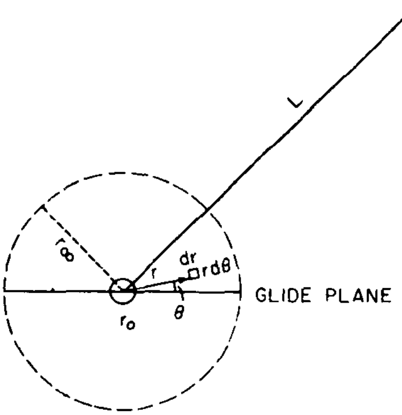

Figure 13. Schematic representation of an edge dislocation of unit strength with the surrounding stress field. L is the length of the dislocation, r_0 the radius of the core, and r_∞ the radius of the limiting circle of the stress field, θ the angle of any point in the stress field with respect to the glide plane and $r\,d\theta\,dr\,dL$, a volume element, in the cylindrical stress field.

The integral with respect to x in Eq. (78) is obtained as†

$$\int_{x_0}^{x_\infty} \exp(K'x)\frac{dx}{x^3} = \left[-\exp\left(\frac{K'x}{2x^2}\right) - K'\exp\left(\frac{K'x}{2x}\right) + \frac{K'^2}{2}(\ln x) + \frac{K'x}{1\cdot 1!} + \frac{K'x}{1\cdot 1} + \frac{K'^2x^2}{2\cdot 2} + \cdots \frac{K'^nx^n}{n\cdot n!} + \cdots\right]_{x_0}^{x_\infty} \tag{79}$$

Expanding the exponentials and inserting the limits in Eq. (79),

$$\begin{aligned}\int_{x_0}^{x_\infty} \exp(K'x)\frac{dx}{x^3} = \Bigg[&\frac{1}{2x_0^2}\left(1+\sum_1^\infty \frac{K'^nx_0^n}{n!}\right) - \frac{1}{2x_\infty^2}\left(1+\sum_1^\infty \frac{K'^nx_\infty^n}{n!}\right)\\ &+\frac{K'}{2x_0}\left(1+\sum_1^\infty \frac{K'^nx_0^n}{n!}\right) - \frac{K'}{2x_\infty}\left(1+\sum_1^\infty \frac{K'^nx_\infty^n}{n!}\right)\\ &+\frac{K'^2}{2}\ln\left(\frac{x_\infty}{x_0}\right) + \frac{K'^2}{2}\sum_1^\infty \frac{K'^nx_\infty^n}{n\cdot n!} - \frac{K'^2}{2}\sum_1^\infty \frac{K'^nx_0^n}{n\cdot n!}\Bigg]\end{aligned} \tag{80}$$

In order to carry out the integration with respect to θ in Eq. (78) K' is expressed as $K \sin\theta$. Since only even powers of $\sin\theta$ remain after integration, the results can be expressed as

---

† In the original publication of this calculation⁽³⁷⁾ the two terms $[-\exp(K'x)/2x^2 - K'\exp(K'x)/2x]_{x_0}^{x_\infty}$ were eliminated while imposing the limits of integration on the assumption that their relative contributions were small. Dr. J. P. Hirth of Ohio State University pointed out that those terms make appreciable contributions. In the following calculations, these terms are retained. Their contributions appear to be appreciable. The author wishes to express his thanks to Dr. Hirth.

$$\bar{C}_{H,\perp} = -\frac{C_{H,0}}{\pi(r_\infty^2 - r_0^2)}\left\{\frac{\pi}{x_0^2}\left[1 + \sum_1^\infty \left(\frac{Kx_0}{2}\right)^{2m} \frac{1}{(m!)^2}\right]\right.$$

$$-\frac{\pi}{x_\infty^2}\left[1 + \sum_1^\infty \left(\frac{Kx_\infty}{2}\right)^{2m} \frac{1}{(m!)^2}\right] + \frac{\pi}{x_0^2}\sum_1^\infty \left(\frac{Kx_0}{2}\right)^{2m} \frac{2m}{(m!)^2}$$

$$-\frac{\pi}{x_\infty^2}\sum_1^\infty \left(\frac{Kx_\infty}{2}\right) \frac{2m}{(m!)^2} + \frac{\pi}{2}K^2 \ln\left(\frac{x_\infty}{x_0}\right) + \frac{\pi}{x_\infty^2}\sum_1^\infty \left(\frac{Kx_\infty}{2}\right)^{2m+2} \frac{(m+1)(2m+1)}{m[(m+1)!]^2}$$

$$\left.-\frac{\pi}{x_0^2}\sum_1^\infty \left(\frac{Kx_\infty}{2}\right)^{2m+2} \frac{(m+1)(2m+1)}{m[(m+1)!]^2}\right\} \tag{81}$$

In Eq. (81) the substitution $2m = n$ has been made. Upon further simplification and finally replacing x_0 by $1/r_0$ and x_∞ by $1/r_\infty$:

$$\bar{C}_{H,\perp} = \frac{C_{H,0}}{\pi(r_\infty^2 - r_0^2)}\left\{\pi r_0^2\left[\sum_1^\infty \left(\frac{K}{2r_0}\right)^{2m+2} \frac{1}{m[(m+1)!]^2} - 3\left(\frac{K}{2r_0}\right)^2 - 1\right]\right.$$

$$\left.+ \pi r_\infty^2\left[1 + 3\left(\frac{K}{2r_\infty}\right)^2 - \sum_1^\infty \left(\frac{K}{2r_\infty}\right)^{2m+2} \frac{1}{m[(m+1)!]^2}\right] + \pi\frac{K^2}{2}\ln\left(\frac{r_\infty}{r_0}\right)\right\} \tag{82}$$

In Eq. (82), $K = [\tau b(1+\nu)/3\pi(1-\nu)](\bar{V}_H/RT)$. If K is set equal to $K_0 b$, the value of K_0 at room temperature × 17.2 for $\bar{V}_H = 2.66\ \text{cm}^3$. For a numerical evaluation, the values of r_0 and r_∞ may be set to be integral multiples of b. Let us take the radius of the core of the dislocation $r_0 = 1b$, which is a reasonable assumption. The outer radius of integration can be taken arbitrarily. However, we will take the minimum value of it to be $2b$. For $r_0 = 1b$ the maximum value of the predominant term in Eq. (82), i.e.,

$$\sum_1^\infty \left(\frac{K}{2r_0}\right)^{2m+2} \frac{1}{m[(m+1)!]^2} = 4.3 \times 10^5$$

The maximum possible value of the corresponding term in r_∞ is when $r_\infty = 2b$ and is equal to 296. For all other values of r_∞, the summation gives much smaller values. The term $\pi(K^2/2)\ln(r_\infty/r_0) = \frac{1}{2}\pi b^2(17.2)^2 \ln(r_\infty/r_0)$ is the only term that increases in magnitude as r_∞ increases. For $r_\infty = 2b$ to $r_\infty = 1000b$ (which is sufficiently large), the magnitude of the term increases from $104\pi b^2$ to $1040\pi b^2$. Therefore, Eq. (82) can be simplified as

$$\bar{C}_{H,\perp} = \frac{C_{H,0}}{\pi(r_\infty^2 - r_0^2)}[\pi r_0^2(4.3 \times 10^5) + \pi r_\infty^2(-240 \rightarrow 1) + \pi r_0^2(104 \rightarrow 1040)] \tag{83}$$

When r_∞ increases the second term in Eq. (83) reduces to 1 and the last term becomes negligible. Therefore, Eq. (83) can be rewritten as

$$\bar{C}_{H,\perp} = \frac{C_{H,0}}{\pi(r_\infty^2 - r_0^2)}[\pi r_\infty^2 + \pi r_0^2(4.3 \times 10^5)] \tag{84}$$

Or in the general form,

$$\bar{C}_{\mathrm{H},\perp} = \frac{C_{\mathrm{H},0}}{\pi(r_\infty^2 - r_0^2)}\left[\pi r_\infty^2 + \pi r_0^2 \sum_1^\infty \left(\frac{K}{2r_0}\right)^{2m+2} \frac{1}{m[(m+1)!]^2}\right] \tag{85}$$

The values of $\bar{C}_{\mathrm{H},\perp}/C_{\mathrm{H},0}$ for $r_0 = 1b$ and r_∞ up to $1000b$ are as given in Table 5. The concentration of H thus decreases exponentially with distance. It also shows that there exists a higher degree of enrichment of hydrogen at the core of the dislocation. The core of the dislocation is essentially a dilated region. There is no rigorous way of calculating the enrichment at the core. We will assume that the stress inside the core is the same as that at $r_0 = 1b$. Further, we will neglect the dependence of stress on θ. However, we will assume that half of the core volume is under uniform compressive stress and the other half is under uniform dilation. The concentration at the core of the dislocation, therefore, is

$$C_{\mathrm{H},\perp\mathrm{core}} = C_{\mathrm{H},0} \cosh\left[\frac{\tau(1+\nu)}{3(1-\nu)} \frac{\bar{V}_\mathrm{H}}{RT}\right] \tag{86}$$

This should be added to Eq. (85) to obtain the total enrichment. Hence the final result is

$$\frac{C_{\mathrm{H},\perp\mathrm{total}}}{C_{\mathrm{H},0}} = \frac{1}{\pi r_\infty^2}\left\{\pi r_\infty^2 + \pi b^2 \cosh K_0 + \pi b^2 \sum_1^\infty \left(\frac{K}{2r_0}\right)^{2m+2} \frac{1}{m[(m+1)!]^2}\right\} \tag{85a}$$

For $K_0 = [(1+\nu)/3(1-\nu)](\bar{V}_\mathrm{H}/RT) = 17.2$, the enrichment at this core is, therefore, $C_{\mathrm{H},\perp\mathrm{core}}/C_{\mathrm{H},0} = 1.47 \times 10^7$. If this is included in the results given in Table 5, the enrichment will be considerably higher. For the final case considered in this table for $r_\infty = 1000b$, the enrichment increases from 1.428 to 6.25. All these facts indicate that there is a high degree of H enrichment at the core and its immediate neighborhood. The maximum possible concentration of H in α-Fe lattice is when the ratio of H/Fe = 3. This corresponds to filling all the interstitial holes with H and is equal to a concentration of 0.4225 g-at./cm^3.

Table 5
Enrichment of H in the Stress Field of an Edge Dislocation as a Function of r_∞ in Terms of b for $r_0 = 1b$

r_∞ in terms of b	2	4	6	8	10	15	20	30	50	500	1000
$\frac{\bar{C}_{\mathrm{H},\perp}}{C_{\mathrm{H},0}}$	1.4×10^5	2.8×10^4	1.2×10^4	4321	1910	1073	476	162	44	2.71	1.428
$\frac{\bar{C}_{\mathrm{H},\perp}}{C_{\mathrm{H},0}}$ in dilative part of the stress field	28×10^5	5.7×10^4	2.4×10^4	8641	3819	2145	951	328	87	4.42	1.856

The lattice concentration $C_{H,0}$ that will saturate the core is obtained from $1.47 \times 10^7\, C_{H,0} = 0.4225$ g-at./cm^3. Therefore $C_{H,0} = 2.8 \times 10^{-8}$ g-at./cm^3. Even if the core is saturated, H can still be distributed in the field of the dislocation. Experimentally, an anomalous behavior in H permeation is observed when $C_{H,0} = 1.5 \times 10^{-7}$ g-at./cm^3,(13,37) which is about five times the concentration corresponding to core saturation. This indicates that at the onset of anomalous permeation, molecular H_2 may form in the interior of the metal.

11. Hydrogen Embrittlement of Metals

The phenomenon of hydrogen embrittlement of a metal is manifested primarily as a loss in the ability of the metal to undergo deformation under applied stress. Normally this is measured as a decrease in the ductility of the metal or as a percentage reduction in the area of cross section at fracture, i.e., $[(A_0 - A_f)/A_0]$. Here A_0 is the initial cross section and A_f is the cross section at fracture. A lower value of this percentage means higher degree of embrittlement. In the presence of H in the metal, the value of A_f remains high.

Hydrogen embrittlement of mild steel was discovered around the year 1871 by W. H. Johnson.†(15) This happened rather soon after the discovery of H permeation through steel by Cailetet in 1864.(14) Hydrogen embrittlement is a complex phenomenon. It has been studied very widely.(1–6,81–88) Four different theories on mechanisms have been proposed to explain this phenomenon. These theories are (1) pressure theory, (2) adsorption theory, (3) decohesion theory, and (4) hydride theory. A brief discussion of these theories is attempted here. A more detailed discussion of these mechanisms is given elsewhere.(75)

11.1. Pressure Theory of Hydrogen Embrittlement

Historically this was the first theory proposed to explain the phenomenon of hydrogen embrittlement. It was formally proposed by Benneck *et al.*(89) in 1935. Hydrogen dissolved in metal during corrosion or processing at higher temperatures is supposed to form molecular hydrogen in cavities or microcracks within the metal and to develop high pressures. As a result of this pressure, a crack could spread spontaneously or with the help of a smaller external stress. The external stress and the internal pressure of H_2 are additive. The theoretical model for crack propagation in the pressure theory is based on Griffith's theory of brittle fracture. If a solid body under the action of external stresses can reduce its potential energy by undergoing fracture, then the equilibrium state of the body is the one in which rupture of the solid has occurred.(90) The critical stress, σ_{cr} for spreading an elliptical crack of length l is(91)

---

† It was generally believed that hydrogen embrittlement was discovered by Heyn at the turn of the century. In the light of the article by Johnson,(15) this can no longer be considered to be true.

$$\sigma_{cr} = \left[\frac{2Y\gamma}{\pi(1-\nu)}\right]^{1/2} \tag{87}$$

where γ is the surface energy of the metal, ν the Poisson's ratio and Y the Young's modulus. Suppose the pressure of H_2 within this crack is P_{H_2}. Then the condition for crack spreading is modified as

$$P_{H_2} + \sigma > \sigma_{cr} \tag{88}$$

where σ is the applied stress which is assumed to act normal to the plane of the crack. During the course of fracture, a metal undergoes plastic deformation. This is considerably less in the presence of H. However, the surface energy parameter may need modification to take into account the work of plastic deformation at the crack surface. An effect that runs contrary to this is the lowering of surface energy due to adsorption of H_2 at the crack surface. This is the essence of Petch's theory and will be considered later in this section.

Many investigators have contributed to the development of the pressure theory.(13,92–95) According to Bilby and Hewitt(94) and Garafalo *et al.*,(93) microcracks or cavities need not be present to initiate embrittlement process. Microcracks could nucleate from dislocation pile-ups under the influence external stress. In presence of H, a microcrack formed from three to five edge dislocations could become unstable and spread. The central idea of the pressure mechanism can be represented as

$$\perp H + \perp H + \perp H + \perp H \perp\perp\perp\perp H_2 \tag{a}$$

where $\perp$ H stands for an edge dislocation of unit strength with hydrogen at the core. The symbol on the right-hand side represents a Stroh crack containing molecular H_2 under pressure. Since H interacts very strongly with the lattice of α-Fe, Bockris *et al.* suggested that diffusion of H into the stress field of dislocations could cause them to move and coalesce.(37) During H permeation through iron, iron–nickel alloys of low nickel content and steel, Bockris and co-workers(13,96,97) observed an anomalous behavior with respect to the flux of H. An example of the permeation transient without and with the anomalous pattern is shown in Figure 14.(97) When the concentration of H in the lattice exceeds a certain critical value, microcracks nucleate and spread. Consequently, part of the diffusing flux of H is withheld as H_2 in the cracks, thereby bringing about a decrease in permeation rate. During decay of the permeation transient, the lattice H diffuses out easily as expected. The hydrogen remaining as molecular H_2 in cracks or H remaining adsorbed at the crack surfaces begins to diffuse out slowly when the lattice H is out. This situation gives rise to the hump in the decay transient. The critical concentration of H required to nucleate and spread microcracks is characteristic of the metal and the temperature of charging. The pressure of H_2 in the cracks corresponding to

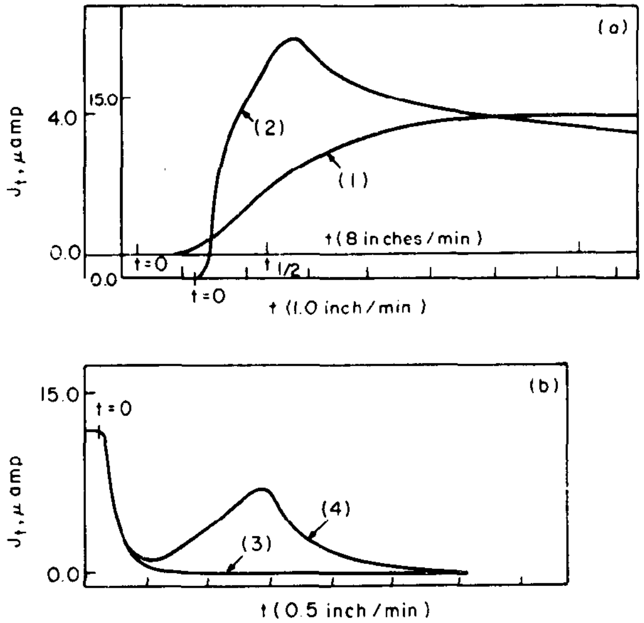

Figure 14. Laboratory records of H permeation transients. (a) represents the normal (1) and abnormal (2) buildup transients. The abnormal buildup transient shows a characteristic peak. For the abnormal transient cathodic current density = 108 mA/cm^2. (b) shows the normal (3) and abnormal (4) decay transients. The abnormal decay transient shows a characteristic hump. Cathodic current density in the case of the abnormal transient was 88.0 mA/cm^2 and charging time 11.0 min. (Membrane material 5% Ni + 95% Fe by wt., $L = 0.09$ cm, temperature 50°C and 0.1 M NaOH solution.)

the critical concentration can be calculated provided that Sievert's law constant is known. The critical pressure necessary to cause spreading of an elliptical crack can be related to the overpotential as$^{(97)}$

$$p_{H_2} > \left[\frac{2Y\gamma}{\pi_{cr}(1-\nu^2)}\right]^{1/2} = 10^{3/2}\exp\left(\frac{-\eta_{cr}F}{2RT}\right) \tag{89}$$

for the coupled discharge–recombination mechanism. Beck *et al.*$^{(13)}$ deduced the following expression for the critical concentration of H:

$$C_{cr} = \left(\frac{2Y\gamma}{\pi l_{cr}}\right)^{1/2} k \exp\left(\frac{-\Delta H_s}{RT}\right) \tag{90}$$

where k is the Sievert's law constant. From the temperature variation of C_{cr}, the value of ΔH_s was obtained as 4.12 kcal/mol of H. This is lower for the heat of solution of H in α-Fe, which is 7.0 kcal/mol of H. However, considering the probable variation of l_{cr}, the value of 4.12 kcal/mol should be considered reasonable. Bockris, Genshaw, and Fullenwider obtained a value of

5.0 kcal/mol for ΔH_s in α-Fe[96] For Pt, Bockris *et al.*[98] found the value of ΔH_s to be 0.3 kcal/mol of H from the measurements of C_{cr}. The heat of solubility of H in Pt from gas phase solubility measurements is found to be a small negative quantity. All this evidence points out that the anomalous permeation is associated with formation of H_2 at a certain critical pressure. The critical solubility of H in α-Fe at room temperature is about $1.4–1.5 \times 10^{-7}$ g-at./cm^3.[96,97]

11.2. Petch's Theory of Hydrogen Embrittlement[99,100]

Petch utilized a suggestion by Orowan[101] that adsorbed gases could reduce surface energy of metals. This is now widely accepted. For a crack formed from a pile-up of dislocations (Stroh crack) the well-known Petch equation for fracture stress is

$$\sigma_f = \sigma_0 + 4\left[\frac{3\tau\gamma_0}{\pi(1-\nu)l}\right]^{1/2} \tag{91}$$

where σ_f is the fracture stress, σ_0 is a constant, γ_0 is the surface energy, and τ the rigidity modulus. The other quantities have the usual significance. In presence of H, the value of the surface energy γ_0 is reduced. The lowering of surface energy $(\gamma_0 - \gamma)$ is given by

$$(\gamma_0 - \gamma) = 2\Gamma_s kT \ln[1 + (AP)^{1/2}] \tag{92}$$

where Γ_s is the number of H atoms adsorbed per unit area of surface. A is a constant originating from Langmuir adsorption isotherm and P the pressure of H_2. The final expression for fracture stress in presence of H can now be deduced as

$$\sigma_f = \sigma_0 + 4\left[\frac{3\tau}{\pi(1-\nu)l}\{\gamma_0 - 2\Gamma_s kT \ln[1 + (AP)^{1/2}]\}\right]^{1/2} \tag{93}$$

This reduced to the following form:

$$\sigma_f = \sigma_0 + Kl^{-1/2} \tag{94}$$

In agreement with this theory, Petch found the values of σ_0 and K to decrease in presence of H. The effect of lowering surface energy on crack propagation is a universal one. This will be present also when the pressure mechanism is functional. The pressure theory and lowering of surface energy should be considered simultaneously as done by Bilby and Hewitt.[94] It is possible, however, sometimes pressure has an overwhelming influence compared to the effect of adsorption and vice versa. The unusual embrittlement phenomenon observed by Hancock and Johnson[102] in the presence of H_2 gas at less than 1 atm pressure is in all probability a manifestation of Petch's theory rather than anything else.

11.3. Decohesion Theory of H Embrittlement(81)

This theory was developed by Troiano. The essence of this theory is that on application of an external stress, H is supposed to diffuse preferentially into regions of triaxial stress. The applied stress produces the driving force for diffusion of H. Hydrogen accumulates at triaxial stress regions and thereby brings about a weakening of the metal–metal bond (i.e., gives rise to decohesion). That H diffuses to regions of dilating stress has been proven by Bockris *et al.*(36) The solubility of H is higher in such regions. However, it has not been proven that the increased solubility of H in iron and steel produces decohesion. This is still a hypothesis.

A prominent defect in metals is the edge dislocation, the density of which could vary from 10^5 to $10^9/\text{cm}^2$. The core of the edge-type dislocation is probably the most stressed region in a lattice, and it will be saturated with H. Therefore we would expect the core to have undergone cracking already before applying the external stress. The external stress is supposed to be effective in producing embrittlement only if it is greater than a minimum level. The increase in solubility of H due to application of a tensile or dilatational stress is relatively much smaller than the solubility levels attainable at the core of dislocations. The externally applied stress can produce new dislocations and it can make the dislocations mobile. This situation will take us to the pressure theory again. The function of the externally applied stress in the decohesion theory is not clear.

11.4. Hydride Embrittlement

Certain metals and alloys, for example, Nb, Ti, Zr, V, U, Ta, $LaNi_5$, $LaCO_5$, Fe-Ti, etc., form hydrides. Moduli of elasticity of these hydrides are lower than that of the matrix metal. Further, the pmv of hydride is larger than that of the metal. As a result of these factors, the metal undergoes hydride embrittlement. Even without the application of external stresses, the materials will break. This is known to happen in the case of $Fe\text{-}Ti\text{-}H_2$, $LaNi_5H_x$, $LaCO_5H_y$, etc.

11.5. Stress Corrosion and Hydrogen Embrittlement(103,104)

Generally when a metal undergoes corrosion, there is simultaneous evolution of hydrogen. Part of this hydrogen will find its way to the stressed region in the metal. This situation will expedite the failure of the metal. The failure of the structural member could occur due to a combination of hydrogen embrittlement and penetration of corrosion. Sometimes, hydrogen embrittlement could be the dominant factor. At other times penetration of corrosion could be decisive. However, both could be acting simultaneously.

11.6. Concluding Remarks

For materials like iron and steel, the pressure mechanism with lowering of surface energy appears to be the more realistic mode of embrittlement. This theory is now becoming more widely accepted.

On the basis of strain energy introduced into the metal by the dissolution of H in α-Fe, Bockris *et al.*(37) suggested that when the concentration of H attains a critical limit, the dislocations could become mobile without the application of external stress. These investigators deduced an equation relating the critical concentration C_{cr} with the yield point (Y.P.) of the metal as

$$\frac{\sigma^2_{\text{Y.P.}}}{2(1-\nu)Y} = \frac{3}{2}K\frac{(\bar{V}_{\text{H}})^2}{V_{\text{Fe}}}C_{\text{Cr}} \tag{95}$$

where K is the bulk modulus. The critical concentration of H calculated to produce a strain energy density equivalent to that produced by subjecting the metal to the yield point (Y.P.) is 1.5 ppm. At a concentration of 1 ppm, the anomalous behavior of H permeation becomes observable, indicating that the embrittlement process has commenced.

12. Usefulness of the Study of Hydrogen in Metals

Foremost in importance of all possible applications of the study of hydrogen in metals is the one relating to the alleviation of the hydrogen embrittlement of structural materials. Recently, the embrittlement due to H_2 gas environment has been recognized also to be an important area for investigations because of the potential of H_2 becoming the fuel of the future and the need for transporting it over long distances. Some of the other applications of the study of hydrogen in metals relate to (a) storage of H in metals, (b) rechargeable H electrodes, (c) fusion reactors, (d) fast H-permeating membranes, (e) materials impermeable to H, (f) codeposition of H in electrodeposition of metals, (g) study of changes in the crystal structure of metals and alloys, and (h) development of materials for H_2-burning internal combustion engines. In the following, these applications will be discussed briefly.

12.1. Storage of H in Metals

This is an approach of great industrial value in storing hydrogen. In the atomic form, H could be stored in metals more efficiently than liquid H_2 or even solid H_2 on the basis of volume. H is supposed to form a weakly bonded hydride that will dissociate and release H_2 easily. In 1970, Van Vucht *et al.*(105) reported the unusual ability of intermetallic compounds such as $LaNi_5$, $SmCo_5$, etc., of the general composition AB_5 to absorb and desorb large volumes of H_2 reversibly even at room temperature. The present writer in 1973 emphasized the possibility of storing H in metals in the atomic form and the search for such materials as an important aspect of the study of H in metals.(75) The compound $LaNi_5$ absorbs H_2 to the extent of forming $LaNi_5H_{6.7}$. The heat of absorption of H_2 in $LaNi_5$ is about 7.4 kcal/mol and the process is exothermic.(106) The equilibrium pressure of the hydride at 25°C is about 2.5 atm and that at 60°C is about 10.0 atm.(107) A number of studies on the rare earth 3*d* transition intermetallic compounds with respect to their capacity to absorb H_2 and the effect of H_2 absorption on their physical properties has been made.(106–109) Some of the compounds which have high capacity for storing H are $Y_3NiH_{8.0}$, $Y_3COH_{8.0}$, $Y_4Co_3H_{11.6}$, $YFe_2H_{4.2}$, $La_3NiH_{8.8}$, $Ce_3Ni_{8.4}$, $GdCo_2H_{4.2}$, etc. Bockris and co-workers had studied the permeability of H through a series of iron nickel alloys and iron and nickel.(109) Hydrogen has a much higher solubility in Ni (approx. 10^{-5} g-at./cm^3) than in α-Fe (3.6×10^{-9} g-at./cm^3) at 27°C; the solubilities in both cases corresponding to a pressure of 1.0 atm H_2. But the diffusion coefficient of H in α-Fe is much higher (6.62×10^{-5} cm^2/sec) than in nickel (1.1×10^{-9} cm^2/sec) at 27°C. A basic idea involved in this study was that a certain combination of Fe and Ni, i.e., a metal with high diffusivity and low solubility and another with a low diffusivity and high solubility would give rise to a composition that would have higher permeability than either constituent.(75,111) Fe–Ni alloy with 5 wt % Ni was found to be slightly higher in permeability. (Incidentally, no single metal is known to have high diffusivity and high solubility.) However, the idea of such a combination seems to have worked very well with Fe–Ti alloy of 46.4 wt % Ti and 53.6 wt % Fe developed at Brookhaven National Laboratories.(112,113) This combination corresponds to the composition FeTi and could form a hydride with almost two H atoms as

$$\text{(a)}\quad 2.13FeTiH_{0.10} + H_2 \rightleftarrows 2.13FeTiH_{1.04}$$

$$\text{(b)}\quad 2.20FeTiH_{1.04} + H_2 \rightleftarrows 2.20FeTiH_{1.95}$$

The diffusion coefficient of hydrogen in α-$TiH_{0.1}$ is $5.60 \pm 1.92 \times 10^{-7}$ cm^2/sec at 20°C. The heat of formation of FeTiH is about 3.36 kcal/mol and that of $FeTiH_2$ is approximately 7.3 kcal/mol. The absorption of H_2 in FeTi is an exothermic reaction. The alloy absorbs or desorbs hydrogen readily. The equilibrium pressure of the hydride at 0°C is about 1.5 atm and the same at 70°C is about 17.0 atm. The heat of absorption and desorption are about the same;(114) however, there appears to be a small irreversibility with respect to the equilibrium pressure in the absorption–desorption process.(113) Fe–Ti alloy is a much more practical and economical material than $LaNi_5$ or any of those rare earth, 3*d* transition metal alloys. It appears to be a practical solution to the problem of hydrogen storage.(115) Another practical material for storing H_2 could be Mg or Mg containing a small amount of Ni.(113)

12.2. Rechargeable H Electrode

Bronoel *et al.* studied the possibility of using $LaNi_5H_x$ compound as a rechargeable H electrode.(116) When $LaNi_5$ is charged with H, either electrolytic alloy or from gas phase, the material is comminuted as a result of considerable volume expansion and internal stress. The same is true for $Fe_xTi_{1-x}H_y$. So the electrodes have to be prepared with the alloy powder particles. Potential of the electrode, $LaNi_5H_{6.5}$, in 5 *N* KOH is found to be approximately 1.160 V vs. SCE and has a capacity of 320 mA hr g^{-1}. As the temperature of the solution increases, the capacity of the electrode material decreases. The kinetics of oxidation of H dissolved in the electrode material needs to be studied further. It appears that $LaNi_5H_x$ has the potential to function as a good rechargeable hydrogen storage electrode. The structural stability and cycle life of the rechargeable hydrogen electrodes, however, need to be established for applications.

12.3. Fusion Reactors

Hydrogen embrittlement and hydrogen permeability of materials are serious problems in thermonuclear reactors. Of the four probable fusion reactions with H and its isotopes, the one with the lowest ignition temperature (50,000,000°C) is the following reaction(117):

$$\text{(c)} \quad \mathrm{D} + \mathrm{T} \rightarrow \mathrm{He}^4 + n + 17.6\,\mathrm{MeV}$$

This reaction could be used in conjunction with the following tritium-breeding reactions for power generation:

$$\text{(d)} \quad n + \mathrm{Li}^6 \rightarrow \mathrm{T} + \mathrm{He}^4 + 4.8\,\mathrm{MeV}$$

$$\text{(e)} \quad n + \mathrm{Li}^7 \rightarrow \mathrm{T} + \mathrm{He}^4 + n - 2.5\,\mathrm{MeV}$$

Tritium is a very expensive isotope and also it is radioactive with a half life of 12.3 years. The loss of tritium to the surroundings by permeation through materials of construction is, therefore, a very serious problem. Conceptually, reaction (c) is carried out in a magnetically confined plasma to form He^4 and 14.1 MeV neutrons.(118) Surrounding the plasma there is a vacuum space followed by a blanket of liquid lithium. Reaction of the neutrons from the plasma with lithium blanket generates tritium. At the same time, liquid lithium functions as a heat transfer medium also. Following this, there are additional stages in the reactor such as a thermal shield, a neutron shield, a superconducting magnet, a potassium loop, a steam loop and a separate tritium recovering, processing, and storing system. Owing to high temperatures (600–1000°C) the permeability of T through the first wall and through the lithium–potassium heat exchanger will be quite high. It is proposed to allow T to permeate into the potassium loop from which it is removed by cold trapping. But it is extremely important to prevent the possible T loss into the steam loop which, if it happened, would be extremely difficult to recover. At all stages, there is the need for developing materials of low H permeability. In this respect, therefore, the study of H permeation is vitally important. There is also the danger of hydrogen embrittlement due to blister formation from bombardment with H ions, the formation of helium from the decay of T, and precipitation of hydrides. At the normal operating temperatures, blister formation and precipitation of hydrides may not occur. But during shutdown periods, chances of embrittlement are higher. Helium bubble formation can, however, occur during operation of the reactor. The proposed materials of construction of the reactor are W, Mo, V, and Nb.

12.4. Fast Hydrogen-Permeating Membranes

Pd and Pd–Ag alloys are well known to dissolve large amounts of H and to permeate H at high rates. These materials are used industrially to purify hydrogen for food, pharmaceutical applications, etc. It is conceivable that the demand for purified H_2 would increase in the future. In many respects, it may be necessary to separate it from other impurities such as O_2, CO, CO_2, CH_6, C_2H_6, etc. The best method for purifying H_2 is the permeation method. It is important to have less expensive materials for the membranes in purification batteries. Beck *et al.* in a study of H permeation through a series of Fe–Ni alloys and Fe and Ni observed that an alloy of Fe–5%Ni (wt %) has better permeability than either Fe or Ni.(110) According to their calculations, Fe–5%Ni alloy should permeate more H at 200°C or above than Pd at the same temperatures. There is a need for more experimental studies in this respect. Perhaps a certain alloy of Fe and Ti may have superior permeability and still remain intact and strong unlike the alloy (Fe–Ti) that is used for H_2 storage, especially at elevated temperatures.

12.5. Materials Impermeable to Hydrogen

There exists an acute need for materials which are impermeable to H. This is usually not recognized. The main function of such a material is to alleviate or eliminate hydrogen embrittlement. The probable method of achieving this is by applying it as a coating or as a lining which will prevent ingress of H into the bulk material. With the advent of hydrogen fuel, the need for such materials will become more acute with respect to the transportation of H_2 through pipelines and storage in tanks under pressure. Beck *et al.* observed that certain alloys of Fe and Ni (40–60 wt % Ni) show extremely low permeability compared to that of either Fe or nickel (about three orders of magnitude smaller than that of Fe).(110) Similarly, the permeability of H decreasing with the addition of Cr to Fe was observed by Bockris, Gershaw, and Fullenwider.(96) This aspect of hydrogen permeation studies certainly deserves more attention. In certain oxide films such as Fe_2O_3 and Cr_2O_3 the diffusion coefficients of H were found to be 1×10^{-18} cm^2/sec and 9.2×10^{-16} cm^2/sec, respectively, by Piggott and Siarkowski using the electrochemical method.(119) These films were produced on 302 and 347 stainless steels by thermal oxidation and were found to be losing effectiveness as barriers as their thickness increased beyond 1000 Å. This may be due to cracks in the films as they grow thicker. Besides cracks, the long-term stability of the oxides themselves in the presence of H_2 under pressure is not known and deserves further study.

12.6. Codeposition of Hydrogen in Electrodeposition of Metals

The electrochemical method for H permeation is ideally suitable for studying codeposition of H with metal deposition. This is possible because of the direct relationship of permeation rate to H coverage θ. By obtaining a blank current density-permeation rate plot without metal deposition (by substituting, say, Na^+ or K^+ for metal ion in the solution) and a similar plot during metal deposition, it should be possible to deduce the partial current i_H, due to hydrogen evolution reaction. It is easy to study by this method the effectiveness of additives in suppressing h.e.r. Devanathan, Stachurski, and Beck utilized this method to study hydrogen evolution during deposition of Cd and Fe.(11) More recently, Parthasaradhy has extended this technique to study hydrogen embrittlement in depositing copper from cyanide bath and nickel from Watts bath.(120) Nityanandan *et al.* have considered the design of a commercial unit for the measurement of H ingress into metals during electrodeposition.(121)

12.7. Study of Changes in the Crystal Structure of Metals and Alloys

The diffusion coefficient of H in a metal changes considerably when the crystal structure changes, for example, after an α–γ transformation. The solubility of H also changes accordingly; however, diffusivity is more sensitive to changes in crystal structure than solubility.(110) A simple measurement of diffusivity of H in the test material will be able to provide evidence of changes in crystal structure. The test specimen should be well annealed to eliminate the effect of cold work on diffusion coefficient. The electrochemical method of studying H permeation is simple and convenient for this. However, it appears that changes in diffusivity of H have not been used as a diagnostic parameter so far for studying structural changes.

12.8. Development of Materials for H_2-Burning Internal Combustion Engines

It appears that H_2 could be burned with good efficiency and smooth performance in internal combustion engines.(122) Liquid H_2 is an ideal fuel for aviation. With the tapping of solar, nuclear, and geothermal energies, hydrogen is expected to be easily available and to substitute for the dwindling supplies of petroleum. This again points to the problems related to hydrogen embrittlement of the materials of construction of engines. Since hydrogen embrittlement is absent at elevated temperatures (for example, 200°C or higher for steels), this may not be a problem for the materials where the temperature is high enough. However, at the regions where the temperature is lower, embrittlement could occur. There could be chances of embrittlement when the engine is cooling due to precipitation of molecular H_2. Therefore it is necessary to use materials which are impermeable to H to reduce or eliminate the possibility of hydrogen embrittlement.

Acknowledgments

The author wishes to thank Gould, Inc., for permission to publish this chapter and for the help received in the preparation of it. He would like to mention, in particular, his thanks to Mr. H. V. Pochapsky, Retired Manager, Physical Chemistry and Dr. M. P. Makowski, Vice President, Gould, Inc., and formerly Director, Gould Laboratories, Cleveland, for their encouragement and interest in this work.

References

1. R. W. Buzzard and H. E. Cleaves, Hydrogen Embrittlement of Steel (review of literature), National Bureau of Standards Circular 511, Washington, D.C. (1951).
2. D. P. Smith, *Hydrogen in Metals,* Chicago University Press, Chicago (1948).
3. M. Smialowski, *Hydrogen in Steel,* Addison-Wesley, Reading, Massachusetts (1962).
4. J. L. Carpenter, Jr. and W. F. Stuhrke, Hydrogen Embrittlement of Structural Alloys—A Technology Survey, NASA-CR-134962, U.S. Dept. of Commerce, NTIS (1976).
5. American Society for Metals, *Hydrogen in Metals,* Proceedings of an International Symposium, September, 1973.
6. American Society for Metals, *Hydrogen Damage,* C. D. Beachem, ed., ASTM, Metals Park, Ohio (1977).
7. J. G. Mavroides, D. I. Tchernev, J. A. Kafalas, and D. F. Kolesar, *Mat. Res. Bull.* **10**, 1023 (1975). J. F. Juliao, F. Decker, and M. Abramovitch, *J. Electrochem. Soc.* **127**, 2264 (1980).
8. K. L. Hardee and A. J. Bard, *J. Electrochem. Soc.* **123**, 1024 (1976). J. H. Kennedy, R. Shinar, and J. P. Ziegler, *J. Electrochem. Soc.* **127**, 2307 (1980).
9. J. O'M. Bockris and M. A. V. Devanathan, ONR Technical Reports 551 (22), 1957.
10. M. A. V. Devanathan and Z. Stachurski, *Proc. R. Soc. London* **270A**, 90 (1962).
11. M. A. V. Devanathan, Z. Stachurski, and W. Beck, *J. Electrochem. Soc.* **110**, 886 (1963).
12. M. A. V. Devanathan and Z. Stachurski, *J. Electrochem. Soc.* **111**, 619 (1964).
13. W. Beck, J. O'M. Bockris, J. McBreen, and L. Namis, *Proc. R. Soc. London* **290A**, 220 (1965).
14. L. Cailetet, *Compt. Rend.* **58**, 327 (1864).
15. W. H. Johnson, *Proc. R. Soc. London* **23** (1875).
16. J. O'M. Bockris, *Energy: The Solar Hydrogen Alternative,* Halsted Press, New York (1975).
17. J. O'M. Bockris, Lectures in Electrochemistry, University of Pennsylvania, Fall, 1965.
18. R. C. Frank, D. E. Swets, and D. L. Fry, *J. Appl. Phys.* **20** (1958).
19. R. Frauenfelder, *J. Chem. Phys.* **48**, 3955 (1968).
20. R. Gibala, *Trans. Met. Soc. AIME* **239**, 1574 (1967).
21. J. A. Peterson, R. Gibala, and A. R. Troiano, *J. Iron Steel Inst.* **207**, 86 (1969).

22. K. Skold and G. Nelin, *Phys. Chem. Solids* **28**, 2369 (1967).
23. W. Gissien, G. Alefold, and T. Springer, *J. Phys. Chem. Solids* **31**, 2361 (1970).
24. G. M. Padawer and P. N. Adler, Development of a nuclear microprobe technique for hydrogen analysis in selected materials, U.S. Nat. Tech. Inf. Serv., A. D. Report No. 770856/35A (1973).
25. R. Gauthier and P. Pinard, *Phys. Status Solidi A* **38**, 85 (1976).
26. A. Benninghove, K. H. Muller, C. Plög, M. S. Chamer, and P. Steffens, *Surf. Sci.* **63**, 403 (1977).
27. T. K. G. Namboodhiri and L. Nanis, Hydrogen permeation and embrittlement in ferrous materials, Office of Naval Research, Technical Report, UPH2-004, (November 1972), NR036-077.
28. J. J. Deluccia, Electrolytic hydrogen in beta titanium, U.S. NTIS.AD. Rep. AD-A028496 (1976).
29. M. G. Fontana and R. W. Staehle, Stress corrosion cracking of metallic materials. Part III—Hydrogen entry and embrittlement in steel, NTIS No. AD/A-010 265, National Technical Information Service, 5285 (1975).
30. M. R. Piggott and A. C. Siarkowski, *J. Iron Steel Inst.*, 901 (1972).
31. N. V. Parthasarathy, *Met. Finish. J.* 36 (1974).
32. J. P. Nityanandan, H. V. K. Uduppa, H. N. V. Rao, Y. Mahadevan, and K. R. Ramakrishnan, *Met. Finish. J.* 190 (1974).
33. Y. Saito and K. Nobe, Abstract No. 126, in Extended Abstracts of the Fall Meeting, Electrochemical Society, Atlanta, October, 1977.
34. Materials Science Research Programs, M.I.T. Research Programs for 1980. R. Kirchheim and R. B. McLellan, *J. Electrochem. Soc.* **127**, 2419 (1980). P. Kedzierzawski,, Z. Szklarska-Smiabowska, and M. Smialowski, *J. Electrochem. Soc.* **127**, 2550 (1980).
35. J. McBreen, L. Nanis, and W. Beck, *J. Electrochem. Soc.* **113**, 1218 (1966).
36. E. Gileadi, M. Fullenwider, and J. O'M. Bockris, *J. Electrochem. Soc.* **113**, 928 (1966).
37. J. O'M. Bockris, W. Beck, M. A. Genshaw, P. K. Subramanyan, and F. S. Williams, *Acta Metall.* **19**, 1209 (1971).
38. L. Nanis and T. R. G. Namboodhiri, *J. Electrochem. Soc.* **119**, 691 (1972).
39. J. Deluccia, Electrolytic hydrogen in beta titanium, U.S. NTIS AD Rep. AD-A028496 (1976).
40. T. K. G. Namboodhiri and L. Nanis, Hydrogen permeation and embrittlement in ferrous materials, Technical Report, UPD2-004, NR 036-077 (November 1972).
41. C. D. Kim and B. E. Wilde, *J. Electrochem. Soc.* **118**, 202 (1971).
42. T. C. Franklin and A. W. Beyerlein, *Denki Kagaku* **41**, 186 (1973).
43. B. Baranowski, S. Majchrzak, and T. B. Flanagan, *J. Phys. F. Metal Phys.* **1** 258 (1971).
44. M. Kuballa and B. Baranowski, *Ber. Bunsen. Gesellsch. Phys. Chem.* **78**, 335 (1974).
45. J. McBreen, Ph.D., thesis, University of Pennsylvania, 1965.
46. J. O'M. Bockris and P. K. Subramanyan, *Electrochem. Acta* **16**, 2169 (1971).
47. W. H. Trapnal, *Chemisorption*, Butterworths, London (1955).
48. H. Podgurski, private communication.
49. C. E. Holley, W. J. Worlton, and R. R. Ziegler, U.S.A.E.C. Report, LA-2271 (August 1958).
50. M. Smialowski, in Proceedings of the First International Symposium on Corrosion, held at Ohio State University, Columbus, Ohio, 1967.
51. J. O'M. Bockris, J. McBreen, and L. Nanis, *J. Electrochem. Soc.* **112**, 1125 (1965).
52. J. McBreen and M. A. Genshaw, in Proceedings of the First International Symposium on Corrosion, held at Ohio State University, Columbus, Ohio, 1967.
53. B. V. Tilak and B. E. Conway, *Electrochem. Acta* **21**, 745 (1976).
54. B. V. Tilak, C. G. Rader, and B. E. Conway, *Electrochem. Acta* **22**, 1167 (1977).
55. J. O'M. Bockris, *Modern Aspects of Electrochemistry*, Vol. 1, Butterworths, London (1954), p. 180.

56. D. B. Matthews, Ph.D. thesis, University of Pennsylvania, 1965.
57. T. P. Radhakrishnan and L. L. Shreir, *Electrochem. Acta* **11**, 1007 (1966).
58. M. Smialowski and Z. Sklarska-Smialowska, *Bull. Acad. Pol. Sci. Cl.*, 111, **2**, 73 (1954).
59. W. Baukloh and G. Zimmerman, *Arch. Eisenhutten Wis.* **9**, 459 (1936).
60. V. V. Kuznetzov and V. V. Frolov, *Zh. Prikl. Rhim. Mosk.* **35**, 582 (1962).
61. P. Bardenheur and H. Ploum, *Mitt. Kelmwilh-Inst. Eisenforsch. Dusseld.* **16**, 129 (1934).
62. J. F. Newman and L. L. Shreir, *Corros. Sci.* **9**, 631 (1969).
63. K. E. Shuler and K. J. Laidler, *J. Chem. Phys.* **17**, 212 (1949).
64. S. M. Beloglazov and M. I. Polukarov, *Zh. Prikl. Chim. Mosk.* **33**, 389 (1960).
65. V. P. Alikin, *Uchen. Zap. Perm. Gos. Univ.* **19**, 3 (1961).
66. U. R. Evans, The corrosion and oxidation of metals, in *Scientific Principles and Practical Applications*, Arnold, London (1961), p. 397.
67. J. O'M. Bockris and R. Thacker, Technical Report No. 3, Office of Naval Research Contract No. NR 551 (22) NRO 36–028 (1958).
68. L. Nanis and J. J. Deluccia, Materials performance and the deep sea, ASTM STP 445, Am. Soc. Testing Materials, (1969), p. 155.
69. J. J. Deluccia, K. Yamakawa, and L. Nanis, Technical Report, UP H 2-001, NR 036-077 (October 1969).
70. F. de Kazinczy, *Jernkont Annlv.* **139**, 885 (1955).
71. J. C. M. Li, R. A. Oriani, and L. S. Darken, *Z. Phys. Chem.* N.F. **49**, 926 (1968).
72. J. W. Gibbs, *The Collected Works*, Vol. 1, Yale University Press, Hew Haven, Connecticut (1948).
73. J. O'M. Bockris and P. K. Subramanyan, *Acta Metall.* **19**, 1205 (1971).
74. J. O'M. Bockris and P. K. Subramanyan, *Scripta Met.* **6**, 947 (1972).
75. P. K. Subramanyan, in *MTP International Review of Science*, Vol. 6, J. O'M. Bockris, ed., Butterworths, London (1973), Chap. 4, p. 181.
76. W. A. Tiller and R. Schrieffer, *Scripta Met.* **4**, 57 (1970).
77. W. A. Tiller, in *Stress Corrosion Cracking and Hydrogen Embrittlement of Iron Base Alloys*, R. Staehle, ed., NACE, Houston (1974).
78. W. A. Tiller, *Scripta Mat.* **8**, 487 (1974).
79. P. K. Subramanyan, *Electrochim. Acta*, to be published.
80. H. G. Van Bueren, *Imperfections in Crystals*, North-Holland, Amsterdam (1961).
81. A. R. Troiano, *Trans. ASM.* **47**, 892 (1955).
82. J. A. Peterson, R. Gibala, and A. R. Troiano, *J. Iron Steel Inst.* **207**, 86 (1969).
83. P. Cotterril, *Prog. Met. Sci.* **9**, 205 (1961).
84. A. S. Tetelman and A. J. McEvily, Jr., *Fracture of Structural Materials*, John Wiley and Sons, New York (1970).
85. H. C. Rogers, *Science* **159**, 1057 (1968).
86. I. M. Bernstein, *Mater. Sci. Eng.* **6**, 1 (1970).
87. J. P. Hirsh and H. H. Johnson, *Corrosion (Houston)* **32**, 3 (1976).
88. A. W. Thompson, *Int. J. Hydrogen Energy* **2**, 299 (1977).
89. H. Benneck, H. Schenck, and H. Muller, *Stahl Eisen* **55**, 321 (1935).
90. A. A. Griffith, *Philos. Trans.* **A221**, 163 (1920–1921); *Proc. Int. Congr. Appl. Mech. Delft*, 55 (1924).
91. I. N. Sneddon, *Proc. R. Soc.* **187**, 229 (1945).
92. F. de Kazinczy, *J. Iron Steel Inst.* **177**, 85 (1954).
93. F. Garafalo, Y. T. Chotu, and V. Ambegaokar, *Acta. Metall.* **8**, 504 (1960).
94. B. A. Bilby and J. Hewitt, *Acta Metall.* **10**, 587 (1962).
95. F. Karnel and A. G. Quarrel, *J. Iron Steel Inst.* **187**, 1002 (1965); K. Farrel, *J. Iron Steel Inst.* **188**, 457 (1965).
96. J. O'M. Bockris, M. A. Gershaw, and M. A. Fullenwider, *Electrochem. Acta* **15**, 47 (1970).
97. J. O'M. Bockris and P. K. Subramanyan, *J. Electrochem. Soc.* **118**, 1114 (1971).
98. E. Gileadi, M. A. Fullenwider, and J. O'M. Bockris, *J. Electrochem. Soc.* **113**, 926 (1966).

99. N. J. Petch and P. Stables, *Nature* (*London*) **169**, 842 (1952).
100. N. J. Petch, *Philos. Mag.* **1**, 186 (1956); **1**, 331 (1956); **3**, 1089 (1958).
101. E. Orowan, *Nature* (*London*) **154**, 341 (1944).
102. G. G. Hancock and H. H. Johnson, *Trans. A.I.M.E.* **236**, 513 (1966).
103. M. G. Fontana and N. D. Greene, *Corrosion Engineering*, McGraw-Hill, New York (1967).
104. Y. A. Marichev and I. L. Rosenfeld, *Corrosion* (*Houston*) **32**, 423 (1976).
105. J. H. N. Van Vucht, F. A. Kujpers, and H. C. A. M. Burming, *Philips Res. Rep.* **25**, 133 (1970).
106. A. Biris, R. V. Bucur, P. Ghete, E. Indrea, and D. Lupu, *J. Less Common Met.* **49**, 477 (1976).
107. O. Boser, *J. Less Common Met.* **46**, 9 (1976).
108. H. H. Van Mal, K. H. J. Buschow, and A. R. Meidema, *J. Less Common Met.* **49**, 473 (1976).
109. A. R. Meidema, K. H. J. Buschow, and H. H. Van Mal, *J. Less Common Met.* **49**, 463 (1976).
110. W. Beck, J. O'M. Bockris, M. A. Genshaw, and P. K. Subramanyan, *Met. Trans.* **2**, 883 (1971).
111. P. K. Subramanyan, Ph.D. thesis, Hydrogen in ferrous metals and alloys, University of Pennsylvania, Philadelphia, 1970.
112. R. H. Wiswall, Jr. and J. J. Reilly, in *Proceedings of the 7th Intersociety Energy Conversion Engineering Conference, San Diego*, September, 1972, American Chemical Society, Washington, D.C. (1973), p. 1342.
113. K. C. Hoffman, J. J. Reilly, F. J. Solzano, C. H. Waide, R. H. Wiswall, and W. E. Winsche, *Int. J. Hydrogen Energy*, **1**, 133 (1976).
114. M. A. Pick and H. Wenzl, *Int. J. Hydrogen Energy* **1**, 413 (1976).
115. A. H. Beaufrere, F. J. Salzano, R. J. Isler, and W. S. Yu, *Int. J. Hydrogen Energy* **1**, 307 (1976).
116. G. Bronoel, J. Sarradin, M. Bonnemay, A. Pecheron, J. C. Achard, and L. Schlapbach, *Int. J. Hydrogen Energy* **1**, 251 (1976).
117. W. C. Gough, in *The Chemistry of Fusion Technology*, D. M. Gruen, ed., P'enum Press, New York (1972), Chap. 1.
118. J. D. Lee, in *The Chemistry of Fusion Technology*, D. M. Gruen, ed., Plenum Press, New York (1972), Chap. 2. T. Kammash, *Fusion Reactor Physics*, Ann Arbor Science Publishing Inc., Ann Arbor, Michigan (1976). B. L. Doyle and F. L. Vook, *Thin Solid Films* **63**, 277 (1979).
119. M. R. Piggot and A. C. Siarkowski, *J. Iron Steel Inst.* 901 (December 1972).
120. N. V. Parthasaradhy, *Met. Finish.* 36 (August 1974).
121. J. P. Nityanandan, H. V. K. Udarfoa, H. N. Venkoba Rao, Y. Mahadevan, and K. R. Ramakrishnan, *J. Met. Finish.* 194 (September 1974).
122. P. C. T. DeBoer, W. J. McLean, and H. S. Homan, *Int. J. Hydrogen Energy* **1**, 153 (1976).

9

Triboelectrochemistry

V. GURUSWAMY and J. O'M. BOCKRIS

1. Introduction

The effect of changing friction by applying an electrochemical potential is a phenomenon of theoretical interest and practical application. Triboelectrochemistry, the study of friction with applied electrochemical potential, may be used to study contact adsorption on solid electrodes. Until now, techniques for studying the double-layer structure and contact adsorption on solid electrodes have been less precise than the electrocapillary techniques for mercury.

The industrial potential in reducing the friction by as much as half(1) in the machining and drilling industry is apparent. Wear and tear and energy use would be reduced.(2)

2. Historical

The first studies on the variation of friction with potential in electrolytes were carried out by Edison(3) in 1877, who observed the variation of the coefficient on lead, thallium, and platinum. Koch(4) in 1879 observed an increase in the friction of platinum against glass (with an anodic potential).

V. GURUSWAMY and J. O'M. BOCKRIS • Department of Chemistry, Texas A&M University, College Station, Texas 77843.

Waitz(5) in 1882 measured the friction of gold, palladium, and nickel against glass in different electrolytic solutions and observed also an increase of friction for anodic potentials and a decrease for cathodic potentials. Krouchkoll(6) in 1889 obtained quantitative measurements of the sliding friction of a platinum brush against glass in an acid electrolyte, where the coefficient of friction increased from 0.10 to 0.30 at a potential of 120 mV with respect to the rest potential of platinum. Clark(7) reported the sliding friction of tungsten and platinum wires on a Perspex drum in various electrolytes.

3. The Rehbinder Effect on Hardness

Rehbinder *et al.*,(8,9) using a Herbert-type pendulum where a spherical glass was in contact with a metal surface surrounded by an electrolyte, found found that there was a logarithmic decrement in the amplitude of the oscillations with potential. Rehbinder *et al.* attributed this effect to the variation of the hardness of the metal, owing to the formation of "reversible micro fissures" in a metal surface under deformation. The electrode double layer penetrated the fissures formed, which reduced the cohesion and hardness of the metal. This concept of a potential effect on hardness was new to the West. However, subsequent work by Bockris and Argade(10) lead to the concept that many of the effects observed are due to potential effects on friction. The Russians consider hardness in relation to wearing(2) and fret corrosion(11) in relation to the electrochemical potential.

4. The Dependence of Friction on Potential

Bowden and Young(12) in 1950 measured the coefficient of static friction of platinum against platinum in 0.1 *M* sulfuric acid. The method involved a small cylinder on a wire in a cell, the apparatus tilted at an angle such that the cylinder just slid down the wire. They concluded that a maximum of static friction at the point of zero charge accompanied an increase in the damage to the surface. This was interpreted as corresponding to the maximum of adhesion.

Bockris and Parry-Jones(13) in 1953, investigating the Rehbinder effect with a cine-camera, found that the glass fulcrum oscillated laterally on the metal when a potential was applied, thereby suggesting both friction and hardness. To clarify the position further, experiments were carried out with a Vickers hardness tester, using an electrolyte in between the sharp metal point and the metal on which it was to make an indentation. A potential was applied to see if there were any changes in hardness, and none was found. Bockris and Parry-Jones went on to show that it was the friction which varied with potential in a parabolic manner similar to that found by Bowden and Young.

Staicopolus(14) in 1961, when developing the above concepts, designed an apparatus for measuring the dynamic friction (Figure 1). It consists of a fulcrum *F* in the shape of a sphere which fits into a conical cavity *C*, the test electrode. During measurement, the electrode is rotated about its vertical axis by a constant speed motor *M*. The motion is counterbalanced by weights. Staicopolus showed that the friction was a function of the potential and that these curves were similar to the electrocapillary curves. The preferential adsorption of CrO_4^{2-} over chloride was shown in the friction curves. Corrosion inhibitors or steel showed unusually high friction values. However, in general, the

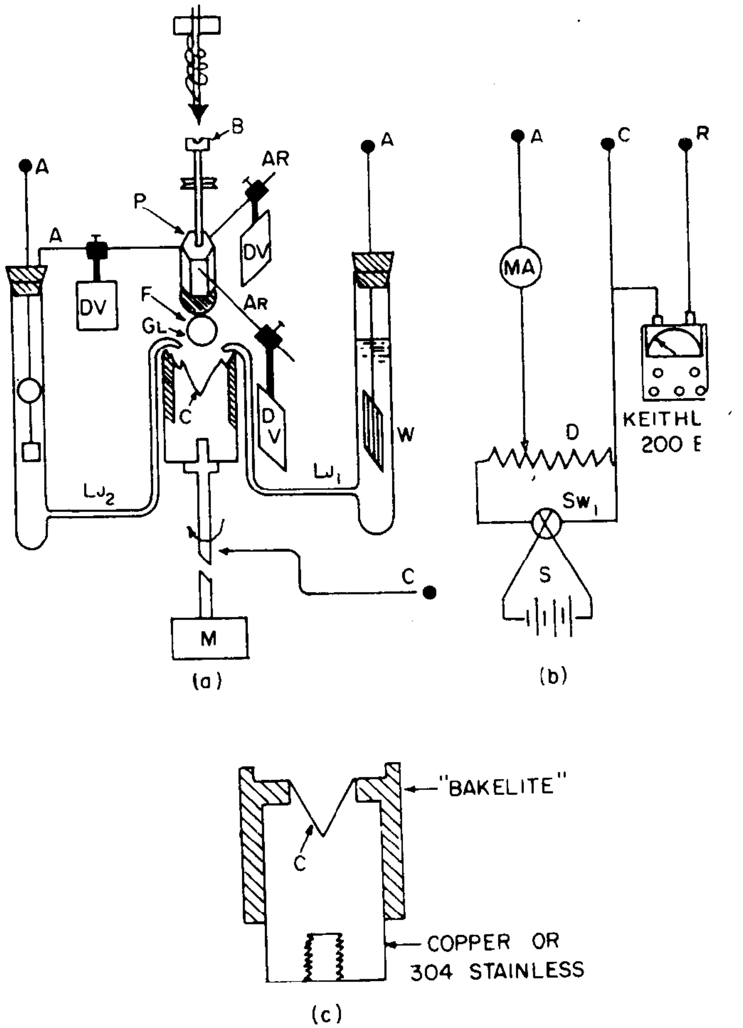
B
A
AR
P
A
A
DV
DV
F
GL
AR
C
D
V
W
LJ2
LJ1
C
M
(a)
A
C
R
MA
KEITHL
200 E
D
Sw1
S
(b)
"BAKELITE"
C
COPPER OR
304 STAINLESS
(c)

Figure 1. Friction apparatus (schematic).(13)

application of a potential greater than the p.z.c. reduced the friction by amounts as large as one-half. Staicopolus concluded that this technique would be of value in the study of adsorption.

Bockris and Argade(15,16) studied a number of techniques to evaluate the p.z.c. and used a sliding friction method to determine the coefficient of friction.

The apparatus (Figure 2) consisted of a slider that was made to slide down the interface—which involved a working electrode—by changing the inclination of the electrode gradually.

Bockris and Argade(15) and Bockris and Sen(16) deduced a mathematical expression for the friction in terms of the double-layer characteristics and the potential applied.

Thus

$$\mu_f = F/R \tag{1}$$

Then, $F = \alpha_T A_0$, where α_T is the tensile strength of the softer of the two metals in contact and A_0 is the area of micro contact. R is the normal reaction, given as

$$R = [w \cos\theta - F_a(A - A_0)] - \rho_0 A_0 + F_{el}(A - A_0) \tag{2}$$

However, if Amonton's law is valid, the coefficient of friction is independent of the geometric area of contact, and the weight of the slider is

$$w \cos\theta + F_{el}(A - A_0) \gg \rho_0 A_0 + F_a(A - A_0) \tag{3}$$

So, Eq. (1) becomes

$$\mu_f = \frac{\rho_T A_0}{w \cos\theta + F_{el}(A - A_0)} \tag{4}$$

Let it be assumed that the force on the slider due to specific adsorption is small. Then, the interaction between the two Gouy layers would be predominant. This repulsion can be calculated by getting the double-layer field

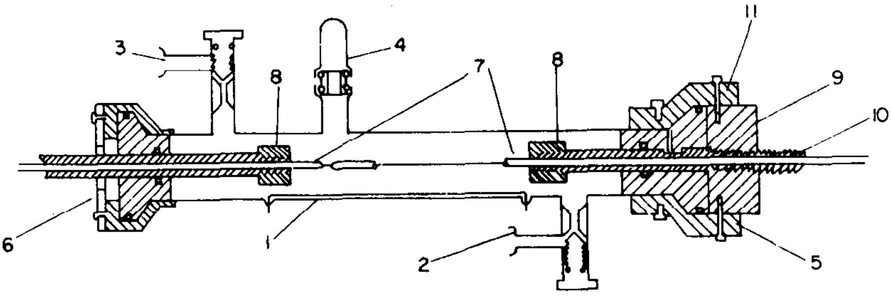

Figure 2. Electrochemical cell for static friction measurements.(14) 1, Counterelectrode; 2, inlet; 3, outlet; 4, reference electrode connection; 5, right end piece; 6, left end piece; 7, metal supports; 8, Kel-F nuts to make seals; 9, Teflon nut; 10, threaded Teflon rod; 11, Kel-F sleeve with screws.

due to one double layer at x, finding out the force it exerts on the other double layer, taking q_{diff} to be localized as a sheet of charge at $1/\kappa$ distance from the solid surface. Hence

$$F_{\text{el}} = -q_{\text{diff}}(-\kappa\psi_0\, e^{-\kappa x}) + q_M[-\kappa\psi_0\, e^{-\kappa(x+1/\kappa)}] \tag{5}$$

if $q_M = q_{\text{diff}}$

$$F_{\text{el}} = q_{\text{diff}}\kappa\psi_0[e^{-\kappa x} - e^{-\kappa(x+1/\kappa)}] \tag{6}$$

Substituting

$$q_{\text{diff}} = \frac{(\varepsilon n_0\kappa T)^{1/2}}{(2\pi)^{1/2}}\psi_0\frac{ze_0}{\kappa T} \tag{7}$$

in Eq. (6) yields

$$F_{\text{el}} = \kappa\left(\frac{\varepsilon n_0\kappa T}{2\pi}\right)^{1/2}\frac{ze_0}{\kappa T}\psi_0^2\{\exp(-\kappa x) - \exp[-\kappa(x + 1/\kappa)]\} \tag{8}$$

On the other hand, expressing $\kappa\psi_0$, Eq. (6), in terms of q_{diff} yields

$$F_{\text{el}} = \frac{4\pi q_{\text{diff}}}{\varepsilon}\{\exp(-\kappa x) - \exp[-\kappa(x + 1/\kappa)]\} \tag{9}$$

Introducing Eq. (8) or (9) into Eq. (4) yields Eqs. (10) and (11):

$$\mu_f = \frac{\rho_T A_0}{w\cos\theta + \kappa(\varepsilon n_0\kappa T/2\pi)^{1/2}(ze_0/\kappa T)\psi_0^2[e^{-\kappa x} - e^{-\kappa(x+1/\kappa)}](A - A_0)} \tag{10}$$

and

$$\mu_f = \frac{\rho_T A_0}{w\cos\theta + (4\pi q_{\text{diff}}/t)[e^{-\kappa x} - e^{-\kappa(x+1/\kappa)}](A - A_0)} \tag{11}$$

Using this equation, Bockris and Sen obtained fair agreement (Figure 3) between experiment and theory for Pt on Pt in $HClO_4$. This treatment may be extended for an intrinsic semiconductor,

$$n_{\text{in}} = (N_c N_v)^{1/2}\exp(-E_g/2\kappa T) \tag{12}$$

and

$$\kappa_i = (8\pi n_{\text{in}} e_0^2/\varepsilon\kappa T)^{1/2} \tag{13}$$

and in this case

$$F_{\text{el}} = \left(\frac{\varepsilon n_0\kappa T}{\pi}\right)^{1/2}\frac{ze_0}{\kappa T}\psi_0^2[e^{-\kappa x} - e^{-\kappa(x+1)}] \tag{14}$$

The agreement with experimental data is fair, but not so good as for the metal–metal interface.

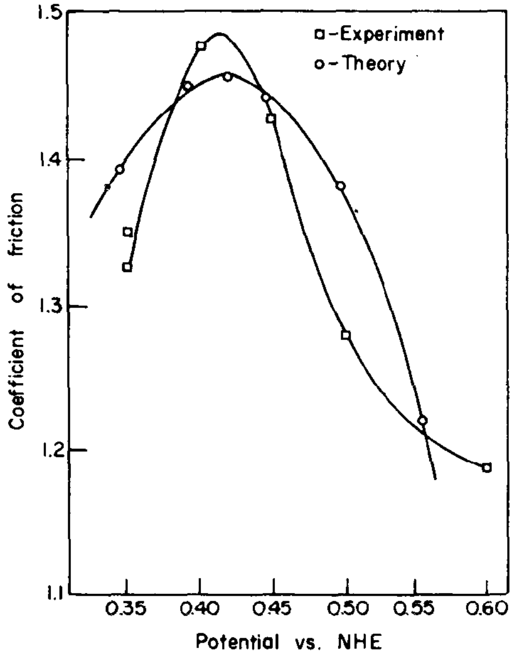

Figure 3. Coefficient friction versus potential for Pt on Pt in $HClO_4$.(14)

In recent Soviet literature it has now become more customary to discuss friction and its dependence on electrochemical potentials.(11) Applications have been made in relation to cooling lubricants(17,18) and the chain lengths of their fatty acid components.

The theory needs to be developed, particularly in the direction of nonpolarizable surfaces. The possibilities of utilizing this technique for such studies has been understressed.

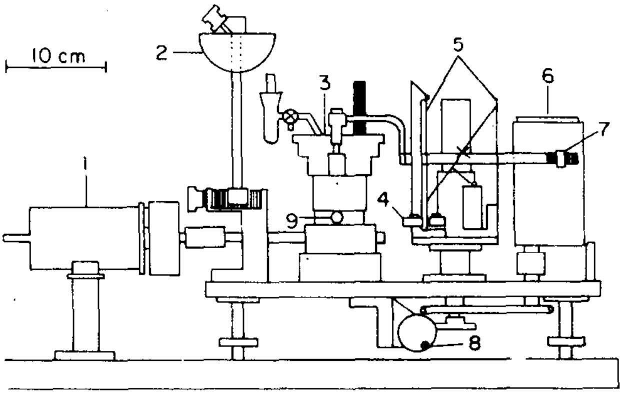

Figure 4. Polaromicrotribometer. 1, Translation drive motor; 2, protractor for calibration; 3, cell; 4, displacement transducers; 5, spring blades; 6, friction measurement bead lift motor; 7, counterbalance; 8, manual height adjustment for the friction contact, 9, micrometer screw for lateral positioning (displacement of the friction contact between successive passes).(19)

刊 T277 B 21

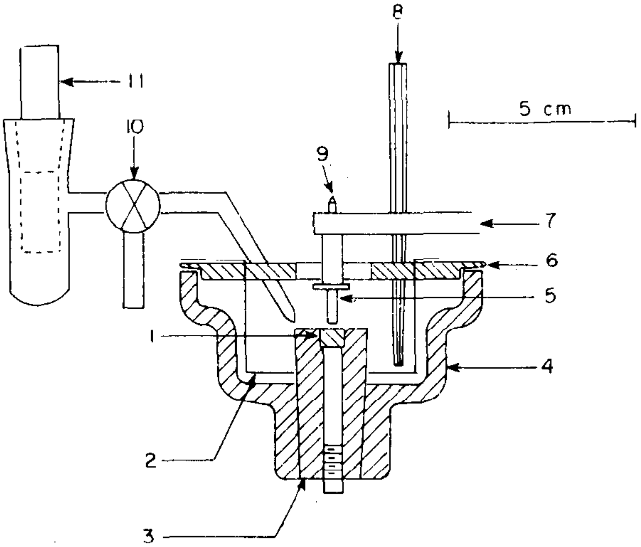

Figure 5. Electrochemical cell. 1, Sample; 2, wire counterelectrode; 3, Teflon sample holder; 4, Pyrex cell; 5, rubbing contact (silica or gold, etc.); 6, cell cover; 7, arm to measure force; 8, nitrogen gas; 9, centering pin for weights; 10, stop-cockbridge; 11, reference electrode.(19)

In 1975, Dubois and Lacaze *et al.*(19) coined the term *polaromicrotribometry* for the study of polarized metal surfaces. Their instrument was a refinement of the Bockris-Argade technique (Figures 4 and 5). Although detailed experimentation has been presented to show variation of surface, material and potential, there has been no theoretical development after that of Bockris and Sen.

Triboelectrochemistry may be developed into a technique for studying the interfacial properties of solid state electrodes.

5. Wear Resistance and Surface Deformation

The studies of Bakradze and Ivanov(2) show that the resistance of copper is a function of the electrochemical potential applied.

This work is in agreement between the Rehbinder effect and the friction effect. Bagotski *et al.*(20) have shown that surface deformations do not affect the friction in electrolytes.

6. Practical Usage of Friction Dependence on Potential

In all mechanically driven devices, a *reduction* in friction among the moving parts is an advantage.

T277 A 21

In ships and hydrofoils, if the propellor of the ship could be held at a suitable potential so that the friction is reduced, considerable savings in fuel energy could be effected.

Another area which is being developed in the U.S.S.R. is the use of greases as electrolytes in lathes and mechanical drills (held at specific potentials) to reduce the energy involved in drilling.

A wider area would be coal mining, rock drilling, and drilling into the ocean beds for oil exploration. In rock drilling, the drill has to grind out more earth and make a penetration into the earth downward in its rotation and make frictional contact with the surroundings. In the first case, a lowered friction would increase the capability of the rock drill, in the second, higher friction. The area is one for research.

Recent Russian work indicates that by reducing friction, the wear resistance and fretting corrosion is reduced as well.

7. Conclusion

It appears that the technique of the variation of friction with electrochemical potential would allow an enhanced understanding of adsorption phenomena and the double layer at solid interfaces, especially nonpolarizable electrodes. There are many practical applications not yet exploited by this technique.

Auxiliary Notation

π	conductance
μ_f	coefficient of friction
z	number of charges per electron
F	tangential force
R	normal force
α_1	tensile strength of the softer of the two metals in contact
A_0	area of micro contact
w	weight of the slider
θ	angle of contact
ρ_0	attractive surface field force per unit area in the micro-contact region
F_{el}	net repulsion between the double layers per unit area
ψ	potential component due to the work function
q_{diff}	charge on the diffuse layer
$1/\kappa$	Debye length
ε	dielectric constant of the medium
n_0	concentration of ions in the double layer relative to the bulk

References

1. D. H. Buckley, *J. Appl. Phys.* **39**, 4224 (1968).
2. I. I. Bakradze and M. K. Ivanov, *Soobschch. Akad. Nauk Gruz. S.S.R. Saknah* **76**(3), 673 (1974).

3. T. Edison, *Teleg. J.* **5**, 189 (1877); *Teleg. J.* **7**, 332 (1879); *C. R. Acad. Sci.* **87**, 270 (1879); *Nature (London)* **19**, 471 (1879).
4. K. R. Koch, *Weidemann's Ann.* **7**, 92 (1879).
5. M. K. Waitz, *Weidemann's Ann.* **7**, 92 (1879).
6. M. Krouchkoll, *C. R. Acad. Sci.* **95**, 177 (1882); *Ann. Chim. Phys.* **17**, 182 (1889).
7. R. E. D. Clark, *Trans. Faraday Soc.* **42**, 449 (1946).
8. Rehbinder and Wenstrom, *Acta Physochim.* **19**, 36 (1944).
9. Rehbinder and Wenstrom, *Dokl. Akad. Nauk.* **68**, 329 (1949).
10. J. O'M. Bockris and S. D. Argade, *J. Chem. Phys.* **50**(4), 1623 (1968).
11. G. E. Movsesov and V. D. Evdokimov, *Fiz-Khim. Mekh. Mater.* (*FKMMAJ*) **9**(6), 103 (1973).
12. F. P. Bowden and L. Young, *Research* **3**, 235 (1950).
13. J. O'M. Bockris and R. Parry-Jones, *Nature* **171**, (May 23, 1953).
14. D. N. Staicopolus, *J. Electrochem. Soc. Electrochem. Sci. Tech.* **108**(9), 903 (1975).
15. J. O'M. Bockris and S. D. Argade, *J. Chem. Phys.* **40**, 1622 (1969).
16. J. O'M. Bockris and R. K. Sen, *Surf. Sci.* **30**, 237 (1972).
17. Yu M. Korobov, V. A. Kuznetsov, Yu G. Kotlov, G. A. Preis, and A. A. Moiseenko, *Probl. Treniya Eznashivaniya* (*PTIAQT*) **8**, 61 (1975).
18. G. N. Uchuvatkin and M. M. Khrushicov, in "*Nauka*" *Moscow Conference Proceedings* (1973), p. 35.
19. J. E. Dubois, P. C. Lacaze, R. Courtel, C. C. Herrmann, and D. Mougis, *J. Electrochem. Soc. Electrochem. Sci. Tech.* **11**, 1458 (1975).
20. V. S. Bagotski, Yu B. Vassiliev, and I. I. Pyshnograeva, *Electrochim. Acta* **16**, 2141 (1971).

10

Nonmetallic Electrode Materials

J. P. RANDIN

1. Introduction

This chapter is devoted to nonmetallic electrode materials, i.e., electrode materials which are neither metallic, nor semiconducting. A large portion of this chapter deals with materials which have proved their worth in actual processes, e.g., carbon and graphite, and another part describes new materials that may prove of much value to the scientist and technologist in the near future.

The characteristics required of an electrode material for industrial processes are easily defined. The electrode material should be:

(a) a good electronic conductor,
(b) an efficient electrocatalyst for the reaction studied,
(c) corrosion resistant and otherwise free from chemical attack,
(d) mechanically rigid (in most cases),
(e) inexpensive (ideally).

Nonmetallic materials usually satisfy conditions (a), (d), and (e), and many efforts have been devoted in recent years to finding materials with both electrochemical stability and electrocatalytic activity. These recent works have generated considerable information about the electrochemistry of nonmetallic materials.

J. P. RANDIN • ASULAB SA, CH 2001 Neuchâtel, Switzerland.

2. Carbon and Graphite Electrodes

Graphite is the only electrochemically important form of the two best-known thermodynamically stable forms of carbon: diamond and graphite. The well-known lattice structure, built up of layers of honeycomb-type planes, imparts high anisotropy to crystals; for example, the electrical resistivity is $4 \times 10^{-5}\ \Omega$ cm in the a-axis and $0.15\ \Omega$ cm in the c-axis direction.(1) The plane parallel to the layers is called the basal (or cleavage) plane, while the plane perpendicular to the layers is known as the edge orientation. The weak bonds between the layers may relax to intercalate a variety of molecules or ions. Such complexes are called intercalation or lamellar or interstitial compounds of graphite.

Graphite is a semimetal in which the valence and conduction bands overlap slightly (about 0.03 eV), so that a few holes and electrons are always available to carry current, regardless of the temperature. In ideal graphite the electron and hole densities are small and equal, and the carrier-effective masses are low. Described as a degenerate semiconductor in one case and a metal with a small Fermi volume in the other, graphite can be considered as intermediate between covalent semiconductors and metals.

Besides graphite, which is the thermodynamically stable crystalline form of the solid element carbon at ordinary pressures, carbon exists metastably in a wide range of disordered or imperfectly ordered structures, the so-called "amorphous" or microcrystalline carbons. Structural disorder is characteristic of synthetic carbons such as charcoal, carbon blacks, soot, and lampblack, produced by a variety of methods. On heating to elevated temperatures, all carbons tend to evolve toward the ordered, equilibrium structure of graphite by the process of graphitization. These materials display a great range of properties when viewed as adsorbents, catalysts, and reagents. The critical factors appear to be surface area, surface heterogeneity, degree of graphitization, and surface complexes, particularly surface oxides.

The general properties and uses,(2-5) electronic properties,(1,3,4,6,7) and electrochemistry(8) of carbon and graphite have been exhaustively described in several treatises.

2.1. Electrochemical Stability in Aqueous Solutions

In aqueous solution, elementary carbon in the form of graphite has no thermodynamically stable domain and corrosion may occur by gasification.(9) However, the corrosive reactions are highly irreversible and, although energetically possible, do not occur readily under normal temperature and pressure conditions.

The surface of any solid may be considered as a borderline case of lattice defect. The regular array of atoms is terminated abruptly at the surface of an ideal crystal and the degree of coordination of the superficial atoms must be different from that of the bulk atoms. As a result, the surface carbon atoms will exhibit unsatisfied valences of great reactivity. Usually most of these valences react immediately with any suitable element present. The most important and best-known surface compound of carbon are those with oxygen, although hydrogen, nitrogen, chlorine, bromine, iodine, and sulfur can also serve as end groups.

Thus, for most carbon or graphite electrodes, the structure of the double layer will be determined mainly by the chemistry of the surface groups or adsorbed gases. The only electrode material on which the surface chemistry is not expected to play a major role is the basal plane of a perfectly oriented graphite monocrystal. The high-pressure, stress-annealing technique has produced graphite of excellent structured characteristics.(10) This material has near-perfect orientation along the *c* axis, that is, across the layer planes. The basal plane of this material therefore provides a rare opportunity to study the double-layer properties of a surface in which all the surface valences are satisfied in the plane of the surface, unlike the surface of other types of carbon electrodes where unsatisfied valences at the surface give rise to chemical interactions with solution phase species.

2.1.1. Electrode–Electrolyte Interface at the Basal Plane of Graphite

The work of Hennig,(11) Montet,(12) Lander and Morrison,(13) and, more recently, Thomas and co-workers(14) has shown that no oxygen, i.e., no functional group, is bound at the basal plane of the highly oriented graphite. A more recent study performed by Barber, Evans, and Thomas(15) using X-ray-induced photoelectron spectroscopy (ESCA) provides the first direct evidence for the existence of chemisorbed oxygen at the basal plane of single crystals of graphite. However, the amount of chemisorbed oxygen is very small at 673 K and "immeasurably small at 300 K."(15)

The electrode–electrolyte interface on the basal plane of stress-annealed pyrolytic graphite has been studied using the ac impedance method(16–18) and by means of electrocapillary measurements.(19) With this highly oriented material, a fresh basal plane surface can be exposed for each experiment by peeling off a layer of graphite with a plastic adhesive tape. The graphite surface exposed in this way was black, mirrorlike in appearance. The differential capacitance has a near parabolic dependence on the electrode potential with the minimum corresponding to about 3 μF/cm^2 in solutions of ionic strength above 10^{-3} *M* (Figure 1). In NaF solutions of $<10^{-4}$ *M* concentration, the capacitance goes through a minimum at potentials essentially the same as those found for higher electrolyte concentrations.

The minimum capacity of about 3 μF/cm^2 observed on the basal plane of stress-annealed pyrolytic graphite is far too low to be explained on the basis of

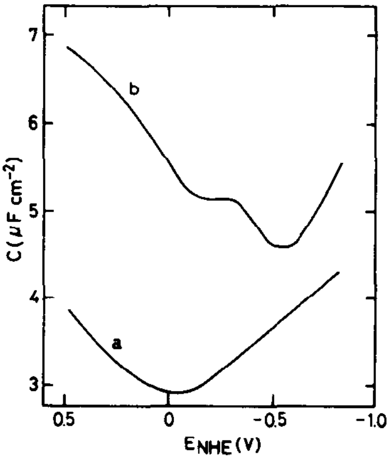

Figure 1. Capacity–potential curves for the basal plane of (a) stress-annealed pyrolytic graphite and (b) boronated stress-annealed pyrolytic graphite (boron content 0.3 wt %) in 0.9 *N* NaF (pH ≃ 6) at 25°C, from ac measurements at 1 kHz. After Randin and Yeager,(18,21) reprinted with permission of Elsevier Scientific Publishing Company.

the usual ionic double-layer structure within the electrolyte. Randin and Yeager(17,18) explained this low capacitance value by assuming that a substantial fraction of the potential change between the electrode and the solution occurs across a space-charge layer within the graphite. The theory of semiconductor electrodes indicates that the capacitance of the space-charge layer in a pure intrinsic semiconductor should exhibit a minimum value given by the expression

$$C_0 = (2\varepsilon\varepsilon_0 e^2 n_i/kT)^{1/2} \qquad (1)$$

with the dependence of the capacity on potential given as

$$C_{sc} = C_0 \cosh(\Delta\phi_s e/2kT) \qquad (2)$$

where ε is the dielectric constant, ε_0 is the permittivity, e is the absolute value of electronic charge, n_i is the intrinsic concentration of electrons and holes, k is Boltzmann's constant, T is the absolute temperature, and $\Delta\phi_s$ is the potential drop in the space-charge layer. Using the value of 6×10^{18} carrier/cm^3 for the electronic carrier concentration(7) and 3 for the dielectric constant,(20) C_0 is 4.5 μF/cm^2. To compare the experimental capacitance value C with the calculated value C_0, i.e., the minimum value of C_{sc}, the value of the Helmholtz double layer, C_H, should be known and computed in the following equation:

$$C^{-1} = C_{sc}^{-1} + C_H^{-1} \qquad (3)$$

Unfortunately, C_H is not known. In the absence of specific adsorption, however, a value of $C_H \simeq 20$ μF/cm^2 seems a reasonable estimate. The capacitance of the Helmholtz layer on the basal plane of graphite may differ appreciably from this value owing to the nonpolar nature of the graphite surface, but it seems quite unlikely that C_H would be sufficiently small as to become the predominant quantity in the series equivalent circuit for the interfacial impedance. By replacing C by 3 μF/cm^2 and C_H by 20 μF/cm^2 in Eq. (3), the space-charge capacitance within the graphite should be 3.6 μF/cm^2, as compared with 4.5 μF/cm^2 calculated from Eq. (1).

The values are in reasonable agreement considering the assumptions involved in the calculations. Thus the low capacity observed on the basal plane of highly oriented graphite at high electrolyte concentrations is best attributed to the space-charge component within the graphite. This conclusion is further confirmed by results obtained on the basal plane of boronated stress-annealed pyrolytic graphite.(21) Electrically active impurities and defects are expected to produce strong alterations in the intrinsic properties of pure graphite since this material has a comparatively small density of states at the Fermi level. Substitutional impurities such as boron slightly increase the carrier concentration and change the semiconductor properties from intrinsic to *p*-type. Figure 1 shows that the potential at the minimum capacity of the capacity–potential curve shifts toward more negative potentials by about 0.5 V relative to that measured on the nonboronated graphite. This finding is in good agreement with the semiconductor interpretation proposed to explain the low value of the capacitance of the graphite–electrolyte interface.(17,18,21) The boronation of graphite results in *p*-type semiconductor characteristics and therefore should shift the potential of the capacity minimum toward more negative values relative to that observed for the basal plane of nondoped graphite.

Studies in NaF solutions at concentrations as low as 10^{-5} M indicated that in the range of potential studied (0.5 to -0.5 V_{NHE}) the minimum capacitance was not associated with a corresponding minimum in the capacity of the diffuse ionic layer. This has been accounted for by assuming that some type of surface heterogeneity broadens the minima in the space-charge capacity as well as the diffuse ionic-layer capacity, and that therefore the potential of zero charge (p.z.c.) does not show up as the sharp minimum found on such surfaces as mercury, or that the p.z.c. for the ionic double layer is outside the potential range studied.(18)

The potential dependence of the space-charge capacity represented by Eq. (2) is much greater than that observed experimentally (Figure 1). The most likely explanation(17,18,21) is that, at the high charge-carrier concentrations involved in the graphite, the semiconductor theory, upon which Eq. (2) and similar equations are based, fails. An alternative explanation involves the nonpolar nature of graphite surface as revealed by the low value of the surface tension of graphite, i.e., $\simeq$34.6 dyn/cm.(19,22)

The capacitance value and potential at the minimum of the capacity–potential curve for the basal plane of highly oriented graphite do not depend appreciably on pH or on the type of anions present in the aqueous electrolyte.(18) This finding is in contrast to the behavior reported with semiconductor and metal electrodes, and suggests that the basal plane of highly oriented graphite is relatively free of functional groups such as OH, H, and other surface species which strongly interact with ions of the electrolyte.

The p.z.c. on the basal plane of stress-annealed pyrolytic graphite has been found to be −0.03 V with the meniscus rise technique(19) and 0.00 V with the ac impedance method.(17,18)

2.1.2. *Electrode–Electrolyte Interface at Other Graphite and Carbon Surfaces*

As mentioned previously, for all carbon and graphite surfaces, except the basal plane of highly oriented graphite, the structure of the double layer is mainly determined by the chemistry of the surface functional groups and adsorbed gases. An extremely large amount of research effort has gone into the study of the surface chemistry of carbon. A full report of these numerous investigations is beyond the scope of this chapter and may be found in several recent reviews.(8,23–31) However, since the surface functional groups play an important role in most electrochemical processes occurring at the carbon and graphite electrode, it seems appropriate to review briefly the most pertinent results of these studies.

Surface oxides arise both from air oxidation at temperatures of 400–1000°C and anodic oxidation, and should be viewed as intermediates in the combustion of carbon. The most extensive studies have been carried out on activated carbon surfaces, where surface oxygen may account for 2–25% of the overall composition of the carbon material.

Chemisorption of oxygen on carbon is irreversible at temperatures greater than about −40°C, and chemisorbed oxygen cannot be removed easily. On heating carbon on which oxygen is chemisorbed and bound, oxygen evolves as CO and CO_2. Thermal breakdown of the adsorbed oxygen layer takes place rather than the desorption of oxygen.

On oxidation, carbon can acquire acid or basic properties. *Acidic surface oxides* result from the treatment of carbon with oxygen at temperatures near its ignition point, i.e., ~400°C. Acidic groups are also formed upon reaction with oxidizing solutions at room temperature. *Basic surface oxides* are formed when a carbon surface, freed from all surface compounds by heating in a vacuum or in an inert atmosphere, comes into contact with oxygen only after cooling at low temperatures.(24)

The principal functional groups suggested as being present on the surface of activated carbon are carboxyls, phenols, quinones, hydroquinones, aldehydes, lactones of the fluorescein type (*f*-lactones), normal lactones, ethers, peroxides, and esters. A schematic representation of some of these groups is shown in Figure 2. The different methods used to determine the various groups have not yielded comparable results and the entire amount of bonded oxygen has not been accounted for.(32) The identification and quantitative determination of the surface functional groups have usually been performed by

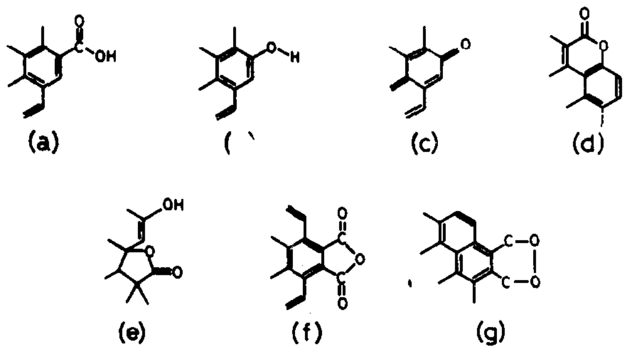

Figure 2. Some of the various possible functional groups on the surface of carbon: (a) carboxyl, (b) phenolic hydroxyl, (c) quinone, (d) normal lactone, (e) fluoresceinlike lactone, (f) carboxylic acid anhydride, and (g) cyclic peroxide. Reprinted from Reference 29, p. 39, by permission of Marcel Dekker, Inc.

applying purely organic chemical methods. The validity of this approach has been questioned on the basis that the functional groups present on graphite crystallites may react only slowly and incompletely because of the possible association between adjacent groups and steric hindrances. The existence of ether-type oxygen bridges between carbon layers of one stack is another possible way of accounting for the difference observed between the oxygen content of oxidized carbon and the oxygen accounted for by the identified functional groups.

The presence of quinone and hydroquinone on carbon blacks has been found by polarography(33) and potentiodynamic sweep technique.(34) Various spectroscopic methods were also used for the direct identification of surface functional groups.(29) Several models have been suggested for the carbon–oxygen surface complexes(24,25,32,33,35,36); however, a realistic model is very difficult to describe because sufficient evidence has not yet been obtained on the relative position of the various groups. The nature of the pretreatment of the carbon seems to have an effect on the spatial arrangement of the groups resulting from oxidation.(35)

Solution adsorption phenomena at the carbon surface have been studied extensively, in particular by Frumkin *et al.*(37) and Garten and Weiss.(38) Excellent reviews are available.(28,29)

Certain classes of reactants, e.g., 9,10-phenanthrenequinone, adsorb very strongly on graphite electrodes to produce electroactive surface species which can be examined in the absence of any diffusing reactant.(39)

The surface functional groups on carbon or graphite electrodes have been evaluated by several workers using standard electrochemical techniques.(8,40,41) All report an irreversible peak at about 0.6 V, attributed to a quinone–hydroquinone couple, despite the variety of carbons studied. This peak practically disappears when only the basal plane of a highly oriented graphite electrode is used.[18] A maximum of three peaks was reported on a low-porosity graphite electrode in 1 *N* H_2SO_4 solutions by means of cyclic voltammetry.[40] The anodic peaks in the potential ranges 0.59–0.91 V, 0.97–1.15 V, and 1.35–1.45 V were associated with cathodic peaks in the potential ranges 0.47–0.79 V, 0.83–1.01 V, and 0.25 V, respectively. They were attributed to the oxidation or reduction of hydroquinone- or quinonelike groups in different environments on the graphite electrode surface.

The apparent differential capacitance for the edge orientation of highly oriented graphite is much higher (typically $>50\ \mu F/cm^2$) than on the basal plane because of higher surface roughness, or capacitive contribution of the surface groups, or both. A model has been put forward[41] to explain the capacitive behavior of the edge orientation; it involves penetration of ions into fissures perpendicular to the surface. Contrary to the behavior of the basal plane of graphite, the potential of the minimum of the capacity–potential curve is pH dependent for the edge orientation. This property, along with the dependence of the differential capacitance on potential, indicates that the chemistry of the surface functional groups plays a predominant role in the interfacial behavior of the edge orientation of graphite. Investigations of the double-layer properties on powdered carbon electrodes have also been reported using the triangular voltage sweep method,[42,43] a low-frequency ac impedance technique,[44] the charging curve method,[45] the measurement of ion adsorption,[37] and the detection of the electrocapillary maximum.[46]

Chemically modified carbon electrode surfaces are the focus of current research in attempts to induce useful analytical, chemical, catalytic, and optical properties.[39,47] Evidence for the successful attachment of various compounds to the surface of carbon has been offered.

The main electrochemical characteristics of both the basal and edge orientation of highly oriented graphite has been summarized in Table 1. For a

Table 1
Comparison of the Main Electrochemical Characteristics of the Basal and Edge Orientations of Highly Oriented Graphite[a]

Characteristic	Basal plane	Edge orientation
Functional groups	None (ideal case)	Numerous
Double-layer capacity (C_{dl})	$3\ \mu F/cm^2$	$50\ \mu F/cm^2$
C_{dl} mainly determined by	Semiconductor properties	Chemistry of surface groups and adsorbed gases
Specific adsorption	None	Strong
Wettability	Poor	Good
p.z.c.	0.00 to −0.03 V	0.16 to 0.20 V
Electrocatalytic properties	Poor	Good

[a] The electrochemical behavior of the edge orientation of graphite can roughly be associated with the behavior of all the carbon and graphite surfaces except for the basal plane of graphite. Reprinted from Reference 8, p. 38, by permission of Marcel Dekker, Inc.

rough comparison, the carbon and graphite surfaces other than the basal plane of graphite can be associated with the behavior of the edge orientation.

2.1.3. Electrochemical Oxidation of Carbon or Graphite

2.1.3.1. In Chloride-Free Electrolytes

Carbon materials corrode when used as anodes. Most attention has been directed toward the graphite anode, where corrosion, particularly in acid solution, not only involves loss of peripheral carbon through surface "combustion" to CO and CO_2, but also involves corrosion associated with swelling and eventually exfoliation of the graphite. One must apparently reckon with intercalation as well as surface dissolution.

Chemical reactions may occur (1) at edge atoms, i.e., at plane boundaries or defects, (2) at exterior intraplanar atoms, or (3) by intrusion between the planes. The edge attack is generally heaviest on the more amorphous carbons and in the more acidic electrolytes. The attack by interplanar intrusion is more pronounced with highly oriented graphite electrodes, provided that some edge planes are exposed to the electrolyte. Amorphous carbons are protected from such attack by their defects, some of which are analogous to the cross-links in polymers. Interplanar intrusion has been observed only in strongly acid solutions containing oxyanions. Some acids (sulfuric, nitric, perchloric, and others) have a strong tendency to form intercalation compounds whereas others (e.g. phosphoric, acetic, hydrochloric) have a weak tendency to intercalate. Strong anodic treatment can lead to the formation of graphite oxide.(48) The conditions for the formation of graphite oxide overlap those for the formation of graphite salts. Croft(49) has suggested that the salt is the precursor of the oxide; in other words, the formation of the oxide occurs only after acid anions have been intercalated into the graphite layer structure. This may explain why the graphite salt is stabilized only under near-anhydrous conditions.

Anode corrosion in alkaline solution, particularly of graphite, is far less intense than in acid solution. CO and CO_2 make up only a small part of the anode gas. CO_2 formed may be retained as surface carbonate.

Early work(50) on the anodic processes occurring on a carbon electrode showed the nature of the reactions to depend on the kind of carbon, on the electrolysis conditions, and on the pH, concentration, and specific nature of the electrolyte. The reason for the anodic destruction of graphite in aqueous solutions has been universally attributed to the oxidation of its surface by adsorbed atomic oxygen before the latter recombines into an oxygen molecule. The source of oxygen is the electrochemical oxidation of water molecules or of hydroxyl ions.

Kokhanov(51–53) and Krishtalik(54–58) and their co-workers have recently studied the kinetic aspects of these reactions. Their investigations were carried

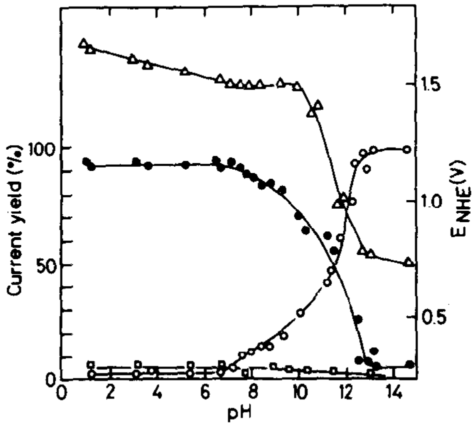

Figure 3. Composition of the anodic gases and graphite electrode potential as a function of the pH value of the phosphate buffer solution at 50°C. Current density 3.7 mA/cm^2. Current yields for CO_2 (●), CO (□), and O_2 (○); anodic potential (△). After Kokhanov and Milova.[51]

out mostly in phosphate electrolytes where intercalation effects are small and the water (or hydroxyl ion) oxidation reaction predominates. The gas composition as a function of the pH of the electrolyte during the anodic polarization of graphite at a fixed current density is given in Figure 3. The product of reaction is mainly CO_2 in acid solution changing to oxygen in alkaline solution, the transition between pH 7 and 13 being accompanied by a sharp drop in anode potential. This transition reflects the change from water molecules to hydroxyl ions as the oxidizing species. In acid solutions the Tafel slope is independent of pH with a value of about $2RT/F$. A linear decrease in the Tafel slope with increasing pH is noted in alkaline solutions until a value of about RT/F is reached at pH > 13.[52]

An interesting comparison between the polarization behavior, the nature of the anodic surface film, and the composition of the anodic product formed as a function of pH and potential was made by Ngo Dai Viet, Kokoulina, and Krishtalik.[56–58] Several potential–pH curves were obtained at various current densities ranging from $\log i = -1.5$ to $\log i = -5$ A/cm^2 at polyethylene-impregnated graphite electrodes in phosphate solutions at 20°C (Figure 4). Three typical potential–pH domains, bounded by dashed lines, can be distinguished in which the potential is independant of pH (I), the potential–pH dependence is small (II), and the potential is strongly dependent on pH (III). In addition, four regions corresponding to different types of oxygen surface films are defined from the characteristics of the cathodic charging curves: (a) no arrest, (b) arrest at 1.58 V, (c) arrest at about 0.5 V, and (d) no arrest but a more reversible behavior. The four regions are denoted by different types of shading. Changes in the intensity of shading correspond qualitatively to changes in the amount of surface oxygen uptake.

Ngo Dai Viet *et al.*[56–58] have defined the main characteristics of these regions as follows. In the first domain, (I), the potential is independant of pH but decreases with increasing ionic strength of the solution. Up to 1.9 V,

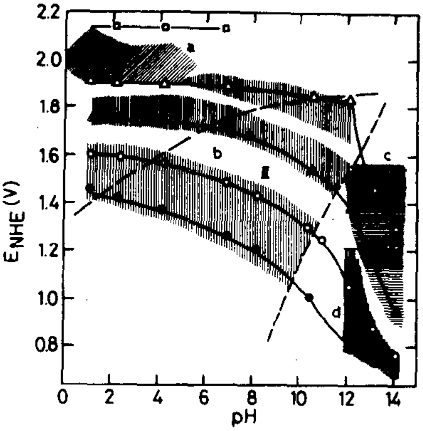

Figure 4. Potential–pH dependence of a polyethylene-impregnated graphite electrode at constant current density in phosphate solutions at 20°C. Log $i = -1.5$ (□), -2.0 (△), -3.0 (▲), -4.0 (○), and -5.0 (●), with i in A/cm^2. After Ngo Tai Piet, Kokoulina, and Krishtalik.(58)

(region a), the same type of oxygen surface film is present and it is most likely that the electroactive species is water molecule. Above 1.9 V (region b) the type of surface film changes causing a decrease in the CO_2 yield and a sharp increase in the crumbling of the graphite.

More complex behavior is observed in domain (II) where the anode potential depends on pH. The reaction rate is directly related to the amount of oxygen adsorbed. This may indicate that some step following the discharge of H_2O or OH^- plays an essential role in the overall mechanism.

In domain (III), which covers alkaline solutions, the electrode potential strongly depends upon pH and increases with increasing ionic strength (adding sulfate). The discharge of hydroxyl ions appears to be the main electrode process in the pH range 13–14. At low potential (region d) the oxygen current efficiency is high (97%), the CO_2 efficiency low, and the charging curves show a reversible behavior attributed to an equilibrium of the type $OH^- \rightleftharpoons OH_{ads} + e^-$ on the electrode. At high potentials (region c) a change in surface states occurs accompanied by an increase in the CO_2 current efficiency (to 40%).

The anodic behavior of glassy carbon in acid solution has been studied by a simultaneous combination of specular reflectance from the electrode surface and usual electrochemical measurements.(59) The anodic oxidation is the sum of three processes: a redox couple formation due to the chemical adsorption of oxygen, the irreversible redox reaction of existing surface groups, and the evolution of oxygen.

Kokhanov(53) has recently discussed the mechanism of anodic oxygen evolution at a graphite electrode using the aforementioned data. The difference between the degree of combustion of graphite in acid and alkaline media is determined by the nature of the discharged species rather than by the anode potential. At low pH values water molecules are discharged and the anodic reaction is the oxidation of carbon with CO_2 evolution. At high values of pH, hydroxyl ions are discharged to adsorbed oxygen atoms from which oxygen molecules are evolved without CO_2 formation. Both processes occur in the intermediate pH range around pH = 9. As the current density is increased, the amount of O_2 evolved is increased while that of CO_2 is decreased.

Oxygen discharged from water molecules is much more active than that discharged from hydroxyl ions. The great difference in the oxygen activities in acid and alkaline solutions suggests that the first step in the evolution of oxygen from water molecule is

$$C + H_2O \rightarrow C(O)_{ads} + 2H^+ + 2e^- \tag{4}$$

while that for the discharge of hydroxyl ions is

$$C + OH^- \rightarrow C(OH)_{ads} + e^- \tag{5}$$

$C(O)_{ads}$ symbolizes chemically adsorbed oxygen without entering into the details of the bonding present, $C(OH)_{ads}$ represents possible reduction products.

The formation of CO_2 following reaction (4) can proceed according to the chemical path

$$2C(O)_{ads} \rightarrow CO_2 + C \tag{6}$$

or to the electrochemical reactions

$$C(O)_{ads} + H_2O \rightarrow CO_2 + 2H^+ + 2e^- \tag{7}$$

or

$$C(O)_{ads} + OH^- \rightarrow CO_2 + H^+ + 2e^- \tag{8}$$

or

$$C(OH)_{ads} + OH^- \rightarrow C(OH)_{2,ads} + e^- \rightarrow CO_2 + 2H^+ + 3e^- \tag{9}$$

The mechanism of oxygen evolution by the discharge of hydroxyl ions is possible either with or without the participation of surface graphite compounds.(53) In acid solutions, oxygen evolution proceeds at glassy carbon without the participation of the chemically adsorbed oxygen.(59)

2.1.3.2. *In Chloride-Containing Electrolytes*

Graphite is used as anode in the chlorine industry, first, because it is in a passive state which inhibits thermodynamically possible corrosion reactions and, second, because it exhibits a low chlorine overpotential. Graphite is preferred to carbon because of its better mechanical and chemical resistance. Since the introduction of dimensionally stable anodes (DSA†) the amount of graphite anodes used in the production of chlorine (in 1976) has declined to about one-half of that used formerly.

The chlorine evolution reaction at graphite electrodes is a moderately fast electrochemical reaction with Tafel parameters $i_0 = 10^{-5}$ A/cm² and $\beta \approx 0.5$ at 25°C.(60–64) The kinetic behavior was shown to change in a stepwise manner as the chloride concentration in the electrolyte was lowered or the pH and temperature raised.(65–68) The change was attributed to an increase in the oxygen evolution reaction and to modifications in surface states. Janssen and Hoogland(62,69–70) have carried out a comprehensive study of the reaction in highly acidic brines (4 *M* NaCl + 1 *M* HCl). They showed that the kinetics changes as the electrode ages. The charge transfer $Cl^- \rightarrow Cl_{ads} + e^-$, and electrochemical desorption, $Cl_{ads} + Cl^- \rightarrow Cl_2 + e^-$, are simultaneously rate determining at a fresh graphite surface. At an aged graphite anode, the electrochemical desorption step becomes rate controlling. Two different surface compounds seem to be formed. In the stationary state, one form is present in the low potential range of chlorine evolution, i.e., below about 1.5 V, and another one at potentials higher than about 1.6 V.(70)

---

† DSA is a noble metal oxide, particularly ruthenium oxide, coated on titanium.

Aqueous brines are electrolyzed in basically two types of cells.(71) The diaphragm cell is composed of graphite or dimensionally stable anodes and mild steel cathodes separated by asbestos diaphragms. The mercury cell involves a two-stage electrochemical operation. In the first stage the brine solution is electrolyzed in a cell consisting of an inclined trough of mild steel on the baseplate of which mercury is flowed. The graphite or DSA anodes are constructed in rows parallel to the running mercury. Chlorine is liberated at the anode and sodium deposited into the mercury to form a sodium amalgam. The latter is transferred into a decomposer vessel where the sodium of the amalgam reacts with water to give the hydroxide and hydrogen. This is a short-circuited galvanic reaction in which graphite acts as a depolarizer.

The graphite consumption is about 4 kg/ton of Cl_2 in diaphragm cells and 2.5 kg/ton in mercury cells.(72) The corrosion of graphite anodes under these conditions can be attributed to three distinct processes:

(1) electrochemical attack due to the reaction of graphite with atomic oxygen resulting from the discharge of H_2O,
(2) chemical attack by hypochlorous acid present in the electrolyte,
(3) mechanical erosion due to the chemical attack within the pores which weakens the intercrystalline bonds and causes the graphite to spall off.

In a normal anolyte with a NaCl concentration of about 220 g/liter, the formation of O_2 and CO are almost totally inhibited, while the formation of CO_2 is low, i.e., about 2.3% of chlorine at pH 1.7 and 93°C.(73) The rate of the electrochemical attack varies with temperature(68) and the presence of specifically adsorbed impurity anions such as sulfate.(74–76) Chlorate ion may also promote graphite consumption(74,77) but the effect is much less than that of sulfate.

Chemical attack of the graphite by hypochlorous acid and hypochlorite occurs to a substantial extent, some 28% of the total consumption being reported.(78) The global reactions involved are

$$C + 2HClO \rightarrow CO_2 + 2HCl \qquad (10)$$

$$C + 2ClO^- \rightarrow CO_2 + 2Cl^- \qquad (11)$$

Hypochlorous acid and hypochlorite ion form part of the "active" chlorine present in the electrolyte and are produced and removed according to the following reactions:

$$Cl_2 + H_2O \rightleftharpoons HClO + HCl \tag{12}$$

$$HClO + OH^- \rightarrow ClO^- + H_2O \tag{13}$$

$$HClO + 2ClO^- \rightarrow ClO_3^- + H^+ + 2Cl^- \tag{14}$$

$$6ClO^- + 3H_2O \rightarrow 2ClO_3^- + 4Cl^- + \tfrac{3}{2}O_2 + 6H^+ + 6e^- \tag{15}$$

Chemical oxidation involving hypochlorous acid or hypochlorite ion occurs particularly in the pores of the graphite anode. Impregnation with oils (e.g., dried linseed oil) is sometimes used to reduce the internal attack (see, e.g., References 8 and 79).

The electrochemical loss of graphite in acidic solution varies little with pH if all the other parameters are constant.(76,77,80) The observed variation of graphite consumption with pH in chlorine cells(67,68,81) is mainly due to the variation in the chemical attack.(77,80) As pH increases through the normal chlorine cell operating range of 2–4 and beyond, consumption first increases before falling at pH ≃ 4 and eventually raising again at pH > 7. This changing consumption pattern closely parallels the variations in the concentrations of hypochlorous acid and hypochlorite in the electrolyte by the reactions given above.

As internal attack by chemical action of hypochlorous acid proceeds, the pores widen and consequently the graphite structure changes. A corrosion front moving with time develops and advances within the graphite structure. The density of the graphite behind the corrosion front decreases until the external layer eventually crumbles.(73,82,83)

The influence of pore structure, surface area, and degree of graphitization,(69,83,84) as well as the graphite manufacturing variables and properties,(73) on consumption have been investigated. The resistance of the graphite to anodic oxidation was found to increase with increasing coke particle size, increasing pitch impregnation, and increasing final heat treatment temperature up to 3000°C. Unpaired electron spin density was the property found best to correlate with the graphite resistance to anodic oxidation.(73)

2.2. Electrocatalytic Activity for the Oxygen Reduction Reaction

2.2.1. Oxygen Reduction Reaction

In oxygen-saturated solutions the rest potential of a carbon or graphite electrode is about 0.1–0.3 V less noble than the reversible oxygen potential of 1.23 V.(50d–50e) This potential is usually unstable and difficult to reproduce. On the contrary, if H_2O_2 is added to an oxygenated alkaline electrolyte, the rest potential becomes highly reproducible and reversible to HO_2^- ions.(85–87) It was found that the rest potential was determined by the oxygen–peroxide couple in alkaline solution:

$$O_2 + H_2O + 2e^- \rightleftharpoons HO_2^- + OH^- \tag{16}$$

since the experimental results gave $\partial E/\partial \log(HO_2^-) \approx 0.03$ V/decade,(85–87) $\partial E/\partial pH \approx 0.03$ V/pH,(85) and $\partial E/\partial \log(P_{O_2}) \approx 0.03$ V/decade.(86)

Oxygen is quantitatively reduced at carbon electrodes to peroxide.(88–90) The isotopic analysis of ^{18}O (Reference 90) demonstrated that both oxygens in HO_2^- originate from the same oxygen molecule. Consequently the O–O bond of the oxygen molecule is not broken during the electroreduction on carbon electrodes.

Several authors have studied the mechanism of the oxygen reduction reaction on nonporous pyrolytic graphite,(91–96) and glassy carbon(92,97,98) electrodes. Typical current–potential curves for the oxygen reduction on a stationary pyrolytic graphite electrode in acidic and alkaline solutions are shown in Figure 5. In alkaline solutions two plateaus of the limiting diffusion current are observed: the first corresponds to the reduction of O_2 to HO_2^- and the second to the reduction of HO_2^- to OH^-. The limiting current density of the second plateau is about twice that of the first one. At $pH < 4$ the current–potential curves exhibit only the first plateau corresponding to the limiting current for a two-electron process. A further increase of potential in the cathodic direction results in the hydrogen evolution and not in the reduction of H_2O_2.

The rotating ring-disk electrode was used to detect the peroxide intermediate.(92) In 1 N H_2SO_4 on pyrolytic graphite electrodes, and at potentials >-0.2 V, oxygen reduction takes place by a two-electron process without any further reduction of H_2O_2. In 0.1 N KOH at potentials more positive than 0.3 V_{RHE}, i.e., in the range of the first wave for the reduction of O_2 to HO_2^-, the reduction of oxygen proceeds to HO_2^- while the peroxide formed does not react further. The influence of the reduction of peroxide can be seen at potentials between 0.1 and -0.4 V_{RHE}.

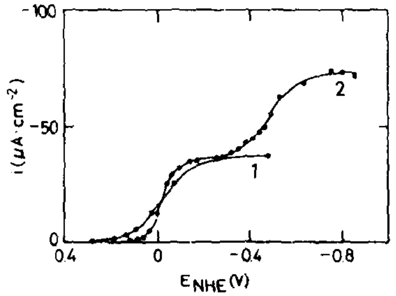

Figure 5. Current–potential curves for the oxygen reduction on pyrolytic graphite electrode in O_2-saturated 0.01 N H_2SO_4 + 0.99 N K_2SO_4, pH = 3.2 (curve 1); and 0.01 N KOH + 0.99 N K_2SO_4, pH = 12.1 (curve 2) at 20°C. After Tarasevich, Sabirov, and Burshtein.(95)

The Tafel slope is about $-2RT/F$(86,91,95,96,98) and the reaction is first order in oxygen(91,92,94,96,98) but independent of pH.(95–96) From these observations the primary electron-transfer step

$$(O_2)_{ads} + e^- \rightarrow (O_2^-)_{ads} \tag{17}$$

is favored as the rate-determining step(86,94,95,98,99) followed by the reduction of $(O_2^-)_{ads}$ to HO_2^- through the following steps(86,96):

$$(O_2^-)_{ads} + H_2O \rightleftharpoons (HO_2)_{ads} + OH^- \tag{18}$$

$$(HO_2)_{ads} + e^- \rightleftharpoons HO_2^- \tag{19}$$

or

$$2(HO_2)_{ads} + OH^- \rightleftharpoons HO_2^- + O_2 + H_2O \tag{20}$$

The superoxide radical ion (O_2^-) might be stable enough in a paraffin–oil medium used as a binder in a carbon paste electrode to be detected as an oxidation peak when the cathodic direction of polarization is reversed at a value close to the limiting current of the first oxygen wave.(99) On glassy carbon the reaction mechanism may differ at low and high pH values.(98) The absence of any significant variation in the exchange current density on cathodes made from different types of carbon was taken as evidence that the rate-determining step does not involve the participation of carbon–oxygen surface functional groups.(100)

Morcos and Yeager(96) found that the electrocatalytic activity of various types of graphite increases in the following order: basal plane of naturally occurring single-crystal graphite < basal plane of stress-annealed pyrolytic graphite ≪ basal plane of ordinary pyrolytic graphite ≃ edge orientation of stress-annealed pyrolytic graphite. They attributed the inhibition of the oxygen reduction on the basal plane of the highly oriented graphite relative to the other surfaces to a lack of favorable chemisorption sites for O_2 or some reaction intermediate on the basal plane.

2.2.2. Uses in Low-Temperature H_2–O_2 Fuel Cells

Carbon may be used as an electrocatalyst for the oxygen reduction in alkaline solutions where its performance is sufficient for certain applications such as in small zinc–air cells. The electrocatalytic activity decreases rapidly with decreasing pH values, and in acidic solutions the activation of carbon with various electrocatalysts is required.

Carbon electrodes are stable on open circuit in alkaline media. Air-depolarized cells standing on open circuit fail only if the temperature rises over the melting point of the wet-proofing material or if subjected to 100% humidity for long periods of time.(101) The presence of Pt catalysts may lead to carbon oxidation of KOH-wet electrodes in the presence of pure oxygen.

Under light continuous load conditions (10–25 mA/cm^2) the lifetime of carbon cathodes is of the order of 1–2 years. It usually decreases with increasing current density. Hydrogen peroxide slowly attacks the carbon of the oxygen electrode. Consequently a good catalyst for the H_2O_2 reduction will improve the lifetime of the carbon electrode by lowering the peroxide concentration. Kordesch(102) has studied the longevity of hydrogen–air fuel cells operating an electric car. He has shown that intermittent use of the fuel cell is possible over 5000 operating hours, i.e., possibly 100,000 or more miles of actual driving, provided that the active gases and the electrolyte are removed from the cells while on standby.

The various treatments developed to improve the performances of carbon–oxygen electrodes have been reviewed.(8,101,103) The catalytic activity can be improved both in alkaline(104) and acidic(105) media by activation with ammonia at 900–1000°C. The current density can be increased by as much as a factor of 2 using such a process. The effect of the NH_3 activation apparently depends on the incorporation of nitrogen-containing groups on the carbon surface, which are more stable than the oxygen-containing groups.

The oxygen electrode operating in a fuel cell must be designed to favor the consumption of oxygen by electrochemical reduction on the electrode surface and to prohibit the diffusion of oxygen from the cathode area to the anode area where oxygen could be consumed by chemical oxidation of the fuel without producing electrical energy. The name *gas-diffusion electrode* was given to such a system(106) composed of a porous diaphragm with one side in contact with the electrolyte and the other side in contact with gaseous oxygen in which oxygen can be electrochemically reduced on the electrolyte side of the electrode before migration to the anode could occur. The reader is referred to recent reviews(107,108) for a general treatment of porous gas-diffusion electrodes.

Diffusion electrodes have been made from porous graphite slabs or thin porous carbon with the solution side of the electrode coated with a catalytically active material to improve the activity for the reduction of oxygen. The preparation and characteristics of various porous carbon gas-diffusion electrodes have been the subject of numerous investigations reviewed by Kordesch.(101,103)

2.3. Electrochemical Stability in Fused Salts

2.3.1. Electrode–Electrolyte Interface

Only a small amount of information is available on the properties of the double layer of carbon in molten salt systems. In cryolite–alumina melts the basal plane of pyrolytic graphite is ideally polarized only in a fairly narrow potential range, i.e., between about 0.7 and 1.1 V vs. the aluminum reference electrode.(109) The capacity exhibits a minimum of about 20 $\mu F/cm^2$ around 0.9 V. At potentials below 0.7 V the capacity rises steeply because of specific adsorption of cations. It also rises slightly at potentials anodic to the minimum in the capacity–potential curve and stabilizes at about 60 $\mu F/cm^2$. In this potential range, i.e., 1.1–1.4 V, gas evolution disturbs the measurement. The double-layer capacity of pyrolytic graphite seems to remain unaffected by carbon dioxide evolution, while that of baked carbon changes because of variations in the surface area.(109) The double-layer capacity of carbon,(110,111) graphite,(112) and glassy carbon(111,113) in cryolite–alumina melts was usually found to be approximately 40 $\mu F/cm^2$.

The capacity–potential curves at glassy carbon electrodes exhibit roughly parabolic shapes in NaCl, KCl,(114) and AgCl(115) melts. In NaCl, KCl, and a mixture of these the minimum capacity rises when passing from KCl to NaCl and decreases with decreasing temperatures.(114) The minimum capacity is relatively high, ≃48 $\mu F/cm^2$, in a silver chloride melt, and is practically constant from 475 to 750°C. The high value of the minimum capacity has been attributed to a higher polarizability of the silver ions compared to the alkali ions with a possibility of specific interactions with the carbon surface.(115) The potential range where the electrode is ideally polarizable becomes smaller at higher temperatures in accordance with the behavior of metal electrodes.(116)

2.3.2. *Electrochemical Oxidation in Oxygen-Containing Melts*

In molten salts the carbon anode is partly oxidized to CO and CO_2. The primary anodic process is the formation of intermediates of chemisorbed carbon oxides of the type C_xO. The decomposition of these surface compounds releases CO and CO_2.

2.3.2.1. *Cryolite–Alumina Melts*

The electrolytic production of aluminum in a cell containing a cryolite–alumina ($Na_3AlF_6 + Al_2O_3$) melt, a carbon anode, and an aluminum cathode is based on the following overall cell reaction:

$$2Al_2O_3 + 3C \rightarrow 4Al + 3CO_2 \qquad (21)$$

The primary anode gas is CO_2(117–119) despite the fact that the formation of CO, according to the reaction

$$Al_2O_3 + 3C \rightarrow 2Al + 3CO \qquad (22)$$

is thermodynamically favored. The equilibrium potential of reaction (21) at 1010°C is 1.163 V as compared to 1.024 V for reaction (22).(120)

The anode gas should consist of the production of CO_2 only. In fact, some formation of CO does occur since the gas from industrial cells contains as much as 30–50% CO. Most of the CO is formed by reaction of the primary anode gas, CO_2, with dissolved aluminum according to the overall reaction(118,119)

$$2Al + 3CO_2 \rightarrow Al_2O_3 + 3CO \qquad (23)$$

which is responsible for part of the loss of current efficiency in aluminum electrolysis.

The nature of the species present in cryolite–alumina melts has not been unequivocally determined. While Na^+ has been shown to be the main current-carrying species, there is still some controversy over the nature of the anionic species, particularly from the viewpoint of the anode reaction. The overall reaction for the anode process may be written as

$$C + 2O^{2-} = CO_2 + 4e^- \tag{24}$$

The use of an oxide ion O^{2-} symbolism is a simplification since complex oxy- and oxyfluoride ions may exist in such melts. Among them AlO_2^-, AlO_3^{2-}, $AlOF_n^{(n-1)-}$, in particular $AlOF_2^-$ have been proposed, the latter being the most probable species.(121)

A substantial amount of work has been devoted to the understanding of the anode reaction. The efforts to unravel it have not always been successful because of experimental difficulties such as the elimination of the resistive voltage drop in the melt between the working electrode and the reference electrode, the presence of a sheath of gas bubbles rising around the electrode distorting the current flows, and the roughness and porosity of the working electrode.

Steady-state current–potential curves have recently been studied by Thonstad(120) (who gives numerous references to earlier work), and Dewing and van der Kouwe.(122) The latter authors overcame the problem of eliminating the ohmic resistance by measuring simultaneously (a) the resistive voltage drop by superimposing an alternating current on the dc and using an ac bridge to determine the resistance, and (b) the harmonic distortion of the superimposed ac. This gave a value for $d^2\eta/di^2$. For graphite the Tafel's law was obeyed over a wide range of dc current densities with $b \simeq RT/F$ but the exchange current density varies from 1.5 mA/cm^2 for current densities below 0.1 A/cm^2 to 5 mA/cm^2 for $i > 0.5$ A/cm^2. This effect could be due to changing CO–CO_2 ratio in the gas bubbles generated or to the changing coverage of the surface by bubbles.(122) Thonstad(120) studied different kinds of graphite and carbon electrodes and found the i_0 values not to depend significantly on the crystal orientation of pyrolytic graphite. The overvoltage is usually smaller for carbon than for graphite(120,122) but it is not clear to what extent this may be due to greater effective surface areas. Thonstad(120) found the exchange current density to be nearly proportional to the alumina concentration in the cryolite melt.

Faradaic impedance measurements were performed by various authors.(111–113,123) According to Dewing(123) this technique fails to give new insights to the anode reaction because of difficulties in the interpretation owing to the porous nature of the electrode surface and to the presence of gas bubbles on the surface.

The reaction mechanism of the anode process on carbon in cryolite–alumina melts has been discussed by numerous authors(111-113,123,124) and reviewed recently.(8) In the absence of identification of the rate-determining step and a model for the faradaic impedance measurements, the mechanisms can only be speculative. A feature common to all the proposed mechanisms is a path involving surface oxides of carbon of the type C_xO.

Anode effect. The anode effect observed on carbon anodes during the electrolysis of molten salts is characterized by a sudden rise of the cell voltage under galvanostatic control, or decrease of the current density for a potentiostatic drive (see Figure 6), nonwetting at the anode–melt interface, and arcing across the gas film separating the anode from the electrolyte during the anode effect. The anode effect occurs when the current exceeds a critical current density which is primarily a function of the melt composition. In the cryolite–alumina melt depletion of dischargeable oxygen-containing ions in the vicinity of the anode leads to fluoride ion discharge once the limiting current density for alumina discharge is exceeded. The anode becomes covered with a film of gas and the current is carried across it by small arcs and locally the temperature is very high, the potential reaching about 40 V. The anode gas contains CF_4, and much higher amounts of CO than normal. The critical current density (for a given alumina content) depends on the stirring at the anode, but a typical commercial cell would exhibit an anode effect when the alumina content drops to about 2%. Numerous authors have studied the anode effect, Thonstad(125,126) being among the most recent.

From a practical point of view the occurrence of the anode effect increases the anode consumption, decreases the current efficiency and produces anomalously high evaporation of the bath because of localized heating. These disadvantages are partly compensated for by the fact that the occurrence of an anode effect establishes that the alumina content has decreased to about 2%

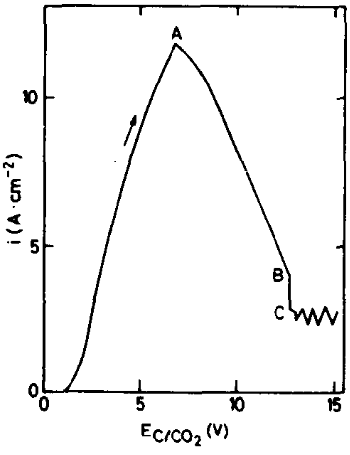

Figure 6. Current–potential curve for a high-density graphite anode in a cryolite melt containing 5 wt % Al_2O_3 at 1010°C with a sweep rate of 0.4 V/sec. The peak current *A* is the critical current density. As the potential raises above this, the current decreases until the anode effect suddenly occurs at *B*. The length of the line *BC* represents the instantaneous decrease in current at the onset of the anode effect. After Thonstad,(125) reprinted with permission of Pergamon Press.

(this is the only form of routine analysis ever performed) and cleans up the cell by burning off pieces or areas of carbon projecting from the anode.(123)

Anodes in the alumina reduction cell. The main advantages of carbon as an anode in aluminum electrowinning are as follows(127): (1) its anode products, CO_2 and CO, are expelled from the system and do not contaminate the electrolyte; (2) it withstands the high operating temperature (~1000°C); (3) it is insoluble in cryolite–alumina melts; (4) it is a good electronic conductor; and (5) it is cheap. The chief disadvantage is the anode consumption, which is between 0.5 and 0.8 kg of carbon per kg of aluminum.

Two types of carbon anode are used in alumina reduction cells. The first is the prebaked carbon block, in which the binder percentage is relatively low. Individual blocks of carbon are attached to upper rods by baking the raw materials, coke or anthracite, in a separate anode baking furnace. As the carbon is consumed, the anodes are lowered further into the melt. The second is the Söderberg anode or self-baking electrode, made with carbon paste, in which the percentage of binder is high. The anode consists of a rectangular steel container, open at top and bottom, suspended over the molten electrolyte bath. The paste containing the coke–pitch mixture is introduced from the top. The heat at the bottom of the anode bakes and binds the mixture. The current is applied to the electrode through iron studs penetrating into the soft paste in the upper part of the anode.

Since most impurities pass into the electrolyte and eventually into the aluminum, the carbon must be of high purity. In fact, it has been observed that the carbon rather than the alumina is usually the main source of contaminants. Petroleum coke is generally used as the anode aggregate because of its high purity and low cost. Coal tar pitch is employed as a binder.

The reader is referred to recent reviews for more details on anode manufacture and carbon quality,(5,118) and on the effects of operating variables on the anode consumption.(8,79)

Cathodes in the alumina reduction cell. The cathode forming the cell lining of the alumina reduction cell is made of carbon because of the unique capability of this material to serve as a low-cost, electrically conductive container for both molten aluminum and cryolite. In operation, carbon cathodes are slowly consumed. The lining failure is of particular importance since it determines the lifetime of the cell as a whole which is of the order of 3–4 years.(128)

The following phenomena are responsible for the consumption of carbon cathodes(123):

(1) swelling due to penetration into the carbon lattice of sodium atoms generated by the reaction

$$3NaF + Al = AlF_3 + 3Na \qquad (25)$$

(2) crystallization of the cryolite absorbed in the pores and cracks of the cathode resulting in structural disruption in a manner analogous to the frost heave of wet porous soils in winter,

(3) formation of aluminum carbide, Al_4C_3, and subsequent dissolution in cryolite,
(4) slow oxidation due to traces of air diffusing into the lining from the underside.

A graphite cathode would absorb less cryolite than a carbon electrode and be less subject to the frost heave phenomenon. Its cost, brittleness, and softness make graphite uncompetitive for the cell lining as compared to carbon.(128)

2.3.2.2. Other Melts

The anodic reaction occurring during the electrolysis of molten nitrates on graphite electrodes at temperatures from 220 to 470°C has been studied by Arvia, Triaca, and Sustersic.(129) The electrochemical combustion of the graphite anode occurs between 230 and 320°C according to the overall reaction

$$C + 2NO_3^- = CO_2 + 2NO_2 + 2e^- \qquad (26)$$

The current–potential curve fits a Tafel line with a slope of $2RT/F$ and an exchange current density of 1.25×10^{-4} A/cm^2 at 269°C. The apparent heat of activation of the process is 6.5 ± 1.0 kcal/mol. A mechanism involving the participation of superficial oxides of graphite has been put forward.

The electrochemical oxidation of graphite in $KHSO_4$ or the eutectic mixture $NaHSO_4$–$KHSO_4$ has been studied by Arvia, Triaca, and Videla.(130) The main gaseous products are CO_2 and CO, with only traces of SO_2. The CO_2–CO ratio is about 2 and is independent of the current density between 0.8 and 45 mA/cm^2. Tafel's law is obeyed with a slope of RT/F and an exchange current density of 7.6×10^{-8} A/cm^2 at 235°C. The apparent heat of activation is 42.5 ± 5 kcal/mol and suggests a thermal process as the rate-determining step since it coincides with the values obtained for the thermal oxidation of graphite to volatile compounds in the same temperature range, i.e., 45–50 kcal/mol between 250 and 450°C.(131) The thermal reaction involves the desorption of intermediates following either a first-order or a second-order reaction depending on the type of adsorption obeyed. The thermal reaction is the rate-determining step irrespective of the preceding steps.

2.3.3. Electrochemical Studies in Halide Melts

2.3.3.1. Fluoride Melts

Fluorine gas is prepared industrially by electrolysis of a molten mixture of potassium fluoride and hydrogen fluoride of the approximate composition KF·2HF (40.8% HF) at 80–110°C with carbon anode and mild steel cathode.(132) The kinetics of the evolution of fluorine at a carbon or graphite anode has been studied by Watanabe, Inoue, and Yoshizawa(133) in KF·2HF at a temperature which is unspecified but probably 100°C and by Arvia and de

Cusminsky(134) in KF·HF at 250–280°C. A Tafel relationship with a slope of $RT/\alpha F$, an exchange current density of about 10^{-4}–10^{-6} A/cm², and a transfer coefficient of 0.8 were found at current densities lower than 10 mA/cm². At higher current densities the resistance due to fluorine gas bubbles on the electrode causes the curve to deviate from linearity.(133) Both Arvia *et al.*(134) and Watanabe *et al.*(133) reported anomalies in the measurements which were attributed to some kind of interaction of fluorine with carbon.

The anode current density of the industrial cells is kept below 0.10–0.18 A/cm² since the anode effect occurs at higher current densities and electrolysis must be stopped. The anode effect is due to a significant diminution of the electrode area available for the fluorine evolution reaction caused by the formation of a film of the intercalation compound $(CF)_n$ which has a very low surface energy and is an electrical insulator.(135–137) It has not yet been established whether the anode effect results of a lack of wettability of the anode surface by the electrolyte or of a lack of conductivity of carbon, or both, masking off larger and larger areas of the anode surface. The involvement of some type of intercalation compound in the anode effect was demonstrated by Rüdorff and co-workers(138) using X-ray analysis, and more recently by Watanabe *et al.*(136) by means of ESCA. The latter authors showed that the carbon monofluoride, $(CF)_n$, film was formed on the surface of the carbon and graphite anodes under normal electrolysis conditions and not only during the anode effect. The following reactions may occur simultaneously on the anode surface:

Fluorine evolution

$$2F^- \rightarrow F_2 + 2e^- \tag{27}$$

Formation of $(CF)_n$ film

$$nF^- + nC \rightarrow (CF)_n + ne^- \tag{28}$$

Decomposition of $(CF)_n$ film

$$(CF)_n \rightarrow C + CF_4 + C_2F_6 + \cdots \tag{29}$$

The ESCA spectra of the electrodes polarized at various potentials indicate that reaction (28) proceeds at a potential less anodic than the equilibrium potential of the F^-–F_2 couple.(136,137) The rate of formation [reaction (28)] and decomposition [reaction (29)] of the $(CF)_n$ film is much larger on the edge orientation of pyrolytic graphite than on the basal plane.(137) The recovery of current at the carbon and graphite anodes during the polarization toward negative potentials after the onset of anode effect was attributed to the fast decomposition reaction of the $(CF)_n$ film [reaction (29)] on the portions of these anodes where the edge orientation is in contact with the electrolyte.

The anode effect in fluoride melts and the methods of avoiding it have recently been reviewed by Rudge(132) and Watanabe and Kanaya.(139)

2.3.3.2. Chloride Melts

The evolution of chlorine on carbon and graphite from molten chloride has been investigated by several authors (see, e.g., References 140–142). At low current densities, steady state current–potential curves exhibit a straight line with a slope close to $RT/2F$, while Tafel slopes greater than $RT/2F$ are observed at high current densities, especially with porous anodes. Several factors can explain the latter behavior: the presence of an ohmic potential drop or a transport process in the pores of the anodes, variation in the surface area owing to bubbles adhering to the anode, and change in the reaction mechanism. The most likely mechanism at low current densities involves a fast discharge of chloride ions followed by a slow combination of adsorbed radicals.

The anode effect also occurs in chloride melts.(142–144) Its appearance during the electrolysis of chlorine has been related to the formation of C_xCl_y-type compounds on the anode surface(143) or the appearance of gas bubbles around the anode.(144)

The chlorine dissolution reaction has been studied in a number of melts on various substrates.(8) At high current densities the cathodic dissolution of chlorine is limited by the diffusion of Cl_2 in the LiCl melt to the carbon surface.(140) Holleck(145) used glassy carbon in an $AlCl_3$–KCl–NaCl (57.5–12.5–30 mol%) melt because it did not show any attack contrary to the graphite-containing electrodes which exhibited swelling and disintegration. He used the rotating disk electrode and obtained good Tafel behavior up to high overvoltages with a slope of $-2.5RT/F$. The reaction is first order with respect to Cl_2 and has an apparent heat of activation of 12 kcal/mol. The most probable rate-determining step is the charge transfer to the Cl_2 molecule with a low chlorine coverage of the electrode.

3. Carbide, Boride, Nitride, Phosphide, and Sulfide Electrodes

Various metal–metalloid compounds have recently received considerable research effort because of their very attractive properties in several fields of modern technology. Some of their unusual properties are high melting temperature, great hardness, wear resistance, corrosion resistance, and high electrical conductivity. Their applications are numerous as hard alloys, refractory materials, corrosion-resistant materials for the chemical industry, wear resistant materials, and materials for nuclear energy production. Possible applications of these materials in electrochemistry is a result of their electrochemical stability, electrocatalytic activity, and electrical conductivity. The chief behavior of these materials which will make them successful candidates for a given application is usually their electrochemical stability.

Various books are available covering the structure, properties, production and applications of carbides,(146,147) borides,(147,148) phosphides,(147,148) and chalcogenides.(149) The electrochemistry of carbide electrodes has been reviewed recently.(8)

3.1. Electrochemical Stability

3.1.1. Carbides

The carbides of transition metals, boron, and silicon bear some electrochemical interest, the others being decomposed by water. Transition metal carbides have a high chemical resistance and are not decomposed by most of the mineral acids, by mixture of them, or by alkaline solutions. Boron and silicon carbides have even higher chemical resistance since they are not decomposed by the nitric and hydrofluoric acid mixture which decomposes almost all the transition metal carbides.

In seawater solutions, TiC, ZrC, Cr_3C_2, Mo_2C, and WC showed a high anodic stability at a current density of 10 mA/cm^2, while HfC and NbC were less resistant.(150) During anodic polarization of the same transition metal carbides in HNO_3, the metal of the carbide was oxidized and oxide film formed, thus preventing further oxidation. In both seawater and HNO_3 solutions, Cr_3C_2 and WC had the best stability.(150) Titanium carbide was found to be the most stable carbide among TiC, VC, WC, Cr_3C_2, and TiB_2, in 5 and 50% NaOH solutions at 83°C, in the presence and absence of air.(151) The presence of oxygen accelerated corrosion, especially in the initial phase.

Titanium carbide seems to be the carbide whose electrochemical stability has been studied the most extensively. The steady state current–potential curve in sulfuric acid reveals a sharp current peak at about 1 V (see Figure 7). The height of this current peak decreases in neutral solutions and vanishes in alkaline media.(152) The current peak indicates the anodic dissolution of TiC, and the current decrease with further anodic polarization (Figure 7) shows the formation of a passive film. At potentials more anodic than the passive region, i.e., at about 1.8 V in H_2SO_4 solutions, severe corrosion is observed. In alkaline solutions the passive state is reached under steady state conditions of anodic polarization as shown in Figure 7.

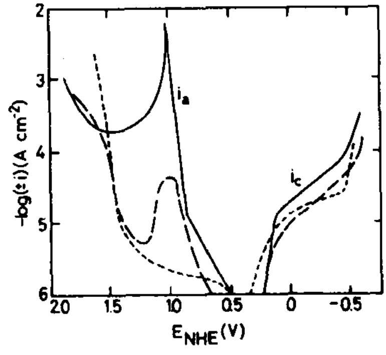

Figure 7. Steady-state current–potential curves for a TiC electrode in nitrogen-saturated 1 M NaOH (——), 0.5 M Na_2SO_4 (— — —), and 0.5 M H_2SO_4 (- - -) solutions at 25°C. After Yoneyama, Ishikawa, and Tamura,(152) reprinted with permission of The Electrochemical Society of Japan.

A Tafel relationship for the dissolution of TiC has been reported in the short potential range 0.9–1.05 V with a slope of about 75 mV/decade(152,153) and a $d(\log i)/d(\text{pH})$ value of 0.68.(152) The pH dependence of the potential at the peak maximum of the potentiodynamic profile was found to be -45 ± 5 mV/pH unit at pH ≤ 1.5.(154) The apparent heat of activation for the maximum current of the anode dissolution, i.e., the curve $\log i_{\text{peak}}$ vs. $1/T$, was found to be 12.7 and 3.6 kcal/mol in sulfuric and nitric acids, respectively.(155) Hintermann and co-workers(156) suggested the following overall reactions for the anodic dissolution of TiC in acidic solutions between about 0.8 and 1 V:

$$TiC(s) + H_2O \rightleftharpoons Ti^{3+}(aq) + CO_{ads} + 2H^+ + 5e^- \qquad (30)$$

$$Ti^{3+}(aq) + H_2O \rightleftharpoons TiO^{2+}(aq) + 2H^+ + e^- \qquad (31)$$

$$CO_{ads} \rightleftharpoons CO(aq) \qquad (32)$$

or

$$CO_{ads} + H_2O \rightleftharpoons CO_2(aq) + 2H^+ + 2e^- \qquad (33)$$

Rotating ring-disk experiments using a platinum ring and a single-crystal TiC disk provided evidence supporting the participation of the intermediate ion Ti^{3+}.(153) Cowling and Hintermann(154) found the presence of both CO and CO_2 in the anode gas evolved during galvanostatic polarization at $E < 1.3$ V, while Yoneyama *et al.*(152) found only CO in the anode gas evolved at 1.05 V. Veselovskaya and co-workers(157) also found no significant amount of CO_2 in the anode gas in chloride electrolytes. It is not clear, therefore, whether CO is desorbed according to reaction (32), further oxidized following reaction (33), or a joint evolution of both gases occurs.

The following reaction was proposed to occur in the passive region between about 1.1 and 1.7 V(154):

$$TiO^{2+}(aq) + 2H_2O = TiO_2 \cdot H_2O(s) + 2H^+ \qquad (34)$$

The passive film formed in H_2SO_4 is relatively soluble.(154) It cannot be reduced in the hydrogen evolution region, and it exhibits high electrical conductivity and consequently does not show any detectable photocurrent on irradiation by uv light.(152) These characteristics strongly indicate that the passive film on TiC is different from the anodic film on Ti, i.e., TiO_2. Cowling and Hintermann(154) proposed the formation of a hydrated oxide $TiO_2 \cdot H_2O$.

The severe corrosion of TiC observed at potentials above about 1.8 V has been proposed to be associated with the oxidation of Ti(IV) to Ti(VI):

$$TiO_2 \cdot H_2O(s) \rightleftharpoons TiO_2^{2+}(aq) + H_2O + 2e^- \qquad (35)$$

Impedance measurements performed at a TiC electrode in 1 *N* H_2SO_4 suggest that the electrode surface is covered with an oxide layer at potentials between -0.3 and 0.6 V.(158) The surface is covered with a firmly bound oxygen corresponding possibly to an oxycarbide.

The electropolishing of TiC has been investigated because the latter is an extremely hard material whose mechanical polishing is very difficult. The best results were obtained at 2.6–2.8 V in 0.4 M aqueous oxalic acid solutions at 40°C for 4 min. The anodic film formed during electropolishing is easily removed by a brief immersion into a dilute hydrofluoric acid solution which does not attack the TiC layer.(159)

Titanium carbide electrodes are reduced under cathodic polarization and the following reactions were proposed as occurring in conjunction with the hydrogen evolution reaction(160):

$$\mathrm{TiC} + x\mathrm{H_2O} + xe^- \rightleftharpoons \mathrm{TiCH}_x + x\mathrm{OH}^- \qquad (x < 1) \tag{36}$$

$$\mathrm{TiCH}_x + \mathrm{H_2O} + e^- \rightarrow \mathrm{TiH} + \mathrm{OH}^- + \mathrm{C}_n\mathrm{H}_{(2n+2)} \qquad (n = 1\text{–}4) \tag{37}$$

The steady state current–potential curves for WC in acidic solutions do not show the anodic peak found for TiC. The photocurrent of passivated WC closely resembles that of passivated tungsten.(161) The following reactions may correspond to the corrosion processes in acidic(161,162) and alkaline(161) solutions:

$$\mathrm{WC} + 5\mathrm{H_2O} = \mathrm{WO_3} + \mathrm{CO_2} + 10\mathrm{H}^+ + 10e^- \tag{38}$$

$$\mathrm{WC} + 10\mathrm{OH}^- = \mathrm{WO_4}^{2-} + \mathrm{CO} + 5\mathrm{H_2O} + 8e^- \tag{39}$$

In aerated alkaline solutions, WC dissolves via a local cell process involving reaction (39) in conjunction with the reduction of dissolved oxygen.(163)

In acidic and neutral solutions, tantalum carbide forms a passive film which breaks down at about 1.7 V and oxygen evolution occurs simultaneously. In alkaline solutions, the carbide passivates at a more anodic potential but is active at relatively less anodic potentials.(164)

The anodic dissolution of NbC in KCl–NaCl melts proceeds at low current densities according to the following process:

$$\mathrm{NbC} \rightarrow \mathrm{Nb}^{n+} + \mathrm{C} + ne^- \tag{40}$$

The formation of a carbon crust on the anode brings about a considerable polarization which favors the passage of niobium ions into the solution in the form of the higher valence ion (pentavalent). At higher current densities the evolution of chlorine may occur.(165)

3.1.2. Sulfides

The anodic dissolution of $\mathrm{Cu_2S}$(166) and NiS(167) was studied in sulfuric acid solutions. The metal ion is formed as well as elemental sulfur or sulfate, depending on the experimental conditions. The electrochemical behavior of NiS, NiAs, NiSb, and NiSi was also reported in perchlorate solutions.(168) The active dissolution at low anodic potentials is followed by a transition to a passive state where the anodic current density is nearly independent of potential. The passive film is either a nickel oxide or a mixed oxide.

3.2. Electrocatalytic Activity

The electrochemical conversion in a fuel cell requires catalytically active electrode materials, especially for the oxygen reduction reaction. Acid electrolytes are favored because of difficulties in feeding the cells with alkaline electrolytes. The choice for electrocatalysts is very much restricted because of severe corrosion problems in acid electrolytes, particularly in the potential range in which the cathode has to operate. Only a few conducting substances, such as noble metals and carbon, are stable in acid electrolytes in the presence of oxygen. The noble metals are generally discarded for mass production for economic and availability reasons. In the absence of a general theory of electrocatalysis as a guide in the search for new materials, a wide search of new compounds has been initiated in the last decade. Some promising results have been reported with carbide, boride, nitride, phosphide, and sulfide electrodes.

3.2.1. Hydrogen Dissolution Reaction

3.2.1.1. Carbides

Bianchi, Mazza, and Trasatti(169) observed that tungsten carbide adsorbs atomic hydrogen up to about 0.3 V. Later Böhm and Pohl(170) proposed WC electrodes for the anodic oxidation of molecular hydrogen in fuel cells. Since then a significant amount of work has been devoted to this reaction on WC(171–184) and other carbides.(170,172,177,178,184) Among the carbides of Ti, Zr, V, Nb, Ta, Cr, Mo, and W, only WC was found to adsorb dissociatively and oxidize molecular hydrogen. The adsorption of hydrogen at the WC electrode is slower, and the exchange current density for its oxidation is smaller than at a platinum electrode.(173) The direct determination of hydrogen adsorbed on WC powders compared with the amount of charge calculated from galvanostatic charging or potentiodynamic curves indicates that the main part of the charge is associated with hydrogen chemisorption but some part of the total charge is consumed for other nondefined redox processes occurring in the hydrogen region on the WC surface.(180) The rate of the hydrogen dissociation reaction was found to be first order with respect to molecular hydrogen and independent of the pH of the solution.(181) The rate-determining step is the dissociative chemisorption or the adsorption of the hydrogen molecule, depending on the activity of the material.(173,181)

Levy and Boudart(185) reported that WC exhibited platinumlike behavior for the chemisorption of hydrogen. They suggested that the catalytic activity of WC as contrasted by the nonactivity of W is due to a change in the electron distribution in tungsten by addition of carbon, making the valence band structure of WC similar to that of Pt. The core level chemical shifts found in X-ray photoelectron spectra(186) indicate electron transfer from W valence orbitals to C_{2p} orbitals. Ross and Stonehart(187) have shown, however, that the platinumlike catalytic properties of WC are not characteristic of every form of WC but only forms with a carbon deficient surface composition. The only electrocatalytically active tungsten carbides had a surface W/C stoichiometry close to 2, suggesting that W_2C was the "active" form of tungsten carbide.(187,188) Richter, von Sturm, and Mund(189) suggested earlier that the carbides of Ti, Zr, V, and Nb are able to adsorb and oxidize atomic hydrogen if formation of a carbohydride phase is possible owing to carbon deficiency. Besides a carbon-deficient surface composition (W_2C) and a hydrogen-containing tungsten carbide, tungsten trioxide and hydrogen tungsten bronzes have been suggested as the active surface layer on WC.(161,162,175,176,179) The two latter compositions are unlikely possibilities because of their known poor electrocatalytic activity for the hydrogen oxidation reaction.(178,190,191) A high concentration of surface defects has also been proposed(178) as creating active centers increasing the catalytic activity.

The specific electrocatalytic activity of tungsten carbide electrodes for hydrogen oxidation and electrochemical stability in acid depends on the method of preparation of the WC.(171,172,175–177,179) Carbides with a bulk deficiency of carbon are indicated to be more active than stoichiometric forms.(175,179,192) The activity and stability can be increased by prepolarization at a potential of 0.6–0.8 V for a fairly long time in the presence of a reducing agent, e.g., hydrogen bubbling.(179) A technique for the preparation of highly dispersed tungsten carbide has been described recently.(193) Tungsten carbide alloyed with silver shows improved electrocatalytic activity for the oxidation of hydrogen as compared to WC.(194)

The tungsten carbide electrode presents the advantage of not being poisoned by carbon monoxide in acidic electrolytes.(172,174,179,182) This property is of considerable technical importance since CO is a constituent of steam-reformed hydrocarbons and other cracked gases. At low polarizations CO behaves like an inert gas, while at high polarizations, i.e., above 0.3 V, tungsten carbide itself is apparently oxidized (see Figure 8). The latter conclusion has been proposed recently by Palanker *et al.*,(182) while earlier studies(172,174,179) attributed the anodic current at potentials higher than 0.3 V to the electrochemical oxidation of CO. Hydrogen sulfide has little effect on the rate of hydrogen oxidation.(172,174,183) Tungsten carbide behaves therefore as a unique catalyst since it adsorbs a considerable amount of hydrogen and catalyzes its oxidation, which could previously be catalyzed only by platinum metals, but does not adsorb CO, C_2H_4, and C_2H_2, which do adsorb strongly on platinum metals and poison them.

The characteristics of experimental fuel cells made of WC anodes and C(Pt) cathodes (containing 4 mg Pt/cm^2) in 2 *N* H_2SO_4 at 60–70°C and fed with either pure H_2 and O_2 or crude gas and air have recently been investigated.(195)

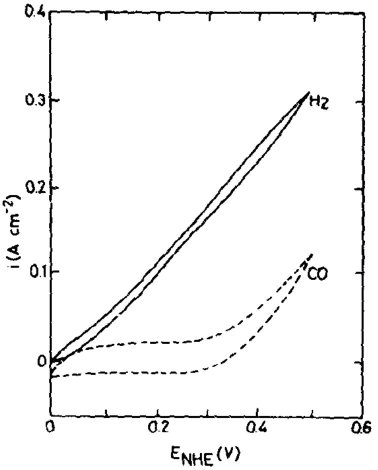

Figure 8. Current–potential curves for the anodic oxidation of hydrogen before and after addition of CO (solid line) and in the presence of carbon monoxide alone (dashed line) at a WC electrode in acidic solutions. After *Böhm and Pohl*,(174) reprinted with permission of AEG-Telefunken.

The construction of bipolar batteries of fuel cells with ten cells has been described. The electrode area is 150 or 260 cm^2 and the power output reaches 30 W at a gas flow rate of about 100 liter/hr. A WC/C(Pt)–H_2SO_4 fuel cell has been in operation for more than 4300 hr without any decline in power.

3.2.1.2. Sulfides, Borides, and Phosphides

The sulfides of tungsten and molybdenum, WS_2 and MoS_2, can also catalyze the hydrogen oxidation reaction.(196,197) The catalytic activity for the oxidation of CO is quite high as compared to that for oxidation of hydrogen. Suitably prepared WS_2 and MoS_2 electrodes can yield the same current densities for the oxidation of H_2 and CO. However, the maximum activity, i.e., 20 mA/cm^2 at 0.2 V polarization, is too low for use in fuel cells.

A mixed electrocatalyst made from molybdenum oxides and sulfides has been claimed to show high catalytic activity toward the oxidation of hydrogen, carbon monoxide, and a variety of unpurified reformed fuels. These materials are highly corrosion resistant and invulnerable to poisoning.(198,199)

Nickel boride, Ni_2B, has been investigated as a hydrogen anode catalyst in alkaline solutions.(200) It was found that the performance of the relatively expensive nickel boride catalyst was no better than that of a 1 : 1 palladium-black-graphite mixture.

Various phosphides of the iron group metals and ternary compounds of these metals with two metalloids from the groups P, As, Sb and S, Se, Te have been studied as electrocatalysts for the hydrogen oxidation.(201) FeP_2, CoP_3, and CoPS exhibited the most promising behavior. Among the arsenides only the cobalt compounds $CoAs_2$ and $CoAs_3$ showed some catalytic activity, while the series of antimonides, selenides, and tellurides were inactive.(202) The range of stability under the corrosive attack of 2.5 *M* H_2SO_4 at 70°C extends up to

0.15 V for CoP_3 and 0.3 V for CoPS. The exchange current density for the hydrogen evolution reaction is of the order of 10^{-5} A/cm^2. CoP_3 is described as the most active anode with a current density of 150 mA/cm^2 at 0.08 V polarization in 2.5 *M* H_2SO_4 at 70°C with a catalyst loading of 0.2 g/cm^2 and a H_2 pressure of 20 N/cm^2. Carbon monoxide is partially adsorbed on the CoP_3 catalyst surface and retards the reaction rate of hydrogen oxidation. It seems therefore that CoP_3 could be classified between tungsten carbide and platinum with respect to CO poisoning.

3.2.2. Oxygen and H_2O_2 Reduction Reactions

Boron carbide(203) and tungsten carbide(169,204,205) were reported to show some activity for the cathodic reduction of oxygen. The exchange current density for the oxygen reduction in 1 *M* $HClO_4$ at a WC electrode was found to be in the 10^{-9} A/cm^2 range, i.e., the same order of magnitude as on platinum.(205) The electrode surface had to be conditioned by sweeping the potential at least 10 cycles between 0 and 0.7 V under nitrogen to obtain stable results.

The electrochemical reduction of oxygen on sulfides has been studied mainly because of its importance in both the flotation and leaching of minerals. Metal dissolution constitutes the anodic reaction in the latter process. The electrocatalytic activity of various rotating disk electrodes has been found to increase in the order $PbS < FeS < CuFeS_2 < FeAsS < Cu_5FeS_4 < CuS < (Fe,Ni)_9S_8 < FeS_2 < Cu_2S$ at pH 1.0 and $CuFeS_2 < PbS < FeS < Cu_5FeS_4 < FeAsS < CuS < (Fe,Ni)_9S_8 < Cu_2S < FeS_2$ at pH 9.2.(206) In assessing sulfides as electrocatalysts for oxygen reduction, it should be noted that the better catalysts, namely, FeS_2 and Cu_2S, have very poor activity, i.e., comparable to that of gold. In general, complete reduction to water takes place on sulfides but hydrogen peroxide has been identified as a fairly stable intermediate.

Kinetic parameters for the electrochemical reduction of oxygen at a rotating FeS_2 electrode were obtained from current–potential measurements at low overpotentials.(207) In oxygen-saturated acid solutions, the Tafel slope is $-2RT/F$ and the exchange current density of the order of 10^{-11} A/cm^2. In acidic solutions the first electron transfer step to form O_2^- is rate determining, while in alkaline media the rates of subsequent steps become important. At low rotation speeds, the limiting current density corresponds to the four-electron reduction of oxygen to water, while at higher rotation speeds complications arise because of the participation of hydrogen peroxide.

Various sulfides(208,209) and thiospinels(209) of transition metals were investigated for their electrocatalytic activity toward the oxygen reduction reaction. The sulfides of cobalt, iron, and nickel show the highest activity. A considerable decrease in activity is observed when sulfur is partly or totally replaced by oxygen, selenium, or tellurium. The same effect is observed with disulfides. The CoPS has also been shown to exhibit some activity for the electrochemical reduction of oxygen.(202) All these compounds, however, were unsufficiently stable to be considered for an application in fuel cells with acid electrolytes at current densities higher than 5 mA/cm^2.

The order of catalytic activity for the electroreduction of oxygen on various compounds is Ni > NiAs > NiSi in acid solutions, and NiS > Ni > NiSi ≃ NiSb > NiAs in alkaline solutions. The reaction occurs in the potential range where a passive film is stable.(168)

The reduction of oxygen was studied on titanium nitride.(204,210) This material was more active than TiC and pure Ti but not as active as a Pt- or Ag-catalyzed cathode.

3.2.3. Other Reactions

Tungsten carbide has been found to be a good electrocatalyst for the oxidation of formaldehyde, acetaldehyde, formic acid, and hydrazine in acidic solutions,(176,177,179,184,211) but the direct conversion of methanol and other alcohols is not possible. The reduction of nitric acid at TiC and WC as well as at various metal carbide–metal mixtures was reported.(212) The rate of the reduction of nitric acid rises with an increase in the TiC concentration in the TiC–Ti mixture, and reaches a maximum for pure TiC. Similar results were obtained with tungsten electrodes containing WC. The catalytic and electrochemical reduction of perchlorate(213) and sulfuric(214) ions by molecular hydrogen in the presence of tungsten carbide powders has been investigated.

Nickel boride, Ni_2B, is a suitable catalyst for the electrochemical oxidation of hydrazine in alkaline medium.(215,216) This catalyst, however, is easily deactivated by hydrogen peroxide ions formed as an intermediate in the reduction of oxygen at the cathode of a hydrazine–oxygen fuel cell.(216)

Nickel sulfide, Ni_3S_2, exhibits good electrocatalytic activity for the anodic oxidation of carbon monoxide in alkaline solutions.(217) Furthermore, it is quite stable below 0.33 V at 75°C and does not catalyze the oxidation of hydrogen, ammonia, methanol, or formate ion. This selectivity implies that Ni_3S_2 could be used to remove electrochemically CO from H_2–CO_2 mixtures and to measure potentiometrically the amount of CO in H_2, N_2, or other inert gases.

3.3. Electroanalytical Applications

Boron carbide has been proposed as a solid electrode for use in electroanalytical investigations. Initial reports(218) claimed that B_4C electrodes exhibit low residual currents in a variety of aqueous electrolytes, and yield reproducible data for several electroanalytical techniques. Later studies(219–221) failed to confirm these properties and showed, on the contrary, that the reproducibility and sensitivity of the B_4C electrodes were poor. Some oxide formation on the electrode which could lead to erroneous interpretation of data has been reported.(220) The behavior of the electrode depended very much upon pretreatment. Tantalum, tungsten, and silicon carbides were also investigated for possible use in voltammetry.(222) None of the carbides showed any advantage over the glassy carbon or pyrolytic graphite electrodes. The carbide electrodes have little utility in electrochemical analysis because the material is expensive and difficult to machine, and the general response and reproducibility are poor.

A comprehensive study of various borides, carbides, and nitrides as potentiometric indicator electrodes for simple redox systems has been carried out by Pungor and Weser.(223) The materials with face-centered-cubic NaCl-type structures were generally satisfactory, while the others were not. Electrodes found suitable for the ferri-ferrocyanide system were TiC, TiC + C, ZrC, $WTiC_2$, W_2C, NbC, TaC, Fe_3C, VN, CrN, TiB_2, Ti_2BN, $MoSi_2$, Cr_3Si, and TiSi. Others tested but found unsuitable were SiC, B_4C, MoC, WC, Cr carbides, VC, Mo_2C, TiN, ZrN, Ti_2B_2N, MoS_2, and Mn_3Si. Among several sulfides studied, FeS_2 was found suitable.

Several chalcogenide materials have been used in recently developed solid state ion-selective electrodes which are sensitive to a number of cations, such as Ag^+, Pb^{2+}, Cr^{3+}, Ni^{2+}, Co^{2+}, Cd^{2+}, Zn^{2+}, Cu^{2+}, and Mn^{2+}.(224,225) Some solid state ion-selective electrodes which respond to Ag^+, Cu^{2+}, Pb^{2+}, and Cd^{2+} are commercially available. The silver sulfide, β-Ag_2S, membrane electrode responds to either silver ion or sulfide ion in aqueous solutions. It is used because it is an ionic conductor with a very low solubility product in water, i.e., 1.6×10^{-49} at 18°C. The principal advantage of this electrode over a simple silver metal electrode for determination of silver ion is its freedom from interference by complexing and precipitating agents, such as thiosulfate and iodide, and by oxidizing or reducing agents. Silver sulfide is also used as a matrix material in conjunction with a number of metal sulfides to give membrane selectivity to the metal ion of the second metal sulfide. The second metal sulfide must satisfy two conditions: (a) its solubility product must be larger than that of Ag_2S, and (b) the sulfides of the membrane phase should equilibrate rapidly with the ions of the solution in order for the electrode to have a reasonable time response. The principles and applications of ion-selective electrodes have been described recently.(224–226)

3.4. Intercalation Compounds as the Cathode of Reversible Batteries

Solids which possess unusually high diffusion coefficients and conductances for specific ions have recently been proposed as cathodes in which the diffusing cation forms a ternary phase by an intercalation reaction. These solids should not be confused with solid electrolytes for which the ionic conductivity is high, but the electronic conductivity must be extremely low to avoid short circuiting the cell internally. On the contrary, the solid of an ionic cathode should ideally have high values of both the ionic and electronic conductivities.

The basic principles of mixed conduction in solids have been formulated by Heyne.(227) Suitable materials are those with layer or tunnel structures in which ionic diffusion is fast; they include inorganic bronzes (e.g., M_xWO_3, $M_xV_2O_5$), graphite intercalation compounds [e.g., $(CF)_n$, C_8CrO_3], and transition metal chalcogenides (e.g., TiS_2, TaS_2). A review of possible candidates is included in a paper by Whittingham,(228) while Dell(229) has reviewed the applications of solid state ionics to the field of batteries.

The tunnel structures of tungsten and vanadium bronzes do not satisfy the rapid mass transport requirements with the alkali metal ions as the electroactive species.(230) The fluorographite intercalation cathodes present several problems associated with their low electronic conductivity, slow electrochemical reaction rate, and polarization by the reaction products.(231) At present the most attractive materials are the transition metal chalcogenides such as TiS_2, which exhibits a relatively low density and is inexpensive, both important features if the compound is to be used in a lightweight battery.

The di- and trichalcogenides of the transition metals Ti, Nb, Ta, Mo, and W are being investigated as possible ionic cathodes for lithium–nonaqueous(232–235) and sodium–β-Al_2O_3(235) secondary batteries. TiS_2 and $Cu_{1.8}S$ have been considered as cathodes for reversible copper solid state cells.(236) These compounds have a layer structure in which anion layers are held together by weak van der Waals forces and between which many electron donors can be intercalated including metals such as Li and Na and many nitrogen molecules, e.g., ammonia and pyridine.(237) The lithium and sodium diffusion coefficient in TiS_2 is about 10^{-7} cm^2/sec at room temperature.(233,234) The presence of an excess of titanium with respect to the stoichiometric composition exerts a profound influence upon the rate of intercalation of the alkali metals.(234) X-ray analysis of the discharge products in the case of a Li^+-containing electrolyte showed that reaction proceeds by intercalation of the lithium into the TiS_2 lattice with a maximum expansion of the structure of about 10% in the c-axis direction.(238) The single-phase reaction can be represented by the equation

$$TiS_2 + xLi \rightarrow Li_xTiS_2 \tag{41}$$

An experimental cell in which the anode was lithium, the electrolyte $LiPF_6$ dissolved in propylene carbonate, and the cathode a single crystal of TiS_2 gave an emf of 2.5 V and an initial current density of 10 mA/cm^2 of active crystal area.(233) A similar cell with powder TiS_2 has been cycled more than 1100 times in shallow cycles operating at 4% of the full capacity. After this treatment the TiS_2 maintained more than 70% of its theoretical capacity, indicating a remarkable reversibility.(233) The theoretical energy density of the Li–TiS_2 couple is 480 Wh/kg. Further work is required on these intercalation compounds to establish whether the organic electrolyte enters into the reaction and whether solid electrolytes can be used without interface polarization.

Some sulfides have also been used in the high-temperature ($\geq 400°C$) lithium–metal sulfide cells in the LiCl–KCl eutectic where, for example, CuS was cycled at 50 mA/cm^2, FeS_2 and FeS at 40 mA/cm^2, and NiS and Cr_2S_3 at 10 mA/cm^2.(239)

4. Mixed Transition Metal Oxide Electrodes

Many oxides have metalliclike conductivity.(240–242) Among them, some transition metal dioxides with rutile structure, e.g., TiO_2, MnO_2, RuO_2, β-PbO_2, etc., have found wide applications in electrochemistry.(79,243) The behaviors of these oxides will not be treated here.

Most of the vast number of oxides having two or more different kinds of cations occur in three basic structural types: the perovskite, spinel, and ilmenite structures. The name of these structures is derived from the first or principal compound to have that type of structure, i.e., $CaTiO_3$, $MgAl_2O_4$, and $FeTiO_3$, respectively. Only the first two of these structures are relevant to the field of electrochemistry.

In the perovskite structure, symbolized ABO_3, the oxide ions and the large cation A form a close-packed cubic array with the smaller cation B occupying those octahedral holes formed exclusively by oxide ions. This structure is often slightly distorted. It is adopted by numerous ABO_3 oxides in which one cation is comparable in size to O^{2-} and the other much smaller, with the cation charges variable so long as their sum is +6.

The spinel AB_2O_4 structure is also based on a close-packed cubic arrangement of oxide ions. One-eighth of the tetrahedral holes are occupied by the A ions and one-half of the octahedral holes are occupied by the B ions. This structure is adopted by many mixed metal oxides of the type $M(II)M(III)_2O_4$, e.g., $Co(II)Co(III)_2O_4$. In certain other spinels half of the B ions are in tetrahedral interstices and the A ions are in the octahedral positions along with the other half of the B ions. These "inverse" spinels are formulated $B(AB)O_4$ to distinguish them from those of the first type. This structure occurs when the A ions have a stronger preference for octahedral coordination than do the B ions, e.g., in $M(IV)M(II)_2O_4$ ($Mn(II)[Ni(II)Mn(IV)]O_4$) and $M(II)M(III)_2O_4$ ($Fe(III)[Co(II)Fe(III)]O_4$, $Fe(III)[Fe(II)Fe(III)]O_4$).

The singular features of oxides and mixed oxides that most interest the electrochemist is their electronic conductivity. The origin of this conductivity has been the subject of sophisticated treatments by physicists for many years and the authoritative review by Goodenough(240) covers the present state of the art. The conduction band in transition metal perovskites results from interactions between d orbitals, t_{2g}, of the transition metal and p_π orbitals of the oxygen. Electrons are donated to the conduction band by the interstitial element A. Metallic or semiconducting properties may appear in ionic crystals if one type of metal ions is present in different valency states. This condition can be satisfied by forming solid solutions of two perovskites, ABO_3 and $A'BO_3$, where A and A′ are nontransition metal of different valency but nearly the same ionic size. B is typically a first-row transition metal with stable +3 or +4 oxidation states such as Ti, V, Cr, Mn, Fe, Co, or Ni. As an example, solid solutions of the two nonconductive perovskites La(III)Ti(III)O_3 and Ba(II)Ti(IV)O_3 are conductive because these solutions, which may be represented as $La_{1-x}Ba_xTiO_3$, contain both trivalent and tetravalent titanium at equivalent lattice sites (the octahedral holes). Electrical conductivity of semiconductivity results from electron (or hole) exchange between the higher-valence-state atoms and the more numerous ones in the normal valence state.

4.1. Transition Metal Oxides of the Perovskite Structure

Considerable attention has been focused recently on transition metal oxides of the perovskite structure because of their possible utility as electrocatalysts and catalysts in the gas phase for controlling automobile exhaust emission (e.g., Reference 244). Although it is generally believed that the catalytic properties of these materials are associated with the *d* electrons (see, e.g., Reference 245), the detailed mechanisms of catalysis are not well understood.

The reader interested in the structure, properties, and preparation of perovskite-type compounds is referred to a recent review.(246)

4.1.1. Oxide Bronzes and Related Compounds

The prototype of oxide bronzes is the nonstoichiometric compound Na_xWO_3 where x is a continuous variable between 0 and 1. The name "bronze" was apparently given to these compounds because $Na_{0.8}WO_3$ has a gold color with metallic luster similar to the Cu–Sn alloys. In the approximate composition range $0.49 < x < 0.93$ Na_xWO_3 has a cubic structure intermediate between the hypothetical $NaWO_3$ and undistorted WO_3 structures and with a fraction $(1 - x)$ of the sodium atoms missing from the cube corners of the $NaWO_3$ unit cell. The composition $x = 1$ is never reached but if it were the structure would be perovskite. As the sodium content of the bronze decreases, the structure goes through various lower symmetry modifications (tetragonal, orthorhombic, and monoclinic), all based on the WO_3 lattice. Sodium tungsten bronzes in which x is >0.25 behave as metallic conductors, while *n*-type semiconductor characteristics with an energy band gap of about 0.5 eV are observed when x is ≤ 0.25. The mechanical properties are more typical of nonmetals: the crystals are hard, brittle, and exhibit weak cleavage planes. The general aspects of oxide bronzes,(247) as well as their preparation,(248) crystal structure,(249) electronic properties,(240,250) and electrochemistry(251) have been described in recent excellent reviews.

Sodium tungsten bronzes can be prepared either by a solid-state reaction between a mixture of fine powders of Na_2WO_4, WO_3, and W at a temperature between 500 and 1000°C(252) or by electrolysis of a molten mixture of Na_2WO_4 and WO_3 between 700 and 900°C.(253) The bronzes produced by the first method are in the form of fine powders, while the second method generates large single crystals very convenient for electrochemical studies.

4.1.1.1. Electrochemical Stability

The chemical stability of Na_xWO_3 resembles that of the parent oxide, WO_3. It is "quite stable" in acidic solutions but dissolves under oxidizing conditions in alkalis. The chemical stability of various oxide bronzes A_xBO_3 in contact with numerous reagents depends on the nature of the metals A and B. McHardy and Stonehart(251) have summarized the published data. The dissolution rate of sodium tungsten bronzes in oxygen-saturated hot azeotropic hydrochloric acid increases with the sodium content of the sample.(254)

The anodic dissolution of sodium tungsten bronzes occurs in acids at a low rate, i.e., about 10^{-8} mol/cm^2 hr at 2 V_{NHE} and room temperature.(255) A net loss of sodium takes place leaving a sodium-depleted layer on the surface. This conclusion has been reached by many authors using various chemical and electrochemical techniques.(191,256–261) Radiotracer data on sodium transfer to solution indicate that the rate of the process at 1.2 V_{NHE} in 1 M H_2SO_4 decays with time.(257) The anodic reaction for sodium depletion may be written as

$$Na_xWO_3 \rightarrow WO_3 + xNa^+ + xe^- \qquad (42)$$

On open circuit, a corrosion mechanism involving the reduction of oxygen or the creation of electron–hole pairs in the electrode under the influence of light(258) may also occur.

Ion probe mass spectrometry performed on polished crystals, which had been cycled between 0.5 and 2.0 V in 0.1 N $HClO_4$, revealed that the surface concentration of sodium had fallen from $x = 0.7$ to $x \leq 0.25$ and that the depth of the depleted layer was between 500 and 2000 Å.(258) For a crystal containing traces of platinum, the surface layer was reported to have an x value of about 0.05 and a depth between 200 and 400 Å.

Capacitance measurements have also been used to determine the sodium concentration in the surface layer.(258–260) Sodium tungsten bronze being a semiconductor when $x < 0.25$, the Mott–Schottky approximation for exhaustive depletion of charge carrier should be valid at potentials sufficiently anodic. This behavior has indeed been observed and a typical plot appears in Figure 9 for an electrode previously oxidized. Donor concentrations determined from the slopes of the Mott–Schottky plots below 2.0 V (assuming a roughness factor of 5) were of the order of 10^{20} carrier/cm^3, which corresponds to an x value of about 0.01.(260) The lack of control of the surface oxidation of the electrode and the strong influence of the prior history of the bronze electrode cause important variations in the slope of the Mott–Schottky plots from one measurement to the

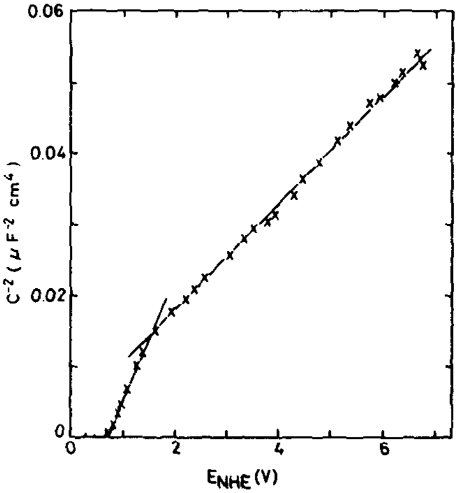

Figure 9. Mott–Schottky plot at 1 kHz for a $Na_{0.82}WO_3$ electrode previously oxidized at 20 mA/cm^2 for 30 min in helium-saturated 1 *N* H_2SO_4. After Randin,(260) reprinted with permission of Pergamon Press.

other. The break observed at about 1.5 V on strongly oxidized electrodes (Figure 9) indicates that a second donor level is activated as the potential is made more anodic. The nature of the deeper level is not clear at the moment. The behavior depicted in Figure 9 is qualitatively similar to results obtained for a single-crystal WO_3 electrode.(262)

The flatband potential estimated by extrapolating Mott–Schottky plots to $1/C^2 = 0$ was found to be 0.6 ± 0.1 V by Randin,(259,260) while McHardy and Bockris(258) obtained values in the range 0.4–0.6 V using data from ac bridge measurements and in the range 0.8–0.9 V using data from galvanostatic pulses measurements. The higher values of the flatband potentials seem to correspond to the more strongly oxidized surfaces.(260) Photocurrent measurements gave an estimated flatband potential of 0.5–0.6 V.(258)

The response of the sodium tungsten bronze electrode to light also provides evidence for the existence of an *n*-type semiconducting layer on the surface.(258) Anodic photocurrents were produced at potentials above 0.5–0.6 V in 0.1 *M* $HClO_4$ upon irradiation with light of frequency greater than 5×10^{14} Hz. The minimum light frequency required to produce a photocurrent corresponds to a band gap of the semiconductor of about 2 eV. By comparison, the fundamental absorption edge of WO_3 is about 2.7 eV (see, e.g., Reference 263).

The potential of an anodically polarized sodium tungsten bronze electrode reaches about 40 V at a current density of 0.2 A/cm^2 and the rate of oxide growth follows a logarithmic law.(259) In this respect, the behavior of sodium tungsten bronze electrodes resembles that of valve metals, including tungsten. At high anodic potentials, the anodic oxidation of the electrolyte, particularly those containing sulfate, may occur.(264)

Potentiodynamic,(190,255,265,266) galvanostatic,(255) and ac impedance(260) measurements show the existence of a pseudofaradaic process at about 0.3 V, which exhibits high pseudocapacitance. Hydrogen bronze, $Na_xH_yWO_3$, or H_xWO_3 formation has been proposed to occur at this intermediate potential.(190,255) The rate-determining step is the electron transfer on a preoxidized, i.e., sodium-depleted, electrode. On an electrode containing sodium in the surface layer the process is controlled by the diffusion of protons in the bronze electrode.(255) This behavior was explained by the fact that the diffusion of protons in Na_xWO_3 is hindered by the presence of sodium at the corners of the cubic lattice. The similarity of the redox reactions of the Na_xWO_3 surface with the reversible reduction of tungsten heteropolyanions has been pointed out.(251)

Reflectance spectroscopy indicates that the largest changes occur below $-0.2\,V_{NHE}$ where it is known that hydrogen enters the surface layer.(190,191) The color turns bluish at potentials more cathodic than about $-0.2\,V_{NHE}$ from the goldish tone of a polished crystal with $x \approx 0.8$. The color change is reversible.

In alkaline solutions sodium tungsten bronze is anodically oxidized with the formation of sodium and tungstate ions. The kinetics of the process has been studied recently.(267)

4.1.1.2. Electrocatalytic Activity

Tungsten bronzes have been shown to possess catalytic activity for a number of reactions, in particular for certain organic processes,(268) the oxygen atom recombination,(269) and the ortho–para hydrogen conversion.(270) The electrochemical oxygen reduction reaction on sodium tungsten bronzes was first examined by Sepa, Damjanovic, and Bockris.(271) They concluded that these materials were about as active as platinum in dilute sulfuric acid. As a result of this work, the tungsten bronzes were studied by a number of workers for electrocatalytic oxygen reduction,(190,254–256,265,266,272–279) as well as hydrogen(190,191,265) and carbon monoxide(190,280) oxidation. Fishman and coworkers(266) showed that the activity for the oxygen reduction was due to the presence of traces of noble metals, in particular platinum.

There is a general consensus that tungsten bronzes free of platinum show little activity for the oxygen reduction reaction.(190,256,265,266,273–279) The overpotential is high, i.e., about 1 V, the background current significant, typically 10^{-6}–10^{-5} A/cm^2,(255) and the dependence upon electrode pretreatment very complex.(274,279)

The presence of platinum in Na_xWO_3 at concentrations in the 100-ppm range has been shown to increase significantly the catalytic properties of the bronze electrodes for the oxygen reduction reaction,(256,265,266,274,279) although some workers(275,276) failed to confirm these findings. Platinum has been incorporated to a low bulk concentration by using a platinum anode (or crucible) during the preparation of the bronzes by electrolysis of a polytungstate melt.(256,274,276,279) A relatively high surface concentration of platinum was also achieved by extended potential cycling in acid solutions containing platinum metal ions(266) or by electrodeposition from chloroplatinic acid.(275) The platinum is believed to be present in the metallic state since it has no effect on the band gap or the flatband potential of the semiconducting surface layer.(258,260) Bockris and McHardy(274) found that the rate of oxygen reduction at a given potential on a sodium tungsten bronze containing about 400 ppm Pt approached that of metallic platinum on a geometric surface area basis. The anodic activity, however, was only 6% that of pure Pt. These authors attributed the increase in cathodic activity with platinum content to synergism between the platinum and the bronze. A model was proposed(274) in which surface diffusion (spillover) of adsorbed reaction intermediates from platinum to the bronze enhanced the rate of oxygen reduction on the platinum surface.

High-surface-area fuel cell electrocatalysts made from Na_xWO_3 with high and low platinum contents showed no activity toward the oxygen reduction reaction.(251,272,275) The ohmic resistance of the surface films and the chemical instability of the bronze, particularly in phosphoric acid,(279) may be worse with high-surface-area electrocatalysts than with single-crystal electrodes. Most workers(190,259,260,265,266,273,275–279) consider that the activity and stability of tungsten bronze, whether with or without platinum, are too low for the materials to be used as oxygen electrode catalysts in conventional acid fuel cells.

Tungsten bronzes have been shown to exhibit rather good electroactivity for the reduction of H_2O_2.(273,275–277,281) In contrast to other electrodes the cathodic reduction of H_2O_2 on tungsten bronze occurs at potentials less cathodic than those required for the reduction of oxygen. The reaction is first order with respect to the H_2O_2 concentration(273,276,277,281) and zero-order with respect to the H^+ concentration.(276) A Tafel relationship is observed between 0.5 and 0.2 V_{NHE} with a slope close to $-2RT/F$.(273,276,277,281) This linear part of the current–potential curve does not depend significantly on the nature of the electrode material for Na_xWO_3, $Ni_{0.03}WO_3$, $Co_{0.03}WO_3$, $Ce_{0.1}WO_3$, $Yb_{0.1}WO_3$, and WO_3.(273,277) At potentials more cathodic than about 0.2 V an interesting inhibition effect (see Figure 10) depending substantially on the electrode material has been observed by the present author.(276,277,281) The inhibition effect was attributed to a competition for available surface sites between hydrogen peroxide and protons. The competing reaction was suggested to be the formation of a reduced form of the bronze electrode, i.e.,

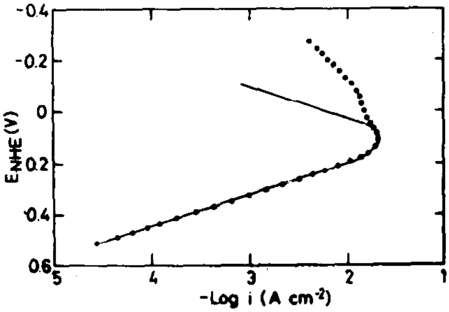

Figure 10. Steady-state potentiostatic current–potential relationship on $Na_{0.65}WO_3$ in He-saturated 1 *N* H_2SO_4 + 0.18 *M* H_2O_2 at 900 rpm (experimental points). The solid line indicates the theoretical relationship for inhibition by competing hydride formation reaction under Langmuirian conditions of adsorption. Reproduced by permission of the National Research Council of Canada from the *Canadian Journal of Chemistry* **52**, 2542–2545 (1974).

hydrogen tungsten bronze $Na_xH_zWO_3$.(276,277,281) The reaction mechanism for the reduction of hydrogen peroxide on tungsten bronzes may be formulated as follows(281):

$$S + H_2O_2 \rightleftharpoons S(H_2O_2)_{ads} \tag{43}$$

$$S(H_2O_2)_{ads} + e^- \xrightarrow{\text{rds}} S(OH)_{ads} + OH^- \tag{44}$$

$$S(OH)_{ads} + e^- \rightleftharpoons S + OH^- \tag{45}$$

where S represents an undefined surface adsorption site at the bronze electrode. The OH^- are neutralized in a homogeneous reaction with H_3O^+. The above sequence of reactions (43)–(45) proceeds in competition with the following parallel reaction:

$$S + H^+ + e^- \rightarrow SH \tag{46}$$

Gilroy and Conway(282) have described numerous cases of anodic oxidations in competition with oxide formation. The inhibition of the cathodic reduction of H_2O_2 on Na_xWO_3 is a cathodic analog of the anodic inhibition process, i.e., a cathodic reduction occurring in competition with hydride formation. The experimental current–potential relationships fit with the theoretical curves calculated under Langmuirian conditions of adsorption to a point 30–40 mV on the cathodic side of the current maximum (see Figure 10).

The hydrogen evolution reaction on sodium tungsten bronzes has been investigated by several authors.(191,283,284) The current–potential curves indicate the presence of several distinct Tafel relationships. This complicated situation arises because of various compositions and structures of the hydride surface layer(191) or adsorption of atomic hydrogen in the bronze.(284) Sodium tungsten bronzes show no activity for the hydrogen oxidation reaction,(190,191) while $M_{0.1}WO_3$ where M is Ce, Sm, Eu, Gd, Dy, Ho and Yb, and $Ni_{>0.24}WO_3$ show some catalytic activity.(265) Synergism between platinum and WO_3 for the electrochemical oxidation of hydrogen has been claimed and attributed to the formation of hydrogen tungsten bronze intermediate by a mechanism such as(285,286)

$$H_2 + 2Pt \rightarrow 2Pt{-}H \tag{47}$$

$$xPt{-}H + WO_3 \rightarrow H_xWO_3 + xPt \tag{48}$$

$$H_xWO_3 \rightarrow WO_3 + xH^+ + xe^- \tag{49}$$

Part of the charge transfer process takes place on the WO_3 surface extending the effective area of the platinum onto the support. However, since the rate-determining step for hydrogen oxidation at a platinum electrode is step (47),(287) the benefit of the above-mentioned mechanism would be limited to platinum particles that are out of contact with the electrolyte.(251)

Enhancement in the electrochemical oxidation of CO was reported with PTFE-bonded electrodes containing mixtures of platinum black and various tungsten oxides(285,288) or sodium tungsten bronzes.(280) The mixed electrocatalyst is less vulnerable to poisoning by the CO than an anode containing platinum alone. It was postulated that the transition metal oxide provides adsorption sites for water molecule adjacent to CO molecules on the platinum. The simultaneous adsorption of CO and H_2O is necessary for the occurrence of the CO oxidation according to the reaction

$$CO_{ads} + H_2O_{ads} \rightarrow CO_2 + 2H^+ + 2e^- \qquad (50)$$

The kinetics of various simple redox couples in aqueous solutions has been studied at sodium tungsten bronzes with different x values.(257,289,290) The rate constants for the $Fe(CN)_6^{4-}$–$Fe(CN)_6^{3-}$, $W(CN)_8^{4-}$–$W(CN)_8^{3-}$, and Fe^{2+}–Fe^{3+} are essentially insensitive to the sodium content of the tungsten bronze but in all cases the electron transfer is considerably slower at Na_xWO_3 than at platinum. Attempts to correlate the rate constants and parameters such as the density of states of electrons at the Fermi level of the bronzes and their work functions have not been successful because slight variations in rate constant with sodium content are not the same for each of the redox couples and the surface composition is not that of the bulk material.

Sodium tungsten bronzes are suitable electrode materials for electrochemical studies in aprotic solvents.(290)

4.1.1.3. *Electroanalytical Applications*

Sodium tungsten bronze has been used as an indicator electrode for electron exchange reactions,(257,289–291) for pH measurements in both aqueous and nonaqueous media,(292) for determination of metal ion concentrations for reducible species such as Ag(I) and Hg(II),(292) for following potential changes involved in some oxidation–reduction systems,(292,293) and in ethylenediamine tetraacetic acid (EDTA) titrations.(294) Even more significant, with respect to possible applications in pollution, is the use of sodium tungsten bronze as oxygen sensitive electrodes.(294) In basic solutions of pH 12, Na_xWO_3 responds potentiometrically to dissolved oxygen in the concentration range 0.2–8 ppm with an unusually large concentration dependence of 120 mV/decade. The potential of the Na_xWO_3 electrode is a mixed potential resulting from the anodic oxidation of Na_xWO_3 and the cathodic reduction of dissolved oxygen.(295) Both the large potential response to dissolved oxygen and the potential break in EDTA titrations are unique to the cubic Na_xWO_3 ($x = 0.65$) among the following highly conducting alkali metal tungsten bronzes: cubic $Li_{0.35}WO_3$, hexagonal $K_{0.3}WO_3$, $Rb_{0.3}WO_3$, and $Cs_{0.3}WO_3$, and tetragonal $K_{0.5}WO_3$.

4.1.1.4. *Electro-optical Applications*

Transparent, amorphous films of WO_3, MoO_3, and other transition metal oxides can be colored dark blue by electroreduction in an acid electrolyte. The process, which is reversible and exhibits a memory in both the colored and bleached state, is one of several electrochromic systems. Electrochromism is a generic term embracing a variety of phenomena which cause a reversible color change in a material by the application of an electric field or the passage of a current.(296–298) The coloration of the WO_3 is due to a double injection of electrons and protons to form the hydrogen tungsten bronze H_xWO_3 or $WO_{3-x}(OH)_x$ according to the reaction

$$\underset{\text{(transparent)}}{WO_3} + xH^+ + xe^- \rightarrow \underset{\text{(blue)}}{H_xWO_3} \tag{51}$$

The process is not limited to the injection of protons from acid electrolytes, but similar systems have been obtained with the injection of Li^+, Ag^+, and Na^+ from $LiClO_4$ dissolved in nonaqueous solvents,(299) and from $RbAg_4I_5$ and sodium–β-alumina(300) solid electrolytes, respectively.

The coloration (reduction) dynamics of WO_3 at low potentials has been explained in terms of barrier-limited proton transfer across the electrolyte–WO_3 interface.(301) The kinetics of the bleaching (anodic) process is mainly determined by a space-charge-limited flow of protons in the WO_3; the interfacial barrier does not limit the current in this case.(302)

Electrochromic systems based on WO_3–H_xWO_3 are being developed for small-size passive display applications. The voltage required to drive the cell is of the order of a typical galvanic cell voltage, i.e., about 1 V, and the optical density is proportional to the injected charge. The power required is from 1 to 20 mW/cm^2 per cycle for a 3:1 contrast ratio and the response time in the 100-msec range.(298) The technologically most advanced system (in 1976) uses an acid electrolyte and the main problem preventing its commercialization is the lifetime which is limited by the lack of chemical and electrochemical stability of the WO_3 film. Lack of reversibility associated with aging of the WO_3 and side reactions may also play a role in the long term stability of the system. In fact, an electrochromic device is nothing else than a battery with a visible state of charge. The challenge is to obtain a system capable of being charged (colored) and then completely discharged (bleached) for millions of cycles despite the fact that no battery exists which is capable of undergoing so many cycles. This rough comparison of electrochemical display devices with batteries illustrates the inherent difficulty in obtaining a long-life electrochromic device.

4.1.2. Other Mixed Transition Metal Oxides of the Perovskite Structure

Perovskite-type compounds, such as strontium-doped $LaCoO_3$, were proposed as electrocatalysts for the oxygen reduction reaction. Meadowcroft,(303) Tseung and Bevan,(304) and Matumoto, Yoneyama, and Tamura(305) found that strontium-doped $LaCoO_3$(303,304) and $LiNiO_3$(305) gave results comparable to, or even better than, platinum in alkaline media. Other studies, however, failed to confirm these results.(306–308) Steady state polarization curves and open-circuit potential measurements(304) were generally used to investigate the electrocatalytic activity. A potentiodynamic study of $La_{0.9}Sr_{0.1}CoO_3$ electrodes seems to indicate the occurrence of a redox process possibly associated with the reduction and oxidation of the electrode material itself.(309) The method of preparation might explain discrepancies from one author to the other, for example, by favoring an ion deficiency, or a particular structure. Sintered electrodes have been shown to give much better results than powdered samples, most likely because of some contact resistance between particles in the latter.(307,309) On the other hand, Tseung and Bevan(304) found encouraging results with freeze-dried samples.

The choice of compounds of the type $(La,Sr)(Co,Ni)O_3$ is related to the possible influence of paramagnetism for catalysis of the oxygen reduction reaction. Paramagnetic susceptibility has long been recognized as a feature of many good catalysts and electrocatalysts (see, e.g., Reference 310). Goldenstein and Tseung(311) have proposed a model based on an idea of Evans(312) to account for the importance of paramagnetism for the electrocatalysis of the oxygen reduction. The paramagnetic electrons in the electrode are supposed to couple with the paramagnetic electrons in the oxygen molecule and, thus, facilitate "side-on" adsorption of the oxygen molecule: O–O, in preference to "end-on" adsorption: $\begin{matrix}\text{O}\\ |\\ \text{O}\end{matrix}$. In the side-on orientation, easy cleavage of the O–O bond is possible by a mechanism involving a chain of hydrogen bonds and resulting in the direct O_2–OH^- reaction. This mechanism has been called the "pseudosplitting" mechanism by Evans.(312) End-on oxygen adsorption permits the O_2–HO_2^- reaction to occur by a joint pseudosplitting–peroxide mechanism.(311) The pseudosplitting mechanism is limited to scarce favorable sites on the electrode surface such as kink sites. It represents an interesting approach to the oxygen reduction reaction but further supporting evidence is required before it can be fully accepted.

It was postulated that for the $(La,Sr)CoO_3$ compounds the existence of strong ferromagnetic exchange between Co(III) and Co(IV) (Reference 313) satisfied an important condition for the splitting of the O–O bond. The substitution of Sr^{2+} for some of the La^{3+} in the $LaCoO_3$ lattice will produce more Co(IV). The electron hopping between Co(III) and Co(IV) by superexchange via the intermediate oxygen ions leads to an enhanced electrical conductivity and improved magnetic characteristics. Typical resistivity of sintered (porous) $La_{0.5}Sr_{0.5}CoO_3$ is $3 \times 10^{-4}\ \Omega$ cm.(314)

Perovskite compounds of the type $(La,Sr)(Co,Ni)O_3$ are chemically stable in alkaline media but dissolve quite rapidly in acidic solutions. They offer therefore no promise for an electrocatalyst in acidic media, which are usually preferred for practical fuel cells because of the carbonation occurring in alkaline solutions when air is used as a depolarizer. It would consequently be of interest to investigate the activity of other perovskite-type compounds in acidic media. $LaCrO_3$ is one of the very few perovskite-type compounds chemically stable in acids as well as in alkalis.(315) Single crystals of $(La,Sr)CrO_3$ prepared by the flux growth method did not show any promising electrocatalytic activity in either H_2SO_4 or NaOH, however.(308)

Some cobaltites with perovskite structure are ionic–electronic mixed conductors with high oxygen ion diffusion coefficient, i.e., $D = 10^{-11}$–10^{-13} cm^2/sec at 25°C, compared with ordinary oxides and also with an electronic conductivity far greater than the ionic conductivity. Thus $Nd_{1-x}Sr_xCoO_3$ is electrochemically reduced in an aqueous alkaline solution to the oxygen deficient compound $Nd_{1-x}Sr_xCoO_{3-y}$.(316)

Kinetic parameters have been determined for the ferro-ferricyanide couple on lanthanum cobaltite electrodes.(317) Various electronically conducting mixed oxides with the perovskite structure have been suggested as cathode materials for high-temperature zirconia electrolyte fuel cells.(318)

4.2. Transition Metal Oxides of the Spinel Structure

Oxides of the spinel structure have been proposed as catalysts for the heterogeneous chemical decomposition of hydrogen peroxide formed during oxygen reduction, especially at a carbon cathode.(101,103,319,320) The oxide is added to the carbon in the proportion of about 10–20% as an activator. At such a composite electrode the electroreduction of oxygen may proceed directly to water without the liberation of hydrogen peroxide, or to hydrogen peroxide by a parallel reaction. The hydrogen peroxide may diffuse out into the solution or undergo a further conversion at the electrode by catalytic chemical decomposition or electrochemical reduction. The extent of each process depends on the nature of the oxide and of the substrate. As an example, on graphite the O_2–HO_2^- reaction proceeds reversibly, while cobalt–iron oxides, $Co_xFe_{3-x}O_4$, are good hydrogen peroxide decomposition catalysts in alkaline solutions with a negligible oxygen and HO_2^- electroreduction activity.(320) On this particular mixed catalyst oxygen is initially reduced at graphite to give hydrogen peroxide:

$$O_2 + H_2O + 2e^- = HO_2^- + OH^- \tag{52}$$

which is then catalytically decomposed at the $Co_xFe_{3-x}O_4$ surface, yielding oxygen:

$$2HO_2^- = O_2 + 2OH^- \tag{53}$$

The product oxygen may be recycled via reaction (52) and consequently increase slightly the exchange current density by increasing the flux of oxygen.

Electrocatalytically active catalysts with the spinel structure have been looked for. Only cobalt cobaltite and the nickel–cobalt oxides have been found to be active for the oxygen reduction reaction. The maximum of the Ni–Co oxides system was found for the 2Co:Ni composition.(321–323) A summary of the information available from the literature is given in Table 2.

Investigations using rotating ring-disk electrodes have shown that the oxygen reduction on cobalt and nickel cobaltites proceeds mainly to OH^-.(324,325,330) This result indicates that dissociative chemisorption of oxygen takes place on Co_3O_4 and $NiCo_2O_4$. By contrast, a two-electron reduction to HO_2^- is observed on nickel oxide, NiO,(324) and possibly on cobalt cobaltite doped with nickel oxide.(326,327)

Cobalt and nickel cobaltites are also good catalysts for the chemical decomposition and cathodic reduction of hydrogen peroxide.(324,331) The rate of the latter reaction is comparable with that of the electroreduction of molecular oxygen.

The role of the trivalent cobalt or nickel ions in the reaction mechanism for the oxygen(323,329,332) and hydrogen peroxide(331) reductions has been pointed out. According to a model proposed by Trunov and Presnov,(332) oxygen chemisorption in solutions and oxygen electroreduction occur chiefly along a pathway involving cobalt surface cations, Co^{3+}, functioning as acceptor sites toward bulk crystal electrons and donor sites toward the oxygen molecules.

Table 2

Activity of Co_3O_4 and $NiCo_2O_4$ Electrocatalysts for the Oxygen Reduction Reaction at Ambient Temperature Unless Otherwise Stated

Electrode	Form	Preparation	Electrolyte	Main reaction product	Refs.
Co_3O_4	Films	Thermochemical or electrochemical oxidation of CoC	0.1 *N* KOH	OH^-	324
$Co_3O_4(15\%) + C$	Powders	—	0.1 *N* KOH	OH^-	325
$Co_3O_4 + \leq 0.3$ at.% Li	Films	Thermochemical oxidation of CoLi	1 *N* KOH	HO_2^-	326
$Co_3O_4 +$ 10 at.% Li	Powders	—	7 *N* KOH	HO_2^-	327
$NiCo_2O_4$	Films	Thermochemical oxidation of CoNi	0.1 *N* KOH	OH^-	324
$NiCo_2O_4$	Powders	Calcination of hydroxides	30% KOH	—	323
$NiCo_2O_4$	Powders	Decomposition of oxysalts	3 *N* KOH (60°C)	—	321
$NiCo_2O_4$	Powders	Decomposition of mixed nitrates	75% KOH (200°C)	—	328
$NiCo_2O_4$	Powders	Decomposition of mixed nitrates	5 *N* KOH	—	322, 329
$NiCo_2O_4(15\%) + C$	Powders	—	0.1 *N* KOH	OH^-	330

The rate-determining step most likely involves some electron transfer from the crystal surface to the oxygen molecule, but not a transfer from the bulk of the crystal to its surface.

Cobalt and nickel cobaltites lack the long-term stability required for a room temperature oxygen electrocatalyst.(329) Cobalt cobaltite is reduced to $Co(OH)_2$ or CoO(331,333) and nickel cobaltite to NiO, CoO, and Co_3O_4,(330) leading to a partial breakdown of the spinel structure and a decrease of the electrocatalytic properties.

The electrochemical activity and stability of some thiospinels have been discussed in Section 3.2.2.

Teflon-bonded $NiCo_2O_4$ electrodes have been shown to be stable enough to be used for the evolution of oxygen.(334) A current density of 1.3 A/cm^2 was obtained at 1.63 V_{DHE} in 5 *N* KOH at 70°C. The kinetics of the ferro-ferricyanide couple has been investigated on $CuMn_2O_4$, $NiMn_2O_4$, $AlMn_2O_4$,(335) and $Cu_{1.2}Mn_{2.8}O_4$.(336)

The solid state reduction of various manganites, $MeMn_2O_4$, and cobaltites, $MeCo_2O_4$, with Me = Ni, Co, Mn, Zn, and Cu, in sulfuric acid solutions occurs in a manner similar to that of the manganese dioxides used in classical Leclanché batteries.(337) The presence of both Mn^{3+} and Mn^{4+}, as well as other cations with two valence states, e.g., Co^{2+}–Co^{3+}, explains the discharge reactions of the manganites.(338)

5. Conclusions

Among the various materials described in this chapter, carbon and graphite represent a unique situation for they have been used and studied since the early days of electrochemistry. On the contrary, investigation of the electrochemistry of carbides, borides, phosphides, sulfides, and mixed oxides began relatively recently. Our knowledge on carbon is consequently much wider than on the other materials.

Despite the huge amount of experimental data regarding the electrochemistry of carbon, several aspects require further investigation. For example, the nature and structure of the surface oxides are not completely understood and the strong influence which the various functional groups exercise in altering the electrochemical properties (and other surface properties) of carbon and graphite needs further study.

A coherent set of interpretations on the numerous studies on the surface chemistry of the materials discussed in the present chapter is missing because their surface is not reproducible, owing undoubtedly to the diversity in the sources of the raw materials (particularly for carbon), in the processes of preparation and in the pretreatment. In this respect studies connected with well-characterized surfaces will prove very helpful. Thus highly oriented pyrolytic graphite and isotropic pyrolytic carbons constitute very suitable varieties of carbon for investigating, respectively, the behavior of the basal plane of graphite and the behavior of a surface which behaves similarly to active carbons. Unfortunately no such well-characterized surfaces exist for the other materials described in this chapter for which there is the uncertainty as to whether the composition of the surface layer is a simple reflection of the bulk.

In addition to better characterized surfaces, improved techniques should be used for examining them, e.g. X-ray photoelectron spectroscopy (XPS or ESCA) and other surface techniques, and *in situ* specular reflection spectroscopy.

The numerous materials described in the present chapter exhibit a certain chemical and electrochemical stability which is usually not sufficient for a fuel cell electrocatalyst. Thus the most limiting factor in the performance of nonnoble metal materials, e.g., carbon, oxide bronzes, sulfides, spinels, and thiospinels, has been the long-term electrochemical stability. Disappointing results have been obtained in the search of new cathodes for the oxygen reduction reaction, with the possible exception of perovskites of the type $La_{1-x}Sr_xCoO_3$ which show interesting behavior under certain experimental conditions, but further supporting evidence is required before this electrocatalyst can be fully recognized. On the other hand new hopes exist for the hydrogen oxidation reaction in acid media with the development of tungsten carbide and various transition metal phosphides (e.g., CoP_3) as electrocatalysts.

Although dimensionally stable anodes (DSA) have not been discussed in this chapter, it is worth mentioning that this novel electrode, based largely on ruthenium oxide coated on a titanium framework, is rapidly replacing the graphite anodes in the chloralkali industry. The advantages of the DSA are a lower overpotential, a longer life, and the ability to use higher current densities. As a result, an average power saving of about 15% can be achieved.

Nonmetallic electrode materials may prove very useful in various electroanalytical applications, i.e., oxide bronzes as indicator electrodes and silver sulfide as solid state ion-specific electrodes. Other new applications might involve reversible batteries using the lamellar compound TiS_2 as a cathode, and electro-optical devices based on the amorphous WO_3–H_xWO_3 system. The latter two devices are based on materials that have high values of both the ionic and electronic conductivities in which the diffusing cation interacts to form an intercalation compound.

While investigations of the electrochemistry of nonmetallic electrodes began relatively recently, several interesting results have evolved and the field promises to remain a fruitful area of research for many years.

Acknowledgment

The author wishes to thank Mr. A. Beyner, Technical Director of Ebauches SA, for permission to publish this review.

References

1. I. L. Spain, A. R. Ubbelohde, and D. A. Young, Electronic properties of well oriented graphite, *Philos. Trans. R. Soc. London Ser. A.* **262**, 345–386 (1967).
2. P. L. Walker, Jr, ed., *Chemistry and Physics of Carbon*, Vols. 1–7, Marcel Dekker, New York (1965–1971); P. L. Walker, Jr. and P. A. Thrower, eds., *Chemistry and Physics of Carbon*, Vols. 8–12, Marcel Dekker, New York (1973–1975).
3. A. Pacault, ed., *Les Carbones*, Vols. 1 and 2, Masson, Paris (1965).
4. L. C. F. Blackman, ed., *Modern Aspects of Graphite Technology*, Academic Press, London (1970).
5. C. L. Mantell, *Carbon and Graphite Handbook*, Wiley-Interscience, New York (1968).
6. I. L. Spain, in *Chemistry and Physics of Carbon*, Vol. 8, P. L. Walker, Jr. and P. A. Thrower, eds., Marcel Dekker, New York (1973), pp. 1–150.
7. C. A. Klein, Electrical properties of pyrolytic graphites, *Rev. Mod. Phys.* **34**, 72–79 (1962); C. A. Klein, Pyrolytic graphites: their description as semimetallic molecular solids, *J. Appl. Phys.* **33**, 3338–3357 (1962).
8. J. P. Randin, in *Encyclopedia of Electrochemistry of the Elements*, Vol. 7, A. J. Bard, ed., Marcel Dekker, New York (1976), pp. 1–291.
9. J. van Muylder and M. Pourbaix, in *Atlas d'équilibres électrochimiques*, M. Pourbaix, ed., Gauthier-Villars, Paris (1963), pp. 449–457.
10. A. W. Moore, in *Chemistry and Physics of Carbon*, Vol. 11, P. L. Walker, Jr. and P. A. Thrower, eds., Marcel Dekker, New York (1973), pp. 69–187.
11. G. R. Hennig, in *Proceedings of the 5th Conference on Carbon*, 1961, Vol. 1, Pergamon Press, Oxford (1962), pp. 143–145.
12. G. L. Montet, in *Proceedings of the 5th Conference on Carbon*, 1961, Vol. 1, Pergamon Press, Oxford (1962), pp. 116–119.
13. J. J. Lander and J. Morrison, Low-energy electron diffraction study of graphite, *J. Appl. Phys.* **35**, 3593–3598 (1964).
14. J. M. Thomas, E. L. Evans, M. Barber, and P. Swift, Determination of the occupancy of valence bands in graphite, diamond and less-ordered carbons by X-ray photo-electron spectroscopy, *Trans. Faraday Soc.* **67**, 1875–1886 (1971).
15. M. Barber, R. L. Evans, and J. M. Thomas, Oxygen chemisorption on the basal faces of graphite: an XPS study, *Chem. Phys. Lett.* **18**, 423–425 (1973).
16. H. H. Bauer, M. S. Spritzer, and P. J. Elving, Double-layer capacity at a pyrolytic graphite disk electrode, *J. Electroanal. Chem.* **17**, 299–307 (1968).
17. J. P. Randin and E. Yeager, Differential capacitance study of stress-annealed pyrolytic graphite electrode, *J. Electrochem. Soc.* **118**, 711–714 (1971).
18. J. P. Randin and E. Yeager, Differential capacitance study on the basal plane of stress-annealed pyrolytic graphite, *J. Electroanal. Chem.* **36**, 257–276 (1972).
19. I. Morcos, Electrocapillary phenomena at the stress-annealed pyrolytic graphite electrode, *J. Phys. Chem.* **76**, 2750–2753 (1972).
20. S. Ergun, J. B. Yasinsky, and J. R. Townsend, Transverse and longitudinal optical properties of graphite, *Carbon (Oxford)* **5**, 403–408 (1967).
21. J. P. Randin and E. Yeager, Effect of boron addition on the differential capacitance of stress-annealed pyrolytic graphite, *J. Electroanal. Chem.* **54**, 93–100 (1974).
22. I. Morcos, Surface tension of stress-annealed pyrolytic graphite, *J. Chem. Phys.* **57**, 1801–1802 (1972).
23. R. N. Smith, The chemistry of carbon-oxygen surface compunds, *Q. Rev. Chem. Soc.* **13**, 287–305 (1959).
24. H. P. Boehm, in *Advances in Catalysis*, Vol. 16, D. D. Eley, M. Pines, and P. B. Weisz, eds., Academic Press, New York (1966), pp. 179–274.
25. H. P. Boehm, Functional groups on the surfaces of solids, *Angew. Chem. Int. Ed.* **5**, 533–544 (1966).
26. J. B. Donnet, The chemical reactivity of carbons, *Carbon (Oxford)* **6**, 161–176 (1968).

27. J. B. Donnet, Surface chemical groups, *Bull. Soc. Chim. Fr.* **1970**, 3353–3366.
28. B. R. Puri, in *Chemistry and Physics of Carbon*, Vol. 6, P. L. Walker, Jr., ed., Marcel Dekker, New York (1970), pp. 191–282.
29. J. S. Mattson and H. B. Mark, Jr., *Activated Carbon*, Marcel Dekker, New York (1971).
30. V. L. Snoeyink and W. J. Weber, Jr., in *Progress in Surface and Membrane Science*, Vol. 5, D. F. Danielli, M. D. Rosenberg, and D. A. Cadenhead, eds., Academic Press, New York (1972), pp. 63–119.
31. R. E. Panzer and P. J. Elving, Nature of the surface compounds and reactions observed on graphite electrodes, *Electrochim. Acta* **20**, 635–647 (1975).
32. H. P. Boehm, E. Diehl, W. Heck, and R. Sappok, Surface oxides of carbon, *Angew. Chem. Int. Ed.* **3**, 669–677 (1964).
33. J. V. Hallum and H. V. Drushel, The organic nature of carbon black surfaces, *J. Phys. Chem.* **62**, 110–117 (1958).
34. K. Kinoshita and J. A. S. Bett, Potentiodynamic analysis of surface oxides on carbon blacks, *Carbon (Oxford)* **11**, 403–411 (1973).
35. H. P. Boehm, E. Diehl, and W. Heck, Oberflächenoxyde bei Russ und anderen Kohlenstoffen, *Rev. Gen. Caoutchouc* **41**, 461–466 (1964).
36. V. A. Garten, D. E. Weiss, and J. B. Willis, A new interpretation of the acidic and basic structures in carbons—I. Lactone groups of the ordinary and fluorescein types in carbons, *Aust. J. Chem.* **10**, 295–328 (1957).
37. B. Bruns and A. Frumkin, The relation between the ability of activated charcoal to adsorb electrolytes and the kind of gas with which it is charged, I, *Z. Phys. Chem.* (*Leipzig*) **A141**, 141–157 (1929); R. Burshtein and A. Frumkin, II, *Z. Phys. Chem.* (*Leipzig*) **A141**, 158–166 (1929); R. Burshtein and A. Frumkin, The behavior of outgassed activated carbon toward electrolytes, *Z. Phys. Chem.* (*Leipzig*) **A141**, 219–220 (1929); A. Frumkin, Ueber die Adsorption von Elektrolyten durch aktivierte Kohle, *Kolloid. Z.* **51**, 123–129 (1930); E. Kuchinsky, R. Burshtein, and A. Frumkin, Adsorption of electrolytes on charcoal, *Acta Phys. Chim. URSS* **12**, 795–830 (1940); R. Burshtein and A. Frumkin, Hydrogen peroxide formation in the adsorption of acids by activated charcoal, *C.R. Acad. Sci. URSS* **32**, 327–329 (1941); A. N. Frumkin, E. A. Ponomarenko, and R. Kh. Burshtein, The chemisorption of oxygen and the adsorption of electrolytes on activated carbon, *Dokl. Akad. Nauk SSSR* **149**, 1123–1126 (1963); R. Kh. Burshtein and E. A. Ponomarenko, The mechanism of the adsorption of electrolytes on charcoal, *Russ. J. Phys. Chem.* **39**, 140–142 (1965).
38. V. A. Garten and D. E. Weiss, A new interpretation of the acidic and basic structures in carbons, II. The chromene–carbonium ion couple in carbon, *Aust. J. Chem.* **10**, 309–328 (1957).
39. A. P. Brown, C. Koval, and F. C. Anson, Illustrative electrochemical behavior of reactants irreversibly adsorbed on graphite electrode surfaces, *J. Electroanal. Chem.* **72**, 379–387 (1976).
40. K. F. Blurton, An electrochemical investigation of graphite surfaces, *Electrochim. Acta* **18**, 869–875 (1973).
41. J. P. Randin and E. Yeager, Differential capacitance study on the edge orientation of pyrolytic graphite and glassy carbon electrodes, *J. Electroanal. Chem.* **58**, 313–322 (1975).
42. S. Evans, Differential capacity measurements at carbon electrodes, *J. Electrochem. Soc.* **113**, 165–168 (1966).
43. E. G. Gagnon, The triangular voltage sweep method for determining double-layer capacity of porous electrodes, IV, Porous carbon in potassium hydroxide, *J. Electrochem. Soc.* **122**, 521–525 (1975).
44. J. McHardy, J. M. Baris, and P. Stonehart, Investigations of hydrophobic porous electrodes—I. Differential capacitance by a low frequency a.c. impedance technique, *J. Appl. Electrochem.* **6**, 371–376 (1976).
45. L. N. Mokrousov, N. A. Urisson, and G. V. Shteinberg, Hydrophobic properties of carbon materials studied by the charging curve method, *Elektrokhimiya* **9**, 683–685 (1973).

46. A. Soffer and M. Folman, The electrical double layer of high surface porous carbon electrode, *J. Electroanal. Chem.* **38**, 25–43 (1972).
47. C. M. Elliott and R. W. Murray, Chemically modified carbon electrodes, *Anal. Chem.* **48**, 1247–1254 (1976); B. F. Watkins, J. R. Behling, E. Kariv, and L. L. Miller, A chiral electrode, *J. Am. Chem. Soc.* **97**, 3549–3550 (1975); B. E. Firth, L. L. Miller, M. Mitani, T. Rogers, J. Lennox, and R. W. Murray, Anodic and cathodic reactions on a chemically modified edge surface of graphite, *J. Am. Chem. Soc.* **98**, 8271–8272 (1976).
48. J. O. Besenhard and H. P. Fritz, On the reversibility of the electrochemical oxidation of graphite in acids, *Z. Anorg. Allg. Chem.* **416**, 106–116 (1975).
49. R. C. Croft, Lamellar compounds of graphite, *Q. Rev. Chem. Soc.* **14**, 1–45 (1960).
50. (a) I. Ya. Sirak, Testing graphite anodes used in alkali-chlorine cells, *Zh. Prikl. Khim.* **6**, 808–822 (1933); (b) V. Sihvonen, The primary process in the oxidation of graphite, *Z. Elektrochem.* **40**, 456–460 (1934); (c) V. Sihvonen, The mechanism of oxidation of carbon, *Ann. Acad. Sci. Fennicae* **A51**(4), 1–40 (1938); (d) H. Thiele, Ueber die Quellung von Graphit, *Z. Anorg. Allg. Chem.* **206**, 407–415 (1932); (e) H. Thiele, Die Quellung des Graphit an der Anode und die mechanische Zerstörung von Kohlenanoden, *Z. Elektrochem.* **40**, 26–33 (1934); (f) H. Thiele, The oxidation of carbon in electrolytes at normal temperature, *Trans. Faraday Soc.* **34**, 1033–1039 (1938); (g) H. Thiele and E. Weise, Graphit als Anode, *Z. Elektrochem.* **55**, 193–199 (1951).
51. G. N. Kokhanov and N. G. Milova, Influence of pH on the process of anodic oxidation of graphite, *Elektrokhimiya* **5**, 93–96 (1969).
52. G. N. Kokhanov and N. G. Milova, Effect of pH on the kinetics of oxygen evolution on a graphite anode, *Elektrokhimiya* **6**, 73–77 (1970).
53. G. N. Kokhanov, Anodic evolution of oxygen on graphite, *Elektrokhimiya* **7**, 1606–1609 (1971).
54. N. G. Bardina and L. I. Krishtalik, Kinetics of oxygen generation on graphite at low anode potentials, *Elektrokhimiya* **2**, 216–221 (1966).
55. N. G. Bardina and L. I. Krishtalik, The kinetics of the anodic evolution of oxygen on graphite, *Elektrokhimiya* **2**, 334–339 (1966).
56. Ngo Dai Viet, D. V. Kokoulina, and L. I. Krishtalik, Electrochemical oxidation of a graphite anode—I. Polarization behavior of the anode as a function of solution composition and temperature, *Elektrokhimiya* **8**, 221–224 (1972).
57. Ngo Dai Viet, D. V. Kokoulina, and L. I. Krishtalik, Electrochemical oxidation of a graphite anode—II. State of the anode surface, *Elektrokhimiya* **8**, 225–228 (1972).
58. Ngo Tai Piet, D. V. Kokoulina, and L. I. Krishtalik, Electrochemical oxidation of the graphite anode—III. Composition of the anodic products as a function of the surface state of the anode and of its polarization characteristics, *Elektrokhimiya* **8**, 384–387 (1972).
59. D. Laser and M. Ariel, The anodic behavior of glassy carbon in acid solution. A spectroelectrochemical study, *J. Electroanal. Chem.* **52**, 291–303 (1974).
60. R. G. Erenburg and L. I. Krishtalik, Investigation of the kinetics of the anodic evolution of chlorine on nonporous graphite, *Elektrokhimiya* **4**, 923–929 (1968).
61. M. Franz and A. L. Rotinyan, Overvoltage during chlorine evolution at pyrographite, *Elektrokhimiya* **5**, 925–928 (1969).
62. L. J. J. Janssen and J. G. Hoogland, The electrolysis of an acidic NaCl solution with a graphite anode. III. Mechanism of chlorine evolution, *Electrochim. Acta* **15**, 941–951 (1970).
63. F. Hine, M. Yasuda, and M. Iwata, Chlorine and oxygen electrode processes on glasslike carbon, pyrolytic graphite, and conventional graphite anodes, *J. Electrochem. Soc.* **121**, 749–756 (1974).
64. F. Hine and M. Yasuda, Studies on the mechanism of the chlorine electrode process, *J. Electrochem. Soc.* **121**, 1289–1294 (1974).
65. L. I. Krishtalik and Z. A. Rotenberg, Overpotential of the anodic evolution of chlorine on graphite. I. Influence of pH, *Zh. Fiz. Khim.* **39**, 328–334 (1965).

66. L. I. Krishtalik and Z. A. Rotenberg, Overpotential of the anodic evolution of chlorine on graphite. II. Kinetic relations in various potential ranges, *Zh. Fiz. Khim.* **39**, 907–912 (1965).
67. G. N. Kokhanov and L. A. Khanova, Influence of pH on the combustion of a graphite anode in the simultaneous discharge of chlorine and oxygen at 40°C, *Elektrokhimiya* **6**, 1492–1496 (1970).
68. G. N. Kokhanov and L. A. Khanova, Dependence of the wear of a graphite anode in a chlorine electrolysis vessel on the conditions of electrolysis, *Elektrokhimiya* **8**, 1159–1162 (1972).
69. L. J. J. Janssen and J. G. Hoogland, Electrolysis of acidic NaCl solution with a graphite anode—I. The graphite electrode, *Electrochim. Acta* **14**, 1097–1108 (1969); II. Atomic chlorine present in a graphite electrode, *Electrochim. Acta* **15**, 339–351 (1970); IV. Chlorine evolution at a graphite electrode after switching off current, *Electrochim. Acta* **15**, 1667–1676 (1970).
70. L. J. J. Janssen, The mechanism of the chlorine evolution on different types of graphite anodes during the electrolysis of an acidic NaCl solution, *Electrochim. Acta* **19**, 257–265 (1974).
71. A. T. Kuhn, in *Industrial Electrochemical Processes*, A. T. Kuhn, ed., Elsevier, Amsterdam (1971), pp. 89–126.
72. L. E. Vaaler, Graphite-electrolytic anodes, *Electrochem. Technol.* **5**, 170–174 (1967).
73. J. H. Entwisle, Consumption of graphite anodes in chlorine manufacture by brine electrolysis, *J. Appl. Electrochem.* **4**, 293–303 (1974).
74. L. I. Krishtalik, G. L. Melikova, and E. G. Kalinina, Investigation of the effect of electrolysis conditions on the stability of graphite electrodes in the chlorine cell, *Zh. Prikl. Khim.* **34**, 1543–1547 (1961).
75. M. M. Flisskii, I. E. Veselovskaya, and R. V. Dzhagatspanyan, Breakdown of graphite anodes in electrolysis of sodium chloride in presence of sulfate ions, *Zh. Prikl. Khim.* **33**, 1901–1903 (1960); M. M. Flisskii, I. E. Veselovskaya, R. V. Dzhagatspanyan, and O. V. Chernyavskaya, Investigations of the anode process on graphite in the electrolysis of sodium chloride in presence of sulfate ions, *Zh. Prikl. Khim.* **34**, 2483–2487 (1961); I. E. Veselovskaya, M. M. Flisskii, R. V. Dzhagatspanyan, and L. V. Morochko, An investigation of the adsorption of sulfate ions on a graphite anode during electrolysis involving chlorine production, *Zh. Prikl. Khim.* **36**, 2179–2183 (1963); B. Wallen and G. Wranglen, Influence of pH and sulfate content of the solution on the corrosion of graphite anodes in alkali chloride electrolysis, *Electrochim. Acta* **10**, 43–48 (1965).
76. A. L. Goldinov, M. A. Gorovits, and G. G. Smirnova, Wear of graphite anodes during electrolysis of sodium chloride solutions with the use of mercury cathodes, *Zh. Prikl. Khim.* **46**, 1249–1253 (1973).
77. F. Hine, M. Yasuda, I. Sugiura, and T. Noda, Effects of the active chlorine and the pH on consumption of graphite anode in chlor-alkali cells, *J. Electrochem. Soc.* **121**, 220–225 (1974).
78. A. Tasch, L. E. Vaaler, and J. M. Finn, Jr., A laboratory cell for testing anode materials, *J. Electrochem. Soc.* **117**, 219–222 (1970).
79. A. T. Kuhn and P. M. Wright, in *Industrial Electrochemical Processes*, A. T. Kuhn, ed., Elsevier, Amsterdam (1971), pp. 525–574.
80. Ngo Tai Piet, D. V. Kokoulina, and L. I. Krishtalik, Wear of graphite anodes in industrial electrolysis, *Elektrokhimiya* **8**, 387–390 (1972).
81. M. M. Jasic, The effect of pH on graphite wear in a chlorate cell process, *J. Appl. Electrochem.* **3**, 219–225 (1973).
82. B. M. Bulygin, Chemical and mechanical destruction of graphite anodes under various conditions of hydroxyl ion discharge, *J. Appl. Chem. USSR* **31**, 1821–1825 (1958); B. M. Bulygin, Influence of electrolyte composition on the distribution of current inside a graphite anode and on its internal wear, *J. Appl. Chem. USSR* **32**, 122–128 (1959); B. M. Bulygin, Alteration of the structure of an anode surface in the course of destruction, *J. Appl. Chem.*

USSR **32**, 521–527 (1959); E. M. Kuchinskii, N. P. Lipikhin, and M. M. Flisskii, A study of the porous structure of graphite electrodes, *J. Appl. Chem. USSR* **37**, 468–470 (1964); D. V. Kokoulina and L. I. Krishtalik, Distribution of current and composition of the electrolyte along the depth of a porous graphite electrode in reactions of anodic liberation of oxygen and chlorine, *Elektrokhimiya* **3**, 848–855 (1967).

83. M. M. Flisskii, Structure of graphite electrodes used in electrolysis of sodium chloride, *J. Appl. Chem. USSR* **38**, 2738–2740 (1965).
84. V. V. Stender and O. S. Ksenzhek, Graphitized anodes in the electrolysis of aqueous chloride solutions, *J. Appl. Chem. USSR* **32**, 111–121 (1959); W. A. Nystrom, Electrolytic degradation and electrode structure, *J. Electrochem. Soc.* **116**, 17–24 (1969).
85. W. G. Berl, A reversible oxygen electrode, *Trans. Electrochem. Soc.* **83**, 253–270 (1943).
86. E. Yeager, P. Krouse, and K. V. Rao, The kinetics of the oxygen-peroxide couple on carbon, *Electrochim. Acta* **9**, 1057–1070 (1964).
87. V. V. Sysoeva, N. N. Storchak, E. N. Smirnova, and V. I. Gants, Cathodic reduction of oxygen on carbon electrodes in KOH solution, *Zh. Prikl. Khim.* **42**, 1098–1104 (1969).
88. E. Berl, A new cathodic process for the production of H_2O_2, *Trans. Electrochem. Soc.* **76**, 359–369 (1939).
89. G. Bianchi, Contribution expérimentale à la connaissance des phénomènes de réduction cathodique de l'oxygène et de l'eau oxygénée, *Corros. Anticorros.* **5**, 146–152 (1957).
90. M. O. Davies, M. Clark, E. Yeager, and F. Hovorka, The oxygen electrode—I. Isotopic investigation of electrode mechanisms, *J. Electrochem. Soc.* **106**, 56–61 (1959).
91. M. R. Tarasevich, F. Z. Sabirov, A. P. Mertsalova, and R. Kh. Burshtein, Ionization of oxygen on pyrographite in alkaline solutions, *Elektrokhimiya* **4**, 432–437 (1968).
92. F. Z. Sabirov and M. R. Tarasevich, Kinetics of oxygen ionization on pyrographite and glassy carbon in acid and alkaline solutions, *Elektrokhimiya* **5**, 608–611 (1969).
93. M. R. Tarasevich and F. Z. Sabirov, Kinetics of ionization of oxygen on pyrographite in alkaline solutions, *Elektrokhimiya* **5**, 643–649 (1969).
94. F. Z. Sabirov, M. R. Tarasevich, and R. Kh. Burshtein, Mechanism of oxygen reduction on pyrographite in acidic solutions, *Elektrokhimiya* **6**, 1130–1133 (1970).
95. M. R. Tarasevich, F. Z. Sabirov, and R. Kh. Burshtein, Mechanism of electrochemical reduction of oxygen on pyrographite, *Elektrokhimiya* **7**, 404–407 (1971).
96. I. Morcos and E. Yeager, Kinetic study of the oxygen-peroxide couple on pyrolytic graphite, *Electrochim. Acta* **15**, 953–975 (1970).
97. M. Brezina and A. Hofmanova, Study of the electrochemical reduction of oxygen on glassy carbon in an alkaline medium, *Collect. Czech. Chem. Commun.* **38**, 985–993 (1973).
98. R. J. Taylor and A. A. Humffray, Electrochemical studies on glassy carbon electrodes. II. Oxygen reduction in solutions of high pH (pH > 10), *J. Electroanal. Chem.* **64**, 63–84 (1975); III. Oxygen reduction in solutions of low pH (pH < 10), *J. Electroanal. Chem.* **64**, 85–94 (1975); IV. Influence of solution pH and buffer capacity on reduction of oxygen, *J. Electroanal. Chem.* **64**, 95–105 (1975).
99. M. Brezina and A. Hofmanova-Matejkova, Electrochemical generation of superoxide ion on carbon paste electrodes, *J. Electroanal. Chem.* **44**, 460–462 (1973).
100. E. Yeager and A. Kozawa, in *Sixth AGARD Combustion and Propulsion Colloquium*, Cannes, March 16–20, 1964, Pergamon Press, Oxford (1965), pp. 769–793.
101. K. Kordesch, in *Fuel Cells*, W. Mitchell, ed., Academic Press, New York (1963), pp. 329–370.
102. K. Kordesch, Hydrogen-air/lead battery hybrid system for vehicle propulsion, *J. Electrochem. Soc.* **118**, 812–817 (1971); K. Kordesch, in *Modern Aspects of Electrochemistry*, J. O'M. Bockris and B. E. Conway, eds., Plenum Press, New York (1975), pp. 339–443.
103. K. V. Kordesch, in *Handbook of Fuel Cell Technology*, C. Berger, ed., Prentice-Hall, Englewood Cliffs, New Jersey (1968), pp. 359–421.
104. J. Mrha, Study of catalysts for fuel cell electrodes, IV. Active carbon electrodes for oxygen in alkaline electrolytes, *Collect. Czech. Chem. Commun.* **32**, 708–719 (1967).

105. H. Böhm, Sauerstroffelektroden für elektrochemische Zellen, *Wiss. Ber. AEG-Telefunken* **43**, 241–245 (1970).
106. A. Schmid, *Die Diffusion-Gas-Elektrode*, Enke Verlag, Stuttgart (1923); Diffusion Gas Elektrodes, *Helv. Chim. Acta* **7**, 370–373 (1924).
107. J. O'M. Bockris and S. Srinivasan, *Fuel Cells: Their Electrochemistry*, McGraw-Hill, New York (1969), Chap. 5, pp. 230–288.
108. V. Vielstich, *Fuel Cells, Modern Processes for the Electrochemical Production of Energy*, translated by D. J. G. Ives, Wiley, London (1970).
109. J. Thonstad, Double-layer capacity of graphite in cryolite-alumina melts and surface area changes by electrolyte consumption of graphite and baked carbon, *J. Appl. Electrochem.* **2**, 315–319 (1973).
110. S. I. Rempel and L. P. Khodak, The mechanism for origin of overvoltage on the carbon anode in cryolite-alumina melts, *J. Appl. Chem. USSR* **26**, 857–865 (1953).
111. J. Thonstad, The electrode reaction on the C, CO_2 electrode in cryolite-alumina melts. II. Impedance measurements, *Electrochim. Acta* **15**, 1581–1595 (1970).
112. P. Drossbach and T. Hashino, Die Anodenvorgänge bei der Elektrolyse von in Kryolith gelöster Tonerde, II, *J. Electrochem. Soc. Jpn.* **33**, 229–246 (1965).
113. M. M. Vetyukov and F. Akgva, Impedance of a carbon anode in a cryolite-alumina melt, *Elektrokhimiya* **6**, 1886–1889 (1970); Relationship of vitreous carbon electric double-layer capacitance to cryolite-alumina melt composition, *Tsvet. Metal* **43**, 27–28 (1970).
114. N. G. Bukun and N. S. Tkacheva, The double-layer capacity of a graphite electrode in molten chlorides, *Elektrokhimiya* **5**, 596–598 (1969).
115. T. Berge and R. Tunold, The chlorine/carbon electrode in a silver chloride melt in the temperature range 475–820°C. II. The double-layer capacitance of a carbon electrode in the silver chloride melt, *Electrochim. Acta* **19**, 483–484 (1974).
116. A. G. Graves and D. Inman, The electrical double layer in molten salts, Part 2. The double-layer capacitance, *J. Electroanal. Chem.* **25**, 357–372 (1970).
117. T. G. Pearson and J. Waddington, Electrode reactions in the aluminum reduction cell, *Discuss. Faraday Soc.* **1**, 307–320 (1947).
118. T. G. Pearson, *The Chemical Background of the Aluminum Industry*, The Royal Institute of Chemistry, London (1955).
119. J. Thonstad, On the anode gas reactions in aluminum electrolysis, II, *J. Electrochem. Soc.* **111**, 959–965 (1964).
120. J. Thonstad, The electrode reaction on the C, CO_2 electrode in cryolite-alumina melts. I. Steady-state measurements, *Electrochim. Acta* **15**, 1569–1580 (1970).
121. P. A. Malachesky, in *Encyclopedia of Electrochemistry of the Elements*, Vol. 6, A. J. Bard, ed., Marcel Dekker, New York (1976), pp. 63–165.
122. E. W. Dewing and E. Th. van der Kouwe, Anodic phenomena in cryolite-alumina melts. I. Overpotentials at graphite and baked carbon electrodes, *J. Electrochem. Soc.* **122**, 358–363 (1975).
123. E. W. Dewing, The chemistry of the alumina reduction cell, *Can. Metall. Q.* **13**, 607–618 (1974).
124. M. M. Vetyukov and R. G. Chuvilyaev, Anodic processes during electrolysis of cryolite-alumina melts, *Izv. Vyssh. Ucheb. Zaved. Tsvet. Met.* **8**, 65–71 (1965); P. Drossbach and T. Hashino, Die Anodenvorgänge bei der Elektrolyse von in Kryolith gelöster Tonerde. I, *J. Electrochem. Soc. Jpn.* **33**, 101–130 (1965; N. E. Richards and B. J. Welch, in *Proceedings of the First Australian Conference on Electrochemistry*, Sydney, February 13–15, 1963, Pergamon Press, Oxford (1964), pp. 901–922; R. G. Chuvilyaev, Mechanism of the anode process during the electrolysis of cryolite-aluminum oxide melts, *Tr. Leningrad Politekhn. Inst.* **272**, 79–84 (1967).
125. J. Thonstad, Critical current densities in cryolite-alumina melts, *Electrochim. Acta* **12**, 1219–1226 (1967).

126. J. Thonstad, Chronopotentiometric measurements on graphite anodes in cryolite-alumina melts, *Electrochim. Acta* **14**, 127–134 (1969); J. Thonstad, A. Solbu, and A. Larsen, The decomposition voltage of aluminum reduction cells. The influence of the alumina content in the bath, *J. Appl. Electrochem.* **1**, 261–268 (1971); J. Thonstad, F. Nordmo, and K. Vee, On the anode effect in cryolite-alumina melts. I. *Electrochim. Acta* **18**, 27–32 (1973); J. Thonstad, F. Nordmo, and J. K. Rodseth, On the anode effect in cryolite-alumina melts. II. The initiation of the anode effect, *Electrochim. Acta* **19**, 761–769 (1974).
127. M. L. Kronenberg, Gas depolarized graphite anodes for aluminum electrowinning, *J. Electrochem. Soc.* **116**, 1160–1164 (1969).
128. V. L. Bullough, L. O. Daley, and C. J. McMinn, Aluminum cell cathodes, *Electrochem. Technol.* **5**, 182–185 (1967).
129. A. J. Arvia and W. E. Triaca, Electrolysis of molten nitrates on graphite electrodes: kinetics of the anodic reaction, *Electrochim. Acta* **11**, 975–986 (1966); M. G. Sustersic, W. E. Triaca, and A. J. Arvia, Potentiodynamic behavior of graphite and platinum electrodes in molten sodium nitrate–potassium nitrate eutectic, *Electrochim. Acta* **19**, 1–17 (1974).
130. A. J. Arvia, W. E. Triaca, and H. A. Videla, Kinetics and mechanism of the electrochemical oxidation of graphite in bisulfate melts, *Electrochim. Acta* **15**, 9–24 (1970).
131. A. R. Ubbelohde and F. A. Lewis, *Graphite and Its Crystal Compounds*, Oxford University Press, London (1960), p. 163.
132. A. J. Rudge, in *Industrial Electrochemical Processes*, A. T. Kuhn, ed., Elsevier, Amsterdam (1971), pp. 1–69.
133. N. Watanabe, M. Inoue, and S. Yoshizawa, Electrode kinetics on the fluorine evolution, *J. Electrochem. Soc. Jpn.* **31**, 168–173 (1963).
134. A. J. Arvia and J. B. de Cusminsky, Kinetics of the electrochemical formation of fluorine at carbon electrodes, *Trans. Faraday Soc.* **58**, 1019–1032 (1962); Galvanostatic studies on fluorine evolution on carbon electrodes, *J. Chem. Phys.* **36**, 1089–1090 (1962).
135. N. Watanabe, M. Ishii, and S. Yoshizawa, Studies on the preparation of fluorine and its compounds. III. Relations between the wettability of anode and the anodic polarization in the electrolytic generation of fluorine, *J. Electrochem. Soc. Jpn.* **29**, E180–E186 (1961); N. Watanabe, Y. Koyama, and S. Yoshizawa, Studies on the preparation of fluorine and its compounds. VIII. The formation reaction of graphite fluoride, *J. Electrochem. Soc. Jpn.* **32**, 17–25 (1964).
136. H. Imoto, T. Nakajima, and N. Watanabe, A study of the anode effect in KF–2HF system. I. ESCA spectra of carbon and graphite anode surfaces, *Bull. Chem. Soc. Jpn.* **48**, 1633–1634 (1975).
137. H. Imoto and N. Watanabe, A study of the anode effect in KF–2HF system. II. Difference in anodic behavior between edge plane and layer plane of pyrolytic graphite, *Bull. Chem. Soc. Jpn.* **49**, 1736–1739 (1976).
138. W. Rüdorff, U. Hofmann, G. Rüdorff, J. Endell, and G. Ruess, Ueber die Störungen an Graphitanoden bei der elektrolytischen Fluordarstellung, *Z. Anorg. Allg. Chem.* **256**, 125–144 (1948).
139. N. Watanabe and Y. Kanaya, Anode effect in fused salt electrolysis, *Denki Kagaku* **39**, 139–147 (1971).
140. W. E. Triaca, C. Solomons, and J. O'M. Bockris, The mechanism of the electrolytic evolution and dissolution of chlorine on graphite, *Electrochim. Acta* **13**, 1949–1964 (1968).
141. P. Dossbach and H. Hoff, Chlorine overvoltage on graphite electrodes during electrolysis of fused chlorides, *Electrochim. Acta* **14**, 89–100 (1969).
142. R. Tunold, H. M. Boe, K. A. Paulsen, and J. O. Yttredal, Chlorine evolution on graphite anodes in a sodium chloride–silver chloride melt, *Electrochim. Acta* **16**, 2101–2120 (1971).
143. Yu. I. Aleksandrov and V. P. Mashovets, Wettability of the graphite electrode in molten chlorides, *Zh. Prikl. Khim.* **39**, 2591–2596 (1966); V. P. Mashovets and Yu. I. Aleksandrov, Influence of the nature of the gas on the anode effect in molten NaCl, *Zh. Prikl. Khim.* **43**,

811–815 (1970); Y. Kanaya and N. Watanabe, Theoretical analysis of the anode effect in chloride melts, *Denki Kagaku* **40**, 417–421 (1972); **41**, 267–271 (1973).

144. P. Drossbach and P. Krahl, Zur Kenntnis des Anodeneffekts, II, *Z. Elektrochem.* **62**, 178–180 (1958); R. Tunold and T. Berge, The anode effect in a silver chloride/sodium chloride melt, *Electrochim. Acta* **19**, 849–854 (1974).
145. G. L. Holleck, The reduction of chlorine on carbon in $AlCl_3$–KCl–NaCl melts, *J. Electrochem. Soc.* **119**, 1158–1161 (1972).
146. T. Ya. Kosolapova, *Carbides, Properties, Production and Application*, Plenum Press, New York (1971); W. S. Williams, in *Progress in Solid State Chemistry*, Vol. 6, H. Reiss and J. O. McCaldin, eds., Pergamon Press, Oxford (1971), pp. 57–118; H. H. Hausner and M. G. Bowman, eds., *Fundamentals of Refractory Compounds*, Plenum Press, New York (1968); E. K. Storms, *The Refractory Carbides*, Academic Press, New York (1967); H. J. Goldschmidt, *Interstitial Alloys*, Plenum Press, New York (1967); P. T. B. Shaffer, *High Temperature Materials*, Vol. 1, *Materials Index*, Plenum Press, New York (1964); G. V. Samsonov, *Refractory Transition Metal Compounds*, Academic Press, New York (1964); G. V. Samsonov, *Handbook of High-Temperature Materials*, Plenum Press, New York (1964); R. Kieffer and F. Benesovsky, *Hartstoffe*, Springer, Vienna (1963); P. Schwarzkopf and R. Kieffer, *Refractory Hard Metals*, Macmillan, New York (1953).
147. R. Ward, in *MTP International Review of Science, Inorganic Chemistry Series One*, Vol. 5, *Transition Metals*, Part 1, D. W. A. Sharp, ed., Butterworths, London (1972), pp. 93–174.
148. B. Aronsson, T. Lundström, and S. Rundqvist, *Borides, Silicides and Phosphides*, Methuen, London (1965).
149. F. Jellinek, in *MTP International Review of Science, Inorganic Chemistry Series One*, Vol. 5, *Transition Metals*, Part 1, D. W. A. Sharp, ed., Butterworths, London (1972), pp. 339–396.
150. A. A. Semenov-Kobzar, V. A. Obolonchik, and Z. S. Akinina, Stability of transition metal carbides under anodic polarization conditions, *Porosh. Met.* **9**, 75–78 (1969).
151. I. Paseka and J. Balej, Materials for acceleration of alkali metal amalgams. Chemical stability of TiC, VC, WC, Cr_3C_2 and TiB_2 in sodium hydroxide solutions, *Chem. Prum.* **23**, 235–238 (1973).
152. H. Yoneyama, Y. Ishikawa, and H. Tamura, Electrochemical properties of titanium carbide, *Denki Kagaku* **39**, 816–820 (1971).
153. R. D. Cowling and H. E. Hintermann, The anodic oxidation of titanium carbide, *J. Electrochem. Soc.* **118**, 1912–1916 (1971).
154. R. D. Cowling and H. E. Hintermann, The corrosion of titanium carbide, *J. Electrochem. Soc.* **117**, 1447–1449 (1970).
155. V. Cihal, A. Desestret, M. Froment, and G. H. Wagner, Anode dissolution characteristics of titanium, niobium and chromium carbides, *Collect. Czech. Chem. Commun.* **38**, 827–832 (1973).
156. H. E. Hintermann, A. C. Riddiford, R. D. Cowling, and J. Malyszko, The anodic behavior of titanium carbide in sulfuric acid solutions, *Electrodepos. Surf. Treat.* **1**, 59–69 (1972).
157. I. E. Veselovskaya, S. D. Khodkevich, L. G. Khromenkov, V. A. Sokolov, and S. G. Shagina, Anodic behavior of titanium carbide, *Elektrokhimiya* **6**, 954–960 (1970).
158. I. Paseka, Impedance of titanium carbide electrode, *Collect. Czech. Chem. Commun.* **39**, 1974–1979 (1974).
159. A. Tvarusko and H. E. Hintermann, in *Proceedings of the 9th International Congress of Chronometry*, Stuttgart, 16–20 September 1974, Deutsche Gesellschaft für Chronometrie, Stuttgart (1974), pp. 691–695.
160. V. P. Pancheshnaya, Ya. M. Kolotrykin, V. M. Knyazheva, and Ya. B. Skuratnik, Reaction of titanium carbide with hydrogen during cathodic polarization, *Elektron. Str. Fiz. Svoistva Tverd. Tela* **1972**, 98–105; I. Paseka and J. Balej, Electrochemical properties of titanium carbide, *Collect. Czech. Chem. Commun.* **38**, 3600–3609 (1973).

161. H. Yoneyama, M. Kaneda, and H. Tamura, Electrochemical properties of tungsten carbide in aqueous solutions, *Denki Kagaku* **41**, 719–723 (1973).
162. J. D. Voorhies, Electrochemical and chemical corrosion of tungsten carbide (WC), *J. Electrochem. Soc.* **119**, 219–222 (1972).
163. H. Yoneyama, S. Marakami, and H. Tamura, Corrosion of tungsten carbide in aqueous alkaline solutions containing dissolved air, *Denki Kagaku* **42**, 178–180 (1974).
164. M. Morita, C. Iwakura, H. Yoneyama, and H. Tamura, Electrode characteristics of tantalum carbide, *Denki Kagaku* **43**, 740–745 (1975).
165. L. E. Ivanovskii and A. F. Plekhanov, Behavior of niobium carbide anodes during electrolysis of chloride melts, *Electrochem. Molten Solid Electrolytes* **6** 82–86 (1968).
166. P. Brennet, S. Jafferali, J. M. Vanseveren, J. Vereecken, and R. Winand, Study of the mechanism of anodic dissolution of Cu_2S, *Met. Trans.* **5**, 127–134 (1974).
167. T. Kato and T. Oki, Anodic dissolution of metal sulfides. 5—Anodic reaction of nickel sulfide and pyrrhotite in acid solutions, *Nippon Kinzoku Gakkaishi* **38**, 663–668 (1974).
168. A. K. M. S. Huq and A. J. Rosenberg, Electrochemical behavior of nickel compounds, I. The hydrogen evolution reaction on NiSi, NiAs, NiSb, NiS, $NiTe_2$ and their constituent elements, *J. Electrochem. Soc.* **111**, 270–278 (1964); A. K. M. S. Huq, A. J. Rosenberg, and A. C. Makrides, Electrochemical behavior of nickel compounds, II. Anodic dissolution and oxygen reduction in perchlorate solutions, *J. Electrochem. Soc.* **111**, 278–286 (1964).
169. G. Bianchi, F. Mazza, and S. Trasatti, Anodic behavior and passivity of some interstitial niobium, tantalum, titanium and tungsten compounds, *Z. Phys. Chem. (Leipzig)* **226**, 40–58 (1964).
170. H. Böhm and F. A. Pohl, Wolframcarbid, ein Elektrokatalysator für saure Brennstoffzellen, *Wiss. Ber. AEG-Telefunken* **41**, 46–49 (1968).
171. F. A. Pohl and H. Böhm, in *Comptes Rendus, Troisièmes Journées Internationales d'Etude des Piles à Combustible*, 16 June 1969, Brussels, Presses Academiques Européennes, Brussels (1969), pp. 180–182.
172. H. Böhm and F. A. Pohl, in *Comptes Rendus, Troisièmes Journées Internationales d'Etude des Piles à Combustible*, 16 June 1969, Brussels, Presses Academiques Européennes, Brussels (1969), pp. 183–186.
173. H. Böhm, Adsorption und anodische Oxydation von Wasserstoff an Wolframcarbid, *Electrochim. Acta* **15**, 1273–1280 (1970).
174. H. Böhm and F. A. Pohl, Anode catalysts for acid fuel cells, *Battelle Frankfurt Inform. Bull.* **11**, 44–46 (1971).
175. H. Binder, A. Köhling, W. Kuhn, W. Linder, and G. Sandstede, Tungsten carbide electrodes for fuel cells with acid electrolyte, *Nature* **224**, 1299–1300 (1969).
176. H. Binder, A. Köhling, W. Kuhn, W. Linder, and G. Sandstede, Das Verhalten von Wolframcarbid in Elektroden für Brennstoffzellen mit sauren Elektrolyten, *Energy Convers.* **10**, 25–28 (1970); J. von Benda, H. Binder, W. Faul, and G. Sandstede, Ueber das elektrochemische Verhalten von Wolframcarbid in Kalilauge, *Chem.-Ing.-Tech.* **43**, 1223–1227 (1971).
177. J. Heidemeyer, D. Baresel, W. Gellert, and P. Scharner, Electrocatalytic oxidation and reduction of hydrogen on carbides, silicides, and nitrides of various transition metals, *Collect. Czech. Chem. Commun.* **36**, 944–947 (1971).
178. R. D. Armstrong, A. F. Douglas, and D. E. Keene, The anodic oxidation of hydrogen in aqueous acids by conducting compounds of the transition elements, *J. Electrochem. Soc.* **118**, 568–571 (1971).
179. K. von Benda, H. Binder, A. Köhling, and G. Sandstede, in *From Electrocatalysis to Fuel Cells*, G. Sandstede, ed., University of Washington Press, Seattle (1972), pp. 87–100.
180. V. Sh. Palanker, E. N. Baybatyrov, and D. V. Sokolsky, A thermodesorption method for the investigation of hydrogen adsorption on electrodes; its application to tungsten carbide, along with electrochemical methods, *Electrochim. Acta* **20**, 51–55 (1975).

181. D. V. Sokolsky, V. Sh. Palanker, and E. N. Baybatyrov, Electrochemical hydrogen reactions on tungsten carbide, *Electrochim. Acta* **20**, 71–77 (1975); V. Sh. Palanker and R. A. Gadzhiev, Mechanism of the ionization of hydrogen on tungsten carbides, *Elektrokhimiya* **11**, 503–504 (1975).
182. R. A. Radzhiev, V. Sh. Palanker, and D. V. Sokolskii, Adsorption and electrooxidation of the simplest carbon compounds on tungsten carbides, *Elektrokhimiya* **11**, 1340–1343 (1975).
183. V. Sh. Palanker and R. A. Gadzhiev, Adsorption of hydrogen sulfide on tungsten carbide and its effect on electrolytic oxidation of hydrogen, *Elektrokhimiya* **11**, 1075–1076 (1975).
184. D. Baresel, W. Gellert, W. Sarholz, and G. Schulz-Ekloff, Adsorptionsverhalten und katalytische Aktivität von Uebergangsmetallcarbiden, *Chem.-Ing-Tech.* **46**, 573 (1974).
185. R. B. Levy and M. Boudart, Platinum-like behavior of tungsten carbide in surface catalysis, *Science* **181**, 547–549 (1973).
186. R. J. Colton, J. T. J. Huang, and J. W. Rabalais, Electronic structure of tungsten carbide and its catalytic behavior, *Chem. Phys. Lett.* **34**, 337–339 (1975).
187. P. N. Ross, Jr. and P. Stonehart, Surface characterization of catalytically active tungsten carbide (WC), *J. Catal.* **39**, 298–301 (1975).
188. P. N. Ross, Jr., J. Macdonald, and P. Stonehart, Surface composition of catalytically active tungsten carbide (WC), *J. Electroanal. Chem.* **63**, 450–455 (1975).
189. G. Richter, F. von Sturm, and K. Mund, Anode catalysts, *Battelle Frankfurt Inform. Bull.* **11**, 43–44 (1971).
190. R. D. Armstrong, A. F. Douglas, and D. E. Williams, A study of the sodium tungsten bronzes for use as electrocatalysts in acid electrolyte fuel cells, *Energy Convers.* **11**, 7–10 (1971).
191. J. P. Randin and A. K. Vijh, Hydrogen evolution reaction on sodium-tungsten bronzes, *Electrochim. Acta* **20**, 37–43 (1975).
192. M. Svata and Z. Zabransky, Preparation of WC catalysts with carbon deficient crystal lattice, *Collect. Czech. Chem. Commun.* **39**, 1015–1019 (1973).
193. V. Sh. Palanker, D. V. Sokolsky, E. A. Mazulevsky, and E. N. Baybatyrov, Highly dispersed tungsten carbide for fuel cells with an acidic electrolyte, *J. Power Sources* **1**, 169–176 (1976).
194. K. Mund, G. Richter, and F. von Sturm, Aktivitätvergleich an Katalysatoren für saure Brennstoffzellen und Entwicklung einer Ag-WC-Elektrode für die H_2-Oxydation, *Collect. Czech. Chem. Commun.* **36**, 439–453 (1971).
195. H. Böhm, Fuel cell assemblies with acidic electrolytes, *J. Power Sources* **1**, 177–192 (1976).
196. H. Böhm, W. Diemer, J. Heffler, F. A. Pohl, and W. Sigmund, Molybdändisulfid und Wolframdisulfid, Katalysatoren für Brennstoffzellen, *Energy Convers.* **10**, 119–122 (1970).
197. H. Böhm, New non-noble metal anode catalysts for acid fuel cells, *Nature* **227**, 483–484 (1970).
198. W. R. Wolfe, Jr., K. B. Keating, V. Mehra, and L. H. Cutler, A new class of fuel cell anode catalysts, *8th Intersociety Energy Conversion Engineering Conference, Conference Proceedings*, American Institute of Aeronautics and Astronautics, New York, pp. 91–95 (1973).
199. W. R. Wolfe, Jr., Fuel cell electrode, U.S. Pat. 3,492,164 (1970).
200. R. J. Jasinski, A new fuel cell anode catalyst, *Adv. Chem. Ser.* **47**, 95–105 (1965).
201. K. Mund, G. Richter, R. Schulte, and F. von Sturm, Elektrokatalyse an Phosphiden der Eisengruppe und einigen ternären Verbindungen, *Ber. Bunsenges. Phys. Chem.* **77**, 839–842 (1973).
202. G. Luft, K. Mund, G. Richter, R. Schulte, and F. von Sturm, New electrocatalysts for acid fuel cells, *Siemens Forsch. Entwicklungsber.* **3**, 177–184 (1974).
203. D. T. Sawyer and E. T. Seo, Reduction of dissolved oxygen at boron carbide electrodes, *J. Electroanal. Chem.* **3**, 410–412 (1962); S. G. Meibuhr, Performance of oxygen fuel cell cathodes catalyzed with boron carbide, *Nature* **210**, 409–410 (1966).
204. F. Mazza and S. Trassatti, Tungsten, titanium and tantalum carbides and titanium nitride as electrodes in redox systems, *J. Electrochem. Soc.* **110**, 847–849 (1963).
205. M. Voïnov, D. Bühler, and H. Tannenberger, Oxygen reduction on tungsten carbide, *J. Electrochem. Soc.* **118**, 1137–1138 (1971).

T277

206. J. R. Gardner, D. A. J. Rand, and R. Woods, Electrochemistry of sulfide flotation, in *International Symposium on Characterization of Adsorbed Species in Catalytic Reactions*, Ottawa, Canada, 17-20 June 1974, Abstract No. 39.

207. T. Biegler, D. A. J. Rand, and R. Woods, Oxygen reduction on sulfide minerals, I. Kinetics and mechanism at rotated pyrite electrode, *J. Electroanal. Chem.* **60**, 151-162 (1975).

208. D. Baresel, W. Sarholz, P. Scharner, and J. Schmitz, Uebergangs-Metallchalkogenide als Sauerstoff-Katalysatoren für Brennstoffzellen, *Ber. Bunsenges. Phys. Chem.* **78**, 608-611 (1974).

209. H. Behret, H. Binder, and G. Sandstede, Electrocatalytic oxygen reduction with thiospinels and other sulfides of transition metals, *Electrochim. Acta* **20**, 111-117 (1975).

210. J. Giner and L. Swette, Oxygen reduction on titanium nitride in alkaline electrolyte, *Nature* **211**, 1291-1292 (1966).

211. H. Binder, A. Köhling, W. Kuhn, and G. Sandstede, Electrochemical oxidation of aldehydes, formic acid and carbon monoxide at tungsten carbide electrodes in 2 *N* sulfuric acid, *Angew. Chem. Int. Ed.* **8**, 757-758 (1969); J. Jindra, On the catalytic activity of tungsten carbide in anodic oxidation of CHO compounds in acid electrolyte, *Chem. Zvesti.* **27**, 766-769 (1973).

212. I. A. Kedrinskii and A. J. Avgustinik, Effect of carbon on the electrochemical reduction of nitric acid, *Zh. Prikl. Khim.* **38**, 2443-2448 (1965).

213. G. Horanyi and G. Vertes, Experimental study of the electrocatalytic behavior of tungsten carbide. Reduction of perchlorate ions, *J. Electroanal. Chem.* **63**, 359-364 (1975).

214. G. Horanyi and E. M. Rizmayer, Catalytic reduction of sulfuric acid by molecular hydrogen in the presence of tungsten carbide and platinum catalysts, *J. Electroanal. Chem.* **70**, 377-379 (1976).

215. W. Wiesener, Untersuchung zur anodischen Hydrazin-Oxidation an porösen Kohleelektroden unter Verwendung von Nickel- und Nickelboridkatalysatoren, *Electrochim. Acta* **15**, 1065-1077 (1970).

216. J. Jindra, M. Svata, and J. Mrha, in *Power Sources 2*, D. H. Collins, ed., Pergamon Press, Oxford (1970), pp. 503-509.

217. R. Jasinski, The anodic oxidation of CO on nickel sulfide in base, *J. Electrochem. Soc.* **116**, 452-453 (1969).

218. T. R. Mueller and R. N. Adams, Voltammetry at inert electrodes. I. Analytical applications of boron carbide electrodes, *Anal. Chim. Acta* **23**, 467-479 (1960); II. Correlation of experimental results with theory for voltage and controlled potential scanning, controlled potential electrolysis, and chronopotentiometric techniques. Oxidation of ferrocyanide and *o*-dianisidine at boron carbide electrode *Anal. Chim. Acta* **25**, 482-497 (1961).

219. W. R. Mountcastle, Jr., Voltammetry and controlled-potential coulometry with boron carbide electrodes, *Anal. Chim. Acta* **32**, 332-338 (1965).

220. A. M. Hartley and H. D. Axelrod, Observations of a boron carbide electrode, *J. Electroanal. Chem.* **18**, 115-121 (1968).

221. E. Jackson and D. A. Pantony, Electrochemical performance of boron carbide electrodes, *J. Appl. Electrochem.* **2**, 353-354 (1972).

222. J. F. Alder, B. Fleet, and P. O. Kane, Evaluation of a range of electrode materials for solid electrode voltammetry, *J. Electroanal. Chem.* **30**, 427-431 (1971).

223. E. Pungor and A. Weser, Suitability of borides, carbides, and nitrides as indicator electrodes for potentiometric measurements, *Acta Chim. Acad. Sci. Hung.* **61**, 241-255 (1969); Criteria for the suitability of chemical compounds as indicator electrodes for potentiometric methods based on simple redox systems, *Anal. Chim. Acta* **47**, 145-148 (1969).

224. J. W. Ross, Jr., in *Ion-Selective Electrodes*, R. A. Durst, ed., N.B.S. Special Publication 314, U.S. Government Printing Office, Washington, D.C. (1969).

225. J. Koryta, *Ion-Selective Electrodes*, Cambridge Monographs in Physical Chemistry, No. 2, Cambridge University Press, Cambridge (1975); Theory and applications of ion-selective electrodes, *Anal. Chim. Acta* **61**, 329-411 (1972).

226. R. P. Buck, Ion-selective electrodes, *Anal. Chim.* **48**, 23R-39R (1976).

227. L. Heyne, in *Fast Ion Transport in Solids*, W. van Gool, ed., North-Holland, Amsterdam (1973), pp. 123–139.

228. M. S. Whittingham, Mechanism of fast ion transport in solids, *Electrochim. Acta* **20**, 575–583 (1975).

229. R. M. Dell, in *Electrode Processes in Solid State Ionics*, M. Kleitz and J. Dupuy, eds., Reidel, Dordrecht (1976), pp. 387–410.

230. B. C. H. Steele, in *Mass Transport Phenomena in Ceramics*, A. R. Cooper and A. H. Heuer, eds., Plenum Press, New York (1975), pp. 269–283.

231. W. Tiedemann, Electrochemical behavior of the fluorographite electrode in nonaqueous media, *J. Electrochem. Soc.* **121**, 1308–1311 (1974).

232. J. Broadhead, in *Power Sources 4*, D. H. Collins, ed., Oriel Press, Newcastle-upon-Tyne, England (1973), pp. 469–482.

233. M. S. Whittingham, Electrical energy storage and intercalation chemistry, *Science* **192**, 1126–1127 (1976).

234. D. A. Winn, J. M. Shemilt, and B. C. H. Steele, Titanium disulfide: a solid solution electrode for sodium and lithium, *Mat. Res. Bull.* **11**, 559–566 (1976).

235. M. S. Whittingham, Batterie à base de chalcogénures, Belg. Pat. 819,672 (1973).

236. M. Lazzari, G. Razzini, and B. Scrosati, An investigation on various cathodic materials in copper solid-state power sources, *J. Power Sources* **1**, 57–63 (1976).

237. M. S. Whittingham, Electrointeraction in transition-metal disulfides, *J. Chem. Soc. Chem. Commun.* **1974**, 328–329.

238. M. S. Whittingham, The role of ternary phases in cathodic reactions, *J. Electrochem. Soc.* **123**, 315–320 (1976).

239. D. R. Vissers, Z. Tomczuk, and R. K. Steunenberg, A preliminary investigation of high temperature lithium/iron sulfide secondary cell, *J. Electrochem. Soc.* **121**, 665–667 (1974); L. Heredy and L. R. McCoy, Lithium-molten salt cell with transition metal chalcogenide positive electrode, U.S. Pat. 3,898,096 (August 5, 1975).

240. J. B. Goodenough, in *Progress in Solid State Chemistry*, Vol. 5, H. Reiss, ed., Pergamon Press, Oxford (1971), pp. 145–399.

241. C. N. R. Rao and G. V. Subba-Rao, Electrical conduction in metal oxides, *Phys. Stat. Sol.* **A1**, 597–652 (1970).

242. J. M. Honig, in *Fast Ion Transport in Solids*, W. van Gool, ed., North-Holland, Amsterdam (1973), pp. 311–329.

243. K. V. Kordesch, ed., *Batteries, Vol. 1: Manganese Dioxide and Vol. 2: Lead Acid Batteries and Electrical Vehicles*, Marcel Dekker, New York (1974–1977); J. P. Carr and N. A. Hampson, The lead dioxide electrode, *Chem. Rev.* **72**, 679–703 (1972); T. F. Sharpe, in *Encyclopedia of Electrochemistry of the Elements*, Vol. 1, A. J. Bard, ed., Marcel Dekker, New York (1973), pp. 235–347; C. C. Liang, in *Encyclopedia of Electrochemistry of the Elements*, Vol. 1, A. J. Bard, ed., Marcel Dekker, New York (1973), pp. 349–403.

244. W. F. Libby, Promising catalyst for auto exhaust, *Science* **171**, 499–500 (1971); L. A. Pedersen and W. F. Libby, Unseparated rare-earth cobalt oxides as auto exhaust catalysts, *Science* **176**, 1355–1356 (1972); R. J. H. Voorhoeve, J. P. Remeika, P. E. Freeland, and B. T. Matthias, Rare-earth oxides of manganese and cobalt rival platinum for the treatment of carbon monoxide in auto exhaust, *Science* **177**, 353–354 (1972); R. J. H Voorhoeve, J. P. Remeika, and D. W. Johnson, Jr., Rare-earth manganites: catalysts with low ammonia yield in the reduction of nitrogen oxides, *Science* **180**, 62–64 (1973); R. J. H. Voorhoeve, J. P. Remeika, L. E. Trimble, A. S. Cooper, F. J. Disalvo, and J. K. Gallagher, Perovskite-like $La_{1-x}K_xMnO_3$ and related compounds: solid state chemistry and the catalysis of the reduction of NO by CO and H_2, *J. Solid State Chem.* **14**, 395–406 (1975); Y. F. Yu Yao, The oxidation of hydrocarbons and CO over metal oxides, *J. Catal.* **36**, 266–275 (1975).

245. T. Wolfram and F. J. Morin, A conceptual model for surface states and catalysis on *d*-band perovskites, *Appl. Phys.* **8**, 125–141 (1975).

246. F. G. Galasso, *Structure, Properties and Preparation of Perovskite-type Compounds*, Pergamon Press, Oxford (1969).

247. P. G. Dickens and M. S. Whittingham, The tungsten bronzes and related compounds, *Q. Rev. Chem. Soc.* **22**, 30–44 (1968); P. Hagenmuller, in *Progress in Solid-State Chemistry*, Vol. 5, H. Reiss, ed., Pergamon Press, Oxford (1971), pp. 71–144.

248. E. Banks and A. Wold, in *Preparative Inorganic Reactions*, Vol. 4, W. L. Jolly, ed., Interscience, New York (1968), pp. 237–268.

249. A. Magnéli, in *The Chemistry of Extended Defects in Non-metallic Solids*, L. Eyring and M. O'Keeffe, eds., North-Holland, Amsterdam (1970), pp. 148–163; A. D. Wadsley, in *Non Stoichiometric Compounds*, L. Mandelcorn, ed., Academic Press, New York (1964), pp. 98–209.

250. M. J. Sienko, in *Nonstoichiometric Compounds*, Advances in Chemistry Series, Vol. 39, R. F. Gould, ed., American Chemical Society, Washington, D.C. (1963), pp. 224–236.

251. J. McHardy and P. Stonehart, in *MTP International Review of Science, Physical Chemistry Series Two*, Vol. 6, *Electrochemistry*, J. O'M. Bockris, ed., Butterworths, London (1976), pp. 171–229.

252. M. E. Straumanis, The sodium tungsten bronzes. I. Chemical properties and structure, *J. Am. Chem. Soc.* **71**, 679–683 (1949).

253. R. A. Fredlein and A. Damjanovic, Electrochemical deposition and dissolution of tungsten oxide bronzes, *J. Solid State Chem.* **4**, 94–102 (1972); H. R. Shanks, Growth of tungsten bronze crystals by fused salt electrolysis, *J. Crystal Growth* **13/14**, 433–437 (1972); J. P. Randin, Electrochemical deposition of sodium tungsten bronzes, *J. Electrochem. Soc.* **120**, 1325–1330 (1973); J. P. Randin, Kinetics of the electrochemical deposition and dissolution of sodium tungsten bronzes, *Electrochim. Acta* **19**, 745–751 (1974).

254. A. Damjanovic, D. Sepa, and J. O'M. Bockris, Electrocatalysis by the bronzes of the electrodic reduction of oxygen to water, *J. Res. Inst. Catalysis, Hokkaido Univ.* **16**, 1–17 (1968).

255. J. P. Randin, A. K. Vijh, and A. B. Chughtai, Electrochemical behavior of sodium tungsten bronze electrodes in acidic media, *J. Electrochem. Soc.* **120**, 1174–1184 (1973).

256. J. McHardy and J. O'M. Bockris, in *From Electrocatalysis to Fuel Cells*, G. Sandstede, ed., University of Washington Press, Seattle, Washington (1972), pp. 109–112.

257. M. V. Vojnovic, D. B. Sepa, and D. S. Ovcin, The surface of sodium tungsten bronze electrodes in acid solutions, *Croat. Chem. Acta* **44**, 89–102 (1972).

258. J. McHardy and J. O'M. Bockris, Electrocatalysis of oxygen reduction by sodium tungsten bronze. I. Surface characteristics of a bronze electrode, *J. Electrochem. Soc.* **120**, 53–60 (1973).

259. J. P. Randin, Kinetics of anodic oxide growth on sodium tungsten bronzes, *J. Electrochem. Soc.* **120**, 378–381 (1973).

260. J. P. Randin, Alternating current impedance characteristics of reduced and oxidized sodium-tungsten bronze electrodes, *Electrochim. Acta* **19**, 87–98 (1974).

261. H. Azuma, M. Saito, T. Kishi, and T. Nagai, Surface layer on sodium tungsten bronzes in acid solutions, *Denki Kagaku* **43**, 51–56 (1975).

262. A. M. Baticle, P. Lemasson, F. Perdu, P. Vannereau, and J. Vernière, Contribution à l'étude du mode de conduction dans l'oxyde de tungstène WO_3 monocristallin, *C.R. Acad. Sci. Paris* **268B**, 1203–1206 (1969).

263. J. M. Berak and M. J. Sienko, Effect of oxygen deficiency on electrical transport properties of tungsten trioxide crystals, *J. Solid State Chem.* **2**, 109–133 (1970).

264. J. Vondrak and J. Balej, Formation of peroxy compounds on anodically polarized sodium tungsten bronze electrodes, *Collect. Czech. Chem. Commun.* **39**, 3030–3035 (1975).

265. B. Broyde, Tungsten bronze fuel cell catalysts, *J. Catal.* **10**, 13–18 (1968).

266. J. H. Fishman, J. F. Henry, and S. Tessore, Activation of sodium tungsten bronzes with noble metals, *Electrochim. Acta* **14**, 1314–1317 (1969).

267. D. B. Sepa, M. V. Vojnovic, D. S. Ovcin, and N. P. Pavlovic, Behavior of sodium tungsten bronze electrode in alkaline solutions, *J. Electroanal. Chem.* **51**, 99–106 (1974); J. Vondrak and J. Balej, Electrochemical behavior of sodium tungsten bronzes in solutions of sodium hydroxide, *Collect. Czech. Chem. Commun.* **41**, 825–833 (1976).
268. E. O. Brimm, J. C. Brantley, J. H. Lorenz, and M. H. Jellinek, Sodium and potassium tungsten bronzes, *J. Am. Chem. Soc.* **73**, 5427–5432 (1951); A. A. Balandin and N. P. Sokolova, Catalytic properties of tungsten bronzes, *Bull. Acad. Sci. USSR Div. Chem. Sci.* **1959**, 198–206; S. S. Moody and D. Taylor, Catalytic decomposition of formic acid on sodium tungsten bronzes, *J. Chem. Soc. Faraday Trans. I* **69**, 289–294 (1973).
269. P. G. Dickens and M. S. Whittingham, Recombination of oxygen atoms on oxide surfaces, Part 2, Catalytic activities of the alkali metal tungsten bronzes, *Trans. Faraday Soc.* **61**, 1226–1231 (1965).
270. F. T. Jones and E. M. Loebl, The orthohydrogen–parahydrogen conversion and hydrogen–deuterium equilibration on sodium tungsten bronzes, *J. Phys. Chem.* **73**, 894–899 (1969).
271. D. B. Sepa, A. Damjanovic, and J. O'M. Bockris, Sodium tungsten bronzes as electrodes for oxygen reduction, *Electrochim. Acta* **12**, 746–747 (1967).
272. J. O'M. Bockris, A. Damjanovic, and J. McHardy, The mechanism and catalysis of the oxygen dissolution reaction, *Proceedings, Third International Symposium on Fuel Cells*, 16 June 1969, Brussels, Presses Academiques Européennes, Brussels (1969), pp. 15–28.
273. M. Voïnov and H. Tannenberger, in *From Electrocatalysis to Fuel Cells*, G. Sandstede, ed., University of Washington Press, Seattle, Washington (1972), pp. 101–108.
274. J. O'M. Bockris and J. McHardy, Electrocatalysis of oxygen reduction by sodium tungsten bronze. II. The influence of traces of platinum, *J. Electrochem. Soc.* **120**, 61–66 (1973).
275. J. Heffler and H. Böhm, Electrocatalytic properties of sodium tungsten bronzes in the reduction of oxygen in 2 *N* sulfuric acid, *Metalloberflaeche Angew. Elektrochem.* **27**, 77–79 (1973).
276. J. P. Randin, The electroreduction of oxygen and hydrogen peroxide on sodium–tungsten bronzes, *J. Electrochem. Soc.* **121**, 1029–1033 (1974); **122**, 742–743 (1975).
277. J. P. Randin, Comparison of the electrocatalytic activity of some tungsten bronzes and tungsten trioxide, *J. Electroanal. Chem.* **51**, 471–476 (1974).
278. J. Vondrak and J. Balej, Electrolytic reduction of oxygen on electrodes containing tungsten bronzes, *Collect. Czech. Chem. Commun.* **40**, 3298–3305 (1975).
279. A. J. Appleby and C. van Drunen, Behavior of pure and platinum-doped sodium tungsten bronze electrodes in oxygen-saturated phosphoric acid, *J. Electrochem. Soc.* **123**, 200–203 (1976).
280. L. W. Niedrach and H. I. Zeliger, Catalytic enhancement of carbon monoxide and reformer gas oxidation in fuel cells by sodium tungsten bronzes, *J. Electrochem. Soc.* **116**, 152–153 (1969).
281. J. P. Randin, Inhibition effects in the electrochemical reduction of hydrogen peroxide on sodium tungsten bronzes, *Can. J. Chem.* **52**, 2542–2545 (1974).
282. D. Gilroy and B. E. Conway, Kinetic theory of inhibition and passivation in electrochemical reactions, *J. Phys. Chem.* **69**, 1259–1267 (1965).
283. J. O'M. Bockris, A. Damjanovic, and R. J. Mannan, Catalysis of the electrode hydrogen evolution and dissolution on rationally chosen substrates, *J. Electroanal. Chem.* **18**, 349–361 (1968); D. B. Sepa, D. S. Ovcin, and M. V. Vojnovic, Hydrogen evolution reaction at sodium tungsten bronzes in acid solutions, *J. Electrochem. Soc.* **119**, 1285–1288 (1972); J. Vondrak and J. Balej, Electrochemical properties of tungsten bronzes. I. Hydrogen absorption in sodium tungsten bronzes, *Electrochim. Acta* **18**, 1017–1023 (1973).
284. J. Vondrak and J. Balej, Electrochemical properties of tungsten bronzes. II. Hydrogen evolution on sodium tungsten bronzes, *Electrochim. Acta* **20**, 283–287 (1975).
285. B. S. Hobbs and A. C. C. Tseung, High performance, platinum activated tungsten oxide fuel cell electrodes, *Nature* **222**, 556–558 (1969).

286. B. S. Hobbs and A. C. C. Tseung, The anodic oxidation of hydrogen on platinized tungsten oxides. II. Mechanism of H_2 oxidation on platinized WO_3 electrodes, *J. Electrochem. Soc.* **120**, 766–769 (1973).

287. W. Vogel, J. Lundquist, P. Ross, and P. Stonehart, Reaction pathways and poisons. II. The rate controlling step for electrochemical oxidation of hydrogen on Pt in acid and poisoning of the reaction by CO, *Electrochim. Acta* **20**, 79–93 (1975).

288. L. W. Niedrach and I. B. Weinstock, Performance of carbon monoxide in low-temperature fuel cells containing oxide catalysts, *Electrochem. Technol.* **3**, 270–275 (1965).

289. M. V. Vojnovic and D. B. Sepa, Effect of electrode materials on the kinetics of electron exchange reactions, *J. Chem. Phys.* **51**, 5344–5351 (1969).

290. M. Amjad and D. Pletcher, Simple redox processes at tungsten bronze electrodes, *J. Electroanal. Chem.* **59**, 61–67 (1975).

291. A. Weser and E. Pungor, Die Eignung von Perowskitphasen als Redoxindikator-elektroden, *Acta. Chim. Acad. Sci. Hung.* **59**, 319–322 (1969).

292. M. A. Wechter, H. R. Shanks, G. Carter, G. M. Ebert, R. Guglielmina, and A. F. Voigt, Use of metal tungsten bronze electrodes in chemical analysis, *Anal. Chem.* **44**, 850–853 (1972).

293. M. A. Wechter, P. B. Hahn, G. M. Ebert, P. R. Montoya, and A. F. Voigt, Chelometric titration of metal cations using the tungsten bronze electrode, *Anal. Chem.* **45**, 1267–1269 (1973).

294. P. B. Hahn. M. A. Wechter, D. C. Johnson, and A. F. Voigt, Sodium tungsten bronze as a potentiometric indicating electrode for dissolved oxygen in aqueous solutions, *Anal. Chem.* **45**, 1016–1021 (1973.

295. P. B. Hahn, D. C. Johnson, M. A. Wechter, and A. F. Voigt, Mixed-potential mechanism for the potentiometric response of the sodium tungsten bronze electrode to dissolved oxygen and in chelometric titrations, *Anal. Chem.* **46**, 553–558 (1974).

296. S. K. Deb, A novel electrophotographic system, *Appl. Opt. Suppl. Electrophotography*, No. 3, 192–195 (1969).

297. B. W. Faughnan, R. S. Crandall, and P. M. Heyman, Electrochromism in WO_3 amorphous films, *RCA Rev.* **36**, 177–197 (1975).

298. I. F. Chang, in *Nonemissive Electrooptic Displays*, A. R. Kmetz and F. K. von Willisen, eds., Plenum Press, New York (1975), pp. 155–196.

299. H. N. Hersh, W. E. Kramer, and J. H. McGee, Mechanism of electrochromism in WO_3, *Appl. Phys. Lett.* **27**, 646–648 (1975).

300. M. Green, W. C. Smith, and J. A. Weiner, A thin film electrochromic display based on the tungsten bronzes, *Thin Solid Films* **38**, 89–100 (1976).

301. R. S. Crandall and B. W. Faughnan, Dynamics of coloration of amorphous electrochromic films of WO_3 at low voltages, *Appl. Phys. Lett.* **28**, 95–97 (1976).

302. B. W. Faughnan, R. S. Crandall, and M. A. Lampert, Model for the bleaching of WO_3 electrochromic films by an electric field, *Appl. Phys. Lett.* **27**, 275–277 (1975).

303. D. B. Meadowcroft, Low-cost oxygen electrode material, *Nature* **226**, 847–848 (1970).

304. A. C. C. Tseung and H. L. Bevan, A reversible oxygen electrode, *J. Electroanal. Chem.* **45**, 429–438 (1973).

305. Y. Matumoto, H. Yoneyama, and H. Tamura, A new catalyst for cathodic reduction of oxygen: lanthanum nickel oxide, *Chem. Lett.* **1975**, 661–662.

306. C. E. Heath, H. H. Horowitz, B. L. Tarmy, C. E. Morrell, J. A. Wilson, W. J. Asher, M. Beltzer, B. Broyde, G. Ciprios, I. M. Feng, M. Lieberman, J. M. Matsen, E. H. Okrent, J. A. Shropshire, H. H. Vickers, E. A. Vogelfanger, and A. A. Zimmermann, Hydrocarbon–air fuel cell, Report No. 8, Contract No. DA 36-039 AMC-03743 (E) ARPA Order No. 247 (1965).

307. C. Pinnington, An assessment of some mixed-oxide systems as low-cost electrocatalysts for oxygen electrodes, in *Fourth International Symposium on Fuel Cells*, Antwerp, Belgium, 2–3 October 1972.

308. J. P. Randin, Unpublished results (1974).
309. T. Kudo, H. Obayashi, and M. Yoshida, Rare earth cobaltites as oxygen electrode materials for alkaline solution, *J. Electrochem. Soc.* **124**, 321–325 (1977).
310. J. M. Thomas and W. J. Thomas, *Introduction to the Principles of Heterogeneous Catalysis*, Academic Press, New York (1967), pp. 131–134; P. W. Selwood, in *Advances in Catalysis and Related Subjects*, Vol. 3, W. G. Frankenburg, V. I. Komarewsky, and E. K. Rideal, eds., Academic Press, New York (1951), pp. 27–105; E. R. S. Winter, Adsorption upon pure and lithium-doped nickel oxide, *J. Catal.* **6**, 35–49 (1966).
311. J. R. Goldenstein and A. C. C. Tseung, A joint pseudo-splitting/peroxide mechanism for oxygen reduction at fuel cell cathodes, *Nature* **222**, 869–870 (1969).
312. U. R. Evans, Cathodic reduction of oxygen in fuel cells and corrosion cells, *Nature* **218**, 602–603 (1968); U. R. Evans, Active centres in the cathodic reduction of oxygen with special reference to fuel cells, *Electrochim. Acta* **14**, 197–201 (1969).
313. J. B. Goodenough, *Magnetism and the Chemical Bond*, Interscience, New York (1963), p. 236.
314. G. H. Jonker and J. H. von Santen, Magnetic compounds with perovskite structure. III. Ferromagnetic compounds of cobalt, *Physica (Amsterdam)* **19**, 120–130 (1953).
315. K. I. Portnoi and N. I. Timofeeva, The preparation and properties of chromites of the rare earth elements, *Izv. Akad Nauk SSSR Neorg. Mat.* **1**, 1593–1597 (1965).
316. T. Kudo, H. Obayashi, and T. Gejo, Electrochemical behavior of the perovskite-type $Nd_{1-x}Sr_xCoO_3$ in an aqueous alkaline solution, *J. Electrochem. Soc.* **122**, 159–163 (1975).
317. H. Nguyen Cong, J. Brenet, and P. Chartier, Kinetics of redox couples at solid electrodes, III. Ferro-ferricyanide system in alkaline media on rotating disk electrode of polycrystalline perovskite cobaltites $La_{1-x}Sr_xCoO_3$, with $x = 0.2$ and O, *Ber. Bunsenges. Phys. Chem.* **79**, 323–326 (1975).
318. C. S. Tedmon, Jr., H. S. Spacil, and S. P. Mitoff, Cathode materials and performance in high-temperature zirconia electrolyte fuel cells, *J. Electrochem. Soc.* **116**, 1170–1175 (1969).
319. K. Kordesch and A. Marko, A new carbon oxygen electrode process, *Oesterr. Chem. Ztg.* **52**, 125–131 (1951); K. Wiesener, Oxygen electrodes made of carbon in acid electrolytes, *Abh. Saechs. Akad. Wiss. Leipzig Math. Naturwiss. Kl.* **49**, 85–95 (1968); J. E. Wynn and H. Knapp, in *Proceedings of the 24th Annual Power Sources Conference*, P. S. C. Publications Committee, Red Bank, New Jersey (1970), pp. 88–91; G. S. Zenin, N. N. Storchak and V. V. Sysoeva, Oscillographic determination of the kinetic parameters of oxygen ionization at carbon electrodes, *Zh. Prikl. Khim.* **44**, 2114–2116 (1971).
320. J. R. Goldstein and A. C. C. Tseung, Kinetics of oxygen reduction on graphite/cobalt-iron oxide electrodes with coupled heterogeneous chemical decomposition of H_2O_2, *J. Phys. Chem.* **76**, 3646–3656 (1972).
321. G. Feuillade, R. Coffre, and R. Outhier, Emploi des oxydes métalliques 3d et 4d comme catalyseurs dans les piles oxygène-hydrogène, *Ann. Radioélectr.* **21**, 105–121 (1966).
322. W. J. King and A. C. C. Tseung, The reduction of oxygen on nickel–cobalt oxides. I. The influence of composition and preparation method on the activity of nickel–cobalt oxides, *Electrochim. Acta* **19**, 485–491 (1974).
323. A. M. Trunov, V. A. Presnov, M. V. Uminskii, O. F. Rakityanskaya, T. S. Bakutina, and A. I. Kotseruba, Oxygen electroreduction at semiconductor catalysts. V. Investigation of the physical and electrochemical properties of mixed nickel–cobalt oxides, *Elektrokhimiya* **11**, 552–559 (1975).
324. V. S. Bagotzky, N. A. Shumilova, and E. I. Krushcheva, Electrochemical oxygen reduction on oxide catalysts, *Electrochim. Acta* **21**, 919–924 (1976).
325. R. Kh. Burshtein, M. R. Tarasevich, V. S. Vilinskaya, F. Z. Sabirov, and A. M. Khutornoi, Mechanism of the promoting action of oxide electrochemical catalysts, *Elektrokhimiya* **9**, 725 (1973); R. Kh. Burshtein, M. R. Tarasevich, A. M. Khutornoi, V. S. Vilinskaya, F. Z.

Sabirov, I. I. Astakhor, and G. G. Teplitskaya, Adsorption and electroreduction of molecular oxygen on oxide catalysts. I. Mechanism of the cathodic reduction of oxygen on cobalt cobaltite, *Elektrokhimiya* **11**, 1064–1068 (1975).

326. M. Savy, Oxygen reduction in alkaline solution on semiconducting cobalt oxide electrodes, *Electrochim. Acta* **13**, 1359–1376 (1968).
327. A. G. Voloshin and N. I. Kramarenko, Electrode reactions in the presence of molecular oxygen on lithium-substituted cobalt cobaltite. *Electrokhimiya* **11**, 1902–1903 (1975).
328. H. G. Oswin, A reversible medium-temperature oxygen electrode, in *Comptes Rendus 2ème Journées Internationales d'Etude des Piles à Combustible*, Société d'Etudes de Recherches et Applications pour l'Industrie, Brussels (1967), pp. 321–325.
329. W. J. King and A. C. C. Tseung, The reduction of oxygen on nickel-cobalt oxides. II. Correlation between crystal structure and activity of Co_2NiO_4 and related oxides, *Electrochim. Acta* **19**, 493–498 (1974).
330. M. R. Tarasevich, V. S. Vilinskaya, A. M. Khutornoi, R. Kh. Burshtein, F. V. Makordei, and Yu. A. Tkach, Adsorption and electrolytic reduction of molecular oxygen on oxide catalysts. II. Mechanism of the cathodic reduction of oxygen on $NiCo_2O_4$, *Elektrokhimiya* **12**, 504–507 (1976).
331. M. R. Tarasevich, A. M. Khutornoi, F. Z. Sabirov, G. I. Zakharkin, and V. N. Storozhenko, Adsorption and electroreduction of molecular oxygen on oxide catalysts. III. Chemical and electrochemical reactions of hydrogen peroxide on Co_3O_4 in alkaline solution, *Elektrokhimiya* **12**, 265–269 (1976).
332. A. M. Trunov and V. A. Presnov, Oxygen electroreduction on semiconductor catalysts, II. Processes at the oxide semiconductor/electrolyte interface, *Elektrokhimiya* **11**, 77–84 (1975).
333. G. Magner and M. Savy, Study of the oxygen reduction on cobalt oxides in alkaline media, *C.R. Acad. Sci. Paris* **267C**, 944–947, 1545–1547 (1968).
334. A. C. C. Tseung and S. Jasem, Oxygen evolution on semiconducting oxides, *Electrochim. Acta* **22**, 31–34 (1977).
335. M. Beley, J. Brenet, and P. Chartier, Kinetics of redox couples at solid electrodes: I. Ferro-ferricyanide system in nearly neutral media on polycrystalline spinel magnetites $MeMn_2O_4$ (Me = Cu, Ni and Al) thermally deposited on platinum grids, *Ber. Bunsenges. Phys. Chem.* **78**, 455–461 (1974).
336. M. Beley, J. Brenet, and P. Chartier, Kinetics of redox couples at solid electrodes: II. Ferro-ferricyanide system in nearly neutral media on rotating disk electrodes of polycrystalline spinel manganites $Cu_xMn_{3-x}O_4$, with $x = 1.2$, *Ber. Bunsenges. Phys. Chem.* **79**, 317–322 (1975).
337. J. Ruch, J. F. Konig, and J. Brenet, in *Power Sources 4*, D. H. Collins, ed., Oriel Press, Newcastle-upon-Tyne, England (1973), pp. 437–451; J. Brenet and J. F. Konig, The influence of the preparation and composition of spinel structure cobaltites (Co, Ni, Zn, Mn and Cu) on their electrochemical reduction, *Z. Phys. Chem. N.F.* **98**, 351–364 (1975); J. P. Brenet, A. K. Mehrotra, and K. Traore, Study of the physicochemical behavior and electrochemical reactivity of nickel manganese spinel oxides and their possible inter-relation, *J. Electroanal. Chem.* **65**, 245–261 (1975).
338. J. Brenet, Electrochemical reactivity of some mixed oxides of transition metals, in 27th Meeting of the International Society of Electrochemistry, Zürich, September 1976, Abstract No. 222 (1976).

Note Added in Proof. This chapter covers the literature and developments in this field up to the end of 1976.

Addendum to Chapter 1

General Bibliography for Section 4

We herewith append a general bibliography relevant to studies on electrochemical equilibrium diagrams for aqueous solutions at 25°C. This bibliography adds to those references contained in publications having the following reference numbers: 3, 8, 23, 33, 34, 57, and 58. The following reference numbers refer to those given at the end of Chapter 1.

Binary Systems at 25°C

$\mathrm{Mn{-}H_2O}$: J. P. Brenet *et al.*(59,60)
$\mathrm{Ni{-}H_2O}$: T. S. de Gromobov and L. L. Shreir(61)
$\mathrm{S{-}H_2O}$: G. Valensi(62,63); P. B. Linkson *et al.*(214)
$\mathrm{Ti{-}H_2O}$: T. R. Beck(64)
$\mathrm{U{-}H_2O}$: F. Letowski and J. Niemiec(65)
$\mathrm{Cu{-}H_2O}$: P. Duby(66); P. B. Linkson *et al.*(214)
$\mathrm{V{-}H_2O}$: J. Serkies, F. Letowski, and J. Niemiec(67);
K. Post and R. G. Robins(68)
$\mathrm{Fe{-}H_2O}$: T. Misawa(69); L. de Miranda(57—RT.221)

R. Garrels(32) has established diagrams for metals and nonmetals with a geological interest: Au, Co, Cu, Fe, Mn, Ni, Pb, S, U, V, W.

Ternary Systems at 25°C

With Cl

$\mathrm{Pb{-}Cl{-}H_2O}$: R. J. Thibeau *et al.*(216)
$\mathrm{Fe{-}Cl{-}H_2O}$: L. Sathler(70); M. H. Froning *et al.*(71);
D. D. MacDonald *et al.*(215)

$Cu{-}Cl{-}H_2O$: J. Van Muylder *et al.*(56); E. Mattsson(72); P. Duby(66); G. Bianchi and P. Longhi(73)
$Ni{-}Cl{-}H_2O$: D. D. MacDonald *et al.*(215)
$Co{-}Cl{-}H_2O$: D. D. MacDonald *et al.*(215)
$Ti{-}Cl{-}H_2O$: D. D. MacDonald *et al.*(215)

With Br

$Cu{-}Br{-}H_2O$: P. Duby(66)

With I

$Cu{-}I{-}H_2O$: P. Duby(66)

With F

$Cu{-}F{-}H_2O$: P. Duby(66)

With S

General overview: Al, Ag, Cd, Cu, Fe, Mg, Mn, Ni, Pb, Sn, $Zn{-}S{-}H_2O$: J. Horvath *et al.*(74–77)
$Cu{-}S{-}H_2O$: P. Duby(65); L. de Miranda(47;58—RT.221)
$Fe{-}S{-}H_2O$: J. Bouet and J. P. Brenet(78); L. de Miranda(47;58—RT.221)

With H_2S

$Ag{-}H_2S{-}H_2O$: F. Letowski, J. Serkies, and J. Niemiec(67)
$Mo{-}H_2S{-}H_2O$: F. Letowski, J. Serkies, and J. Niemiec(67)

With SO_3

$Fe{-}SO_3{-}H_2O$: L. de Miranda(47;58—RT.221); J. Detournay *et al.*(42;58—RT.215)
$Cu{-}SO_3{-}H_2O$: A. Bustorff and J. Van Muylder(79)
$Pb{-}SO_3{-}H_2O$: P. Delahay *et al.*(80); P. Rvetschi and R. P. Angstadt(181); A. C. Simon(217)

With CO_2

$Fe{-}CO_2{-}H_2O$: E. Deltombe and M. Pourbaix(58—RT.8)
$Pb{-}CO_2{-}H_2O$: P. Delahay *et al.*(80); J. Van Muylder *et al.*(58—RT.13)
$U{-}CO_2{-}H_2O$: F. Letowski and J. Niemiec(65)
$Zn{-}CO_2{-}H_2O$: P. Delahay *et al.*(80)
$Cu{-}CO_2{-}H_2O$: J. Van Muylder *et al.*(55;58—RT.133)

With NH_3

$Ag-NH_3-H_2O$: J. H. Sluyters *et al.*(81)
$Cu-NH_3-H_2O$: H. E. Homig and G. Glass(82)
$Zn-NH_3-H_2O$: P. B. Brouillet and F. Jolas(83)

With P_2O_5

$Mg-P_2O_5-H_2O$: J. Van Muylder *et al.*(58—RT.39)

R. M. Garrels(32) has established diagrams for ternary systems having a geological interest:

With Cl: Au
With CO_2: Co, Fe, Mn, Ni, Pb, U
With S: Au, Co, Cu, Fe, Mn, Ni, Pb, W, FeCu
With SO_3: Pb
With SiO_2: Fe

Quaternary Systems at 25°C

With NH_3 and SO_3

$Cu-NH_3-SO_3-H_2O$: F. Letowski and J. Niemiec(84,90)
$Ni-NH_3-SO_3-H_2O$: F. Letowski and J. Niemiec(85,90)
$Ag-NH_3-SO_3-H_2O$: F. Letowski and J. Niemiec(86)
$Co-NH_3-SO_3-H_2O$: F. Letowski and J. Niemiec(87)
$Zn-NH_3-SO_3-H_2O$: F. Letowski and B. Kozlowska-Kolodziej(88)
$Cd-NH_3-SO_3-H_2O$: Б. Kozlowska-Kolodziej and F. Letowski(89)

With NH_3 and Cl

$Cu-NH_3-Cl-H_2O$: R. Bartonicek and M. Lukasovska(91)

With H_2S and SO_2

$Ni-H_2S-CO_2-H_2O$: F. Letowski *et al.*(67)
$Co-H_2S-CO_2-H_2O$: F. Letowski *et al.*(67)
$Mn-H_2S-CO_2-H_2O$: F. Letowski *et al.*(67)
$Pb-H_2S-CO_2-H_2O$: F. Letowski *et al.*(67)
$Zn-H_2S-CO_2-H_2O$: F. Letowski *et al.*(67)

With Cl and S

$Fe-Cl-S-H_2O$: H. M. Froning *et al.*(71)

R. Garrels(32) has established diagrams for quaternary systems having a geological interest:

With CO_2 and S: Au, Cu, Pb, Zn
With CO_2 and SO_3: Pb

Quintuple Systems at 25°C

With Cl, CO_2, and SO_3

$Cu–Cl–CO_2–SO_3–H_2O$: J. Van Muylder *et al.*(92)

With CO_2, S, and SO_2

$Fe–CO_2–S–SO_2–H_2O$: R. M. Garrels(32)

With H_2S and CO_2

$Cu–Fe–H_2S–CO_2–H_2O$: J. Serkies *et al.*(93)

Some general descriptions of the applications of potential–pH equilibrium diagrams have been published by P. Delahay *et al.*(94) and by A. G. Guy and F. N. Rhines.(95) U. A. Campbell and R. A. Whiteker(96) have published the preparation, in the form of tables suitable for use in wall exhibits. The periodic system of the elements making up these diagrams and an analogous representation has been made by Klara Kovacs(97) and is titled, "The periodic system from the point of view of corrosion." Potential–pH equilibrium diagrams have been used by E. Mattson for the study of stress corrosion(72) and by J. Horvath for the study of bacterial corrosion under anaerobic conditions.

General Bibliography for Section 5

We give below a general bibliography of potential–pH equilibrium diagrams for aqueous solutions at higher temperatures (above 25°C and up to 300–350°C). Although we have tried to make this as complete as possible, it is certainly not exhaustive.

Simple Systems

H_2O: D. Lewis(112,113,114); R. T. Lawson(115); D. D. MacDonald, G. R. Shierman, and P. Butler(116); M. Pourbaix and Yang Xi-Zhen(218)

Binary Systems

Fe–H_2O: R. G. Robins(117); H. E. Townsend(118); V. Ashworth and P. J. Boden(119); G. D. Manning and J. Helling(100); D. Lewis(114,120,121,122); P. A. Brook(123); E. Bardal(124); R. J. Biernat and R. G. Robins(125); D. D. MacDonald, G. R. Shierman, and P. Butler(126); J. T. Harrison and C. J. Mason(127); M. Pourbaix and Yang Xi-Zhen(218)
Ni–H_2O: R. G. Robins(117); R. L. Cowan and R. W. Staehle(128); P. A. Brook(123); D. D. MacDonald(129)
Cr–H_2O: R. G. Robins(117); P. A. Brook(123)
Co–H_2O: R. G. Robins(117); D. D. MacDonald, G. R. Shierman, and P. Butler(130)
Cu–H_2O: P. A. Brook(123); P. Duby(66); D. D. MacDonald, G. R. Shierman, and P. Butler(116); P. B. Linkson *et al.*(214)
Mn–H_2O: D. D. MacDonald(131)
Ti–H_2O: P. A. Brook(123)
Al–H_2O: P. T. Lawson(132,133); D. D. MacDonald and P. Butler(134)
S–H_2O: R. J. Biernat and R. G. Robins(109); I. E. Dyatchkova and I. L. Khodakovski(135); H. Magima and E. Peters(136); R. C. H. Ferreira(137); P. B. Linkson *et al.*(214)
Se–H_2O: I. E. Dyatchkova and I. L. Khodakovski(135)
Te–H_2O: I. E. Dyatchkova and I. L. Khodakovski(135)
As–H_2O: E. F. Sergeieva and I. L. Khodakovski(138)

Ternary Systems

Fe–S–H_2O: R. J. Biernat and R. G. Robins(125); R. C. M. Ferreira(137)
Cu–S–H_2O: O. J. Kwor and R. G. Robins(139); R. C. M. Ferreira(137)
Cu–Cl–H_2O: H. Kanetani and A. Aoki(140); P. B. Linkson *et al.*(214)
Fe–Cl–H_2O: D. D. MacDonald *et al.*(215)
Ni–Cl–H_2O: D. D. MacDonald *et al.*(215)
Co–Cl–H_2O: D. D. MacDonald *et al.*(215)
Ti–Cl–H_2O: D. D. MacDonald *et al.*(215)
Fe–C–H_2O: M. Pourbaix(162); C. J. Cron *et al.*(219)
Cr–C–H_2O: C. J. Cron *et al.*(219)

Quaternary Systems

Pb–S–Cl–H_2O: F. Baratin, E. Peters, and M. Morris(141)

Electrochemical potential–pH equilibrium diagrams at high temperatures for aqueous systems given here were established on the basis of three methods of determining free energies, formation, and of reaction explained here. These methods are due to A. J. de Bethune, C. M. Criss, J. W. Cobble, and I. L. Khodakovski.

To formulate an estimate of the relative merits of each of these methods could only involve personal study of each of them and verification of results which are known from other methods. It seems better, therefore, to indicate to the reader where he can find expressed opinions and analyses by experienced investigators of the various methods: G. D. Manning and J. Helling(105); R. T. Lawson(106); H. L. Barnes and G. Kullerud(108); H. C. Heldelson(110); D. Lewis(112,143); R. G. Robins(109,117); H. E. Townsend.(142)

Index

Activation energy, and crack growth, 405
Active-passive behavior, of oxides, 255
Activity of hydrogen, as a function of pressure, 429
Additives, effect on permeation, 436
Adsorption, of O^{2-} ions, 321
Affinity, 14
Ahmed, and the oxide–electrolyte interface, 275
Alkire, and mass transfer kinetics in pits, 142
Alloys, high-strength, and cracking thereof, 405
Aluminum alloys, in fatigue cracks, 403
Aluminum reduction cell
  and anodes, 493
  and cathodes, 493
Amorphous films
  and conduction, 287
  conduction of, 268
Anderson, and corrosion of copper, 130
Anderson and Eyring, and electrode kinetics of copper dissolution, 135
Angerstein-Kozlowska, and anodic film formation, 297
Anions
  as species in corrosion, 313
  their effect on passivation, 212
Anode effect, 492
  in chloride melts, 496
Anode gas, its composition, 498
Anode oxide films, porous, 289
Anodes, and alumina reduction cell, 493
Antropov, and summary of inhibitor adsorption, 320
Armstrong and Firman, and the dissolution of titanium, 205
Armstrong and Henderson, and the dissolution of nickel, 205
Armstrong, Henderson, and Thirsk; and the dissolution of chromium, 205
Armstrong, Porter, and Thirsk; and the anodic dissolution of sulfides, 228
Arvia *et al.*, and Tafel relationships in molten salts, 495
Ashworth and Fairhurst, and three-dimensional growth of nuclei, 300
Atmospheric corrosion, 74
Autocatalysis, 179

Baccarella, and copper dissolution, 120
Baccarella and Greiss, and Tafel slopes, 125
Bakradze and Ivanov, and resistance of copper, 469
Baranowski, and hydrogen in metals, 422
Barber, Evans, and Thomas; XPS work upon graphite electrodes, 475
Barriers, of passive films, ionic current through, 226
Barsom, Imhof, and Rolfe; and environment-enhanced fatigue cracks, 401
Batteries, and intercalation compounds, 505
Battery metal, behavior of, 255
Baylis, and corrosion of copper, 56
Bean
  and mobility of defects in conduction, 263
  and the theory of conduction, 261

Beck
  and error made in calculation of numerical value for partial molar volume, 437
  and the investigation of hydrogen in dissolved iron, 437
Beck, Bockris, Nanis, and McBreen; first determination of partial molar volume of H in metals, 421
Belanger and Vijh, and anodic film formation on platinum, 297
Bell-shaped curves, 180
Benneck, and the pressure theory, 449
Bertocci
  and copper literature, 129
  and electrochemistry of copper, 115
Bianchi, Mazza, and Trasatti; their work on tungsten carbides, 500
Biegler, and anodic film formation, 297
Bilby and Hewitt
  and hydrogen embrittlement, 449
  pressure and the surface energy of metals, 452
Binary diagrams, for corrosion, 16
Binary systems, potential–pH diagrams, 36
Bockris
  analysis of compressive stress, 443
  and details of the reduction process in corrosion, 115
  and entry of hydrogen into metal lattice, 430
  and equation for effect of stress upon solubility, 437
  and first kinetic theory of corrosion, 107
  and hydrogen in α-Fe, 453
  and interaction of hydrogen with lattice and α-Fe, 449
  and investigations of poisons on hydrogen permeation, 435
  and iron dissolution kinetics, 111
  and iron nickel alloys, hydrogen content of, 449
  and mechanism of iron dissolution, 199
  and mechanisms of various metal dissolutions, 114
  and partial molar volume determination, 421
  and permeation of hydrogen into metals, 435
  and proof of diffusion of hydrogen to regions of high stress, 453
  and rate-determining step in copper reduction kinetics, 115
  and tungsten bronzes, 509
Bockris and Argade
  and the sliding friction method, 465
  and the theory of friction as a function of potential, 464
Bockris, Despic, and Drazic; their mechanism for iron dissolution, 167
Bockris, Drazic, and Despic; and the FeOH$^+$ ion intermediate, 204
Bockris, Gershaw, and Fullenwider
  and heat of activation for hydrogen and α-Fe, 449
  and permeability of hydrogen through various metals, 457
Bockris and McHardy, and rate of reduction of oxygen on tungsten bronzes as function of platinum content, 511
Bockris and Parry-Jones, their work on the Rehbinder effect, 464
Bockris and Pentland, and Tafel slopes, 125
Bockris and Reddy, and the Butler–Volmer equation, 114
Bockris and Sen, and the theory of friction; as a function of potential, 466
Bockris and Subramanyan
  and classical thermodynamics for hydrogen in metals, 437
  and hydrogen permeability transients, 449
Bockris and Thacker, and hydrogen evolution mechanism, 435
Böhm and Pohl
  their work on anodic oxidation of hydrogen, after addition of CO, 501
  their work on tungsten carbide in fuel cells, 500
Boiler technology, and corrosion, 3
Bonfiglio, and Tafel slopes, 125
Bonhoeffer, and the Flade potential, 206
Boride electrodes, 496, 502
Boron carbide, in electroanalytical applications, 504
Bowden and Young, their work on friction and potential, 464
Braun and Nobe, and copper dissolution, 120
Breakdown, chemical; of passive layers, 228
  for films, models of, 234
  of film, and pit initiation, 232
Brightening, anodic, 237
Bronoël, and hydrogen storage by electrochemical means, 455
Bronzes, in related structures, 508
Brown
  and cracking mechanisms, 61
  and his clogged corrosion pillars, 57

Brown (*cont.*)
  on the pH in cracks, 329
Brown and Nobe
  and copper dissolution, 120
  and Tafel slopes, 125
Brussels, corrosion in its water, 50
Bucci and Paris, on crack growth in a saturation regime, 378
Burshtein, and oxygen on graphite, 487
Butler–Volmer equation, 103, 104
  applied to corrosion, 114
  and corrosion expressions, 145
  linearized for kinetic studies, 143
  used in pitting theory, 341

Cailetet (1864), and permeation of steel, 411
Calcium titanate, as electrode, 507
Capacitance measurements, and tungsten bronzes, 509
Carbide electrodes, 496
Carbides, stability of, 497
Carbon
  classic behavior, thereat, 483
  in cryolite, 492
    steady-state curves, 491
  in cryolite-alumina, 490
  and functional groups attached to, 479
Carbon blacks, models for surface, 479
Carbon dioxide, its effect on potential–pH diagrams, 26
Carbon electrodes
  and graphite surfaces, 480
  and stability in cryolite, 489
Carbon fibers, and effect on crack growth, 398
Carbon monoxide
  and tungsten bronze electrodes, 511
  and tungsten bronzes, 514
Carbon surfaces, work still to be done, 519
  on crack growth rate and stress intensity, 389
  experiments on cracking, 376
Carter and tests of cracking in maraging steel, 376
Cathodes, and aluminum reduction cell, 493
Cathodic currents
  in crevices, 140
  at galvanic corrosion cells, 142
Cathodic polarization, its effect on potential–pH diagrams, 60
Cathodic protection, and theory by Newman, 141
Cavities
  and hydrogen, 426
  and kinetics of hydrogen evolution, 426
Cell, for static friction measurements, 466
Cell assembly, and stress measurements, 419
Chalcogenide electrodes, 496
Chalcogenides, and ion-selective electrodes, 505
Characteristics of oriented graphite surfaces, tabulated, 480
Chemical passivation, 193
Chemical potential
  and hydrogen evolution kinetics, 425
  of hydrogen in metals, 424
Chemical thermodynamics, basic reactions relevant to corrosion, 4
Chemisorption
  on the graphite surface, 478
  of oxygen, on oxide electrodes, 518
Cherepanov
  and the effect of passivation on crack growth, 395
  and fracture mechanics for pits, 346
  theory of elasticity, and cracking, 351
Chloride, effect on pitting, 231
Chloride melts, and Tafel slopes, 496
Chlorine
  attack on graphite, 486
  dissolution reaction, 496
Chlorine industry, and graphite electrodes, 484
Chromates
  and influence on corrosion, 48
  as inhibitors, 308
Chromium
  corrosion of, 203
  its passivation data described, 221
  and passive film therefrom, 221
Chromium-nickel, corrosion of, 73
Cobalt
  corrosion of, 203
  its passivation data obtained ellipsometrically, 220
  passivity of, 220
Cobalt phosphosulfide, as electrocatalyst, 503
Computer simulation technique, 176
Conditions for equilibrium, 13
Conduction, high-field, 248
Conduction in oxides, comparison of theories with data, 285
Conduction, of oxides; second-order effects, 266

Conductivity, electrical; mechanism of in spinels, 508
Control, for oxide growth; interfacial vs. bulk, 278
Conway
  and anodic film formation, 297
    on platinum, 297
  and the theory of adsorption on platinum, 297
Copper
  corrosion of, 26
  in presence of water, localized corrosion, 49
  its potential-pH diagram, 25
  passivation of, 26
  pitted, and the mixed potential, 55
  potential-pH diagram, 55
Copper and iron, corrosion of, 49
Copper corrosion
  in deoxygenated sulfuric acid, 121
  and oxygenated HCl, 126
Copper dissolution
  in acid chloride solutions, kinetic treatment, 118
  its mechanism, 116
  and the Tafel slope, 116
Copper manganate, and electrocatalysis, 519
Copper-water system, and potential-pH diagram, 51
Correspondence principle, 33
Corrosion, 21
  atmospheric, 74
  basic kinetic conditions, 105
  and cathodic reactions, 113
  and chemical thermodynamics, 4
  of chromium, 203
  of cobalt, 203
  of copper, 26
    as a function of oxygen concentration, 128
  of copper and iron, 49
  cracks, their propagation, 62
  differential aeration and pitting, 141
  economic importance, 2
  efficiency of inhibitors, 45
  environmental, 323
  of graphite, 486
  immunity and passivation, 72
  localized, inhibition of, 323
  of iron
    diagramed, 20
    in presence of chlorine, 56
  of metalloids, 41
Corrosion (*cont.*)
  nonuniform, in heterogeneous systems, 136
  and polarization curves, 69
  and solvent, 100
  by stress, 333
  of titanium carbide, 498
  of tungsten bronzes, 509
Corrosion domains, of metals; classified, 41
Corrosion fatigue
  catastrophic, 403
  mechanism of, 403
Corrosion inhibitors, oxidizing, 46
Corrosion kinetics
  and rotating disk studies, 123, 124
  in copper dissolution, 134
Corrosion potential
  as function of area ratio in galvanic couples, 145
  mixed potential, 143
Corrosion studies, and measurements of electrode potential, 63
Coupled-discharge recombination, and mechanism of hydrogen evolution, 431
Coupled reactions, 104
Cowling and Hintermann, on CO and CO_2 in anode gas, 498
Crack front
  its electrochemical kinetics, 361
  propagation of, 357
Crack growth
  and activation energy, 405
  caused by hydrogen embrittlement, 399
  and cycling, 398
  detection by measurement of potential, 405
  in distilled water, 389
  and humidity, 394
  and tensile stress, 396
  and theoretical considerations of hydrogen, effects on, 384
  as a function of stress, 389
  kinetic theory of, 398
  subcritical, model for, 393
  tunnel model, 368
Crack growth rate
  in saline solution, 391
  and stress intensity, 389
  theoretical dependence on stress, 387
Crack initiation, tests, 358
Crack tip
  as affected by presence of hydrogen, diagramed, 385
  portrayed, 349
Crack twinning, 354

- Cracking
  - caustic, and corrosion inhibitors, 326
  - in commercial metals, mechanism of, 370
  - corrosion crack growth rate, 363
  - data in, 375
  - diagramed, 335
  - due to stress, 371
  - electrochemical mechanism of, 364
  - experimental determination of its velocity, 355
  - flow of ions in tunnels, 369
  - and inhibition, 328
  - of metal surfaces, 371
  - in periodic jumps, 387
  - and porous structure, 382
  - specimens diagramed, 356
  - test data, 388
  - theory of
    - and assumptions, 359
    - and Laplace equation, 380
  - and Volmer–Tafel theory, 360
  - zone in which electrochemical reaction occurs, 367
- Cracking mechanisms, 51
- Cracks
  - due to fatigue, 397
  - fatigue, in titanium alloys, 377
  - and hydrogen, 426
  - and hydrogen embrittlement, 383
  - pH in, 329
- Crevice, and potential in, 140
- Crevice cells, artificial; diagramed, 62
- Crevice corrosion
  - device for studying, 57
  - kinetic treatment, 140
  - and porous electrode theory, 141
- Criss and Cobble, on the entropy of ions, 32
- Critical potentials, in corrosion, 74
- Crocker and Lange, and cracking in high-strength steels, 399
- Cryolite, and stability of carbon electrodes therein, 489
- Cryolite-alumina melts, 490
- Cupric ions, generated during dissolution of copper, 132
- Current–potential curves
  - as a function of inhibitor, 308
  - on graphite electrodes in cryolite, 492
- Current–time curves, after addition of inhibitor, 329
- Cyclic voltammogram, for oxide electrode formation; on platinum, 297
- Cycling
  - and effect on crack growth, 398, 402
  - and the spreading of cracks, 349

- Damjanovic, and tungsten bronzes, 509
- de Béthune
  - and equilibrium potentials, 27
  - and the "isothermic coefficient," 35
- Decohesion, and hydrogen embrittlement, 453
- Defect, mobile
  - effect on conduction, 263
  - and the theory of conduction, 261
- Deformation, and fresh surface at crack tip, 386
- de Kazinczy, and stress of hydrogen in metals, 437
- Dekker and Middelhoek, and transport numbers in films, 290
- Dell, and intercalation compounds, 506
- Deluccia
  - and double potentiostatic circuit for hydrogen in β-titanium, 418
  - and effects of hydrostatic pressure, 437
- de Miranda
  - and the influence of isolation periods, 79
  - and a layer of goethite, 21
  - and polarized light studies of corrosion, 85
- Despic, and iron dissolution kinetics, 111
- Devanathan, and diffusion equation for hydrogen, 415
- Devanathan and Bockris, method for examining hydrogen permeation, 411
- Devanathan and Stachurski, and hydrogen evolution mechanism, 435
- Devanathan, Stachurski, and Beck; and hydrogen evolution on cadmium, 457
- Device
  - rotating, for studying atmospheric corrosion of alloys, 76
  - for studying crevice corrosion, 57
- Dewald
  - and transients in oxide film growth, 280
  - and transport through solids, 259
- Dewing
  - and gas bubbles, 491
  - and steady-state curves on carbon in cryolite, 491
- De Wit, and structure model, 287
- De Wit, Wijenberg, and Crevecoeur; and conduction in oxides, 284
- Dielectric relaxation, model for conduction in oxides, 284

Differential capacitance, for highly oriented graphite surfaces, 480
Diffuse double layer theory, and pitting, 338
Diffusion
  and growth of cracks, 382
  of oxygen into pits, 344
Diffusion equation
  after shutting off current, 417
  for hydrogen, 414
Dignam
  and migration of defect through vitreous layers, 269
  and point defects, 268
Dignam, Barrett, and Nagy; and electropolishing of silver, 256
Dignam and Gibbs, effect of distortion on potential energy barrier, 267
Dignam and Goad, aluminum in glycol buffer under oxidizing conditions, 251
Dignam and Ryan
  on anodic oxidation of aluminum, 249
  and growth of aluminum films in borate, 278
Dimensionally stable anodes, 520
Dislocations
  and effect on hydrogen, 448
  and stress field, 445
Dissolution
  of copper, and corrosion studies, 131
  of nickel, and Vetter's work, 224
  and non-steady-state, 224
  of oxide, 253
  of passive metals, 222
  precipitation mechanism, for silver oxide growth, 291
  of thin rods, perpendicular to body surface, 381
  of zinc-plate inclusions on copper-based metal, 362
Distribution of charge, 276
Dodero, and demonstrations of corrosion, 3
Doig and Flewitt
  and corrosion of coplanar electrodes, 145
  and radially symmetric galvanic couples, 146
Double layer, thickness of, and model for pitting, 338
Double-layer capacity, of carbon electrodes, 490
Drazic, and iron dissolution kinetics, 111
Dubois and Lacaze, and polaromicrotribometry, 469
Duby, a simplifying hypothesis in integration of the van't Hoff equation, 31
Ebersbach, Schwabe, and Ritter; and kinetics of potentiostatic passivation, 209
Edeleaunu and Evans, and corrosion of copper, 56
Edison, and variation of friction with potential (1877), 463
Elastic bodies, and tunnels, 352
Electroanalysis, and tungsten bronzes, 514
Electrocatalysis
  on lanthanum chromite, 517
  mixed, containing molybdic oxide, 502
  and nickel cobaltites, 519
  and paramagnetism, 516
  and spinel structure, 517
  by traces of platinum, 511
  of tungsten bronzes, 511
Electrocatalytic activity, 511
  of nonmetallic electrode materials, 500
  of thiospinels, 503
Electrochemical impedance, 155
Electrochemical interface, stability, 161
Electrochemical method, for hydrogen; principles of, 413
Electrochemistry, and mechanism of cracking, 358
Electrochromism, and tungsten bronzes, 515
Electrode kinetic equations, basic, stated, 102
Electrode kinetics, applied to corrosion, described, 101
Electrode materials, nonmetallic, 473
  and electrocatalytic activity, 500
Electrode potential
  definitions, 10
  during wetting and drying, 74
  and electrochemical reactions, involving iron, 66
  measurements of, in corrosion studies, 63
Electrode reactions, temperature coefficient of, 35
Electron transfer, at passive metals, 238
Electroneutrality, and corrosion systems, 138
Electrons in metals, and the chemical potential, 440
Electro-optical applications of tungsten bronzes, 514
Electropolishing, of titanium carbide, 498
Ellipsometry
  and determination of oxide thickness on films, 295
  in examination of passive layers, 219
  work of McBee and Kruger, 233
Ellison, and nonuniform corrosion, 140

Elovich equation
  applied to oxide film formation, 272
  for solids, 272
Embrittlement, 411
  of metals, by hydrogen, 449
Energy, and the hydrogen–metal system, 411
Energy method, for consideration of crack spreading, 350
Environment, effect on crack growth, 395
Environmental effects, on crack growth, 397
Epelboin, Gabrielli, Keddam, and Takenouchi; reaction scheme for passivation of iron, 205
Epelboin and Keddam
  and capacitative impedance, 204
  and consecutive mechanism for iron dissolution, 153
Equilibrium
  formulated, 9
  general formula for, 8
Equivalent circuits, for electrode reactions, 157
Eshelby, and theory of elasticity applied to cracking, 351
ESCA; use of, in molten salts, 495
Evans
  and the alleged strangeness of corrosion reactions, 3
  and basic demonstration of corrosion, 2
  classical experiments in corrosion, 8
  and corrosion of copper, 56
  and poisons, in permeation, 435
  and "pseudo-splitting," 516

Faita, dissolution of copper and sodium chloride, 129
Faraday, and passivation, 193
Fast-charge–slow-recombination mechanism, for hydrogen, 427
Fast-discharge–slow-combination mechanism, and hydrogen evolution, 432
Fatigue, corrosion, 324
Fatigue crack growth, theory of, 400
Fatigue cracks, 397
  in aluminum alloys, 403
Feeney and Blackburn, their tests on titanium alloys, 377
Feller, Kesten, and Krupki; and effective anions on passivation, 212
Fermi level, and tungsten bronzes, 514
Ferrous titanate, as electrode, 507
Field, in oxides; decay of, with time, 280
Film, limitingly thin; and space charge, 265
Film, thin; and negligible space charge, 264
Film growth
  galvanostatic, 249
  measured by ellipsometry, 219
  potentiodynamic, 249
  potentiostatic, 251
Finkelstein, and pioneering work on passive electrodes, 153
Fisher, and theory of conduction through films, 265
Fishman, evidence that oxygen reduction on tungsten bronzes is due to platinum traces, 511
Fissures, micro; and effect upon potential, 464
Flade potential, 206
  in passivity of iron, 173
Flatband potential, and Mott–Schottky plot, 510
Fleischmann and Thirsk, and nucleation of oxides, 299
Fletcher, and three-dimensional film growth, 301
Fluctuations, of field for conduction in oxides, 271
Fluoride melts, electrochemical studies, 494
Fluorine on carbon, and ESCA studies, 495
Fontana and Staehle, on hydrogen permeation and promoters, 435
Formaldehyde, oxidized at tungsten carbide, 504
Fourier transfrom, 415
Fracture mechanics
  for pits, 346
  and the theory of spreading of pits, 345
Fracture stress, in titanium alloys, 395
Franck
  on active and passive states, 235
  and the Flade potential, 207
Franck and Weil, and passive layers, 240
Franke, Forker, and Schultheiss
  and anodic dissolution of iron, 199
  and transpassive dissolution, 201
Frenkel, contribution to ionic conduction theory, 261
Frenkel defects, effect on conduction, 263
Free energy relationships, and corrosion, 98
Freier, and operation of boiler without corrosion, 3
Friction
  as a function of potential
    its uses, 470

Friction (*cont.*)
  as a function of potential (*cont.*)
    measured, 469
  its dependence on potential, experimental, 468
  its relation to potential, 464
  its variation with interfacial potential, 466
Frumkin, and adsorption on carbon surfaces, 479
Frumkin and Bagotskaya, and entry of hydrogen into metal lattice, 430
Fuel cells, and electrocatalysis, 512
Fujii, and ion corrosion, 58
Fusion, and difficulties with hydrogen damage, 456
Fusion reactor, and storage of hydrogen, 456

Galvele
  and the mathematical theory of pit formation, 344
  and the mathematical theory of pits, 343
  and pitting, 336
  and transport equations in passive layers, 236
Garafalo, and hydrogen embrittlement, 450
Garten and Weiss, and adsorption on carbon surfaces, 479
Gas phase charging, and hydrogen, 412
Gerberich and Hartbower, and low-alloy steel, 391
Gerischer and Mehl
  and Faradaic impedance, 156
  and a non-steady-state technique for hydrogen, 153
Gibbs, work on nucleation step sites for deposition of oxide on film, 295
Gibbs *et al.*, and formation of silver oxide film, 292
Gibbs–Helmholtz equation, integration of, 29
Gileadi, Bockris, and Fullenwider; hydrogen diffusion in platinum, 449
Gilroy and Conway, anodic oxidation with oxide formation, 513
Glassy carbon, reactions on, 486
Gobrecht, Paatsch, and Thull
  and modulation spectroscopy, 218
  and modulation spectroscopy on nickel, 218
Gohr and Lange, and the Flade potential, 207
Goldstein, and peaks for oxide formation on platinum, 297
Goldstein and Tseung, and paramagnetism, 515
Goodenough, and electrochemical features of spinels, 507
Gould and Evans, and corrosion fatigue, 324
Gouy–Chapman equation, used in considerations of pitting, 337
Grahame, and the situation in 1950, 153
Graphite
  and chlorine evolution, 485
  and double layer at special types of surfaces, 478
  and electrochemical loss in acidic solutions, 486
  electrochemical oxidation, chemical reactions occurring at edge atoms, 481
  as electrode, 473
  of use in chlorine industry, 484
Green's formula, used in theory of cracking, 380
Griffith theory, and cracking, 371
Growth, or cracks; tunnel theory, 379
Growth kinetics
  for copper oxide, 299
  for oxides, 277
Growth of films, on valve metal oxides, 278
Gutmann, and negative resistance, 172

Haber, and early work on electrode potentials in corrosion, 63
Halide melts, electrochemical studies, 494
Hancock and Johnson
  activity of oxygen in crack growth, 397
  hydrogen embrittlement, 452
Hardness, its relation to potential, 464
Hartman, and tunneling through passive layers, 238
Heat treatment, and hydrogen embrittlement, 391
Hennig, and his work upon graphite, 475
Heterogeneous systems, and corrosion, 136
Heusler, mechanism of dissolution of iron, 199
Heusler and Schoner, transformation of nickel hydroxide, 218
Heyn
  and discovery of hydrogen embrittlement, 449
  and intercalation compounds, 506
Hirth, and extra terms in stress analysis, 446
Histogram, frequency of pit generation in stainless steel, 235
Hoar
  and active dissolution in passive layers, 237
  and corrosion of copper, 56

Hoar (*cont.*)
  and economics of corrosion, 2
  and kinetic reduction of oxygen, 115
  and metal anode behavior, 237
  and premature passivation, 45
  and stress corrosion cracking, 333
Hoar and Evans, and incorporation of chromate into iron oxide, 48
Hoar and Holiday, and corrosion of mild steel, 313
Hoar and Khera, and lateral interaction between adsorbed species, 317
Holleck, and chlorine dissolution in aluminum chloride melts, 496
Humidity, and crack growth, 394
Hurlen, and copper dissolution, 120
Hydrides, 454
  and hydrogen storage, 455
Hydrochloric acid, and dissolution of copper, 124
Hydrogen
  and chemisorption in hydrogen embrittlement, 383
  and the diffusion equation, 414
  diffusion of, into metals; effect on cracking, 404
  effect upon cracking, 387
  entry into lattice, and hydrogen evolution, 430
  and fusion reactor, 456
  and internal combustion engine, 458
  metallurgical effects, 388
  most difficult materials problem for fusion, 456
  and reactions in tungsten bronzes, 511
  storage of, 454
  and the University of Pennsylvania, 412
  and vacuum extraction, 412
Hydrogen bonds, action as electrode, 511
Hydrogen dissolution reaction, on carbides, 500
Hydrogen effects, on subcritical crack growth, 393
Hydrogen embrittlement
  among the various metals, 453
  and crack growth, 399
  and decohesion, 453
  and growth of cracks, 382
  and heat treatment, 391
  and Petch's theory, 452
Hydrogen evolution, on various metals, mechanism of, 434
Hydrogen evolution kinetics
  and chemical potential, 425
Hydrogen evolution kinetics (*cont.*)
  mechanisms of, 429
Hydrogen evolution reaction
  on sodium tungsten bronze, 513
  and Tafel lines, 110
Hydrogen in metals, 411
  its chemical potential, 424
  schematic for the dissolution of hydrogen, 422
  solubility, 421
  study of, 412
  theoretical considerations, 384
  thermodynamic analysis, 440
  usefulness of the study, 453
Hydrogen in steels, stress analysis, 447
Hydrogen in stress fields, 445
  near edge dislocations, 448
Hydrogen ingress, and crystal structure, 458
Hydrogen–metal system, and energy, 411
Hydrogen–oxygen fuel cells, in graphite electrodes, 487
Hydrogen permeability, as function of charge in current density, 431
Hydrogen permeability–stress relationship, for Armco iron, 444
Hydrogen permeation
  and background currents, 420
  experimental method for, 419
  in iron, and hydrostatic pressure, 436
Hydrogen permeation apparatus, and palladium deposition, 420
Hydrogen permeation method, 413
Hydrogen peroxide
  formation from oxygen, 503
  formation at spinels, 517
Hydrogen pump, and tensile stress, 440
Hydrostatic pressure, and the kinetics of hydrogen evolution reaction, 436

Ilmenite, as electrode, 507
Immersion time, and effect on corrosion, 50
Immunity, 21, 41
Immunity domains, of metals; tabulated, 41
Impedance
  electrochemical, 155
  electrode, at electrodes, 204
  of electrodes, at high frequencies, 183
  and passivation, 155
Impedance diagrams
  on carbon electrodes, 491
  for iron, 178
  during iron passivation, 185
Impedance measurements, 163

Impedance measurements (*cont.*)
  and transfer function generator, 165
Impurities, and effect on graphite surfaces, 477
Incubation, of crack growth, 395
Induction, for pit initiation, 232
Inhibition
  of corrosion, 307
  of localized corrosion, 323
  mechanism of, 322
  and polarization curves, 308
  of stress corrosion cracking, 326
Inhibitors
  and adsorption isotherms, 320
  anodic, 312
  and attachment to electrode surface, 317
  cathodic, 312
  and concentration, 311
  and coverage of anodes and cathodes, 316
  and coverage of electrode surface, 313
  and current–potential curves, 308
  effect of concentration on, performance of, 310
  and effect upon oxygen reduction, 321
  and Frumkin's isotherm, 313
  and hydrogen adsorption, 312
  mechanism of their effect, 317
  and stress corrosion cracking, 323
  and Tafel slopes, 320
  theory of their behavior, 311
Integration, of Gibbs–Helmholtz equation, 29
Intercalation compounds, and reversible batteries, 505
Interface
  metal–oxide, 272
  oxide–electrolyte, 275
Internal combustion engine, and materials for use with hydrogen, 458
Internal field, for conduction in oxides, 270
Internal high-field equations, 272
Internal pressure calculations of hydrogen, as a function of mechanism, 427
International Union of Pure and Applied Chemistry, their convention, 12
Iron
  corrosion of, 3
  and electrochemical reactions, 66
  experimental circumstances of its immunity, 70
  and passive films, 213
Iron column, in Delhi, India, 1
Iron crevices, corrosion in, 58
Iron passivation, details, 185
Iron surface, seen in the microscope, 200
Ion conduction, field-assisted, 226
Ion probe, examination of tungsten bronzes, 509
Ionic conduction, intrinsic, 261
Irwin, and fracture mechanics for pits, 347

JANAF Thermodynamic Tables, 99
Janssen and Hoogland, and the graphite electrode, 484
Johnson (1871), and permeation of steel, 411
Johnson and Willner, and subcritical crack growth, 388

Kaesche, and aggressive ions present in solution, 324
Kelly
  and the dissolution of titanium, 111
  and iron dissolution kinetics, 111
Khodakovski, his correspondence principle, 33
Kim and Wild, experimental determination of hydrogen in metals, 421
Kinetic model, for the steady state, 181
Kinetics
  of copper dissolution
    detailed, 133
    under diffusion control, 119
    and resulting corrosion, 134
  of corrosion reactions, 100
  at electrodes, and dissolution of copper, 131
  of formation of copper oxide films, 299
  of hydrogen evolution, and cavities, 426
  for oxide film growth and aqueous species, 300
  transient, isothermal for oxide film growths, 280
Kirchhoff's equation, applications in electrochemical thermodynamics, 28
Koch (1879), and variation of friction with potential, 463
Kodama and Ambrose, their work on molybdates, 48
Kokhanov
  and kinetics of reactions at graphite, 481
  and mechanism of anodic oxygen evolution at graphite, 484
Kokoulina, and reactions at graphite interfaces, 482
Kolotyrkin, and zirconium dissolution, 230
Kordesch
  and longevity of hydrogen–air fuel cells, 489
  and review of porous electrodes, 489

Krishtalik, and kinetics of reactions at graphite, 481
Krouchkoll (1889), and sliding friction measurements as function of potential, 464
Kruger, and film breakdown models, 234
Kruger and Colbert, and growth of passive layers, 211
Kuznetsov and Dogonazade, impedance across Helmholtz and passive layers, 228

Lander and Morrison, their work upon graphite, 475
Landsberg and Hollnagel, and mechanisms of passivation, 209
Lanthanum chromite, and stability in acid and alkaline solutions, 517
Lanthanum cobaltite, as an electrode, 517
Laplace equation, used in theory of cracking 379
Laplace transform, 415
Latimer
  and entropies of ions, 33
  his valuable book, 99
Law and Newman, Ohmic drops, 180
Leckie and Uhlig, and anodic polarization curves for austenitic stainless steel, 230
Levy and Boudart, and the platinumlike behavior for the chemisorption of hydrogen, 500
Levich and Frumkin, and theory of distribution of current at electrodes, 144
Levine and Smith, and the oxide–electrolyte interface, 275 and the oxide–solution interface, 275
Lewis, Randall, Pitzer, and Brewer; tabulation of thermodynamic data, 99
Li, and effect of stress upon solubility, 437
Linder, his thesis on threshold stress intensity, 348
Linear polarization, and the technique of Stern and Geary, 111
Lissajous figures, use in ac impedance methods, 153
Lithium nitrate, and electrocatalysis, 515
Loadings, cyclic; and effect on pit propagation, 348
Local field
  for conduction in oxides, 270
  model for conduction in oxides, 270
Logan, his book on corrosion, 368
Lowsan, and dissolved species, effect on corrosion, 27
Luggin's capillary, 11

Magnesium aluminate, as electrode, 507
Makrides, and passive layers, 240
Manning and Helling, specific heats in solution, 31
Mansfeld and the Stern–Geary method, 112
Mass spectroscopic method, and hydrogen, 412
Mass transport kinetics, in copper dissolution, 120
Materials, impermeable to hydrogen, 457
Matumoto, Yoneyama, and Tamura; and strontium-doped lanthanum cobaltate, 515
Maurer, and growth of oxide films, 279
May, and interpretation of effects of flow on corrosion, 56
Mayne and Pryor, and iron corrosion, 18
McBee and Kruger, and passive layers for iron, 232
McBreen
  and potentiostatic control of hydrogen, 418
  and solution of diffusion equation for hydrogen, 415
McEvily, Clark, and Bond; and subcritical crack growth, 392
McHardy and Bockris, on tungsten bronzes, 510
McHardy and Stonehart, and bronzes, 509
Meadowcraft, and perovskite structures, 515
Mechanism
  of catastrophic corrosion fatigue, 403
  electrochemical, of spreading of cracks, 365
  of hydrogen evolution, and permeation of hydrogen, 429
  of hydrogen evolution, diagnostic parameters, 433
  and internal pressure calculations, 427
  of production in oxides, conclusion, 289
Melts
  and electrochemical oxidation, 490
  and use of carbon electrodes, 494
Metalloid electrodes, 496
Metal–oxide interface, 272
Metal–oxide systems, 289
Metals, active and passive, 44
Miller, and copper dissolution, 120
Miller and Bellavance
  rotating disk studies involving copper, 129
  and Tafel slopes, 125

Mixed potential, 143
  for copper dissolution, 123
  and copper pits, 55
Model, local field, for growth in oxide films, 279
Modeling
  of corrosion systems, 137
  of galvanic corrosion cells, 142
  of nonuniform corrosion, 139
Models, for impedance curves, 179
Molten salts, and use of ESCA for evolution of fluorine on carbon, 495
Molybdates, and influence on corrosion, 48
Molybdenum, its dissolution, 205
Montet, his work on graphite, 475
Morcos and Yeager, and electrocatalytic activity on graphite, 487
Morphology
  of copper, and its interaction with sulfur, 81
  of copper–sulfur interaction, 80
    and rust, 79
  of corrosion cracks, 374
Moshtev
  and function of electric field on passivity, 226
  and passive layers, 240
  his work on passive films, 226
Mössbauer spectroscopy, of anodic film, 221
Mostovoy, Smith, Lingwall, and Rippling; and their tests on maraging steel, 376
Mott and Cabrera
  and high field conduction, through solids, 258
  mechanism for oxide film growth, 277
  model for oxide growth, 277
Mott–Schottky plot, and measurements on tungsten bronzes, 509

Nagayama and Cohen, and the dependence of the Flade potential upon pH, 208
Namboodhiri and Nanis, hydrogen in Armco iron, 421
Nanis and Deluccia, and hydrostatic pressure effect for hydrogen permeation, 437
Nanis and Kesselman, and corrosion near a disk, 144
Nanis and Namboodhiri, and hydrogen diffusion from the interface, 418
National Bureau of Standards, Technical Series on Corrosion, 98
Nernst, and the dissolution potential, 8
Nernst equation
  applied to the oxide–solution interface, 275
Nernst equation (*cont.*)
  and hydrogen, 424
Network defects, and conduction in solids, 268
Neutron scattering, and hydrogen, 412
Newman
  and basic step in copper reduction, 115
  and copper electrode kinetics, 115
  and corrosion near a disk, 144
  and current distribution during corrosion, 142
  and flow-related corrosion, 140
  and penetration of corrosion into a pipe, 141
Ngo Dai Viet, and reactions at graphite interfaces, 481
Nickel
  its corrosion, 201
  and modulation spectroscopy thereof, 218
  its passivation, 213
    data, 217
  passive films compared with iron, 216
  passivity thereof, 217
  polarization, in boric solution, 202
  transpassivity, 171
Nickel anode, ellipsometry thereon, 219
Nickel boride, and oxidation of hydrazine, 504
Nickel cobaltates
  and electrocatalysis, 519
  their preparation as electrocatalysts, table, 518
Nickel sulfide, and oxidation of carbon monoxide, 504
Nikiforchin, and adsorption effects in high-strength steels, 372
Niobium carbide, and anodic dissolution, 499
Nitrates, as inhibitors, 309
Nitride electrodes, 496
Nityanandan, and hydrogen ingress into metals, 458
Nobe, and dissolution of iron in chloride solutions, 111
Nobility, practical, 40
Noise spectrum, for passive layers, 233
Non-steady-state techniques, in passivation, 152
Novakovski and Likkackev, and dissolution of passive layers, 224, 225

O'Grady and Bockris
  and first Mössbauer measurements in electrochemistry, 215

O'Grady and Bockris (*cont.*)
  first suggestion of water in passive films, 215
Ohmic drop, 180
Ohmic effects, in corrosion, 111
Ohtsuka
  and bilayered film, 221
  and passivity of chromium, 221
  and passivity of cobalt, 220
Okamoto and Sato, polarization curve for nickel, 197
Oldham and Mansfeld, and galvanic corrosion, 144
Ord
  and quadratic term, in conduction of solids, 267
  and theory of oxide growth, 285
Ord, DeSmet, and co-workers; and open-circuit transients in oxide growth, 282
Oriani, and thermodynamic analysis of hydrogen in metals, 439
Orowan, and gases on internal surfaces of metals, 452
Oshe, Rosenfeld, and Doroskenko; and photoelectric polarization of iron anodes, 215
Osterwald, and negative resistance, 171
Outside nuclei, growth of, 296
Overpotential, 14
  as function of current density, in film growth, 294
Oxidation, in oxygen containing melts, 490
Oxide–electrolyte interface, 275
Oxide films; vitreous, anodic, and conduction, 268
Oxide growth kinetics, 277
Oxides, growth of, 247
Oxygen
  discharged from water molecules, on graphite, 484
  influence of, on corrosion, 47
  reduction of, and inhibitors, 321
  and reduction to hydrogen peroxide, 503
Oxygen deposition, on platinum, electrode, 297
Oxygen electrode, as a gas diffusion electrode, 489
Oxygen electrode reaction at passive metals, 238
Oxygen evolution, on valve metal, 253
Oxygen evolution reaction, on nickel cobaltates, 519
Oxygen reduction, and electrocatalytic activity, 486
Oxygen reduction reaction, on graphite, 486

Palanker, and poisoning by CO in fuel cells, 501
Palmer, on mixtures of inhibitors, 316
Paramagnetism
  and electrocatalysis, 516
  and the work of Tseung, 515
Parrish, and the potential-pH diagram for iron, 62
Parthasaradhy, and hydrogen evolution during copper deposition, 458
Partial molar volume, of hydrogen at different temperatures, 444
Passivation, 21, 151
  affected by anions, 212
  of copper, 26
  galvanostatic, 208
  and impedance, 155, 156
  of iron
    mechanism, 205
    in passivation studies, 173
    in weakly acid medium, 166
  of metals, 43
  models, 193
  under potentiostatic conditions, 211
  of titanium, 168
Passivation domains, of metals, tabulated, 41
Passive films
  on chromium, 221
  and dissolution rate, 223
  formed on iron, their composition, 215
  as a function of thickness, 218
  growth of, 210
  on iron, 213
    description of, 215
  their thickness, as a function of current density, 216
  on zirconium, 239, 240
Passive layers, and redox reactions, 240
Passive metals, in oxygen electrode reactions, 238
Passivity
  of cobalt, 220
  on nickel, 217
  of nickel anodes, 219
  theory of, 226
Permanganate, influence on corrosion, 47
Permeation current, and mechanism of hydrogen evolution reaction, 431

Permeation method, electrochemical; and hydrogen solubility, 423
Permeation of hydrogen
  and mechanism for hydrogen evolution, 429
  in metals, and ambient solution, 434
Permeation transient, for hydrogen, and build-up, 420
Perovskite structures, 508
  and electrodes, 507
  and high-temperature zirconia fuel cells, 517
  and mixed transition metal oxides, 515
Perovskites, as electrodes, 507
Peroxide, effect in copper dissolution; found by Anderson and Eyring, 136
Petch, his theory of hydrogen embrittlement, 452
pH changes, in cracks, 329
pH in pits, 343
Phosphide electrodes, 496, 502
Phosphides of iron group, and electrocatalysis, 502
Photoelectric response, of nickel anodes, 220
Pickering and Frankenthal, and pitting, 336
Pit
  corrosion in, on copper, 49
  its initiation, 54
Pits
  cylindrical, 352
  diagramed, 344
  formation of, 141
  and fracture mechanics, 345
  pH in, 343
Pitting, 336
  basic mechanism, 342
  determination of parameters and the theory of, 343
  and differential aeration corrosion, 141
  and diffuse double-layer theory, 338
  stability of, 235
Pitting potential, 343
Pitting processes, one-dimensional, 340
Pitting theory, and Butler–Volmer equation, 341
Platinum, its effect on tungsten bronzes, 511
Platinum electrode, oxygen deposition of, 297
Podgurski
  and activity of hydrogen, 429
  and fugacity of hydrogen, 428
Point defect theory of ionic conduction in vitreous anodic oxide films, 268
Poisons, and inhibition of corrosion, 329
Poisson's ratio and cracking, 352
Polarization, of iron, 177
Polarization curves
  for corrosion of iron, 196
  inhibition, 308
  involving corrosion, 69
  for iron, 183, 198
Polarization parameters, and corrosion systems, 138
Polaromicrotribometer, 468
Pores, used in cracking theory, 382
Porous electrode theory, and crevice corrosion, 141
Porous film, idealized model, 290
Pourbaix
  and the activation of metals, 43
  and basic demonstration of corrosion, 2
  and the classification of metal nobility, 43
  and corrosion equations, 6
  and inhibitors, 46
  and kinetic studies, 61
  and localized corrosion, 58
  and thermodynamics of corrosion, 1
Pourbaix diagrams, 17
Potential
  across thin semiconductors, 228
  breakthrough, of aluminum in presence of chromate, 324
  in crevice, 140
  and detection of crack growth, 405
  during corrosion, and inhibitors, 315
Potential–current relationship, in presence of inhibitors, 311
Potential–pH dependence at polyethylene-impregnated graphite, 483
Potential–pH diagram, 15
  for binary systems, 36
  for copper, 55
  for copper–water system, 51
  and the effects of stirred solutions, 59
  of a general kind, passivation, corrosion, and immunity, 65
  involving copper, with influences from Cl, CO_2, and SO_3, 53
  involving copper and chloride, 52
  for iron, 72
  and passivation of iron, 38
  of systems involving copper, 25
  taking into account films of iron oxide, 39
  and the three-component system, 52
Potential regions, in iron corrosion, 56

Potential–time curves
  during stressing, 325
  influence of temperature, 78
Pressure, developed during electrolysis, 429
Pressure theory, of hydrogen embrittlement, 449
Pringle, and conduction in tantalum oxide, 270
Promoters, of cracking, 327
Propagation, brittle, 374
Protons, diffusing out of crack tips, 387
Pryor, and the Flade potential, 208
"Pseudo-splitting," and Evans, 516
Pungor and Weser, and borides, 505
Pyrolytic graphite, reactions on, 486

Radhakrishin and Shreir, and permeation of hydrogen, 434
Randall, Bernard, and Wilkinson; and oxide film growth, 280
Randin
  and inhibition effects on tungsten bronzes, 512
  and Mott–Schottky plot for tungsten bronzes, 509
Randin and Yeager, and the capacity-potential curve for pyrolytic graphite, 476
Reaction model
  for iron passivation, 166, 186
  in passivation studies, 173
  for passivity of iron, 174
  for titanium passivation, 169
Reactions
  coupled, 104
  parallel or simultaneous, 104
Redox reactions, and passive layers, 240
Reduction, on various manganites, 519
Reflection spectroscopy, 511
Rehbinder, his effect, 464
Reiss, and the analysis of stress and strain, 351
Revie, Baker, and Bockris
  Auger verification of water in passive layers, 215
  and first Auger measurements in electrochemistry, 215
Richards, and steady-state curves on carbon in cryolite, 491
Richter, von Sturm, and Mund; their work on transition metal elements and atomic hydrogen adsorption, 501
Ring disk studies, on passivation, 178
Ritchie, and chemisorption on oxide films, 272
Rosenfeld and Marchakov, corrosion of copper, 56
Ross and Stonehart, the platinumlike catalytic properties of WC, 501
Rotating disk studies
  for copper dissolution, 120
  of pyrolytic graphite, 486
Rudge, and fluoride melts, 495
Rust
  and copper, 79
  and morphology, 82
  under polarized light, 84
Ruthenium oxide, 520
Ryder and Gallagher
  and fatigue crack growth, 399
  and subcritical crack growth, 388

Sato and Kudo
  secondary passivation, 218
    of nickel, 218
  theory of passivity, 228
  work on time interval, 235
Sato, Kudo, and Nishimura; and passive films of iron, 213
Sato, Kudo, and Noda; verification of water in passive films, 215
Schenk, and pit density in stainless steel, 231
Schultze, and potential ranges in passivation, 154
Schultze and Stimming, and passive layers, 240
  on titanium, 241
Selenates, and influence on corrosion, 48
Sen, theory of friction as a function of potential, 464
Sepa, and tungsten bronzes, 509
Sepa, Damjanovic, and Bockris; first examination of sodium tungsten bronzes, 511
Shank, and water intensity, 348
Shuler and Laidler, and effective inhibitors on permeation, 435
Siejka, Nadai, ~~and~~ Amsel; and control of growth in oxide films, 278
Sievert's law, and hydrogen in metals, 422
Silicon carbide, and voltammetry, 505
Silver oxide
  film formation as a function of current density, diagram, 293
  formed under galvanostatic conditions, 296
Simmons, and numerical techniques, 145

Simons, Kellerman, and Leidheiser; Mössbauer spectroscopy of anodic film, 221
Simulation curves, for passivity, 176
Slow-discharge–fast-recombination mechanism, for hydrogen, 427
Smialowski
  and hydrogen under high pressures, 429
  and mechanism of effective inhibitors on hydrogen permeation, 435
Smith, Peterson, and Brown; and propagation of corrosion cracks, 62
Smith, Piper, and Downey; and catastrophic sensitivity to water, 348
Smyrl, and corrosion of copper, 115
Smyrl and Newman
  and the Butler–Volmer equation, 146
  and potential distribution in corrosion reactions, 139
  and treatment of disks in a plane, 145
Sneddon, and fracture mechanics for pits, 346
Soderberg anodes, 493
Sodium, permeation into carbon, 491
Sodium tungsten bronze
  and activity in hydrogen evolution, 513
  its use in electrochemistry, 508
Solids, and network defect; conduction consequences, 268
Solubility, and stress, 443
Solubility of hydrogen
  as a function of overpotential, 423
  and measurement by means of electrochemical permeation method, 423
  in metals, 421
    determination of, 421
  in stress fields, 449
Solubility of tenorite, as a funtion of pH, 23
Space charge
  and conduction of solids, 260
  and film conduction, 265
  in graphite electrodes, 477
Specific heats, of dissolved substances, 30
Specific molar heat
  and constancy of variation, 31
  and temperature, 34
  variation of, 32
Spectroscopy, modulation; of film on nickel, 218
Speidel, and energy assumptions made in cracking theory, 373
Sphere, hollow; and Nernst equation for hydrogen pressure in, 425
Spillover, and model of tungsten bronzes, 511
Spinels, as electrodes, 507
Stability
  and the electrochemical interface, 161
  and fused salts, 489
  of nonmetallic electrodes in aqueous solution, 474
Staehle, and inhibitors for hydrogen permeation, 435
Staicopolus
  his apparatus for friction measurements in solution, 465
  and the variation of friction with potential, 465
Stainless steel
  its passivation described, 222
  passivity thereon, 222
Standard equilibrium potentials
  and corrosion, 6
  and temperature, 34
Standard free energies of formation, 29
Steady state, accessibility, 160
Steady-state curves, on carbon in cryolite, 491
Steels, and cracking, 402
Steiggerwald, and catastrophic sensitivity to water, 348
Stern
  corrosion potential and logarithmic dependence upon current density, 145
  and galvanic corrosion potential, 144
  his application of the Butler–Volmer equation to practical determinations of corrosion, 108
  and the linear polarization method, 111
Stern and Geary
  and linear polarization, 111
  their method for corrosion determination, 68
  their method for practical determination of corrosion, 108
Stirring, and growth of pits, 142
Storage of hydrogen
  by an electrochemical method, 455
  in metals, 454
Stress
  and chemical potential of hydrogen and metals, 437
  in cracking, 371
  critical, and hydrogen embrittlement, 449
  and solubility, 443
Stress analysis, for hydrogen in steels, 447
Stress corrosion, and hydrogen embrittlement, 453

Stress corrosion cracking, 333
  general considerations, 333
  and inhibitors, 323
  intergranular, and inhibition, 326
  velocities, 326
Stress field, near dislocation, 445
Stress-induced potential, for hydrogen in metals, 443
Stress intensity, and crack growth rate, 389
Stress measurements, of metals; and hydrogen permeation, 419
Stress-velocity relationship in cracking, 377
Subramanyan
  and the hydrogen method, schematic presentation, 416
  and stress-induced potential, 443
Sugimoto, Kishi, Ikeda, and Sawada; and high passivation potentials, 222
Sulfide electrodes, 496, 502
Sulfides, 499
  electrochemical behavior in perchlorate solution, 499
  and high-temperature electrolytes, 507
Surface films, and electrocatalysis, 512
Surfaces, fresh
  after cracking, 406
  and high rate of reaction thereon, 406
Surface species
  mobile, at metal–electrolyte interface, 300
  and oxide films, 299
Synergism
  between platinum and bronze, 511
  and reactions of hydrogen with tungsten bronze, 513
System stability, plotted, 164
Szklarska-Smialowska and Kaminiski, their work upon the electronic structure of inhibitors, 318
Szklarska-Smialowska and Wieczorek, and application of the Frumkin isotherm to adsorption, 319

Tafel behavior, of chlorine reaction; in alkali halide melts, 496
Tafel equation, and corrosion studies, 143
Tafel extrapolation, and the technique of Stern and Geary, 111
Tafel extrapolation technique, 124
Tafel format, and corrosion control, 108
Tafel kinetics
  and dangers of overlinearization, 146
  and nonuniform current densities, 145
Tafel line
  and corrosion, 68
  and corrosion control, 108
  for oxygen reduction reaction, 503
  and tungsten bronzes, 512
Tafel polarization
  and corrosion, 110, 144
  and corrosion studies, 143
Tafel relationships
  in fluoride melts, 495
  and hydrogen evolution reaction, 513
  involving the dissolution of titanium carbide, 498
  and use of tungsten bronzes, 512
Tafel slope
  and copper dissolution, 117
  in corrosion kinetics with copper, 123
  and mechanisms determining corrosion, 117
  observed in copper dissolution, 120
  for oxygen on graphite, 487
Tarasevich, and work concerning oxygen and graphite, 487
Teflon bonding, of nickel cobaltate electrodes, 519
Temperature, elevated; and electrochemical equilibrium, 27
Temperature coefficient, of electrode reactions, 35
Tensile stress
  and a crack growth, 396
  and a hydrogen pump, 440
Ternary diagrams, 21
Thermodynamic analysis, of hydrogen in metals, 440
Thermodynamics
  basic equations, corrosion, 5
  of corrosion, 1, 97
Thickness
  of double layer, and model for pitting, 338
  of films, for passive films of iron, 214
Thiospinels, 519
  and their electrocatalytic activity, 503
Thomas, and his work on graphite, 475
Thomas and Nurse, on the critical potential for passivation, 322
Thonstad
  graphite in carbon electrodes, 491
  and steady-state curves on carbon in cryolite, 491
Threshold stress intensity factor, 394
Tip
  of crack
    portrayed, 349

Tip (*cont.*)
  of crack (*cont.*)
    and tension, 440
  during cracking, and components, 373
Titanium alloys, in cracking, 395
Titanium carbide, 498
  and electric polishing, 498
  reduction of, during cathodic polarization, 498
Titanium dissolution, and Kelley, 111
Titanium disulfide, and intercalation compounds, 506
Titanium passivation, 168, 171
  reaction model, 169
Tilak and Conway, theoretical analysis of overpotential-decay behavior for hydrogen evolution, 434
Tiller and Schrieffer; and chemical potential, of electrons in metal, 440
Tomashov, and corrosion rate of iron, 195
Tonstadt, and the theory of the anode effect, 492
Townsend, his potential-pH diagram for iron, 38
Tracey, and copper corrosion, 129
Transients
  and hydrogen permeation method, 417
  isothermal, and oxides film growth, 283
  nature of, in oxide film growth, 280
  thermally induced, 288
Transition metal oxide electrodes, and metallic conductivity, 507
Transition metal oxides
  and fuel cells, 517
  perovskite structures, 508
Transpassivity, 236
  of nickel, 171
Transport
  controlled by injection processes, 259
  in first few layers, 272
  ionic
    equations for, 272
    through solids, 256
Transport numbers, in oxide film growths, 280
Transport processes, in pits, 336
Transport through solids, theory of, 257
Triboelectrochemistry, 463
Troiano, and the decohesion theory, 453
Trunov and Presnov, and mechanism of oxygen reduction, 518
Tseung and Bevan, their work on perovskite structures, 515
Tungstates, and influence on corrosion, 48
Tungsten bronzes, 509
  and activity in fuel cells, 512
  and capacitance measurements, 509
  and electrochromism, 515
  and hydrogen peroxide reduction, 512
  and Mott-Schottky plots, 510
  nature of surface, 510
  and polarization by light, 510
Tungsten carbide, as electrocatalyst for oxidation of formaldehyde, 504
Tunnel growth, theory of, 378
Tunnels, in elastic bodies, 352
Turner and Brook, and Tafel slopes, 125
Twinning, in cracking, 354

Uhlig
  and chemisorbed atoms, affecting the Flade potential, 208
  and economics of corrosion, 2
  and stress corrosion cracking, 333
  and Tafel slopes, 114
University of Ferrara, and quinquennial conferences on inhibitors, 308
University of Pennsylvania, and foundation of electrochemical techniques for hydrogen, 412

Vacuum extraction, and hydrogen, 412
Valve metal behavior of, 249
  limited, 252
Valve metal oxides, growth of films on, 278
Van Rysselberghe, and the reduction potential, 46
Vanadates, and influence on corrosion, 48
Vegger
  and dissolution of passive films, equation for, 223
  and potential dependence of transpassive dissolution, 224
Velocity, of crack spreading, electrochemical theory, 366
Vermilyea
  and control of growth in oxide films, 279
  and first explanation of transients in film growth, 283
  and theory of conduction through films, 265
  and transport numbers in oxide film growth, 280
Verwey, and treatment of transport through solids, 259
Veselovskaya, and the composition of anode gas, 498

Vetter
  and dissolution rate, of passive films, 223
  and kinetic information on metals, 114
  and Tafel polarization data, 114
  and transpassivity, 224
Vetter and Gorn
  and dissolution current densities in the passive state, 225
  ellipsometric measurements of passive films, 215
  their work on dissolution of passive ions, 225
Vetter and Schultze, and formation of oxides on platinum, 297
Vetter and Strehblow, and pitting, 336
Visscher and Damjanovic, 219
Voids, and hydrogen, 426
Volmer–Tafel theory, and cracking, 360

Wagner
  and corrosion, 18
  and current distribution in cathodic protection, 139
  and definition of passivation, 194
  and the Flade potential of iron, 208
Wagner and Traud
  and discussion of the corrosion reaction for zinc, 107
  and first discussion of reaction kinetics in corrosion, 106
  and original current–voltage curves, 64
Waitz, and variation of friction with potential (1882), 464
Water
  its effect on anodic polarization curves in acetic acid solution, 197
  oxygenated, influence on corrosion, 47
Water sensitivity, catastrophic; for high-strength steels, 348
Watanabe and Kanaya, and fluoride melts, 495
Watanabe, Inoue, and Yoshizawa; their work on the evolution of fluorine on carbon, 494
Weathering, of steels, 77
Weathering steel, under atmospheric corrosion in Brussels, 83
Weil
  and function of electric field on passivity, 226
  his work on passive films, 226
Welch, steady-state curves on carbon in cryolite, 49
West, and adsorption of quinoline, 314
Wettability, and crack growth, 394
Williams, and fracture mechanics, 346
Wittingham, and intercalation compounds, 506

XPS technique, necessary, 520

Yeager and Randin, and the capacity-potential curve base for graphite, 476
Yolken, Kruger, and Calvert
  and iron corrosion, 18
  and water in passive films, 215
Yoneyama *et al.*, and CO in anode gas, 498
Yoneyama, Ishikawa, and Tamura; their work on steady-state current–potential curves, using titanium carbide, 497
Young
  and autocatalytic effects in film growth, 283
  contribution to ionic conduction theory, 261
  and form of potential difference in films, 279
  and generalization of Dewald's treatment, 259
  growth of tantalum oxide films, 278
  and model film growth according to Adams, Van Rysselberghe, and Willis, 283
  and second-order effects in conduction of oxides, 266
Young and Smith, and the tantalum oxide system, 286
Young's modulus, and cracking, 352

Zone, embrittled, 385